P

Vol

THE PHYSICAL REVIEW

A journal of experimental and theoretical physics established by E. L. Nichols in 1893

Published by the American Physical Society
at
AMERICAN PHYSICAL SOCIETY

Officers

President

C. C. LAURITSEN
California Institute of Technology
Pasadena, California

Vice-President

J. H. VAN VLECK
Harvard University
Cambridge, Massachusetts

Secretary

K. K. DARROW
Bell Telephone Laboratories
Office:
Columbia University
New York 27, New York

Treasurer

G. B. PEGRAM
Columbia University
New York 27, New York

Local Secretary
for the Pacific Coast

J. KAPLAN
University of California at Los Angeles
Los Angeles, California

Manager of Publications

S. A. GOUDSMIT
Brookhaven National Laboratory
Upton, Long Island
New York

Entered as second-class matter at Office and Lemon Streets, Lancaster, Pennsylvania
Acceptance for mailing at special rate of postage provided for in Section 1103, Act of October 3, 1917, authorized on July 31, 1918

BOARD OF EDITORS

Editor

S. A. Goudsmit

Associate Editors

J. Bardeen — Harvey Brooks
T. Bonner — R. F. Christy
R. G. Fowler — C. L. Critchfield
W. E. Lamb, Jr. — M. Deutsch
A. J. P. Meyer — T. H. Johnson
W. E. Shoupp — Bruno Rossi

Manuscripts for publication should be submitted to S. A. Goudsmit, Brookhaven National Laboratory, Upton, Long Island, New York. Authors' institutions are requested to pay a publication charge of $10 per page which, if received, entitles them to 100 free reprints. Additional reprints may be sent with galley proofs.

Send all correspondence concerning papers in the process of publication should be addressed to the Publication Manager, American Institute of Physics, 57 East 55 Street, New York 22, New York.

Subscription Price

United States and Canada $15.00
Elsewhere $16.00

Back Numbers[1]

Yearly back number rate when complete year is available:
Prior to 1949: $20.00
Thereafter: $27.00

Single issues: $2.00 each, prior to July, 1939;
$1.00 each, July, 1939–December, 1941;
$3.00 each, January, 1942–December, 1946;
$1.00 each, January, 1947–December, 1948;
$1.25 each, thereafter.

Volumes I–XXX, 1893–1930: $6.00.

Subscriptions, renewals, and orders for back numbers should be addressed to the American Institute of Physics, 57 East 55 Street, New York 22, New York.

Changes of address in the case of members of the American Physical Society should be addressed to the Treasurer; in the case of other subscribers, to the American Institute of Physics.

[1] Prepared by Issues of Physics Department, Cornell University, Ithaca, New York.

THE
PHYSICAL REVIEW

A journal of experimental and theoretical physics established by E. L. Nichols in 1893

SECOND SERIES, VOL. 83, NO. 6 SEPTEMBER 15, 1951

A Proton–Gamma-Ray Coincidence Study of Si^{30} and B^{11}

H. H. LANDON*†
Sloane Physics Laboratory, Yale University, New Haven, Connecticut‡
(Received June 11, 1951)

The excited states of the Si^{30} and B^{11} nuclei were studied by means of a proton–gamma-ray coincidence technique for the purpose of determining the nature of the gamma-ray decay scheme. The nuclei were formed under cyclotron bombardment using the $Al^{27}(\alpha,p)Si^{30}$ and $B^{10}(d,p)B^{11}$ reactions. The transitions from the first two excited states of Si^{30} are directly to the ground state, while the transition from the third excited state takes place by means of a cascade to the second state and then to the ground state. The decay scheme in the B^{11} nucleus is most likely the same as for the Si^{30} nucleus for the first two excited states, while the third and the prolific fifth and sixth states show cascade transitions as most probable.

INTRODUCTION

IN the study of nuclear energy levels, knowledge of the scheme of de-excitation by gamma-radiation is becoming increasingly important as the level properties other than energy are accumulated. In general, two approaches to the problem of ascertaining decay schemes are possible. Transitions can be deduced by careful separate measurements of both level positions and gamma-ray energies. The assignments are then made on the basis of corresponding energy differences. Gamma-ray energy measurements are difficult to make to a high degree of accuracy, however, particularly when the experiment is to be performed under cyclotron bombardment, since a number of competing processes are possible, in general, under charged particle bombardment.

A second approach has advantages under these conditions. It is possible to use an energy measurement on a charged particle reaction product to determine a level position and at the same time obtain an approximate energy measurement of any gamma-rays which occur in time coincidence with the reaction product. The obvious advantage is that the gamma-ray is indisputably associated with the level being studied. The coincidence event is rare, however, because of the low detection efficiencies obtainable for gamma-rays. The method has its limitations when the number of states is large and the spacing between states small, because of the many transitions possible if the gamma-rays should cascade.

The familiar $Al^{27}(\alpha,p)Si^{30}$ reaction was chosen as a suitable one with which to test the possibilities of the method. This reaction has been thoroughly studied and proton–gamma-ray coincidences have already been observed[1] for the three excited states which can be excited by the 7.5-Mev alpha-particles available from the Yale cyclotron.

The reaction $B^{10}(d,p)B^{11}$ was also chosen to permit a test under the more exacting requirements of deuteron bombardment.

APPARATUS AND TECHNIQUE

In order to study the decay scheme of Si^{30} it was first necessary to perform the familiar proton group structure experiment to determine the relative ranges in aluminum and air of the four different proton groups associated with the ground state and three excited states. The technique used was the so-called peaked proportional counter method. The protons were observed at an angle of 90° with respect to the incident beam by means of a proportional counter filled with 20 cm pure argon. The pulses were amplified and then put through a biased diode discriminator and into a blocking oscillator for shaping before recording. The discriminator could then be adjusted so that only those protons

*Part of a dissertation presented to the faculty of the Graduate School of Yale University in partial fulfillment of the requirements for the degree of Doctor of Philosophy.

† Now at Rensselaer Polytechnic Institute, Troy, New York.

‡ Assisted by the joint program of the AEC and ONR.

[1] B. B. Benson, Phys. Rev. 73, 7 (1948).

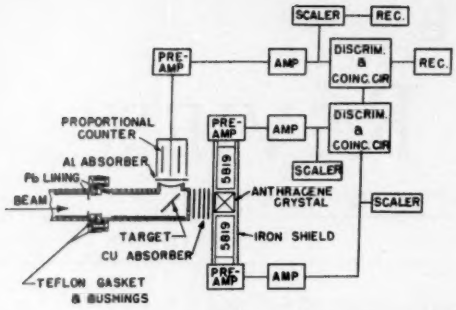

FIG. 1. Schematic diagram of apparatus for proton–gamma-ray coincidence experiment.

which ended their range in the counter volume would produce sufficient ionization to be counted.

By varying the amount of aluminum absorber in the path of the protons it was then possible to count preferentially only those protons from any of the four groups.

The detection of the gamma-rays was achieved by the use of scintillation counters. Two 5819 photomultipliers viewed a large anthracene crystal as shown in Fig. 1. The output pulses from these were amplified and shaped in the same manner as the proportional counter pulses. The shaped phototube pulses were then applied to a coincidence circuit,[2] the output of which was fed into a similar coincidence circuit along with the proton pulses. This arrangement was used to reduce the number of random thermal noise pulses counted by the system. The resolving time of each coincidence circuit was approximately 0.2 microsecond with a coincidence efficiency very nearly 100 percent. The output of the second coincidence tube was fed into a multivibrator pulse lengthener and into a driving stage for a mechanical recorder. Provision was made in both coincidence circuits for monitoring of single pulses generated at the blocking oscillators. It was therefore possible to record the number of coincidences per proton stopping in the proportional counter, and also to calculate the number of accidental coincidences to be expected from each circuit.

The gamma-ray detector was placed as near as possible to the target, leaving space only for sufficient absorption path for the gamma-rays to allow good energy measurements on the basis of measured absorption coefficient.

Since the gamma-rays to be expected are all above 1.5 Mev, the absorber chosen was copper, which is dense but for which absorption by pair production is relatively small up to almost 5 Mev. Lead was found to be satisfactory for the third excited state of Si^{30}.

The general operating procedure was the following. After the choice of excited state was made by placing aluminum absorber in the path of the protons, a series of runs was made counting the number of triple coincidences per proton for each of several different gamma-ray absorber thicknesses. Special care was taken to shield the gamma-ray counters with Pb to limit the number of stray or scattered gamma-rays detected. Careful monitoring of the number of accidental coincidences to be expected was made and the resolving time checked before and after each run. This measurement was checked in three ways. Separate random sources were used to supply pulses to each channel of the coincidence circuits and the rate of accidentals recorded was compared to the individual channel rates. Cyclotron target gamma-rays were then used as one of the random sources to check for any possible bunching effect in the beam. A measurement was made using a synchroscope and a delay line to measure the effective width of the shaped pulses. Finally, a random source was placed near the gamma-ray detector during one of the runs to increase the effective background a known amount.

It was found for the aluminum reaction that even at maximum beam intensity (0.003 microampere) the ratio of real to accidental coincidences was 10 to 1 or greater. This was not true for the deuteron reaction, however, because of the greater number of states excited. A consequent large increase in the number of gamma-rays was observed. Furthermore, a considerable number of neutrons, which are produced in the vacuum chamber of the cyclotron in deuteron bombardment, were added to the background counting rate in the gamma-ray detector. However, except for a few minor changes which were made to maximize the net counting efficiency of the system, the operating procedure was the same in the deuteron bombardment as in the case of the alpha-particle reaction.

The target in the $B^{10}(d,p)B^{11}$ reaction was a thin layer (3 mm air equivalent) of elemental B^{10} evaporated onto a thin gold backing. The B^{10} isotope, concentrated to 96 percent, was supplied by the Oak Ridge National Laboratory through the AEC.

In order to clarify possible ambiguity in the decay scheme, it was found necessary to set up an experiment whereby proton–gamma-gamma-coincidences could be observed. This was done to detect suspected cascade gamma-ray transitions. For this experiment two separate scintillation phosphors were used, each with its own corresponding photomultiplier. Only one photomultiplier was used with each phosphor, since the

TABLE I. Proton–gamma-ray coincidences for the ground state and three excited states of Si^{30}.

State	Aluminum absorber thickness (cm air equivalent)	Excitation energy (Mev)	Proton–gamma-ray coinc./10^4 protons
0	71.7	0	0.32
1	42.2	2.3	5.95
2	28.2	3.6	7.25
3	14.7	4.9	11.9

[2] H. L. Schultz and E. C. Pollard, Rev. Sci. Instr. **19**, 617 (1948).

resolving time of the first coincidence circuit was sufficient to discriminate at least partially against the random noise pulses from each tube. Owing to the inherent inefficiency of any gamma-ray detector, this triple coincidence event is extremely rare; but with two coincidence circuits sufficient resolution was obtained to enable a real effect to be detected. This experiment was performed for both reactions.

RESULTS

After the mean range of each proton group associated with the excited states of the residual nucleus of the reaction was determined, each group was examined for proton–gamma-ray coincidences. The results for Si^{30} are tabulated in Table I.

The total number of coincidences observed for each state except the ground state was several hundred, so that the standard deviation for each observation was

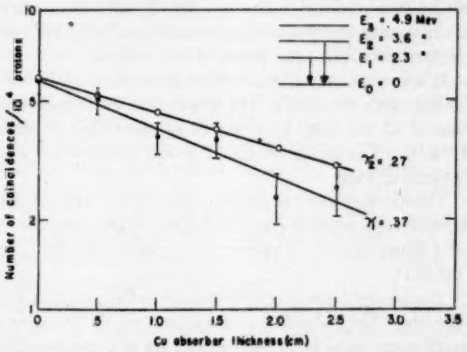

FIG. 2. Proton–gamma-ray coincidences as a function of copper absorber thickness for the first and second excited states. The energy level diagram shows schematically the gamma-ray transitions.

5 percent or less. The coincidence rate shown is that actually observed without correction for accidentals. The lack of coincidences for the long-range group is expected if this is the ground state. The number of coincidences per proton from the first and second excited states are seen to be approximately equal. This is the first evidence that the transition from the second state probably consists of a single gamma-ray. The third state shows a coincidence rate which is almost twice that of the first two states. Since the detector efficiency for these gamma-rays should be less or at least no greater on the basis of the Compton cross section than for the first two states, we have the first evidence of a complex nature for the decay scheme of this state.

The results of the gamma-ray absorption experiment for the first two excited states are shown plotted in Fig. 2. The average number of coincidences observed at each point was approximately 100 giving the standard deviations shown. The absorption coefficients τ as calculated from the slope of the indicated straight lines are shown on the graph. The necessary lack of collimation of the absorbed gamma-ray beam is an unavoidable disadvantage for this type of energy measurement. It is to be expected from this that an absorption coefficient measurement will probably include in it a nearly constant component due to scattered rays which will tend to decrease the slope of the measured absorption curve, particularly at the higher energies.

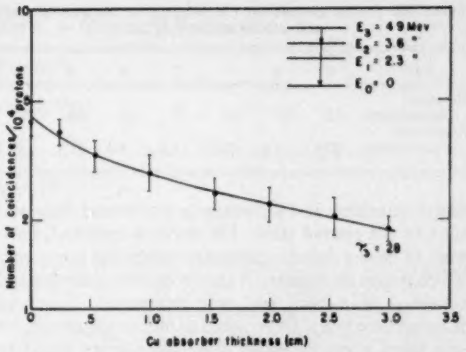

FIG. 3. Proton–gamma-ray coincidences as a function of copper absorber thickness for the third excited state. The corresponding gamma-ray transitions are shown on the energy level diagram.

The data shows, however, that certainly different energy gamma-rays enter into the transitions with that from the second state being of greater energy. A cascade to the first state is therefore excluded except for a possible branching process in which the cascade transitions are of minor importance.

Data was then taken for the third excited state and a characteristic set is shown in Fig. 3. The number of possible transitions from this state is increased to four, exclusive of branching processes. The data allows elimination immediately of two of these. A single straight line can be drawn through these experimental points with the standard deviations as measured. The slope this line would have is shown on Fig. 3. This represents an energy in the minimum of the absorption curve. A cascade transition to the first state is therefore excluded, since this would yield two nearly equal energy gamma-rays whose absorption coefficient would be greater than that observed. A multiple cascade to the ground state is more strongly excluded for the same reason. The slope as quoted above could not distinguish between a

TABLE II. Proton–gamma-gamma-coincidences for the second and third excited states of Si^{30}.

State	Observed coincidences	Accidental coincidences	No. of protons
2	6	3.7	1.85×10^6
3	36	4.2	2.39×10^6

TABLE III. Proton–gamma-ray coincidences for the ground state and excited states of B^{11}.

State	0	1	2	3	4	5	6
Observed coincidences	21	17	30	52	18	86	267
Accidental coincidences	20.1	4.8	9.2	15.6	3.9	41.7	80.7

direct transition and a cascade to the second state and then to the ground state. The curve is observed, however, to have a definite curvature toward the upper end, which would be expected if the decay were complex and consisted of a hard and soft component. Excessive running time would be required to reduce the deviations to a point where exclusion of a simple decay would be possible. Another complete set of data, however, showed the same curvature at the upper end. If a straight line is subtracted from the above data, a component of energy less than 2 Mev remains.

A series of runs was made using lead as the absorber with the gamma-ray detector moved in to increase the counting rates. The results indicated a slope which was greater than would be expected if no low energy component were present.

The proton–gamma-gamma-coincidence experiment was then performed with results as shown in Table II.

This event is extremely rare, as is seen from the total number of protons counted. The results confirm conclusively that the transition from the third excited state is indeed complex, while that from the second state is direct to the ground state.

The method of examination used above was then applied to the more difficult $B^{10}(d,p)B^{11}$ reaction. Work just completed in this laboratory by Bateson[3] shows that the number of resolved levels in B^{11} for the case of 90° observation was six, exclusive of the ground state. The relative intensities vary considerably, with the fifth and sixth levels being very prolific.

The number of gamma-rays observed per proton for this reaction was very much greater than for the previous reaction. The proton–gamma-ray coincidence rate at each level is tabulated in Table III. The accidental coincidences expected are listed as well as the number actually observed because of the low ratio of genuine to accidentals that it was possible to achieve. The separation of the fourth and fifth state protons was not expected to be complete because of their close spacing.

TABLE IV. Proton–gamma-gamma coincidences for the excited states of B^{11}.

State	2	3	5	6
Observed coincidences	9	8	9	24
Accidental coincidences	7.6	2.9	4.7	8.7

The ground-state group was seen to yield no genuine coincidences outside the statistical deviation of the observed data. This confirms the assignment of this as the probable ground state and permits the evaluation of the mass difference between the B^{10} and B^{11} nuclei. Data similar to this for the ground state and first two excited states has been reported by Thirion.[4]

It was possible to measure an absorption coefficient on the sixth state only. The absorption coefficient was that of an energetic gamma-ray of more than 5 Mev. It was not possible to tell if a soft component was present as well.

The proton–gamma-gamma-coincidence experiment allowed for a possible partial solution for the assignment of a decay scheme, however. The results are shown in Table IV.

The second state probably decays to the ground state directly. The transitions from the third, fifth, and sixth states appear to be complex. It was not possible to make a decision in the case of the fourth state because of the close proximity of the intense fifth state.

The author wishes to acknowledge the guidance and direction of Professor E. C. Pollard during the progress of this research.

[3] W. O. Bateson, Phys. Rev. **80**, 982 (1950).

[4] J. Thirion, Compt. rend. **229**, 1007 (1949).

Measurement of the Positive π-Meson Lifetime*

CLYDE E. WIEGAND†
Department of Physics, Radiation Laboratory, University of California, Berkeley, California
(Received February 7, 1951)

The time intervals between the succession of events: stopping of a π^+ meson in a stilbene crystal, $\pi \rightarrow \mu$-decay and $\mu \rightarrow \beta^+$ decay are used to identify the pulses produced by π^+ mesons and to measure the mean life of the $\pi^+ \rightarrow \mu$-decay. For this mean life we find $(2.58 \pm 0.14) \times 10^{-8}$ sec.

INTRODUCTION

THE first evidence of the decay of a heavy (π) meson into a lighter (μ) meson was tracks in a photographic emulsion which had been exposed to cosmic rays by Lattes, Muirhead, Occhialini, and Powell.[1] From the length of time the heavy meson spent in the emulsion they set a lower limit on the lifetime as 10^{-11} sec.

Later, working with π-mesons produced artificially in the Berkeley 184-inch cyclotron, Lattes was able to establish an experimental lower limit of 5×10^{-9} sec for the lifetime. The first direct measurement of the π-meson lifetime was made by Richardson.[2] His method was to measure the fraction of negative π-mesons which survived various times of flight in the cyclotron vacuum tank. He detected the mesons by photographic plates and reported the mean lifetime of $(1.11_{-0.35}^{+0.48}) \times 10^{-8}$ sec. Later, Martinelli and Panofsky[3] using a technique similar to that of Richardson measured the mean lifetime of positive π-mesons. They found τ equals $(1.97_{-0.28}^{+0.21}) \times 10^{-8}$ sec.

In the light of recent developments in electronic techniques it was natural to plan experiments to determine the lifetime of the π-mesons by means of electronic detectors because of the expected improvement in accuracy over previous methods. A classic example of electronic technique for the measurement of a mean lifetime in the microsecond region is that of Rasetti's[4] work on "slow mesons," which are now identified as μ-mesons.

A preliminary measurement of the positive π-meson lifetime using a method similar to the one presently described was reported by Kraushaar, Thomas, and Henri.[5] On the basis of 57 $\pi \rightarrow \mu$-decays they obtained for the mean lifetime $(1.65 \pm 0.33) \times 10^{-8}$ sec.

More recently at this laboratory Jakobson, Schulz, and Steinberger[6] measured the mean lifetime of positive π-mesons in connection with the development of improved apparatus for electronic detection and counting of π-mesons. They found $\tau = (2.54 \pm 0.11) \times 10^{-8}$ sec based upon the results of counting 5641 mesons.

The present paper describes in more detail the work reported by Chamberlain, Mozley, Steinberger, and Wiegand.[7]

EXPERIMENTAL METHOD

The 322-Mev (maximum) x-ray beam of the Berkeley synchrotron was used to produce π-mesons in a target of polyethylene. Figure 1 is a diagram of the arrangement of the apparatus. The x-ray beam was collimated by lead shielding to produce a beam 1 inch in diameter incident upon the polyethylene target, which was in size and shape a 2-inch cube. The detectors consisted of two crystals of *trans*-stilbene arranged to form a counter "telescope" at right angles to the beam. The phosphorescent radiation caused by an ionizing particle which passed through either of the crystals was detected by multiplier phototubes associated with each crystal. The entire apparatus was surrounded by lead shielding 6 to 8 inches thick. Each crystal measured 4.5×4.1 cm and was 1.8 cm thick. An aluminum absorber 1 inch thick was placed between the target and the detectors in order to reduce the energy of the emitted mesons. This had the effect of increasing the probability that a meson would stop in the crystal detector.

The object of this experiment was to determine the

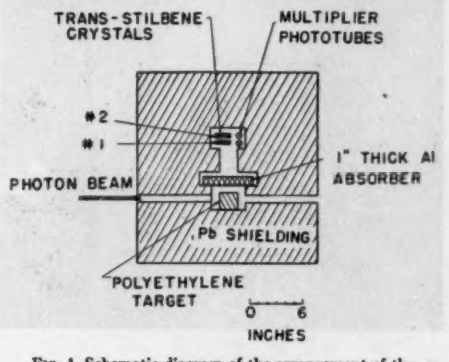

FIG. 1. Schematic diagram of the arrangement of the detecting apparatus.

* This work was performed under the auspices of the AEC.
† Submitted in partial satisfaction of the requirements for the degree of Doctor of Philosophy.
[1] Lattes, Muirhead, Occhialini, and Powell, Nature **159**, 694 (1947); **160**, 486 (1947).
[2] J. Richardson, Phys. Rev. **74**, 1720 (1948).
[3] E. A. Martinelli and W. K. H. Panofsky, Phys. Rev. **77**, 465 (1950).
[4] F. Rasetti, Phys. Rev. **59**, 706 (1941); **60**, 198 (1941).
[5] Kraushaar, Thomas, and Henri, Phys. Rev. **78**, 486 (1950).
[6] Jakobson, Schulz, and Steinberger, Phys. Rev. **81**, 894 (1951).
[7] Chamberlain, Mozley, Steinberger, and Wiegand, Phys. Rev. **79**, 394 (1950).

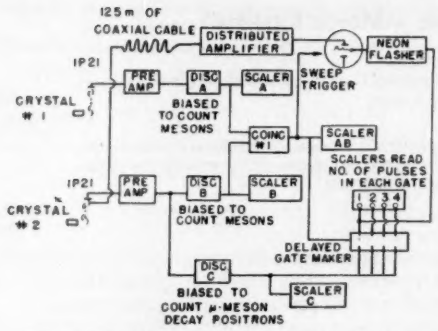

FIG. 2. Block diagram of the electronic apparatus.

mean lifetime of positive π-mesons by measurement of the time intervals between the stopping of π-mesons and the emission of μ-mesons. In order to be certain that the observed pulses were due only to π-mesons, the μ-decay positrons were detected and recorded by an apparatus developed by Steinberger.[8] The time intervals corresponding to the lifetime of the π-mesons were measured by recording photographically the pulses from the second crystal detector displayed on the screen of a cathode-ray oscillograph.

APPARATUS

A block diagram of the electronic apparatus is presented in Fig. 2. The design of the electronic components was for the most part based upon standard techniques employing resistance-capacitance coupling and high transconductance miniature tubes to obtain sufficiently rapid response in the coincidence and gate-forming circuits. However, sufficient resolution of the π- to μ-decay pulses requires a vertical deflection amplifier capable of producing pulses which have a time of rise of 10^{-8} sec or less. The deflection amplifier used in this experiment made use of the traveling wave concept and its design was based upon principles discussed by Ginzton, Hewlett, Jasberg, and Noe[9] in their paper on distributed amplification. The time of rise of the oscillograph deflection system was about 5×10^{-9} sec. The amplifier was operated with a gain of 15.

FIG. 3. Photographic reproduction of a typical oscillograph trace showing the π-μ-meson decay pulses and the neon flash bulb marking. The pulse separation is about 4×10^{-6} sec.

Let us review the electronic events due to the detection of a π-μ-decay: If a meson passed through crystal number 1 and stopped in number 2 and the pulses were accepted by discriminators A and B, there was produced at the output of coincidence number 1 a pulse which started the sweep and intensifying circuits of the oscillograph for π-μ-decay and at the same time initiated a circuit which opened a series of four delayed gates beginning 0.5 μsec later for μ-β^+ decay. The length of the delayed gates was 2×10^{-6} sec. On account of its limited resolution, coincidence number 1 treated the two pulses from the stopping of the π-meson and the emission of the μ-meson as one event. The output of detector number 2 was also connected to another discriminator, C, biased to accept μ-meson decay positron pulses. If a particular pulse were accepted by discriminator C, it was fed to the delayed gate circuit; and, if a gate were open, the pulse was recorded by the register associated with the open gate. When a pulse was recorded in the first delayed gate, an additional circuit was actuated and caused a small neon lamp to flash momentarily. The neon lamp was placed near the face of the oscillograph tube and in the field of view of the recording camera. Its flash would thus produce a dot on the film at the end of the sweep trace. The dot appearing at the end of the trace would then indicate that the pulse of the positron from the μ-meson decay had been detected. A third connection to detector number 2 was made to a section of 125 ohms impedance RG 63/U coaxial cable 125 meters long and thence to the distributed amplifier, the output of which was connected as directly as possible to the vertical deflection plates of the oscillograph. The purpose of the long cable was to delay the pulse about 0.5 microsecond in order to allow the oscillograph sweep and intensifier circuits to become operative. The sweep duration was 0.8×10^{-6} sec. The oscillograph trace thus displayed the pulses which occurred in detector number 2 during a time interval of about 0.8×10^{-6} sec after the passage of a particle through detector number 1 and into or through number 2. Figure 3 is a reproduction of a typical trace.

The sweep speed of the oscillograph was calibrated by applying a sine wave voltage of known frequency to the vertical deflection plates. Such calibrations were made several times during the course of the experiment. The standard frequency source was a General Radio type 605-B signal generator accurately calibrated

[8] J. Steinberger and A. S. Bishop, Phys. Rev. **78**, 493 (1950).

[9] Ginzton, Hewlett, Jasberg, and Noe, Proc. Inst. Radio Engrs. **36**, 956 (1948).

to within ± 0.3 percent. Also, we allowed a slight amount of extraneous pick-up from the synchrotron radiofrequency system which provided a practically continuous calibration by its presence on the pulse base line. The frequency of the synchrotron was constant and by a different signal generator was found to be 47.34 ± 0.02 megacycles per second. The two measurements agreed and showed the sweep speed to be linear within ± 0.5 percent and to amount to 1.3×10^{-8} sec mm^{-1} at the screen of the cathode-ray tube.

The apparatus was adjusted by trial to give a reasonable rate of traces exhibiting π-μ-decay pulses and at the same time a reasonably low background of spurious traces. A typical run was as follows: During a $1\frac{1}{2}$-hour exposure the standard length of 100 feet of film was run continuously through the camera, and there were recorded upon this film 5232 traces of which 168 bore the neon lamp flash marker.

A microfilm reader was used to examine the processed film. Images of the traces were projected onto a piece of graph paper upon which the distance between two pulses could easily be determined to within 1 mm. With the particular camera and projector arrangement employed, 1 mm on the projector screen represented 0.362×10^{-8} sec.

The distance between pairs of pulses was interpreted as indicated by Fig. 4. Points halfway up the leading slopes were determined, and the distance between pulses was taken to be the distance between the projections upon the base line of these two points. All double pulses marked by the flash were included in the tabulation of the data. Only in a very few instances was it questionable that a pulselike disturbance on the baseline was due to a μ-meson. The heights of the μ-meson pulses were fairly uniform, as is indicated by a plot of the number of pulses *versus* their height in Fig. 5.

The slope of the baseline due to the first pulse influences the apparent height of the second pulse and this accounts largely for the small pulses of Fig. 5. However, the time separation was not affected, since the distance between the pulses was measured using the middle of the rise as illustrated in Fig. 4. Furthermore, since the amplifier was always operated well within its linear region, we believe there was no distortion by the amplifier of the pulse separation times.

Considering all the traces marked by the neon flash bulb, it was not possible in every instance to observe two distinct pulses. This was interpreted as being due to π-meson decays occurring within the resolving time of the system and, consequently, the stopping of the π-meson and emission of the μ-meson appearing as one pulse. The treatment of such unresolved decays will be discussed later.

RESULTS

During the course of the experiment a total of 1419 separate traces marked with the neon flash bulb were accumulated. A total of 691 of the marked traces exhibited two clearly separated pulses between which the distance could be measured, and the remainder were unresolved. The distances between the pairs of pulses were tabulated to the nearest millimeter on the projector screen. A histogram of the number of pulses which occurred with various time separations is presented in Fig. 6.

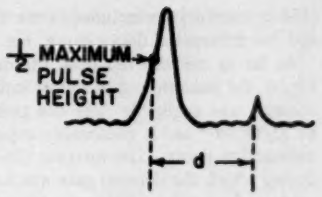

FIG. 4. Illustration of the method of measuring the separation d between two pulses.

An integral representation of the same data is given in Fig. 7 in which the total number of pulses occurring after a certain time is plotted as a function of this time upon semilogarithmic paper. This number is given by $N(t) = N_0 e^{-\lambda t}$, where N_0 is the total number of recorded traces due to π-mesons stopping in the detector and λ is the meson decay constant.

In Fig. 8 the data are shown in differential form, where the logarithm of ΔN, the number of pulses occurring in the constant time interval 1.45×10^{-8} sec, is plotted *versus* time. The expression τ is the time for ΔN to diminish by the factor $1/e$ and by inspection of the curve is seen to amount to about 2.6×10^{-8} sec.

a. Analysis of Differential Curve

Inspection of the histogram Fig. 6 and the integral curve Fig. 7 reveals that apparently all of the π-μ-decay pulses were resolved after 2.17×10^{-8} sec. Therefore, only pulses which occurred after 2.17×10^{-8} sec

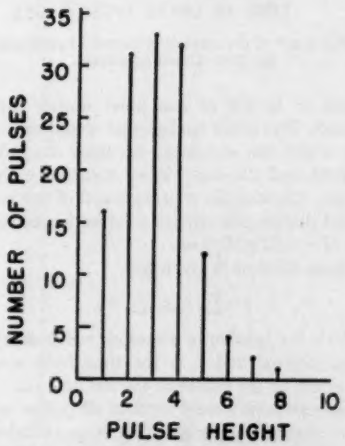

FIG. 5. Histogram of the number of μ-meson pulses *versus* the height of the pulses.

(554 in number) are included in the lifetime calculation and the differential decay curve, Fig. 8.

As far as one can tell from the decay histogram of Fig. 6, the background of pulses from extraneous phenomena was negligible. The one pulse which occurred at 25.3×10^{-8} sec is reasonably expected from a pure radioactive decay. The interval $(26 \text{ to } 36)\times10^{-8}$ sec, during which the delayed gate was known to be closed, contained no pulses. Using the known counting rate in scaler C and the beam on time, it is calculated that there should be a probability of 0.3 of getting one accidental pulse in the accepted time interval of the whole experiment.

A different background arising from mesons stopped in detector 2 and accompanied by an accidental pulse in the first delayed gate and flashing the neon bulb is

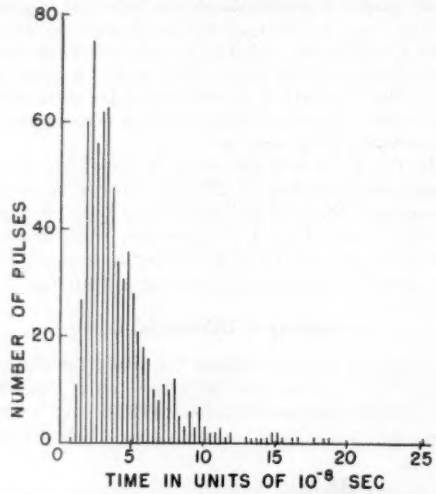

FIG. 6. Histogram of the number of measured pulse pairs *versus* the time of their separation.

calculated to be 0.6 of one pulse during the whole experiment. This latter background would arise only in cases in which the π-μ-decay occurred too quickly to be resolved and the μ-β^+ decay occurred within 25.3×10^{-8} sec. Allowing for a background of one pulse out of the 554 decays will require a correction to the mean lifetime of -0.02×10^{-8} sec.

The mean lifetime is given by

$$\tau=\sum_i N_i t_i/\sum_i N_i,$$

where N_i is the number of π-mesons which decay in the ith time interval and t_i is the time from a suitably chosen origin to the center of the ith interval.

The summations should include all pulses occurring after the chosen time origin. (We have included those from 2.17×10^{-8} through 25.34×10^{-8} sec.) The correction due to exclusion of all pulses after 25.34×10^{-8} sec has been calculated and is negligible (-0.1 percent error). The error due to taking finite time intervals is also negligible ($+0.16$ percent).

Since not all of the pulses were resolved until after the sixth interval of 0.362×10^{-8} sec, we have chosen as time 0 the center of the sixth interval. We have then

$$\tau=\sum_{i=6}^{70} N_i t_i \Big/ \sum_{i=6}^{70} N_i, \quad \tau=2.65\times10^{-8} \text{ sec.}$$

The statistical error in the result for τ is obtained by a method pointed out by Peierls.[10] The percentage error in τ is given by $1/\sqrt{N}$, where N is the number of measured pulses used (554):

$$\tau=(2.65\pm0.11)\times10^{-8} \text{ sec.}$$

A correction for a systematic error and a discussion of the reliability of the measurements will be given later.

b. Analysis of the Integral Curve

The integral representation of the data allows us to make use of the unresolved pulses in the first few time intervals providing we know the total number of mesons which stopped in the detector. This procedure gives a point of high statistical accuracy and is important in determining the slope of the decay line. However, it may be reduced in effectiveness by the uncertainty of the necessary corrections for background.

Of the 1419 recorded traces marked by the neon bulb, 691 showed two resolvable pulses leaving 728 unresolved single appearing pulses. However, not all the unresolved pulses were due to π-mesons stopped in the detector because there was a background of spurious pulses which could fall within the delayed gate time, initiate the flash bulb, and thus give false impressions of arising from μ-meson decay positrons. Another source of single background pulses originated from the decay of π-mesons while in flight from the polyethylene target to the detectors. Such events could lead to μ-mesons coming to rest in the detector and making single pulses, and then their decay positrons activating the neon bulb flasher.

An estimate of the number of spurious unresolved pulses can be made as follows: If all the pulses arriving at the delayed gates are due to positrons from μ-meson decay, they should accumulate in the four gates according to the law $N_i=N(0)\exp(-\lambda\mu t_i)$ $(i=1, 2, 3, 4)$, where t_i is the time at the center of the gate. A departure from this law can be attributed to the background. If we assume $\lambda_\mu=4.65\times10^5$ sec^{-1} $(\tau_\mu=2.15\times10^{-6}$ sec) and attempt to fit the expected curve to the experimental data, we find that a background of about 5 percent of the total number of pulses must be subtracted.

Another calculation of the background pulses falling into the delayed gates and flashing the neon bulb can

[10] R. Peierls, Proc. Roy. Soc. (London) **149**, 467 (1935).

be made from the auxiliary counters indicated on the block diagram of Fig. 2. The number of gates made was equal to the number of pulses in coincidence accepted by discriminators A and B and registered in scaler AB. The number of pulses which could fall into a delayed gate was the number accepted by discriminator C and registered in scaler C. Then, if τ was the time in seconds that a gate remained open each time it was made and T was the time during which the number of counts N_{AB} and N_C were accumulated, the number expected to randomly fall into a gate is given by

$$N_{accid}=N_{AB}N_C\tau/TF,$$

where F is the fraction of time the synchrotron beam was actually on and is sometimes referred to as the duty cycle. The beam pulses came at a rate of 6 per second and had a duration of about 2×10^{-3} sec. Hence,

$$F=1.2\times10^{-2}.$$

A typical run lasted 87 minutes, during which 4217 pulses were received in scaler AB and 73,820 in scaler C. The value of τ was 2×10^{-6} sec for each of the four delayed gates. Putting these values into the formula, we find the expected number of accidentals to be 9.94.

During this run 160 pulses were registered in the first delayed gate. If then 10 of these were background, as we have just computed, 10/160 or about 6 percent of the pulses were accidental; and this agrees within statistical accuracy with the previously estimated value. The average background of spurious unresolved pulses for the entire experiment came to 7 percent of the total number of pulses marked by the neon flash bulb.

The second correction needed to establish the total number of stopped π-mesons is obtained by evaluating the fraction of π-mesons which decayed in flight from the target to the detector. The kinetic energy of the emitted π-mesons lies in the region of 60 Mev and their rest energy m_0c^2 is about 140 Mev. Then, it follows that $v/c=0.72$, where v is the velocity of the meson and c is the velocity of light. Since the energy of the emitted mesons is not constant, it will be sufficient to consider the velocity constant during the flight. The probability that a meson decay while traversing the distance $d=20$ cm from the target to the detector is

$$(1-v^2/c^2)^{\frac{1}{2}}d/\tau v=0.025,$$

where τ is the approximate mean lifetime. We have finally a background of about 10 percent to subtract from the total number of recorded traces marked by the neon flasher. This leaves 1277 pulses for the first point on the integral curve.

The data of the integral representation can be conveniently analyzed by calculating the average lifetime of the unresolved pulses and combining this point with the differential curve. The average lifetime τ' of the

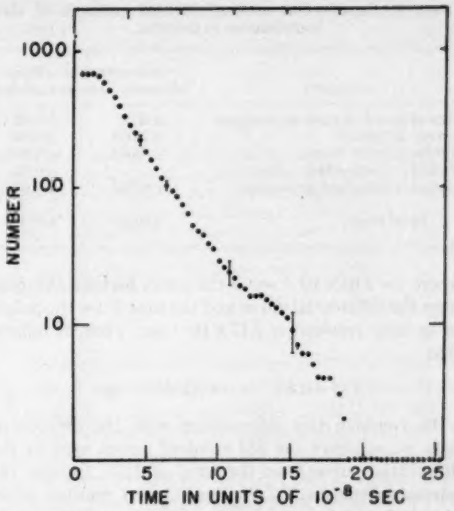

FIG. 7. Plot of the total number of pulses occurring after a certain time *versus* this time.

unresolved pulses can be expressed as follows:

$$\tau'=\frac{\int_0^T\lambda e^{-t/\tau}tdt]}{\int_0^T\lambda e^{-t/\tau}dt}=\tau\left[1+\frac{T/\tau}{1-e^{T/\tau}}\right],$$

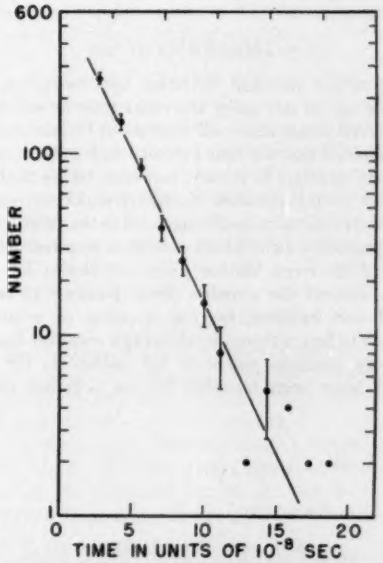

FIG. 8. Plot of the number of pulses occurring in time intervals of 1.45×10^{-8} sec *versus* the time.

TABLE I. Experimental uncertainties and estimates of their contributions to the error.

Uncertainty	Estimated relative errors Differential data	Integral data
Measurement of pulse separations	±0.02	±0.02
Sweep calibration	±0.005	±0.005
Nonlinearity of sweep	±0.005	±0.005
Number of unresolved pulses		±0.04
Statistics (standard deviations)	±0.043	±0.028
Total errors	±0.048	±0.053

where $\tau=2.65\times10^{-8}$ sec is the mean lifetime obtained from the differential curve and the time T for the pulses to be fully resolved is 2.17×10^{-8} sec. Then, it follows that

$$T/\tau=0.82, \quad \tau'=0.91\times10^{-8} \text{ sec.}$$

To combine this information with the differential data we subtract the 554 resolved pulses used in the differential curve from the total of 1277, leaving 723 unresolved pulses N_s. We must insert another term, $N_i\times2.17\times10^{-8}$ sec, in the numerator of the mean lifetime relation, so that the origins of the time scales will coincide. Finally, the mean lifetime including the unresolved pulses is given by

$$\tau=\sum N_i t_i+6\times0.352\times10^{-8}\times N_i/\sum N_i+N_s$$
$$=2.60_5\times10^{-8} \text{ sec.}$$

In the above analysis a total of 1277 measurements are involved, so that if we apply Peierls' method of determining the error, we find a standard deviation of ±2.8 percent, or

$$\tau=(2.60_5\pm0.07)\times10^{-8} \text{ sec.}$$

The actual standard deviation is somewhat larger, because we do not know the exact time at which the unresolved pulses occurred, whereas in Peierls' analysis it is assumed that the time at which each pulse occurred is known exactly. It is easy, however, to see that this addition to the standard deviation under our experimental conditions is small compared to the term $1/\sqrt{N}$.

A systematic error which caused an apparent lengthening of the mean lifetime arose as follows: The gate which allowed the μ-meson decay positron to be detected was initiated by the stopping of π-mesons, whereas to be consistent in allowing a constant fraction of decay positron pulses to fall within it, the gate should have been initiated by the μ-meson pulses. Consequently, the longer a π-meson lived in the detector, the higher was the probability that its μ-meson decay positron pulse would fall within the delayed gate and actuate the neon flash circuit. A detailed calculation shows that our arrangement actually measured the difference between the decay constants of the π- and μ-mesons.

We have found the π-meson decay constant to be approximately 3.85×10^{7} sec^{-1}. The μ-meson decay constant is 4.65×10^{5} sec^{-1}. Therefore, the effect of the above correction is to reduce the measured mean lifetimes by 1 percent.

There are uncertainties in all the operations involved in the tabulation of the data. For instance, it is possible that the distances between the pairs of pulses have been on the average over- or underestimated. The sweep calibration could not be determined exactly and there was a slight nonlinearity in the sweep speed. The number of unresolved pulses involved the fraction of time the synchrotron emitted its photon beam. This duty cycle was not accurately known and probably was not constant.

Various uncertainties and estimates of their contributions to the error are listed in Table I.

We have found from the differential data $\tau=2.65\times10^{-8}$ sec and from the integral data $\tau=2.60_5\times10^{-8}$ sec. Then, subtracting one percent for the systematic correction and 0.02×10^{-8} sec for background effects and applying the above errors, we find the final results of this measurement of the mean lifetime of positive π-mesons:

$$\tau=(2.60\pm0.13)\times10^{-8} \text{ sec (differential data),}$$

$$\tau=(2.56\pm0.14)\times10^{-8} \text{ sec (integral data),}$$

and correspondingly for the half-life:

$$T_{\frac{1}{2}}=(1.80\pm0.09)\times10^{-8} \text{ sec,}$$

$$T_{\frac{1}{2}}=(1.77\pm0.10)\times10^{-8} \text{ sec.}$$

The author gratefully acknowledges the considerable assistance of Dr. Owen Chamberlain, Dr. R. F. Mozley, and Dr. J. Steinberger in analyzing the photographic records. The incorporation of Dr. Steinberger's meson-detecting equipment into the apparatus greatly accelerated the progress of the experiment. Thanks are extended to Professors E. McMillan and E. Segrè for their encouragement and many helpful discussions. The cooperation of the synchrotron operating staff is deeply appreciated.

Neutron Thresholds from the Reactions $T^3(p,n)He^3$, $Li^7(p,n)Be^7$, $Be^9(d,n)^*B^{10}$, and $O^{16}(d,n)F^{17}$

T. W. Bonner and J. W. Butler
*Rice Institute, Houston, Texas**

(Received June 11, 1951)

Techniques are described for observing low energy (15–60 kev) "threshold" neutrons in the presence of fast neutrons. The threshold of the $T^3(p,n)He^3$ reaction was found to be 1020.3 kev, which gives a Q-value of the reaction equal to -764.7 kev and a neutron-hydrogen mass difference of 783.2 kev. Interpretation of data near the threshold of the $Li^7(p,n)Be^7$ reaction gives indication of a level in Be^8 near 18.90 Mev. Three neutron thresholds have been observed in the reaction $Be^9(d,n)^*B^{10}$ at deuteron energies of 920, 985, and 1916 kev. The corresponding Q-values are -752, -805, and -1566 kev; these give excited states in B^{10} at 5.110, 5.163, and 5.924 Mev. The threshold of the reaction $O^{16}(d,n)F^{17}$ was determined to be 1836 kev, giving a Q value of -1631 kev and a mass of F^{17} equal to 17.007506.

INTRODUCTION

NEUTRON thresholds for endothermic reactions have been investigated in the case of a number of nuclear reactions.[1] The absolute determination of these threshold energies give the Q-values of the reactions and, therefore, the mass differences between the initial and final systems. The accuracy of establishing the position of the threshold is limited only by the absolute bombarding energy scale, which is known to about a tenth of one percent. This is in contrast to an accuracy of the order of one percent in measuring the Q-values of exothermic neutron emitting reactions.

The experiments reported herein concern the neutron thresholds from proton bombardment of T^3 and Li^7 and deuteron bombardment of Be^9 and O^{16}. All of these reactions except deuterons on Be^9 are endothermic and thus cannot occur at all below a certain reaction threshold. The deuteron disintegration of Be^9 is highly exothermic, but the residual nucleus may be left in a higher excited state than would be possible from the energy available from the reaction energy. One would expect such "threshold neutrons" (15–60 kev) to exhibit threshold characteristics similar to the endothermic reaction thresholds except that the sharpness of the threshold would depend on the width of the excited state of the residual nucleus.

The experimental problem of observing new "thresholds" is complicated somewhat by the presence of the faster neutrons from lower energy states and the ground state. These faster neutrons are essentially background as far as the new group of threshold neutrons is concerned, and in most cases outnumber them. If one is to establish accurately the position of the threshold, he must discriminate strongly against the fast neutrons in favor of the slower ones.

The application of threshold techniques to these new groups of slower neutrons presents a method capable of resolving closely spaced energy levels in the residual nucleus because the resolution is limited primarily by the target thickness, which for the very light elements can be reduced to a few kev and still give satisfactory intensity. Essentially, the same accuracy of establishing the position of the threshold can be attained as in the case of the endothermic reaction threshold.

The usefulness of the method of neutron thresholds is enhanced by the cone effect of the neutron emission which gives a very favorable factor in the forward direction just above threshold.[1] This cone effect is discussed in the Appendix.

According to theory[2] the cross section for emission of a neutron near threshold is proportional to $E^{l+\frac{1}{2}}$, where E is the neutron energy in the center-of-mass system and l is the angular momentum of the neutron, and so one might expect to be able to determine the angular momenta of the neutrons by examination of the experimental yield curve. However, because of the very high centrifugal barrier[3] in the region just above threshold for neutrons with nonzero angular momentum, there will be at most a small contribution from such neutrons unless neutrons with zero angular momentum were forbidden or made improbable by selection rules. If a group of neutrons, known by other methods, fails to show a threshold, it might be taken as an indication that neutrons with zero angular momentum are forbidden by the selection rules.

APPARATUS

The bombarding particles used in these experiments were accelerated by the Rice Institute pressure Van de Graaff generator, which was stabilized by a magnetically focused beam of electrons going down the vacuum tube in the opposite direction to the positive ions.[4]

For all the absolute voltage determinations and for most of the excitation curves, the slit width of the magnetic beam analyzer was 0.005 inch which allowed

* A preliminary report of these results has been given by Bonner, Butler, and Risser, Phys. Rev. **79**, 240(A) (1950), and in Proceedings of the Harwell Nuclear Physics Conference (September, 1950), unpublished.

[1] R. F. Taschek and A. Hemmendinger, Phys. Rev. **74**, 383 (1948); Hanson, Taschek, and Williams, Revs. Modern Phys. **21**, 635 (1949); Bonner, Evans, and Hill, Phys. Rev. **75**, 1398 (1949); Richards, Smith, and Browne, Phys. Rev. **80**, 524 (1950); H. B. Willard and W. M. Preston, Phys. Rev. **81**, 480 (1951).

[2] E. P. Wigner, Phys. Rev. **73**, 1002 (1948).

[3] Feshbach, Peaslee, and Weisskopf, Phys. Rev. **71**, 145 (1947).

[4] S. J. Bame and L. M. Baggett, Rev. Sci. Instr. **20**, 839 (1949).

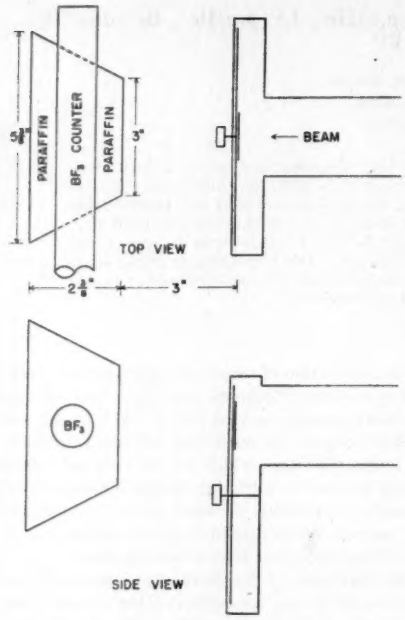

FIG. 1. Target-counter arrangement for 27° geometry.

an energy spread of 0.08 percent in the incident beam. For the Be^9 excitation curve below the 920-kev threshold and above the 985-kev threshold, the slit width was 0.012 inch.

In order to obtain accurate data from thin targets which are bombarded by deuterons, it was necessary to take steps to reduce the background. A deflecting magnet was placed across the vacuum tube about one meter before the analyzing magnet. This magnet separated the beam into its various mass components, while adjustable quartz plates on each side of the beam were moved in to stop the unwanted portions of the beam and to permit only the desired mass component to pass through to the analyzing magnet.

The ion source of the electrostatic accelerator was supplied with either hydrogen or deuterium by means of a $\frac{1}{8}$-in. Saran tube going from the storage bottle outside the accelerator tank up to the palladium leak inside the central electrode. When the absolute value of the deuteron-neutron thresholds in terms of the standard calibration reactions using protons as bombarding particles was determined, it was necessary to switch from protons to deuterons, or vice versa, with as little delay as possible.

The target holder was a brass disk capable of holding five targets simultaneously and was contained in a short brass cylinder as shown in Fig. 1. Target positions could be changed by rotating the target holder from outside the vacuum system by means of a knob connected to the shaft passed through a Teflon seal to the vacuum system.

The background counting rate was determined by rotating into the path of the beam a silver blank and recording the counting rate in the same manner as with a target.

COUNTING TECHNIQUE

Various materials, shapes, sizes, and orientations of moderators around a BF_3 counter were tried in an effort to attain an optimum geometry, the optimum conditions being (1) a good counting rate and (2) the highest ratio of counts from threshold neutrons (15–60 kev) to that from fast neutrons. A bare BF_3 counter satisfies the second condition, but gives a very low counting rate. Cylindrical paraffin moderators coaxial with the counter tube were tried, but were abandoned in favor of a truncated cone of paraffin because of better defined boundary of the "counting cone" in the case of a truncated cone. A well-defined counting cone is important when we try to compare the experimental curve with theory. The "cone effect" near threshold caused by the moving center of mass, is discussed in the Appendix. The final version of the counting arrangement is shown in Fig. 1; thin cadmium sheets completely cover the paraffin moderator.

A graphite moderator was tried with the hope that it would give a very high ratio of threshold neutron counts to fast neutron counts; but it actually gave about the same ratio as the paraffin moderator, and the total counting rate was so low as to make the graphite moderator of little value. A heavy water moderator was tried in order to avoid neutron capture by the moderator as in the case of paraffin, but it too gave a lower counting rate than the paraffin and gave no higher ratio of "threshold" to fast neutrons than did the paraffin. The arrangement in Fig. 1 is hereinafter referred to as the "27° geometry."

$T^3(p,n)He^3$

It was thought that this reaction would be a particularly good one for testing the counting technique, because the high center-of-mass velocity confines the total neutron yield to a cone of half-angle 27° until a bombarding energy of 24 kev above threshold is reached. This reaction provided a region (large compared with target thickness) over which the shape of the rising slope of the curve could be critically compared with a calculated curve. This is important to determine whether or not the effective cone of the counter is the same as the geometric cone. Furthermore, the reaction is almost ideal as regards certain assumptions which are made in calculating a theoretical curve. Because of the low coulomb barrier (about 400 kev) and because no excited states of the intermediate nucleus He^4 have been reported in the energy range involved here, one would expect the cross section for formation of the intermediate nucleus to remain practically constant

over a small range of bombarding energies. In calculating the geometrical effect of the neutron cone on the counting rate, it was assumed that the neutrons were emitted isotropically in the center-of-mass system. Taschek *et al.*[5] have shown that the neutrons from this reaction show approximate symmetry in the center-of-mass system near the threshold.

The tritium targets were made by evaporating thin deposits of zirconium onto ½-in. diameter polished tungsten disks and allowing the zirconium to take up tritium by first heating it, then cooling it in an atmosphere of the gas.[6]

The circles in Fig. 2 give the experimental neutron counting rates for a target which was 40 micrograms of Zr per cm² thick (about 4 kev). The background counting rate was negligible. The counting rate rises smoothly until a bombarding energy of 15 kev about threshold is reached, after which the points fall rather slowly until 24 kev above threshold is reached. At this energy the neutron cone has opened up to 27°, and therefore the neutrons start missing the cone of the counter entirely at higher energies, and the yield falls more rapidly. Apparently then, the outer layer of paraffin between 21° and 27° (at 15 kev above threshold, the cone has opened up to 21°) is not so effective in contributing to the counting rate as the inner cone (less than 21°).

The curve in Fig. 2 represents the expected theoretical counting rate, assuming a counter cone of half-angle 21°, which appears to be approximately the effective cone of the counter. The curve was calculated by multiplying the geometrical effect by the square root of the neutron energy in the center-of-mass system and integrating the product curve over a 4-kev target thickness. Since both the solid angle (as a function of cone half angle) and the neutrons per unit solid angle are concentrated toward the outer edge of the cone near threshold, one would expect the experimental counting rate above 1035 kev to be somewhat higher than the calculated curve based on an effective cone of 21°.

Above 1060 kev the experimental points drop faster than the calculated curve; this can be explained qualitatively on the basis of the counter efficiency as a function of neutron energy. By making a rough extrapolation of the curves of Hanson and McKibben[7] for the counting efficiency of various sizes of paraffin cylinders as a function of neutron energy, it is estimated that the efficiency of the counter is almost flat up to an energy of about 100–200 kev and decreases for higher energies. The neutrons emitted just above threshold have an energy of about 60 kev in the laboratory system. At a bombarding energy of 1080 kev, the neutrons emitted in the forward direction have an energy of 200 kev in the laboratory system; and for a bombarding energy of 1120 kev, the maximum neutron energy is about 250 kev.

Experiments to determine accurately the threshold of this reaction were made with thin tritium targets. The absolute value of the threshold energy is based on the accurate work of Herb, Snowdon, and Sala,[8] who determined the voltages of the 873.5-kev resonance in the reaction $F^{19}(p,\alpha,\gamma)O^{16}$, the 993.3-kev resonance in $Al^{27}(p,\gamma)Si^{28}$, and the threshold for the reaction $Li^{7}(p,n)Be^{7}$ at 1882.2 kev to an over-all accuracy of about 0.1 percent.

To determine the value of the $T^{3}(p,n)He^{3}$ threshold, the beam analyzing magnet currents required for the fluorine and aluminum resonances were determined by bombarding a target of LiF about 0.4 microgram per cm² thick (about 100 volts thick for 900-kev protons) and a freshly cleaned disk of commercial 2*S* aluminum. The tritium threshold was then studied using the geometry of Fig. 1. For the range of magnet currents which were used in the calibration, the bombarding energy is given by the following equation:

$$E=AI^{2}+B,$$

where E is the bombarding energy, I the magnet current, and A and B are constants determined by the two resonance calibration points. A typical run is shown in Fig. 3.

The half-width of the F^{19} resonance was about 4.3 kev; and the total rise of the thick target Al^{27} resonance took place in about 1.5 kev, thus confirming the value of the beam energy resolution determined by the setting of the resolution slit. The half-width of the Al^{27} resonance is known to be about 0.4 kev or less.

For a thick target yield above threshold, the (neutron yield)$^{\frac{1}{2}}$ is a linear function of bombarding energy. The position of the tritium threshold was determined by plotting the (neutron yield)$^{\frac{1}{2}}$ and extrapolating to the abscissa. This relation applies to the threshold data, since all points taken were less than 4 kev (target thickness) above the threshold. The values of the tritium threshold thus determined for five different

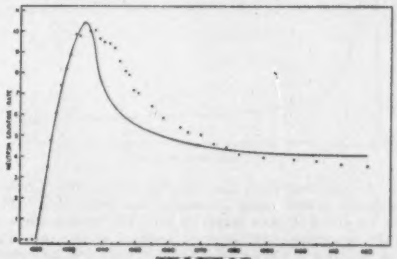

FIG. 2. Neutrons from the reaction $T^{3}(p,n)He^{3}$. Circles give experimental points using a counter half-angle of 27° and a 4-kev target. The curve gives the calculated values for an effective counter half-angle of 21°.

[5] Taschek, Jarvis, Hemmendinger, Everhart, and Gittings, Phys. Rev. **75**, 1361 (1949).
[6] A. B. Lillie and J. P. Conner, Rev. Sci. Instr. **22**, 210 (1951).
[7] A. O. Hanson and J. L. McKibben, Phys. Rev. **72**, 673 (1947).
[8] Herb, Snowdon, and Sala, Phys. Rev. **74**, 246 (1949).

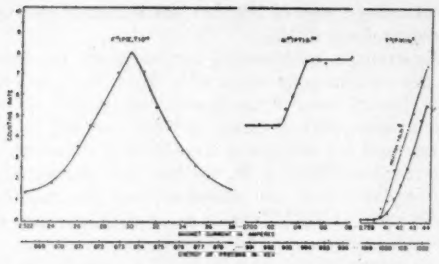

FIG. 3. Typical run on absolute determination of threshold energy for the reaction $T^3(p,n)He^3$. Targets used on this run: LiF (about 0.1 kev thick), thick Al disk, and a 4-kev tritium target.

runs are 1019.9, 1019.7, 1020.6, 1021.1, and 1020.3 kev. The average value is 1020.3 kev, with an estimated limit of error of 1.5 kev.

This value of the threshold agrees very well with that obtained by Taschek *et al.*[9] (1019 kev). When the average threshold value of 1020.3 kev is used, the Q-value of the reaction is -764.7 kev; and the neutron-hydrogen mass difference is found to be 783.2 ± 2 kev when 18.5 kev[10] is used as the end point of the beta-spectrum from T^3 and the neutrino rest mass is neglected.

$Li^7(p,n)Be^7$

This reaction has been investigated rather thoroughly by Taschek and Hemmendinger[1] and others. Breit and Bloch[11] have discussed the possibility of a resonance below threshold on theoretical considerations and on the basis of the cross section for the reaction obtained by Taschek and Hemmendinger. Their values of total cross section were constant from about 50 kev about

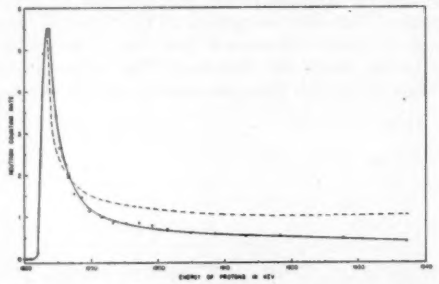

FIG. 4. Neutrons from the reaction $Li^7(p,n)Be^7$. Circles give experimental points using a counter half-angle of 5° (effective angle: 4°) and a 0.6-kev target of LiF. The broken curve represents the theoretical counting rate assuming an isotropic distribution of neutrons in the center-of-mass system and assuming that the cross section increases as the neutron velocity.

[9] Taschek, Argo, Hemmendinger, and Jarvis, Phys. Rev. **76**, 325 (1949).
[10] Hornyak, Lauritsen, Morrison, and Fowler, Revs. Modern Phys. **22**, 299 (1950).
[11] G. Breit and I. Bloch, Phys. Rev. **74**, 397 (1948).

threshold to about 190 kev above, indicating that either the probability of neutron emission is independent of bombarding energy in this range, or that the cross section for formation of the compound nucleus is a decreasing function of energy. Since the behavior of the cross-section curve below 23 kev above threshold was unknown, it was felt that by determining the trend of the cross-section curve closer to threshold, one might draw more definite conclusions as to the possibility of existence of an excited state in the Be^8 nucleus corresponding to a bombarding energy in the neighborhood of the threshold.

A target of LiF, 4 micrograms per cm^2 thick (about 600 volts for 1.9-Mev protons), was bombarded with protons from the threshold to 1940 kev. The geometry was the same as in Fig. 1 except the counter was moved back until the average solid angle subtended by the paraffin was a cone of half-angle 5°. Figure 4 shows the experimental data.

Since the outside layer of paraffin seemed to be rather ineffective in contributing to the counting rate in the

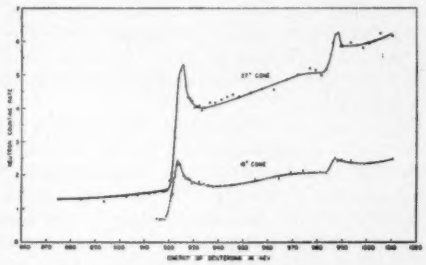

FIG. 5. Neutrons from the reaction $Be^9(d,n)^*B^{10}$ using counter half-angles of 27° and 15° and a 4-kev target.

$T^3(p,n)He^3$ reaction, the theoretical curve for the reaction was calculated using an effective angle of 4° (that is, the same "effective volume") instead of the geometrical angle of 5°. The calculated results using a 5° cone were found to be not appreciably different from the 4° curve, which is shown in Fig. 4.

Since the experimental points above 1890 kev drop faster than the theoretical curve, there is an indication that the cross section for formation of the compound nucleus is a decreasing function of energy in this interval. This is consistent with the results of Taschek and Hemmendinger at higher energies, and it lends support to the existence of a level in Be^8 near 18.90 Mev.[12]

$Be^9(d,n)^*B^{10}$

The neutrons from this reaction have been previously investigated by other methods,[13,14] and the group of

[12] Calculated with Bainbridge's 1951 *Table of Masses*.
[13] T. W. Bonner and W. M. Brubaker, Phys. Rev. **50**, 308 (1936).
[14] Evans, Malich, and Risser, Phys. Rev. **75**, 1161 (1949).

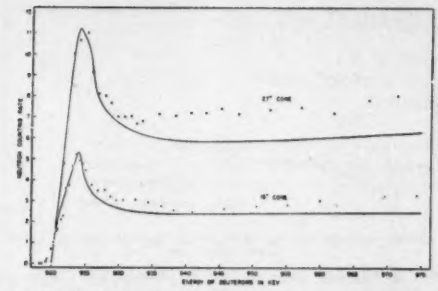

FIG. 6. "Threshold" neutrons from the reaction $Be^9(d,n)^*B^{10}$. Circles and crosses give data for counter cones of 27° and 15°. Experimental points show only "threshold" neutrons (fast neutrons have been subtracted) corrected for the cross section for formation of the compound nucleus. The curves represent the theoretical counting rates.

neutrons having a threshold at about 0.9 Mev reported.[14]

The targets were made by evaporating metallic beryllium onto silver disks Targets which were used varied in weight from 8 to 50 micrograms per cm^2.

Figure 5 gives results obtained with an 8-microgram per cm^2 target, which is about 4 kev thick for 900-kev deuterons. Curves are given for 15° and 27° cones. The data at 15° were obtained by moving the counter and moderator back from the target until the average solid angle subtended by the paraffin was a cone of half-angle 15°.

Two thresholds are indicated—one at 920-kev bombarding energy, the other at 985 kev. The calculated Q values are -752 kev and -805 kev, respectively. These thresholds indicate a doublet energy level in the residual nucleus B^{10} at 5.110 Mev and 5.163 Mev, calculated on the basis of a reaction Q-value of 4.358 Mev.[12] Since the curves exhibit sharp breaks at the thresholds, these states in B^{10} are quite narrow, probably 3 kev or less, although they usually break up into Li^6 and an alpha-particle.[15]

In order to determine how well a theoretical curve will fit the experimental data, it is necessary to correct the experimental data for the fast neutron counts and for the cross section for formation of the intermediate nucleus. The total yield was determined by the use of a flat energy response neutron detector[7] at 90° to the deuteron beam. The corrected data is given in Fig. 6.

The theoretical values shown in Fig. 6 are equal to the integrated effects over a 4-kev target of the product of the geometrical factors and the square root of the neutron energy in the center-of-mass system.

The calculated curves fall below the experimental points. This discrepancy can be explained in a number of ways. If one assumes a small percentage of p-neutrons, a very good fit can be made with the experimental points. However, the high centrifugal barrier for p-neutrons with such low energies makes it very unlikely that these neutrons make any appreciable contribution to the yield. A more likely explanation of this relatively small deviation is the difficulty in subtracting out accurately the effects of the fast neutrons.

Figure 7 gives data obtained at bombarding energies from 480 to 2130 kev. No thresholds were observed below 920 kev, although Ajzenberg,[16] using a bombarding energy of 3.4 Mev, found a group of neutrons corresponding to a level in B^{10} at 4.79 Mev. This group should have a threshold at about 525 kev. Since our data showed no threshold at this energy, a reasonable conclusion is that s-neutrons are forbidden at such low bombarding energies. s-deuterons are expected to be predominant, leaving the excited B^{11} intermediate nucleus with odd parity. If the 4.79-Mev state of B^{10} has even parity, then s-neutron emission is forbidden near threshold. Figure 7 shows that there is another

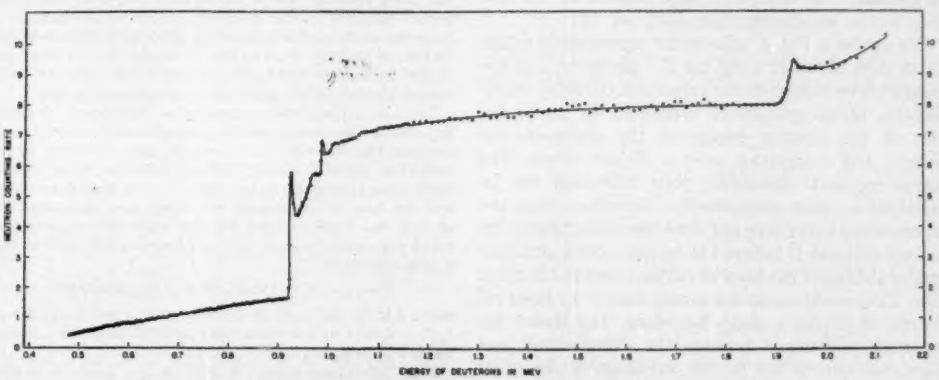

FIG. 7. Neutrons from the reaction $Be^9(d,n)^*B^{10}$ over a wide range of bombarding energies. Target thicknesses ranged from 8 to 50 micrograms per cm^2.

[15] Chao, Lauritsen, and Rasmussen, Phys. Rev. **76**, 582 (1949).
[16] Fay Ajzenberg, Phys. Rev. **82**, 45 (1951).

TABLE I. Data on the neutron "thresholds" in the reaction $Be^9(d,n)^*B^{10}$.

Be^9 threshold (kev)	Q-values (kev)	B^{10} energy levels (Mev)	Level spacing (Mev)
920±2	− 752±2	5.110	0.053
985±2	− 805±2	5.163	0.761
1916±4	−1566±4	5.924	

threshold at a bombarding energy of 1916 kev, giving a Q-value of −1566 kev and an energy level of 5.924 Mev in the B^{10} nucleus.

The 920-kev threshold was calibrated in terms of the 1882.2-kev threshold of the $Li^7(p,n)Be^7$ reaction using the mass-one beam, the 446-kev resonance in the $Li^7(p,\gamma)Be^8$ reaction, and the 485-kev resonance in the reaction $F^{19}(p,\alpha,\gamma)O^{16}$, using the mass-two beams. The respective results were 920, 919, and 920 kev.

The value of the 1916-kev threshold was measured by comparing it with the 873.5 kev $F^{19}(p,\alpha,\gamma)O^{16}$ resonance using the mass-two beam. The values of all three thresholds, their probable errors, Q-values, and corresponding B^{10} energy levels are given in Table I.

$O^{16}(d,n)F^{17}$

This reaction has been observed by Heydenburg and Inglis[17] and others, but the thin target excitation curve in the region just above threshold has not previously been investigated. A target of $Ca(OH)_2$, 85 micrograms per cm^2 thick (about 20 kev for 1.8-Mev deuterons), was prepared by evaporating metallic calcium onto a silver disk and allowing the calcium deposit to become oxidized and slaked by exposure to the air. The target was then bombarded with deuterons with energies from 1800 kev to 2077 kev and the counting rates recorded with the 27° geometry previously described. The background was relatively large because of the low cross section for this reaction.

The circles in Fig. 8 indicate the experimental values which were obtained using the 27° geometry, and the broken curve represents the values calculated by multiplication of the geometrical correction by the square root of the neutron energy in the center-of-mass system, and integration over a 20-kev target. The curves are quite dissimilar; their differences can be explained at least qualitatively. The reason that the experimental curve does not show the characteristic dip beyond the peak is believed to be incomplete oxidation and/or slaking of the layer of calcium next to the silver disk. This would cause the target density to taper off instead of having a sharp boundary. The reason for the major difference between the experimental and calculated curves lies in the variation of the cross section for the formation of the compound nucleus. The data of Heydenburg and Inglis[17] for the short-range proton yield from deuterons on O^{16} show a resonance at about 1.7 Mev, a minimum at 1.95 Mev,

[17] N. P. Heydenburg and D. R. Inglis, Phys. Rev. 73, 230 (1948).

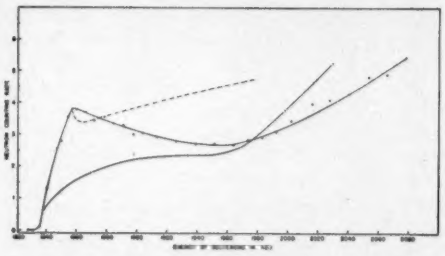

FIG. 8. Neutrons from the reaction $O^{16}(d,n)F^{17}$. Circles give experimental points using the 27° geometry and a 20-kev target of $Ca(OH)_2$. The broken curve represents the calculated counting rate assuming constant cross section for formation of the compound nucleus. The crosses give the total cross section for the reaction by measurement of positron activity of F^{17}. Units are arbitrary.

and another resonance at about 2.2 Mev. Similar resonance effects are evident in the neutron curve.

The absolute value of the threshold was determined by calibration of the beam analyzing magnet with the 873.5-kev resonance in F^{19} by means of the molecular hydrogen beam. Two runs were made, both giving a threshold value of 1836 kev. The error is estimated to be 3 kev.

When the value of 1836 kev is used for the reaction threshold, the Q-value is −1631 kev, which gives the mass of F^{17} as 17.007506±0.000018, when the values of deuteron and neutron masses given by Bainbridge[12] are used. The probable error in this mass is mostly due to the uncertainty in the masses of the neutron and the deuteron.

We are indebted to the Research Corporation and the joint ONR-AEC program for financial aid.

APPENDIX

Because of the center-of-mass velocity, the neutrons emitted just above threshold will be concentrated in a small cone in the forward direction in the laboratory system of coordinates. As the energy of the bombarding particle is increased above threshold, the cone of neutrons opens up until it reached 2π steradians. Any further increase in bombarding energy causes neutrons to be emitted throughout the entire solid angle of 4π steradians.

To derive a quantitative expression for the effect of this changing cone on the counting rate, we determine the fraction F of the neutrons that lie within the constant cone subtended by the counter as the total cone of neutrons opens up. If an isotropic distribution of neutrons in the center-of-mass system is assumed and the laws of conservation of energy and momentum are applied, the fraction F for the case when the center-of-mass velocity is greater than the neutron velocity in the center-of-mass system is given by

$$F=1-\cos\theta[1-(M_1M_4/M_3M_3)(E_1/\Delta E_1)\sin^2\theta]^{\frac{1}{2}},$$

where θ is the half-angle of the counter cone and the subscripts 1, 2, 3, 4 refer to the bombarding particle, bombarded nucleus, residual nucleus, and emitted particle.

When the center-of-mass velocity is less than the neutron velocity in the center-of-mass system, F is given by

$$F=\frac{1}{2}\left[1+\left(\frac{M_1M_4}{M_2M_3}\frac{E_1}{\Delta E_1}\right)^{\frac{1}{2}}\sin^2\theta-\cos\theta\left(1-\frac{M_1M_4}{M_2M_3}\frac{E_1}{\Delta E_1}\sin^2\theta\right)^{\frac{1}{2}}\right].$$

When the two velocities are equal, both forms reduce to

$$F=\sin^2\theta.$$

The Disintegration Scheme of Au^{199}

P. M. Sherk and R. D. Hill
Physics Department, University of Illinois, Urbana, Illinois*
(Received May 28, 1951)

The disintegration of 3.3-day Au^{199} has been investigated using beta-ray spectrometers and counting techniques. The beta-ray spectrum was observed to be complex. Determinations were made of the conversion electron and γ-ray intensities of three γ-transitions of 50, 159, and 209 kev. A consistent disintegration scheme is given.

INTRODUCTION

THE 3.3-day beta-activity of Au^{199} was discovered by McMillan, Kamen, and Ruben.[1] In 1948, Mandeville, Scherb, and Keighton[2] reported that the beta-spectrum was simple, with an upper energy end point of 380 kev. In 1949, Meem and Maienschein[3] concluded that the beta-spectrum was simple and had an end point of 320 kev. They also observed γ-rays of 140 and 214 kev. In 1949, Beach, Peacock, and Wilkinson[4] investigated the beta- and γ-ray emission of Au^{199}. They observed a simple beta-spectrum of 320-kev end point and γ-rays corresponding to energies of 24, 52, 76, 154, 206, and 230 kev. More recent work[5] has seemed to indicate only the existence of 50-, 159-, and 209-kev γ-rays. Because of this and the interest attached to the disintegration scheme of Au^{199} in evaluating the neutron capture cross section[6] of Au^{198}, the present investigation was undertaken.

SPECTROMETER MEASUREMENTS

A. Electron Spectrum

The combined beta- and conversion electron spectrum was observed with a 180° variable field spectrometer of approximately 1.4 percent resolution. The detector was a Geiger counter having an 0.12 mg/cm² Nylon window. The source was ~0.01 mg/cm² thick and was mounted on a conducting plastic backing of 0.025 mg/cm² thickness. Sources were prepared by chemically separating gold from platinum metal which had been irradiated by neutrons in the Oak Ridge pile. The spectrum, after correction for known factors, is shown in Figs. 1 and 2.

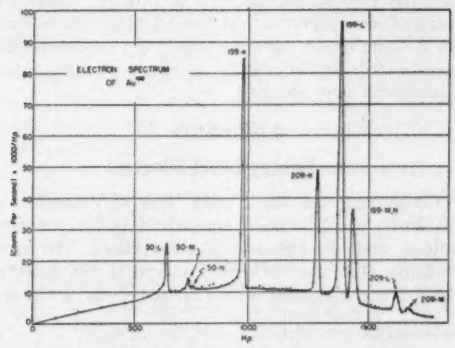

FIG. 1. Electron spectrum of Au^{199}.

Fermi plots of the beta-spectrum are shown in Figs. 3 and 4. Analysis of these plots, assuming as a first approximation allowed-shape spectra, indicates the existence of three components with upper energy end points of 250, 300, and 470 kev. Errors up to 25 kev would be possible for these energy values. The existence of the highest energy component is definite and the value of its upper energy limit is consistent with a transition to a level 159 kev below that reached by the main beta-ray component. The existence of the lowest energy component is less certain. Its existence is again supported by the value of its upper energy limit being 50 kev less than the main component.

The conversion lines corresponding to γ-transitions of 50, 159, and 209 kev confirm the experimental work of earlier observers.[4,5] The intensities of the lines were obtained by decomposing them from the beta-spectrum and then integrating the counting rates with respect to $H\rho$. These intensities are listed in Table I.

B. Photoelectron Spectrum

This spectrum was measured using a lens spectrometer of approximately 1 percent transmission and 3

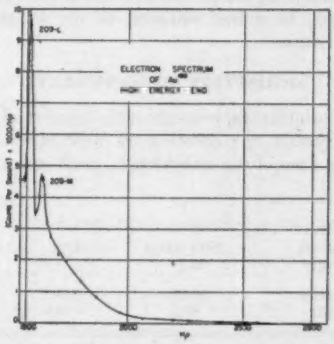

FIG. 2. Electron spectrum of Au^{199}: high energy end.

* Assisted in part by the joint program of the ONR and AEC.
[1] McMillan, Kamen, and Ruben, Phys. Rev. 52, 375 (1937).
[2] Mandeville, Scherb, and Keighton, Phys. Rev. 74, 601 (1948).
[3] J. L. Meem and F. Maienschein, Phys. Rev. 76, 328 (1949).
[4] Beach, Peacock, and Wilkinson, Phys. Rev. 76, 1585 (1949).
[5] R. D. Hill, Phys. Rev. 79, 413 (1950).
[6] R. D. Hill and J. W. Mihelich, Phys. Rev. 79, 275 (1950).

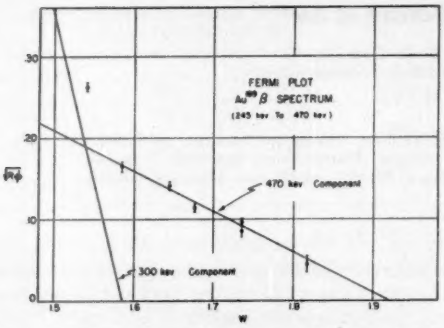

FIG. 3. Fermi plot of Au^{199} beta-spectrum (245 kev to 470 kev). [R is the normalized counting rate and $\phi=(\eta^3F)^{-1}$.]

percent resolution. In order to resolve the photoelectron lines from the 159- and 209-kev γ-rays to the greatest extent possible a tin radiator was used. The spectrum obtained from a 15.7 mg/cm² tin radiator, with no counting rate corrections applied, is shown in Fig. 5. The lines marked K_α-L and K_β-L arise from the conversion of K x-rays of mercury in the L-shell of tin. The small peak at $H\rho=1370$ is due to a trace of source material deposited on the outside of the container. This peak is the strong 159-L conversion line, and corrections for the presence of the unshielded Au^{199} were made on the basis of its intensity.

The peak heights of the photoelectron lines were measured and corrected for known factors such as background, decay of source, and window absorption. The ratio of the peak heights of the K lines of the 159- and 209-kev γ-rays was determined to be 6.1. Using Richardson's thick target formula,[7] this ratio was then used to calculate the true ratio of the 159-kev γ-ray intensity to the 209-kev γ-ray intensity. The final value obtained was 4.2. Gamma-ray intensities are shown in Table I.

No trace of a 230-kev γ-ray, such as reported by Beach *et al.*[4] was found. The strong line interpreted by these workers as the K line of a 230-kev γ-ray can be attributed, for a lead radiator, to the L line of the 159-kev γ-ray.

ABSORPTION MEASUREMENTS

Using scintillation counters with 2-mm thick sodium iodide crystals, γ-γ-coincidences were observed. The resolving time of the coincidence circuit was 1.2×10^{-7} second. Both counters were shielded with enough aluminum so as to prevent the passage of 500-kev electrons.

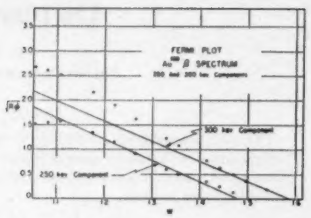

FIG. 4. Fermi plot of Au^{199} beta-spectrum (250- and 300-kev components). [R is the normalized counting rate and $\phi=(\eta^3F)^{-1}$.]

An absorption curve of the γ-rays in coincidence was obtained by introducing copper absorbers in front of one counter. The curve showed that a soft γ-ray component of ~50 kev was in coincidence with an x-ray of ~70 kev and a γ-ray of ~160 kev. Copper absorbers placed in front of both counters showed that there was no appreciable coincidence rate between γ-rays ~200 kev.

The intensity of the 50-kev γ-ray relative to the 159-kev γ-ray was estimated by comparing coincidence and singles rates. With no absorber, the coincidence rate was 0.059 count per second, as compared with a singles rate of 276 counts per second. Using the solid angle and efficiency factors of the crystals, it was then estimated that the 159-kev γ-ray was ~120 times more intense than the 50-kev γ-ray.

This result assumes that the lifetime of the level intermediate between the 50- and 159-kev γ-transitions is shortlived compared with the resolving time of the coincidence circuit. This point was verified by showing that the γ-γ-coincidences were as prompt, within the limits of our experiment, as the β-γ-coincidences from Au^{198}. Coincidences between beta- and γ-rays were also investigated, but no significant results of their interrelationship were obtained.

DISCUSSION

A. Energy Level Diagram

Considering the three main lines of evidence: γ-transition energy values, component beta-ray energy values, and γ-γ-coincidence observations, the most probable Hg^{199} level scheme involved in the decay of Au^{199} is one consisting of two excited levels of 159 and

TABLE I. Radiation intensities.

Radiation	(250+300)β	470β	50γ	159γ	209γ	50-L	50-M
Intensity	96.2	3.8	0.4	47.9	11.4	2.46	0.5
Radiation	50-N	159-K	159-L	159-M, N	209-K	209-L	209-M, N
Intensity	0.15	9.0	15.0	5.2	6.14	1.14	0.3

[7] H. O. W. Richardson, Proc. Phys. Soc. (London) **63A**, 234 (1950).

209 kev above the ground state. This scheme is shown in Fig. 6. It is found to lead to a consistent interpretation of the intensities of all transitions and also to assignments of spin values for the levels which are consistent with interval conversion and radiation theory.

B. Radiation Intensities

The observed radiation intensities are shown in Table I. The intensities have been normalized so that the total beta-ray intensity is 100. The γ-ray and conversion electron intensities have been related to each other and to the beta-ray intensities by assuming that the 159- and 209-kev total transition intensities equal the sum of the 250- and 300-kev beta-intensities, i.e., on the basis of the level diagram in Fig. 6.

C. Conversion Coefficients

The conversion coefficients calculated from the above intensity data are shown in Table II. Limits of errors involved in these coefficients were arrived at after

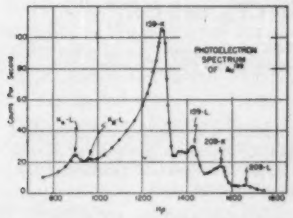

FIG. 5. Photoelectron spectrum of Au^{199}.

trying a number of decompositions of beta-spectra and conversion lines, as well as after considering the inaccuracies arising from the observations alone. The different upper and lower limits arose primarily from the decomposition process. For example, the lowest intensity limits of the lines were obtained when the continuous beta-ray spectrum was drawn as far as feasible up into the bases of the lines.

Although the divergence of the experimental conversion coefficients from the theoretical value is admittedly large, the experimental values favor the electric 2^2 assignment for the 159-kev transition, and, to be in line with this, an assignment of either 2^1 magnetic or 2^4 electric for the 209-kev transition. These assignments are also supported by a consideration of the N_K/N_L ratios for these two transitions. Although the present state of the theory does not seem to warrant an accurate comparison with experimental N_K/N_L ratios, it would appear that a value of 0.6 for the 159-kev transition is in better agreement with one of ~ 2 for electric 2^2 than with one of ~ 8 for electric 2^1. And for the 209-kev transition, the experimental value of $N_K/N_L = 5.4$ agrees better with a value ~ 12 for

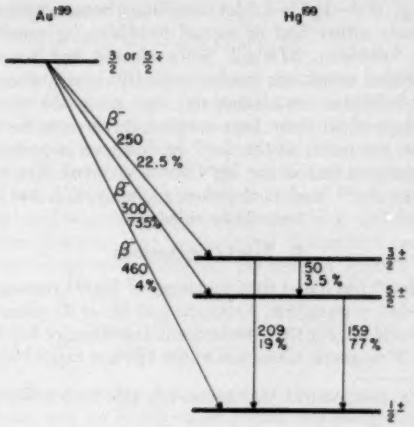

FIG. 6. Proposed disintegration scheme of Au^{199}.

magnetic 2^1 than with 0.7 or less for either electric 2^3 or 2^4.

D. Spin and Parity Assignments

The ground-state spin of Hg^{199} is known[8] to be 1/2. Thus considering the multipolarities assigned to the transitions, the 159-kev excited level must have spin 5/2, and the 209-kev excited level must have spin 3/2, both levels being of the same parity as the ground level.

On this basis, the 50-kev transition is magnetic 2^1. If the L conversion coefficient is increased from the experimental value of 6 to ~ 10, so as to be in line with the probable values of the other K conversion coefficients, it would not seem to be inconsistent with one of ~ 10 for the theoretical[9] L_I conversion coefficient.

The experimental branching ratio of the 209- to 50-kev γ-ray transitions is 28. The theoretical ratio, based on a $(2l+1)$ energy dependence, is 73, which is in reasonable agreement with experiment.

The logft values of 6.3 and 6.0 for the 250 and 300-kev beta-components indicate either allowed or first-forbidden transitions. The values of log$ft = 7.8$ or

TABLE II. Conversion coefficients.

Transition (kev)	50	159	209
K-conversion coeff. (expt.)	—	$0.19+0.15-0.06$	$0.54+0.8-0.19$
K-conversion coeff. (theor.)	—	0.11, 2^1 el[a] 0.30, 2^2 el[a]	1.15, 2^1 mag[a] 0.42, 2^3 el[b] 1.18, 2^4 el[b]
L-conversion coeff. (expt.)	6	0.31	0.10

[a] J. R. Reitz, Phys. Rev. **77**, 10 (1950).
[b] Rose, Goertzel, Spinrad, Harr, and Strong, Phys. Rev. **76**, 184(A) (1949); **83**, 79 (1951).

[8] Schuler *et al.*, Z. Physik **72**, 423 (1931); **74**, 631 (1932).
[9] Gellman, Griffith, and Stanley, Phys. Rev. **80**, 866 (1950).

of $\log[(W_0^2-1)ft]=8.5$ for the 470-kev beta-component indicate either first or second forbidden, or possibly first forbidden, $\Delta I=\pm 2$. Since allowed and second-forbidden transitions involve no parity change, whereas first-forbidden transitions do, and since the parity changes of all three beta-components have to be the same, the parity of the Au^{199} ground level is probably opposite to that of the Hg^{199} levels involved. The spin of the Au^{199} level is therefore probably 3/2, but the possibility of 5/2 cannot be ruled out.

E. Final Conclusions

Hole[10] has found that the decay of Hg^{199m} contains a 159-kev γ-transition. From the half-life of 43 minutes, it would appear that the isomeric transition of 370 kev is a 2^4 magnetic transition to the 159-kev excited level. This would identify the spin of the isomeric level as 13/2 and the parity as opposite to that of the lower levels.

Another point concerns the neutron capture cross section of Au^{198}. If the intensity of the 159-K line is accepted as being present to the extent of 9 percent of the Au^{199} decays, then the cross section is estimated to be 3.8×10^4 barns.

In conclusion, it is significant to point out that if the ground state of Hg^{199} is $p_{1/2}$, as is suggested by Mayer's shell structure model,[11] then the 159-, 209-, and 529-kev excited levels are $f_{5/2}$, $p_{3/2}$, and $i_{13/2}$, respectively, all levels being consistently predicted by the model.

We are indebted to Dr. F. R. Metzger for the use of scintillation counting equipment and for his interest in the problem.

[10] N. Hole, Arkiv. f. Mat. Astron. Fys. **36A**, No. 9 (1948).

[11] M. G. Mayer, Phys. Rev. **78**, 16 (1950).

PHYSICAL REVIEW VOLUME 83, NUMBER 6 SEPTEMBER 15, 1951

Neutron Diffraction by the Gases N_2, CF_4, and CH_4*

N. Z. Alcock† and D. G. Hurst
National Research Council of Canada, Chalk River Laboratory, Chalk River, Ontario

(Received June 4, 1951)

Neutron diffraction patterns for the gases nitrogen, carbon tetrafluoride, and methane are given for a neutron wavelength of 1.063A. It is found that the coherent scattering cross sections of nitrogen and fluorine are nearly equal to the total cross sections, and that the C—F bond length in carbon tetrafluoride is 1.33A. The error in a semiclassical form of the differential scattering cross section is discussed.

I. INTRODUCTION

NEUTRON diffraction by gases may be used to determine nuclear scattering cross sections and details of molecular structure. In the present paper diffraction patterns are given for nitrogen, carbon tetrafluoride, and methane. From these the bond lengths in carbon tetrafluoride, and the ratio of coherent to total scattering for nitrogen and fluorine are derived.

The present results, together with the patterns for deuterium,[1] oxygen and carbon dioxide,[2] are the only published diffraction patterns for gases. The deuterium measurements were analyzed according to the complete quantum-mechanical formulation.[3–5] Such an approach cannot be used for every gas because in many cases the necessary formulas have not been derived or because of the large amount of computation required even when the formulas are known. This theoretical complexity and the experimental requirement of large neutron fluxes are probably the reasons why the subject has not been developed previously.

The proof that a semiclassical approximation is often applicable[3,4] greatly simplifies the equations and removes one of the obstacles to structure determinations. The error in this approximation is examined below in the light of experimental and theoretical results for nitrogen, and an elementary application is made to the measurement of bond lengths in carbon tetrafluoride.

II. THEORY

In the quantum-mechanical treatment of the scattering of monoenergetic neutrons by molecules of a gas[3,4] a differential cross section is calculated for each possible molecular transition. The formulas given in reference (3) are for deuterium in the center-of-mass system, but Spiers[5,1] has derived the transformation to the laboratory system for a maxwellian distribution of molecular velocities. Similar formulas could be applied to nitrogen because 99.2 percent of the molecules are $N^{14}N^{14}$, the same type of molecule as D_2, but the greater mass and size of the nitrogen molecule would increase the amount of computation for the

* The results published in this paper were given at the Harwell Nuclear Physics Conference, Oxford, September, 1950, and are summarized in the Report on that Conference—Report A.E.R.E. G/M 68, p. 105 (September, 1950), unpublished.

† Now with Isotope Products Ltd., Oakville, Ontario.

[1] D. G. Hurst and N. Z. Alcock, Can. J. Phys. **29**, 36 (1951).

[2] N. Z. Alcock and D. G. Hurst, Phys. Rev. **75**, 1609 (1949).

[3] M. Hamermesh and J. Schwinger, Phys. Rev. **69**, 145 (1946).

[4] J. A. Spiers, Phys. Rev. **75**, 1765 (1949).

[5] J. A. Spiers, National Research Council (Canada) Report CRT-417 (April, 1949). (N.R.C. No. 1940), unpublished.

following reasons. Rotational transitions, which are the only type possible with the neutron energies used in these experiments, involve transfer of angular momentum between the neutron and molecule, the important transitions being those in which the change in rotational quantum number is small. This can be interpreted in terms of classical impact parameters, the principal limitation on the change in angular momentum corresponding to the requirement that the neutron hit the molecule; for example, the maximum change in the rotational quantum number for 90° scattering is given roughly by 2π (nuclear separation/wavelength in the center-of-mass system) which follows from equating the angular momentum change to the angular momentum of the neutron when its impact parameter equals the nuclear separation. From this it can be seen that the larger nuclear separation (1.11A compared to 0.75A) and the smaller neutron wavelength in the center-of-mass system for nitrogen as compared to deuterium increase the possible change in quantum number and consequently the number of transitions from each initial state. Because nitrogen is heavier and larger, the spacing between the rotational energy levels is less and many more initial states are populated at the same temperature. When, as was the case experimentally, the nitrogen is at a higher temperature the number of initial states is still larger. The combination of more initial states and more transitions from each initial state gives about ten times as many transitions to be computed for nitrogen at room temperature as for deuterium at 77.4°K[1] with 0.072-ev neutrons. The need of a simpler method of analysis is thus apparent for nitrogen. For other types of molecule the exact scattering formulas have not yet been given explicitly. However, earlier measurements,[2] were found to agree reasonably with a simple formula discussed in the next paragraph.

In the semiclassical treatment of coherent scattering of x-rays and electrons by molecules[6] the molecule is considered to have a definite orientation and the wavelets scattered by the constituent atoms are added in the direction of observation. The intensity is then calculated and is averaged over all molecular orientations. The semiclassical treatment of neutron scattering is similar,[2,5] but the calculation is performed in the center-of-mass system and a transformation must be made to the laboratory system, taking into account the thermal motions of the molecules. For heavy molecules this transformation is a small correction. The intensity of coherent x-ray scattering through an angle φ is proportional to

$$I(\varphi)=\sum_j \sum_i f_i f_j \sin x_{ij}/x_{ij},$$

where i and j refer to atoms in the molecule, f_i is the scattering amplitude of the ith atom, and the sum is taken over all values of i and j, including $i=j$. The quantities x_{ij} are given by

$$x_{ij}=(4\pi r_{ij}/\lambda)\sin(\varphi/2),$$

where r_{ij} is the distance between the atoms i and j, and λ is the wavelength. A similar formula applies for neutron scattering in the center-of-mass system, but because of the effect of nuclear spin, which occurs specifically with neutrons, the scattering amplitude used is the coherent scattering amplitude[7] if $i\neq j$ and is the total scattering amplitude if $i=j$.

More precisely, the semiclassical differential cross section for neutron scattering through an angle θ in the center-of-mass system is

$$\sigma(\theta)=\frac{1}{4\pi}\left(\frac{M}{M+1}\right)^2\sum_i\sum_j(\sigma_i\sigma_j)^{\frac{1}{2}}\frac{\sin x_{ij}}{x_{ij}}, \qquad (1)$$

where M is the ratio of the masses of the molecule and neutron, and σ_i is the total bound scattering cross section of the nucleus i if $i=j$, otherwise it is the coherent cross section. In the calculation of x_{ij} the wavelength is that of the incident neutron in the center-of-mass system. This general form is due to Pope;[8] the special case of diatomic molecules having like nuclei with spin 1 has already been given[6] and is discussed in further detail in the Appendix.

The discussion in the preceding paragraphs has ignored the effect of molecular vibration which reduces the scattering at large angles. For x-ray and electron diffraction[9] the extent of the electron cloud and the angular dependence of Rutherford scattering cause the scattering to decrease so steeply with increasing angle as to make the reduction due to vibration very difficult to measure. For neutrons, however, the nuclei act as points and would scatter spherically except for the effect of vibration. The reduction due to vibration is then more in evidence, and the approximation involved in the assumption of a rigid molecule requires investigation. In many molecules only the ground-state vibration occurs at room temperature and the energy of the neutrons (0.072 ev for the present series of measurements) is insufficient to cause transitions to higher vibrational levels. The nuclear scattering then has the structure factor of the probability density of the ground-state vibration. When the neutrons have sufficient energy to cause vibrational transitions, or when more than the ground-state vibration is present, the effect is more complicated.

Deuterium and nitrogen belong to the simpler case and calculations have been made for these molecules. The result for deuterium has been given,[1] and the modification to fit nitrogen is straightforward and was applied to the measurements reported in this paper.

Carbon tetrafluoride is more complicated because one of the four fundamental vibration frequencies corre-

[6] M. H. Pirenne, *The Diffraction of X-rays and Electrons by Free Molecules* (Cambridge University Press, London, 1946).

[7] E. O. Wollan and C. G. Shull, Phys. Rev. 73, 830 (1948).

[8] N. K. Pope (unpublished).

[9] R. W. James, *The Optical Principles of the Diffraction of X-rays* (G. Bell & Sons Ltd., London, 1948), Chap. IX.

TABLE I. Corrected experimental intensities with standard deviations.

Scattering gas	Pressure (atmos)	Scattering angle 7.7°	15.7°	23.7°	31.7°	39.7°	47.7°	55.7°	63.7°	71.7°	79.7°	87.7°
N_2	30	300.0 ±10.0	299.2 ±7.6	210.8 ±4.4	161.2 ±4.0	141.2 ±3.6	154.8 ±4.0	163.2 ±4.8	173.6 ±4.4	176.0 ±4.0	174.0 ±5.2	161.6 ±4.8
CF_4	31	602.4 ±12.0	303.2 ±7.6	134.4 ±4.0	162.0 ±3.6	173.2 ±2.8	164.0 ±2.8	202.0 ±3.2	230.8 ±3.6	200.0 ±3.2	150.0 ±2.8	134.0 ±2.4
CH_4	14.7	1043 ±16	1068 ±15	984 ±13	940 ±12	872 ±10	764 ±10	674 ±8	584 ±9	490 ±8	434 ±6	390 ±5
CH_4	5.0	398 ±12	397 ±10	409 ±9	384 ±9	334 ±7	308 ±5	274 ±10	227 ±5	206 ±6	173 ±5	152 ±4

sponds to 0.054 ev which is comparable to thermal energies. Consequently there is an appreciable population in the second level at room temperature, and moreover neutrons of 0.072 ev can induce transitions in this mode. As an approximation to the scattering the difference caused by these deviations from the simple case was neglected and it was assumed that the vibration of each nucleus could be represented by the ground state of a three-dimensional harmonic oscillator. The radial density of this state is $\exp[-(r/a)^2]$ where a is $(\hbar/m\omega)^{\frac{1}{2}}$, m being the mass of the oscillator and $\hbar\omega$ the separation of the energy levels. The intensity of elastic scattering is proportional to $\exp[-8(\pi a/\lambda)^2 \sin^2(\varphi/2)]$ where φ is the scattering angle. The observed pattern of CF_4 was about 0.93 of the semiclassical curve at 90°. This factor was ascribed to vibration and equated to the intensity ratio just given, with the result that $a=0.045$A, a reasonable value for the mean amplitude of the modes of the CF_4 molecule. In nitrogen the vibration changed the scattering by only about 0.7 percent at 90°; the larger effect in CF_4 is due not to a larger amplitude of vibration, but to the fact that the vibration is three-dimensional instead of linear as in nitrogen.

Another departure from the formula for an isolated rigid molecule occurs because the measurements were made with gases at high pressure. Under these conditions the scattering pattern shows evidence of intermolecular interference. Debye,[10] discussing the corresponding phenomenon in x-ray scattering, named it "the outer effect" and gave a formula for diatomic molecules. This has been used for nitrogen, and has been modified for polyatomic molecules and applied to CF_4.

III. EXPERIMENTAL PROCEDURE

The spectrometer, scattering chamber, and operating procedure have been previously described.[1] The measurements on N_2, CF_4, and CH_4 were made immediately after those on D_2 with similar experimental conditions except that the gases were at room temperature (23°C). The average wavelength of the neutrons was 1.063A with a spread of about ±0.05A. The spectrometer was operated automatically, counts being recorded every 8° through the angular range 7.7° to 87.7°. As with deuterium, the counts from a primary neutron flux monitor were recorded during the time taken for one thousand counts to accumulate in the spectrometer counter, though on some background runs a one hundred count setting was used.

Bottled compressed gases were used for the measurements with no additional purification, except that nitrogen was passed through a dry ice trap to remove traces of water vapor. Samples of the gases were drawn from the gas cell and analyzed in a mass spectrometer. The gas pressures remained constant during the measurements, the slow leak mentioned in connection with the deuterium having been repaired.

The reduction of the measured angular distributions for comparison with theory was carried out as for deuterium:[1] (i) background, which was measured with the cell evacuated, was separated experimentally into fast and slow neutron components, and each treated separately, the fast component being subtracted directly from the total intensity, the slow component being subtracted from the total intensity after correction for loss in transmission through the scattering gas; (ii) the geometry of the scattering system was taken into account by dividing the intensity at each angle by the effective scattering volume; (iii) double scattering was allowed for after the manner described for D_2; the angle whose intensity corresponds to the average intensity due to single scattering was found for N_2 and CF_4 by a numerical integration of the semiclassical

TABLE II. Experimental details.

Gas	Pressure (atmos)	Analysis[a]	Background (percent of meas. intensity)	Double scattering correction
N_2	30	Impurities <0.2 percent	50% at 7.7° 16% at 87.7°	2% to 4%
CF_4	31	0.2 percent CF_3H Trace of water vapor and atmospheric gases	34% at 7.7° 18% at 87.7°	1% to 4%
CH_4	14.7	Impurities <1	23% at 7.7° 7% at 87.7°	3% to 11%
	5.0		44% at 7.7° 16% at 87.7°	2% to 5%

[a] See reference 11.

[10] P. Debye, Physik. Z. 28, 135 (1927)

angular distribution over 4π-steradians, for CH_4 by integration of an estimated pattern based on the experimental distribution.

IV. EXPERIMENTAL RESULTS

The corrected experimental intensities (expressed as counts per 10^4 monitor counts per cubic inch of scattering gas) are given in Table I. Other experimental information,[11] including some background and double scattering corrections to indicate their magnitude, are given in Table II. The intensities are plotted on Figs. 1 to 3 as functions of the scattering angle.

In Fig. 1, which contains the nitrogen results, the experimental points are shown fitted at 23.7° to a semiclassical diffraction pattern. This is the broken line marked "Theory—1st approximation" and it has been transformed from the center-of-mass coordinates and corrected for thermal motion of the molecules. The

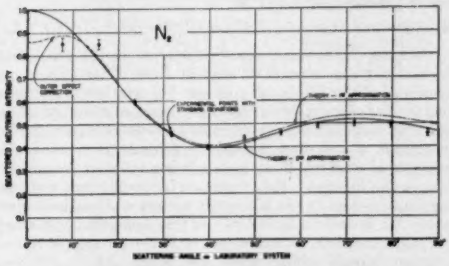

FIG. 1. The scattering of neutrons of wavelength 1.063A from nitrogen at 23°C and 30 atmos pressure. The curves shown are for spin-independent semiclassical scattering uncorrected (1st approximation), and corrected for vibration and deviations from the exact spin-independent formula (2nd approximation). At small angles the calculated effect of intermolecular diffraction is shown dotted. The experimental points are normalized so that the point at 23.7° lies on the curve.

curve marked "Theory—2nd approximation" has been corrected for the error in the semiclassical approximation according to the calculations in the Appendix and also for the effect of molecular vibration. At small angles the dotted line shows the "outer effect." The theoretical curves were calculated on the assumption that the coherent scattering cross section equals the total cross section, i.e., $\sigma_{coh}/\sigma_T=1$. The molecular parameters used were 1.11A for the internuclear distance and 1.78A for the molecular (collision) radius.

Figure 2 shows the carbon tetrafluoride results fitted in the region of small angles to a semiclassical formula. The coherent cross section of fluorine was assumed to equal the total bound cross section which was taken as 4.1 barns, and the bound cross section of carbon was taken as 5.52 barns. The curve as drawn is for a carbon-fluorine distance of 1.33A. The "outer effect" was calculated for a molecular radius of 2A.

[11] We are indebted to the Chemical Control Laboratory, Chalk River, for the analyses.

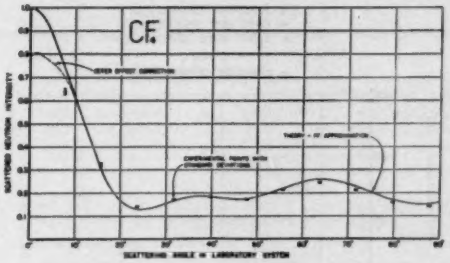

FIG. 2. The scattering of neutrons of wavelength 1.063A from carbon tetrafluoride at 23°C and 31 atmos pressure fitted to a semiclassical equation for spin-independent scattering. The dotted line is the calculated effect of intermolecular diffraction. A value of 1.33A was used for the carbon-fluorine bond length.

The experimental points for methane are plotted in Fig. 3 where the high pressure point for 7.7° has been fitted to unity and the low pressure points have been normalized for best average fit to the high pressure run.

V. DISCUSSION

(a) Nitrogen

The fit of the points to the theoretical curves shows that the 2nd approximation is quite good. Besides the value $\sigma_{coh}/\sigma_T=1$ for which the curve is plotted, other values of this ratio were tried, and it is estimated that the ratio of coherent to total bound scattering cross section lies between 0.9 and 1.0. This was at variance with previous measurements but is in agreement with the most recent results.[12]

(b) Carbon Tetrafluoride

The general run of the experimental points is in agreement with the semiclassical equation. There is a decrease of the experimental values relative to the theoretical curve at large angles, and this is attributed

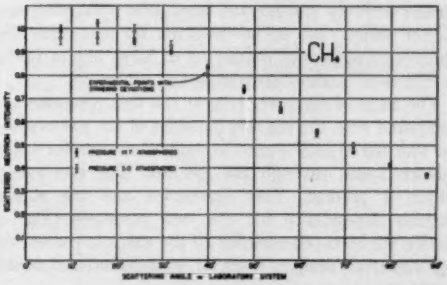

FIG. 3. The scattering of neutrons of wavelength 1.063A from methane at 23°C for 14.7 atmos and 5.0 atmos pressure. The high pressure point at 7.7° has been fitted to unity and the low pressure results normalized for best average fit.

[12] G. H. Goldschmidt and D. G. Hurst, Phys. Rev. 83, 88 (1951). C. G. Shull and E. O. Wollan, Phys. Rev. 81, 527 (1951). A.W Reynolds and G. W. Johnson, Phys. Rev. 82, 344 (1951).

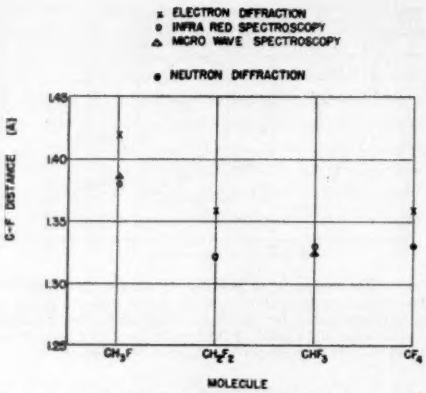

FIG. 4. The carbon-fluorine bond lengths in the fluoro-methanes as observed by various methods (see reference 13).

to vibration and to the approximate nature of the theoretical formula. The simple treatment of vibration, outlined in Sec. II, in which the decrease at 90° was taken as 7 percent (Fig. 2), shows that vibration can account for the major part of this difference.

The carbon-fluorine bond length of 1.33A on which the curve of Fig. 2 is based is smaller than the generally accepted value of this quantity as found by electron diffraction. A comparison of bond lengths in the fluoro-methanes is given in Fig. 4.[13] It will be seen that electron diffraction has given consistently greater bond lengths than other methods and that the present result is in agreement with an extrapolation of the spectroscopic results.

The "outer effect" corrections for both CF_4 and N_2 give the general trend of the scattering at small angles, but they do not seem to fit in detail.

(c) Methane

Because slow neutron scattering by hydrogen is almost entirely incoherent, negligible diffraction and "outer effect" are to be expected for methane. The observed decrease of scattering at large angles is due to effects of inelastic scattering and vibration.

The ratio of the scattering at the two pressures was compared with the relative densities of the gas as given by Van der Waals' equation with allowance for transmission losses through the gas cell. The two agreed within 1 percent. This agreement and the similar angular dependence for the two pressures (Fig. 3) justify the methods used for all the gases to correct the experimental counting rates for background and double scattering.

VI. CONCLUSION

It has been shown that measurements of the differential cross sections of gases for monoenergetic neutrons can be analyzed to give coherent cross sections and information about molecular structures. The semiclassical formulas apply to many gases with sufficient accuracy to be used for such analyses.

We thank the Minnesota Mining and Manufacturing Company for supplying the carbon tetrafluoride and an infrared spectrographic analysis of impurities. We are indebted to Dr. N. K. Pope for helpful discussions, and to Mr. R. Semple for computing assistance.

APPENDIX

The semiclassical equation for gas scattering is very simple and a knowledge of its error is of interest because of the complexity of the exact formulas. In this Appendix an approximate expression is derived for the error in the special case of rigid diatomic molecules with like nuclei of spin 1 to which the formulas for deuterium, suitably modified for the mass and size of the molecule, are applicable. The cross section for scattering of a neutron through an angle φ in the laboratory system by such a molecule which undergoes a rotational transition in which the rotational quantum number changes from J to J' is

$$\sigma_{JJ'}(\varphi)=\mu_{JJ'}X(\varphi)(p/p_0)\Sigma_L(2L+1)(2J'+1)C_{LJJ'}j_L^2(kr). \quad (A.1)$$

This is Eq. (35) of Spiers' report[5] with some changes in notation. The quantity $\mu_{JJ'}$ depends on whether J and J' are even or odd according to Table III; in this table σ_T is the total bound scattering cross section and σ_{coh} is the coherent bound cross section of the nuclei, M is the ratio of the mass of the molecule to the mass of the neutron. p_0 and p are respectively the neutron momentum in the center-of-mass coordinate system before and after the collision. $X(\varphi)$ is the function which transforms from the center-of-mass coordinate system to the laboratory system and has been given exactly for deuterium by Spiers;[5] as this Appendix applies only if $M\gg1$, a sufficient approximation is $X(\varphi)=1+2p_0/(Mp)\cos\varphi$. L is an integer which takes the values $J+J'$, $J+J'-2$, $\cdots|J-J'|$. $C_{LJJ'}=\frac{1}{2}\int_{-1}^{1}P_L(z)P_J(z)P_{J'}(z)dz$ where $P_n(z)$ is the Legendre function of degree n. $j_L(x)=((\pi/2x))^{\frac{1}{2}}J_{L+\frac{1}{2}}(x)$, where $J_{L+\frac{1}{2}}(x)$ is the bessel function of order $L+\frac{1}{2}$, r is the internuclear distance in the molecule, and $k=(\pi/h)(p_0^2+p^2-2pp_0\cos\theta)^{\frac{1}{2}}$ where h is Planck's constant and θ is the scattering angle in the center-of-mass system.

The differential cross section $\sigma(\varphi)$ is the sum of all the cross sections $\sigma_{JJ'}(\varphi)$ and the computation can involve many terms. Spiers[5] showed that the semiclassical result is obtained if the energy change in the transition $J\to J'$ is ignored, i.e., if p is put equal to p_0, for then

$$\sigma_{J,\alpha}^*(\varphi)=\Sigma_{J'}{}^{\alpha}\sigma_{JJ'}{}^*(\varphi)=\mu_{J,\alpha}X^2(\varphi)\tfrac{1}{2}\{1\pm\sin2k^*r/(2k^*r)\} \quad (A.2)$$

where an asterisk is used to denote a quantity which has been calculated with $p=p_0$. The sum is taken either for $J-J'$ even, corresponding to the plus sign inside the brackets, or for $J-J'$ odd, corresponding to the negative sign, the symbol α being used to indicate this partition of the values of J'. The differential cross section is the sum over J of these $\sigma_{J,\alpha}{}^*(\varphi)$. At room temperature two-thirds of the molecules have even values of J and the differential cross section is

$$\begin{aligned}\sigma^*(\varphi)&=X^2(\varphi)\tfrac{1}{2}\{(\tfrac{2}{3}\mu_{oo}+\tfrac{1}{3}\mu_{pp})(1+\sin2k^*r/(2k^*r))\\&\quad+(\tfrac{2}{3}\mu_{op}+\tfrac{1}{3}\mu_{po})(1-\sin2k^*r/(2k^*r))\}\\&=X^2(\varphi)[M/(M+1)]^2\{\sigma_T+\sigma_{coh}\sin2k^*r/(2k^*r)\}/(2\pi). \quad (A.3)\end{aligned}$$

The semiclassical differential cross section is calculated on the basis of elastic scattering and is sometimes assumed to represent a physical process of coherent scattering without change in wavelength.[6] A study of the contributions from (A.1) to the curves of Fig. 3, however, shows that although at angles less than 30° essentially only elastic scattering contributes, between 45° and 80° most of the scattering is associated with a transfer of energy resulting in transitions to $J'=J\pm2$. These changes in

[13] H. J. Bernstein and G. Herzberg, J. Chem. Phys. 16, 30 (1948). Gilliam, Edwards, and Gordy, Phys. Rev. 75, 1014 (1949).

energy may not be negligible in neutron diffraction, even when (A.3) is a good approximation to the differential cross section.

The difference between $\sigma(\varphi)$ and $\sigma^*(\varphi)$ is

$$\Delta\sigma=\sigma(\varphi)-\sigma^*(\varphi)=\Sigma_J\Sigma_{J'}[\sigma_{JJ'}(\varphi)-\sigma_{JJ'}{}^*(\varphi)]$$
$$=\Sigma_J\Sigma_{J'}(2J'+1)\mu_{JJ'}\Sigma_L(2L+1)C_{LJJ'}$$
$$\times\{X(\varphi)(p/p_0)j_L{}^2(kr)-X^*(\varphi)j_L{}^2(k^*r)\}$$

where Σ_J means average over the Boltzmann distribution. The semiclassical equation was obtained on the assumption that $p=p_0$. The quantity in the braces $\{\ \}$ is a function of the difference p_0-p, and to the first power of $\epsilon=(p_0-p)/p_0$,

$$X(\varphi)(p/p_0)j_L{}^2(kr)-X^*(\varphi)j_L{}^2(k^*r)$$
$$=-\epsilon X^*(\varphi)\left\{\frac{1}{2x}\frac{d}{dx}(x^2j_L{}^2(x))-2j_L{}^2(x)M^{-1}\cos\varphi\right.$$
$$\left.+xj(x)j'(x)M^{-1}\cos^2(\varphi/2)\right\}=-\epsilon X^*(\varphi)F_L \qquad (A.4)$$

where

$$F_L=\{(1/2x)(d/dx)x^2-2M^{-1}\cos\varphi\}j_L{}^2(x)$$
$$+xj(x)j'(x)M^{-1}\cos^2(\varphi/2)$$

and

$$x=k^*r=2\pi(r/\lambda)[M/(M+1)]\sin(\theta^*/2).$$

Powers of $1/M$ higher than the first arising from $X(\varphi)$ have been neglected in (A.4). The quantity ϵ is approximately given by

$$\epsilon=-((M+1)/M)(E_1/E)\{J(J+1)-J'(J'+1)\}/4 \qquad (A.5)$$

where E_1 is the energy of the first rotational level and E is the energy of the incident neutrons, $E_1/E=(2/M)(\lambda/\pi r)^2$.

For neutrons of 0.07 ev scattered by nitrogen $\epsilon=-1.7\times10^{-4}\times\{J(J+1)-J'(J'+1)\}$ and having regard to the distribution of J values at room temperature and the vanishingly small probability for $\varphi<90°$ of transitions involving $|J-J'|>6$, it appears that all values of ϵ which merit consideration are $\ll1$. The equation for $\Delta\sigma$ to the first power of ϵ is

$$\Delta\sigma=X^*(\varphi)\frac{M+1}{M}\frac{E_1}{4E}\sum_J\sum_{J'}(2J'+1)\mu_{JJ'}\sum_L(2L+1)C_{LJJ'}$$
$$\times\{J(J+1)-J'(J'+1)\}F_L. \qquad (A.6)$$

The order of summation over L and J' may be changed and

$$\Delta\sigma=X^*(\varphi)\frac{M+1}{M}\frac{E_1}{4E}\sum_J\sum_L(2L+1)F_L\sum_{J'}\mu_{JJ'}(2J'+1)C_{LJJ'}$$
$$\times\{J(J+1)-J'(J'+1)\}. \qquad (A.7)$$

From the definition of $C_{LJJ'}$ it follows that

$$\Sigma_{J'}(2J'+1)C_{LJJ'}P_{J'}(s)=P_L(s)P_J(s). \qquad (A.8)$$

Differentiation of both sides with respect to s and use of the formula $(d/ds)P_n(s)=(\pm)^{n+1}n(n+1)/2$ for $s=\pm1$, yields

$$\Sigma_{J'}(2J'+1)C_{LJJ'}J'(J'+1)=L(L+1)+J(J+1).$$

From (A.8) with $s=1$, $\Sigma_{J'}(2J'+1)C_{LJJ'}J(J+1)=J(J+1)$. The difference is $\Sigma_{J'}(2J'+1)C_{LJJ'}[J(J+1)-J'(J'+1)]=-L(L+1)$. With the notation μ_{Je} for $\mu_{JJ'}$ when $J-J'$ is even, μ_{Jo} when $J-J'$ is odd, this gives from (A.7)

$$\Delta\sigma=-X^*(\varphi)((M+1)/M)(E_1/4E)\Sigma_J(\mu_{Je}z_e+\mu_{Jo}z_o)$$

where

$$z_e=\Sigma_{L\ \mathrm{even}}L(L+1)(2L+1)F_L,\quad z_o=\Sigma_{L\ \mathrm{odd}}L(L+1)(2L+1)F_L.$$

With $y_\pm=z_e\pm z_o=\Sigma_L(\pm)^LL(L+1)(2L+1)F_L$ the formula for $\Delta\sigma$ becomes

$$\Delta\sigma=-X^*(\varphi)(M/(M+1))(E_1/4E)(y_+\sigma_T+y_-\sigma_C)/2\pi. \qquad (A.9)$$

$y_\pm$ is readily found from[3]

$$\Sigma_L(2L+1)j_L{}^2(x)P_L(s)=\sin s/s \quad\text{where}\quad s=x[2(1-s)]^{\frac{1}{2}}.$$

Differentiation of both sides with respect to s at $s=\pm1$ leads to

$$\Sigma_L(\pm)^LL(L+1)(2L+1)j_L{}^2(x)=\tfrac{1}{3}x^2 \text{ for the } + \text{ sign}$$
$$=\tfrac{1}{2}(\cos2x-\sin2x/2x) \text{ for the } - \text{ sign.}$$

To obtain $y_\pm$ it is only necessary to operate on both sides so as to transform $j_L{}^2(x)$ to F_L by Eq. (A.4). Then

$$y_+=(4/3)x^2$$
$$y_-=\tfrac{1}{2}\{\cos2x-[(2x)^2+1]\sin2x/2x\}$$

neglecting terms in M^{-1}.

The value of $\Delta\sigma=\sigma(\varphi)-\sigma^*(\varphi)$ follows from (A.9) with these values of $y_\pm$, and has been applied to the nitrogen results as shown in Fig. 1.

In the range of x where $\Delta\sigma$ is important y_- is small compared to y_+. A rough value of $\Delta\sigma$ is obtained by retaining only y_+ and also neglecting $1/M$ compared to unity. Then

$$\Delta\sigma=-(8/3M)(\sigma_T/2\pi)\sin^2(\varphi/2) \qquad (A.10)$$

and for nitrogen the difference between this and the full result as given by (A9) is experimentally unimportant.

The smallness of y_- means that the error in the semiclassical equation is largely independent of coherent effects because, to the extent that (A.10) holds, $\Delta\sigma$ is independent of σ_{coh}. When $\sigma_{coh}=0$, the semiclassical result except for the reduced mass term is practically billiard ball scattering. This suggests that the chief source of error in the semiclassical equation is in the assumption of a molecular model which is fixed in orientation so that transfer of angular momentum cannot occur.

TABLE III. The values of $\mu_{JJ'}$.

J	J'	Transition	Designation	μ
even	even	ortho-ortho	μ_{oo}	$[M/(M+1)]^2(5\sigma_T+3\sigma_{coh})/8\pi$
odd	odd	para-para	μ_{pp}	$[M/(M+1)]^2(\sigma_T+3\sigma_{coh})/4\pi$
even	odd	ortho-para	μ_{op}	$3[M/(M+1)]^2(\sigma_T-\sigma_{coh})/8\pi$
odd	even	para-ortho	μ_{po}	$3[M/(M+1)]^2(\sigma_T-\sigma_{coh})/4\pi$

Field Corrections to Neutron-Proton Scattering in a New Mixed Meson Theory

D. B. BEARD* AND H. A. BETHE
Cornell University, Ithaca, New York

(Received April 18, 1951)

The principal relativistic correction to neutron-proton scattering has been computed to fourth order for nonrelativistic energies by calculating the matrix elements using the Feynman method and then subtracting off the appropriate order Born approximation to the Yukawa potential. A new meson theory was used, namely a mixture of pseudovector mesons and pseudoscalar mesons with pseudovector coupling; it is shown that by suitable choice of the coupling constants the divergent terms could be eliminated in all orders (disregarding possible electromagnetic couplings). The mesonic field corrections to neutron-proton scattering were found to be of order μ/M smaller than the static Yukawa potential cross section; in practical applications, they could be treated as a perturbing potential to the static Yukawa interaction.

I. INTRODUCTION

CHRISTIAN and Hart[1] have calculated neutron-proton scattering quite accurately using a static Yukawa potential, $e^{-\mu r}/r$. The most important correction to this form of the interaction should be because of the field effect, that is, noninstantaneous interactions or rather what might be called virtual phenomena occurring in times too short for energy to be conserved.

Using Feynman's[2] approach to quantum electrodynamics one might consider expanding the solution in a series in powers of $g^2/\hbar c$ in analogy to quantum electrodynamics. Unfortunately such a series converges very slowly for values of $g^2/\hbar c$ which fit the experimental total cross section; for each term includes the appropriate order Born approximation to the static Yukawa potential, and this, as will be apparent in Sec. III, is rather large. Since Christian and Hart have already calculated the static interaction quite accurately what one can do is to make the calculation in terms of powers of $g^2/\hbar c$ anyway and then subtract from each order the appropriate order Born approximation to the static interaction. The remainder is the mesonic field correction to neutron-proton scattering.[3]

FIG. 1. Feynman diagram for a possible complex process.

The final cross section will be:

$$\sigma(\theta)=\left(\frac{m}{2\pi\hbar^2}\right)^2\left|\begin{array}{l}\text{Christian and Hart result with appropriate spin and charge dependence}\end{array}+\begin{array}{l}\text{pure field effect to the order one cares to compute it}\end{array}\right|^2. \tag{1}$$

II. DISCUSSION OF THE INTERACTION

Though the method may be taken over for scalar, neutral vector, and other convergent meson theories, the calculation was based on a new mixture theory of pseudoscalar and pseudovector mesons with equal pseudovector coupling which eliminates the divergence occurring in either theory alone.

The interaction for the emission of a pseudovector meson with pseudovector coupling polarized in the μth direction is, according to the Feynman theory, $\gamma_5(\gamma_\mu-\mathfrak{q}q_\mu\mu_0^{-2})$, where γ_5 is the product of the three Dirac matrices α_x, α_y, α_z times i $(=i\gamma_x\gamma_y\gamma_z\gamma_t)$, $\mathfrak{q}$ is the product, $q_\mu\gamma_\mu$, and μ_0 is the meson mass. For absorption the interaction is simply $\gamma_5\gamma_\mu$.

The divergence arises, in all higher orders, from integrating the $\mathfrak{q}q_\mu\mu_0^{-2}$ part of the interaction over d^4q. The other part of the coupling, $\gamma_5\gamma_\mu=\beta\sigma_\mu$, does not give rise to divergences. The coupling of the pseudoscalar mesons is taken to be $\gamma_5\mathfrak{q}$, for both absorption and emission.

The elimination of divergences by this mixture may be shown in the following way: Consider a complex process in which many virtual pseudovector mesons are emitted and absorbed (see Fig. 1). If one of the mesons is polarized in the μth direction the matrix element will be: $\mathfrak{A}\gamma_5\gamma_\mu\mathfrak{B}\gamma_5(\gamma_\mu-\mathfrak{q}q_\mu\mu_0^{-2})\mathfrak{C}$ where $\mathfrak{A}$, $\mathfrak{B}$, and $\mathfrak{C}$ may be products of many $\mathfrak{q}$'s and γ-matrices belonging to either nucleon and represent the emission and absorption interactions for the other virtual mesons in the process. The particular meson polarized in the μth direction may or may not be absorbed by the same nucleon which emitted it. The matrix element may be rewritten as: $\mathfrak{A}\gamma_5\gamma_\mu\mathfrak{B}\gamma_5\gamma_\mu\mathfrak{C}-\mu_0^{-2}\mathfrak{A}\gamma_5\mathfrak{q}\mathfrak{B}\gamma_5\mathfrak{q}\mathfrak{C}$. To this one adds the matrix element for the possibility of this particular meson having been a pseudoscalar meson with pseudovector coupling, $+\mu_0^{-2}\mathfrak{A}\gamma_5\mathfrak{q}\mathfrak{B}\gamma_5\mathfrak{q}\mathfrak{C}$,

* Now at The Catholic University of America, Washington, D. C.

[1] R. S. Christian and E. W. Hart, Phys. Rev. **77**, 441 (1950).

[2] R. P. Feynman, Phys. Rev. **76**, 749 (1949); *ibid.* **76**, 769 (1949).

[3] A similar calculation has been made by Y. Nambu in the Prog. Theor. Phys. **5**, 614 (1950).

and gets: $\mathfrak{A}\gamma_5\gamma_\mu\mathfrak{B}\gamma_5\gamma_\mu\mathfrak{C}$. If one repeats this addition for the emission and absorption of a pseudoscalar meson wherever the emission and absorption of a pseudovector meson is treated in $\mathfrak{A}$, $\mathfrak{B}$, or $\mathfrak{C}$ the resulting matrix will contain only $\gamma_5\gamma_\mu$ type couplings. Therefore, if in any process *having virtual mesons only* one adds the contributions from these two types of mesons the effective coupling will always be merely $\gamma_5\gamma_\mu$.

Thus the divergent terms are identically removed in all orders. It should be noted, however, that in this process the entire tensor interaction, which occurs in first order and is necessary to explain the electric quadrupole moment of the deuteron, is lost also. The central force which is left predicts a symmetrical deuteron, but this is quite close to what has been experimentally observed.

It should also be remembered that there are difficulties in the treatment of the interaction of a charged meson of spin 1 with the electromagnetic field. As Salam has shown,[4] this theory cannot be renormalized with the standard procedure which is successful for the electrodynamics of particles of spin zero or $\frac{1}{2}$. It is therefore doubtful whether charged mesons of spin 1 can exist. There would of course be no trouble in a *neutral* meson theory which is mixed pseudoscalar and pseudovector; however, in this case the *experimental* evidence shows that at least the neutral *pi*-meson has spin zero which rules out the pseudovector.

III. SECOND ORDER MATRIX ELEMENT AND THE BORN APPROXIMATION

The matrix element for the second order[5] is according to Feynman's theory (see Fig. 2):

$$-4\pi\hbar^3c^3(g^2/\hbar c)\gamma_5{}^A\gamma_\mu{}^A[q^2-\mu_0{}^2]^{-1}\gamma_5{}^B\gamma_\mu{}^B, \qquad (2)$$

where q is the energy-momentum 4-vector of the meson exchanged by the two nucleons. In the center-of-mass system q^2 equals $-\mathbf{Q}^2$, where $\mathbf{Q}$ is the momentum 3-vector, since q is the energy-momentum exchanged by the two nucleons and therefore q_4 is zero in the center-of-mass system. Since the nonrelativistic approximation to $\overline{U}_2\gamma_5\gamma_\mu U_1$ is $\overline{U}_2\sigma_\mu U_1$, the matrix element for the second-order process is:

$$4\pi\hbar^3c^3(g^2/\hbar c)\boldsymbol{\sigma}^A\cdot\boldsymbol{\sigma}^B[\mu^2+\mathbf{Q}^2]^{-1}, \qquad (3)$$

a purely central spin dependent force corresponding to a potential $g^2(e^{-\mu r}/r)\boldsymbol{\sigma}^A\cdot\boldsymbol{\sigma}^B$. The first-order[5] Born approximation to this potential which we must subtract from the matrix element [Eq. (3)] is identical to this matrix element and, therefore, in this nonrelativistic approximation one gets no contribution to the field corrections to this order.

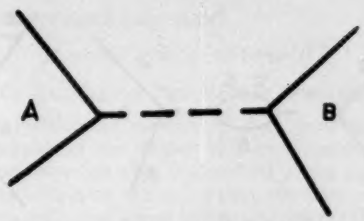

FIG. 2. Feynman diagram of second-order process.

The second-order Born approximation is the convolution in momentum space of the potential and the first-order approximation to the wave function:

$$\hbar^3c^3\int W(\mathbf{Q}_a)\varphi_1(\mathbf{P}_2-\mathbf{Q}_a)d^3Q_a, \qquad (4)$$

where $W(\mathbf{Q}_a)$ is the fourier transform of the potential and $\varphi_1(\mathbf{P}_2-\mathbf{Q}_a)$ is the transform of the first-order approximation to the wave function. This second-order term is, therefore:

$$\hbar^3c^3(g^2/\hbar c)^2 2M(\boldsymbol{\sigma}^A\cdot\boldsymbol{\sigma}^B)^2\pi^{-1}\int[\mu^2+\mathbf{Q}_a{}^2]^{-1}$$

$$\times[\mathbf{Q}_a{}^2-2\mathbf{Q}_a\cdot\mathbf{P}_2]^{-1}[\mathbf{Q}_a{}^2-2\mathbf{Q}_a\cdot\mathbf{Q}+\mathbf{Q}^2+\mu^2]^{-1}d^3Q_a, \qquad (5)$$

where $\mathbf{P}_2$ is the space momentum after the collision, $\mathbf{P}_1$ the momentum before collision, and $\mathbf{Q}=\mathbf{P}_2-\mathbf{P}_1$, the momentum exchanged by the two nucleons. The denominator of (5) can be transformed into an easier integrand by Feynman's parameter integration scheme.

$$\frac{1}{acb}=\int_0^1\int_0^1\frac{2(1-x)dxdy}{[(a-b)(1-x)(1-y)+(b-c)(1-x)+c]^3} \qquad (6)$$

and the integral in Eq. (5) becomes:

$$2\int_{-\infty}^{\infty}\int_0^1\int_0^1\frac{(1-x)dxdyd^3Q_a}{\{[2\mathbf{Q}\cdot\mathbf{Q}_a-\mathbf{Q}^2][1-x][1-y]+[\mathbf{Q}^2+\mu^2-2\mathbf{Q}\cdot\mathbf{Q}_a+2\mathbf{P}_2\cdot\mathbf{Q}_a][1-x]+[\mathbf{Q}_a{}^2-2\mathbf{P}_2\cdot\mathbf{Q}_a]\}^3}$$

$$=\int_{-\infty}^{\infty}\int_0^1\int_0^1\frac{(1-x)dxdyd^3Q_a}{\{\mathbf{Q}_a{}^2-2\mathbf{Q}_a\cdot[\mathbf{P}_2x+\mathbf{Q}(1-x)y]+[\mu^2(1-x)+\mathbf{Q}^2(1-x)y]\}^3}. \qquad (7)$$

[4] Private communication to H. A. Bethe.

[5] By the order of a process we refer to the number of vertices in a Feynman diagram. In this development the order corresponds to the power of the coupling constant (e, in electromagnetic theory, g, in meson theory) in the matrix element. In the Born approximation, however, the order refers to the power of the potential and therefore corresponds to half the power of the coupling constant.

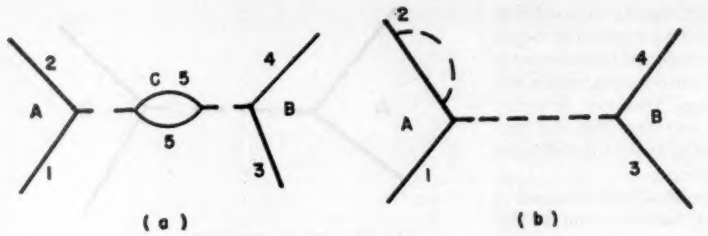

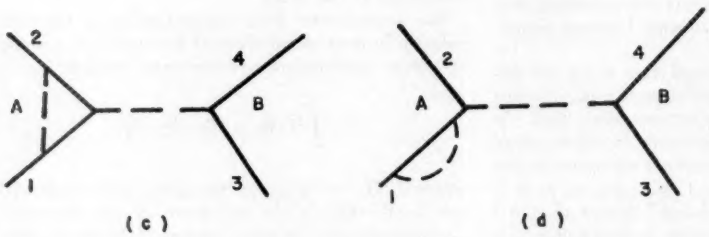

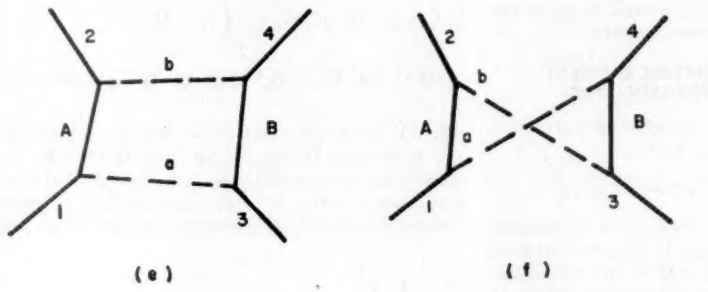

FIG. 3(a). Feynman diagram of vacuum polarization correction to second-order process.

FIGS. 3(b), 3(c), and 3(d). Feynman diagram of radiative correction to second-order process.

FIG. 3(e). Feynman diagram for successive exchange of two mesons (process I).

FIG. 3(f). Feynman diagram for crossed exchange of two mesons (process II).

The integral can be evaluated:

$$\int_{-\infty}^{\infty}\{\mathbf{Q}_a^2-2\mathbf{P}\cdot\mathbf{Q}_a+L\}^{-3}d^3Q_a$$

$$=\int_{-\infty}^{\infty}\{\mathbf{Q}'^2_a+(L-\mathbf{P}^2)\}^{-3}d^3Q'_a$$

$$=4\pi\int_0^{\infty}\{\mathbf{Q}'^2_a+(L-\mathbf{P}^2)\}^{-3}\mathbf{Q}'^2_a dQ_a'$$

$$=4\pi(8)^{-1}(L-\mathbf{P}^2)^{-\frac{1}{2}}(\pi/2)=(\tfrac{1}{4})\pi^2(L-\mathbf{P}^2)^{-\frac{1}{2}}. \quad (8)$$

Since $|\mathbf{P}_2|=|\mathbf{P}_1|$ in the center-of-mass system, we have

$$\mathbf{Q}^2=2\mathbf{P}_2^2-2\mathbf{P}_1\cdot\mathbf{P}_2=2\mathbf{P}_2\cdot\mathbf{Q}.$$

(7) becomes then:

$$\tfrac{1}{2}\pi^2\int_0^1\int_0^1(1-x)dxdy\{\mu^2(1-x)+\mathbf{Q}^2(1-x)y$$

$$-\mathbf{P}_2^2x^2-\mathbf{Q}^2(1-x)xy-\mathbf{Q}^2(1-x)^2y^2\}^{-\frac{1}{2}}$$

$$=\tfrac{1}{2}\pi^2\int_0^1\int_0^1(1-x)dxdy\{-\mathbf{Q}^2(1-x)^2y^2$$

$$+\mathbf{Q}^2(1-x)^2y+\mu^2(1-x)-\mathbf{P}_2^2x^2\}^{-\frac{1}{2}}$$

$$=\tfrac{1}{2}\pi^2\int_0^1(1-x)dx\{\mu^2(1-x)+\tfrac{1}{4}\mathbf{Q}^2(1-x)^2-\mathbf{P}_2^2x^2\}^{-1}$$

$$\times\{\mu^2(1-x)-\mathbf{P}_2^2x^2\}^{-\frac{1}{2}}. \quad (9)$$

Therefore (5) is:

$$\hbar^3c^3(g^2/\hbar c)^2 2M(\sigma^A\cdot\sigma^B)(\pi/2)$$
$$\times\int_0^1(1-x)dx[\mu^2(1-x)+\tfrac{1}{4}Q^2(1-x)^2-\mathbf{P}_2^2x^2]^{-1}$$
$$\times[\mu^2(1-x)-\mathbf{P}_2^2x^2]^{-\frac{1}{2}}. \quad (10)$$

This is the term which must be subtracted from the fourth-order expression which includes the Born approximation to the Yukawa potential (see Fig. 3(e)).

IV. FOURTH-ORDER CALCULATION

In the fourth order there are several possible processes. To begin with there are the processes for vacuum polarization and radiative corrections to scattering (see Figs. 3(a), 3(b), 3(c), and 3(d)).

A. Vacuum Polarization

As in quantum electrodynamics, vacuum polarization gives rise to two kinds of terms, namely an infinite charge renormalization and a term which vanishes as q^2 for small momentum change. Terms of the latter kind are considered negligibly small compared with the square of the nucleon mass in our approximation. The charge renormalization was calculated with regulators[6] satisfying the conditions

$$\sum C_j=\sum C_jM_j^2=\sum C_jM_j^2\ln M_j=0.$$

The charge renormalization then turns out to be proportional to[7]

$$\sum C_j(M_j^2+M^2)\ln M_j, \quad (11)$$

which can be made zero by imposing an additional condition on the coupling constants C_j,

$$\sum C_j\ln M_j=0.$$

B. Radiative Corrections to Scattering

These are represented by Figs. 3(b), 3(c), and 3(d). As usual they give rise to another charge renormalization and to a term which vanishes as q^2. The latter term is neglected in our approximation. The charge renormalization which is zero in electrodynamics, is finite in this problem and has the value[7]

$$(g^2/\pi\hbar c)[8\ln(M/\mu)-7+6\pi\mu/M]. \quad (12)$$

C. Exchange of Two Mesons (General)

The fourth-order calculation, then, involves only the exchange of two mesons. This can happen in two different ways (see Figs. 3(e) and 3(f)). For purposes of identification we will call the process shown in Fig. 3(e) process I, that shown in Fig. 3(f) process II.

Some general relationships for the exchange of two mesons:

$$p_2-p_1=p_3-p_4=q_b-q_a=q. \quad (13)$$

From this and the fact that all $p_i^2=M^2$ it follows that:

$$p_1\cdot p_2=p_3\cdot p_4,\quad p_2\cdot p_3=p_1\cdot p_4,\text{ and }\quad p_1\cdot p_3=p_2\cdot p_4, \quad (14)$$
$$q^2=q\cdot(p_2-p_1)=(p_2-p_1)^2=2M^2-2p_1\cdot p_2$$
$$=2M^2-2p_3\cdot p_4.$$

Therefore,

$$q^2=2p_2\cdot(p_2-p_1)=-2p_1\cdot(p_2-p_1)$$
$$=2p_3\cdot(p_3-p_4)=2p_4\cdot(p_3-p_4), \quad (15)$$
$$q^2=2p_2\cdot q=-2p_1\cdot q=2p_3\cdot q=-2p_4\cdot q.$$

Here p_1 and p_3 represent the four-momenta of the neutron and proton before collision; p_2 and p_4 represent the two four-momenta after collision; q_b and q_a represent the four-momenta of the two mesons which are exchanged, and q represents the four-momentum exchanged between the two nucleons.

We shall carry out the calculation in the center-of mass coordinate system; this involves further simplifying relations:

$$p_1\cdot p_3=E^2-\mathbf{P}\cdot(-\mathbf{P})=E^2+\mathbf{P}^2=M^2+2\mathbf{P}^2, \quad (16)$$
$$M^2+p_1\cdot p_3=2E^2;\quad p_1\cdot p_3-M^2=2\mathbf{P}^2, \quad (17)$$

where E and $\mathbf{P}$ are the energy and space-momentum respectively of each of the two nucleons in the center-of-mass coordinate system, and as before $-q^2=Q^2$.

Since this calculation is a nonrelativistic one, $\mu\simeq\frac{1}{6}M$, μ^2, $\mathbf{P}^2$, and Q^2 are all assumed small compared to M^2, and $E^2\simeq M^2$.

We shall represent the operator $p_\mu\gamma_\mu$ by $\not{p}$.

D. Successive Exchange of Two Mesons (Process I)

$$4\left(\frac{\hbar^3c^3}{i}\right)\left(\frac{g^2}{\hbar c}\right)^2\int_{-\infty}^{\infty}(q_b^2-\mu^2)^{-1}(q_a^2-\mu^2)^{-1}\gamma_5^B\gamma_\nu^B(\not{p}_3+\not{q}_a-M)^{-1}\gamma_5^B\gamma_\mu^B\gamma_5^A\gamma_\nu^A(\not{p}_1-\not{q}_a-M)^{-1}\gamma_5^A\gamma_\mu^Ad^4q_a$$
$$=4\left(\frac{\hbar^3c^3}{i}\right)\left(\frac{g^2}{\hbar c}\right)^2\int_{-\infty}^{\infty}(q_a^2-2q_a\cdot q+q^2-\mu^2)^{-1}(q_a^2-\mu^2)^{-1}\gamma_\nu^B\frac{\not{p}_3+\not{q}_a-M}{q_a^2+2p_3\cdot q_a}\gamma_\mu^B\gamma_\nu^A\frac{\not{p}_1-\not{q}_a-M}{q_a^2-2p_1\cdot q_a}\gamma_\mu^Ad^4q_a. \quad (18)$$

These four fractions, $(c\,d\,a\,b)^{-1}$, may now be transformed into easier integrals by Feynman's parameter integration

[6] W. Pauli and F. Villars, Revs. Modern Phys. **21**, 434 (1949).
[7] Professor R. P. Feynman has also obtained this result (private communication).

scheme.[2]

$$(abcd)^{-1}=6\int_0^1 dz\int_0^1 dy\int_0^1 x(1-x)dx\{[ay+b(1-y)]x+[cz+d(1-z)][1-x]\}^{-4}, \tag{19}$$

$$4\left(\frac{\hbar^3c^3}{i}\right)\left(\frac{g^2}{\hbar c}\right)^2\int_{-\infty}^{\infty}\int_0^1\int_0^1\int_0^1 \frac{6x(1-x)dxdydzd^4q_a\gamma_\nu{}^B(\not p_3+\not q_a-M)\gamma_\mu{}^B\gamma_\nu{}^A(\not p_1-\not q_a-M)\gamma_\mu{}^A}{\{2\boldsymbol{q}_a\cdot(\boldsymbol{p}_1+\boldsymbol{p}_3)xy+[2\boldsymbol{q}_a\cdot\boldsymbol{q}+\boldsymbol{q}^2]z(1-x)-[2\boldsymbol{p}_1\cdot\boldsymbol{q}_a-\mu^2]x+\boldsymbol{q}_a{}^2-\mu^2\}^4},$$

$$=4\left(\frac{\hbar^3c^3}{i}\right)\left(\frac{g^2}{\hbar c}\right)^2\int_{-\infty}^{\infty}\int_0^1\int_0^1\int_0^1 \frac{6x(1-x)dxdydzd^4q_a\gamma_\nu{}^B[(\not p_3-M)+\not q_a]\gamma_\mu{}^B\gamma_\nu{}^A[(\not p_1-M)-\not q_a]\gamma_\mu{}^A}{\{\boldsymbol{q}_a{}^2-2\boldsymbol{q}_a\cdot[-\boldsymbol{q}z(1-x)+\boldsymbol{p}_1x(1-y)-\boldsymbol{p}_3xy]-[-\boldsymbol{q}^2z(1-x)+\mu^2(1-x)]\}^4}. \tag{20}$$

The integration over $d^4q_a(=(2\pi)^{-2}dq_{ax}dq_{ay}dq_{az}dq_{at})$ has been done by Feynman,[2] and yields:

$$\left(\frac{\hbar^3c^3}{6}\right)\left(\frac{g^2}{\hbar c}\right)^2\int_0^1\int_0^1\int_0^1 6x(1-x)dxdydz\{[-\boldsymbol{q}z(1-x)+\boldsymbol{p}_1(1-y)x-\boldsymbol{p}_3xy]^2+[-\boldsymbol{q}^2z(1-x)+\mu^2(1-x)]\}^{-2}$$

$$\times\{\gamma_\nu{}^B(\not p_3-M)\gamma_\mu{}^B\gamma_\nu{}^A(\not p_1-M)\gamma_\mu{}^A+\gamma_\nu{}^B[-\not pz(1-x)+\not p_1x(1-y)-\not p_3xy]\gamma_\mu{}^B\gamma_\nu{}^A(\not p_1-M)\gamma_\mu{}^A$$

$$-\gamma_\nu{}^B(\not p_3-M)\gamma_\mu{}^B\gamma_\nu{}^A[-\not pz(1-x)+\not p_1x(1-y)-\not p_3xy]\gamma_\mu{}^A-\gamma_\nu{}^B[-\not pz(1-x)+\not p_1x(1-y)-\not p_3xy]\gamma_\mu{}^B\gamma_\nu{}^A$$

$$\times[-\not pz(1-x)+\not p_1x(1-y)-\not p_3xy]\gamma_\mu{}^A\}+\left(\frac{\hbar^3c^3}{6}\right)\left(\frac{g^2}{\hbar c}\right)^2\left(\frac{\delta_{\sigma\tau}}{2}\right)\gamma_\nu{}^B\gamma_\sigma{}^B\gamma_\mu{}^B\gamma_\nu{}^A\gamma_\tau{}^A\gamma_\mu{}^A$$

$$\times\int_0^1\int_0^1\int_0^1 \frac{6x(1-x)dxdydz}{\{[-\boldsymbol{q}z(1-x)+\boldsymbol{p}_1x(1-y)+\boldsymbol{p}_3xy]^2+[-\boldsymbol{q}^2z(1-x)+\mu^2(1-x)]\}}. \tag{21}$$

We will consider the matrix element term by term. In the nonrelativistic approximation only the time component of $\boldsymbol{p}$ gives an appreciable result and since $q_t=0$, $\boldsymbol{q}$ in the numerator becomes zero since it is to be compared with M, while in the denominator where it occurs with μ^2, $\boldsymbol{q}^2=-\mathbf{Q}^2$. Since $\not p_3=M\gamma_4{}^B$, $\not p_1=M\gamma_4{}^A$; and $\gamma_\nu\gamma_4=-\gamma_4\gamma_\nu$ for $\nu\neq4$, $\gamma_\nu\gamma_4=\gamma_4\gamma_\nu$ for $\nu=4$; $(\overline{U}_4\gamma_\nu(\not p_3-M)\gamma_\mu U_3)$ becomes 0 for $\nu=4$, while for $\nu\neq4$ it is $-2M(\overline{U}_4\gamma_\nu\gamma_\mu U_3)=-2M(\overline{U}_4\sigma_{\mu\nu}U_3)$; and the first term becomes, using (15):

$$\hbar^3c^3(g^2/\hbar c)^2 4M^2(\sigma_{\mu\nu}{}^A\sigma_{\mu\nu}{}^B)\int_0^1\int_0^1\int_0^1 x(1-x)dxdydz[M^2x^2(1-2y)^2-\mathbf{P}^2x^2+\mu^2(1-x)+\mathbf{Q}^2(1-x)^2z(1-z)]^{-2}. \tag{22}$$

The second and third terms may be considered together. The integral

$$\int_0^1\{M^2x^2[(1-y)-y]^2-\mathbf{P}^2x^2+\mu^2(1-x)+\mathbf{Q}^2(1-x)^2z(1-z)\}^{-2}ydy$$

equals the integral

$$\int_0^1\{M^2x^2[(1-y)-y]^2-\mathbf{P}^2x^2+\mu^2(1-x)+\mathbf{Q}^2(1-x)^2z(1-z)\}^{-2}(1-y)dy, \tag{23}$$

and as a result the second and third term are both equal to zero.

The fourth term becomes, leaving out the coefficient of the integral:

$$\gamma_\nu{}^B\gamma_t{}^B\gamma_\mu{}^B\gamma_\nu{}^A\gamma_t{}^A\gamma_\mu{}^A\int_0^1\int_0^1\int_0^1 \frac{M^2x^2(1-2y)^2x(1-x)dxdydz}{\{M^2x^2(1-2y)^2+\mu^2(1-x)-\mathbf{P}^2x^2+\mathbf{Q}^2(1-x)^2z(1-z)\}^2}$$

$$=\gamma_\nu{}^B\gamma_t{}^B\gamma_\mu{}^B\gamma_\nu{}^A\gamma_t{}^A\gamma_\mu{}^A\int_0^1\int_0^1\int_0^1 \frac{x(1-x)dxdydz}{M^2x^2(1-2y)^2+\mu^2(1-x)-\mathbf{P}^2x^2+\mathbf{Q}_z{}^2(1-x)^2z(1-z)}, \tag{24}$$

omitting remainder terms of order μ^2/M^2, $\mathbf{Q}^2/M^2$, and $\mathbf{P}^2/M^2$.

It can be easily shown that this integral, which also occurs in the fifth term is small compared to the first term. We note that the terms with μ^2 and $\mathbf{Q}^2$ are comparable to the first term only when the latter is small, i.e., for x small, so that the factor $(1-x)$ can be replaced by one of these terms; the same can be done in the numerator.

If we let $k^2=\mu^2+\mathbf{Q}^2z(1-z)$, the integrations over x and y give:

$$\int_0^1\int_0^1[M^2x^2(1-2y)^2+k^2]^{-1}xdxdy\simeq\pi\int_0^1[Mxk]^{-1}xdx=(\pi/Mk) \tag{24a}$$

whereas the integrations of the first term yield:

$$M^2\int_0^1\int_0^1[M^2x^2(1-2y)^2+k^2]^{-2}xdxdy=\tfrac{1}{2}\int_0^1[1-2y]^{-2}[k^{-2}-\{M^2(1-2y)^2+k^2\}^{-1}]dy$$
$$=(M^2/2k^2)\int_0^1[M^2(1-2y)^2+k^2]^{-1}dy=(M^2/2k^2)(\pi/Mk). \tag{25}$$

The first term (25) is larger by about a factor $(M/k)^2\simeq M^2(\mu^2+\mathbf{Q}^2)^{-1}$. The field effect, as we shall see, is smaller than the main term by a factor μ/M, but the fourth and fifth terms are *still* smaller by another factor μ/M and therefore can be neglected.

We are left, then, with only the first term:

$$\hbar^3c^3\left(\frac{g^2}{\hbar c}\right)^2 4M^2\sigma_{\mu\nu}{}^B\sigma_{\mu\nu}{}^A\int_0^1\int_0^1\int_0^1\frac{x(1-x)dxdydz}{\{M^2x^2(1-2y)^2-\mathbf{P}^2x^2+\mu^2(1-x)+\mathbf{Q}^2(1-x)^2z(1-z)\}^2} \tag{22}$$

letting $s=Mx(1-2y)$:

$$\hbar^3c^3\left(\frac{g^2}{\hbar c}\right)^2 4M^2\sigma_{\mu\nu}{}^B\sigma_{\mu\nu}{}^A\int_0^1\int_0^1\int_{-Mx}^{Mx}(2M)^{-1}\{s^2+\mu^2(1-x)+\mathbf{Q}^2(1-x)^2z(1-z)-\mathbf{P}^2x^2\}^{-2}(1-x)dxdzds$$
$$=\hbar^3c^3\left(\frac{g^2}{\hbar c}\right)^2 2M\sigma_{\mu\nu}{}^B\sigma_{\mu\nu}{}^A\int_0^1dx\int_0^1(1-x)dz\{Mx[\mu^2(1-x)+\mathbf{Q}^2(1-x)^2z(1-z)-\mathbf{P}^2x^2]^{-1}[M^2x^2+\mu^2(1-x)$$
$$+\mathbf{Q}^2(1-x)^2z(1-z)]^{-1}+[\mu^2(1-x)+\mathbf{Q}^2(1-x)^2z(1-z)-\mathbf{P}^2x^2]^{-1}$$
$$\times\tan^{-1}[Mx\{\mu^2(1-x)+\mathbf{Q}^2(1-x)^2z(1-z)-\mathbf{P}^2x^2\}^{-1}]\} \tag{26}$$
$$=\hbar^3c^3\left(\frac{g^2}{\hbar c}\right)^2 2M\sigma_{\mu\nu}{}^B\sigma_{\mu\nu}{}^A\int_0^1(1-x)dx\int_0^1dz\{(\pi/2)[\mu^2(1-x)+\mathbf{Q}^2(1-x^2)z(1-z)-\mathbf{P}^2x^2]^{-\frac{1}{2}}$$
$$-[\mu^2(1-x)+\mathbf{Q}^2(1-x)^2z(1-z)-\mathbf{P}^2x^2]^{-\frac{1}{2}}\tan^{-1}[\{Mx\}^{-1}\{\mu^2(1-x)+\mathbf{Q}^2(1-x)^2z(1-z)-\mathbf{P}^2x^2\}^{\frac{1}{2}}]$$
$$+Mx[\mu^2(1-x)+\mathbf{Q}^2(1-x)^2z(1-z)-\mathbf{P}^2x^2]^{-1}[M^2x^2+\mathbf{Q}^2(1-x)^2z(1-z)+\mu^2(1-x)]^{-1}\}. \tag{27}$$

The first term is exactly the Born approximation Eq. (9) with the correct factor. To see this, and to carry out the summation over μ and ν in (26), it is convenient to use the relation between Pauli spin operators, $\sigma_{\mu\nu}\equiv\gamma_\nu\gamma_\mu=\sigma_\mu\sigma_\nu$, so that we have:

$$\sigma_\mu{}^B\sigma_\nu{}^B\sigma_\mu{}^A\sigma_\nu{}^A=(\boldsymbol{\sigma}^A\cdot\boldsymbol{\sigma}^B)^2. \tag{28}$$

Since process I contains the second-order Born approximation to the Yukawa potential we must subtract the Born approximation from it in computing the field effect corrections. We are left then with the other two terms, which taken together may be neglected for large x since, for large x, they equal roughly:

$$\{\mu^2(1-x)+\mathbf{Q}^2(1-x)^2z(1-z)-\mathbf{P}^2x^2\}^{-1}\{Mx[M^2x^2+\mathbf{Q}^2(1-x)^2z(1-z)+\mu^2(1-x)]^{-1}-[Mx]^{-1}\}$$
$$\simeq-[\mu^2(1-x)+\mathbf{Q}^2(1-x)^2z(1-z)-\mathbf{P}^2x^2]^{-1}\frac{\mu^2(1-x)+\mathbf{Q}^2(1-x)^2z(1-z)}{Mx[M^2x^2+\mu^2(1-x)+\mathbf{Q}^2(1-x)^2z(1-z)]}, \tag{29}$$

which for large x can be neglected. These terms contribute, then, only for small x of order μ/M. Neglecting terms of relative order μ/M, we can neglect x in $(1-x)$ everywhere. Our result becomes:

$$\hbar^3c^3(g^2/\hbar c)^2 2M\sigma_{\mu\nu}{}^B\sigma_{\mu\nu}{}^A\int_0^1\{\mu^2+\mathbf{Q}^2z(1-z)\}^{-1}dz\int_0^1dx\{Mx[M^2x^2+\mu^2+\mathbf{Q}^2z(1-z)]^{-1}$$
$$-[\mu^2+\mathbf{Q}^2z(1-z)]^{-\frac{1}{2}}\tan^{-1}[(\mu^2+\mathbf{Q}^2z(1-z))^{\frac{1}{2}}(Mx)^{-1}]\}$$
$$=\hbar^3c^3(g^2/\hbar c)^2 2M\sigma_{\mu\nu}{}^B\sigma_{\mu\nu}{}^A\int_0^1\{\mu^2+\mathbf{Q}^2z(1-z)\}^{-1}dz\{(2M)^{-1}\ln[M^2\{\mu^2+\mathbf{Q}^2z(1-z)\}^{-1}]$$
$$-(2M)^{-1}\ln[M^2\{\mu^2+\mathbf{Q}^2z(1-z)\}^{-1}]-[\mu^2+\mathbf{Q}^2z(1-z)]^{-\frac{1}{2}}\tan^{-1}[\{\mu^2+\mathbf{Q}^2z(1-z)\}^{\frac{1}{2}}M^{-1}]\} \tag{30}$$

$$\simeq -\hbar^3c^3(g^2/\hbar c)^2 2M\sigma_{\mu\nu}{}^B\sigma_{\mu\nu}{}^A\int_0^1 M^{-1}[\mu^2+Q^2z(1-z)]^{-1}dz \tag{30a}$$

$$=-\hbar^3c^3(g^2/\hbar c)^2\sigma_{\mu\nu}{}^B\sigma_{\mu\nu}{}^A[(\tfrac{1}{2}Q)(\mu^2+\tfrac{1}{4}Q^2)^{\frac{1}{2}}]^{-1}\ln\frac{(\mu^2+\frac{1}{4}Q^2)^{\frac{1}{2}}+\frac{1}{2}Q}{(\mu^2+\frac{1}{4}Q^2)^{\frac{1}{2}}-\frac{1}{2}Q}. \tag{31}$$

where $Q=(\mathbf{Q}^2)^{\frac{1}{2}}$.

This expression (31) is of order μ/M smaller than (10), the second-order Born approximation term. For the evaluation of $\sigma^B{}_{\mu\nu}\,\sigma_{\mu\nu}{}^A$, see the appendix.

E. Crossed Exchange of Two Mesons (Process II)

$$4\left(\frac{\hbar^3c^3}{i}\right)\left(\frac{g^2}{\hbar c}\right)^2\int_{-\infty}^{\infty}(q_b{}^2-\mu^2)^{-1}(q_a{}^2-\mu^2)^{-1}\gamma_5{}^B\gamma\mu^B(\not p_2-\not q_b-M)^{-1}\gamma_5{}^B\gamma_\nu{}^B\gamma_5{}^A\gamma_\nu{}^A(\not p_1-\not q_a-M)^{-1}\gamma_5{}^A\gamma_\mu{}^A d^4q_a$$

$$=4\left(\frac{\hbar^3c^3}{i}\right)\left(\frac{g^2}{\hbar c}\right)^2\int_{-\infty}^{\infty}(q_a{}^2+2q_a\cdot q+q^2-\mu^2)^{-1}(q_a{}^2-\mu^2)^{-1}\gamma_\nu{}^B\frac{\not p_2-\not q_a-\not q-M}{q_a{}^2-2q_a\cdot(p_2-q)}\gamma_\nu{}^B\gamma_\nu{}^A\frac{\not p_1-\not q_a-M}{q_a{}^2-2q_a\cdot p_1}\gamma_\mu{}^A d^4q_a, \tag{32}$$

and from Eq. (19)

$$\begin{aligned}&=4\left(\frac{\hbar^3c^3}{i}\right)\left(\frac{g^2}{\hbar c}\right)^2\int_0^1\int_0^1\int_0^1\int_{-\infty}^{\infty}\frac{6x(1-x)dxdydz[\gamma_\mu{}^B(\not p_2-\not q_a-\not q-M)\gamma_\nu{}^B\gamma_\nu{}^A(\not p_1-\not q_a-M)\gamma_\mu{}^A]d^2q_a}{\{2q_a\cdot(-p_2+p_1+q)xy+(2q_a\cdot q+q^2)z(1-x)-(2q_a\cdot p_1-\mu^2)x+q_a{}^2-\mu^2\}^4}\\&=4\left(\frac{\hbar^3c^3}{i}\right)\left(\frac{g^2}{\hbar c}\right)^2\int_0^1\int_0^1\int_0^1\int_{-\infty}^{\infty}\frac{6x(1-x)dxdydz[\gamma_\mu{}^B(\not p_2-\not q_a-\not q-M)\gamma_\nu{}^B\gamma_\nu{}^A(\not p_1-\not q_a-M)\gamma_\mu{}^A]d^4q_a}{\{q_a{}^2-2q_a\cdot[-qz(1-x)+x(p_2y+p_1(1-y))-qxy]-[\mu^2-q^2z(1-x)-\mu^2x]\}^4};\end{aligned} \tag{33}$$

This integration over d^4q_a has been done by Feynman.[2]

$$\begin{aligned}&\hbar^3c^3\left(\frac{g^2}{\hbar c}\right)^2\int_0^1\int_0^1\int_0^1 x(1-x)dxdydz\{[-qz(1-x)+x\{p_2y+p_1(1-y)\}-qxy]^2+[\mu^2-qz(1-x)-\mu^2x]\}^{-2}\\&\times\{\gamma_\mu{}^B(\not p_2-\not q-M)\gamma_\nu{}^B\gamma_\nu{}^A(\not p_1-M)\gamma_\mu{}^A-\gamma_\mu{}^B(-\not pz[1-x]+x[\not p_2y+\not p_1\{1-y\}]-\not pxy)\gamma_\nu{}^B\gamma_\nu{}^A(\not p_1-M)\gamma_\mu{}^A\\&-\gamma_\mu{}^B(\not p_2-\not q-M)\gamma_\nu{}^B\gamma_\nu{}^A(-\not pz(1-x)+x[\not p_2y+\not p_1\{1-y\}]-\not pxy)\gamma_\mu{}^A\\&+\gamma_\mu{}^B(-\not pz(1-x)+x[\not p_2y+\not p_1\{1-y\}]-\not pxy)\gamma_\nu{}^B\gamma_\nu{}^A(-\not pz(1-x)+x[\not p_2y+\not p_1\{1-y\}]-\not pxy)\gamma_\mu{}^A\}\\&+\hbar^3c^3(g^2/\hbar c)^2(\delta_{\sigma\tau}/2)\gamma_\mu{}^B\gamma_\sigma{}^B\gamma_\nu{}^B\gamma_\tau{}^A\gamma_\nu{}^A\gamma_\mu{}^A\\&\qquad\times\int_0^1\int_0^1\int_0^1\frac{x(1-x)dxdydz}{\{-qz(1-x)+x[p_2y+p_1(1-y)]-qxy\}^2+\{\mu^2(1-x)-\mathbf{q}^2z(1-x)\}}.\end{aligned} \tag{34}$$

In the nonrelativistic approximation only the time component of $\not p$ gives an appreciable result, and since $q_4=0$, q in the numerator is dropped while in the denominator $q^2=-\mathbf{Q}^2$ and q^2x^2 is neglected since it is always much less than $M^2x^2+\mu^2(1-x)$. The matrix element is now considered term by term.

As in process I (21–25) the first term gives:

$$\hbar^3c^3\left(\frac{g^2}{\hbar c}\right)^2 4M^2\sigma_{\mu\nu}{}^B\sigma_{\nu\mu}{}^A\int_0^1\int_0^1\int_0^1\{M^2x^2+\mu^2(1-x)+\mathbf{Q}^2(1-x)^2z(1-z)\}^{-2}x(1-x)dxdydz. \tag{35}$$

The second and third terms yield:

$$-\hbar^3c^3\left(\frac{g^2}{\hbar c}\right)^2 4M^2\sigma_{\mu\nu}{}^B\sigma_{\nu\mu}{}^A\int_0^1\int_0^1\int_0^1\{M^2x^2+\mu^2(1-x)+\mathbf{Q}^2(1-x)^2z(1-z)\}^{-2}x^2(1-x)dxdydz. \tag{36}$$

The fourth term, neglecting the coefficient of the integral, becomes:

$$M^2\sigma_{\mu\nu}{}^B\sigma_{\nu\mu}{}^A\int_0^1\int_0^1\int_0^1\{M^2x^2+\mu^2(1-x)+\mathbf{Q}^2(1-x)^2z(1-z)\}^{-2}x^3(1-x)dxdydz$$
$$=\sigma_{\mu\nu}{}^B\sigma_{\nu\mu}{}^A\int_0^1\int_0^1\int_0^1\Big\{[M^2x^2+\mu^2(1-x)+\mathbf{Q}^2(1-x)^2z(1-z)]^{-1}$$
$$-\frac{\mu^2(1-x)+\mathbf{Q}^2(1-x)^2z(1-z)}{[M^2x^2+\mu^2(1-x)+\mathbf{Q}^2(1-x)^2z(1-z)]^2}\Big\}x(1-x)dxdydz. \quad (37)$$

According to (24), (24a), and (25), this integral and the fifth term integral are of order μ^2/M^2 or $\mathbf{Q}^2/M^2$ less than the other terms and are therefore neglected.

The matrix element for process II is then:

$$\hbar^3c^3\left(\frac{g^2}{\hbar c}\right)^2 4M^2\sigma_{\mu\nu}{}^B\sigma_{\nu\mu}{}^A\int_0^1\int_0^1\int_0^1[M^2x^2+\mu^2(1-x)+\mathbf{Q}^2(1-x)^2z(1-z)]^{-2}x(1-x)^2dxdydz$$
$$=\hbar^3c^3\left(\frac{g^2}{\hbar c}\right)^2 4M^2\sigma_{\mu\nu}{}^B\sigma_{\nu\mu}{}^A\int_0^1\int_0^1[M^2x^2+\mu^2(1-x)+\mathbf{Q}^2(1-x)^2z(1-z)]^{-2}x(1-x)^2dxdz. \quad (38)$$

For large x this integral is of order $M^2/M^4=M^{-2}$; therefore it is quite safe to replace $(1-x)$ by 1 everywhere. Since the only sizable contribution comes from small x:

$$\hbar^3c^3\left(\frac{g^2}{\hbar c}\right)^2 4M^2\sigma_{\mu\nu}{}^B\sigma_{\nu\mu}{}^A\int_0^1\int_0^1[M^2x^2+\mu^2+\mathbf{Q}^2z(1-z)]^{-2}xdxdz$$
$$=\hbar^3c^3\left(\frac{g^2}{\hbar c}\right)^2 4M^2\sigma_{\mu\nu}{}^B\sigma_{\nu\mu}{}^A\int_0^1(\tfrac{1}{2})M^{-2}\{[\mu^2+\mathbf{Q}^2z(1-z)]^{-1}-[M^2+\mu^2+\mathbf{Q}^2z(1-z)]^{-1}\} \quad (39)$$
$$\simeq\hbar^3c^3\left(\frac{g^2}{\hbar c}\right)^2\sigma_{\mu\nu}{}^B\sigma_{\nu\mu}{}^A\int_0^1[\mu^2+\mathbf{Q}^2z(1-z)]^{-1}2dz, \quad (39a)$$

or, from Eqs. (30a) and (31):

$$\hbar^3c^3\left(\frac{g^2}{\hbar c}\right)^2\sigma_{\mu\nu}{}^B\sigma_{\nu\mu}{}^A[(\tfrac{1}{2}Q)(\mu^2+\tfrac{1}{4}Q^2)^{\frac{1}{2}}]^{-1}\ln\frac{(\mu^2+\frac{1}{4}Q^2)^{\frac{1}{2}}+\frac{1}{2}Q}{(\mu^2+\frac{1}{4}Q^2)^{\frac{1}{2}}-\frac{1}{2}Q}. \quad (40)$$

V. CHARGE THEORY

What charge is assumed for the meson field, has little effect on the magnitude of the maxima and minima nucleon-nucleon scattering as a function of angle; it has effect only on their relative positions. In order to explain the near-symmetry of the n-p scattering about the equatorial plane, Serber and others at Berkeley have suggested that the nuclear force contains a factor $1+P$. This charge dependence was, e.g., employed by Christian and Hart.[1] To obtain this symmetry in meson theory, we assume that neutral and charged mesons are exchanged with equal[8] probability and almost attain symmetry. That we do not quite obtain symmetry, is because the crossed exchange of two charged mesons is forbidden, thus favoring scattering in the backward direction.

The contribution to the cross section of the field effect is the cross-product between the static Yukawa potential result of Christian and Hart and the field effect:

$$2\times\text{Yukawa potential result }(\sigma^B\cdot\sigma^A)(1+P)$$
$$\times[8\sigma^B\cdot\sigma^A(1+P)-(2\sigma^B\cdot\sigma^A+3)]\hbar^3c^3(g^2/\hbar c)^2$$
$$\times[(\tfrac{1}{2}Q)(\mu^2+\tfrac{1}{4}Q^2)^{\frac{1}{2}}]^{-1}\ln\frac{(\mu^2+\frac{1}{4}Q^2)^{\frac{1}{2}}+\frac{1}{2}Q}{(\mu^2+\frac{1}{4}Q^2)^{\frac{1}{2}}-\frac{1}{2}Q}. \quad (41)$$

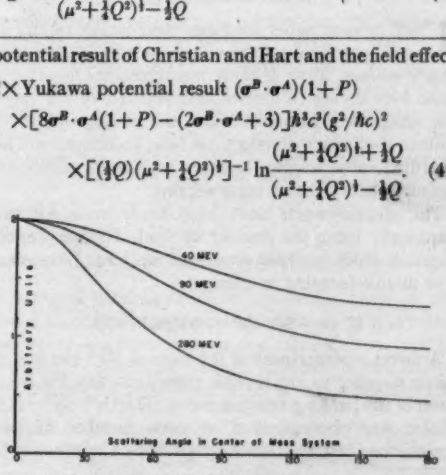

FIG. 4. Matrix element for the field effect at various energies in the laboratory system.

[8] In Kemmer's theory, the emission of charged mesons is twice as probable as that of neutral ones.

VI. RESULTS

The leading relativistic corrections to the static interaction of two nucleons by a Yukawa potential have been computed by examining the effect of retarded interactions in nonrelativistic approximation; this field correction was found to be of order μ/M, not $(\mu/M)^2$, smaller than the static Yukawa potential. The function

$$[(\tfrac{1}{2}Q)(\mu^2+\tfrac{1}{4}Q^2)^{\frac{1}{2}}]^{-1}\ln\frac{(\mu^2+\frac{1}{4}Q^2)^{\frac{1}{2}}+\frac{1}{2}Q}{(\mu^2+\frac{1}{4}Q^2)^{\frac{1}{2}}-\frac{1}{2}Q}$$

has been plotted as a function of scattering angle in the center-of-mass system for 40, 90, and 280-Mev neutron energies in the laboratory system in Fig. 4. The mass of the meson, μ, was taken to be the experimentally determined mass of the π-meson,[9] 276±6 electron masses =141 Mev.

[9] Gardner, Barkas, Smith, and Bradner, Science 111, 191 (1950).

On the basis of this work it may be concluded that at these energies the main part of the neutron-proton scattering may be computed as Christian and Hart have done, *viz.*, by calculating the scattering in a Yukawa potential. A rather accurate and moderately important correction could then be obtained by treating the matrix element for the field effect as a perturbing potential to the simple Yukawa interaction problem.

We would like to take this opportunity to express our sincere thanks to Professor R. P. Feynman for many enlightening discussions during the course of this work.

APPENDIX

$$\sigma_{\mu\nu}{}^B\sigma_{\mu\nu}{}^A=3+(i\sigma_x{}^B)(i\sigma_x{}^A)+(-i\sigma_y{}^B)(-i\sigma_y{}^A)+\cdots$$
$$=3-2\sigma_x{}^B\sigma_x{}^A-2\sigma_y{}^B\sigma_y{}^A-2\sigma_z{}^B\sigma_z{}^A$$
$$=3-2\boldsymbol{\sigma}^B\cdot\boldsymbol{\sigma}^A,$$
$$\sigma_{\mu\nu}{}^B\sigma_{\tau\mu}{}^A=\Sigma_\mu\Sigma_\tau(2\delta_{\mu\nu}-\sigma_{\mu\nu}{}^B\sigma_{\mu\nu}{}^A)=3+2\boldsymbol{\sigma}^B\cdot\boldsymbol{\sigma}^A,$$

since $\Sigma_\mu\Sigma_\nu\delta_{\mu\nu}=3$.

PHYSICAL REVIEW VOLUME 83, NUMBER 6 SEPTEMBER 15, 1951

Some New Values of Atomic Masses, Principally in the Region of 82 Neutrons*

HENRY E. DUCKWORTH, CORT L. KEGLEY, JOHN M. OLSON, AND GEORGE S. STANFORD
Scott Laboratory of Physics, Wesleyan, University, Middletown, Connecticut

(Received May 29, 1951)

Some new mass comparisons are described which lead to atomic mass values for twenty-nine stable nuclides. There is shown to be a definite mass effect associated with the closing of the 82 neutron shell and probably also with the closing of the 58 proton shell. There is evidence that the minimum of the packing fraction curve occurs at $_{28}Ni^{62}$. Recent microwave data are used to obtain the masses of Ge^{74} and Ge^{76} from the mass spectrographically determined masses of Ge^{70} and Ge^{72}.

I. INTRODUCTION

THE present paper describes some recent results in our general program of precise measurement of atomic masses. Most of these measurements have been made with a view to determining whether or not there is a mass effect associated with the closing of the 82 neutron shell. Such an effect has been found and will be described subsequently, together with some additional measurements in other mass regions.

The measurements have been made mass spectrographically using the doublet method. The mass spectrograph which has been employed is a large Dempster-type double-focusing instrument.[1]

II. $O^{16}-S^{32}-Ni^{64}$ COMPARISON

A direct measurement of the mass of Ni^{64} was undertaken in order to locate with more certainty the minimum in the packing fraction curve. The $O_2{}^{16}-S^{32}-Ni^{64}$ triplet was photographed at mass number 32, the desired ions being obtained by allowing a mixture of O_2 and CS_2 to leak into a high frequency spark between nickel electrodes. From nine photographs, the $O^{16}-Ni^{64}$ and $S^{32}-Ni^{64}$ packing fraction differences are $\Delta f=8.25\pm0.03$ and $\Delta f=2.65\pm0.02$, respectively. Assuming for S^{32} a value[2] of $f=-5.547\pm0.01$, the packing fraction of Ni^{64} is computed from the $S^{32}-Ni^{64}$ doublet to be -8.20 ± 0.03, a figure which is reasonably consistent with the result of the $O^{16}-Ni^{64}$ comparison. Assuming the packing fraction of Ni^{64} to be -8.23 ± 0.03, it is possible, by use of excellent transmutation data,[3-10] to compute the f's of Cu^{63}, Zn^{64}, and Cu^{65} to be -8.16

* This work has been done under contract with the AEC.
[1] H. E. Duckworth, Rev. Sci. Instr. 21, 54 (1950).

[2] This is the mean of recent precise measurements made by H. Ewald (private communication) and A. O. Nier, Phys. Rev. 81, 624 (1950).
[3] McElhinney, Hanson, Becker, Duffield, and Diven, Phys. Rev. 75, 542 (1949).
[4] Johns, Katz, Douglas, and Haslam, Phys. Rev. 80, 1062 (1950).
[5] "Nuclear data," NBS Circular 499, September 1, 1950 (unpublished).
[6] Kinsey, Bartholomew, and Walker, Phys. Rev. 78, 481 (1950).
[7] J. A. Harvey, Phys. Rev. 81, 353 (1951).
[8] Hanson, Duffield, Knight, Diven, and Palevsky, Phys. Rev. 76, 578 (1949).
[9] G. C. Baldwin and H. W. Koch, Phys. Rev. 67, 1 (1945).
[10] H. Kubitschek and S. N. Dancoff, Phys. Rev. 76, 351 (1949).

± 0.03, -8.04 ± 0.03, and -8.08 ± 0.03, respectively. This last value is to be compared with -7.87 ± 0.05 obtained through a $Pt^{195}-Cu^{65}$ comparison[11] which is at present somewhat under suspicion.

If the decay scheme of Cu^{62} were known it would be possible to compute the packing fraction of Ni^{62} from that of Cu^{63}. However, a reported γ-ray of 0.56-Mev energy[12] accompanying the 2.88-Mev positron[13,14] is of doubtful authenticity. If there were such a γ-ray the packing fraction of Ni^{62} would be -8.63 ± 0.03, whereas, if there were not, the packing fraction would be -8.53 ± 0.03.

A recent, precise measurement[15] of the mass of Si^{28}, when combined with accurate Q-values[16,17] for the $Si^{28}(d,p)Si^{29}$ and $Si^{29}(d,p)Si^{30}$ reactions, has shown that our value[18] for the mass of Si^{30} is about 0.35 mMU too small. This leads, through the $Si^{30}-Ni^{60}$ comparison,[19] to corrected packing fraction for Ni^{60} of -8.43 ± 0.03 and suggests that, unless either Zn^{66} or Zn^{68} should be found to be exceptionally stable, the minimum in the packing fraction curve is at Ni^{62}. This agrees with the experiments of Shaw,[20] although our packing fractions for nickel are all algebraically larger than his.

III. Cu–Zn–Te–Pt COMPARISON

The masses of Te^{126}, Te^{128}, and Te^{130} were obtained in the following way. An electrode was prepared by packing a thin-walled steel tube with a mixture of brass and tellurium fillings (1:6 by volume) and the desired ions were produced by running a high frequency spark between this electrode and one made of platinum. After a good deal of difficulty, chiefly because of the uncooperative behavior of the tellurium in the spark, a few fair photographs were obtained of the $Te^{126}-Cu^{63}$ doublet at mass number 63, the $Te^{128}-Zn^{64}$ doublet at mass 64 and the $Pt^{195}-Te^{130}-Cu^{65}$ triplet at mass 65. The following packing fraction differences were found: $Te^{126}-Cu^{63}$, $\Delta f=3.61\pm 0.07$ (3 doublets); $Te^{128}-Zn^{64}$, $\Delta f=3.91\pm 0.07$ (5 doublets); $Te^{130}-Cu^{65}$, $\Delta f=3.98\pm 0.06$ (6 doublets); and $Pt^{195}-Te^{130}$, $\Delta f=5.45\pm 0.11$ (5 doublets). Using the f's of Cu^{63}, Zn^{64}, and Cu^{65} previously listed, and the value[11] for Pt^{195} of 1.35 ± 0.04, the packing fractions of Te^{126}, Te^{128} and Te^{130} are found to be -4.55 ± 0.08, -4.13 ± 0.08, and -4.10 ± 0.07, respectively.

IV. Zr–Ba COMPARISON

Using a spark between a barium electrode and one of zirconium, five satisfactory photographs were obtained of the $Ba^{138}-Zr^{92}$ doublet at mass number 46. These give a packing fraction difference of 3.58 ± 0.05. Assuming for Zr^{90} that[21] $f=-7.49\pm 0.05$, and making use of Harvey's Q's for the $Zr^{90}(d,p)Zr^{91}$ and $Zr^{91}(d,p)Zr^{92}$ reactions,[7] the packing fraction of Ba^{138} is found to be -3.65 ± 0.07. The masses of Ba^{136} and Ba^{137} may be computed from that of Ba^{138} by means of the (γ,n) thresholds measured[22] by Sher, Halpern, and Stephens.

V. Ti–Pr COMPARISON

The $Pr^{141}-Ti^{47}$ doublet at mass number 47 was photographed using a spark between a titanium electrode and one of neodymium with a strong praseodymium impurity. Six doublets yield a packing fraction difference of 3.64 ± 0.03. The mass of Ti^{47} can be computed from that of Ti^{48} by means of the Q[7] for the $Ti^{47}(d,p)Ti^{48}$ reaction and the threshold[22] for the $Ti^{48}(\gamma,n)$ reaction. In this way the packing fraction of Pr^{141} is found to be -3.45 ± 0.06. The (γ,n) threshold of Pr^{141} has been measured by Ogle, *et al.*,[23] and Hanson, *et al.*,[5] to be 9.8 ± 0.3 and 9.4 ± 0.1 Mev, respectively. Since Pr^{140} is known to emit a β^- of 2.5-Mev energy,[5] the upper limit for the packing fraction of Ce^{140} is computed to be -3.65. With better knowledge of the decay scheme of Pr^{140}, the packing fraction of Ce^{140} could be calculated more accurately. Using the measured $Ce^{142}(\gamma,n)$ threshold[22] and the known decay scheme[5] of Ce^{141}, the packing fraction of Ce^{142} is computed from that of Pr^{141} to be -3.26 ± 0.06.

VI. Mo–Pr–Nd COMPARISON

With a spark between one electrode of molybdenum and a second of neodymium containing a considerable praseodymium impurity, the following doublets were photographed: $Pr^{141}-Mo^{94}$ at mass number 47, $Nd^{144}-Mo^{96}$ at mass 48, and $Nd^{150}-Mo^{100}$ at mass 50. The measured packing fraction differences are $\Delta f=2.54\pm 0.05$ (4 doublets), $\Delta f=3.66\pm 0.03$ (5 doublets), and $\Delta f=4.09\pm 0.04$ (7 doublets), respectively. The Δf's, when combined with the value of Pr^{141} and previously reported values[18] for Mo^{96} and Mo^{100}, give the following results: Mo^{94}, $f=-6.99\pm 0.08$; Nd^{144}, $f=-3.06\pm 0.06$; and Nd^{150}, $f=-2.08\pm 0.06$.

VII. Sr–Y–Hf COMPARISON

A nickel tube was packed with equal parts of SrO and Y_2O_3 and used as one electrode in a spark in which the other electrode was a rod of hafnium metal.[24] Satisfactory photographs were obtained of the $Hf^{176}-Sr^{88}$ doublet at mass number 88, and fair photographs

[11] Duckworth, Woodcock, and Preston, Phys. Rev. **78**, 479 (1950).
[12] G. T. Seaborg and I. Perlman, Revs. Modern Phys. **20**, 585 (1948).
[13] Becker, Kirn, and Buck, Phys. Rev. **76**, 1406 (1949).
[14] Katz, Penfold, Moody, Haslam, and Johns, Phys. Rev. **77**, 289 (1950).
[15] H. Ewald (private communication).
[16] Endt, Van Patter, and Buechner, Phys. Rev. **81**, 317 (1950).
[17] Van Patter, Sperduto, and Enge, Phys. Rev. **83**, 212 (1951).
[18] Duckworth, Preston, and Woodcock, Phys. Rev. **79**, 188 (1950).
[19] Duckworth, Johnson, Preston, and Woodcock, Phys. Rev. **78**, 386 (1950).
[20] A. E. Shaw, Phys. Rev. **75**, 1011 (1949).
[21] From reference 18 corrected for the change in the mass of Si^{30}.
[22] Sher, Halpern, and Stephens, Phys. Rev. **81**, 154 (1951).
[23] Ogle, Brown, and Carson, Phys. Rev. **78**, 63 (1950).
[24] We are grateful to Mr. E. B. Meservey for obtaining the hafnium wire for us.

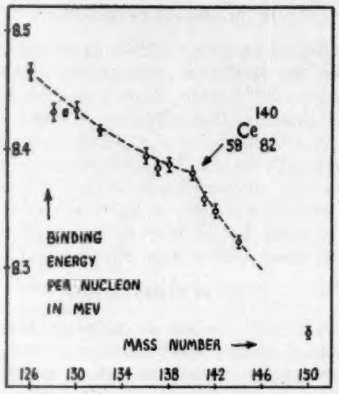

FIG. 1. Plot of the binding energy per nucleon *versus* the mass number in the 82 neutron region.

of the $Hf^{188}-Y^{89}$ doublet at mass number 89 were obtained on some exposures. From five photographs the $Hf^{176}-Sr^{88}$ packing fraction difference is $\Delta f=7.11\pm0.04$, whereas from three photographs the $Hf^{178}-Y^{89}$, $\Delta f=7.07\pm0.05$. These differences, when combined with a previous value[25] for Sr^{88} and transmutation data[5,7] leading to Y^{89} from Sr^{88}, result in packing fractions for Hf^{176} and Hf^{178} of -0.44 ± 0.06 and -0.36 ± 0.07, respectively.

VIII. Ni–Zr–Hf COMPARISON

Spark electrodes of hafnium and zirconium gave well-matched $Hf^{180}-Zr^{90}$ doublets at mass number 90. Subsequently, $Hf^{180}-Ni^{60}$ doublets at mass number 60 were obtained with hafnium and stainless steel electrodes. The measured packing fraction differences are 7.70 ± 0.03 and 8.57 ± 0.03, respectively, and lead, by use of the above value for Ni^{60} and a previously reported value[21] for Zr^{90}, to two values for the packing fraction of Hf^{180}. These are 0.19 ± 0.06 from the first comparison and 0.14 ± 0.05 from the second, giving a weighted mean of 0.16 ± 0.04.

IX. Zr–W COMPARISON

Using a spark between one electrode of tungsten wire and a second consisting of a nickel tube packed with zirconium metal, satisfactory photographs were taken of the $W^{182}-Zr^{91}$ and $W^{184}-Zr^{92}$ doublets at mass numbers 91 and 92. The measured packing fraction differences are 7.45 ± 0.04 (7 doublets) and 7.53 ± 0.04 (8 doublets), respectively. These doublet separations were studied previously by Dempster[26] who obtained $\Delta f=7.85\pm0.2$ for the first and $\Delta f=8.05\pm0.2$ for the second. Masses for Zr^{91} and Zr^{92} may be computed from that of Zr^{90} using the Q-values[7] for the appropriate dp reactions, and these lead to a value for the packing fraction of W^{182} of $f=0.18\pm0.06$ and for W^{184} of $f=0.28\pm0.06$.

The recent measurement of the $W^{183}(\gamma,n)$ threshold[22] permits the calculation of the mass of W^{183} from that of W^{182}. The resulting packing fraction is 0.32 ± 0.07. Also, from a knowledge of the Q of the $Ta^{181}(d,p)Ta^{182}$ reaction[7] and the decay scheme[27] of Ta^{182}, the packing fraction of Ta^{181} may be computed to be 0.17 ± 0.07.

X. Ge–Ce–Nd COMPARISON AND THE MASSES OF THE GERMANIUM ISOTOPES

$Nd^{144}-Ge^{72}$ and $Nd^{146}-Ge^{73}$ doublets of not very good quality were photographed at mass numbers 72 and 73, the ions arising from a spark between a neodymium electrode and one consisting of germanium[28] in a nickel tube. $Ce^{140}-Ge^{70}$ doublets were photographed using a cerium electrode and a nickel tube enclosing a rod of germanium. The nickel tube partially shielded the germanium from the spark and had the effect of diluting the germanium. The resultant packing fraction differences are: $Nd^{144}-Ge^{72}$, $\Delta f=4.85\pm0.07$ (5 doublets); $Nd^{146}-Ge^{73}$, $\Delta f=4.64\pm0.08$ (4 doublets); and $Ce^{140}-Ge^{70}$, $\Delta f=4.25\pm0.03$ (6 doublets). Using the packing fractions for Nd^{144} and Ce^{140} cited, those of Ge^{72} and Ge^{70} are computed to -7.91 ± 0.09 and 7.90 ± 0.08, respectively.

Geschwind and Gunther-Mohr, by a microwave study[29] of the isotopic shift in the pure rotational spectrum of GeH_3Cl^{35}, have determined that the $Ge^{72}-Ge^{70}$, $Ge^{74}-Ge^{72}$, and $Ge^{76}-Ge^{74}$ mass differences are in the ratio of 1:1.00059:1.0018. The $Ce^{140}-Ge^{70}$ and $Nd^{144}-Ge^{72}$ mass comparisons already described were undertaken to determine the absolute values of the Ge^{70} and Ge^{72} masses, with the intention of combining them with the microwave data to compute the masses of Ge^{74} and Ge^{76}. Although the present mass spectrographic results are not very accurate, they can be thus used to compute packing fractions for Ge^{74} and Ge^{76} of -7.76 ± 0.12 and -7.46 ± 0.12, respectively. Also, a recent study[30] of the decay of As^{74} and knowledge of the threshold[23] of the $As^{75}(\gamma,n)$ reaction enable one to compute for Se^{74}, $f=-7.59\pm0.12$, and for As^{75}, $f=-7.57\pm0.12$.

The prospect of combining mass spectrographic and microwave results in this manner is very attractive to the mass spectroscopist, especially in the study of elements which possess many isotopes, such as Cd, Sn, Te, etc. It is hoped that the accuracy of the mass spectrographic part of this dual project for germanium will be improved in the near future.

[25] H. E. Duckworth and R. S. Preston, Phys. Rev. **82**, 468 (1951).
[26] A. J. Dempster, Phys. Rev. **53**, 64 (1938).
[27] Engelkemeir, Freedman, and May, ANL-4473 (1950) (unpublished).
[28] We are indebted to Dr. N. B. Hannay for the germanium electrodes.
[29] S. Geschwind and R. Gunther-Mohr, Phys. Rev. **81**, 882 (1951).
[30] Johansson, Cauchois, and Siegbahn, Phys. Rev. **82**, 275 (1951).

XI. DISCUSSION OF MASSES IN THE 82 NEUTRON REGION

The new mass values from Te^{128} to Nd^{150} are plotted in Fig. 1 on a binding energy per nucleon curve. Also plotted on this curve are the binding energies of Xe^{129} and Xe^{132} recently measured[31] in this laboratory. The recent measurements[32] by Goudsmit, Richards, and Hays of the masses of I^{127} and several of the isotopes of xenon are not plotted in Fig. 1 because they do not seem to be consistent with ours. Regardless of whether these measurements are more or less reliable than ours, it is important in searching for a change in nuclear stability to use a consistent set of mass values.

The curve in Fig. 1 is drawn to pass through the points representing even-even nuclides. Three of the four points lying below the curve are either even-odd or odd-even nuclides and would be expected to be less stable than their even-even cousins. The fourth low-lying point is Te^{128}, and it must be concluded that this mass has been poorly measured. Figure 1 shows a sudden change in the binding energy curve at $_{58}Ce^{140}$. Sudden changes of this sort have been observed[33,28] at $_{40}Zr^{90}$ and $_{82}Pb^{208}$, nuclides which are "doubly-magic," or possess closed shells of both protons and neutrons. Since Ce^{140} possesses a closed shell of 82 neutrons it is tempting to ascribe to it a "doubly-magic" character, and in this way identify 58 protons as a closed shell configuration, representing the completion[34] of the $1g_{7/2}$ subshell. Nuclear spins of 7/2 are common[35] among nuclides in the $Z=51$ to $Z=57$ range and, in particular, $_{57}La^{139}$ has a spin of 7/2. When one considers that the pairing-energy is thought to increase[34] with increasing values of spin, so that the addition of the 58th proton to $_{57}La^{139}$ should lower the energy of the $1g_{7/2}$ state still further with respect to the competing $2d_{3/2}$, $2d_{5/2}$, and $3s_{1/2}$ states, it seems reasonable to conclude on the basis of spin evidence that Ce^{140} does indeed represent a completed proton shell. If so, the data represented in Fig. 1 give further proof of the usefulness of investigating nuclear shell structure by studying atomic masses. The rather obvious comment might be made in this connection that, although studies of spins have been made so very fruitful in the identification of nuclear energy levels, they have given and give no promise of yielding information about ground states in even-even nuclei, since it appears that in these cases the spins are always zero. The approach to the nuclear energy level problem by a study of masses suffers from no such limitation.

[31] C. L. Kegley and H. E. Duckworth, Nature **167**, 1025 (1951).
[32] S. A. Goudsmit (private communication).
[33] A. J. Dempster, Phys. Rev. **53**, 869 (1938).
[34] M. G. Mayer, Phys. Rev. **78**, 16 (1950).
[35] See, for example, the list of spins compiled by J. E. Mack, Revs. Modern Phys. **22**, 64 (1950).

TABLE I. New mass values reported in this paper.

Cu^{63}	62.94862±0.00020	Ba^{137}	136.9502±0.0010
Zr^{64}	63.94852±0.00019	Ba^{138}	137.9498±0.0009
Ni^{64}	63.94733±0.00019	Ce^{140}	139.9489±0.0009
Cu^{65}	64.94749±0.00021	Pr^{141}	140.9514±0.0008
Ge^{70}	69.9447 ±0.0006	Ce^{142}	141.9537±0.0009
Ge^{72}	71.9430 ±0.0006	Nd^{144}	143.9560±0.0008
Ge^{74}	73.9426 ±0.0009	Nd^{150}	149.9687±0.0008
Se^{74}	73.9439 ±0.0009	Hf^{176}	175.9923±0.0011
As^{75}	74.9432 ±0.0010	Hf^{178}	177.9936±0.0013
Ge^{76}	75.9433 ±0.0009	Hf^{180}	180.0029±0.0007
Mo^{94}	93.9343 ±0.0008	Ta^{181}	181.0031±0.0013
Te^{126}	125.9427 ±0.0010	W^{182}	182.0033±0.0011
Te^{128}	127.9471 ±0.0010	W^{183}	183.0059±0.0013
Te^{130}	129.9467 ±0.0009	W^{184}	184.0052±0.0011
Ba^{136}	135.9488 ±0.0010		

XII. SUMMARY OF RESULTS

The new mass values resulting from the work described in this paper are listed in Table I.

XIII. CONCLUDING REMARKS

The new mass values listed in Table I supplement previous atomic mass measurements made in this laboratory. With these new masses there are now available sufficient mass spectrographic and transmutation data to compute the masses of approximately 40 percent of the stable nuclides with $A>45$. A review of the mass information available in this region is now in preparation.

The authors appreciate greatly the indispensable help given during the course of these experiments by Mr. Clifford Gieselbreth.

On the Reactions $\pi^+ + d \rightleftarrows p + p$*

W. B. CHESTON
University of Rochester, Rochester, New York
(Received April 5, 1951)

The reactions $\pi^+ + d \rightleftarrows p + p$ have been investigated in weak-coupling approximation. Using detailed balancing arguments it is shown that comparison of the total cross sections for both processes at appropriate energies allows a unique determination of the spin of the charged π-meson independent of weak coupling theory. It is also shown that the angular distributions of the final state particles and the energy variation of the total cross sections also provide information as to the charged π-meson spin.

1. INTRODUCTION

COMPARISON of the theoretical predictions[1] regarding the absorption of a π^- meson from the K shell of the mesic-deuterium atom with the observed ratio of 2 to 1 for nonradiative to radiative absorption[2] leads to the conclusion that the charged π-meson is either pseudoscalar (spin zero and odd parity) or pseudovector (spin one and even parity). This conclusion follows from quite general selection rules associated with the properties of a π^- meson in a K shell rather than from detailed quantitative predictions of weak-coupling theory. It is clear that at sufficiently low energies (say, below 5 Mev) the same selection rules operate for the absorption of π^+ mesons by deuterons and nonradiative and radiative absorption complete on almost equal terms. However, if an experiment is carried out for π^+ energies greater than 5 Mev (which is experimentally more feasible) the nonradiative process $\pi^+ + d \rightarrow p + p$ becomes dominant and of great interest for studying the properties of the π^+ meson.

In this paper we treat the reaction $\pi^+ + d \rightarrow p + p$ phenomenologically and compute both the total cross section as a function of energy and the angular distribution of the two final protons for the fields and couplings considered by Tamor[1] [$S(S)$, $PS(PS)$, $PS(PV)$, $V(V)$, and $PV(PV)$]. We restrict ourselves to meson energies greater than 5 Mev[3] but low enough (say, less than 100 Mev) so that the nucleons can be treated nonrelativistically. We also calculate the cross section for the inverse reaction $p + p \rightarrow \pi^+ + d$ at corresponding energies and determine the angular distribution of the π^+ mesons in the laboratory system.[4] It will be shown that the method of detailed balancing applied to the two reactions permits a unique determination of the spin of the π^+ meson.

2. THE REACTION $\pi^+ + d \rightarrow p + p$

We perform a first-order phenomenological calculation similar to that used by Tamor[1] in his investigation of the analogous process of the absorption of the π^- meson from the K shell of the mesic-deuterium atom. The matrix element M for the absorption of a π^+ meson by the deuteron may be written:

$$M = \int \Psi_f^*(\mathbf{r}_1, \mathbf{r}_2; \sigma_1, \sigma_2; \tau_1, \tau_2)\vartheta(\mathbf{r}_1, \mathbf{r}_2; \sigma_1, \sigma_2; \tau_1, \tau_2) \times \Psi_0(\mathbf{r}_1, \mathbf{r}_2; \sigma_1, \sigma_2; \tau_1, \tau_2) d\mathbf{r}_1 d\mathbf{r}_2 \quad (1)$$

where $\mathbf{r}_i$, σ_i, τ_i are the space, spin, and isotopic spin of the ith nucleon; ϑ is the operator which takes the two nucleon system in the initial state (deuteron) into the

TABLE I. Meson-nucleon interaction operators.

Theory	Interaction operator	Nonrelativistic approximation
$S(S)$	$(4\pi)^{\frac{1}{2}} g \beta \phi$	$(4\pi)^{\frac{1}{2}} g \phi$
$PS(PS)$*	$i(4\pi)^{\frac{1}{2}} f' \beta \gamma^5 \phi$	$i(4\pi)^{\frac{1}{2}} \frac{f'}{2} \left\{ \sigma \cdot \mathbf{k} - \frac{E - 2J(r)\Delta}{2} \sigma \cdot (\mathbf{p}' + \mathbf{p}^0) \right\} \phi$
$PS(PV)$	$i(4\pi)^{\frac{1}{2}} \frac{f}{\mu} \beta \gamma^5 \gamma_\mu \frac{\partial}{\partial x_\mu} \phi$	$-i(4\pi)^{\frac{1}{2}} \frac{f}{\mu} \left\{ \sigma \cdot \mathbf{k} - \frac{E}{2} \sigma \cdot (\mathbf{p}' + \mathbf{p}^0) \right\} \phi$
$V(V)$	$i(4\pi)^{\frac{1}{2}} g' \beta \gamma_\mu \phi_\mu$	$(4\pi)^{\frac{1}{2}} \frac{g'}{2} \left\{ \left(\mathbf{p}' + \mathbf{p}^0 - \frac{2}{E} \mathbf{k} \right) \cdot \boldsymbol{\phi} + i\sigma \cdot (\mathbf{p}' - \mathbf{p}^0) \times \boldsymbol{\phi} \right\}$
$PV(PV)$	$i(4\pi)^{\frac{1}{2}} f'' \beta \gamma^5 \gamma_\mu \phi_\mu$	$(4\pi)^{\frac{1}{2}} f'' \sigma \cdot \boldsymbol{\phi}$

* The equivalence theorem between the $PS(PS)$ and $PS(PV)$ theories does not hold because the potential contains charge exchange operators [see F. J. Dyson, Phys. Rev. 73, 929 (1948)]. We have assumed that the two nucleon potential may be written:

$$V(r, \sigma, \tau) = \tfrac{1}{2}(1 + P_M) J(r),$$

where P_M is the Majorana operator.

* This work was sponsored by the AEC.
[1] S. Tamor, Phys. Rev. 82, 38 (1951).
[2] Aamodt, Hadley, and Panofsky (private communication).
[3] This has the additional advantage that the coulomb barrier of the deuteron may be neglected.
[4] The angular distribution in the c.m. system is the same for the inverse reaction (see below).

TABLE II. Differential cross section for the reactions $\pi^+ + d \rightleftarrows p + p$ in the c.m. system.

Type of meson-nucleon coupling	$dN(\theta)/d(\cos\theta)$ unnormalized
$S(S)$	$\{a_- - a_+\}^2$
$PS(PS)$	$\{2\lvert[E\mathbf{K}+\mathbf{k}]a_+ + [\mathbf{K}-\tfrac{1}{2}\mathbf{k}]c_+\rvert^2$ $+2\lvert[E\mathbf{K}-\mathbf{k}]a_- + [\mathbf{K}+\tfrac{1}{2}\mathbf{k}]c_-\rvert^2$ $+4([E\mathbf{K}+\mathbf{k}]a_+ + [\mathbf{K}-\tfrac{1}{2}\mathbf{k}]c_+)\cdot([E\mathbf{K}-\mathbf{k}]a_- + [\mathbf{K}+\tfrac{1}{2}\mathbf{k}]c_-)$ $+\lvert[E\mathbf{K}+\mathbf{k}]\rvert^2 a_+^2 + \lvert[E\mathbf{K}-\mathbf{k}]\rvert^2 a_-^2 + 2[k^2 - E^2K^2]a_+a_-\}$
$PS(PV)$	$\{3\lvert E\mathbf{K}+\mathbf{k}\rvert a_+^2 + 3\lvert E\mathbf{K}-\mathbf{k}\rvert a^2$ $-2[k^2 - E^2K^2]a_+a_-\}$
$V(V)$	$(1/E^2)\{\lvert E\mathbf{K}+\mathbf{k}\rvert^2 a_+^2 + \lvert E\mathbf{K}-\mathbf{k}\rvert^2 a_-^2 - 2[k^2 - E^2K^2]a_+a_-\}$
$PV(PV)$	$\{3a_-^2 + 3a_+^2 - 2a_+a_-\}$

final state (two protons) and represents the absorption of a π^+ meson; Ψ_0; Ψ_f are the wave functions of the initial and final states of the two nucleon system. For Ψ_f we chose appropriately antisymmetrized plane wave functions neglecting the interaction of the two nucleons in the final state, which is assumed small because of the high kinetic energy (>70 Mev) of the final protons.[5] In considering Ψ_0 we note that the deuteron ground state is predominantly ${}^3S_1$ with a few percent admixture of ${}^3D_1$. We shall first neglect the ${}^3D_1$ contribution to Ψ_0 and estimate the error introduced later. For the space part of $\Psi_0(r)$, we chose therefore the S-state solution of Schrödinger's equation corresponding to Hulthen's potential:

$$V(r) = \frac{\gamma^2 - \beta^2}{e^{(\beta-\gamma)r} - 1}; \quad \Psi_0(r) = \frac{N}{(4\pi)^{\frac{1}{2}}} \frac{e^{-\gamma r} - e^{-\beta r}}{r} |\text{triplet}>$$

where γ = reciprocal radius of the deuteron; and β is defined in terms of r_0, the effective range of nuclear forces, thus:

$$r_0 = 2/(\gamma+\beta) - 1/\beta.$$

Since our calculation is phenomenological and treats the two nucleons nonrelativistically, it is necessary to find nonrelativistic expressions for the meson-nucleon interaction operators which are valid to first order in v/c of the nucleons. The nonrelativistic approximations to those interactions which contain only even operators, i.e., $S(S)$ and $PV(PV)$ are immediate. For those interactions which contain odd operators, i.e., $PS(PS)$,[6] $PS(PV)$, and $V(V)$ the method we use is due to Foldy and Wouthuysen.[7] The nonrelativistic approximations for the various theories are given in Table I. The

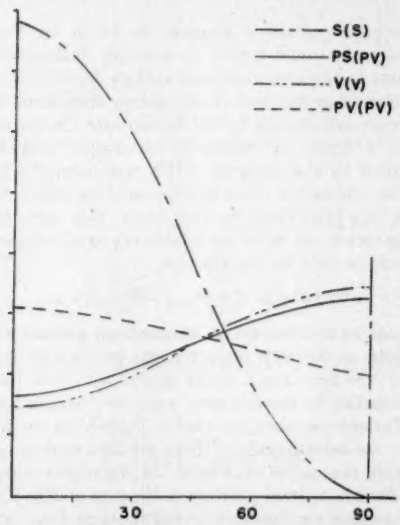

FIG. 1. Angular distribution of protons in c.m. system for absorption of 22.7 Mev π^+ mesons by the deuteron. The ${}^3D_1$ contribution to the deuteron ground state is neglected.

TABLE III. Differential cross section for the reactions $\pi^+ + d \rightleftarrows p + p$ in the c.m. system evaluated for four different incident π^+ kinetic energies (laboratory system).

$\sigma(0°):\sigma(45°):\sigma(90°)$.[a]

Theory \ π Kinetic energy (Mev)	5		22.7		50		100	
	45°	90°	45°	90°	45°	90°	45°	90°
$S(S)$	0.49	0	0.47	0	0.44	0	0.38	0
$PS(PS)$[b]			1.18	1.23				
$PS(PV)$	1.13	1.26	1.52	1.97	1.80	2.33	1.88	2.22
$V(V)$	1.10	1.19	1.71	2.33	5.12	7.90	6.01	8.40
$PV(PV)$	0.96	0.92	0.84	0.70	0.71	0.48	0.56	0.27

[a] All values normalized to $\sigma(0°) = 1$.

[b] Values in this table and Tables V and VII for the $PS(PS)$ theory were calculated using $J(r) = -V'/\alpha^2 e^{-\alpha r}/\alpha r$. The values of V_0 and α used are based on a value of $r_0 = 1.74 \times 10^{-13}$ cm. [Hughes, Burgy, and Ringo, Phys. Rev. 77, 291 (1950); Hughes, Phys. Rev. 78, 315 (1950).]

[5] The effect of the distortion of the final wave function caused by the interaction of the two protons was estimated and found to change the total and differential cross sections by at most a few percent.

[6] It should be noted that a phenomenological calculation employing the $PS(PS)$ theory is likely to lead to misleading results if nuclear forces are due to an exchange of virtual mesons. This follows because for the $PS(PS)$ theory, the exchange terms (i.e., the terms involving the absorption of the real meson between the emission and absorption of the virtual mesons) dominate the nonexchange terms and when the nuclear force is replaced by a potential, these exchange terms are ignored. Nevertheless, we give some results for the $PS(PS)$ theory for the sake of comparison.

[7] L. Foldy and S. Wouthuysen, Phys. Rev. 78, 29 (1950).

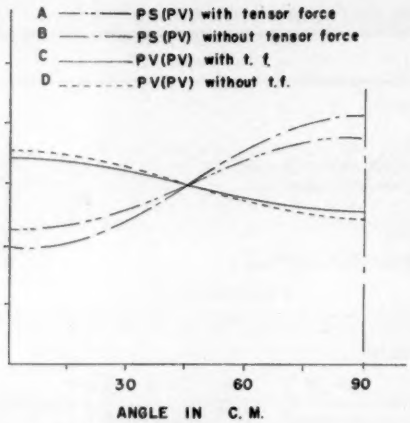

FIG. 2. Angular distribution of protons in c.m. system for absorption of 22.7-Mev π^+ mesons by the deuteron. Curves A and C include the ${}^3D_1$ contribution for the $PS(PV)$ and $PV(PV)$ theories respectively, whereas curves B and D neglect the ${}^3D_1$ contribution for the $PS(PV)$ and $PV(PV)$ theories.

symbols in Table I are defined as: ϕ=meson wave function (incoming plane wave); $\mathbf{k}$=meson momentum; E=meson energy; σ=Pauli spin matrix; $\mathbf{p}^0$, $\mathbf{p}'$=initial and final nucleon momenta; $\hbar=c=M=1$. Λ is defined by: $<\text{triplet}|\Lambda=<\text{triplet}|$; $<\text{singlet}|\Lambda=0$. For the process to occur, the interaction operators must be symmetrized with respect to the space, spin, and isotopic spin coordinates of the two nucleons. Since the initial state is antisymmetric in isotopic spin and the final state symmetric in this coordinate, the interaction operators must be antisymmetrized in the space and spin coordinates of the two nucleons. The angular distribution of the final protons follows directly from the differential cross section and is expressable in terms of two integrals $a^{\pm}$ and $c^{\pm}$ defined by:

$$a^{\pm}=\int\frac{u_0(R)}{R}\exp[i(\mathbf{K}\pm\tfrac{1}{2}\mathbf{k})\cdot\mathbf{R}]d\mathbf{R},$$
$$c^{\pm}=\int\frac{u_0(R)}{R}J(R)\exp[i(\mathbf{K}\pm\tfrac{1}{2}\mathbf{k})\cdot\mathbf{R}]d\mathbf{R}, \tag{2}$$

where $\mathbf{K}$=momentum of a final proton in the center-of-mass system; $\mathbf{R}$=relative distance between the two nucleons; and $u_0(R)$=solution of the radial part of Schrödinger's equation for the S-state of the deuteron.

TABLE IV. Coefficients in expressions for total absorption cross section (see formula 4).

Theory	A	B	C
$S(S)$	1	0	-1
$PS(PV)$	$\frac{1}{3\mu^2}[E^2K^2-k^2]$	$\frac{E}{\mu^2}$	$\frac{1}{\mu^2}[E^2K^2+k^2]$
$V(V)$	$\frac{1}{3E^2}[E^2K^2-k^2]$	$\frac{1}{3E}$	$\frac{1}{3E^2}[E^2K^2+k^2]$
$PV(PV)$	1	0	$-\frac{1}{3}$

The angular distributions predicted by the four theories are listed in Table II. Curves for the angular distribution of the protons in the center-of-mass system at 22.7-Mev meson kinetic energy are given in Fig. 1. Table III lists $\sigma(0°):\sigma(45°):\sigma(90°)$ in the center-of-mass system for incident mesons whose kinetic energy is 5, 22.7, 50, and 100 Mev in the laboratory. Figure 2 shows the effect of the inclusion of the ${}^3D_1$ contribution to the ground state of the deuteron on the angular distributions in the c.m. system for the $PS(PV)$ and $PV(PV)$ theories. The effect on the total cross section for the processes $\pi^++d\rightleftarrows p+p$ is negligible. It is to be noted that at the lowest energy, the angular distributions for the PS, V, and PV theories are much more isotropic than the curve for the S theory. This can be understood in a qualitative way as follows: at the lowest energy, the π^+ meson is predominantly in an angular momentum state described by $l=0$. The states which may be occupied by two identical nucleons are limited in number by the Pauli principle and are ${}^1S_0$; ${}^3P_{2,1,0}$; ${}^1D_2$; etc. For S-state π^+ mesons, the final states of the two proton system to which transitions occur, are determined by conservation of total angular momentum and parity. They are, for the four theories, S—none; PS—${}^3P_1$; V—${}^3P_{2,1,0}$ and ${}^3F_2$; PV—${}^1S_0$ and ${}^1D_2$.

Since the meson is assumed to be in an S-state initially, we would expect an isotropic distribution of protons in the center-of-mass system for PS, V, and PV mesons in the limit of zero energy since there is no reference axis defined by the initial state. On the other hand, a scalar π^+ meson in an S-state cannot be absorbed by the deuteron. (This was pointed out by Tamor, reference 1.) Any absorption of the scalar meson must take place from the $l>0$ states. This supplies for scalar mesons an initial state reference axis, and general arguments yield for the reaction,

$$\pi^+(l>0)+d\rightarrow 2p({}^3P_{2,1,0}+{}^3F_{4,3,2}+\text{etc.}),$$

an angular distribution of the resultant protons which vanishes at 90° with respect to the incident π^+ meson beam; the fact that a scalar meson with $l=0$ cannot be absorbed by the deuteron is also responsible for the smaller cross sections recorded in Table V for the scalar case (see subsequently). These remarks explain qualitatively the curves at 5 Mev. At the higher energies, the deviations from isotropy in the case of PS, V, and PV mesons are due to the contributions from orbital angular momentum states with $l>0$. Therefore, the anisotropy should increase as the kinetic energy of the absorbed meson increases. In addition, the relatively large anisotropy of the $PS(PV)$ and $V(V)$ angular distribution shows that even for low energy mesons, the absorption of mesons from the p-state competes strongly with absorption from the s-state: this is due

to the presence of gradient operators in the interaction for the $PS(PV)$ and $V(V)$ theories.

The total absorption cross section is evaluated using the relationship:

$$\sigma = (2\pi/v)\int \langle |M|^2 \rangle_{Av} d\mathbf{p}/dE_f, \tag{3}$$

where v is the relative velocity of the π^+ meson and the deuteron and $d\mathbf{p}/dE_f$ = density of states per unit final energy $= \frac{1}{2}Kd\Omega/(2\pi)^3$ (the direction of the incoming meson is chosen as the polar axis in $d\Omega$). The indicated integrations are straightforward and lead to

$$\sigma = \frac{2\pi g^2 N^3}{v}\frac{K}{E}\left\{A\left[\frac{1}{\Gamma_1^+\Gamma_1^-}+\frac{1}{\Gamma_2^+\Gamma_2^-}+\frac{1}{kK(\Gamma_2-\Gamma_1)}\ln\frac{\Gamma_1^-\Gamma_2^+}{\Gamma_1^+\Gamma_2^-}\right]+B\left[\frac{\Gamma_1+\Gamma_2}{kK(\Gamma_1-\Gamma_2)}\ln\frac{\Gamma_1^+\Gamma_2^-}{\Gamma_1^-\Gamma_2^+}\right]+C\left[\frac{1}{2kK\Gamma_1}\ln\frac{\Gamma_1^+}{\Gamma_1^-}+\frac{1}{2kK\Gamma_2}\ln\frac{\Gamma_2^+}{\Gamma_2^-}-\frac{1}{kK(\Gamma_1+\Gamma_2)}\ln\frac{\Gamma_1^+\Gamma_2^+}{\Gamma_1^-\Gamma_2^-}\right]\right\}, \tag{4}$$

TABLE V. Total π^+ absorption cross section evaluated for four different incident π^+ kinetic energies (laboratory system). $\sigma/(g^2/\hbar c)\times 10^{-27}$ cm^2.

π Kinetic energy (in Mev) / Theory	5	22.7	50	100
$S(S)$	1.5	2.0	2.2	1.9
$PS(PS)$[a]		6.9		
$PS(PV)$	20.6	9.6	7.1	4.4
$V(V)$	8.2	1.9	0.70	0.23
$PV(PV)$	58.6	19.4	9.8	6.0

[a] Absorption cross section for the $PS(PS)$ theory was only evaluated at 22.7 Mev for comparison with the reaction $P+P\rightarrow D+\pi^+$ at 340 Mev.

where

$$\begin{pmatrix}\Gamma_1\\ \Gamma_2\end{pmatrix} = \begin{pmatrix}\gamma^2\\ \beta^2\end{pmatrix} + K^2 + \tfrac{1}{4}k^2$$

$$\Gamma_i^{\pm} = \Gamma_i \pm Kk$$

and A, B, C, for the different theories are listed in Table IV. The numerical values for the absorption cross section for incident π^+ mesons of 5, 22.7, 50 and 100-Mev kinetic energy are listed in Table V.

Since the transition probability for the absorption of π^- mesons from the K-shell of the mesic-deuteron atom is finite in all cases except for the scalar field, the cross sections for the π^+ absorption should go as $1/v$ for small v, as indeed they do.[8]

TABLE VI. Observed angular distribution of π^+ mesons in the laboratory system produced in 340-Mev $p-p$ collisions. $\sigma\times 10^{28}$ cm^{-2} steradian.

Angle in laboratory (in degrees)	σ
0	2.0
18	1.63
30	0.58
60	<0.17

3. THE REACTION $p+p\rightarrow\pi^++d$

Experiments at Berkeley[9] indicate that in 340-Mev $p-p$ collisions, the cross section for the reaction $p+p\rightarrow\pi^++d$ is comparable to the cross section for the reaction $p+p\rightarrow\pi^++n+p$. Table VI lists the total cross section of these two reactions at four different angles. The contribution to the production cross section of the first reaction can be predicted theoretically on the basis of Tables II and IV, using detailed balancing arguments. The total production cross section may be obtained from the absorption cross section using the relationship:

$$\sigma^{\text{prod}} = \tfrac{3}{4}(2S+1)(k^2/K^2)\sigma^{\text{abs}},$$

where S is the spin of the π^+-meson, k is the momentum of the meson in the c.m. system, and K is the momentum of the proton in the c.m. system. Table VII lists the total cross sections for the reaction $p+p\rightarrow\pi^++d$ for incident proton energies in the laboratory system corresponding to the four meson energies used in the computations of Sec. 2. The ratios $\sigma^{\text{abs}}/\sigma^{\text{prod}}$ are also recorded in this table for $S=0$; for $S=1$, every ratio is reduced by a factor of 3. Thus the spin of the charged π meson will be uniquely determined[10] when the pro-

TABLE VII. Total π^+ production cross section evaluated for $p-p$ collisions at four different energies. $\sigma^{\text{prod}}/(g^2/\hbar c)\times 10^{-28}$ cm^2.

Proton kinetic energy (Mev)	302	340	394	494
Meson kinetic energy (Mev)	5	22.7	50	100
$\sigma^{\text{abs}}/\sigma^{\text{prod}}$	95.4	18.0	8.9	5.1
Theory				
$S(S)$	0.15	1.1	2.4	2.8
$PS(PS)$		3.8		
$PS(PV)$	2.2	5.3	7.9	8.6
$V(V)$	0.85	1.1	0.75	0.47
$PV(PV)$	6.1	10.8	11.2	11.8

[8] It should be remembered that the correct cross sections at very low energy would behave quite differently because of the coulomb barrier of the deuteron.

[9] Cartwright and Richman (private communication).

[10] It seems to us that this method provides a much more clearcut method for determining the meson spin than the Wentzel experiment (see G. Wentzel, Phys. Rev. 75, 1810 (1949)). Dr. M. H. Johnson has informed us that he independently suggested the measurement of the cross sections for the two reactions $\pi^0+d\leftrightarrows p+p$ as a means of determining the meson spin.

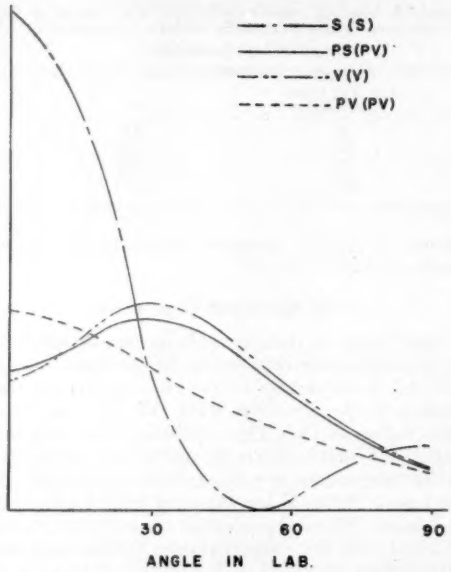

FIG. 3. Angular distribution of π^+ mesons in the laboratory at 340 Mev for the reaction $p+p\rightarrow\pi^++d$. Same remarks apply here as for Fig. 1.

duction and absorption cross sections are known within a factor of three (unless, of course, the spin is greater than 1 in which case the accuracy will have to be better). Once the spin of the charged meson is known, the parity is automatically determined by the results of the π^- meson absorption in deuterium referred to previously. The angular distribution of the π^+ mesons in the c.m. system is the same as the protons but the kinematics changes the laboratory distribution: the results for 340-Mev protons in the laboratory system are given in Figs. 3 and 4.[11] When the data in Table VI are analyzed as to the relative contributions of the two competing reactions, it is hoped that it will be possible

[11] The angular distributions for the reaction $\pi^++d\rightarrow p+p$ were given only in the c.m. system since the transformation to the system in which the deuteron is at rest only changes the distributions slightly for 22.7-Mev mesons.

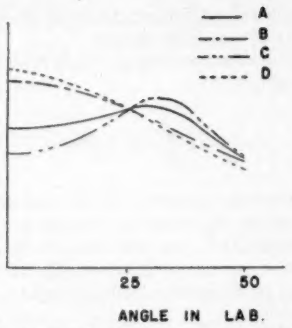

FIG. 4. Angular distribution of π^+ mesons in the laboratory at 340 Mev for the reaction $p+p\rightarrow\pi^++d$. Same remarks apply here as for Fig. 2.

to determine the nature of the charged π-meson. If we consider just the two meson theories which are compatible with the $\pi^-(K$ shell$)+d$ reactions, reference to Fig. 4 shows that the $PV(PV)$ theory predicts a slightly more isotropic distribution of π^+ mesons in the laboratory than does the $PS(PV)$ theory in the reaction $p+p\rightarrow\pi^++d$. However, a more feasible method of deciding between the PS and PV theories is suggested by Tables V and VII. The absorption cross section for the PS theory is essentially constant in the meson energy range of 5 to 100 Mev, whereas the PV theory predicts a decrease of a factor ten. This has as a consequence that the production cross section increases by a factor of ten for the PS theory in the energy region 300 to 500 Mev whereas the PV production cross section remains essentially constant. Either effect can be checked experimentally and the results could offer another—albeit less conclusive—method for determining whether the charged π-meson is pseudoscalar or pseudovector.

4. ACKNOWLEDGMENTS

The author wishes to express his gratitude to Dr. R. E. Marshak under whose guidance this work was undertaken and to Dr. S. Tamor for many helpful discussions concerning the π^- meson absorption problem.

Slow Neutron Velocity Spectrometer Studies. IV. Au, Ag, Br, Fe, Co, Ni, Zn

W. W. HAVENS, JR., AND L. J. RAINWATER
Columbia University, New York, New York
(Received May 23, 1951)

The spectrometer has been improved, enlarged, and all the operational factors re-evaluated. The principal resonance in gold has been redetermined as $E_0=4.87\pm0.07$ ev, and in silver as 5.13 ± 0.07 ev. Resonances are found in Br at 35.7, 54, 104, and 136 ev. Transmission dips are also observed at higher energies which are probably due to unresolved levels. The thermal cross section of iron is well matched by the relation $\sigma=(11.2+0.33E^{-\frac{1}{2}})$. Crystal interference effects are observed in the thermal region with the Debye-Scherrer rings at 2.3A and 2.8A resolved. The cut-off wavelength predicted to be at 4.04A is in good agreement with experiment. No strong resonances are observed in iron at high energies. Resonances are observed in cobalt at 126 ev and 5000 ev. Ni shows crystal interference effects in the thermal region. No strong resonances were detected at high energies. The thermal cross section of Zn is well matched by the relation $\sigma=3.85+0.14E^{-\frac{1}{2}}$ with crystal interferences effects observed in the thermal region. Resonances in Zn occur at 520 ev, 1100 ev, and 3800 ev.

A. INTRODUCTION

THE results of previous investigations using the Columbia University slow neutron velocity spectrometer have been presented in a number of earlier papers.[1-3] The previous three papers[2] of this series present the results of survey studies of nuclear resonance levels using a spectrometer system, which employs a 100-kc crystal oscillator as the timing standard and permits simultaneous measurement of 16 energy intervals for each of two counter systems. Some of the work which has been published[1,3] was not included in this series, as part of it referred to different types of investigations and part of it was done using the original spectrometer system which had considerably poorer reliability and resolving power.

B. IMPROVEMENT OF THE SPECTROMETER CIRCUITS

The spectrometer system described in the first paper of this series has been improved by replacing the 100-kc crystal oscillator with a 1-megacycle crystal oscillator. The block diagram for the spectrometer system is essentially the same as Fig. 1 of the first paper of this series,[2] except that the 100-kc oscillator and 5-μsec circuit are replaced by a 1-Mc oscillator and five additional timing scale-of-two circuits. This permits timing pulses of 1, 2, 4, 8$\cdots$, 32768 μsec. In practice detection intervals as short as 2 μsec and arc "on times" as low as 4 μsec were used for the highest resolution studies to give an approximately triangular resolution function of about 1 μsec/meter width at the base. A 6-meter path length was used for almost all of the measurements.

An arc "on time" of $\tau_{arc}=4$ μsec rather than 2 μsec is used for intensity reasons. The effective arc "on time" is not a square pulse of 4 microseconds duration because the arc current takes between $\frac{1}{2}$ and 1 μsec to rise to its full value. For very sharp dips there is some advantage in having points more closely spaced than the resolution width of the apparatus to better define the transmission curve. Thus it is better to keep the detection intervals (and spacing) shorter than the arc "on time" for highest resolution work.

In the course of the circuit revision, the speed of operation of the entire system was greatly improved in all parts including the pulse amplifiers, pulse-height selectors, timing coincidence circuits, and other timing circuits.

C. QUENCHING THE ARC PULSE

In normal operation of the spectrometer it was customary to remeasure a sharp resonance dip as a general check on the over-all operation of the system from time to time. Such checks made shortly after the publication of the previous set of papers[2] showed a smearing of the resonance dips of Co, Ag, and Au to give much broader and shallower dips displaced to larger timings, and with slow recovery of the transmission on the low energy side of the dip. This was interpreted as failure of the ion production at the arc to stop at the end of the arc modulation pulse. The magnitude of this effect remained large for a period of time and many attempts were made to locate the cause of the trouble and correct it. The cyclotron used a hooded capillary type arc source and the effect was probably caused by ions produced lower down in the arc source which were gradually blown out after the electron emission from the filament was ended. However, the operating conditions were, as far as was known, the same as for the earlier measurements which had shown no observable smearing effect. Thus, under apparently identical operating conditions, the system developed a bad gradual trailing off of ion production after the arc pulse was over. By keeping the flow of deuterium to the arc to a minimum the effect could be removed. The intensity was greatly reduced but the resonance dips

[1] L. J. Rainwater and W. W. Havens, Jr., Phys. Rev. **70**, 136 (1946); W. W. Havens, Jr., and L. J. Rainwater, Phys. Rev. **70**, 154 (1946).
[2] Rainwater, Havens, Wu, and Dunning, Phys. Rev. **71**, 65 (1947); Havens, Wu, Rainwater, and Meaker, Phys. Rev. **71**, 165 (1947); Wu, Rainwater, and Havens, Phys. Rev. **71**, 174 (1947).
[3] Rainwater, Havens, Dunning, and Wu, Phys. Rev. **73**, 733 (1948); Havens, Rainwater, Wu, and Dunning, Phys. Rev. **73**, 963 (1948).

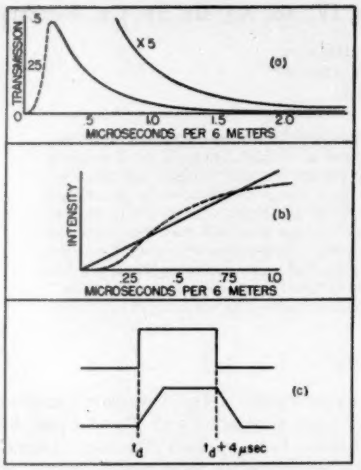

FIG. 1. Calibration of over-all delay time of apparatus. The solid curve in (a) shows the calculated transmission of the thick paraffin sample. The dashed part of the curve indicates the change in neutron intensity. The dashed curve in (b) shows the relative intensity near zero timing; the solid line is the straight line approximation used. The upper curve in (c) shows the theoretical neutron production; the lower curve the approximate neutron production used in the analysis of results.

were restored to the correct timings. The magnitude of the shifts, at worst, was such that the gold and silver resonances were moved from timing values corresponding to ~5 ev to values near 4 ev energy.

The solution which has finally been adopted is to separate the hood on the arc source from the grounded capillary tube and maintain it at a positive potential of about 2000 volts. This potential repels any positive ions in the capillary tube and prevents delayed emission from plasma blown out of the lower part of the arc source. A negative potential was found to make the effect worse and too small a positive voltage did not improve conditions since it could not overcome the effect of the gas flow sweeping the ions out of the capillary. In all measurements using moderately high resolution, the high quenching voltage is now used while the electrode is grounded for low resolution or unmodulated cyclotron operation. Thus, while the effect of delayed ion emission has been cured, the reason why there was no indication of such effects in the earlier work or why the effect suddenly became large is not understood. Such effects appear to be absent from the Cornell cyclotron velocity selector.[4]

D. CALIBRATION OF THE OVER-ALL DELAY TIME

The energy of a resonance dip is determined by the source-detector path length of 6 meters and by the time-of-flight of the neutrons of this energy. The timing of a detection interval after the arc modulation pulse is well known in terms of the basic timing circuits which are precise to ~0.1 μsec. There is, however, a certain over-all delay time, t_d, of the system representing the time required to accelerate the deuterons, etc., and this must be accurately evaluated. Measurements were previously made with the BF_3 counter in a B_4C shield near the source and showed a 7 μsec delay time using 2 μsec arc and detection intervals. Thus, for most of a the subsequent work a 7 μsec correction was used. However, this delay time varies slightly with operating conditions and therefore a technique has been devised to measure the delay time under the same operating conditions and during the same operating period in which the resonance dips are measured. The results of these checks now indicate that a value of between 8.5 and 10.0 μsec is usually obtained with the exact value varying over this range between successive operating periods. The shift from the original value to 9.0 μsec is 2.0 μsec in 6 meters or 0.32 μsec/meter. The position of resonances obtained using this correction now checks very closely the results of Selove *et al.*, using the Argonne mechanical velocity spectrometer system.[5] When the arc and detection intervals are not equal, there is an additional correction of half the difference in the widths if the timings are referred to the start of the intervals rather than to the centers. For $\tau_{arc}=4$ μsec and $\tau_{det}=2$ μsec, this increases the apparent value of t_d by 1 μsec.

The method which is now used to check the delay time is quite simple and consists of using the first detection group[2] and inserting a 2.89 g/cm² paraffin filter in the neutron beam. This gives calculated transmission values of 0.47, 0.237, 0.050, 0.022, 0.011, and 0.0043, at 4×10^6, 10^6, 2×10^5, 10^5, 5×10^4, and 10^4 ev respectively. Thus, only fast neutrons having time-of-flight values of less than 1 μsec for 6 meters will contribute significantly to the counting rate, and the counting rate *vs* timing interval almost gives the experimental resolution function with the delay time shift. In Fig. 1(a) the calculated transmission[6] is given as a function of neutron time-of-flight. If the arc pulse is turned on between $t=0$ and $t=4$ μsec from the start of the timing cycle, the delay time, t_d, will cause the effective neutron production "on time" to be displaced to between t_d and $(t_d+4$ μsec) as shown in the upper curves of Fig. 1(c).

If infinitely short detection intervals were used and there was zero source detector distance, then the plot of detected intensity *vs* timing for fast neutrons should also be zero outside of the region t_d to $(t_d+4$ μsec) and constant within. Again for infinitely narrow detection intervals but with the detector at 6 meters and using the thick paraffin filter, the plot will be broadened as shown in the second curve of Fig. 1(c). This curve may

[4] B. D. McDaniel, Phys. Rev. **70**, 832 (1946).

[5] W. Selove, Phys. Rev. **77**, 557 (1950). Hibdon, Muehlhause, and Selove, Phys. Rev. **77**, 730 (1950).

[6] R. K. Adair, Revs. Modern Phys. **22**, 249 (1950). H. J. Groenewald and H. Groendijk, Physica **XIII**, No. 1–3 (1947).

be understood by noting that the neutrons of a given timing must have originated at the source slab at a time earlier by the amount of the time-of-flight. Since neutrons with times-of-flight between ~0.2 and 1 μsec for 6 meters make up most of the neutrons detected, the expected counting rate will increase roughly linearly for t_d to (t_d+1 μsec) and then remain constant until (t_d+4 μsec) after which it falls off in another microsecond. Thus the expected intensity *vs* timing is not just the experimental resolution function displaced by t_d but is broadened by about 1 μsec extra and is shifted to larger timings by about 0.5 μsec (at 6 meters).

More precisely, to construct the lower curve of Fig. 1(c) the transmission curve of Fig. 1(a) should be multiplied by the curve giving the relative number of neutrons from the source per unit time-of-flight interval times the relative detection efficiency of the BF_3 counter. If the area of this resulting curve is normalized to unity, the integral of the curve should give the form of the rise and fall-off of the lower curve of Fig. 1(c). This is shown in Fig. 1(b) roughly, and a comparison straight line rise between zero and 1 μsec/6 meters is seen to give a good approximation. This approximation was used in Fig. 1(c) and in the analysis of the experimental intensity *vs* timing curve using the thick paraffin.

In Fig. 2, two curves are shown illustrating extreme variations of the measured curves at different operating periods. The procedure which has now been adopted is to check the position of energy levels by frequent measurements using the thick paraffin to determine t_d at the time of the measurements of the position of the resonance dip. The position of the dips for several elements which were previously investigated have been checked by this method, and the results are presented in this and later papers.

E. CALIBRATION OF THE EFFECTIVE SOURCE-DETECTOR DISTANCE

The energy of the neutron groups is determined by the time-of-flight over a measured path length. However, there is a small uncertainty in how this distance should be measured. At the detector end, the center of the 10 cm long active region of the BF_3 counter is used as the detector position while the finite length of the detector contributes an extra term to the resolution broadening, amounting to 1/60 of the time-of-flight. The position to be taken as the effective source location has the main uncertainty due to the small effect of the mean time required for neutrons to cascade from higher energies to the energy of the group being measured. This cascading time is inversely proportional to the velocity of the neutron group being studied, and thus it acts like an extra contribution to the source detector distance to be added to the distance from the front of the source to the detector.

To measure this effective increase in path length, a method of differences has been employed. Using a nominal source detector distance $l_1 \approx 1$ meter, the timing positions of the main resonances at t_{11} and t_{12} for cobalt and indium (126 ev and 1.45 ev) were determined. The same resonances were then studied at $l_2 \approx 6$ meters giving timings t_{21} and t_{22}. The differences $\Delta t_1 = (t_{12} - t_{11})$ and $\Delta t_2 = (t_{22} - t_{21})$ then give the differences in timing for the two resonances at l_1 and l_2. Now l_1 and l_2 can be measured quite precisely aside from the correction effect mentioned above, so the difference $l_2 - l_1 \approx 5$ meters is known with considerable accuracy. The difference $(\Delta t_2 - \Delta t_1)$ accurately corresponds to the timing difference of the two levels for a path length $(l_2 - l_1)$. The effective path l_1 is then given by

$$l_1(\text{effective}) = (l_2 - l_1)\Delta t_1/(\Delta t_2 - \Delta t_1).$$

It should be noted that this method does not require a precise knowledge of the effective time delay or of the energies E_1 and E_2. Such measurements gave a 3 cm effective increase in the path length which is in good agreement with theory. Groenewald and Groendijk[6] [Eq. (23) of their paper] show that the average time a neutron emitted with energy $E \leq E_{\text{initial}}$ has been in paraffin is $\approx 3\tau(E)$. This corresponds to adding three times the mean free path (0.7 cm) for collisions at this energy or 2.1 cm. However, we measure to the part of the source slab which has a plywood front. The equivalent surface of paraffin is thus slightly less than one centimeter further away so that this adds up essentially to 3 cm.

As a by-product of this calibration, when combined with the measurement of the energy of the Co resonance described later, a new value of (1.45±0.02) ev is obtained for the indium resonance. This result is considered to be better established than the previous value[2] of (1.44±0.02) ev. The stated limits of error are now felt to represent extreme limits of uncertainty.

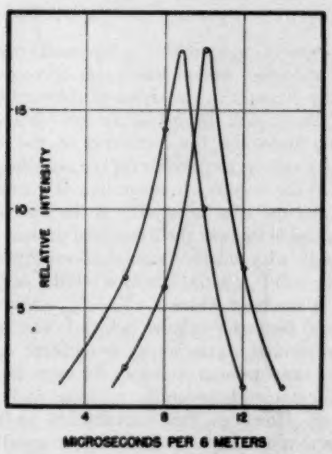

FIG. 2. These two curves show the extreme variations of the measured delay time at different operating periods.

F. ANALYSIS OF RESONANCE LEVEL PARAMETERS

The observation of the time-of-flight corresponding to the minimum of a sharp transmission dip determines the time-of-flight, t_0, and thus the energy, E_0, corresponding to exact resonance. If $n\sigma_0 \gg 1$ where n = sample thickness in atoms/cm^2 and σ_0 = total cross section at exact resonance, calculated for the natural element, the "strength" of the level $\sigma_0\Gamma^2$ can be determined from the area of the transmission dip as described in an earlier paper.[1] Here Γ is the full level width at half-maximum cross section. If $\Gamma \ll E_0$ so the "$(1/v)$ factor" can be neglected, the expression for the total cross section of an element near resonance (neglecting doppler broadening) can be given as

$$\sigma = \sigma_0[1+4(E-E_0)^2/\Gamma^2]^{-1} + \sigma_{\text{const}},$$

$$\sigma_0 = 4\pi\lambda^2 f(\Gamma_n/\Gamma) = \sigma_{0e} + \sigma_{0s},$$

$$\frac{\sigma_{0s}}{\sigma_{0e}} = \frac{\Gamma_n}{\Gamma_\gamma},$$

$$f = \tfrac{1}{2}a[1 \pm (2i+1)^{-1}].$$

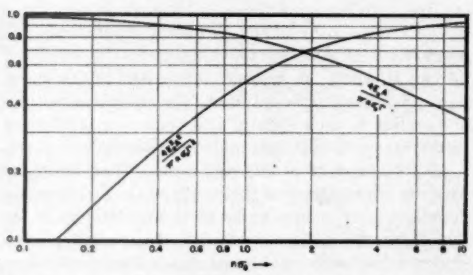

FIG. 3. The deviation of the quantities $(4E_0^2A^2/\pi n\sigma_0\Gamma^2)$ and $(4E_0A/\pi n\sigma_0\Gamma)$ from unity for intermediate values of $n\sigma_0$ are shown. Note that the area A is always smaller than should be obtained.

In the foregoing expressions σ_{const} represents that portion of the total cross section which can be considered as essentially constant in the region of resonance. λ is the neutron wavelength divided by 2π and f is a statistical weighting factor for the formation of the particular compound nucleus responsible for the resonance. f is the product of the isotopic abundance, a, of the responsible isotope and the spin factor. If i is the nuclear spin of the responsible isotope, the compound nucleus can have spin $(i \pm \frac{1}{2})$ with relative statistical weights as given above. Γ_n and Γ_γ are the "neutron width" and "photon width" of the level where $\Gamma = \Gamma_n + \Gamma_\gamma$. Aside from the extra $(1/v)$ factor for capture (which is here neglected) the capture and scattering cross sections, σ_e and σ_s, show the same resonance shape. An extra interference effect[7] is expected between the potential and resonance scattering. However, this contribution to the total cross section averages to zero and is usually unimportant in our measurements. The term σ_{const} includes the total cross section near the resonance due to all other isotopes, to the other spin state, and to the potential scattering for the responsible spin state. Unless there is definite reason for using a different value, σ_{const} is usually taken as the expected value for the potential scattering for the element. If a compound is used as a sample, σ_{const} also includes the contribution from the other elements present.

For most of the resonance levels $E_0 \gg 1$ ev and Γ is less than the resolution width so the experimental curve of σ *vs* E is flattened and broadened relative to the true curve corresponding to infinitely sharp resolution. If the sample is so thin that $n\sigma_0 \ll 1$, the area of the transmission dip is proportional to $n\sigma_0\Gamma$, whereas for $n\sigma \gg 1$ it is proportional to $(n\sigma_0)^{\frac{1}{2}}\Gamma$. Thus, by comparing the areas of a transmission dip for thick and thin samples, it is sometimes possible to evaluate σ_0 and Γ separately.

Let us define a quantity A which we shall call the "relative area" of a transmission dip which is obtained as follows. The experimental transmission values, T, in the region of the dip are divided by T_{const}, due to σ_{const}, and plotted *vs* t. The area above the resultant dip in μsec/meter is divided by t_0 to give A. The analysis then gives

$$n\sigma_0\Gamma^2 = 4E_0^2A^2/\pi \text{ for } n\sigma_0 \gg 1,$$

$$n\sigma_0\Gamma = 4E_0A/\pi \text{ for } n\sigma_0 \ll 1.$$

The deviations of the quantities $(4E_0^2A^2/\pi n\sigma_0\Gamma^2)$ and $(4E_0A/\pi n\sigma_0\Gamma)$ from unity for intermediate values of $n\sigma_0$ are shown in Fig. 3 for $0.1 \leq n\sigma_0 \leq 10$. It is to be noted that the area A is smaller than expected in both cases when the limiting conditions are not satisfied. The method which has been adopted for the routine evaluation of $n\sigma_0$ when measurements have been made on both thick and thin samples is to compute $\sigma_0\Gamma^2$ from A for the thick sample and again for the thin sample, using the thick sample approximation in each case. The ratio of the values $(\sigma_0\Gamma^2)_{\text{thin}}/(\sigma_0\Gamma^2)_{\text{thick}}$ will be <1 because of the bad approximation in using the thick sample formula for the thin sample. However, by comparing the value of this ratio with the curve of Fig. 3, the value of $n\sigma_0$ for the thin sample is obtained directly and thus σ_0 and Γ are separately evaluated.

If the isotope responsible for the resonance is known, then, a is known. If $i \neq 0$ then the spin of the compound nucleus having the resonance is usually not known and only $f\Gamma_n$ can be determined from σ_0 and Γ. For medium atomic weight elements having level spacings of ~ 10 to 1000 ev, the value of Γ_n for levels of a few ev energy is usually much smaller than Γ. Some theories predict that $\Gamma_n E_0^{-\frac{1}{2}}$ should be proportional to the level spacing (for the given compound nucleus spin state). For light elements such as Mn and Co where the level spacing is large and the resonance energy is usually greater than 100 ev, it has been found, in agreement with theory, that $\Gamma_n \gg \Gamma_\gamma$ so σ_0 depends only on E_0 and f. For such cases if it is assumed that $\Gamma_n \approx \Gamma$ and the value of f is

[7] Feshbach, Peaslee, and Weiskopf, Phys. Rev. 71, 145 (1947).

approximately known, the value of σ_0 can be computed and Γ evaluated from the value of $\sigma_0\Gamma^2$. This procedure has been used in a number of cases where it seemed justified.

In cases where only $\sigma_0\Gamma^2$ is known for a resonance in an element of medium atomic weight and $E_0 \ll 100$ ev, the values of σ_0 and Γ_n are sometimes estimated by assuming $\Gamma_n \ll \Gamma_\gamma \sim 0.1$ ev since values of Γ_γ have been measured in many cases and seem to be roughly constant at ~ 0.1 ev. In some cases where this last method is used to estimate σ_0, the value of $n\sigma_0$ for the sample may not satisfy the thick sample condition and the computed value of $\sigma_0\Gamma^2$ may be increased slightly by use of Fig. 3. In cases where the resultant calculated σ_0 is not $\gg \sigma_{max}$ from the experimental transmission curve, the values of σ_0 and Γ for a given $\sigma_0\Gamma^2$ are adjusted to give the best fit between the predicted and experimental values of σ_{max}, the predicted value being obtained by averaging the theoretical transmission curve over the experimental resolution function with the resolution function centered at t_0.

In presenting the results of an analysis of an experimental transmission curve, the appropriate method of those listed above is used. When a curve shows many resonance dips, only the first few can usually be expected to be due to single resonances and the structure at higher energies is due to the fluctuations in the distribution of many levels, the relative resolving power of the instrument decreases rapidly at higher energies while there is not expected to be any systematic change in the level spacing with energy. The maximum energy at which separate resonances can be distinguished is relative and may be a few ev when the level spacing is <10 ev. On the other hand single levels at a few hundreds or thousands of ev may be easily distinguished for the light elements which have very strong ($\Gamma_n \approx \Gamma \gg 1$ ev) widely spaced (>1000 ev) levels. Thus with less than 1 percent of Co or Mn impurities in other samples the Co and Mn dips are still observed.

G. RESULTS

Check of the Positions of the Main Resonances in Gold and Silver

After the development of the technique for measuring t_d using the thick paraffin filter, the positions of the main resonances in Au and Ag were checked. The results are shown in Figs. 4 and 5. The new values for the resonant energies are slightly higher than the previous results[2] and give $E_0 = (4.87 \pm 0.07)$ ev for gold and $E_0 = (5.13 \pm 0.07)$ ev for silver. This last result is in good agreement with the recent determination of Selove.[5] This and other measurements suggest that the earlier reported energy values tended to be slightly low and a uniform decrease of about 0.2 to 0.3 μsec/m in the earlier timing values is indicated as a proper correction. This shift is usually quite small, but not negligible, when precise energy values are desired.

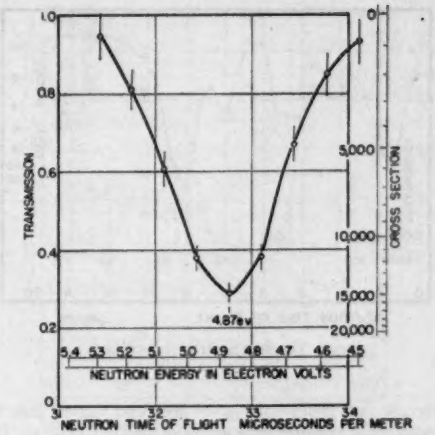

FIG. 4. The slow neutron transmission of 0.02745 g/cm² of gold.

Bromine and Sodium Bromide

Two different samples were used to study Br. The first sample contained 15.0 g/cm² powdered NaBr. The sample was of analytical reagent grade. The results of measurements with this sample are given in Fig. 6 and show sufficient structure so that it was considered of interest to prepare a sample of liquid Br. The sample was analytical reagent grade bromine dried with P_2O_5 and distilled into a quartz sample holder. Analysis showed $I < 0.05$ percent. The sample contained 16.41 g/cm² of bromine. A quartz blank containing the same amount of fused quartz as the sample holder was used as dummy on the "sample out" runs.

The measurements with liquid Br used arc and

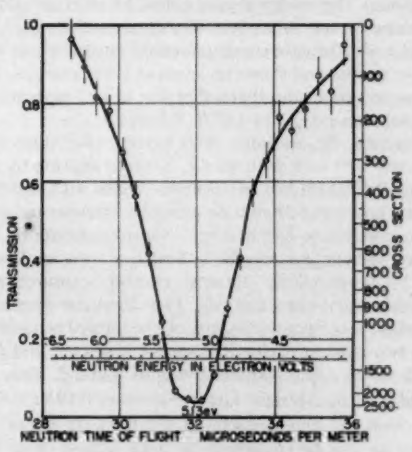

FIG. 5. The slow neutron transmission of 0.252 g/cm² of silver.

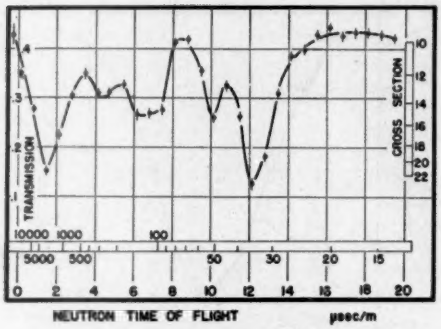

FIG. 6. The slow neutron transmission of 15 g/cm² of NaBr.

detector "on times" of $\tau_{are}=4$ μsec and $\tau_{det}=2$ μsec for a resolution triangle base width of about 1 μsec/m. The measurements of NaBr used $\tau_{are}=\tau_{det}=4$ μsec and extend as low as 13 ev. The two curves agree on the position of the resonance dips at 35.7 ev and 54 ev. A broad dip near 100 ev in NaBr is resolved into dips at 104 ev and 136 ev using the higher resolution for Br. Except for the strong dip near 3000 ev for NaBr, the two samples seem to agree as well as possible for the general behavior of the whole curve, but more detail is seen at higher energies in Fig. 7. The strong dip near 3000 ev clearly must be due to Na, and this has been confirmed by recent work of Selove.[5]

In Fig. 7 Br shows a dip between 4 and 5 μsec/m which is probably due to two or more levels. If two levels are responsible, they are near 260 and 320 ev. The dip near 700 ev and the broad dip at higher energies are probably due to a large number of levels since an average level spacing of less than 100 ev is indicated. Although the energy region below 13 ev is not shown in these curves, it has been measured carefully by I. W. Ruderman (private communication) in connection with other studies and shows no levels at lower energies. The cross section in the thermal region is well matched by the relation $\sigma=(5.95+1.01E^{-\frac{1}{2}})$ barns.

Natural Br contains 50.6 percent Br^{79} and 49.4 percent Br^{81} both with spin $\frac{3}{2}$. Neutron capture by Br^{79} gives Br^{80} which has two isomeric states with half-lives of 4.4 hours and 18 min decaying by electron and positron emission to Kr^{80} and Se^{80}. Neutron capture by Br^{81} gives 34-hour β-active Br^{82}. Both isotopes are known to be produced by thermal neutron capture[5] with roughly equal cross sections. Thus there are four ways in which a compound nucleus can be formed considering the two isotopes each with possible spin $I=1$ and $I=2$ with relative spin statistical weights $\frac{3}{8}$ and $\frac{5}{8}$. Since the total statistical weight factor f is either 0.19 or 0.31 in all cases, the four possibilities, for the purposes of this analysis, can be considered to have almost equal statistical weights and *a priori* chance of being responsible for any given resonance level. However, the four states may not all have levels of the same strengths or spacings. In the analysis of the level strengths only the first few levels have been considered in detail since the other dips are probably due to more than one level. For the first two levels, the analysis was also made using the NaBr curve as a check.

For the first level at 35.7 ev the Br curve gives $\sigma_0\Gamma^2=210$ barns (ev)² while the NaBr curve gives 275 barns (ev)². Since the Br curve seems better for this analysis, a weighted average of 220 barns (ev)² is used. If we assume $\Gamma_n\ll\Gamma_\gamma\approx 0.1$ ev, then $\sigma_0\approx 2.2\times10^4$ b. If we use $f\approx 0.25$ for the responsible isotope, then $\sigma_0\approx 1.9\times10^4\,\Gamma_n/\Gamma$ which gives $\Gamma_n\approx\Gamma$. Thus the original assumptions are not good. If we assume $\Gamma_n=\Gamma_\gamma$ then $\sigma_0\approx 9\times10^3$ b from theory and $\Gamma=2\Gamma_\gamma=2\Gamma_n\approx 0.15$ ev. This corresponds to $\Gamma_nE_0^{-\frac{1}{2}}\approx 0.026$ (ev)$^{\frac{1}{2}}$. (Note that σ_0 always refers to the element.)

The second level at 54 ev has $\sigma_0\Gamma^2=140$ barns (ev)² from the Br curve and 100 barns (ev)² from the NaBr curve. In this case the Br curve is much more reliable and the value 140 is used. If we assume $\Gamma_n\approx\Gamma_\gamma$ and $f\approx 0.25$, then $\sigma_0=6.15\times10^3$ b and $\Gamma\approx 0.15$ ev as for the other level. This corresponds $\Gamma_nE_0^{-\frac{1}{2}}\approx 0.021$ (ev)$^{\frac{1}{2}}$.

For the third level at 104 ev, the Br curve gives $\sigma_0\Gamma^2=250$ b (ev)². Assuming $f\approx 0.25$ and $\Gamma_n\approx 3\Gamma_\gamma$ gives $\sigma_0\approx 4700$ b and $\Gamma\approx 0.24$ ev. The larger value of Γ_n/Γ_γ is assumed to keep Γ_γ about the same as for the other levels whereas Γ_n should increase with energy. This gives $\Gamma_n\approx 0.18$ and $\Gamma_nE_0^{-\frac{1}{2}}\approx 0.018$ (ev)$^{\frac{1}{2}}$.

The fourth level at 136 ev has $\sigma_0\Gamma^2=1000$ b (ev)² which is somewhat larger than the others. Assuming $f\approx 0.25$ and $\Gamma_n\approx\Gamma_\gamma$ gives $\sigma_0\approx 4800$ b and $\Gamma\approx 0.45$ ev and $\Gamma_nE_0^{-\frac{1}{2}}\approx 0.02$ (ev)$^{\frac{1}{2}}$. If this dip were really due to two equal levels, each would have $\Gamma\approx 0.23$ ev which is closer to the values for the other levels.

In the above analysis the value $f\approx 0.25$ rather than $f=0.19$ or 0.31 was used. Thus all calculated values of Γ should be increased or decreased by about 15 percent

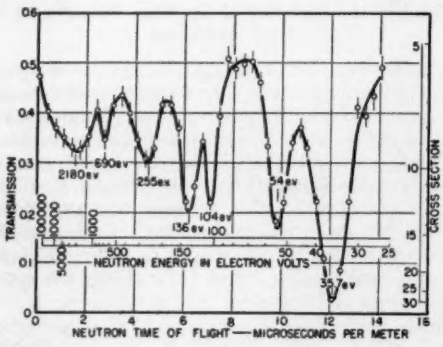

FIG. 7. The slow neutron transmission of 16.41 g/cm² of Br.

[5] National Bureau of Standards Circular 499.

depending on whether $I=1$ or 2 for the compound nucleus. Clearly the assumptions $\Gamma_n \approx \Gamma_\gamma$ are crude and this should be considered in using the resulting values of Γ_n and Γ. However, the resultant values of Γ_γ are reasonable; so the order of magnitude of the results is probably correct.

On the basis of the theory of Feshbach, Peaslee, and Weisskopf,[7] the average level spacing D should be related to $\Gamma_n E_0^{-\frac{1}{2}}$ by the approximate relation $D=5000\ E_0^{-\frac{1}{2}}\Gamma_n$. Since the values of $\Gamma_n E_0^{-\frac{1}{2}}$ are all roughly the same and equal to 0.02 $(\text{ev})^{\frac{1}{2}}$, the predicted level spacing is about 100 ev. A further comparison with the experimental level spacing depends on whether the observed levels are all due to one of the four possible compound nucleus states or are divided among them. If the spacing of 100 ev applies separately to each state then $D=25$ ev is predicted for the element. The experimental level spacings of >35 ev (between the first level and the next at negative neutron incident energy), 18 ev, 51 ev, and 31 ev are consistent with an average spacing in this region of between 25 and 100 ev so that the agreement with theory is reasonably good. It is also of interest to note that Br is the lightest element to show such a close level spacing.

The main results for Br may be summarized as follows:

1. In the thermal region Ruderman obtained $\sigma=5.95+1.01E^{-\frac{1}{2}}$.
2. The first level has $E_0=35.7$ ev with $\sigma_0\Gamma^2=220$ b $(\text{ev})^2$. If $\Gamma_n \approx \Gamma_\gamma$ then $\sigma_0 \approx 9\times10^3$ b, $\Gamma \approx 0.15$ ev and $\Gamma_n E_0^{-\frac{1}{2}} \approx 0.026$ $(\text{ev})^{\frac{1}{2}}$.
3. The second level at 54 ev has $\sigma_0\Gamma^2=140$ b $(\text{ev})^2$. If $\Gamma_n \approx \Gamma_\gamma$ then $\sigma_0 \approx 6\times10^3$ b, $\Gamma \approx 0.15$ ev and $\Gamma_n E_0^{-\frac{1}{2}} \approx 0.02$ $(\text{ev})^{\frac{1}{2}}$.
4. The third level has $E_0=104$ ev and $\sigma_0\Gamma^2=250$ b $(\text{ev})^2$. If $\Gamma_n \approx 3\Gamma_\gamma$, then $\sigma_0 \approx 4700$ b, $\Gamma \approx 0.24$ ev and $\Gamma_n E_0^{-\frac{1}{2}} \approx 0.018$ $(\text{ev})^{\frac{1}{2}}$.
5. The fourth level has $E_0=136$ ev and $\sigma_0\Gamma^2=1000$ b (ev). If it is single and $\Gamma_n \approx \Gamma_\gamma$, then $\sigma_0 \approx 4800$ b, $\Gamma \approx 0.45$ ev and $\Gamma_n E_0^{-\frac{1}{2}} \approx 0.02$ $(\text{ev})^{\frac{1}{2}}$.
6. There is evidence for many more unresolved levels at higher energies.
7. In addition, the NaBr shows a strong level in Na near 3000 ev in agreement with Selove.[6]

In conclusion we also point out that the resolving power of the instrument is well illustrated by the degree of resolution of the dips at 6.2 and 7.1 μsec/m and the sharp rise on the low energy sides of the resonance.

Iron

The slow neutron transmission of the sample of iron containing 9.93 g/cm² has been reinvestigated.[3] The results of the transmission measurements using broad resolution are shown in Fig. 8. Spectroscopic analysis of the sample showed between 0.5 and 1 percent Mn, 0.01 to 0.05 percent Cr, about 0.001 percent Co, between 0.01 percent and 0.1 percent Cu, and traces of Ag and

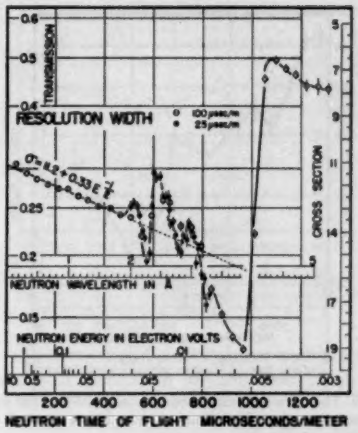

FIG. 8. The slow neutron transmission of 9.93 g/cm² of Fe. The sharp changes are caused by crystal interference effects.

Pb. The results in the region between 2 ev and 0.03 ev are well matched by the relationship $\sigma=(11.2+0.33E^{-\frac{1}{2}})$ barns. This is in good agreement with earlier results.[3]

Below 0.02 ev strong crystal interference effects are observed. At the suggestion of Professor O. Halpern, the wavelength interval between 2A and 3A was investigated with higher resolution than is usually used in order to resolve the discontinuities in the transmission corresponding to the Debye-Scherrer rings at 2.3A and 2.8A predicted by theory. The theory also predicts that the coherent scattering for iron should disappear at the cut-off wavelength of 4.04A. The large change in transmission between 3.8A and 4.2A indicates the close agreement obtained between observed transmission and the theoretical prediction. The agreement between theory and experiment for the passage of neutrons through polycrystalline media is very gratifying.

At 0.003 ev the predicted σ_s from the thermal slope is 6.0 b compared to the measured total cross section of 7.8 b. Thus 1.8 b is due to residual incoherent scattering.

The results of the transmission measurement above 200 ev are shown in Fig. 9. The dips near 330 and 4000 ev are caused by the manganese impurity. From the area of the dip at 330 ev the sample should contain 0.7 percent manganese which is in good agreement with the spectroscopic analysis. The dip at 950 ev cannot be attributed to any specific impurity, as none of the observed impurities have known levels at this energy. However, because of the small magnitude of the dip and the statistical uncertainty of the points involved, no conclusions have been drawn about this level. It might be due to one of the rarer isotopes of iron or to some other impurity.

The scattering cross section in this energy region is

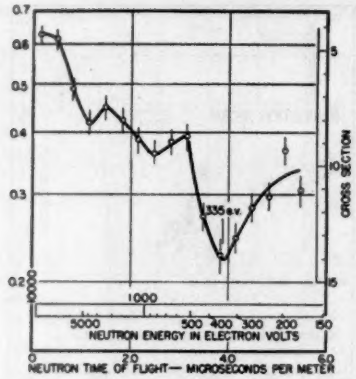

FIG. 9. The slow neutron transmission of 9.93 g/cm² Fe in the higher energy region. The dips in transmission are probably due to impurities in the iron.

much higher than $4\pi R^2$ (5.5 barns) which would indicate that there is interference between potential and resonance scattering. Because of the presence of these impurities it is difficult to determine how the scattering cross section decreases with energy in this region in order to observe the detailed behavior of the interference. Barshall *et al.*[9] found many levels in Fe below 1 Mev with the lowest at 15 kev.

Cobalt

The behavior of the Co cross section above 70 ev was reinvestigated with maximum resolution using the same 1.06 g/cm² sample which was previously studied.[2] Results of these measurements are shown in Fig. 10.

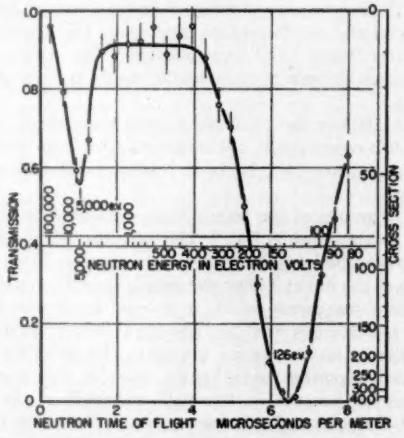

FIG. 10. The slow neutron transmission of 1.06 g/cm² of Co showing the resonances at 126 and 5000 ev.

[9] Barschall, Bockelman, and Seagondollar, Phys. Rev. **73**, 659 (1948).

A spectroscopic analysis of the sample showed about 1 percent Ni, 0.05 percent Mn, less than 0.01 percent Zn and Cr, and traces of Al, Ca, Cu, Fe, Mg, Si, and Na. The results for the cross section at lower energies are given in the earlier paper.[2]

The earlier measurements showed a strong dip at 115 ev which is now placed at 126 ev in line with the above remarks. The curve shows the main resonance dip at 126 ev and a higher energy dip near 5000 ev. The higher energy dip may be due to several levels. It is unlikely that an impurity could give such a strong dip so it is probably due to Co.

The level at 126 ev must be the result of the main (99.83 percent) Co^{59} isotope of spin 7/2. It has also been studied in detail by Seidl[10] using Co as a resonance scattering detector. Seidl has shown that this level has $\Gamma_n \gg \Gamma_\gamma$ and obtains $\Gamma = 2.0 \pm 0.1$ ev if $I=4$ for the compound nucleus and $\Gamma = 5.0 \pm 0.5$ ev if $I=3$. His measured value of $\sigma_0 = 12{,}500 \pm 1250$ b is consistent

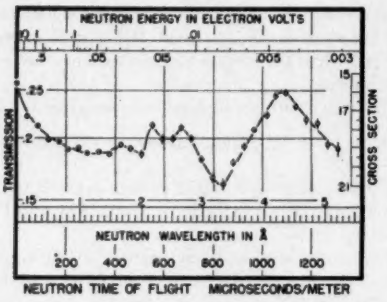

FIG. 11. The slow neutron transmission of 8.47 g/cm² of Ni. The abrupt changes in transmission are caused by crystal interference effects.

only with $I=4$. For 126 ev the predicted values of σ_0 for $\Gamma_n \gg \Gamma_\gamma$ are 9100 b for $I=3$ and 11,600 b for $I=4$.

Analysis of the area of the dip at 126 ev in Fig. 10 gives $\sigma_0 \Gamma^2 = 2.3 \times 10^5$ b (ev)² which gives

$$\Gamma = 5.0 \text{ ev for } I=3, \quad \Gamma = 4.4 \text{ ev for } I=4.$$

These results for Γ, when combined with those of Seidl, argue strongly for $I=3$ in disagreement with his conclusion.

In conclusion, the analysis of the dip at 126 ev, when combined with Seidl's results, favors $I=3$, $\sigma_0\Gamma^2 = 2.3 \times 10^5$ b (ev)², $\sigma_0 = 9100$ b, $\Gamma_\gamma \ll \Gamma_n \approx 5.0$ ev, and $\Gamma_n E_0^{-\frac{1}{2}} = 0.45$ (ev)$^{\frac{1}{2}}$. Analysis of the dip at 5000 ev, assuming that it is a single level, gives $\sigma_0\Gamma^2 \sim 2 \times 10^8$ b (ev) or $\Gamma \sim 900$ ev, which seems unreasonably large. Therefore, probably more than one level is responsible for this dip.

Nickel

The slow neutron transmission of Ni was remeasured using the same samples as in the earlier studies.[3] Spec-

[10] F. P. G. Seidl, Phys. Rev. **75**, 1508 (1949).

trographic analysis of the sample showed 0.9 percent Co, 0.3 percent Mn, 0.02 percent Cr, between 0.1 and 0.9 percent Fe, Hg, and Si, between 0.01 percent and 0.09 percent Al, B, Cu, Ti, and between 0.001 and 0.009 percent Ca, Mg. The measurements in the thermal region were extended to 0.003 ev and the results are shown in Fig. 11. The curve shows strong interference effects over most of the wavelength region.

The earlier measurements[3] had shown a resonance dip near 100 ev and so the region above 90 ev was reinvestigated using highest resolution and the results are shown in Fig. 12. The dips near 130 ev and 330 ev are believed to be due to cobalt and manganese, respectively. From the area of the dip near 130 ev it is calculated that the sample contains 0.85 percent cobalt, which is in good agreement with the result of 0.9 percent obtained for this sample by spectroscopic analysis.

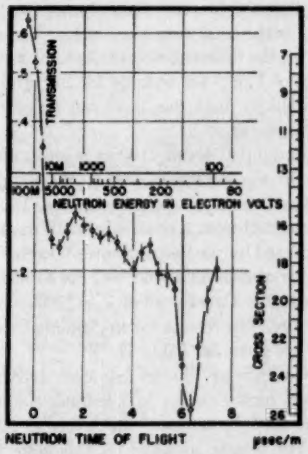

FIG. 12. The slow neutron transmission of 8.47 g/cm² of Ni in the higher energy region. The dip near 130 ev is due to a Co impurity and the other dips are probably due to other impurities.

From the area of the dip at 330 ev the Mn impurity was calculated to be between 0.2 percent and 0.8 percent in agreement with the spectroscopic analysis of 0.3 percent. The dip at 5000 ev probably represents a resonance in one of the nickel isotopes. However, this conclusion is somewhat uncertain as it could be caused by levels in impurities such as Cr, Mn, and Co. An attempt to explain this dip on the basis of any of these elements would require larger amounts of these materials than found from the spectroscopic analysis.

The results for Ni are similar to those for Fe in that the scattering cross section remains relatively constant at ~3 to 4 times the value expected for potential scattering over a wide energy region. The presence of the impurity resonances makes it difficult to observe the details of the decrease in cross section above 1000 ev to give a prediction of the expected level density according

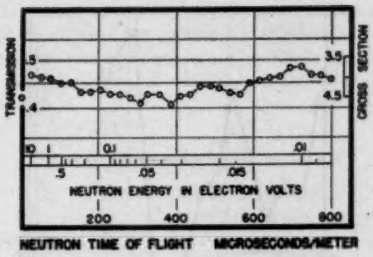

FIG. 13. The slow neutron transmission of 20.93 g/cm² of Zn in the low energy region. The changes in transmission shown are caused by crystal interference effects.

to the theory of Feshbach, Peaslee, and Weisskopf.[7] The results of Barshall *et al.*[9] show many resonances below 1 Mev.

Zinc

The slow neutron transmission of two samples of zinc containing 20.93 g/cm² and 42.29 g/cm² were investigated. The samples were made by casting the analytical reagent grade zinc in a carbon crucible. Spectrographic analysis of the sample showed Mn and Cr to be present to less than 0.01 percent and traces of B, Si, Fe, Sr, Mg, Pb, Cu, Ag, and possibly Cd.

The results of the transmission measurements using broad resolution on the 20.93 g/cm² sample are given in Fig. 13. The results in the region between 2 ev and 0.06 ev are well matched by the relation,

$$\sigma=(3.86+0.17E^{-\frac{1}{2}}) \text{ barns.}$$

The irregularities in the transmission at large times-of-flight are caused by neutron interference effects due to the crystalline structure of the sample.

The energy region above 0.5 ev was studied using high resolution with the results shown in Fig. 14. Below 100 ev the curve agrees well with the straight line determined from the data in Fig. 13. Above 100 ev there are very definite dips in transmission which indicate one or more resonances at higher energies.

The region above 200 ev then was investigated using

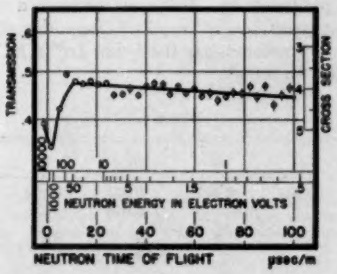

FIG. 14. The slow neutron transmission of 20.93 g/cm² of Zn in the intermediate energy region showing the $1/v$ line $\sigma=(3.86+0.17E^{-\frac{1}{2}})$ and the resonances at higher energy.

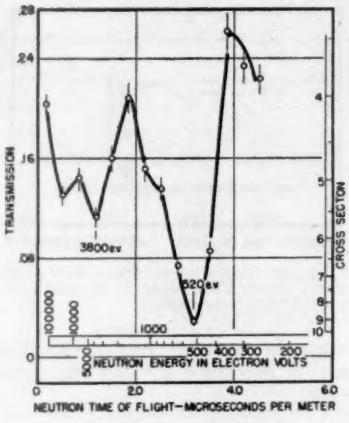

FIG. 15. The slow neutron transmission of 42.29 g/cm² of Zn in the higher energy region.

maximum resolution on the 42.29 g/cm² sample. The results are shown in Fig. 15. The curve shows a strong resonance at 520 ev, a probable partially resolved level near 1100 ev, a dip at 3800 ev, and a dip probably due to many levels above 15,000 ev. Since zinc has about the same atomic weight as Mn, Cr, and Co, therefore the levels would be expected to be strong, widely spaced, and principally due to scattering. The first two or three dips are probably caused by single levels and have been analyzed as such. The dip in transmission above 10,000 ev is probably caused by more than one level; therefore no analysis has been made.

Natural zinc has 5 isotopes: 50.9 percent Zn^{64}, 27.3 percent Zn^{66}, 17.4 percent Zn^{68}, 3.9 percent Zn^{67}, and 0.5 percent Zn^{70}. Four of these isotopes are of the even-even type and probably have spin zero and therefore the f is determined by the isotopic abundance. Zn^{67} has a spin 5/2; therefore the total statistical weight factor would be 0.016 or 0.024, depending on the spin of the compound nucleus.

There are two activities known to be produced by slow neutron reaction in zinc. These are the 57-min period[8] produced by $Zn^{68}(n,\gamma)Zn^{69}$ and a 210-day period[8] produced by $Zn^{64}(n,\gamma)Zn^{65}$. Two other activities[8] produced by neutrons are the 5-min $Zn^{66}(n,p)Cu^{66}$ and 12.5-hr $Zn^{64}(n,p)Cu^{64}$.

TABLE I.

A	64	66	67	68	70
f	0.509	0.273	0.024 0.016	0.174	0.005
Γ(ev)	5.2	7.1	24 29	8.9	52
$\Gamma_n E^{-\frac{1}{2}}$	0.23	0.31	1.3 1.1	0.40	2.3

TABLE II.

A	64	66	67	68	70
Γ	4.4	6.0	20 25	7.6	45
$\Gamma_n E_0^{-\frac{1}{2}}$	0.13	0.18	0.61 0.75	0.23	1.4

The dip in transmission with a minimum at 520 ev does not recover fast enough on the high energy side of the resonance and seems to be caused by two levels, one at 520 ev and the other at 1100 ev. Since the levels have not been completely resolved, the curve was divided into two separate dips by comparing this transmission curve with those of elements having single resonances in this energy region. The area of the dip at 520 ev corresponds to $\sigma_0\Gamma^2=6.9\times10^4$ barns (ev)². Assuming $\Gamma_n\gg\Gamma_\gamma$ gives $\sigma_0=5100\,f$ barns and $\Gamma=3.7\,f^{-1}$ ev where f is the total statistical factor. The results for this level for the different isotopes are given in Table I. The values of $\Gamma_n E^{-\frac{1}{2}}$ are so large for Zn^{67} and Zn^{70} that it seems unlikely that this level can be attributed to these rare isotopes.

The second dip at about 1100 ev is much more uncertain both in the determination of the energy of the resonance and the area of the resonance. The area had to be determined from a relatively small fraction of the total dip caused by the two unresolved levels. The result obtained for this level is $\sigma_0\Gamma^2=2.3\times10^4$ barns (ev)². Again assuming $\Gamma_n\gg\Gamma_\gamma$ gives $\sigma_0=2300\,f$ barns and $\Gamma=3.2\,f^{-1}$ ev. The results for the different isotopes for this level are given in Table II.

The third level at 3800 ev has been separated from the levels at higher energy in a manner similar to that which was used to separate the levels at 520 ev and 1100 ev. The results obtained for this level (see Table III), assuming $\Gamma_n\gg\Gamma_\gamma$ and $\sigma_0\Gamma^2=2.5\times10^6$ barns (ev)², $\sigma_0=700\,f$ and $\Gamma=60\,f^{-1}$. The large values of Γ and $\Gamma_n E^{-\frac{1}{2}}$ compared to those obtained for the other two levels strongly suggest that this dip is caused by more than one level.

The results for zinc give good indication of the resoving power of the system as the resolution triangle was about 1 μsec/meter at the base, but the average spacing of the detectable dips is less than 1 μsec/meter.

The level spacing of Zn on the basis of the theory of Feshbach, Peaslee, and Weisskopf would be between

TABLE III.

A	64	66	67	68	70
Γ	84	115	390 475	144	850
$\Gamma_n E^{-\frac{1}{2}}$	1.4	1.9	6.5 7.8	2.4	14

1000 and 10,000 ev for $\Gamma_n E^{-\frac{1}{2}}$ between 0.2 and 2. This is in rough agreement with the experimental results for the level spacing since this is the level spacing per isotope, for a given spin state.

We wish to thank Miss Miriam Levin who assisted with the numerous calculations involved in this paper and the members of the cyclotron staff who aided with these measurements. Thanks are also due to the United States Atomic Energy Commission for its support of this research.

PHYSICAL REVIEW VOLUME 83, NUMBER 6 SEPTEMBER 15, 1951

The Reaction $C^{14}(p,n)N^{14}$: Excited States in N^{15}

W. D. Roseborough, J. J. G. McCue, W. M. Preston, and C. Goodman
*Laboratory for Nuclear Science and Engineering, Massachusetts Institute of Technology, Cambridge, Massachusetts**

(Received June 7, 1951)

The relative neutron yield from $C^{14}(p,n)N^{14}$ has been measured for proton energies of 1100 to 2600 kev. Resonances occur at nine proton energies: 1165, 1310, 1664, 1789, 1883, 2024, 2079, 2272, and 2451 kev. The form of the yield curve and the calculated energies of the resonance levels in N^{15} are in good agreement with the results of others on the inverse reaction, $N^{14}(n,p)C^{14}$.

I. INTRODUCTION

THE excited states of N^{15} have been studied extensively.[1] As indicated schematically in Fig. 1, the virtual levels in the region of excitation somewhat above the neutron binding energy can be excited by three bombardments: $B^{11}+\alpha$, $N^{14}+n$, and $C^{14}+p$. We are concerned here with two reactions which are inverse to each other: $N^{14}(n,p)C^{14}$ and $C^{14}(p,n)N^{14}$. Both (n,p) and (p,n) reactions on stable, light nuclei lead to residual nuclei which are unstable. The recent availability of radioactive C^{14} in reasonable concentration has made this the first case in which both reactions, leading to the same compound nucleus, can be investigated.

It is expected that the yield curve, number of protons *vs* neutron energy E_n from $N^{14}(n,p)C^{14}$, should be very similar to the yield of neutrons *vs* proton energy E_p from $C^{14}(p,n)N^{14}$. The same resonances should be observed, with identical half-widths, but at higher bombarding energies, in the (p,n) reaction, by an amount equal to the (p,n) threshold energy (see Fig. 1). The cross sections are related by the principle of detailed balance.[2]

The absolute cross section $\sigma_{n,p}$ for $N^{14}(n,p)C^{14}$ has been measured by Johnson and Barschall[3] with fairly good resolution. They found three strong resonances and indications of several weaker ones in the neutron energy range 0.2 to 2.0 Mev. The neutron yield from $C^{14}(p,n)N^{14}$ was investigated by Shoupp, Jennings, and Sun.[4] Three large peaks in the neutron yield were found at energies which correlate with the later results of Johnson and Barschall. Although they used a thin target (estimated thickness 3 kev at $E_p=1.14$ Mev), their beam energy control did not suffice to resolve weaker resonances, and a detailed comparison is not possible. Because of the general interest of the reaction and its connection with parallel work in this laboratory on the total neutron cross section of N^{14}, we decided to remeasure the $C^{14}(p,n)$ yield with the good energy resolution available with the Rockefeller electrostatic generator.[5]

II. EXPERIMENTAL METHOD

Barium carbonate was obtained from Oak Ridge National Laboratory with carbon enriched to about 1.6 percent of C^{14}. This was converted to HCN and then to NaCN in a solution of NaOH.[6] The final material

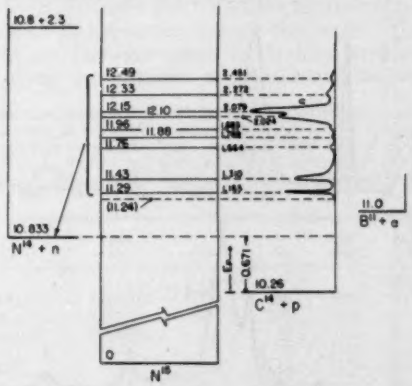

FIG. 1. Energy level diagram for N^{15} in the region somewhat above the neutron binding energy. The energies shown are computed from the results of this paper. *Note added in proof:* The energy of $C^{14}+p$ should read 10.207.

* This work was assisted by the BuShips and ONR.

[1] For a summary, see Hornyak, Lauritsen, Morrison, and Fowler, Revs. Modern Phys. 22, 291 (1950).

[2] H. A. Bethe, *Elementary Nuclear Theory* (John Wiley and Sons, Inc., New York, 1947).

[3] C. H. Johnson and H. H. Barschall, Phys. Rev. 80, 818 (1950).

[4] Shoupp, Jennings, and Sun, Phys. Rev. 75, 1 (1949).

[5] W. M. Preston and C. Goodman, Phys. Rev. 82, 316 (1951).

[6] The chemical conversion was performed by Tracerlab, Inc., Cambridge, Massachusetts.

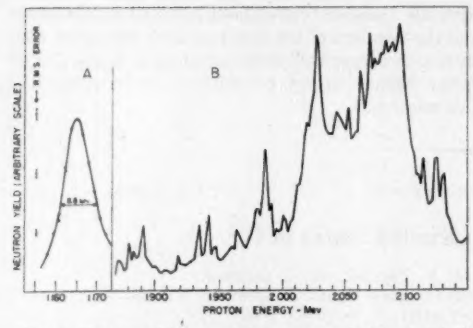

FIG. 2. Neutron yield *vs* proton energy, target No. 1, (A) the $C^{14}(p,n)$ resonance at 1.165 Mev; (B) narrow, closely spaced peaks due to a contaminant, Cl^{37}, superimposed on C^{14} resonances at 2.024 and 2.079 Mev.

consisted of about equal parts NaCN and NaOH, with 0.25 atom-percent C^{14}. It was evaporated[7] onto 10-mil tantalum disks, 6.2 cm in diameter, which fit with rubber gaskets on a rotating target assembly, eccentric to the axis of the proton beam. With a 3-μa beam in a spot about 2×2 mm, the targets lasted many hours with little evaporation, provided a strong air jet was directed on the back face of the target. The (p,n) thresholds of C^{12}, C^{13}, N^{14}, N^{15}, O^{16}, O^{17}, O^{18}, and Na^{23} are all higher than the proton energies used in this experiment.

The neutrons were detected by a 1-inch diameter counter with an active volume 12 inches long, filled to a pressure of 55 cm with enriched BF_3 (95 percent B^{10}). The counter was embedded in a cadmium-covered cylinder of paraffin, 12 inches long and 8 inches in diameter. The latter was mounted with its axis perpendicular to the beam and its side almost touching the target in order to get maximum counting rates. We cannot assume that its efficiency in this position is as independent of neutron energy as that of the "long counter" of Hanson and McKibben.[8]

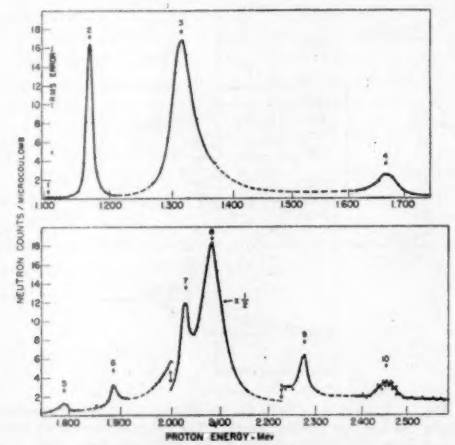

FIG. 3. Neutron yield from $C^{14}(p,n)$ *vs* proton energy, target No. 3 (about 8 kev thick at 1.165 Mev).

[7] The evaporation was carried out by Mr. Edward Barr of Baird Associates, Cambridge, Massachusetts.

The ion beam of the Rockefeller generator is bent through 90 degrees, on a 38-cm radius, by a magnetic analyzer whose field is stabilized by a proton magnetic moment resonance control. The field B at the point of measurement is proportional to the resonant frequency f, which can be measured to about one part in 10^5 by comparison with a standard oscillator. The proton energy is then given by $E=E'(1-E'/M_pc^2)$ to a sufficient approximation, where $E'=kf^2$ is the energy computed without the relativity correction. The constant k is determined by the $Li^7(p,n)$ threshold energy, which is taken as 1882.2 kev.[9] The constancy of k has been checked, for fields well below saturation, by measurements of a sharp resonance with the H^+ and the H_2^+ beams. Drifts in the calibration constant, amounting to 0.1 percent over periods of a few weeks, appear to be the largest source of instrumental error in energy measurements.

The energy resolution of the proton beam is set by the defining slits at the object and image planes of the magnetic analyzer. In the present work, the slit widths were 1 mm, corresponding to a possible energy spread of 0.15 percent. The voltage stabilizer keeps the beam fairly well centered on the slits, and tests on narrow resonances indicate that the effective half-width of the energy distribution is not over 0.075 percent with 1-mm slits.

III. EXPERIMENTAL RESULTS

Figure 2 shows two sections of the neutron yield curve obtained with our first C^{14} target. Two strong resonances appeared, at 1165 and 1309 kev; the first of these is shown on an enlarged scale in Fig. 2A. The background in this region was small, since the proton energy is below the (p,n) threshold of all likely contaminants. Above 1680 kev, however, a spectrum appeared consisting of narrow and closely spaced resonances characteristic of an element heavier than C^{14}. Some of these are shown in Fig. 2B, superimposed on two broader C^{14} peaks. Investigation with targets of NaCl showed that the impurity was C^{37}, which has its threshold at 1640 kev.[10]

Since the Cl^{37} spectrum obscured any weak resonances of C^{14}, the enriched material was processed chemically to remove chlorine.[11] A run with a second target then showed that nearly all of the chlorine had been removed successfully, but that the neutron background from

[8] A. O. Hanson and J. L. McKibben, Phys. Rev. **72**, 673 (1947).
[9] Herb, Snowden, and Sala, Phys. Rev. **75**, 246 (1949).
[10] Richards, Smith, and Browne, Phys. Rev. **80**, 524 (1950).
[11] The purification was performed by Tracerlab, Inc.

TABLE I. The $C^{14}(p,n)$ resonance at 1165 kev. Γ' = observed half-width of resonance, kev. T = target thickness, kev. Γ = calculated natural half-width, kev. Y_{max} = maximum yield at resonance. E_r = proton energy at resonance, kev. $E_{rt} = E_r - \frac{1}{2}T$ = resonance energy corrected for target thickness.

Date of run	Target No.	Γ'	T	Γ	Y_{max}	E_r	E_{rt}
2/8/51	1	8.8	4	7.8	...	1165.5	1163.5
4/17/51	2	8.2	3.0	7.6	7.1	1165.5	1164.0
5/3/51	3	11.3	8.4		16.3	1169.4	1165.2

parts of the machine other than the target was unusually high. This background was reduced by cleaning the slits and shielding with paraffin. Data taken with a third target are shown in Fig. 3, over the energy range 1100 to 2600 kev.

Nine resonances were found in this range. The dashed portions of the yield curve in Fig. 3, up to 1700 kev, were covered with targets No. 1 or 2 and no resonances found above background. A major portion of the yield between resonances is still due to a background from the generator which increases smoothly with energy, as shown by runs with a blank target. This background was somewhat variable, and we did not feel justified in subtracting it from the total yield. The scatter in points in the region of resonance No. 10, which is larger than the expected statistical variations, may be due to background fluctuations. At still higher energies, indications of additional resonances were so masked by the same effect that we have not included the data.

Table I summarizes data taken with all three targets on resonance No. 2 at 1165 kev, from which we can calculate the natural width and the thickness of the targets. The natural width of the chlorine resonances in Fig. 2B is small compared with the target thickness, and from several of the more isolated peaks we can estimate the thickness of target No. 1 as 4 kev at 1165 kev. This gives $\Gamma = 7.8$ kev for the natural half-width of resonance No. 2. The neutron counter was in the same position during the runs with targets 2 and 3, so we can use the observed half-widths of the resonance and the ratio of the peak yields to calculate the natural half-widths and the target thicknesses. The value obtained is $\Gamma = 7.6$ kev, in good agreement with the first estimate. The spread in values of E_{rt}, the resonance energy corrected for target thickness, may be caused by: (a) target contamination, (b) errors in estimating the position of the maxima, (c) long term shifts in the energy calibration of the generator (the same calibration constant has been used for all three runs).

Table II summarizes the data for all resonances observed, taken from Fig. 3. The column headed E_r gives the proton energy at the observed resonance peaks. The target thickness, T, is taken as 8.4 kev for resonance No. 2 (from Table I) and adjusted for higher energy values. Under E_{rt} are given the proton resonance energies corrected for target thickness, based on the $Li(p,n)$ threshold 1882.2 kev. The errors given are estimates; except for the sharp resonance No. 2, instrumental errors should be smaller than the uncertainty in locating graphically the position of a peak. Γ is the width of a resonance at half maximum; its measurement is uncertain in cases of small peaks with large background.

IV. DISCUSSION

Resonance Energies

In order to compare our resonance energies with the results of Johnson and Barschall, we must subtract from the former the threshold energy E_t for the $C^{14}(p,n)$ reaction. For this quantity, we have taken the value $E_t = 671$ kev, from Tollestrup, Fowler, and Lauritsen.[12] It is based on a weighted mean value of 782 ± 1 kev for the $n-H'$ difference and 156 ± 1 kev for the end point of the C^{14} beta-spectrum, giving a Q-value for $N^{14}(n,p)$ of 626 kev. This value agrees, within stated errors, with the direct determination of Johnson and Barschall[3]

TABLE II. Resonances in $C^{14}(p,n)N^{14}$. E_r = proton energy at peak of resonance, measured. T = calculated target thickness. E_{rt} = resonance energy corrected for target thickness. Γ = natural half-width of resonance. $E_n = E_{rt} - 671$, neutron resonance energy, this paper. E_n(JB) = neutron resonance energy, Johnson and Barschall.[a] E_n(SJS) = neutron resonance energy, computed from data of Shoupp, Jennings, and Sun.[b] Y_{max} = observed relative yield at maximum. Y_n = normalized yield (see text). $\sigma_{n,p}$(JB) of $N^{14}(n,p)C^{14}$ reaction, in millibarns, observed by Johnson and Barschall. $E_x(N^{15})$ = excitation energy of level in N^{15}. Quantities in brackets are our own estimates, from Fig. 3 of the paper of Johnson and Barschall.[a]

No.	E_r(kev)	T(kev)	E_{rt}(kev)	Γ(kev)	This paper E_n(kev)	JB E_n	SJS E_n	Y_{max}	Y_n	JB $\sigma_{n,p}$	$E_x(N^{15})$ (Mev)
1			(1105)		(434)			<0.1			(11.238)
2	1169.4	8.4	1165±2	8±1	494±2	499±5	469±20	21	280	125	11.294
3	1313.5	7.4	1310±3	43±5	639±3	640±7	629±20	17	200	200	11.429
4	1667.0	6.2	1664±4	38±10	993±4	993±12	(800±50)	2.0	19	20	11.759
5	1791.9	5.8	1789±4	18±5	1118±4	[1120]	...	0.9	9	[5]	11.876
6	1885.9	5.6	1883±4	15±5	1212±4	[1220]	...	2.0	18	[5]	11.964
7	2026.8	5.4	2024±4	18±5	1353±4	...	...	16	140	...	12.095
8	2081.9	5.2	2079±4	55±10	1408±4	1415±15	1379±20	36	300	190	12.146
9	2274.7	4.8	2272±4	22±5	1601±4	[1610]	1539±50	~4	~33	[5]	12.326
10	2453.6	4.6	2451±10	45±20	1780±10	1800±15	...	~1.6	~13	[5]	12.493

[a] See reference 3.
[b] See reference 4.

[12] Tollestrup, Fowler, and Lauritsen, Phys. Rev. 78, 372 (1950).

(630±50 kev); with that of Franzen, Halpern, and Stephens[13] (630±6 kev); and with the Q-value for the $C^{14}(p,n)$ reaction obtained by Shoupp, Jennings, and Sun[4] (−620±9 kev). In Table II we list our values for $E_n=E_{rt}-671$. The agreement with the results of Johnson and Barschall, in the next column, is quite satisfactory.[14] (The values enclosed in brackets are our own estimates of the positions of weak peaks in Fig. 3 of their article, not mentioned in their text.) The results in the column headed E_n(SJS) are computed from data of Shoupp, Jennings, and Sun.[4] The agreement is almost within their stated error, except for their resonance at 800 kev, which they list as doubtful.

Comparison of Cross Sections

For the purpose of comparing the cross sections for the inverse reactions, $C^{14}(p,n)N^{14}$ and $N^{14}(n,p)C^{14}$, we can use the single-level Breit-Wigner resonance formula:

$$\sigma_J{}^l(E_p)=(C/E_p)(2l+1)\times G_J{}^l\{\Gamma_p{}^l\Gamma_n{}^{l'}/[(E_p-E_{rp})^2+\tfrac{1}{4}\Gamma^2]\}, \quad (1)$$

$$\sigma_J{}^{l'}(E_n)=(C/E_n)(2l'+1)\times G_J{}^{l'}[\Gamma_p{}^l\Gamma_n{}^{l'}/(E_n-E_{rn})^2+\tfrac{1}{4}\Gamma^2], \quad (2)$$

where $\sigma_J{}^l(E_p)$ is the cross section for the reaction: C^{14} (spin $I=0$)+proton (spin $\frac{1}{2}$, angular momentum l)$\rightarrow N^{15}$ (in a state of spin J, appropriate parity, resonant at $E_p=E_{rp}$)$\rightarrow N^{14}$ (spin $I'=1$)+neutron (spin $\frac{1}{2}$, angular momentum l'); $\sigma_J{}^{l'}(E_n)$ is the cross section for the inverse reaction; $C=\hbar^2/8\pi m$, where m is the mass of the proton or neutron; E_p and E_n are the proton and neutron energies; $\Gamma_p{}^l$ and $\Gamma_n{}^{l'}$ are the half-widths for proton and neutron emission; Γ is the total half-width of the level. The lowest reported excited states of N^{14} and C^{14} are at 2.3 and 5.6 Mev, respectively,[1] so in the energy range covered in this paper the compound nucleus must decay to the ground states.

The statistical weight factors are, respectively,

$$(2l+1)G_J{}^l=(2J+1)/2(2I+1)=(2J+1)/2$$

and

$$(2l'+1)G_J{}^{l'}=(2J+1)/2(2I'+1)=(2J+1)/6.$$

Substituting in Eqs. (1) and (2), we obtain, for the ratio of the cross sections at the peak of the same resonance,

$$\sigma(E_{rp})/\sigma(E_{rn})=3E_{rn}/E_{rp}. \quad (3)$$

In Table II, we list under the heading Y_{max} the observed relative maximum yields, taken from Fig. 3. The target thickness T is considerably less than the natural width Γ for all resonances except No. 2; in this case, a correction has been applied to give the correct relative yield for a thin target.

Resonance No. 1 appears strongly in measurements of the total cross section of N^{14} for fast neutrons.[15] The background in this region is very low, and it is possible to set an upper limit of 1 percent for the ratio of the peak yield at this resonance to that at No. 2, in the $C^{14}(p,n)$ reaction.

In order to compare roughly our relative yields with the (n,p) cross sections of Johnson and Barschall, in the column under σ_{np} in Table II, we have divided our peak yields Y_{max} by the value of $\sigma(E_{rp})/\sigma(E_{np})$ from Eq. (3), and normalized to 200 millibarns at resonance No. 3. The results are in the column headed Y_n. (It must be emphasized that (a) the efficiency of our neutron detector was probably not independent of energy and that (b) we measured yields in a large forward angle, whereas Barschall and Johnson measured the integrated yield over all angles.) Resonances 3 and 4 are broad and known to be formed on N^{14} by s neutrons,[16] so their yields should be almost isotropic; the agreement for No. 4 is seen to be good. It seems probable that Johnson and Barschall somewhat underestimated the cross section for the narrow resonance No. 2. Our higher values for No. 5, 6, and 9 may be due partly to better resolution, to an increase in our counter's efficiency at higher energies, and to preferred yield in the forward direction.

Levels in N^{15}

In the last column of Table II we list the computed energies of the levels in N^{15}, where the excitation energy $E_x=[10.833+(14.0076/15.0166)E_n]$ Mev. We have used the adjusted value[16] 10.833±0.007 Mev for the neutron binding energy in N^{15}. The levels are also plotted in Fig. 1.

In conclusion, we wish to express our sincere appreciation to the maintenance staff of the Rockefeller generator: Mr. Donald Thompson, Mr. Gene Slawson, Mr. Richard Spencer, and Mr. John Adams.

[13] Franzen, Halpern, and Stephens, Phys. Rev. **77**, 641 (1950).

[14] Our values average slightly higher. We believe these authors somewhat underestimated the energy spread of their neutron source, as evidenced by their failure to resolve resonances No. 7 and 8; this may make their resonance energies too high.

[15] Measurements made in this laboratory, to be published.

[16] Li, Whaling, Fowler, and Lauritsen, Phys. Rev. **83**, 512 (1951), see Table I; private communication to W. Buechner.

Thick Target Yields from the (d,n) Reaction at 10 Mev*

LYLE W. SMITH† AND P. GERALD KRUGER
Physics Department, University of Illinois, Urbana, Illinois
(Received May 29, 1951)

The neutron yield from thick targets of Be, B, C, Al, Ni, Cu, Mo, Ta, W, Pt, and Au, bombarded with 10-Mev deuterons, has been determined by comparing the manganese activity ($MnSO_4$ in solution, in a large tank) after bombardment, with the activity produced by a standard Ra-Be source placed at the same position as the target. Some less reliable data on P, Mn, and Sb, obtained by a different method, are included.

INTRODUCTION

THE production of neutrons by deuteron bombardment was discovered by Crane and Lauritsen,[1] who used Li and Be targets. This type of source gives, at medium bombarding energies, large neutron intensities and is quite applicable to many types of experiments. Although absolute yields from various targets are of considerable value in planning experiments and add to nuclear knowledge in general, until recently, the only available data were at low energy or were thin target data for some particular reaction in which emitted charged particles could be counted. The present experiments describe a determination of the thick target yields for a number of targets bombarded with 10-Mev deuterons.

EXPERIMENTAL ARRANGEMENT

In order to avoid the troublesome corrections necessary with most available neutron detectors, because of their selective response to neutrons of different energy, this experiment was done by immersing the source in a large tank of water in which all of the neutrons are assumed ultimately to be reduced to thermal energies. A suitable detector is dissolved in the water and the activity induced in this detector, which accurately averages over energy and angle, is a measure of the total number of neutrons produced. The detector in this case was a quantity of manganese (in the form of manganese sulfate), which has a convenient absorption cross section and half-life.

The source of deuterons in this experiment was the magnetically analyzed beam from the University of Illinois cyclotron,[2] the energy of which was determined to be 10.00 ± 0.07 Mev by a range-energy measurement. The physical arrangement of the apparatus is shown in Fig. 1. The deuteron beam emerging from the cyclotron is stopped down to one inch diameter at the main target box T, is magnetically analyzed and stopped down to a one-half inch diameter at the analyzer magnet A. The analyzed beam then passes into a hole E, in the shielding water tanks (which contain a saturated solution of boric acid) around the cyclotron. After the beam traverses the shielding water tanks, it passes into an adjustable brass tube which is insulated by hard rubber bushings from the cyclotron exit tube and the water tank, B. This tube passes through Wilson seals and connects the exit tube of the cyclotron with the experimental tank, B, containing water and manganese sulfate. At the end of this tube, which serves also as a faraday cage, the target is held by means of a threaded Lucite bushing. At the front end of this tube, another aperture is provided which is insulated from the faraday tube and serves to keep deuterons which are scattered by the collimating holes from entering the faraday tube. Figure 2 shows a detail of the target assembly and the connection between the cyclotron exit tube and the tank B. The tank B was a cube approximately one meter on a side and contained 1000 liters of water in which approximately 450 pounds of manganese sulfate was dissolved. The adjustable tube connecting the cyclotron exit tube with the tank B was

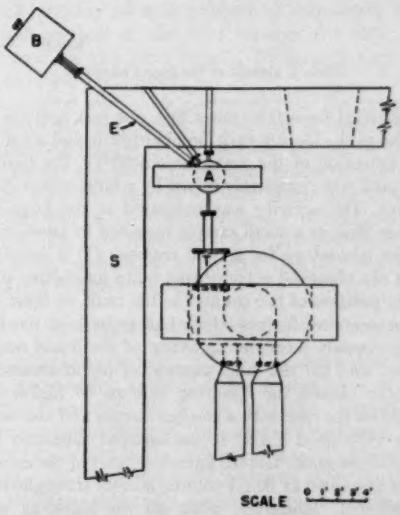

FIG. 1. Physical arrangement of apparatus. T is the main cyclotron target, A the analyzer magnet, E the exit tube, and B the experimental tank containing $MnSO_4$ in 1000 liters of water.

* This work has been supported in part by the ONR.
† Now at Brookhaven National Laboratory, Upton, New York.
[1] Crane, Lauritsen, and Solton, Phys. Rev. 44, 514 (1933); 44, 692 (1933).
[2] Kruger *et al.*, Rev. Sci. Instr. 15, 333 (1944).

electrostatically shielded. Through this shield, electrical contact was made to the tube and to an electronic beam current integrator or Q-meter, which measured the total charge striking the target. The Q-meter was an adaption of a circuit designed by Meagher for another experiment.[3] The Q-meter was calibrated with a standard voltage, measured on a precision meter which was impressed across standard resistors. These resistors were vacuum-sealed Hi-Meg resistors manufactured by the Victoreen Instrument Company, and were calibrated by the National Bureau of Standards at various temperatures with an accuracy of one-half percent. The integrator circuit was found to be linear within experimental accuracy from 10^{-11} to 10^{-7} ampere and the actual beam currents used in the experiment were all between 2×10^{-9} and 3×10^{-10} ampere.

The detection of the induced activity in the $MnSO_4$ solution was done in the following manner: A thin-walled Geiger counter was suspended vertically in the liquid on a level with the center line of the beam and

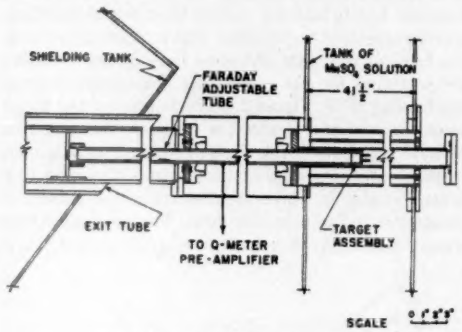

FIG. 2. Details of the target assembly.

equidistant from this center line, one end, and one side of the tank. During each bombardment and all during the detection of the manganese activity, the liquid in the tank was completely mixed by a large motor-driven stirrer. The activity was measured in the large tank rather than in a small sample removed to another part of the laboratory for several reasons: (1) it was found that the observed activity was quite insensitive to the exact position of the counter in the tank, so there were no geometrical factors which had to be kept fixed, (2) no accurately measured quantity of the liquid need be taken, and (3) the large amount of liquid around the counter caused the counting rate to be higher than would be the case with a smaller sample and also served as a very good shield to background radiation from outside the tank. The background count of the arrangement remained at 20 ± 1 counts/minute throughout the experiment. Moreover, when all the shielding water tanks were in place and the analyzer magnet set so that no beam appeared outside the shielding tanks, a ten-microampere beam of deuterons on the main cyclotron target for thirty minutes did not affect the background rate inside the tank of $MnSO_4$ solution.

The method of alignment of apparatus and taking data was as follows: The tank was leveled and lined up visually with the exit tube of the cyclotron; then a thin aluminum foil was coated with willemite and placed at the target position. The whole assembly was pumped down and a deuteron beam obtained. The fluorescent spot on the willemite was observed through a glass plate sealed on the rear of the tank and the final tank adjustment made so that the beam spot was centered on the target and did not move as the position of the target was changed back and forth within the tank. The beam spot did not move as the analyzer magnet field was swung through resonance but simply appeared and disappeared. These visual observations were made frequently during the course of the experiment, and at no time was the beam ever observed to strike any object but the target. In addition, the target was occasionally removed and the beam allowed to pass completely through the tank. During these runs the Q-meter on its most sensitive scale failed to indicate any charge striking the adjustable tube.

Before each bombardment the Q-meter was calibrated and a deuteron beam obtained at the main cyclotron target. When the beam became steady, the cyclotron deflector voltage was turned down and the analyzer magnet turned on. The deflector voltage was then raised to give a beam at the experimental stations. By this method, it was possible to get a beam to the target inside the tank B which rose rapidly to a given value. The beam into the tank was held to approximately 0.01 microampere, which was of the order of 10^{-3} of the beam current to the main cyclotron target. Bombardments lasted usually from ten to thirty minutes, and the external beam and main cyclotron beam were monitored visually and kept constant by small adjustments of the cyclotron magnetic field.

After a bombardment was completed, the activity in the tank was observed with the Geiger counter, and its decay was followed for at least one half-life of the manganese activity. No activity was ever observed other than the 2.59-hour[4] manganese except in the case of the carbon and boron carbide targets, where the activities due to the 9.93-minute N^{13} and the 20.5-minute[4] C^{11} formed in the target were observed.

As a neutron standard, a source consisting of 500 milligrams of radium element (about 900 milligrams of radium salt) intimately mixed with 3 grams of 325 mesh beryllium powder was used. The density of this source was 1.8 g/cc. Since the experiments were performed, this source has been calibrated at Argonne National Laboratory; and, allowing for Po growth between the time of the experiments and the time of calibration,

[3] R. E. Meagher, Phys. Rev. **78**, 667 (1950).

[4] These periods are taken from the Segrè chart.

the strength of this source at the time of the experiment was $6.08\pm0.37\times10^6$ neutrons/second. Bombardments were made frequently during the experiments with this source held in the target assembly at the same position in the tank as the targets during deuteron bombardment.

The counting rates observed as a function of time after the end of bombardment were corrected for counter resolving time in the usual manner. Another correction must be made at low counting rates, for, if in order to get a statistically significant number of counts it is necessary to count for a period of time during which the source decays appreciably, the observed rate is not the true rate at one-half of the time interval, but is equal to the time rate at some earlier time. Thus, let $R(t)$ be the real counting rate at any time t; then the number of counts recorded between t_1 and t_2 is

$$\int_{t_1}^{t_2} R(t)dt=\int_{t_1}^{t_2} R(t_1)\exp(-\lambda t)dt$$
$$=[R(t_1)/\lambda][\exp(-\lambda t_1)-\exp(-\lambda t_2)],$$

so that the average observed rate is

$$[R(t_1)/\lambda(t_2-t_1)][\exp(-\lambda t_1)-\exp(\lambda t_2)].$$

This must equal the true rate at some time t_3 and so is equal to

$$R(t_1)\exp(-\lambda t_3),$$

so that

$$\exp(-\lambda t_3)=[\exp(-\lambda t_1)-\exp(-\lambda t_2)]/\lambda(t_2-t_1)$$

and

$$t_3-t_1=(1/\lambda)\ln\{(t_2-t_1)/1-\exp\lambda(t_2-t_1)\}$$

may be used to find the time at which the observed rate is equal to the true rate.

After the above corrections are made and background and activities due to previous bombardments are subtracted, the activity induced in the manganese can be extrapolated back to the time at which the bombardment ended. If the bombardment was constant, this will give a number which is proportional to

$$(K/\lambda)[1-\exp(\lambda T)],$$

where K is the rate of production of neutrons, λ is the decay constant of the manganese, and T is the bombardment time. Since in these experiments only the activity induced in the manganese is used and the physical arrangement remained the same, if the observed activities at the end of bombardment are divided by $[1-\exp(-\lambda T)]$, the number obtained is proportional to the rate of production of neutrons. If the bombardment was not constant, the activity produced at the end of bombardment will be proportional to

$$(K/\lambda)[1-\exp(-\lambda T)]+\exp(-\lambda T)\int_0^T f(t)\exp(\lambda t)dt,$$

where $f(t)$ is the fluctuation from the average rate, K, of production of neutrons and $\langle f(t)\rangle_{Av}=0$. This additional term is estimated to be less than 2 percent of the total activity in the present experiments, and agreement between different bombardments of the same target confirm this. If the fraction of neutrons absorbed in the manganese is the same for the Ra-Be source as for the (d,n) source, the ratio of the two yields for a bombardment time long compared with $1/\lambda$ is equal to the equivalent number of Kg of Ra-Be per microampere and, knowing the number of neutrons per second emitted by the Ra-Be source, one can determine the number of neutrons per second per microampere emitted from the (d,n) reaction.

In order to check the assumption that the fraction of neutrons absorbed in the manganese is the same for the Ra-Be source as for the (d,n) sources, a number of checks were made:

(1) When the level of manganese solution in the tank was lowered and the yield redetermined from a Be target, no change in the yield was noted.

(2) In order to check whether differential absorption was occurring because of the difference in angular distribution of neutrons from the Ra-Be and (d,n) sources, the position of the sources in the tank of manganese solution was changed in the direction of the incident deuteron beam so that the hole in the tank in the straight through position subtended a larger angle at the target. Although, when the sources were placed sufficiently near the exit hole, a decrease in manganese activity was noted, for each the ratio remained constant within experimental error, indicating that no errors were arising from this source. This point was checked further by using a Lucite plug which completely filled the last one-half of the tube through the tank and redetermining the yield from a Be target; again no change in yield was noted.

All targets were thick compared with the range of the deuterons and, except in the case of boron, were composed of reagent grade material. To get the yield from boron, a quantity of granular boron carbide was packed into a cavity in a brass block and bonded together with a very dilute solution of collodion in acetone. The yield from boron is determined when the yield from carbon and the atomic stopping power of boron and carbon are known.

EXPERIMENTAL RESULTS

A preliminary report[5] of some of these data was given previously. Table I shows a summary of the results expressed in kg Ra-Be equivalent per microampere and neutrons per second per microampere.

The asterisks indicate values which were determined by using a target in the main cyclotron target box and detecting the neutrons by means of a gold foil imbedded in paraffin. These values were normalized to the values

[5] L. W. Smith and P. G. Kruger, Phys. Rev. 74, 1258(A) (1948).

TABLE I. Summary of data of neutron yields from the (d,n) reaction in thick targets.

Target	Z	kg Ra-Be equivalent	$n/\mu a$ sec (10^{-10})
Be	4	2.66	3.23 ±0.24
B	5	1.58	1.91 ±0.14
C	6	0.98	1.19 ±0.22
Al	13	0.72	0.87 ±0.07
P*	15	0.86	1.05 ±0.31
Mn*	25	0.63	0.76 ±0.22
Ni	28	0.26	0.33 ±0.03
Cu	29	0.45	0.55 ±0.05
Mo	42	0.35	0.42 ±0.05
Sb*	51	0.28	0.35 ±0.10
Ta	73	0.062	0.074±0.014
W	74	0.058	0.070±0.005
Pt	78	0.050	0.060±0.008
Au	79	0.039	0.047±0.006

for Be and W targets obtained from the manganese tank detection method after subtracting the continuous neutron background which exists inside the shielding tanks around the cyclotron. This continuous background is approximately 0.4×10^{10} neutrons/second/microampere near the main cyclotron target.

DISCUSSION

There is not much data available for comparison with the above results. In the case of Be, one can extrapolate the low energy data of Amaldi, Hafstad, and Tuve,[6] assuming a Gamow potential and taking into account the increase of range with energy. The result is 3×10^{10} neutrons/sec/μa, and the agreement is probably fortuitous. Lawrence and Cooksey[7] report a yield, with 5-Mev deuterons, of approximately 30×10^{10} neutrons/sec/μa. This value is considerably higher than would be expected from the present data. More recent measurements by Aebersold[8] with an ionization chamber indicate a neutron yield at 8 Mev of 2.38×10^{3} curies of Rn-Be equivalent per microampere. This is in reasonable agreement with the present results although, since the results of Aebersold are for neutrons in the forward direction, his value should be somewhat high. Fermi[9] estimates the yield at 8 Mev to be 10^{10} neutrons/second/microampere.

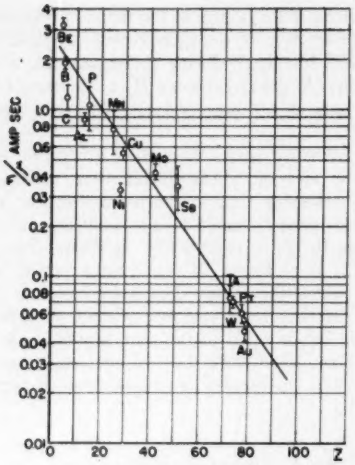

FIG. 3. Neutron yield, showing the number of neutrons per microampere sec$(\times10^{-10})$, *vs* Z.

In the case of carbon, the extrapolation of Amaldi, Hafstad, and Tuve's data gives 0.3×10^{10} neutrons/sec/μa. The agreement is not too bad considering the errors which are introduced in such an extrapolation.

Allen *et al.*[10] have reported the fast neutron yield and angular distribution of various thick targets bombarded with 15-Mev deuterons. They find the yield per second per microampere, N, to decrease with nuclear charge, Z, of the target according to the approximate empirical equation,

$$\log N = 10.18 - 0.0234Z.$$

As shown in Fig. 3, the present data also may be approximated by a curve of the same general nature, although there are deviations as large as a factor of two.

[6] Amaldi, Hafstad, and Tuve, Phys. Rev. **51**, 896 (1937).
[7] E. O. Lawrence and D. Cooksey, Phys. Rev. **50**, 1131 (1936).
[8] P. C. Aebersold and G. A. Anslow, Phys. Rev. **69**, 1 (1946).
[9] E. Fermi, "Neutron physics," MDDC-320 (1946), unpublished.
[10] Allen, Nechaj, Sun, and Jennings, NP-1507 (1950), unpublished.

Neutral Photomeson Production and Nucleon Isobars

KEITH A. BRUECKNER*
Institute for Advanced Study, Princeton, New Jersey
AND
K. M. CASE
Department of Physics, University of Michigan, Ann Arbor, Michigan
(Received May 7, 1951)

The magnitude of the neutral photomeson cross section, which is comparable with the cross section for charged mesons, is not given correctly by weak coupling perturbation theory. In fact, the phenomenon appears to depend on a nonlinear behavior of the meson fields corresponding to intermediate or strong coupling. Accordingly, the effect of the existence of nucleon isobars, which is one of the most characteristic features of strong coupling theory, has been investigated through the use of a classical model and is found to give the general features and magnitude of the neutral cross section correctly. The isobars are predicted to be unstable with an excitation energy of three or four hundred Mev.

I. INTRODUCTION

THE experimental measurements on the production of mesons by photons[1] show (1) that the total cross sections for charged and neutral meson production are about the same and are approximately equal to 10^{-28} cm^2 for a bremsstrahlung spectrum with maximum energy of 320 Mev; (2) that the neutral cross section rises much more steeply with energy than does the charged; and (3) that the angular distribution for charged mesons is roughly isotropic for angles between 45 and 135 degrees in the laboratory system. The angular distribution for the neutral mesons is only very approximately known but appears to be somewhat peaked forward in the laboratory system for mesons of 60 to 70 Mev.

The production of charged mesons might be reasonably expected to depend only on the extent of the charge cloud about the nucleon, the probability of a meson being present, and the strength of the interaction of the photon with the meson charge, i.e.,

$$\sigma(\text{charged}) \simeq \pi(\hbar/\mu c)^2(g^2/\hbar c)(e^2/\hbar c) \sim 2(g^2/\hbar c)10^{-28}\ \text{cm}^2. \quad (1)$$

For $g^2/\hbar c = \frac{1}{2}$, this is indeed the approximate magnitude of the cross section observed. One can similarly argue that if neutral mesons are only weakly affected by the interaction of the photon with the charged mesons, the neutral meson can be produced only through the interaction of the photon with the nucleon magnetic moment. Since this is characterized by a length $\hbar/Mc$, where M is the nucleon mass, the cross section would be

$$\sigma(\text{neutral}) \simeq \pi(\hbar/Mc)^2(g^2/\hbar c)(e^2/\hbar c) \sim (\mu/M)^2\sigma(\text{charged}). \quad (2)$$

Since $\mu/M \simeq 1/7$, one would expect on the basis of this elementary argument to find σ(neutral) one or two orders of magnitude smaller than σ(charged), in contradiction with the observed approximate equality.

A detailed calculation of this effect has been made by Kaplon[2] using weak coupling theory and including the effects of the nucleon anomalous moments by the introduction of a Pauli term[3] of the form,

$$\sigma_{\mu\nu}F_{\mu\nu} = \boldsymbol{\sigma}\cdot\mathbf{H} - i\boldsymbol{\alpha}\cdot\mathbf{E} \quad (3)$$

in the equation of motion of the nucleon field. He finds for symmetrical pseudoscalar theory that the ratio σ(neutral)/σ(charged) is 0.138 for production from protons and 0.062 for production from neutrons at 250 Mev, where the experimental value is approximately 0.6. The theoretical values of Kaplon are therefore considerably lower than those observed, particularly for neutrons. It is possible to obtain agreement with experiment by increasing the neutral coupling constant; we shall, however, restrict ourselves to the symmetrical form of the theory.

The anomalous magnetic moments which make the values computed by Kaplon appreciably larger than the estimate in Eq. (2) are of course themselves thought to be due to charged meson currents; and thus Kaplon's calculations represent one mechanism by which the electromagnetic effects of charged mesons can serve to increase the photoeffect of neutral mesons. We have thought it of interest to investigate other such effects, which will not appear when the photoeffect is treated by perturbation theory in its lowest order, because they correspond to essentially nonlinear terms in the equation. Indeed it appears that the neutral meson distribution can be strongly excited by the interaction of the photon with the charged mesons and with the nucleon magnetic moment. A possible source of such nonlinear behavior of the charged and neutral meson fields might be the existence of unstable nucleon isobars which could be easily excited by a resonant interaction at the frequencies of the electromagnetic radiation. The excited states of the nucleon would then decay with

* Now at the Department of Physics, Indiana University, Bloomington, Indiana.

[1] J. Steinberger and A. S. Bishop, Phys. Rev. **78**, 494(L) (1950). Steinberger, Panofsky, and Steller, Phys. Rev. **78**, 802 (1950). We wish to thank Drs. Steinberger and Panofsky for information on additional recent experimental results.

[2] We are indebted to Dr. Kaplon for communicating his results to us in advance of publication.

[3] W. Pauli, *Handbuch der Physik* **24**, 1 (233).

very short lifetime (of the order of the dimensions of the system divided by the velocity of light) into charged or neutral mesons together with a stable nucleon. The relative probability of production of the charged and neutral mesons would then depend only on the relative strength of coupling of the two fields to the nucleon.

After the completion of this work, it was brought to the attention of the authors that Fujimoto and Miyazawa of the University of Tokyo[4] had independently suggested that the large neutral cross section could be attributed to the existence of nucleon isobars. Their calculations were made with a strong coupling quantum-mechanical treatment of symmetrical pseudoscalar theory. We wish to develop these arguments in greater detail than has been done by Fujimoto and Miyazawa in their letter. We shall also show that a simple classical model gives predictions for this process which, although somewhat different from the strong coupling treatment, lead to essentially the same results that they have obtained. A more detailed comparison of the results of these methods will be given in Sec. II.

To investigate strongly nonlinear effects of this nature, a weak coupling approximation cannot be used. A strong coupling theory of the meson-nucleon interactions is necessary. Unfortunately, however, no rigorous methods have been devised for treating this problem. We therefore shall introduce an approximate model for the calculation which will allow a strong coupling treatment of the meson-nucleon interaction and of the effects of isobars on the phenomena in which we are interested. The method to be used is the classical treatment of the meson field and of the spin variables which was originally suggested by Heisenberg[5] and others.[6] We shall consider only the symmetrical pseudoscalar theory because of other evidence that the charged meson is described by a pseudoscalar field.[7] The application of this method is given in detail in Sec. II. In Sec. III some remarks will be made on the classical theory of meson scattering by nucleons and on the scattering of nucleons by nucleons.

II. CLASSICAL CALCULATION OF MESON PRODUCTION BY PHOTONS

The approximations of the classical method allow a simple solution of this problem without a weak coupling treatment of the meson nucleon interaction.[8] It is necessary to assume that the meson field is unquantized, i.e., that quantum fluctuations of the field are unimportant. This will apparently be so if the coupling is strong leading to many mesons about the nucleon. A severer restriction is the assumption that the nucleon spin and isotopic spin vectors can be treated as classical unit vectors which can take on continuously variable orientations, i.e., that they are also unquantized. It is also necessary to assume that the effects of nucleon recoil can be approximated by the introduction of a cut-off radius corresponding to the distance at which the nucleon recoil will appreciably modify the behavior of the system. Such a distance may reasonably be chosen to be approximately the nucleon Compton wavelength.

The hamiltonian for mesons interacting with one nucleon (at rest) and the electromagnetic field is

$$H=\int d^3x\{\tfrac{1}{2}(\boldsymbol{\pi}\cdot\boldsymbol{\pi}+\nabla\boldsymbol{\phi}\cdot\nabla\boldsymbol{\phi}+\mu^2\boldsymbol{\phi}\cdot\boldsymbol{\phi})$$
$$+(4\pi)^{\frac{1}{2}}(f/\mu)[\boldsymbol{\sigma}\cdot\nabla\boldsymbol{\phi}\cdot\boldsymbol{\tau}+(4\pi)^{\frac{1}{2}}e(\boldsymbol{\sigma}\cdot\mathbf{A})(\boldsymbol{\tau}\cdot\boldsymbol{\phi}\times\mathbf{k})]U$$
$$+(\boldsymbol{\mu}\cdot\mathbf{H})U-\mathbf{A}\cdot\nabla(\boldsymbol{\phi}\times\mathbf{k})\cdot\boldsymbol{\phi}\}. \quad (4)$$

In this expression, the neutral fields φ_1 and φ_2 are the components of the charged field

$$\varphi=(\varphi_1-i\varphi_2)/\sqrt{2} \quad (5)$$

and φ_3 is the neutral meson field. The vector $\boldsymbol{\phi}$ in charge space then has components φ_1, φ_2, φ_3. Similarly $\boldsymbol{\tau}$ is the isotopic spin vector in charge space. We also define $\mathbf{k}$ as a unit vector in the direction of the 3-axis in charge space. $\mathbf{A}$ is the vector potential. U is the nucleon source density; for a point source, U would be a delta-function. The term $\boldsymbol{\mu}\cdot\mathbf{H}$ gives the electromagnetic interaction of the nucleon and is taken to be

$$(4\pi)^{\frac{1}{2}}e(a+b\boldsymbol{\tau}\cdot\mathbf{k})(\boldsymbol{\sigma}\cdot\mathbf{H}) \quad (6)$$

where a and b are determined by the values of the static moments, i.e.,

$$a+b=\gamma_N/2M, \quad a-b=\gamma_P/2M, \quad (7)$$

where

$$\gamma_N=-1.91, \quad \gamma_P=2.79. \quad (8)$$

This assumption, that the static moments represent the interaction of nucleons with photons of energies near the meson rest energy of 140 Mev, is of course valid only if the moments show a negligible energy variation over this energy range. This is true only if the currents about the nucleon which contribute to the moment are confined to regions small compared with the wavelength of the radiation, which (at threshold for meson production) is the meson Compton wavelength. This condition is in fact satisfied for the pseudoscalar theory,[9] which predicts a distribution of the dimensions of the nucleon Compton wavelength for both the meson and the nucleon currents which contribute to the magnetic moment. The ratio of wavelength to the dimensions of the contributing currents is therefore $M/\mu\simeq 7$ and the condition for energy inde-

[4] Y. Fujimoto and H. Miyazawa, Prog. Theor. Phys. **5**, 1052(L) (1950).

[5] W. Heisenberg, Z. Physik **113**, 61 (1939).

[6] J. R. Oppenheimer and J. Schwinger, Phys. Rev. **60**, 150 (1941). H. J. Bhabha and H. C. Corben, Proc. Roy. Soc. (London) **A178**, 273 (1941).

[7] S. Tamor and R. E. Marshak, Phys. Rev. **80**, 766(L) (1950). Brueckner, Serber, and Watson, Phys. Rev. **81**, 575 (1951).

[8] See W. Pauli, *Meson Theory* (Interscience Publishers, Inc., New York, 1946), for a detailed discussion of the method.

[9] K. M. Case, Phys. Rev. **76**, 1 (1949).

pendence is approximately satisfied. Aside from these considerations, however, a change in the magnitude of the moments which is not strongly energy dependent will not change the principal features of this calculation, which has to do with the resonance interaction of nucleon isobars. We shall therefore use the static values for the moments but realize that the quantitative values of our results are somewhat in doubt.

From this hamiltonian we obtain the equation of motion for the meson field by the relations,

$$\dot{\pi}_i = -\partial H/\partial\varphi_i, \quad \dot{\varphi}_i = \partial H/\partial\pi_i. \tag{9}$$

We shall treat the spin and isotopic spin as classical unit vectors with the properties

$$\{\sigma_x, \sigma_y\} = -2\sigma_z, \quad \{\tau_x, \tau_y\} = -2\tau_z, \quad \text{(and cyclic)} \tag{10}$$

where $\{\ \}$ is the classical poisson bracket. The equations of motion for the spins are then given by

$$d\boldsymbol{\sigma}/dt = \{H, \boldsymbol{\sigma}\}. \tag{11}$$

Thus we obtain

$$(\Box - \mu^2)\boldsymbol{\phi} = (4\pi)^{\frac{1}{2}}(f/\mu)\boldsymbol{\sigma}\cdot\nabla U\boldsymbol{\tau} - 4\pi(fe/\mu)\boldsymbol{\sigma}\cdot\mathbf{A}(\boldsymbol{\tau}\times\mathbf{k})U - 2(4\pi)^{\frac{1}{2}}e\mathbf{A}\cdot\nabla(\boldsymbol{\phi}\times\mathbf{k}), \tag{12}$$

$$d\boldsymbol{\sigma}/dt = \boldsymbol{\sigma}\times\mathbf{F}, \quad d\boldsymbol{\tau}/dt = \boldsymbol{\tau}\times\mathbf{G},$$

where

$$\mathbf{F} = -2(4\pi)^{\frac{1}{2}}\int d^3x U\{(f/\mu)\nabla\boldsymbol{\phi}\cdot\boldsymbol{\tau} - (4\pi)^{\frac{1}{2}}(fe/\mu)\mathbf{A}(\boldsymbol{\phi}\times\boldsymbol{\tau})\cdot\mathbf{k} + e(a+b\boldsymbol{\tau}\cdot\mathbf{k})\mathbf{H}\}$$

$$\mathbf{G} = -2(4\pi)^{\frac{1}{2}}\int d^3x U\{(f/\mu)\boldsymbol{\sigma}\cdot\nabla\boldsymbol{\phi} + (4\pi)^{\frac{1}{2}}(fe/\mu)\boldsymbol{\sigma}\cdot\mathbf{A}(\boldsymbol{\phi}\times\mathbf{k}) + eb\mathbf{k}\boldsymbol{\sigma}\cdot\mathbf{H}\}. \tag{13}$$

We shall now introduce the perturbation aspect of the problem. We assume that we can separate the variables into an unperturbed part and a perturbed part, i.e.,

$$\boldsymbol{\phi}(r, t) = \boldsymbol{\phi}_0(r) + (2\pi)^{-\frac{1}{2}}\int d\omega \exp(-i\omega t)\boldsymbol{\phi}_1(\omega) \tag{14}$$

and similarly for $\boldsymbol{\sigma}$, $\boldsymbol{\tau}$, $\mathbf{F}$, $\mathbf{G}$. We then argue that, since the perturbation in the system is introduced by the electromagnetic field, $\boldsymbol{\phi}_1$ will be of order $\alpha(=1/137)$ compared with the unperturbed $\boldsymbol{\phi}_0$. The perturbation approximation will then consist of neglecting terms of order $\boldsymbol{\phi}_1\cdot\boldsymbol{\tau}_1$, etc., which are of order α^2 and retaining only terms of order α. We note that this approximation does not apply to the strong meson-nucleon coupling. We also introduce fourier representations for $\boldsymbol{\phi}$ and U.

$$\boldsymbol{\phi}(\mathbf{r}) = (2\pi)^{-\frac{1}{2}}\int d^3l \exp(i\mathbf{l}\cdot\mathbf{r})\boldsymbol{\phi}_l$$

$$U(\mathbf{r}) = (2\pi)^{-3}\int d^3l \exp(i\mathbf{l}\cdot\mathbf{r})U_l \tag{15}$$

(we note that if $U(\mathbf{r})$ is a delta-function, corresponding to a point nucleon source, $U_l = 1$). We also write

$$\mathbf{A}(\mathbf{r}, t) = [\boldsymbol{\varepsilon}/(2\pi)^{\frac{1}{2}}]\exp[-i(\mathbf{v}\cdot\mathbf{r} - \nu t)] \tag{16}$$

and set

$$\int H(r)U(r)d^3r = H(0). \tag{17}$$

Inserting these definitions for $\boldsymbol{\phi}$ and U and eliminating φ_0 and φ_1 from the equations for F and G, we have

$$\mathbf{F}_0 = -\frac{f^2}{\mu^2\pi^2}\int d^3l \frac{(U_l)^2(\boldsymbol{\sigma}_0\cdot\mathbf{l})}{l^2+\mu^2}$$

$$\mathbf{F}_1 = \frac{f^2}{\mu^2\pi^2}\int d^3l (U_l)^2\left\{\frac{-(\boldsymbol{\tau}_0\cdot\boldsymbol{\tau}_1)(\boldsymbol{\sigma}_0\cdot\mathbf{l})}{l^2+\mu^2} + \frac{(\boldsymbol{\tau}_0\cdot\boldsymbol{\tau}_1)(\boldsymbol{\sigma}_0\cdot\mathbf{l})}{\omega^2-l^2-\mu^2} + \frac{\tau_0^2(\boldsymbol{\sigma}_1\cdot\mathbf{l})}{\omega^2-l^2-\mu^2}\right\} - 2(4\pi)^{\frac{1}{2}}e(a+b\boldsymbol{\tau}_0\cdot\mathbf{k})\mathbf{H}_0(0)\delta(\omega-\nu)$$

$$\mathbf{G}_0 = \frac{-f^2\boldsymbol{\tau}_0}{\mu^2\pi^2}\int d^3l \frac{(U_l)^2(\boldsymbol{\sigma}_0\cdot\mathbf{l})^2}{l^2+\mu^2}$$

$$\mathbf{G}_1 = \frac{f^2\boldsymbol{\tau}_1}{\mu^2\pi^2}\int d^3l \frac{(\boldsymbol{\sigma}_0\cdot\mathbf{l})^2(U_l)^2}{\omega^2-l^2-\mu^2} + (4\pi)^{\frac{1}{2}}\frac{eif^2}{\mu^2\pi^2}(\boldsymbol{\tau}_0\times\mathbf{k})(\boldsymbol{\sigma}_0\cdot\boldsymbol{\varepsilon}) \times\int d^3l U_l U_{l-\nu}\left(\frac{1}{\omega^2-l^2-\mu^2} + \frac{1}{l^2+\mu^2}\right) \times\boldsymbol{\sigma}_0\cdot\mathbf{l}\,\delta(\omega-\nu) - 2(4\pi)^{\frac{1}{2}}\frac{eif^2}{\mu^2\pi^2}(\boldsymbol{\tau}_0\times\mathbf{k}) \times\int d^3l U_l U_{l-\nu}\frac{(\boldsymbol{\sigma}_0\cdot\mathbf{l})\boldsymbol{\sigma}_0\cdot(\mathbf{l}-\mathbf{v})(\boldsymbol{\varepsilon}\cdot\mathbf{l})\delta(\omega-\nu)}{(\omega^2-l^2-\mu^2)[(l-\nu)^2+\mu^2]} - 2b(4\pi)^{\frac{1}{2}}e\mathbf{k}\boldsymbol{\sigma}_0\cdot\mathbf{H}_0(0)\delta(\omega-\nu). \tag{18}$$

In evaluating the integrals over $\mathbf{l}$, we shall assume the convention that in convergent integrals, we can replace U_l by 1, its value for a point source. If an integral diverges, we shall set $U_l = 1$ but change the limits of integration by replacing

$$\int_0^\infty dl \quad \text{by} \quad \int_0^{l_{\max}} dl. \tag{19}$$

This is equivalent to inserting a cut-off radius. In addition, in the terms of order α, we shall retain only the leading (and largest) term in the integrals. These methods for obtaining approximate values for the integrals are valid only in the region where $l_{\max}$ is much greater than the frequencies involved in the process. Since $l_{\max}$ will be assumed to be approximately the nucleon momentum, we will be restricted to photon energies which are small compared to the nucleon rest

energy. We then have

$$\int d^3l \frac{(\boldsymbol{\sigma}_0\cdot\mathbf{l})U_l^2}{\omega^2-\mu^2-l^2}=\frac{4\pi}{3}\boldsymbol{\sigma}_0\int_0^\infty \frac{l^4dlU_l^2}{\omega^2-\mu^2-l^2}$$
$$=\frac{4\pi}{3}\boldsymbol{\sigma}_0\left\{\int_0^{l_{\max}} dl(-l^2-\omega^2+\mu^2)\right.$$
$$\left.+(\omega^2-\mu^2)^2\int_0^\infty \frac{dl}{\omega^2-\mu^2-l^2}\right\}. \quad (20)$$

In evaluating the last integral, we deform the contour about the poles at

$$l=\pm(\omega^2-\mu^2)^{\frac{1}{2}}\equiv\pm q$$

to give a result corresponding to outgoing waves, i.e.,

$$\lim_{\epsilon\to 0}\frac{1}{2}\int_{-\infty}^{\infty}\frac{dl}{(\omega^2-\mu^2-l^2-i\epsilon)}=\frac{\pi i}{2q}. \quad (21)$$

The total integral then is the sum of three contributions

$$(4\pi/3)\boldsymbol{\sigma}_0\{-\tfrac{3}{4}l_{\max}{}^3-(\omega^2-\mu^2)l_{\max}+\tfrac{1}{2}\pi iq^3\}. \quad (22)$$

The integral

$$\int d^3l U_l U_{l-\nu}\left(\frac{1}{\omega^2-l^2-\mu^2}+\frac{1}{l^2+\mu^2}\right)\boldsymbol{\sigma}_0\cdot\mathbf{l} \quad (23)$$

in this approximation is

$$\int_0^{l_{\max}} l^2dl\left(\frac{1}{\omega^2-\mu^2-l^2}+\frac{1}{l^2+\mu^2}\right)\int d\Omega(\boldsymbol{\sigma}_0\cdot\mathbf{l})=0. \quad (24)$$

The failure of this term to contribute can be explained on elementary grounds; the direct coupling term in the hamiltonian $fe\boldsymbol{\sigma}\cdot\mathbf{A}\boldsymbol{\phi}$ leads to emission of mesons in s-states. Then, since the meson is coupled with the nucleon only when in P-states (through the $\boldsymbol{\sigma}\cdot\nabla\boldsymbol{\phi}$ interaction), such s-state mesons cannot react on the spins.

To evaluate the integral

$$\int d^3l\frac{(\boldsymbol{\sigma}_0\cdot\mathbf{l})(\boldsymbol{\epsilon}\cdot\mathbf{l})\boldsymbol{\sigma}_0\cdot(\mathbf{l}-\mathbf{v})U_lU_{l-\nu}}{(\omega^2-l^2-\mu^2)[(\mathbf{l}-\mathbf{v})^2+\mu^2]} \quad (25)$$

we note that it must be proportional to the scalar $(\boldsymbol{\sigma}_0\cdot\boldsymbol{\epsilon})(\boldsymbol{\sigma}_0\cdot\mathbf{v})$ since other scalar products vanish, due to the orthogonality of $\boldsymbol{\epsilon}$ and $\mathbf{v}$. We can, therefore, approximate the integral by

$$(\boldsymbol{\sigma}_0\cdot\mathbf{v})\int d^3l(\boldsymbol{\sigma}_0\cdot\mathbf{l})(\boldsymbol{\epsilon}\cdot\mathbf{l})/l^4=\frac{4}{3}\pi(\boldsymbol{\sigma}_0\cdot\mathbf{v})(\boldsymbol{\sigma}_0\cdot\boldsymbol{\epsilon})l_{\max}. \quad (26)$$

In collecting these results, we observe that since the equations of motion for the spins can be written

$$-i\omega\boldsymbol{\sigma}_1=\boldsymbol{\sigma}_0\times\mathbf{F}_1+\boldsymbol{\sigma}_1\times\mathbf{F}_0,\ -i\omega\boldsymbol{\tau}_1=\boldsymbol{\tau}_0\times\mathbf{G}_1+\boldsymbol{\tau}_1\times\mathbf{G}_0, \quad (27)$$

we can drop terms in $\mathbf{F}_1$ and $\mathbf{G}_1$ proportional to $\boldsymbol{\sigma}_0$ and $\boldsymbol{\tau}_0$ respectively. We introduce the new constant,

$$a=\tfrac{1}{2}\pi l_{\max}, \quad (28)$$

where a is the cut-off radius and define

$$N=\tfrac{2}{3}(f^2/\mu^2a)(\omega^2-a\mu^3+iaq^3). \quad (29)$$

The equations for the spin motion then are

$$i\omega\boldsymbol{\sigma}_1=N\boldsymbol{\sigma}_0\times\boldsymbol{\sigma}_1+2e(4\pi)^{\frac{1}{2}}(a+b\boldsymbol{\tau}_0\cdot\mathbf{k})\boldsymbol{\sigma}_0\times\mathbf{H}_0\delta(\omega-\nu)$$
$$i\omega\boldsymbol{\tau}_1=N\boldsymbol{\tau}_0\times\boldsymbol{\tau}_1+2e(4\pi)^{\frac{1}{2}}b\boldsymbol{\tau}_0\times\mathbf{k}\boldsymbol{\sigma}_0\cdot\mathbf{H}_0\delta(\omega-\nu)$$
$$+\frac{4}{3}\frac{f^2(4\pi)^{\frac{1}{2}}}{\mu^2a}e\boldsymbol{\tau}_0\times(\boldsymbol{\tau}_0\times\mathbf{k})\boldsymbol{\sigma}_0\cdot\mathbf{v}\boldsymbol{\sigma}_0\cdot\boldsymbol{\epsilon}\delta(\omega-\nu). \quad (30)$$

At this point we can introduce some simplification of these expressions. An examination of the derivation of these equations shows that the term in the equation for $\boldsymbol{\tau}_1$ proportional to $\boldsymbol{\tau}_0\times(\boldsymbol{\tau}_0\times\mathbf{k})$ is the result of the virtual emission and reabsorption of mesons which, while virtual, interact with the electromagnetic field. Since we have taken into account of such processes by the introduction of a moment interaction proportional to $\mu\cdot\mathbf{H}$ (the anomalous moment part of which is due to such virtual meson interactions with the electromagnetic field), we can consistently neglect the contribution of this term, assuming that it has been properly represented by the anomalous moment term. An explicit calculation with this term included shows that the contribution in the weak coupling limit although of the same form as that due to the anomalous moments is actually considerably smaller. This is the result of the classical average over the unit vector $\boldsymbol{\tau}_0$ which appears to a high power in this term. Rigorously some sort of expectation value should replace the averaging process. Hence, one might conclude that dropping this term and using the anomalous moments may indeed give a better approximation to the correct cross sections.

We further simplify the equations if we neglect $a/b=(\gamma_P+\gamma_N)/(\gamma_P-\gamma_N)=+0.19$. We can solve for $\boldsymbol{\sigma}_1$ by making the obvious substitution,

$$\boldsymbol{\sigma}_1=A\boldsymbol{\sigma}_0\times\mathbf{H}_0+B\boldsymbol{\sigma}_0\times(\boldsymbol{\sigma}_0\times\mathbf{H}_0), \quad (31)$$

i.e., expressing $\boldsymbol{\sigma}_1$ which is orthogonal to $\boldsymbol{\sigma}_0$ by a linear combination of two mutually orthogonal vectors which are also orthogonal to $\boldsymbol{\sigma}_0$. We find

$$\boldsymbol{\sigma}_1=4be\frac{\pi^{\frac{1}{2}}\boldsymbol{\tau}_0\cdot\mathbf{k}}{N^2-\nu^2}i\nu\left[\boldsymbol{\sigma}_0\times\mathbf{H}_0+\frac{N}{i\nu}\boldsymbol{\sigma}_0\times(\boldsymbol{\sigma}_0\times\mathbf{H}_0)\right]. \quad (32)$$

Similarly

$$\boldsymbol{\tau}_1=4be\frac{\pi^{\frac{1}{2}}\boldsymbol{\sigma}_0\cdot\mathbf{H}_0}{N^2-\nu^2}i\nu\left[\boldsymbol{\tau}_0\times\mathbf{k}+\frac{N}{i\nu}\boldsymbol{\tau}_0\times(\boldsymbol{\tau}_0\times\mathbf{k})\right]. \quad (33)$$

To find the outgoing amplitude of the meson wave,

we have at large distances

$$\phi_1(r)=\frac{1}{(2\pi)^{\frac{1}{2}}}\int d^3l\,\phi_{1l}\exp(i\mathbf{l}\cdot\mathbf{r})$$

$$=\frac{e^{iqr}}{4\pi r}(4\pi)^{\frac{1}{2}}\frac{f}{\mu}\Big[i(\sigma_0\cdot\mathbf{q}\tau_1+\sigma_1\cdot\mathbf{q}\tau_0)-(4\pi)^{\frac{1}{2}}e\sigma_0\cdot\boldsymbol{\varepsilon}\tau_0\times\mathbf{k}$$

$$+2e(4\pi)^{\frac{1}{2}}\frac{\boldsymbol{\varepsilon}\cdot\mathbf{q}\sigma_0\cdot(\mathbf{q}-\mathbf{v})}{(\mathbf{q}-\mathbf{v})^2+\mu^2}\tau_0\times\mathbf{k}\Big] \quad (34)$$

where $q=(\nu^2-\mu^2)^{\frac{1}{2}}$ is the meson momentum.

The differential cross section then is given by

$$d\sigma/d\Omega=\langle|A_s|^2\rangle q/\nu e^2 \quad (35)$$

where A_s is the coefficient of e^{iqr}/r in Eq. (34) and $\langle\ \rangle$ denotes an average over spin directions and over the polarization of the gamma-ray. In carrying out this average, we note that in general

$$\langle(\boldsymbol{\varepsilon}\cdot\mathbf{A})^2\rangle=(A^2-(\mathbf{A}\cdot\mathbf{v})^2/\nu^2)e^2/2$$

$$\langle\sigma_0\cdot\mathbf{A}\sigma_0\cdot\mathbf{B}\rangle=\tfrac{1}{3}\mathbf{A}\cdot\mathbf{B}$$

$$\langle\sigma_0\cdot\mathbf{A}\sigma_0\cdot\mathbf{B}\sigma_0\cdot\mathbf{C}\sigma_0\cdot\mathbf{D}\rangle$$

$$=(\mathbf{A}\cdot\mathbf{B}\mathbf{C}\cdot\mathbf{D}+\mathbf{A}\cdot\mathbf{C}\mathbf{B}\cdot\mathbf{D}+\mathbf{A}\cdot\mathbf{D}\mathbf{B}\cdot\mathbf{C})/15 \quad (36)$$

and that the average of expressions containing an odd number of factors of σ_0 or τ_0 is zero. Carrying out the indicated averages, we find

$$(d\sigma/d\Omega)[(1/9)(q/\nu)(f^2e^2/\mu^2)]^{-1}$$

$$=\left|\frac{2bvq}{N^2-\nu^2}\right|^2\Big\{[2(1+\sin^2\theta)\sin^2\varphi$$

$$+(1+2\cos^2\varphi)(1+\cos^2\theta)]\nu^2/10$$

$$+[2(1+\sin^2\theta)(1+7\cos^2\varphi)$$

$$+2(2-3\sin^2\theta)(1-3\cos^2\varphi)$$

$$+(1+2\cos^2\varphi)(2+7\sin^2\theta)]|N|^2/50$$

$$+\sin^2\varphi\left[1-\frac{2q^2\sin^2\theta}{((\mathbf{q}-\mathbf{v})^2+\mu^2)^2}\right]\Big\} \quad (37)$$

where θ is the angle between the photon and meson directions and φ is the angle in charge space between the meson charge vector and the 3-axis (φ is equal to 0 degrees for neutral mesons and to 90 degrees for charged).

Reinserting the expression for N, and setting[10]

$$\tfrac{2}{3}f^2/\mu^2a=1/\nu_0$$

we have approximately

$$|N^2-\nu^2|^2=(1-\nu_0^2/\nu^2)^2+4(aq^2/\nu_0^2)^2$$

where we have dropped some small terms depending on the cut-off radius. We also insert the definition of b. The result for neutrals is

$$\frac{d\sigma}{d\Omega}\left[\frac{9\nu\mu^2}{qf^2e^2}\right]^{-1}=\frac{q^2}{\mu^2}\left(\frac{\gamma_N-\gamma_P}{2}\right)^2$$

$$\cdot\frac{3/10(1+\cos^2\theta)+\nu^2/\nu_0^2(14+49\sin^2\theta)/50}{(1-\nu_0^2/\nu^2)^2+4(aq^3/\nu_0^2)^2} \quad (38)$$

and for charged (adding two identical contributions corresponding to the meson charge vector lying in the x- or y-direction)

$$\frac{d\sigma}{d\Omega}\left[\frac{9\nu\mu^2}{2qf^2e^2}\right]^{-1}=\frac{q^2}{\mu^2}\left(\frac{\gamma_N-\gamma_P}{2}\right)^2$$

$$\cdot\frac{(5-\cos^2\theta)/10+(\nu^2/\nu_0^2)(8+3\sin^2\theta)/50}{(1-\nu_0^2/\nu^2)^2+4(aq^3/\nu_0^2)^2}$$

$$+1-\frac{2q^2\sin^2\theta}{[(\mathbf{q}-\mathbf{v})^2+\mu^2]^2}. \quad (39)$$

If, in the expression for charged mesons, we neglect the first term, we have

$$\frac{d\sigma}{d\Omega}=\frac{2}{9}\frac{f^2}{\mu^2}e^2\left[1-\frac{2q^2\sin^2\theta}{[(\mathbf{q}-\mathbf{v})^2+\mu^2]^2}\right]_v^q. \quad (40)$$

This is equivalent to the perturbation result[11] except for a factor 2/9 which results from the classical averaging over the spin variables.

We shall in addition at this point compare this result with that of Fujimoto and Miyazawa.[4] They find for the largest contribution to the charged production (from the meson charge interaction) a result identical with ours. For neutral mesons, they give

$$\frac{d\sigma}{d\Omega}=\frac{1}{144}\frac{e^2f^2}{\mu^2}\frac{q^3}{4\nu\nu_0^2}\frac{2+3\sin^2\theta}{(1-\nu/\nu_0)^2+0.114(aq_0^3/\nu_0^2)^2}. \quad (41)$$

We can put this in the form of our result if we make the approximation

$$(1-\nu/\nu_0)^2=\tfrac{1}{4}(1-\nu/\nu_0)^2(1+\nu_0/\nu_0)^2$$

$$\cong\tfrac{1}{4}[1-(\nu/\nu_0)^2]^2 \quad (42)$$

for ν/ν_0 not far from one. Since most of the contribution to the cross section comes from this region, the approximation is a fairly good one. Then we have

$$\frac{d\sigma}{d\Omega}=\frac{1}{144}\frac{e^2f^2}{\mu^2}\frac{q^3}{\nu\nu_0^2}\frac{2+3\sin^2\theta}{[1-(\nu/\nu_0)^2]^2+0.456(aq_0^3/\nu_0^2)^2} \quad (43)$$

which is to be compared with our result

$$\frac{d\sigma}{d\Omega}=\frac{0.459}{144}\frac{e^2f^2}{\mu^2}\frac{q^3}{\nu\mu^2}\frac{2+(7/6)\sin^2\theta(\nu/\nu_0)^2}{[1-(\nu/\nu_0)^2]^2+4(aq_0^3/\nu_0^2)^2} \quad (44)$$

[10] The energy ν_0 is the usual expression for the isobar spacing.

[11] Leslie L. Foldy, Phys. Rev. **76**, 1 (1949).

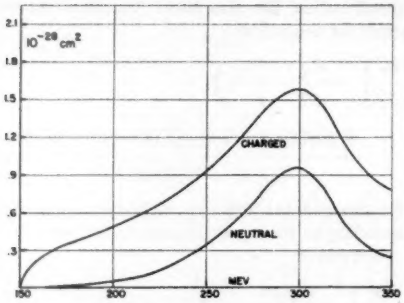

FIG. 1. Variation with photon energy of the total cross section for meson production. The isobar energy is 250 Mev and the cut-off radius is taken to be $(4/3)(\hbar/Mc)$, corresponding to the coupling constant $\frac{1}{4}$. The energies have been related to those in the center-of-momentum system by the proper Lorentz transformation.

where we have inserted the numerical values of γ_N and γ_P. These two results, Eq. (43) and Eq. (44), are then clearly of the same form and of the same magnitude. The difference in the coefficients of the damping term $(aq_0^3/\nu_0^2)^2$ appears to be due to a different approximation in the two calculations in the introduction of the cut-off radius, and not to an essential difference in the methods.

To examine the physical consequences of our results, we first simplify them by averaging them over angles and inserting the numerical values of the various constants, taking the cut-off radius as the nucleon compton wavelength. The cross sections then are

$$\sigma[2.49\times10^{-29}\text{ cm}^2\, qf^2/\nu]^{-1}$$
$$=\frac{(0.400+0.933\nu^2/\nu_0^2)q^2/\mu^2}{(1-\nu^2/\nu_0^2)^2+0.0816(q^3/\mu\nu_0^2)^2},\text{ neutral}$$
$$=\frac{(0.933+0.400\nu^2/\nu_0^2)q^2/\mu^2}{(1-\nu^2/\nu_0^2)^2+0.0816(q^3/\mu\nu_0^2)^2}+16.1,\text{ charged.}\quad(45)$$

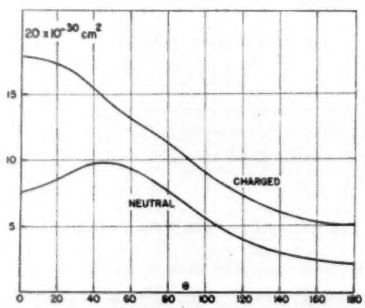

FIG. 2. Differential cross section in the laboratory system at 300-Mev photon energy. The peaking forward is due to the transformation from the center-of-momentum system to the laboratory system.

We can easily obtain the cross sections in the weak coupling ($\nu^2/\nu_0^2\ll1$) and the strong coupling ($\nu^2/\nu_0^2\gg1$) limit. We find

$$\sigma(2.49\times10^{-29}qf^2/\nu\text{ cm}^2)^{-1}$$
$$\left.\begin{aligned}&=0.400q^2/\mu^2,\text{ neutral}\\&\quad0.933q^2/\mu^2+16.1,\text{ charged}\end{aligned}\right\}\text{weak coupling}$$
$$\left.\begin{aligned}&=0.933q^2\nu_0^2/\mu^2\nu^2,\text{ neutral}\\&\quad16.1,\text{ charged}\end{aligned}\right\}\text{strong coupling.}\quad(46)$$

To investigate the validity of these limits, we can determine the numerical consequences of the two approximations at an energy at which the cross sections have been determined experimentally (for example, at 250 Mev in the c.m. system). The predicted results are

$$\left.\begin{aligned}&\sigma(\text{charged})\ll0.451\times10^{-28}\text{ cm}^2\\&\sigma(\text{neutral})\ll0.212\times10^{-30}\text{ cm}^2\end{aligned}\right\}\text{weak coupling}$$
$$\left.\begin{aligned}&\sigma(\text{charged})\gg0.402\times10^{-28}\text{ cm}^2\\&\sigma(\text{neutral})\ll1.47\times10^{-30}\text{ cm}^2\end{aligned}\right\}\text{strong coupling.}\quad(47)$$

These are to be compared with the observed cross sections of approximately 10^{-28} cm^2 for both charged and neutral mesons.[1] The charged cross section indicates that the coupling certainly cannot be considered as weak and that actually we are somewhat into the strong coupling domain. The smallness of the predicted neutral cross section in the two limits, in contradiction with experiment, is, in addition, a strong indication that the coupling is neither strong nor weak.

We can see, however, from the expressions for the cross sections that the neutral cross section can become large in the vicinity of

$$1-\nu^2/\nu_0^2=0$$

or, in terms of the original definition of ν_0,

$$\tfrac{2}{3}f^2/\mu^2a=1/\nu\quad(48)$$

where ν is the frequency of the radiation. If this condition is satisfied, the spin of the nucleon resonates to the imposed frequency and we have a "nucleon isobar" which is unstable against the decay into neutral or charged mesons. For example, if we assume that this condition is exactly satisfied at the energy of 250 Mev, then the cross sections are

$$\begin{aligned}\sigma&=0.869\times10^{-28}\text{ cm}^2\quad\text{(neutral)}\\&=1.271\times10^{-28}\text{ cm}^2\quad\text{(charged).}\end{aligned}\quad(49)$$

These cross sections are, therefore, roughly equal at this energy and approximately equal to the observed cross sections at 10^{-28} cm^2. Characteristic energy and angular spectra are given in Figs. 1 and 2 on the basis of these results. The rapid drop of the neutral cross section on both sides of the resonance should be easily

detected experimentally. The rapid rise of the neutral cross section with energy at energies below the "isobar frequency" has indeed been observed by Panofsky and Steinberger.[1]

III. CONSEQUENCES FOR OTHER PROCESSES

The existence of an unstable nucleon isobar will lead to anomalies in the scattering of mesons by nucleons. Pauli[8] gives for the scattering of neutral pseudoscalar mesons by nucleons the expression for the total cross section

$$\sigma=\frac{8}{9}\frac{f^4}{\mu^4}\frac{q^4}{\nu^2}\frac{1+(\nu/\nu_0)^2}{[1-(\nu/\nu_0)^2]^2+4(aq^3/\nu_0\nu)^2} \tag{50}$$

where ν_0 has been defined as above. With the values of the cut-off radius and ν_0 used in Sec. II, the variation of this cross section with energy is given in Fig. 3. The scattering of charged mesons will also have the same general behavior.

Nucleon-nucleon scattering will also show an anomaly at energies in the laboratory system of twice the resonance frequency, i.e., about 560 Mev. Since the resonance is very broad, nonstatic effects of some importance might also be expected to occur at considerably lower energies, although a quantitative estimate of the effect is difficult to make.

IV. CONCLUSIONS

We have made an application of classical theory of the problem of pseudoscalar meson production by photons. A comparison of the results with the experiments of Steinberger and Panofsky[4] suggests an explanation of the large cross section for neutral mesons in terms of the existence of unstable nucleon isobars with an excitation of approximately 200 to 300 Mev. We find, however, that this condition for the isobar energy implies that the strong coupling condition[8]

$$\tfrac{2}{3}(f^2/\mu a)\gg 1 \tag{51}$$

is not satisfied. It also follows therefore, that the classical approximations are only of very approximate validity since the classical treatment of the spin variables is valid only for large quantum numbers, i.e., in the region of high isobar excitation. In addition, certain other ambiguities due to the classical treatment of the isotopic spin are present, resulting from the average over initial isotopic spin directions. The charged cross section is thus some kind of an average for the production of π^+ and π^- mesons from protons and neutrons, respectively.

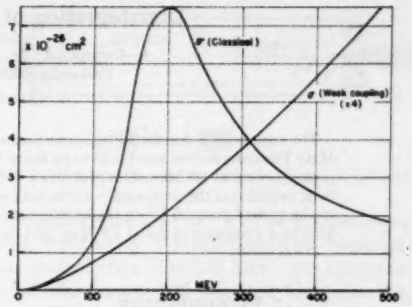

FIG. 3. Total cross section for the scattering of neutral mesons by nucleons. The meson energy in the laboratory system is indicated. The parameters are the same as in Figs. 1 and 2. The weak coupling approximation to the cross section has been multiplied by four.

In addition we wish to emphasize that for pseudoscalar theory a fairly unambiguous nonrelativistic approximation exists only for pseudovector coupling, i.e.,

$$f\psi^*(\boldsymbol{\sigma}\cdot\nabla\varphi-\gamma_4\partial\pi/\partial t)\psi\rightarrow fU(\mathbf{r})\boldsymbol{\sigma}\cdot\nabla\varphi \tag{52}$$

where $U(\mathbf{r})$ is the nucleon source density. It is difficult to obtain a nonrelativistic approximation to the pseudoscalar coupling

$$f\psi^*\gamma_4\gamma_5\psi \tag{53}$$

when the coupling is strong. Our conclusions therefore relate only to the pseudovector coupling form of the theory.

Finally we wish to re-emphasize the crudity of the classical model for the treatment of this problem; the exact results are not to be taken too seriously. We feel that the importance of these results is only in the qualitative ideas introduced and the possibility of using them to get a qualitative agreement with experiment.

We are indebted to Professor J. R. Oppenheimer and to Dr. Abraham Pais for several interesting discussions and helpful comments on this subject.

Disintegration of Boron by Fast Neutrons*

B. PETREE,† C. H. JOHNSON,‡ AND D. W. MILLER§
University of Wisconsin, Madison, Wisconsin

(Received May 31, 1951)

The cross section for the $B^{10}(n,\alpha)$ reaction was measured as a function of neutron energy from 0.35 to 2.6 Mev. The cross section was found to lie below the $1/v$ extrapolation of the thermal cross section except at a peak observed at 1.9 Mev. This peak has a width of about 400 kev and a maximum value of 0.53 barn. The total variation of the cross section at the peak is 0.35 barn. The ratio of the number of disintegrations leading to the ground state of Li^7 to the number leading to the excited state increases smoothly from 0.2 at 0.35 Mev to a maximum of 2.3 at 1.9 Mev, and decreases again to 0.8 at 2.6 Mev.

I. INTRODUCTION

STUDIES of the disintegration of boron by neutrons are of interest because of the common use of boron in neutron detectors and shields. An unexpected feature of the $B^{10}(n,\alpha)Li^7$ reaction is that for thermal neutrons there is a strong preference for the Li^7 nucleus to be formed in the 478-kev excited state rather than in the ground state. Hanna[1] found that for thermal neutrons the ratio of the number of disintegrations leading to the ground state of Li^7 to the number leading to the 478-kev excited state is 0.062. An examination of this branching ratio as a function of neutron energy appeared to be useful for the interpretation of the disintegration process. In addition, the flux of neutrons used in the measurement of the branching ratio was determined, so that the $B^{10}(n,\alpha)$ cross section could be obtained at the same time. This cross section was investigated by Bailey *et al.*[2] at Los Alamos in 1943, but only incomplete results of that work have been published. After the present experiment was begun, measurements of the branching ratio were published by Bichsel *et al.*[3]

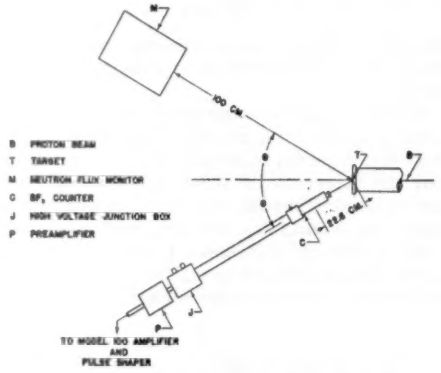

FIG. 1. Experimental arrangement for observing boron disintegrations and measuring neutron flux.

II. EXPERIMENTAL PROCEDURE

The $B^{10}(n,\alpha)$ disintegration cross section was obtained by determination of the number of disintegration pulses in a proportional counter, the number of B^{10} nuclei in the counter, and the number of neutrons per cm^2 causing the disintegrations. Figure 1 shows the geometrical arrangement of the neutron source and the neutron counters used in this experiment. Fast neutrons were produced by bombarding targets at T with a proton beam B accelerated by the electrostatic generator. The energy of the protons was measured by passing them through a one-meter radius electrostatic analyzer.[4] A lithium target, evaporated in place on a tantalum backing, was used to provide monoenergetic neutrons in the energy range from 0.35 to 1.30 Mev. Neutrons with energies from 0.95 to 2.65 Mev were obtained using a target which consisted of tritium absorbed in zirconium film on a tungsten backing. The proportional counter, C, with which the $B^{10}(n,\alpha)Li^7$ and $B^{10}(n,\alpha)Li^{7*}$ disintegrations were observed, and the neutron flux monitor M were mounted along lines making equal angles with respect to the axis of the proton beam.

The flux monitor M was a "long counter" of the type developed by Hanson and McKibben.[5] From 10 kev to 5 Mev, the efficiency of this monitor is nearly independent of neutron energy. By observing the counting rate when a calibrated radium-beryllium neutron source was placed at the position normally occupied by the lithium or tritium target, it was possible to determine the monitor efficiency. A correction was applied to the monitor counting rate for the background of scattered neutrons.

Because of the necessity of distinguishing between disintegrations leading to the ground state of Li^7 and those leading to the excited state, special care was required in the construction of the BF_3 proportional counter. In the most common design of simple proportional counters the small center wire is supported at

* Work supported by the AEC and the Wisconsin Alumni Research Foundation.

† Now at National Bureau of Standards, Washington, D. C.

‡ Now at Oak Ridge National Laboratory, Oak Ridge, Tennessee.

§ AEC Predoctoral Fellow.

[1] G. C. Hanna, Phys. Rev. **80**, 530 (1950).

[2] C. L. Bailey, *et al.*, (unpublished); quoted by R. K. Adair, Revs. Modern Phys. **22**, 249 (1950).

[3] Bichsel, Hälg, Huber, and Stebler, Phys. Rev. **81**, 456 (1951).

[4] Warren, Powell, and Herb, Rev. Sci. Instr. **18**, 559 (1947).

[5] A. O. Hanson and J. L. McKibben, Phys. Rev. **72**, 673 (1947).

each end by larger wires. The supporting wires are usually enough larger than the center wire that the field at their surfaces is too small to produce gas multiplication. Only the ions which are collected on the small wire undergo gas multiplication and produce full-size pulses. For such an arrangement the active volume is about as long as the small wire. This simple construction has two faults which made it undesirable for use in the measurements reported here. The active volume is not easy to determine accurately because of the distortion of the field lines near the ends of the small wire. In addition, a spread in pulse size occurs because the gas multiplication gradually diminishes to unity near the ends of the wire.

These undesirable end effects associated with the termination of the center wire were eliminated by a design similar to that described by Cockroft and Curran.[6] Figure 2 shows a cross-sectional view of the counter used in the present experiment. A thin-walled guard sleeve was installed concentric to the center wire at each end and maintained at an intermediate voltage appropriate to its radius. If the guard sleeves were sufficiently long, the electric field at the surface of the wire would be uniform and radial along its entire exposed length. For shorter lengths of guard sleeve, however, the field at the end of the sleeve is rather sensitive to the radius of the annular gap which separates the guard sleeve from the grounded shell of the counter.

The optimum radius of this gap was determined from electrolytic tank studies of an enlarged model of the counter. It was found that with the gap placed as in Fig. 2 the equipotential lines between counter wall and guard sleeves are straight and parallel at a distance of one-half inch from the gap. One-half inch is, therefore, a sufficient length of guard sleeve to make the field at the wire uniform and radial, provided the wire is smooth, round, and properly centered. Under these conditions the active volume is simply determined by the exposed length of the wire. There is still a spread in the pulse height for a given initial ionization in this counter because of wall effects and the properties of the filling gas, but the serious spread caused by nonuniformity of the field was largely eliminated.

A typical pulse-height distribution curve obtained for slow neutrons is shown in Fig. 3. The groups of pulses at 2.30 and 2.78 Mev, representing $B^{10}(n,\alpha)Li^{7*}$ and $B^{10}(n,\alpha)Li^{7}$ disintegrations in the gas,[7] are sufficiently well resolved that their respective numbers can be determined with little ambiguity. Disintegrations of boron atoms deposited on the wall of the counter are responsible for the groups of pulses at 1.46 and 0.84 Mev. Since the alpha-particle and the Li^7 nucleus are emitted in opposite directions, only one of them can enter the active volume of the counter when a disintegration occurs on the wall. The alpha-particle and the

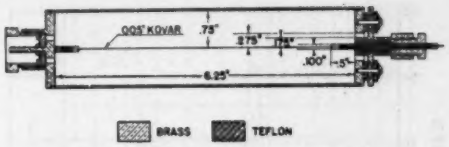

FIG. 2. Proportional counter for observing boron disintegrations.

Li^7 nucleus receive 7/11 and 4/11 of the disintegration energy, respectively. For disintegrations producing Li^7 in the excited state ($Q=2.30$ Mev), the alpha-particle and Li^7 energies are 1.46 and 0.84 Mev. For the less frequent disintegrations producing Li^7 in the ground state ($Q=2.78$ Mev), the alpha-particle and Li^7 energies are 1.77 and 1.01 Mev. The 1.77- and 1.01-Mev pulses are not sufficiently numerous to appear distinctly in Fig. 3.

While a large pressure of BF_3 is desirable for the sake of a large counting rate, it was found that good pulse-height resolution could not be obtained with BF_3 at a pressure greater than two inches of mercury. A deterioration of the resolution with time was also noticed. Fowler and Tunnicliffe[8] have attributed the deterioration to the formation of a gas with strong electron attachment properties by the chemical action of BF_3 on traces of impurities. Because of this effect, it was necessary to refill the counter several times during the course of the experiment. A useful life of two or three days was obtained by limiting the BF_3 pressure to one inch of mercury.

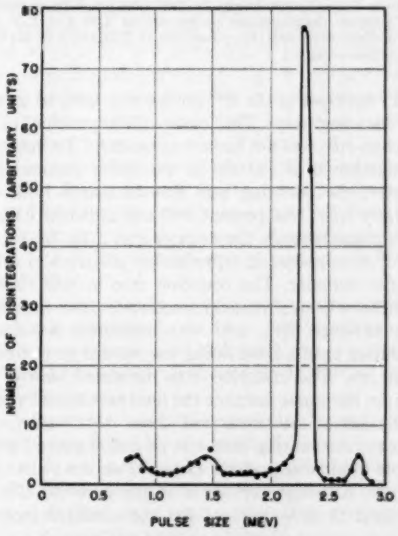

FIG. 3. Pulse-height distribution for slow neutron disintegration of boron.

[6] A. L. Cockroft and S. C. Curran, Rev. Sci. Instr. **22**, 37 (1951).
[7] Hornyak, Lauritsen, Morrison, and Fowler, Revs. Modern Phys. **22**, 291 (1950).
[8] I. L. Fowler and P. R. Tunnicliffe, Rev. Sci. Instr. **21**, 734 (1950).

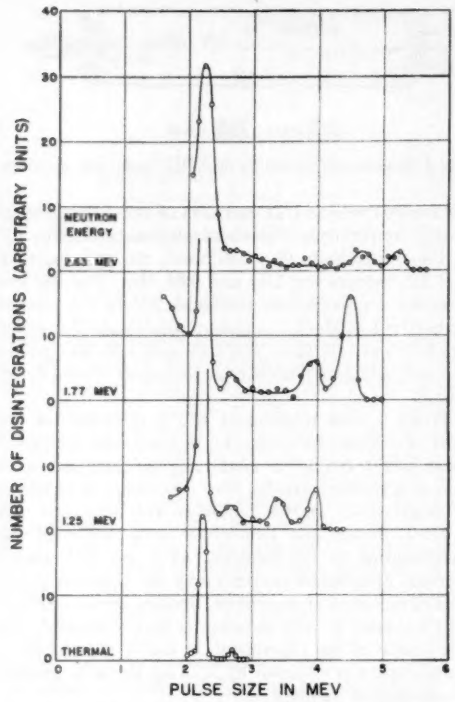

FIG. 4. Typical pulse-height distributions for $B^{10}(n,\alpha)$ reaction. Slow neutron disintegration pulses are at 2.30 and 2.78 Mev. Fast neutron disintegration pulses are at 2.30 and 2.78 Mev plus the neutron energy.

BF_3 enriched in the B^{10} isotope was used to increase the counting rate. The isotopic composition of the enriched BF_3 was not known accurately. To determine the number of B^{10} atoms in the active volume of the counter, the counting rate was measured both with ordinary BF_3 (18.8 percent B^{10}) and enriched BF^3. For these measurements the counter and a Ra-Be neutron source were placed in reproducible positions in a large paraffin cylinder. The counting rate in this standard geometry was determined immediately after each filling with enriched BF_3, and was measured occasionally thereafter until a fresh filling was needed to restore the resolution. The counting rate decreased slowly with time; in the worst instance the final rate was 85 percent of the initial rate measured three days earlier. This decrease in counting rate was probably caused largely by the gradual deposition of boron on the walls of the counter. Although the boron in the enriched BF_3 was supposed to be 96 percent B^{10}, the standard geometry measurements indicated only 50 to 60 percent.

The best pulse-height resolution was obtained with argon at 35 psi as the stopping gas. At this relatively low pressure the wall effect is appreciable. A correction for this effect was estimated by the method described by Rossi and Staub.[9] For thermal neutrons it was calculated that 12 percent of the (n,α) pulses would be reduced in size because of wall effect, in agreement with the experimental results. The wall effect correction at higher neutron energies was found by the same method, taking into account the increased range of the alpha-particles.

In order to make certain that neutron reactions with argon were not producing an appreciable number of pulses, the counter was filled with pure argon at 35 psi and exposed to fast neutrons at several energies covering the range of the experiment. The number of pulses observed in this way was less than 5 percent of the number observed with argon and BF_3.

A closely fitting cadmium shield was installed on the counter to reduce the number of disintegration pulses caused by the background of thermal neutrons. The background of epithermal neutrons scattered from the floor still gave an appreciable number of disintegration pulses at 2.30 and 2.78 Mev. These pulses were useful for calibrating pulse size in terms of disintegration energy.

Disintegration pulses from the proportional counter were amplified with a Model 100 amplifier and recorded photographically.

III. RESULTS

Figure 4 gives the pulse-height distributions obtained at several neutron energies. The bottom curve, obtained with thermal neutrons, shows the two groups of pulses at 2.30 and 2.78 Mev which correspond to the processes $B^{10}(n,\alpha)Li^{7*}$ and $B^{10}(n,\alpha)Li^{7}$. The strong preference for $B^{10}(n,\alpha)Li^{7*}$ is evident. Approximately equal fluxes of fast neutrons were used to obtain the other three curves in Fig. 4. Groups of pulses at 2.30 and 2.78 Mev on these curves were caused by the background of epithermal neutrons. The disintegrations caused by fast neutrons appear at 2.30 and 2.78 Mev plus the neutron energy. At 1.25-Mev neutron energy the reactions $B^{10}(n,\alpha)Li^{7*}$ and $B^{10}(n,\alpha)Li^{7}$ have about equal probability; at 1.77 Mev $B^{10}(n,\alpha)Li^{7}$ predominates, in contrast to the result at thermal energy; at 2.63 Mev the two processes are again about equally probable. Large variations in the (n,α) disintegration cross section can be seen on these curves; the relatively large number of fast neutron disintegrations at 1.77 Mev means a relatively large cross section at that neutron energy.

It will be noted in Fig. 4 that an appreciable number of intermediate size pulses was observed, smaller than the fast neutron pulses and larger than those produced by the slow neutron background. These intermediate size pulses are about twice as numerous as would be expected from wall effect. The pulses are too large to have been caused by neutron reactions with B^{11} or F^{19}, all of which are endothermic, or by the reactions

[9] B. B. Rossi and H. H. Staub, *Ionization Chambers and Counters* (McGraw-Hill Book Company, Inc., New York, 1949), p. 236.

$B^{10}(n,p)Be^{10}$ ($Q=+0.2$ Mev) or $B^{10}(n,2\alpha)H^3$ ($Q=+0.3$ Mev). An appreciable number of these pulses was probably caused by neutrons scattered inelastically from the floor and from the walls of the counter.

Twenty pulse-height distributions were taken at various neutron energies from 0.35 to 2.63 Mev. The pulses produced by fast neutrons were found to increase in size linearly with neutron energy. Below 0.35-Mev neutron energy the cross section could not be measured because the fast and slow neutron disintegration pulses overlapped.

Figure 5 shows the cross sections and branching ratios determined in this experiment. Neutrons from the $Li^7(p,n)$ reaction were used to obtain the data represented by solid circles. Open circles denote data obtained with $T(p,n)$ neutrons. The statistical uncertainty is indicated by the vertical bars. It should be emphasized that the cross section plotted in the upper part of Fig. 5 is for normal boron, which contains only 18.8 percent B^{10}.

Aside from the statistical uncertainty, the accuracy of the cross section is limited by the precision with which the neutron fluxes and the quantity of B^{10} in the counter were determined. The quantity of B^{10} depends on the BF_3 pressure and the standard geometry measurements, both of which were accurate to about 5 percent. A determination of the strength of the Ra-Be source was made by comparison at the Argonne National Laboratory with a standard source whose strength is believed to be known to 7 percent. The efficiency of the monitor was probably equal, within 5 percent, for both Ra-Be neutrons and the fast neutrons with which the cross sections were observed. Background corrections may be in error by as much as 10 percent. The combined effect of these uncertainties is estimated to be about ± 25 percent of the cross sections.

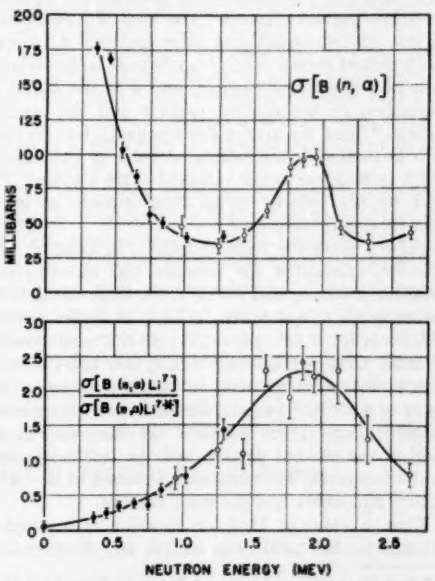

FIG. 5. Upper curve, (n,α) disintegration cross section of ordinary boron. Lower curve, ratio of the number of disintegrations leading to the ground state of Li^7 to the number leading to the 478-kev excited state.

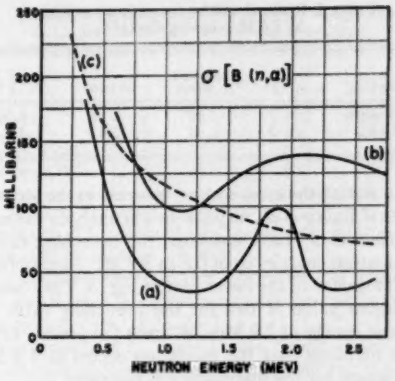

FIG. 6. The (n,α) cross section of ordinary boron. (a) Present experiment; (b) Bailey *et al.* (reference 2); (c) $1/v$ extrapolation of the slow neutron cross section determined by Sutton *et al.* (reference 10).

It is difficult to estimate the accuracy of the branching ratio measurements. The total uncertainty is somewhat greater than the statistical uncertainty indicated in the lower part of Fig. 5 because of the imperfect resolution of the $B^{10}(n,\alpha)Li^7$ and $B^{10}(n,\alpha)Li^{7*}$ pulses. The pulse height distribution curves of Fig. 4 indicate rather clearly, however, that the ratio is about two at 1.77-Mev neutron energy, and that it is about one at neutron energies of 2.63 and 1.25 Mev.

In this experiment, the uncertainty in neutron energy is caused almost entirely by the uncertainty in the angle of observation, which was less than 3 degrees. The energy uncertainty is nearly proportional to the square root of the neutron energy, and at 1.9 Mev is about 60 kev.

Figure 6 shows the (n,α) cross sections determined in the present experiment, the cross sections determined by Bailey *et al.*[2] at Los Alamos, and the $1/v$ extrapolation of the cross sections determined by Sutton *et al.*[10] for slow neutrons.

No information is available regarding the epithermal neutron background for the work of Bailey *et al.*, nor how or if a correction for such a background was applied. If no background correction was applied, it seems likely that their cross sections are too large. In the present experiment only pulses of a size consistent with the energy of the direct neutron flux were counted

[10] Sutton, McDaniel, Anderson, and Lavatelli, Phys. Rev. 71, 272 (1947).

TABLE I. Reduced widths assuming a single level at 1.9 Mev having $J=11/2$.

Particle	L	Particle width	$\gamma^2\times10^{13}$	$\gamma^2+\frac{3}{2}\frac{\hbar^2}{Ma}$
Neutron	2	$\frac{1}{4}\Gamma$	1.14	0.08
Alpha	5	$\frac{3}{4}\Gamma$	5.4	1.2

in calculating the cross section, whereas in the measurements of Bailey *et al.*, no pulse-height analysis was made.

Bichsel *et al.*[3] have measured the branching ratio at five neutron energies from 0.5 to 3.9 Mev, and obtained results similar to the lower part of Fig. 5. They found a maximum value of two for the branching ratio at a neutron energy of 2.9 Mev, whereas the present experiment indicates that the maximum occurs at 1.9 Mev. The reason for the discrepancy is not clear.

It will be noted in Fig. 5 that the maxima in the branching ratio and the B(n,α) cross section appear to coincide at 1.9 Mev. A satisfactory interpretation of this effect has not been found.

IV. DISCUSSION

The peak in the disintegration cross section at 1.9-Mev neutron energy indicates the presence of one or more levels in the B^{11} compound nucleus. This peak has a width of 400 kev, which is more than four times the experimental neutron energy spread. The rise in the cross section at the peak is caused almost entirely by the increased number of disintegrations leading to the ground state of Li.[7]

For an isolated resonance, the maximum value of the disintegration cross section given by the Breit-Wigner formula is

$$\sigma_a^R=[(2J+1)/2(2I+1)](4\pi/k^2)\Gamma_n\Gamma_a/\Gamma^2. \quad (1)$$

I and J are the angular momenta of the target and compound nuclei in units of $\hbar$, k is the wave number for neutrons of resonance energy, and Γ_a and Γ_n are the partial widths for alpha-particle and neutron emission. Γ is the total width, which is observed experimentally, and is the sum of the partial widths for all possible modes of decay of the compound nucleus. In expression (1), σ_a^R denotes the maximum value of the (n,α) cross section for the isotope B^{10}. Figure 5 shows clearly that the peak in the disintegration cross section is not isolated as required by Eq. (1). Broad resonances above and below 1.9 Mev may contribute appreciably at 1.9 Mev and prevent the disintegration cross section from approaching zero on either side. Under the assumption that neighboring levels do not interfere, then, σ_a^R is taken to be the change in the B^{10} disintegration cross section at the peak rather than its maximum value. When defined in this way, σ_a^R is obtained by dividing the change in the cross section at the peak in Fig. 5 by 0.188, the isotopic abundance of B^{10} in normal boron.

A lower bound for J can be obtained from Eq. (1) if it is assumed that $\Gamma_n=\Gamma_a=\Gamma/2$. However, recent measurements by Bockelman *et al.*[11] at this laboratory have shown that the rise in total cross section at 1.9 Mev is no larger than the rise in the disintegration cross section. From this it is concluded that Γ_n is considerably smaller than Γ_a. This result requires that J must be at least 11/2 in order to satisfy Eq. (1). To produce a compound nucleus with that angular momentum, incoming neutrons with at least two units of orbital angular momentum would be necessary. If one assumes a spin of 1/2 for the excited state of Li^7, and that the ground state and the excited state have the same parity, the alpha-particles emitted in the disintegration processes must be emitted with five units of angular momentum.

An estimate of the upper limit for the angular momentum of the compound nucleus can be obtained from an examination of the reduced widths for the various modes of decay. The width for the emission of a particle, s, can be written[12]

$$\Gamma_s=2kT_L\gamma_s^2,$$

where k is the wave number of the emitted particle, T_L is the barrier penetration factor for a particle with orbital angular momentum L, and γ_s^2 is called the reduced width. If the emitted particle is charged, T_L is the coulomb barrier penetration factor for particles of orbital angular momentum L. For neutrons, T_L, the centrifugal barrier penetration factor, can be calculated explicitly.[13] The reduced widths for the emission of various particles from a given level of a compound nucleus are not expected to differ greatly.[14] A reduced width cannot exceed $3\hbar^2/2Ma$, where M is the reduced mass of the emitted particle, and a is the radius of interaction of the emitted particle and the residual nucleus.[14] Since the barrier penetration factors decrease with increasing L, the calculated value of the reduced width increases as larger values of L are assumed. The limit on the reduced width thus imposes an upper limit on L and hence on J.

Table I gives the reduced widths, in units of 10^{-13} Mev-cm, calculated for neutron and alpha-particle emission, assuming that $J=11/2$. For these calculations, the ratio Γ_n/Γ was taken to be $\frac{1}{4}$. A larger neutron width would not be compatible with the measurements of total cross section and absorption cross section. The radius of interaction for neutron emission was taken as 4.5×10^{-13} cm, and for alpha-particle emission, 5.2×10^{-13} cm. These numbers are the sums of the radii of the emitted particle and the residual nucleus in the two cases. The radii were assumed to be $1.43A^{\frac{1}{3}}\times10^{-13}$ cm, where A is the mass number.

Thus, a value of 11/2 for J, which is required to account for the total cross section and disintegration

[11] Bockelman, Miller, Adair, and Barschall, Phys. Rev. **84**, 69 (1951).
[12] R. K. Adair, Revs. Modern Phys. **22**, 249 (1950).
[13] Feshbach, Peaslee, and Weisskopf, Phys. Rev. **71**, 145 (1947).
[14] E. P. Wigner, Am. J. Phys. **17**, 99 (1949).

cross-section data, leads to a reduced width for alpha-particle emission which is 20 percent larger than the theoretical maximum. Although the assumption of other processes besides neutron and alpha-emission may decrease Γ_α, the reduced width for alpha-particle emission will not become smaller. For if Γ_α is reduced while Γ_n and Γ remain fixed, J must be increased to satisfy Eq. (1). The net effect then is to increase rather than to reduce the calculated reduced width. Hence, a state of the compound nucleus with $J=11/2$ does not seem possible.

The single-level scheme is not definitely excluded, however, because under certain rather special conditions the total cross section can show only a small variation in the neighborhood of a resonance with a large neutron width. Although a J value of $7/2$ is somewhat beyond the limit of the experimental uncertainty of the disintegration cross-section data, such a state of the compound nucleus can provide an explanation for the absence of a prominent resonance in total cross section at 1.9 Mev. A state with $J=7/2$ can be produced by both S- and D-neutrons. It is possible for a dip rather than a rise in the scattering cross section for S-neutrons to occur at the resonance energy because of destructive interference between resonance and potential scattering. Since the S-wave potential phase shift for 1.9-Mev neutrons is in the neighborhood of 90 degrees, such a dip would be expected.[15] For D-neutrons, however, the potential phase shift is too small to produce any appreciable interference, and a peak would occur at resonance. If one assumes S- and D-neutron widths of 0.1 and 0.4 of the total width, partial cancellation would reduce the variation in scattering cross section at the 1.9-Mev resonance to about 0.05 barn. In that case total cross-section measurements would be expected to show only the effect of processes other than elastic scattering.

With this scheme, therefore, it is possible to reconcile a large neutron width with the experimental fact that the total cross-section peak is no larger than the (n,α) peak. A J value of $7/2$ permits the alpha-particles to be emitted with only three units of orbital angular momentum. The reduced neutron and alpha-particle widths are tabulated in Table II in units of 10^{-13} Mev-cm, together with the assumed angular momenta of the emitted particles, the assumed widths for the processes, and the ratios of the reduced widths to the theoretical maxima. The two alpha-particle widths were taken in the ratio of two to one, as is indicated by the branching ratio at 1.9 Mev.

[15] M. R. MacPhail, Phys. Rev. **57**, 669 (1940).

TABLE II. Reduced widths assuming a $J=7/2$ level at 1.9 Mev formed by both S- and D-neutrons.

Particle	L	Particle width	$\gamma^2\times10^{13}$	$\gamma^2+\frac{3}{2}\frac{\hbar^2}{Ma}$
S neutron	0	0.1 Γ	0.07	0.0048
D neutron	2	0.4 Γ	1.8	0.12
Long-range alpha	3	0.33Γ	0.27	0.058
Short-range alpha	3	0.17Γ	0.13	0.028

The reduced widths in this scheme are not unreasonable, and there is fair agreement with the disintegration cross-section data. With $J=7/2$, and $\Gamma_n=\Gamma_\alpha=\Gamma/2$, as has been assumed in Table II, the height of the (n,α) peak calculated from Eq. (1) is 30 percent less than the measured height. The percentage difference between calculated and observed heights will increase, however, if Γ_n and Γ_α are reduced to allow for other processes. The somewhat artificial scheme summarized in Table II is the most nearly satisfactory single-level interpretation of the peak at 1.9 Mev.

It is more plausible to assume that the peak is caused by two or more closely spaced levels. With two levels to contribute to the disintegration cross section, small J-values are adequate to account for the height of the absorption peak. For small J-values, the reduced widths are found to be reasonably small. Provided one level is produced by S-neutrons, the small height of the total cross-section peak can be explained as before. Because of the many parameters available in the two-level scheme, the levels cannot be uniquely specified.

A surprising result of this experiment is the apparent scarcity of levels from 0.35- to 2.63-Mev neutron energy. The corresponding interval in the excitation energy of the B^{11} nucleus is 11.74 to 13.81 Mev.[7] In this interval of 2.07 Mev, only the one peak at 1.9 Mev was observed. From an investigation of the $B^{10}(d,p)$ reaction, Van Patter *et al.*[16] list ten excited states in B^{11} below 10 Mev, with a marked trend toward closer spacing at higher excitation energies. In the 2.52-Mev region between 6.76 and 9.28 Mev, seven levels were observed. The interval between 10.2 and 11.46 Mev has not been explored. A level density higher than that found previously around 9 Mev might be expected in the range of energies covered in the present measurement, adding to the plausibility of the two-level interpretation of the (n,α) disintegration peak at 1.9 Mev.

[16] Van Patter, Buechner, and Sperduto, Phys. Rev. **82**, 248 (1951).

Remarks Concerning the Adiabatic Theorem and the S-Matrix*

HARTLAND S. SNYDER
Brookhaven National Laboratory, Upton, Long Island, New York
(Received May 17, 1951)

An improved mathematical formulation and solution of transition rate problems for scattering and reaction problems is given. Difficulties in connecting the time dependent and stationary methods of defining the S-matrix are noted, but not resolved.

I. INTRODUCTION

NEARLY all recent studies[1] in field theory and reaction processes[2] have been based, tacitly or explicitly, on the adiabatic hypothesis. Although the adiabatic hypothesis has been verified by Born[3] for hamiltonians which admit discrete eigenvalues only, a corresponding verification for hamiltonians which have continuous degenerate spectra has not been given. The purpose of the work being reported here is to examine to some extent conditions on the validity of the adiabatic hypothesis and to show that certain important consequences of S-matrix theory do not depend on the adiabatic hypothesis.

II. TIME DEPENDENT PERTURBATION THEORY

In this section we will be concerned with a system described by a hamiltonian

$$H(t)=H_0+Ve^{\alpha t/\hbar}, \tag{1}$$

in which H_0 is the hamiltonian of the non-interacting parts of the system and V is the time independent interaction energy. The factor[4] $e^{\alpha t/\hbar}$ was included to simulate the adiabatic turning off of the interaction as $t\to-\infty$. For simplicity we suppose that the two operators $H(t)$ and H_0 have exactly the same continuous spectrum of eigenvalues, although not, of course, the same eigenfunctions. The eigenfunctions of H_0 are denoted by ϕ_a and satisfy

$$H_0\phi_a=E_a\phi_a, \tag{2}$$

and

$$\int dN_a(\phi_a,\phi_b)=1 \text{ or } 0, \tag{3}$$

where dN_a is a suitably chosen weighting function of the states ϕ_a, so that the right side of Eq. (3) is 1 if the state ϕ_b is contained in the domain of integration over states ϕ_a, otherwise it is zero.

For the time dependent Schroedinger equation

$$i\hbar\dot{\psi}=H(t)\psi \tag{4}$$

we write a solution in the form

$$\psi=\int dN_a C_a(t)\phi_a\exp(-iE_at/\hbar), \tag{5}$$

from which we obtain, using Eqs. (2), (3), and (4), and taking ϕ_a to be time independent,

$$i\hbar\dot{C}_a(t)=\int dN_b(\phi_a, V\phi_b)C_b(t)\times\exp([i(E_a-E_b)+\alpha]t/\hbar). \tag{6}$$

Integrating Eq. (6), we obtain

$$C_a(t)=C_a^0-(i/\hbar)\int_{-\infty}^{t}dt'\int dN_bC_b(t')(\phi_a, V\phi_b)\times\exp([i(E_a-E_b)+\alpha]t'/\hbar), \tag{7}$$

in which C_a^0 is the initial value of $C_a(t)$ at $t=-\infty$. Iteration of Eq. (7) gives the Liouville-Neumann series solution to Eq. (7)

$$C_a(t)=C_a^0+\sum_{n=1}^{\infty}\int dN_bC_b^0\times\frac{V_{ab}^{(n)}(\alpha)\exp([i(E_a-E_b)+n\alpha]t/\hbar)}{E_b-E_a+in\alpha}, \tag{8}$$

in which

$$V_{ab}^{(n)}(\alpha)=\int dN_c\frac{V_{ac}^{(1)}V_{cb}^{(n-1)}(\alpha)}{E_b-E_c+i(n-1)\alpha}, \tag{9}$$

$$V_{ab}^{(1)}=(\phi_a, V\phi_b).$$

Now, the relative probability that the system will be in the group of states about the state ϕ_a at the time t is $W_a(t)dN_a$ in which

$$W_a(t)=|C_a(t)|^2. \tag{10}$$

The quantity of major interest is the rate of transition to state ϕ_a if the system were initially in state ϕ_b, that is

$$w_{ab}(t)=dW_{ab}(t)/dt, \tag{11}$$

for $C_a^0=1_{ab}$, where 1_{ab} is a generalized Dirac δ-function

* Research carried out at Brookhaven National Laboratory, under the auspices of the AEC.

[1] C. Møller, KGL. Danske Videnskab. Selskab, Mat.-fys. 22, No. 1 (1946). R. P. Feynman, Phys. Rev. 76, 744 and 769 (1949). F. J. Dyson, Phys. Rev. 75, 486 (1949). B. A. Lippman and J. S. Schwinger, Phys. Rev. 79, 469 (1950).

[2] The work of Wigner and Eisenbud is the most notable exception to this. E. P. Wigner and L. Eisenbud, Phys. Rev. 72, 22 (1947).

[3] M. Born, Z. Physik 40, 167 (1927).

[4] In the work of Born much more general types of time variations were considered than the simple time variation given by $e^{\alpha t/\hbar}$ which we use.

such that $\int 1_{ab}dN_a=1$ if the state ϕ_b is contained in the region of integration over states ϕ_a. Using Eqs. (8), (10), and (11) we obtain

$$w_{ab}(\alpha,t)=\frac{2}{\hbar}1_{ab}\,\mathrm{Im}\sum_{n=1}^{\infty}V_{ab}^{(n)}(\alpha)\exp(n\alpha t/\hbar)$$
$$+\frac{1}{\hbar}\sum_{n,m=1}^{\infty}V_{ab}^{(n)}(\alpha)V_{ab}^{(m)}(\alpha)$$
$$\times\left(\frac{i}{E_b-E_a+in\alpha}-\frac{i}{E_b-E_a-im\alpha}\right)$$
$$\times\exp((n+m)\alpha t/\hbar). \quad (12)$$

In the limit as $\alpha\to 0$, Eq. (12) becomes

$$w_{ab}=(2\pi/\hbar)\delta(E_a-E_b)|\mathbf{T}_{ab}|^2+(2/\hbar)1_{ab}\,\mathrm{Im}\mathbf{T}_{ab}; \quad (13)$$

in which

$$\mathbf{T}_{ab}=\lim_{\alpha\to 0}\sum_{n=1}^{\infty}V_{ab}^{(n)}(\alpha). \quad (14)$$

The important result given by Eq. (13) shows that in the adiabatic limit the transition rate from a state ϕ_b at $t=-\infty$ to a state ϕ_a at any finite time t, is independent of the time t, and that transitions take place only between states which conserve energy. The usefulness of the results given above depends on the convergence of the power series in Eq. (14) which defines $\mathbf{T}_{ab}$.

We now note that we may write

$$\mathbf{T}_{ab}=(\phi_a, V\psi_b^+) \quad (15)$$

in which

$$\psi_b^+=\lim_{\epsilon\to 0}\psi_b(\epsilon);\quad \epsilon>0, \quad (16)$$

and

$$\psi_b(\epsilon)=\phi_b+\frac{1}{E_b+i\epsilon-H_0}V\psi_b(\epsilon), \quad (17)$$

with $\epsilon>0$. To see that Eqs. (15) and (16) give the same result for $\mathbf{T}_{ab}$ as Eqs. (9) and (14) do, we solve Eq. (17) for $\psi_b(\epsilon)$ by iteration and substitute into Eq. (15), obtaining a power series of exactly the same form as Eq. (14) except that the imaginary part of the energy denominator, $(n-1)\alpha$, in Eq. (9) is replaced by ϵ. This makes no difference in the limit as α and ϵ approach zero since, in an integral such as Eq. (9), the limit as $\alpha\to 0$ implies that the integral over the energy is to be calculated as a principal value, minus πi multiplied by the residue at the point where energy is conserved. It is, of course, necessary that the limit as $\alpha\to 0$ of the series Eq. (14) converge to the same value as the limit as $\epsilon\to 0$ of the series obtained by iteration of Eq. (17) in Eq. (15) in order that Eqs. (14) and (15) give the same result.

The important Eq. (17) is the basis of the stationary method of solving scattering (Lippman and Schwinger[1]) and reaction problems.

III. THE BEHAVIOR OF WAVE FUNCTIONS ON THE ADIABATIC TURNING ON OF THE INTERACTION

In this section we will show that if one starts a system in the state ϕ_b at $t=-\infty$ under the action of the hamiltonian given by Eq. (1) and in the limit as $\alpha\to 0$ it will be in the state ψ_b^+ at any finite time. To prove[5] this we write the solution to the Schroedinger equation of motion, Eq. (4), in the form

$$\psi(t)=\int dN_a b_b(t)\psi_a^+(\alpha t)\exp(-iE_a t/\hbar), \quad (18)$$

in which

$$\psi_a^+(\alpha t)=\lim_{\epsilon\to 0}\psi_a(\alpha t,\epsilon), \quad (19)$$

and

$$\psi_a(\alpha t,\epsilon)=\phi_a+\frac{e^{\alpha t/\hbar}}{E_a+i\epsilon-H_0}V\psi_a(\alpha t,\epsilon). \quad (20)$$

In writing Eq. (18) as a solution of Eq. (4) it is assumed that the functions $\psi_a^+(\alpha t)$ form a complete set. If we differentiate Eq. (20) with respect to time and take ϕ_a to be time independent we obtain

$$\dot\psi_a(\alpha t,\epsilon)=\frac{\alpha e^{\alpha t/\hbar}}{E_a+i\epsilon-H(t)}V\psi_a(\alpha t,\epsilon), \quad (21)$$

a relation which will use later. Applying Eqs. (1) and (4) to Eq. (18) gives

$$i\hbar\dot b_a(t)=\int dN_b b_b(t)(\psi_a^+(\alpha t),\psi_b^+(\alpha t))$$
$$\times\exp[i(E_a-E_b)t/\hbar]. \quad (22)$$

In the derivation of Eq. (22) the assumption is made that $(\psi_a^+(\alpha t),\psi_b^+(\alpha t))=1_{ab}$, an assertion which will be proved later provided certain conditions are satisfied. Integrating Eq. (22) with respect to time gives

$$b_a(t)=b_a^0-(i/\hbar)\int_{-\infty}^{t}dt'\int dN_b b_b(t')(\psi_a^+(\alpha t'),\psi_b^+(\alpha t'))$$
$$\times\exp(i(E_a-E_b)t'/\hbar), \quad (23)$$

in which b_a^0 is the initial value of $b_a(t)$ at $t=-\infty$. Using Eq. (21) in Eq. (23) and integrating by parts with respect to time

$$b_a(t)=b_a^0+\lim_{\epsilon\to 0}\int\frac{\alpha dN_b b_b(t)(\psi_a^+(\alpha t),V\psi_b^+(\alpha t))}{[E_b-E_a+i\alpha][E_b-E_a+i\epsilon]}$$
$$\times\exp\{[i(E_a-E_b)+\alpha]t/\hbar\}$$
$$-\lim_{\epsilon\to 0}\int\frac{\alpha dN_b}{[E_b-E_a+i\alpha][E_b-E_a+i\epsilon]}\int_{-\infty}^{t}dt'$$
$$\times\exp\{[i(E_a-E_b)+\alpha]t'/\hbar\}$$
$$\times\{[(\psi_a^+(\alpha t'),V\psi_b^+(\alpha t'))$$
$$+(\psi_a^+(\alpha t'),V\dot\psi_b^+(\alpha t'))]b_b(t')$$
$$+(\psi_a^+(\alpha t'),V\psi_b^+(\alpha t'))\dot b_b(t')\}. \quad (24)$$

[5] If the series solution Eq. (8) of Eq. (7) converges to a solution of Eq. (7) one can then prove the adiabatic hypothesis as stated above.

We now note that the integration over the state ϕ_b in Eq. (24) of both the second and third terms involves an integration over the energy E_b of the form

$$\lim_{\epsilon\to 0}\int \alpha dE f(E,\alpha,\epsilon)/[(E+i\alpha)(E+i\epsilon)]. \quad (25)$$

In the limit as $\alpha\to 0$ integrals of the form Eq. (25) vanish provided the integral exists for finite α and ϵ and provided $f(E,0,0)$ is regular at $E=0$. For expressions of the form Eq. (25) to vanish in the limit $\alpha\to 0$ and $\epsilon\to 0$ it is necessary that both α and ϵ have the same sign. We thus see that if the time integral in the third term is bounded as a function of α then in the limit as $\alpha\to 0$, $b_a(t)\to b_a{}^0$. This shows that, subject to the boundedness condition above, as an interaction is turned on adiabatically an initial state ϕ_a at $t=-\infty$ changes in the course of time into the state $\psi_a{}^+$ which is a linear combination of the initial state plus outgoing waves.

IV. THE IRRELEVANCE OF THE ADIABATIC HYPOTHESIS

The important and well-known result which is restated in this paper is the transition rate from the state ϕ_b at $t=-\infty$ to the state ϕ_a at a finite time as given by Eq. (13) in terms of the matrix element $\mathbf{T}_{ab}$ as it is determined by Eqs. (15), (16), and (17). The function of the adiabatic hypothesis was to insure that the system would be in the state $\psi_b{}^+$ at a finite time if it started in the state ϕ_b at $t=-\infty$. The use of the adiabatic process may, however, be completely circumvented by imposing the appropriate boundary condition at a finite time.

We will suppose that the system is in the state $\psi_b(\epsilon)$ at $t=0$ with $\psi_b(\epsilon)$ given by Eq. (17) and calculate the transition rate to the state ϕ_a at any finite time in the limit as $\epsilon\to 0$. We now drop the time dependent factor $\exp(\alpha t/\hbar)$ from the hamiltonian Eq. (1). If the system is in the state $\psi_b(\epsilon)$ at $t=0$, then at other time t, it will be in the state

$$\psi_b(\epsilon,t)=e^{-iHt/\hbar}\psi_b(\epsilon). \quad (26)$$

The rate of transition from the state $\psi_b(\epsilon,t)$ to the state ϕ_a is

$$w_{ab}(\epsilon,t)=\frac{d}{dt}|(\phi_a, e^{-iHt/\hbar}\psi_b(\epsilon))|^2$$
$$=-(i/\hbar)(\phi_a,\psi_b(\epsilon,t))^*$$
$$\times(\phi_a, H_b\psi_b(\epsilon,t))+\text{c.c.}, \quad (27)$$

in which

$$H_b=H-E_b. \quad (28)$$

We will now show that

$$\lim_{\epsilon\to 0} w_{ab}(\epsilon,t)=w_{ab}, \quad (29)$$

with w_{ab} given by Eq. (13). According to Eq. (17)

$$H_b\psi_b(\epsilon)=i\epsilon(\psi_b(\epsilon)-\phi_b). \quad (30)$$

Define

$$f_b(\epsilon,t)=\exp(iE_bt/\hbar)\psi_b(\epsilon,t)=\exp(-iH_bt/\hbar)\psi_b(\epsilon). \quad (31)$$

Differentiating Eq. (31) with respect to time and using Eq. (30) one obtains

$$\dot f_b(\epsilon,t)=-(i/\hbar)\exp(-iH_bt/\hbar)H_b\psi_b(\epsilon)$$
$$=(\epsilon/\hbar)f_b(\epsilon,t)-(\epsilon/\hbar)\exp(-iH_bt/\hbar)\phi_b. \quad (32)$$

The solution of differential Eq. (32) subject to the boundary condition $f_b(\epsilon,0)=\psi_b(\epsilon)$ gives

$$f_b(\epsilon,t)=e^{\epsilon t/\hbar}\Big\{\psi_b(\epsilon)$$
$$+i\epsilon\frac{[1-\exp(-i(H_b-i\epsilon)t/\hbar)]}{H_b-i\epsilon}\phi_b\Big\}. \quad (33)$$

Substituting the relation given in Eq. (33) into Eq. (27) and using Eqs. (30) and (17) one obtains

$$w_{ab}(\epsilon,t)=e^{2\epsilon t/\hbar}\Big\{\Big(\phi_a,\phi_b+\frac{1}{E_b-E_a+i\epsilon}V\psi_b(\epsilon)$$
$$+i\epsilon\frac{[1-\exp(-i[H_b-i\epsilon]t/\hbar)]}{H_b-i\epsilon}\phi_b\Big)^*$$
$$\times\Big(\phi_a,\frac{1}{E_b-E_a+i\epsilon}V\psi_b(\epsilon)$$
$$+\frac{[1-\exp(-i[H_b-i\epsilon]t/\hbar)]}{H_b-i\epsilon}H_b\phi_b\Big)+\text{c.c.}\Big\}$$
$$=e^{2\epsilon t/\hbar}\Big\{i1_{ab}[(\phi_a,V\psi_b(\epsilon))^*(\phi_a,V\psi_b(\epsilon))]$$
$$+\frac{2\epsilon}{(E_b-E_a)^2+\epsilon^2}|(\phi_a,V\psi_b(\epsilon))|^2$$
$$+\Big[\epsilon\Big(1_{ab}+\frac{(\phi_a,V\psi_b(\epsilon))^*}{E_b-E_a-i\epsilon}$$
$$-i\epsilon\Big(\phi_a,\frac{1-\exp(-i(H_b-i\epsilon)t/\hbar)}{H_b-i\epsilon}\phi_b\Big)^*\Big)$$
$$\times(\phi_a,[1-\exp(-i(H_b-i\epsilon)t/\hbar)][H_b/(H_b-i\epsilon)]\phi_b)$$
$$-i\epsilon^2\Big(\phi_a,\frac{[1-\exp(-i(H_b-i\epsilon)t/\hbar)]}{H_b-i\epsilon}\phi_b\Big)^*$$
$$\times\Big(\phi_a,\frac{1}{E_b-E_a+i\epsilon}V\psi_b(\epsilon)\Big)+\text{c.c.}\Big]\Big\}(1/\hbar). \quad (34)$$

In the limit as $\epsilon\to 0$, Eq. (34) gives

$$w_{ab}=(2\pi/\hbar)\delta(E_a-E_b)|(\phi_a, V\psi_b^+)|^2 +(2/\hbar)1_{ab}\,\mathrm{Im}(\phi_a, V\psi_b^+), \quad (35)$$

provided the matrix elements $(\phi_a, V\psi_b^+)=\mathbf{T}_{ab}$ are continuous functions of the states ϕ_a and ϕ_b, and provided the matrix elements

$$(\phi_a, ([1-\exp(-i[H_b-i\epsilon]t/\hbar)]/[H_b-i\epsilon])\phi_b)$$

and (36)

$$(\phi_a, [1-\exp(-i[H_b-i\epsilon]t/\hbar)]\phi_b),$$

are bounded as $\epsilon\to 0$. The matrix elements in Eq. (36) will, in fact, be bounded unless the operator H is pathological since the first of these is the time integral of unitary operator and second is the difference of two unitary operators. Thus, the validity of Eq. (29) is proven. The valuable relations

$$\int dN_a w_{ab}(\epsilon, t)=\frac{d}{dt}(\psi_b(\epsilon, t), \psi_b(\epsilon, t))=0$$

$$\int dN_a w_{ab}=0 \quad (37)$$

are here the immediate consequence of the fact that $\phi_b(\epsilon, t)$ satisfies the Schroedinger equation of motion [Eq. (4)].

We now give an independent derivation of the second of the relations given in Eq. (37). Defining the operator $T(\epsilon)$ by the equation

$$T(\epsilon)\phi_a=V\psi_a(\epsilon), \quad (38)$$

we may write Eq. (17) in the form,

$$\psi_a(\epsilon)=\phi_a+\frac{1}{E_a+i\epsilon-H_0}T(\epsilon)\phi_a. \quad (39)$$

From Eq. (30) we see that ψ_a^+ is a solution of the hermitian eigenvalue problem

$$H\psi_a^+=E_a\psi_a^+, \quad (40)$$

from which we may infer that

$$\lim_{\epsilon\to 0}(\psi_a(\epsilon), \psi_b(\epsilon))=0; \quad E_a\neq E_b. \quad (41)$$

Calculating $(\psi_a(\epsilon), \psi_b(\epsilon))$ by Eq. (39) we obtain

$$(\psi_a(\epsilon), \psi_b(\epsilon))=1_{ab}+\frac{1}{E_b-E_a+i\epsilon}[\mathbf{T}_{ab}(\epsilon)-\mathbf{T}_{ba}{}^*(\epsilon)] +\frac{1}{E_b-E_a+2i\epsilon}\int dN_c\mathbf{T}_{ca}{}^*(\epsilon)\mathbf{T}_{cb}(\epsilon) \times\left[\frac{1}{E_c-E_b-i\epsilon}-\frac{1}{E_c-E_a+i\epsilon}\right]. \quad (42)$$

In the limit as $\epsilon\to\infty$, Eq. (42) yields

$$(\psi_a{}^\dagger, \psi_b{}^\dagger)=1_{ab}+\left\{P\frac{1}{E_p-E_a}-\pi i\delta(E_a-E_b)\right\} \times\left\{\mathbf{T}_{ab}-\mathbf{T}_{ba}{}^*+P\int dN_c\mathbf{T}_{ca}{}^*\mathbf{T}_{cb} \times\left(\frac{1}{E_c-E_b}-\frac{1}{E_c-E_a}\right)+\pi i\int dN_c\mathbf{T}_{ca}{}^*\mathbf{T}_{cb} \times[\delta(E_c-E_b)+\delta(E_c-E_a)]\right\}. \quad (43)$$

Equations (41) and (43) give

$$\mathbf{T}_{ab}-\mathbf{T}_{ba}{}^*+P\int dN_c\mathbf{T}_{ca}\delta\mathbf{T}_{cb}\left(\frac{1}{E_c-E_b}-\frac{1}{E_c-E_a}\right) +\pi i\int dN_c\mathbf{T}_{ca}{}^*\mathbf{T}_{cb}[\delta(E_c-E_b)+\delta(E_c-E_a)]=0 \quad (44)$$

for $E_a\neq E_b$. If, however, $\mathbf{T}_{ab}$ is a continuous function of the states ϕ_a and ϕ_b, then Eq. (44) must also hold for $E_a=E_b$. Thus, Eq. (44) gives, for $a=b$,

$$(2\pi/\hbar)\int dN_c\delta(E_c-E_a)|\mathbf{T}_{ca}|^2+(2/\hbar)\,\mathrm{Im}\mathbf{T}_{aa}=0, \quad (45)$$

which is the explicit expression for the second of Eq. (47).

Substitution of Eq. (44) in Eq. (43) gives the relationship

$$(\psi_a^+, \psi_b^+)=1_{ab}, \quad (46)$$

which was assumed in the derivation of Eq. (22).

V. CONNECTION WITH THE S-MATRIX

The results given in this paper are related to the more conventional forms[1] of the Heisenberg S-matrix theory in accordance with the following definitions:

$$T_{ab}=-2\pi i\delta(E_a-E_b)\mathbf{T}_{ab} \quad (47)$$

and

$$S=1+T. \quad (48)$$

The S-matrix defined by the relations given in Eqs. (47) and (48) can be shown to be left unitary by using Eq. (44) as follows:

$$\begin{aligned}(S^\dagger S)_{ab}&=1_{ab}+T_{ab}+T_{ab}{}^\dagger+(T^\dagger T)_{ab}\\ &=1_{ab}-2\pi i\delta(E_a-E_b)(\mathbf{T}_{ab}-\mathbf{T}_{ba}{}^*)\\ &\quad+4\pi^2\int dN_c\mathbf{T}_{ca}{}^*\mathbf{T}_{cb}\delta(E_a-E_c)\delta(E_b-E_c)\\ &=1_{ab}+2\pi\delta(E_a-E_b)\left\{[\mathbf{T}_{ab}-\mathbf{T}_{ba}{}^*]/i\right.\\ &\quad\left.+2\pi\int dN_c\mathbf{T}_{ca}{}^*\mathbf{T}_{cb}\delta(E_c-E_a)\right\}\\ &=1_{ab}.\end{aligned} \quad (49)$$

The proof that $SS^\dagger=1$ required additional relations which will be developed now. If we calculate

$$\mathbf{T}_{ab}(\epsilon)-\mathbf{T}_{ba}{}^*(\epsilon)$$

$$=-\left\{\left(\mathbf{T}(\epsilon)\phi_a\left[\frac{1}{E_a-i\epsilon-H_0}-\frac{1}{E_p+i\epsilon-H_0}\right]\mathbf{T}(\epsilon)\phi_b\right)\right\}$$

or (50)

$$\mathbf{T}_{ab}(\epsilon)-\mathbf{T}_{ba}{}^*(\epsilon)+\int dN_c\mathbf{T}_{ca}{}^*(\epsilon)\mathbf{T}_{cb}(\epsilon)$$

$$\times\left\{\frac{1}{E_c-E_b-i\epsilon}-\frac{1}{E_c-E_a+i\epsilon}\right\}=0.$$

We first note that in the limit as $\epsilon\to 0$, Eq. (50) reduces to Eq. (44) and thus gives an independent proof of Eq. (44). We further note that Eq. (50) is also valid for negative ϵ, from which we get, for $\epsilon>0$,

$$\mathbf{T}_{ab}(-\epsilon)-\mathbf{T}_{ba}{}^*(-\epsilon)+\int dN_c\mathbf{T}_{ca}{}^*(-\epsilon)\mathbf{T}_{cb}(-\epsilon)$$

$$\times\left\{\frac{1}{E_c-E_b+i\epsilon}-\frac{1}{E_c-E_a-i\epsilon}\right\}=0. \quad (51)$$

Another needed relation follows from

$$(\psi_a(-\epsilon),\ V\psi_b(\epsilon))$$

$$=\mathbf{T}_{ba}{}^\dagger(-\epsilon)+\left(\mathbf{T}(-\epsilon)\phi_a,\ \frac{1}{E_b+i\epsilon-H_0}\mathbf{T}(\epsilon)\phi_b\right) \quad (52)$$

$$=\mathbf{T}_{ab}(\epsilon)+\left(\mathbf{T}(-\epsilon)\phi_b,\ \frac{1}{E_a+i\epsilon-H_0}\mathbf{T}(\epsilon)\phi_b\right),$$

from which one sees that

$$\mathbf{T}_{ab}(\epsilon)=\mathbf{T}_{ba}{}^*(-\epsilon), \quad (53)$$

if $E_a=E_b$. We now calculate $(SS^\dagger)_{ab}$ using Eqs. (47), (48), (51), and (53);

$$(SS^\dagger)_{ab}=1_{ab}-2\pi i\delta(E_a-E_b)(\mathbf{T}_{ab}-\mathbf{T}_{ba}{}^*)$$

$$+4\pi^2\int dN_c\mathbf{T}_{ac}\mathbf{T}_{bc}{}^*\delta(E_a-E_c)\delta(E_b-E_c)$$

$$=1_{ab}+2\pi\delta(E_a-E_b)\lim_{\epsilon\to 0}\left\{[\mathbf{T}_{ba}{}^*(-\epsilon)-\mathbf{T}_{ab}(-\epsilon)]/i \quad (54)\right.$$

$$\left.-\pi\int dN_c\mathbf{T}_{ca}{}^*(-\epsilon)\mathbf{T}_{cb}(-\epsilon)\times\left\{\frac{1}{E_c-E_b+i\epsilon}-\frac{1}{E_c-E_a-i\epsilon}\right\}\right\}$$

$$=1_{ab}.$$

In deriving the above relationship we use the fact that, for all relevant matrix elements of $T_{ab}(\epsilon)$ and $T_{ba}{}^*(-\epsilon)$, $E_a=E_b$, hence Eq. (53) holds, and the principal parts in the integral contained in Eq. (54) vanish.

VI. REMARKS

Although these results appear generally valid, severe restrictions must be placed on the interaction energy, V, for some of the conclusions to hold. One of the most limiting of these assumptions, that the functions $\psi_a{}^+$ constitute a complete set, was utilized in proving the adiabatic theorem. For example, the functions $\psi_a{}^+$ will not form a complete set when the operator H_0 has only a continuous spectrum, and $H(t)$ has the same continuous spectrum as H_0 plus additional discrete eigenvalues.

We will show that completeness here is a necessary condition for the adiabatic hypothesis to hold. If the system starts in the state ϕ_b at $t=-\infty$, then under the action of the hamiltonian, Eq. (1), at time t, it will be in the state

$$\psi_b(t,\alpha)=U(t,\alpha)\phi_b, \quad (55)$$

in which $U(t,\alpha)$ is a unitary operator (i.e., $U^\dagger U$ $UU^\dagger=1$). Since $U(t,\alpha)$ is a unitary operator, the set of states $\psi_b(t,\alpha)$ is complete. Thus we see that in the limit as $\alpha\to 0$ the set of states $\phi_b(t,\alpha)$ (if they approach a limit) will approach a complete set and, therefore, cannot approach the set of states $\psi_b{}^+$, if the set of states $\psi_b{}^+$ is not complete. The same argument leads us to conclude that in the limit as $\alpha\to 0$ the states $\psi_b(t,\alpha)$ will not approach stationary states[6] unless the set of states $\psi_b{}^+$ is complete.

The fact that the limit as $\alpha\to 0$ of $\psi_b(t,\alpha)$ differs from $\psi_b{}^+$ does not prove that a transition rate calculated by

$$w_{ab}=\lim_{\alpha\to 0}\frac{d}{dt}|(\phi_a,\psi_b(t,\alpha))|^2, \quad (56)$$

will differ from the transition rate as given by

$$w_{ab}-\lim_{\epsilon\to 0}\frac{d}{dt}|(\phi_a,\ e^{-iHt/\hbar}\psi_b(\epsilon))|^2. \quad (57)$$

We have, however, not succeeded in obtaining a proof of the equivalence of Eqs. (56) and (57) except when expression (12) approaches Eq. (13) in the limit $\alpha\to 0$ and the series of Eq. (14) has the limiting value $(\phi_a,\ V\psi_b{}^+)$, nor have we proven that Eqs. (56) and (57) will not give the same result if the functions $\psi_b{}^+$ do not constitute a complete set. We have merely noted that if one could show that

$$\lim_{\alpha\to 0}\psi_b(t,\alpha)=\exp(-iE_bt/\hbar)\psi_b{}^+$$

$$+\sum_n C_n\phi_n\exp(-iE_nt/\hbar), \quad (58)$$

in which ϕ_n are the discrete eigenfunctions of H and the

[6] In the paper of Lippmann and Schwinger, an essential step in the development of the transition rate formula [Eq. (1.72)] was an assumption equivalent to the requirement that the states $\psi_b(t,\alpha)$ approach stationary states in the limit as $\alpha\to 0$, and consequently that the states $\psi_b{}^+$ form a complete set.

C_n are appropriate constants, then one could demonstrate the equivalence of Eqs. (56) and (57).

Another difficulty is demonstrating rigorously the equivalence between the S-matrix as it is defined by Eqs. (47) and (48) of the stationary method, and its definition as a unitary matrix describing the state of the system at $t=\infty$ in terms of the state at $t=-\infty$; i.e., $\psi(\infty)=S\psi(-\infty)$. Actually, the important conclusions of this paper do not depend on a demonstration of the equivalence of these two definitions of the S-matrices. However, many recent works in field theory have, in effect, depended on the assumption of the equivalence of these two definitions and it would be worthwhile to find a mathematically satisfactory demonstration of the equivalence.

The author wishes to express his hearty appreciation to David A. Kleinman, George A. Snow, Edward J. Kelly, and Maurice Neuman for many helpful discussions and criticisms which occurred during the course of this work.

PHYSICAL REVIEW VOLUME 83, NUMBER 6 SEPTEMBER 15, 1951

Imprisonment of Resonance Radiation in Gases. II

T. HOLSTEIN
Westinghouse Research Laboratories, East Pittsburgh, Pennsylvania
(Received April 12, 1951)

This paper is a continuation of an earlier paper which treated the decay of resonance radiation in optically excited gases for the case of doppler-broadened radiation in plane-parallel enclosures. The treatment is here extended to a second type of enclosure geometry—infinite cylinders—and to a variety of spectral line shapes.

1. INTRODUCTION

THE phenomenon of imprisonment of resonance radiation in gases owes its existence to the selective absorbability of resonance lines by normal atoms of the emitting gas. Over a wide range of gas density this absorbability is so high that a resonance quantum emitted in the interior of a gas-filled enclosure has but a small chance of reaching the walls; hence, the eventual escape of a unit of atomic excitation energy from the enclosure generally takes place only after a large number of repeated emissions and absorptions. Under these conditions the radiation is said to be "imprisoned."

Perhaps the most direct way in which imprisonment manifests itself is in decay experiments with optically excited gases. In this type of experiment an enclosure of gas is irradiated with a beam of resonance radiation, which serves to excite some of the gas atoms to a given resonance state. The incident beam is then abruptly cut off, and the intensity of diffuse radiation, which is proportional to the concentration of atoms in the resonance state, is measured as a function of time. One observes essentially an exponential decay of the form $e^{-\gamma g t}$, where $1/\gamma$ is the radiative lifetime of an isolated atom and g, the "escape factor," is a dimensionless quantity characteristic of the imprisonment process. The quantity g may be regarded as the reciprocal of the number of emission and absorptions of an individual unit of atomic excitation prior to its escape from the enclosure.

In an experiment on the decay of the 6^3P_1 mercury resonance state, which combines optically with the ground state to emit the 2537A resonance line, Zemansky[1] observed values of g as low as 10^{-3}. The quantity g was also found to depend both on vapor density and enclosure geometry.

A theoretical study[2] of the decay problem was recently carried out by the author of the present paper. It was shown that g depends not only upon vapor density and enclosure geometry but also upon the shape of the resonance line. In particular, for an enclosure of the form of an infinite slab of thickness L and for a doppler-broadened resonance line, the following expression for g was obtained:

$$g=1.875/[k_0L(\pi \log\tfrac{1}{2}k_0L)^{\frac{1}{2}}], \tag{1.1}$$

where k_0 is the absorption coefficient at the center of the resonance line. k_0, itself, is specified[3] in terms of the parameters of the system: gas density, gas temperature, wavelength of the line, and lifetime of the resonance state.

More recently,[4] measurements of the imprisonment of resonance radiation in mercury vapor over a wide range of vapor density were carried out at the Westinghouse Research Laboratories. In the region of density for which g had been evaluated—the doppler-broadening region—the agreement between theory and experiment was quite satisfactory.

[1] M. W. Zemansky, Phys. Rev. **29**, 513 (1927).
[2] T. Holstein, Phys. Rev. **72**, 1212 (1947), to be referred to hereafter as "I."
[3] A. C. G. Mitchell and M. W. Zemansky, *Resonance Radiation and Excited Atoms* (The Macmillan Company, New York, 1934) (to be referred to hereafter as "MZ") Chapter III, pp. 99–100 and Eq. (35).
[4] Alpert, McCoubrey, and Holstein, Phys. Rev. **76**, 1257 (1949).

In the course of preparation for these and other experiments to follow, calculations of g were performed for a second type of enclosure geometry—the infinite cylinder—and for a variety of spectral line shapes. These extensions of the theory constitute the subject matter of the present paper.

2. GENERAL METHOD

We present here a brief outline of the approach developed in I for the treatment of imprisonment phenomena with special emphasis on the decay problem.

The radiative transport of resonance excitation is formulated in terms of a Boltzmann-type integro-differential equation for the density of excited atoms, $n(\mathbf{r})$:

$$\partial n(\mathbf{r})/\partial t = -\gamma n(\mathbf{r}) + \gamma \int n(\mathbf{r}')G(\mathbf{r}', \mathbf{r})d\mathbf{r}'. \quad (2.1)$$

In (2.1) the integration goes over all volume elements, $d\mathbf{r}'$, of the enclosure. $G(\mathbf{r}', \mathbf{r})$, which represents the probability of radiation emitted at a point $\mathbf{r}'$ being absorbed in a unit volume element around the point $\mathbf{r}$, is given by the expression,

$$G(\mathbf{r}', \mathbf{r}) = -(1/4\pi\rho^2)(\partial T/\partial\rho), \quad (2.2)$$

where $\rho = |\mathbf{r}'-\mathbf{r}|$, and $T(\rho)$ is the probability of a resonance quantum traversing a distance ρ without being absorbed.

In evaluation of $T(\rho)$ it is necessary to take account of the rapid frequency variation of the absorption coefficient, $k(\nu)$, in the neighborhood of resonance. Denoting by $P(\nu)$ the frequency spectrum of the radiation emitted from a given volume element, we have for $T(\rho)$ the general expression,

$$T(\rho) = \int P(\nu)e^{-k(\nu)\rho}d\nu. \quad (2.3)$$

In the Appendix of Part I it is shown that the proportionality relation,

$$P(\nu) \propto k(\nu), \quad (2.4)$$

may be used when the shape of the resonance line is determined by either doppler- or pressure-broadening; in the latter case, it was assumed that $k(\nu)$ is given by the dispersion formula,

$$k(\nu) \propto 1/(1+[4\pi(\nu-\nu_0)/\gamma_p]^2), \quad (2.5)$$

where γ_p is proportional to the vapor density. In the present paper Eq. (2.4) will be assumed to hold for other types of pressure broadening; this extension is discussed in Appendix A.

The constant of proportionality in (2.4) is readily determined from the "integral absorption" relation,

$$\int k(\nu)d\nu = (\lambda_0^2 N/8\pi)(g_2/g_1)\gamma, \quad (2.6)$$

[see MZ pp. 95–96, Eq. (28); I, Eq. (2.5)] and from the normalization requirement on $P(\nu)$: $\int P(\nu)d\nu = 1$. Thus,

$$k(\nu) \equiv \kappa P(\nu) = (\lambda_0^2 N/8\pi)(g_2/g_1)\gamma P(\nu), \quad (2.7)$$

where λ_0 is the wavelength at the center of the resonance line, N is the vapor density, and g_2, g_1 are the statistical weights of excited and ground states. Inserting Eq. (2.7) into Eq. (2.3), we readily evaluate $T(\rho)$ and, hence, $G(\mathbf{r}', \mathbf{r})$ for various line shapes.

The general solution of Eq. (2.1) may be written as a sum of product solutions of the form,

$$n_i(r)e^{-\gamma g_i t},$$

each of which satisfies an equation of the type,

$$(1-g_i)n_i(\mathbf{r}) = \int G(\mathbf{r}, \mathbf{r}')n_i(\mathbf{r}')d\mathbf{r}'. \quad (2.8)$$

As is discussed in I, the g's form a discrete positive-definite set of numbers; hence, after a sufficiently long time, only the "fundamental mode," with the lowest eigenvalue, is observed experimentally.

The evaluation of g and $n(r)$ for the fundamental mode may be achieved approximately by the Ritz variational method; the general procedure and its use in the derivation of Eq. (1.1) are presented in I.

3. LINE SHAPES FOR DOPPLER- AND PRESSURE-BROADENING

In this section we present a brief survey of the frequency variation of $k(\nu)$ for the cases of doppler- and pressure-broadening.

A. Doppler-Broadening

$k(\nu)$ is given by the relation,

$$k(\nu) = k_0 \exp[-((\nu-\nu_0)/\nu_0)^2(c/v_0)^2]. \quad (3.1)$$

In Eq. (3.1), ν_0 is the resonance frequency of an atom at rest, $v_0 = (2kT/M_{\text{atom}})^{\frac{1}{2}}$ and k_0 is given by the relation [I, Eq. (2.10)],

$$k_0 = \frac{\lambda_0^3 N}{8\pi}\frac{g_2}{g_1}\frac{\gamma}{\pi^{\frac{1}{2}}v_0}. \quad (3.2)$$

B. Pressure-Broadening

We include in our discussion two kinds of broadening: self-broadening (due to the interaction of an absorbing atom with others of the same kind) and foreign gas broadening. In the latter case, we assume that the foreign gas does not quench the resonance excitation of the absorbing atoms by collisions of the second kind.

As was stated in I, pressure broadening can often be represented by the dispersion distribution, which in its most general form reads:[5]

$$k(\nu) = k_p/\{1+[4\pi(\nu-\nu_0-\beta_p)/\gamma_p]^2\}. \quad (3.3)$$

[5] H. M. Foley, Phys. Rev. 69, 616 (1946); E. Lindholm, Arkiv. Mat. Astron. Fysik. 32A, No. 17 (1945).

Here β_p and γ_p are directly proportional to the density, N', of the broadening agent. (For self-broadening $N'=N$.) k_p is obtained from Eq. (2.6); thus,

$$k_p=\frac{\lambda_0^2 N}{2\pi}\frac{g_2}{g_1}\frac{\gamma}{\gamma_p}. \tag{3.4}$$

In discussing Eq. (3.3) we first point out that this line shape is generally unobservable in the immediate core of the line because of doppler-broadening. However, as shown in *MZ*, Appendix I, for frequencies whose distance $\Delta\nu$ from the center of the line is large compared to $\nu_0 v_0/c$, effects of doppler-broadening may be ignored; for such frequencies, since γ_p (as well as β_p) is generally small compared to $\nu_0 v_0/c_0$, Eq. (3.3) takes the simple form,

$$k(\nu)=k_p[\gamma_p/\{4\pi(\nu-\nu_0-\beta_p)\}]^2. \tag{3.3'}$$

In the case of self-broadening β_p is zero,[5] i.e., there is no frequency shift. Foreign gas broadening, on the other hand, usually produces a negative shift.

Deviations from the dispersion distribution occur at high pressures and for large $\Delta\nu$. According to Spitzer[6] these deviations first become appreciable when

$$\Delta\nu > \sim (1/2\pi)(v^n/C_n)^{1/(n-1)}. \tag{3.5}$$

Here, v is the average velocity of perturbing atoms relative to absorbing atoms; C_n and n are defined in terms of an assumed interaction law according to which the presence of a perturbing atom at a distance R from an absorbing atom, produces a change in the absorption frequency,

$$\Delta\nu_p=C_n/R^n. \tag{3.6}$$

(The C_n of Eq. (3.6) is essentially equal to Spitzer's interaction constant, q, divided by $\hbar$; it is not to be confused with the C_n of his equation, which is a dimensionless quantity of the order of magnitude unity.)

Another condition for the validity of the dispersion formula is that the mean free time between collisions be large compared to the time of a collision. This means that for the major fraction of time the absorption frequency of a given absorbing atom is negligibly perturbed. At high pressures such that the mean free time between collisions is so short that the absorption frequency is continually perturbed, the dispersion formula breaks down.

At high pressures or for $\Delta\nu$ larger than (3.5), pressure broadening is customarily treated from the standpoint of the *statistical theory*. The basic premise of this theory may be stated as follows. The system of absorbing atom plus perturbers possesses at any time t an instantaneous absorption frequency $\nu(t)$ equal to ν_0 plus frequency perturbations of the type (3.6). For a specified sequence of collisions of a given type, $\nu(t)$ is a known function of time. The statistical theory assumes that the absorption coefficient $k(\nu)$ is proportional to that fraction of an arbitrarily large time interval, T, for which $\nu(t)$ is contained between ν and $\nu+d\nu$. Since an arbitrarily large number of collisions take place in time T, the general principles of statistical mechanics permit us to equate the defined time fraction to the probability of occurrence, $H(\nu)d\nu$, of those configurations of absorbing and perturbing atoms for which the absorption frequency lies between ν and $\nu+d\nu$. Furthermore, since $H(\nu)$ is by definition a normalized probability function, i.e., $\int H(\nu)d\nu$, we must have

$$P(\nu)=H(\nu), \tag{3.7}$$

since $P(\nu)$ is similarly normalized. The constant of proportionality between $k(\nu)$ and $H(\nu)$ is then the same as that of (2.7).

In simple applications of the statistical theory, one customarily assumes a frequency perturbation of the form (3.6); the following expressions for $P(\nu)$ and $k(\nu)$ are then readily obtained.[7]

$$P(\nu)=(4\pi N'/n)C_n^{3/n}/(\Delta\nu)^{3/n+1}, \tag{3.8}$$

$$k(\nu)=\kappa P(\nu)=\frac{\lambda_0^2}{2}\frac{g_2}{g_1}\frac{\gamma N N'}{n}\frac{C_n^{3/n}}{(\Delta\nu)^{3/n+1}}. \tag{3.9}$$

In a more exact treatment it is necessary to take account of the degeneracy of excited or ground states, which is always present in an actual case. The approach of a perturbing atom then entails not only a shift, but also a splitting of the absorption frequency. Hence, Eq. (3.6) must be replaced by a system of equations,

$$\Delta\nu_p^{(s)}=C_n^{(s)}/R^n, \tag{3.6'}$$

where s takes on a number of values equal to the multiplicity of the splitting. The statistical analysis then yields for $P(\nu)$ and $k(\nu)$ expressions of the form (3.8) and (3.9) wherein the interaction constant C_n is replaced by a more complicated term involving the $C_n^{(s)}$. In the derivation of (3.8) and (3.9) it is further assumed that binary collisions are alone of significance. As shown by Kuhn,[7] this condition is fulfilled for sufficiently large $\Delta\nu$, i.e., in the wings of a spectral line. The treatment of the present paper is restricted to this case.

In practice, two types of interaction are of special importance:

1. *Dipole-dipole interaction.*—This interaction exists when the colliding atoms are of the same kind, i.e., in the case of self-broadening. The resultant frequency perturbation is of the form,

$$\Delta\nu_p=C_3/R^3. \tag{3.10}$$

Inserting Eq. (3.10) into Eqs. (3.8) and (3.9), we obtain

$$P(\nu)=(4\pi N/3)[C_3/(\Delta\nu)^2] \tag{3.11}$$

$$k(\nu)=\frac{\lambda_0^2}{6}\frac{g_2}{g_1}\gamma N^2\frac{C_3}{(\Delta\nu)^2}. \tag{3.12}$$

[5] Lyman Spitzer, Jr., Phys. Rev. **58**, 348 (1940).

[7] H. Kuhn, Phil. Mag. **18**, 987 (1934); Proc. Roy. Soc. (London) **A158**, 212 (1937).

We note that Eq. (3.12) exhibits the same dependence on $\Delta\nu$ and N as the dispersion formula (3.3′) (with $\beta_p=0$). Furthermore, a treatment taking into account the degeneracy of excited and ground states, as outlined, shows (see a forthcoming paper by the present author[8]) that $P(\nu)$ and $k(\nu)$ are symmetrical with respect to the sign of the frequency deviation, $\Delta\nu$. Finally, as has already been demonstrated by Margenau and Watson,[9] the magnitudes of Eqs. (3.3′) and (3.12) are of the same order. Thus, in the case of self-broadening, we may expect the dispersion distribution to be valid for $\Delta\nu$ much larger than the limit set by Spitzer's criterion (3.5), at least as long as the interaction is predominantly dipole-dipole in character.

2. *Van der waals interaction.*—This interaction, which gives a frequency perturbation of the form,

$$\Delta\nu_p=C_6/R^6, \tag{3.13}$$

represents the first term on the expansion, in powers of $1/R$, of the interaction between unlike atoms. For this case Eqs. (3.8) and (3.9) give

$$P(\nu)=\tfrac{3}{2}\pi N'C_6^{\frac{1}{5}}/(\Delta\nu)^{\frac{4}{5}}, \tag{3.14}$$

$$k(\nu)=\frac{\lambda_0^2}{12}\frac{g_2}{g_1}\frac{\gamma_N N'C_6^{\frac{1}{5}}}{(\Delta\nu)^{\frac{4}{5}}}. \tag{3.15}$$

In contrast to the dipole-dipole case, the more exact analysis involving degeneracy considerations shows that $P(\nu)$ and $k(\nu)$ are asymmetrical with respect to the sign of $\Delta\nu$. Usually this asymmetry takes the form of enhanced intensity on the red side of the unperturbed frequency.[10]

Finally, it should be mentioned that in some cases of self-broadening in which the dipole-dipole interaction is weak to begin with, terms in higher powers of $1/R$, such as the van der waals $1/R^6$ term, may predominate for close approaches, which in the statistical theory determine the line shape at large $\Delta\nu$. Thus, Kuhn[10] finds that at 0.6A from the center of the 2537A mercury resonance line, on the red side,

$$k(\nu)\propto(\Delta\nu)^{-\frac{4}{3}},$$

whereas, on the violet side, $k(\nu)$ drops off with increasing $\Delta\nu$ much faster than the dispersion distribution. On the other hand, Gregory[11] finds that the self-broadening of each of the lines of the principal caesium doublet obeys the dispersion formula out to at least 20A from the line center.

The difference between these two cases may be understood[12] in terms of the magnitude of the dipole-dipole interaction, which is directly proportional to the oscillator strength, f, of the resonance line. In the case of Hg 2537A, $f=0.029$, whereas for the D_1 and D_2 lines of Cs, $f=0.33$ and 0.67, respectively.

4. TRANSMISSION OF DOPPLER AND PRESSURE BROADENED RESONANCE RADIATION

The formulas which we obtain in this section for the transmission probability, $T(\rho)$, hold only for ρ large enough so that the core of the resonance line is quite thoroughly absorbed out; the main contribution to (2.3) is then contained in the wings of the line. A necessary and sufficient condition for the prevalence of this situation is

$$T(\rho)\ll 1. \tag{4.1}$$

Now, as has been shown in I for doppler-broadening, and as will be demonstrated more generally subsequently, the escape factor, g, is related to $T(\rho)$ by the order-of-magnitude equation,

$$g\sim T(d), \tag{4.2}$$

where d is the shortest linear dimension of the enclosure. Hence, the calculations of this section will apply to those cases in which the escape factor, is small compared to unity.

A. Doppler-Broadening

The expression for $T(\rho)$, obtained in I, is

$$T(\rho)=1/k_0\rho(\pi\log k_0\rho)^{\frac{1}{2}} \tag{4.3}$$

where k_0 is given by (3.2).

B. Pressure-Broadening

1. *Dispersion distribution.*—We use here the asymptotic form (3.3′) valid in the wings of the line. From Eqs. (2.7), (3.3′), and (3.4) we have

$$P(\nu)=\frac{4}{\gamma_p}\left[\frac{\gamma_p}{4\pi(\nu-\nu_0-\beta_p)}\right]^2. \tag{4.4}$$

Introducing (3.3′) and (4.4) into (2.3) and transforming to a new variable $u=4\pi(\nu-\nu_0-\beta_p)/\gamma_p$ we obtain

$$\begin{aligned}T(\rho)&=\frac{1}{\pi}\int_{-\infty}^{+\infty}\left(\frac{1}{u^2}\right)\exp(-k_p\rho/u^2)du\\&=\frac{2}{\pi}\int_0^{\infty}\exp(-k_p\rho y^2)dy\\&=1/(\pi k_p\rho)^{\frac{1}{2}}.\end{aligned} \tag{4.5}$$

2. *Statistical distributions.*—We use here the general expression (3.8) for $P(\nu)$. We assume for the sake of simplicity that $P(\nu)$ differs from zero for only one sign of $\Delta\nu$. (It is immaterial whether we choose this sign positive or negative.) Then, changing the variable of

[8] T. Holstein, Phys. Rev. **76**, 457 (1949) (preliminary notice).
[9] H. Margenau and W. Watson, Revs. Modern Phys. **8**, 22 (1936).
[10] R. Minkowski, Z. Physik **93**, 731 (1935), H. Kuhn, Proc. Roy. Soc. (London) **A158**, 230 (1937).
[11] Chris Gregory, Phys. Rev. **61**, 465 (1942).
[12] V. Weisskopf, Physik Z. **34**, 1 (1933).

integration from $\Delta\nu$ to $P(\nu)$, we have

$$T(\rho)=\int_0^\infty Pe^{-\kappa\rho P}\left|\frac{d(\Delta\nu)}{dP}\right|dP$$

$$=\left(\frac{4\pi N'}{n}\right)^{n/(3+n)}C^{n/(3+n)}\left(\frac{n}{3+n}\right)\times\int_0^\infty P^{-n/(3+n)}e^{-\kappa\rho P}dP$$

$$=\left(\frac{n}{3+n}\right)\left(\frac{4\pi N'}{n}\right)^{n/(3+n)}C^{3/(3+n)}\times\left(-\frac{n}{3+n}\right)!(\kappa\rho)^{-3/(3+n)}. \quad (4.6)$$

Substituting the explicit expression for κ given by (2.7) into (4.6), we obtain

$$T(\rho)=\frac{\left(\frac{n}{3+n}\right)\left(\frac{4\pi N'}{n}\right)^{n/(3+n)}C^{3/(3+n)}\left(-\frac{n}{3+n}\right)!}{\left(\frac{\lambda_0^2 N}{8\pi}\frac{g_2}{g_1}\gamma\rho\right)^{3/(3+n)}}$$

or

$$T(\rho)\propto N'^{n/(3+n)}/N^{3/(3+n)}\rho^{3/(3+n)}. \quad (4.7)$$

For the purposes of the next section, in which we calculate escape factors for all these cases, we express $T(\rho)$ in the general asymptotic form,

$$T(\rho)=a_m/\rho^m;\quad 0<m\leqq 1, \quad (4.8)$$

where a_m is a function of N, N', and atomic constants. Equation (4.8) embraces all the pressure-broadening cases discussed here. In the case of doppler-broadening, the presence of the logarithmic term in (4.3) does not permit an exact representation of $T(\rho)$ by (4.8). However, as we have already observed in I, the logarithmic term can, in most instances, be treated as constant; for example, in that paper, we replace $\log k_0\rho$ by $\log\frac{1}{2}k_0L$. This approximation will also be used in the present paper in the calculations for infinite slabs; in the case of cylinders, we replace $\log k_0\rho$ by $\log k_0R$, where R is the radius of the cylinder. With these approximations, the transmission of doppler-broadened radiation is represented by (4.8) with $m=1$.

5. ESCAPE FACTORS FOR DOPPLER- AND PRESSURE-BROADENED RADIATION IN INFINITE SLABS AND CYLINDERS

In this section we employ the variational method described in I to calculate the escape factor, g. The variational expression for g reads [see I, Eq. (3.11)]:

$$g=\frac{\int n^2(\mathbf{r})E(\mathbf{r})d\mathbf{r}+\frac{1}{2}\int\int[n(\mathbf{r})-n(\mathbf{r}')]^2G(\mathbf{r},\mathbf{r}')d\mathbf{r}d\mathbf{r}'}{\int n^2(\mathbf{r})d\mathbf{r}}, \quad (5.1)$$

where

$$E(\mathbf{r})=1-\int G(\mathbf{r},\mathbf{r}')d\mathbf{r}'. \quad (5.2)$$

The problem is to find the minimum value of g and the function $n(\mathbf{r})$ for which this minimum is obtained.

A. Infinite Slab

We choose a cartesian system of coordinates whose z axis is perpendicular to the slab; the origin is chosen so that the plane $z=0$ bisects the region. We assume that $n(\mathbf{r})$ is a function of z alone; it is then possible to effect a considerable simplification in Eq. (5.1) by integrating over the other two variables, x and y.

The quantities which have to be evaluated are $\int G(\mathbf{r},\mathbf{r}')dx'dy'$ and $E(\mathbf{r})$. From (2.2) and (4.8) we have

$$G(\mathbf{r},\mathbf{r}')=ma_m/4\pi\rho^{m+2}, \quad (5.3)$$

where $\rho=|\mathbf{r}-\mathbf{r}'|$. We then obtain

$$G(\mathbf{r},\mathbf{r}')dx'dy'=\frac{ma_m}{4\pi}\int_{-\infty}^{+\infty}\int\frac{dx'dy'}{[(x-x')^2+(y-y')^2+(z-z')^2]^{(m+2)/2}}$$

$$=\frac{ma_m}{2(m+1)}\frac{1}{|z-z'|^{m+1}}. \quad (5.4)$$

The calculation of $E(\mathbf{r})$ is not to be performed by a direct evaluation of $\int G(\mathbf{r},\mathbf{r}')d\mathbf{r}'$, since important contributions to the latter integral occur for small values of ρ, for which the asymptotic expression (5.3) is not valid. One gets around this difficulty by observing that the integral of $G(\mathbf{r},\mathbf{r}')$ over an infinite region is unity; this follows from the definition of $G(\mathbf{r},\mathbf{r}')$ given in the text after Eq. (2.1) as well as from (2.2). We then immediately obtain

$$E(\mathbf{r})=\int_{\text{Ext}}G(\mathbf{r},\mathbf{r}')d\mathbf{r}', \quad (5.5)$$

where the subscript "Ext" denotes integration over all volume elements outside the gas enclosure. In the plane case

$$E(z)=\frac{ma_m}{2(m+1)}\left[\int_{\frac{1}{2}L}^\infty\frac{dz'}{|z-z'|^{m+1}}+\int_{-\infty}^{-\frac{1}{2}L}\frac{dz'}{|z-z'|^{m+1}}\right]$$

$$=\frac{a_m}{2(m+1)}\left[\frac{1}{(\frac{1}{2}L-z)^m}+\frac{1}{(\frac{1}{2}L+z)^m}\right] \quad (5.6)$$

where L is the thickness of the slab. Substituting Eqs. (5.5) and (5.6) into Eq. (5.1) and introducing the variable,

$$\xi=2z/L, \tag{5.7}$$

we obtain

$$g=\frac{g_m{}^P}{2^{1-m}}\Big[\int_{-1}^{+1}n^2(\xi)\Big\{\frac{\frac{1}{2}}{(1-\xi)^m}+\frac{\frac{1}{2}}{(1+\xi)^m}\Big\}d\xi$$

$$+\frac{m}{4}\int_{-1}^{+1}\int\frac{[n(\xi)-n(\xi')]^2}{|\xi-\xi'|^{1+m}}d\xi d\xi'\Big]\Big/\int_{-1}^{+1}n^2(\xi)d\xi \tag{5.8}$$

where

$$g_m{}^P=2a_m/(1+m)L^m. \tag{5.8a}$$

(The superscript "P" denotes "plane case" as contracted with the superscript "C" to be used later to denote "cylindrical case.")

We now have to consider the type of function to be used for $n(\xi)$ in the variational calculation of g. In I we found that results good to a few percent can be expected for the two parameter "parabolic" function

$$n_{01}(\xi)=a_0n_0(\xi)=a_1n_1(\xi)$$
$$=a_0+a_1(1-\xi^2). \tag{5.9}$$

TABLE I. g_0, g_1, and g_{01} in units of a_m/L^m for typical values of m.

m	$\frac{1}{3}$	$\frac{1}{2}$	1
g_0	1.125	1.333	∞
g_1	1.085	1.198	1.875
g_{01}	1.077	1.150	1.875

Introducing (5.9) into (5.8), we obtain

$$g/g_m{}^P\equiv\alpha=\sum_{i,j=0,1}a_ia_jK_{ij}{}^P/\sum_{i,j=0,1}a_ia_jH_{ij}{}^P \tag{5.10}$$

where

$$K_{ij}{}^P=\frac{1}{2^{1-m}}\int_{-1}^{+1}n_i(\xi)n_j(\xi)\Big[\frac{\frac{1}{2}}{(1-\xi)^m}+\frac{\frac{1}{2}}{(1-\xi)^m}\Big]d\xi$$

$$+\frac{1}{2^{1-m}}\frac{m}{4}\int_{-1}^{+1}\int\frac{[n_i(\xi)-n_i(\xi')][n_j(\xi)-n_j(\xi')]}{|\xi-\xi'|^{1+m}}d\xi d\xi' \tag{5.11a}$$

and

$$H_{ij}{}^P=\int_{-1}^{+1}n_i(\xi)n_j(\xi)d\xi. \tag{5.11b}$$

The Ritz variational procedure consists in minimizing g with respect to arbitrary variations in the a_i, i.e.,

$$\partial g/\partial a_i=0;\quad i=0,1. \tag{5.12}$$

Equation (5.12) yields two homogeneous equations for the a_i

$$\begin{aligned}(K_{00}-\alpha H_{00})a_0+(K_{01}-\alpha H_{01})a_1&=0\\(K_{01}-\alpha H_{01})a_0+(K_{11}-\alpha H_{11})a_1&=0\end{aligned} \tag{5.13}$$

the nontrivial solution of which requires the vanishing of the determinant of the coefficients, i.e.,

$$\begin{vmatrix}K_{00}-\alpha H_{00} & K_{01}-\alpha H_{01}\\ K_{01}-\alpha H_{01} & K_{11}-\alpha H_{11}\end{vmatrix}=0. \tag{5.14}$$

From Eq. (5.14) we obtain two values for α, and, hence, for g; since we are seeking an absolute minimum, only the smaller of these is significant. Once α is known, we may obtain a_0 and a_1 to within an arbitrary constant from (5.13).

The calculation of the $K_{ij}{}^P$ and $H_{ij}{}^P$ is straightforward.[13] The results are:

$$\begin{aligned}K_{00}{}^P&=1/(1-m) & H_{00}{}^P&=2\\K_{01}{}^P&=4/(2-m)(3-m) & H_{01}{}^P&=4/3\\K_{11}{}^P&=16/(2-m)(3-m)(5-m) & H_{11}{}^P&=16/15.\end{aligned} \tag{5.15}$$

Inserting these expressions into (5.14) and solving for $\alpha=g/g_m{}^P$ we obtain the "two-parameter" approximation to g.

$$g_{01}=\frac{3a_m/L^m[10-m-m^2-m(101-40m+2m^2+m^4)^{\frac{1}{2}}]}{(1-m^2)(2-m)(3-m)(5-m)}. \tag{5.16}$$

One may also calculate "one-parameter" approximations, g_0 and g_1 by taking $n(\xi)=a_0$ and $n(\xi)=a_1(1-\xi^2)$, respectively. The results are:

$$g_0=g_m{}^PK_{00}{}^P/H_{00}{}^P=a_m/(1-m^2)L^m \tag{5.17}$$

$$g_1=g_m{}^PK_{11}{}^P/H_{11}{}^P$$
$$=30a_m/(1+m)(2-m)(3-m)(5-m)L^m. \tag{5.18}$$

In Table I we present the numerical values of g_0, g_1, and g_{01} in units of a_m/L^m for $m=\frac{1}{3}$, $\frac{1}{2}$, and 1. From Table I, it can be seen that g_1 and g_{01} do not differ by more than a few percent. Furthermore, for $m=\frac{1}{3}$ and $\frac{1}{2}$, the discrepancy between g_0 and g_{01} does not exceed 15 percent. We thus see that, with the exception of the g_0 for $m=1$, the one-parameter results are not very different from the more accurate two-parameter values; hence, it is to be expected that the three-parameter function, derived from $n_{01}(\xi)$ by the addition of a term of the type, e.g., $a_2(1-\xi^4)$ will, at best, improve the value for g by only a few percent.

We should point out here that actually g_0 does not become infinite for $m=1$. As shown in I, p. 1220, the asymptotic form of $T(\rho)$ given by (4.8) or (4.3) is not

[13] The calculation of the double-integral term of $K_{11}{}^P$ is facilitated by the introduction of new integration variables, $u=\xi+\xi'$, $v=\frac{1}{2}(\xi-\xi')$.

accurate enough for the evaluation of $K_{00}{}^P$. The detailed treatment presented in I gives for $K_{00}{}^P$ the value $2\log k_0L$ (Eq. (4.7) of I must be multiplied by 4, since the $n_0(\xi)$ of the present paper is twice the $n_0(\xi)$ of I). Hence,

$$g_0=K_{00}{}^P/H_{00}{}^P=\log k_0L.$$

The value of g_{01} is also affected by the modification of $K_{00}{}^P$. From I, (4.18), we have

$$g_{01}=1.875\left(1-\frac{\frac{1}{16}}{\log k_0L-5/4}\right), \tag{5.19}$$

which, for typical values of $\log k_0L$ (~4 to 5), differs from the number 1.875, given in Table I, by only a few percent.

Having obtained g_{01}, or α, we may substitute into Eq. (5.13) and solve for $n_{01}(\xi)$ to within an arbitrary constant. With use of (5.15) we obtain a set of values for the ratio a_0/a_1 (Table II). The two-parameter functions $n_{01}(\xi)$ corresponding to these ratios are plotted as full curves in Fig. 1; here the arbitrary multiplicative constant has been chosen to make $n_{01}(0)$ equal to unity for all m.

As pointed out the correct value of K_{00} for $m=1$ is $2\log k_0L$ instead of infinity. When this correction is taken into account, one obtains

$$\frac{a_0}{a_1}=\frac{\frac{3}{8}}{\log k_0L-15/8} \tag{5.20}$$

which, for a typical value of $\log k_0L$, e.g., 5, gives

$$a_0/a_1=0.12. \tag{5.20'}$$

The density function $n_{01}(\xi)$ corresponding to (5.20') is represented by the dashed curve of Fig. 1.

B. Infinite Cylinder

As in the case of the infinite slab, the starting point of the analysis is the variational expression (5.1) for g, together with the auxiliary relation (5.5) for $E(\mathbf{r})$. Introducing cylindrical coordinates, z, φ, and r, with $-\infty\leqq z\leqq\infty$, $0\leqq\varphi\leqq 2\pi$, and $0\leqq r\leqq R$ (the radius of the cylinder), we have

$$d\mathbf{r}=dzd\sigma;\quad d\mathbf{r}'=dz'd\sigma' \tag{5.21}$$

where $d\sigma$ and $d\sigma'$ are elements of cross-sectional area

$$d\sigma=rdrd\varphi;\quad d\sigma'=r'dr'd\varphi'. \tag{5.22}$$

In view of the symmetry of the problem, we may take $n(\mathbf{r})$ to be a function of the radial coordinate, r, alone. The integrations with respect to z and z' then proceed readily. We have, from (5.3)

$$\int_{-\infty}^{+\infty}G(\mathbf{r},\mathbf{r}')dz'=\frac{ma_m}{4\pi}\int_{-\infty}^{+\infty}\frac{dz'}{\rho^{m+1}}$$

$$=ma_m\int_{-\infty}^{+\infty}\frac{dz'}{[q^2+(z-z')^2]^{(m+1)/2}}$$

Table II. The ratio a_0/a_1 for typical values of m.

m	$\frac{1}{2}$	$\frac{1}{3}$	1
a_0/a_1	0.89	0.31	0

with

$$q=[r^2+r'^2-2rr'\cos(\varphi-\varphi')]^{\frac{1}{2}}. \tag{5.23}$$

Carrying out the integration, we obtain[14]

$$\int_{-\infty}^{+\infty}G(\mathbf{r},r')dz'=C_m/q^{m+2} \tag{5.24a}$$

where

$$C_m=\frac{ma_m}{2^{3+m}}\frac{(m+1)!}{[(m+1)/2]!}. \tag{5.24b}$$

Introducing (5.24a) into (5.5), we obtain

$$E(\mathbf{r})=\int_{\text{Ext}}(C_m/q^{m+2})d\sigma' \tag{5.5'}$$

where the subscript "Ext" denotes integration over the cross-sectional area exterior to a circle of radius R. (When this subscript is absent, the integration is to be taken over the area of the circle, itself.)

From the form of (5.5') and (5.24a) we see that the integrands of all the terms in (5.1) are independent of z; hence, integration with respect to this variable may be ignored and we obtain

$$g=\frac{\left[\int\int_{\text{Ext}}n^2(r)(C_m/q^{m+2})d\sigma'd\sigma+\frac{1}{2}\int\int[n(r)-n(r')]^2(C_m/q^{m+2})d\sigma d\sigma'\right]}{\int n^2(r)d\sigma}. \tag{5.1'}$$

For the variational treatment of (5.1'), we choose for $n(r)$ a two-parameter "parabolic" function,

$$n(r)=a_0n_0(r)+a_1n_1(r)=a_0+a_1(1-r^2/R^2) \tag{5.25}$$

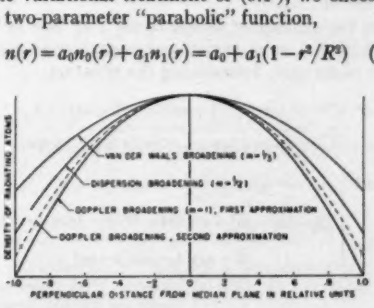

Fig. 1. Spatial distributions of radiating atoms in an infinite slab for different spectral line shapes.

[14] E. Jahnke and F. Emde, *Tables of Functions* (Dover Publications, New York, 1945), Fourth Edition, p. 21, first equation.

TABLE III. g_0, g_1, and g_{01} in units of a_m/R^m for typical values of m.

m	$\frac{1}{3}$	$\frac{1}{2}$	1
g_0	0.964	1.376	∞
g_1	0.893	1.143	1.60
g_{01}	0.880	1.115	1.60

and obtain

$$g=\sum_{i,j=0,1} a_i a_j K_{ij}{}^C/\sum_{ij}{}' a_i a_j H_{ij}{}^C \tag{5.26}$$

with

$$K_{ij}{}^C=\int\int_{\text{Ext}} n_i(r)n_j(r)(C_m/q^{m+2})d\sigma' d\sigma + \tfrac{1}{2}\int\int [n_i(r)-n_i(r')][n_j(r)-n_j(r')] \times (C_m/q^{m+2})d\sigma d\sigma' \tag{5.27}$$

and

$$H_{ij}{}^C=\int n_i(r)n_j(r)d\sigma. \tag{5.28}$$

The $H_{ij}{}^C$ are readily obtained; the more tedious evaluation of the $K_{ij}{}^C$ is relegated to Appendix B. The results may be expressed as follows. If

$$K_{ij}{}^C=\frac{\pi^2}{2^{2+m}}\frac{a_m}{R^{m-2}}\frac{(1+m)!}{[\frac{1}{2}(1+m)]!^2}\frac{(1-m)!}{[1-\frac{1}{2}m]!^2}k_{ij} \tag{5.29}$$

and

$$H_{ij}{}^C=\pi R^2 h_{ij} \tag{5.30}$$

we have

$$\begin{aligned} k_{00}&=(2-m)/(1-m) & h_{00}&=1\\ k_{01}&=4/(4-m) & h_{01}&=\tfrac{1}{2}\\ k_{11}&=16/(4-m)(6-m) & h_{11}&=\tfrac{1}{3}. \end{aligned} \tag{5.31}$$

These expressions for the k_{ij} are fully equivalent to the appendix relations (6B), (8B), and (13B) for the $K_{ij}{}^C$. In the text version, the constant C_m has been eliminated with use of (5.24b).

The two-parameter escape factor may now be determined by the same variational procedure as was used in the plane case. Introducing the notation,

$$g_m{}^C=\frac{\pi}{2^{2+m}}\frac{(1+m)!}{[\frac{1}{2}(1+m)]!^2}\frac{(1-m)!}{[1-\frac{1}{2}m]!^2}\frac{a_m}{R^m} \tag{5.32}$$

we find

$$g_{01}=g_m{}^C\left[\frac{24-8m-m^3-m(304-96m+16m^2+m^4)^{\frac{1}{2}}}{(1-m)(4-m)(6-m)}\right]. \tag{5.33}$$

For the purposes of comparison we give here the one-parameter escape factors

$$g_0=K_{00}{}^C/H_{00}{}^C=g_m{}^C[1-\tfrac{1}{2}m]/(1-m) \tag{5.34}$$

and

$$g_1=K_{11}{}^C/H_{11}{}^C=g_m{}^C 24/(4-m)(6-m). \tag{5.35}$$

In Table III we present the numerical values of g_0, g_1, and g_{01} in units of a_m/R^m for $m=\frac{1}{3}$, $\frac{1}{2}$, and 1.

6. SUMMARY OF RESULTS

In the foregoing sections, the escape factor g has been computed for a variety of line shapes and for two different enclosure geometries. These results will now be summarized.

A. Doppler-Broadening

Here

$$k(\nu)=k_0\exp[-\{(\nu-\nu_0)/\nu_0\}(c/v_0)^2] \tag{6.1}$$

where k_0 is given by (3.2). We have, for plane-parallel geometry

$$g=1.875/k_0L(\pi\log k_0L)^{\frac{1}{2}} \tag{6.2}$$

whereas, for the cylindrical case

$$g=1.60/k_0R(\pi\log k_0R)^{\frac{1}{2}}. \tag{6.3}$$

B. Impact-Broadening

$$k(\nu)=\frac{k_p}{1+[4\pi(\nu-\nu_0-\beta\rho)/\gamma_p]^2} \tag{6.4}$$

where k_p is given by (3.4). The expressions for g then read

$$g=1.150(\pi k_pL)^{-\frac{1}{2}} \tag{6.5}$$

and

$$g=1.115(\pi k_pR)^{-\frac{1}{2}}. \tag{6.6}$$

C. Statistical-Broadening

Starting from the binary interaction law,

$$\Delta\nu_p=\frac{C_n}{R^n} \tag{6.7}$$

one obtains

$$k(\nu)=\kappa\frac{4\pi N'}{n}\frac{C_n{}^{2/n}}{(\Delta\nu)^{(1+2/n)}}, \tag{6.8}$$

where N and N' are the densities of absorbing and perturbing atoms and where κ is given by (2.7). We then have for the two geometries,

$$g=\frac{3a_m/L^m[10-m-m^3-m(101-40m+2m^2+m^4)^{\frac{1}{2}}]}{(1-m^2)(2-m)(3-m)(5-m)} \tag{6.9}$$

and

$$g=\frac{\pi}{2^{2+m}}\frac{(1+m)!}{[\frac{1}{2}(1+m)]!}\frac{(1-m)!}{(1-\frac{1}{2}m)!}\frac{a_m}{R^m} \times\left[\frac{24-8m-m^3-m(304-96m+16m^2+m^4)^{\frac{1}{2}}}{(1-m)(4-m)(6-m)}\right]. \tag{6.10}$$

In these expressions, $m=3/(3+n)$ and, from Eq. (4.6)

$$a_m=\left(\frac{n}{3+n}\right)\left(-\frac{n}{3+n}\right)!C^{3/(3+n)}\times\left(\frac{4\pi N'}{n}\right)^{n/(3+n)}\left(\frac{\lambda_0^2 N}{8\pi}\frac{g_2}{g_1}\gamma\right)^{-3/(3+n)}.$$

APPENDIX A

One of the fundamental assumptions of our theory is the proportionality relationship (2.2),

$$P(\nu)\propto k(\nu), \tag{1A}$$

between the emission spectrum of a given excited atom, $P(\nu)$, and the absorption coefficient $k(\nu)$. The latter quantity is determined by the nature of the absorbing atoms, their thermal motion and their interaction with other atoms. The emission spectrum, on the other hand, depends not only on atomic parameters, but also on the mechanism of excitation. In the case of natural broadening, for example, excitation of a given atom by a "monochromatic" beam (whose spectral width is small compared to the natural width) produces an emission spectrum identical with that of the incident beam. In order to obtain $P(\nu)$ proportional to $k(\nu)$ it is necessary to excite the atom in a "nonresonant" manner. This is accomplished either by collisions with material particles—atoms, ions, or electrons—or by optical excitation with "white" radiation, i.e., radiation whose spectrum is broad compared to the absorption spectrum.[14]

A similar although less drastic situation prevails in the case of doppler-broadening. Here, monochromatic stimulation evokes an emission spectrum which, while not itself monochromatic, still deviates greatly from the typical doppler absorption line shape. As in the natural broadening case, an exact proportionality between $P(\nu)$ and $k(\nu)$ is obtained only with nonresonant excitation. Thus, in both cases the emission spectrum depends appreciably upon the spectrum of the exciting radiation.

Now, in an imprisonment experiment the excitation agent is the imprisoned radiation itself. The latter, in turn, consists of radiation emitted by excited atoms throughout the enclosure. The spectrum of the exciting radiation is thus not known *a priori;* its determination forms an integral part of the whole imprisonment analysis. An analysis of this type for the doppler case and a plane-parallel enclosure (of width L) was carried out in Part B of the Appendix of I (pp. 1229–1233). It was found that over most of the enclosure —exclusive of a small peripheral region—the spectral intensity of imprisoned radiation is essentially constant in a domain of frequencies for which $k(\nu)L>1$. Outside this range the intensity drops off rapidly to negligibly small values. With a distribution of this type for the spectrum of the exciting radiation, $P(\nu)$ and g were calculated. Comparison of the results with (3.1) and (1.1) demonstrated the approximate applicability of (1A) to doppler-broadened resonance radiation.

In the case of impact pressure broadening, as was shown in Part A of the Appendix of I (pp. 1227–1229), $P(\nu)$ is almost independent of the mechanism of excitation. Namely, even with monochromatic excitation, $P(\nu)$ turns out to be essentially proportional to $k(\nu)$. In this appendix we present a semi-quantitative argument for the applicability of (1A) to the case of statistical broadening; a detailed quantitative discussion may be found in a Westinghouse Research Laboratories report.[15]

As pointed out in Sec. III of this paper, the fundamental quantity of the statistical theory is the instantaneous emission-absorption frequency, $\nu(t)$, of a given atom. $\nu(t)$ differs from the unperturbed frequency, ν_0, of an *isolated* atom because of collisions with neighboring atoms. In the course of time, $\nu(t)$ will range over a continuum of frequencies. The occurrence probability defined (see Sec. III) as the fraction of time for which $\nu(t)$ is contained between ν and $\nu+d\nu$, gives directly both the absorption coefficient and the emission spectrum arising from white excitation.

Let us suppose, in accordance with the procedure used in the Appendix of I, that the atoms are excited by a monochromatic beam of frequency ν_1. The statistical theory states that a given atom absorbs energy from the beam only at times t_i such that $\nu(t_i)=\nu_1$. Now, after each such absorption, the atom radiates with an intensity proportional to $\exp[-\gamma(t-t_i)]$; the spectrum of the emitted radiation is thus determined essentially by the variation of $\nu(t)$ over a time interval $\sim 1/\gamma$. The question of the dependence of $P(\nu)$ upon the excitation frequency may then be put in the following form. To what extent is the variation of $\nu(t)$ over the time interval, $1/\gamma$, dependent upon the circumstance that the initial value of $\nu(t)$ is ν_1, i.e., that the atom acquires its excitation energy when $\nu(t)=\nu_1$?

Now, as in Sec. III, we assume that the time dependence of $\nu(t)$ is determined mainly by binary collisions. During each of these $\nu(t)$ is equal to ν_0 plus a perturbation of the form (3.6). Excluding the very special case of $\nu_1=\nu_0$, we observe that absorption takes place only during a collision, in fact, only during those collisions in which $\nu(t)$ attains the value ν_1. This stipulation implies a nonrandom situation in the time interval immediately subsequent to excitation. Namely, the "absorption" collision, during which the newly excited atom begins radiating, is not a random encounter but is selected in a special way. (For example, if $\nu_1-\nu_0$ is large, absorption takes place only in those encounters in which the distance of closest approach is sufficiently small as determined by (3.6).) Hence, the possibility of a correlation between $\nu(t)$ and ν_1 during the absorption collision cannot be ruled out. On the other hand, when the absorption collision is terminated, the further density of $\nu(t)$ becomes the responsibility of new binary encounters, which are completely uncorrelated with each other, or with the absorption collision. Thus, the excited atom "remembers" the excitating frequency at most for an interval of the order of a "time of collision," τ. We thus arrive at the qualitative conclusion that, if $\tau\ll 1/\gamma$, the influence of the exciting frequency on the emission spectrum is small. Now this condition is almost always obeyed in practice ($\tau\sim$collision radius/atomic velocity $\sim<10^{-10}$ sec, $1/\gamma\sim 10^{-8}$ sec); the emission spectrum is thus determined predominantly by collisions whose parameters are uncorrelated with the absorption frequency and, hence, must obey (1A).

APPENDIX B

In the evaluation of the integrals in (5.27) use is made of the relation,

$$1/q^p=[1/(2-p)^2]\nabla^2(1/q^{p-2})=[1/(2-p)]^2\nabla^{2_2}(1/q^{p-4}), \tag{1B}$$

where ∇^2 and ∇^{2_2} are the two-dimensional laplacian operators involving differentiation with respect to r, φ and r', φ', respectively. Thus

$$K_{00}{}^C=\int\int_{\Sigma 1}(C_m/q^{m+2})d\sigma' d\sigma=\int\int_{\Sigma 1}(C_m/m^2)\nabla^{2_2}q^{-m}d\sigma' d\sigma$$

which, with the aid of Gauss' theorem, can be transformed into

$$K_{00}{}^C=-(C_m/m^2)\int\int_s(\partial/\partial r')q^{-m}ds'd\sigma$$

$$=-(C_m/m^2)\int_\sigma ds'(\partial/\partial r')\int q^{-m}d\sigma, \tag{2B}$$

where the subscript "s" indicates a line integration over the circumference of the cross-sectional circle. By further use of (1B) and Gauss' theorem, we obtain

$$K_{00}{}^C=-\frac{C_m}{m^2(2-m)^2}\int\int_\sigma(\partial/\partial r)(\partial/\partial r')q^{-m+2}ds ds'. \tag{3B}$$

The double line integrals of the type exemplified by (3B)can

[15] Westinghouse Research Laboratories, scientific paper 1501, available upon written request.

readily be evaluated; in fact,

$$\int\int_s (\partial/\partial r)(\partial/\partial r')q^{-p}dsds' = \frac{\pi^2\rho^2}{R^p}\frac{(-\rho)!}{(-\frac{1}{2}\rho)!^2}\frac{\rho+2}{\rho+1} \tag{4B}$$

as we shall now verify.

Differentiating with respect to r and r' and setting both these variables equal to R, we obtain for the left-hand side of (4B) the expression,

$$\int_0^{2\pi}\int_0^{2\pi}\{\rho(1+\rho\sin^2[\tfrac{1}{2}(\varphi-\varphi')])/(2R)^{\rho+2}\sin^{\rho+2}[\tfrac{1}{2}(\varphi-\varphi')]\}R^2d\varphi d\varphi'.$$

One now introduces the transformation $\varphi'=\varphi+\theta$ and integrates with respect to φ, obtaining

$$\frac{2\pi\rho}{2^{\rho+2}R^\rho}\int_0^{2\pi}\frac{1+\rho\sin^2\frac{1}{2}\theta}{\sin^{\rho+2}\frac{1}{2}\theta}d\theta = \frac{2\pi\rho}{(2R)^\rho}\int_0^\pi\frac{1+\rho\sin^2X}{\sin^{\rho+2}X}.$$

The remaining integral is evaluated with the aid of the formula quoted in reference 12; minor algebraic manipulation of the resultant factorial terms then yields (4B).

Similarly one may readily show that

$$\int\int_s(\partial/\partial r)q^{-p}dsds' = \int\int_s(\partial/\partial r')q^{-p}dsds' = -\frac{2\pi^2\rho}{R^{p-1}}\frac{(-\rho)!}{(-\frac{1}{2}\rho)!^2}. \tag{5B}$$

Equation (5B) will be used in the evaluation of the other $K_{0l}{}^C$.

Inserting (4B) into (3B), we obtain, after elementary algebraic operations,

$$K_{00}{}^C = \frac{2\pi^2C_m}{mR^{m-2}}\frac{(1-m)!}{(1-\frac{1}{2}m)!^2}\frac{1-\frac{1}{2}m}{1-m}. \tag{6B}$$

To calculate $K_{01}{}^C$ we first apply (1B) and Gauss' theorem to the "primed" integration variables, obtaining

$$K_{01}{}^C = -\frac{C_m}{m^2}\int_s ds'\frac{\partial}{\partial r'}\int\frac{1-(r/R)^2}{q^m}d\sigma$$

We then perform two integrations-by-parts with respect to the unprimed variables, wherein we integrate $1/q^m$ and differentiate $1-(r/R)^2$ with the aid of (1B) and Green's formula,

$$\int(u\nabla^2v - v\nabla^2u)d\sigma = \int_s[u(\partial v/\partial n) - v(\partial u/\partial n)]ds. \tag{7B}$$

This procedure yields

$$K_{01}{}^C = \frac{-(2/R)C_m}{(2-m)^2m^2}\int\int_s\frac{\partial}{\partial r'}\left[\frac{1}{q^{m-2}} - \frac{(2/R)}{(4-m)^2}\frac{\partial}{\partial r}\frac{1}{q^{m-4}}\right]dsds'.$$

The integrals to be evaluated are of the forms of (4B) and(5B). We obtain

$$K_{01}{}^C = \frac{4\pi^2C_m}{mR^{m-2}}\frac{(1-m)!}{(1-\frac{1}{2}m)!^2}\frac{1}{4-m}. \tag{8B}$$

The first term of $K_{11}{}^C$ is evaluated in much the same way except that three partial integrations have to be performed with respect to the unprimed variables. One finds

$$K_{11}{}^{C(1)} = \int E(r)[1-(r/R)^2]d\sigma = \frac{8C_m}{m^2(2-m)^2(4-m)^2R^2}\int\int_s\frac{\partial}{\partial r'}\times\left[\frac{\partial}{\partial r}\left\{\frac{1}{q^{m-4}} - \frac{8}{(6-m)^2R^2}\frac{1}{q^{m-6}}\right\} - \frac{4}{R}\frac{1}{q^{m-4}}\right]dsds'$$

$$K_{11}{}^{C(1)} = \frac{\pi^2C_m}{mR^{m-2}}\frac{(2-m)!}{(2-\frac{1}{2}m)!^2}\frac{8}{6-m}. \tag{9B}$$

Finally, the second term of $K_{11}{}^C$,

$$K_{11}{}^{C(2)} = \left(\frac{C_m}{2R^4}\right)\int\int\left[\frac{(r^2-r'^2)}{q^{m+2}}\right]d\sigma ds' = \frac{C_m}{2R^4}\int_0^R\int_0^R\int_0^{2\pi}\int_0^{2\pi}\frac{(r^2-r'^2)rr'drdr'd\varphi d\varphi}{[r^2+r'^2-2rr'\cos(\varphi-\varphi')]^{\frac{1}{2}m+1}}$$

is evaluated as follows. We express r' and φ' in terms of new variables, $x=r'/r$ and $\theta=\varphi'-\varphi$, and integrate with respect to φ obtaining

$$K_{11}{}^{C(2)} = \frac{\pi C_m}{R^4}\int_0^R dr\int_0^{R/r}dx\int_0^{2\pi}\frac{r^{5-m}(1-x^2)^2drxdxd\theta}{(1+x^2-2x\cos\theta)^{\frac{1}{2}m+1}}.$$

The form of the integrand of this expression indicates the desirability of inverting the order of the integrations over x and r. Performing this inversion and integrating with respect to r, we obtain

$$K_{11}{}^{C(2)} = \frac{\pi C_m}{(6-m)R^{m-2}}\left[\int_0^{2\pi}\int_0^1\frac{(1-x^2)^2xdxd\theta}{[1+x^2-2x\cos\theta]^{\frac{1}{2}m+1}} + \int_0^{2\pi}\int_1^\infty\frac{(1-x^2)^2dxd\theta}{x^{5-m}[1+x^2-2x\cos\theta]^{\frac{1}{2}m+1}}\right]. \tag{10B}$$

With the aid of the transformation $x=1/y$, we can readily establish the equality of the two double integrals in (10B); we then have

$$K_{11}{}^{C(2)} = \frac{2\pi C_m}{(6-m)R^{m-2}}\int_0^1\int_0^{2\pi}\frac{(1-x^2)^2xdxd\theta}{[1+x^2-2x\cos\theta]^{\frac{1}{2}m+1}}$$

or

$$K_{11}{}^{C(2)} = (2\pi C_m/(6-m)R^{m-2})\int_{s_1}[(1-x^2)^2/q^{m+2}]d\sigma \tag{11B}$$

where $q=(1+x^2-2x\cos\theta)^{\frac{1}{2}}$ and the subscript s_1 indicates integration with respect to a circle of radius unity. The technique for evaluating (11B) is the same as has already been employed; three integrations-by-parts yield

$$K_{11}{}^{C(2)} = \frac{16\pi^2C_m}{m^2(2-m)^2(6-m)R^{m-2}}\times\int_0^{2\pi}\left[\frac{\partial}{\partial x}\left\{\frac{1}{q^{m-2}} + \frac{8}{(4-m)^2}\frac{1}{q^{m-4}}\right\} - \frac{4}{q^{m-2}}\right]_{x=1}d\theta.$$

One now utilizes Eqs. (4B) and (5B), obtaining

$$K_{11}{}^{C(2)} = \frac{4\pi^2C_m}{(2-m)(6-m)R^{m-2}}\frac{(2-m)!}{(2-\frac{1}{2}m)!^2}. \tag{12B}$$

Adding (9B) and (12B), we then have

$$K_{11}{}^C = \frac{16\pi^2C_m}{m(6-m)(4-m)R^{m-2}}\frac{(1-m)!}{(1-\frac{1}{2}m)!^2}. \tag{13B}$$

Substituting the text Eqs. (5.24B) into Eqs. (6B), (8B), and (13B), we obtain the results listed in the text Eqs. (5.29) and (5.31).

Cosmic Rays at Airplane Altitudes*

A. T. Biehl and H. V. Neher
California Institute of Technology, Pasadena, California
(Received May 25, 1951)

A continuation of experiments made in a B-29 airplane to investigate the properties of cosmic rays is herein reported. Part I describes results on the latitude effect at 30,000 ft measured with counter telescopes and with both shielded and unshielded ionization chambers, from 64° geomagnetic north to the magnetic equator. A considerably larger latitude effect for the shielded ionization chamber than with the unshielded one or with counter telescopes indicates a definite change in the character of the radiation as one goes toward the equator at this altitude. The "knee" of the latitude effect is investigated in detail by a number of similar flights. Part II describes measurements made on density and formation of extended air showers. The apparatus was of such a nature as to be sensitive to relatively sparse showers. The densities obtained can be fitted to an integral power law spectrum with a negative exponent of 1.50±0.05 for an altitude of 30,000 ft. Intensity-altitude curves are presented, showing that the development of smaller showers takes place nearer the top of the atmosphere than does the development of large showers. Derived zenith-angle dependencies at various altitudes are also given.

I. INTRODUCTION

DURING the summers of 1948 and 1949, a series of flights was made in a B-29 airplane in order to continue the studies of cosmic-ray intensities previously reported.[1] The purposes of these flights were to supplement those parts that required more detailed study. In particular (Part I), it was thought desirable (1) to check the latitude effects obtained with an unshielded Geiger tube telescope and ionization chamber, (2) to investigate further the latitude effect of an electroscope shielded by 11 cm of lead, and (3) to study the knee of the latitude curve in detail. Part II contains information on extended shower densities and intensities.

II. FLIGHT SCHEDULE

Two series of flights were made; one during the summer of 1948, and the other during the summer of 1949. The 1948 flights were all local flights from Inyokern, California, along the 117° W meridian, and were made for the purpose of investigating the "knee" of the latitude curve. The 1949 flights consisted of a trip to the magnetic equator, in Peru, and then up to the Great Slave Lake region in Canada. Table I gives the schedule of the individual flights. In general, the procedure during the individual flights was as previously described,[1] and only deviations from it will be mentioned.

III. DESCRIPTION OF APPARATUS

A. Equipment For Investigating the "Knee" of the Latitude Curve (Summer, 1948)

This equipment consisted of two unshielded telescopes of the type previously used,[1] and an unshielded ionization chamber. The telescopes were interleaved to conserve space, but were otherwise completely independent.

B. Equipment Used During the Summer of 1949

This equipment consisted of two unshielded telescopes, an unshielded and a shielded (11-cm lead) ionization chamber, and a shower array. In our previous experiments the equipment was converted from the former balloon-born apparatus.[2] Some difficulty was encountered with this type of battery-operated electronics and lightly constructed telescopes. For these reasons new equipment was constructed, similar to the old, but of a more rugged and permanent nature.

The unshielded ionization chamber was the same one used in former years, while the shielded ionization chamber consisted of an identical instrument incased completely inside a 11-cm lead shield.

C. Shower Density Equipment (Summer, 1949)

The shower measuring equipment consisted of six trays of Geiger tubes, similar to those used in the telescopes, so arranged that many physical spacings and coincidence arrangements could be used. Two quadruple coincidence channels were provided for, and coincidences between these two channels could be measured. The dispositions used are given in Fig. 1. The whole array was placed against the ceiling of the plane in order to minimize the effects of showers formed in the skin of the plane.

PART I. LATITUDE EFFECT

The measured latitude effect, both with unshielded ionization chamber and vertical counter telescope, was very close to the same as that measured during a similar flight made in 1948.[1] In fact, in each case the agreement in the measured values of the latitude effect was within 0.5 percent of being the same for the two series of flights. This agreement means that at the altitude at which these experiments were made (310 g cm^{-2}) the relative intensity of the primary radiation which could

* Supported in part by the joint program of the ONR and AEC.
[1] Biehl, Neher, and Roesch, Phys. Rev. **76**, 914 (1949).
[2] Biehl, Montgomery, Neher, Pickering, and Roesch, Revs. Modern Phys. **20**, 353 (1948).

TABLE I. Flight record.

Flight number	Date	Starting time	Finishing time	From	To
1-B-48	July 20, 1948	1300 GCT	2100 GCT	Inyokern	Inyokern
2	July 26	1700	2200	Inyokern	Inyokern
3	July 28	1600	2200	Inyokern	Inyokern
4	August 11	1700	2300	Inyokern	Inyokern
5	August 12	1700	2300	Inyokern	Inyokern
6	August 17	1800	2200	Inyokern	Seattle
7	September 23	2000	2300	Inyokern	Inyokern
8	October 21	1700	2400	Inyokern	Inyokern
1-B-49	August 1, 1949	1600	2400	Inyokern	Tampa
2	August 5	1500	2100	Tampa	Panama
3	August 6	1200	1800	Panama	Lima
4	August 9	1500	2200	Lima	Lima
5	August 13	1300	2100	Lima	Lima
6	August 16	1500	1800	Lima	Lima
7	September 20	1500	2100	Lima	Panama
8	September 21	1200	1900	Panama	San Antonio
9	September 21	0000	0400	San Antonio	Inyokern
10	October 27	2000	0200	Inyokern	Great Falls
11	October 29	1100	1900	Great Falls	Great Falls
12	October 31	2100	0600	Great Falls	Inyokern

penetrate to this depth at 51° N and at the equator was the same in August of 1949 as in June of 1948. These flights covered a range of latitude from 64° N to the geomagnetic equator in Peru.

However, the latitude effect with the shielded ionization chamber was found to be considerably larger than without the shield. As shown in Fig. 2, the ionization inside the 11-cm lead shield dropped from a value of 30.5 ions cm^{-3} sec^{-1} $atmos^{-1}$ of air at geomagnetic latitude 51° N to 16.2 at the geomagnetic equator. The unshielded ion chamber gave a decrease of 36.1 percent between these two latitudes compared with the above value of 47 percent for that shielded with 11 cm of lead.

The larger latitude effect for the shielded ion chamber may be explained by a change in the character of the radiation at this altitude as one goes toward the equator. From the work of Simpson, Uretz,[3] and others, it is known that the latitude effect in nuclear events is much larger at this altitude than in the total radiation. Such events will undoubtedly be enhanced by the presence of the 11-cm lead shield.

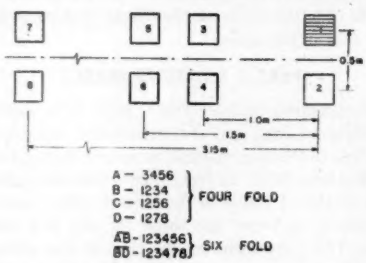

FIG. 1. Disposition of shower array. Each tray of Geiger counters contains eight counters connected in parallel. Coincidence arrangements are as indicated.

[3] J. A. Simpson and R. B. Uretz, Phys. Rev. 76, 569 (1949).

The summer flights of 1948 were made under as nearly identical conditions as possible along the 117° W meridian, between the borders of Mexico and Canada. This was done in order to compare the latitude effect and the relative intensities obtained on successive days. Figures 3 and 4 show the data obtained for the average of the two counter telescopes over ten-minute periods and for the ion chamber. It should be noted that all flights except No. 5 were made at 33,000 ft,—No. 5 having been made at 30,500 ft.

An examination of the data plotted in Figs. 3 and 4 indicates that there is considerable choice as to the manner in which the curves may be drawn through the experimental points. The curves as shown are merely what appears to the authors to be a good fit, but are not necessarily completely justified by the experimental points. For example, flight 1 of Fig. 3 appears to have two plateaus between about 36° to 40°, and 42° to 48°, and possibly a third below 34° geographic latitude. It is interesting to note the correspondence of this particular telescope data with that of the electroscope taken on this same flight. Again, two plateaus are indicated, but the knees do not occur at the same latitude.

In general, it appears that there is fair agreement between corresponding telescope and electroscope data for each of the flights made on the same day (note points going north, and also going south). This is well illustrated by flight 4, where both methods of intensity measurements yielded values considerably below the average of the other flights. However, the lack of agree-

ment between flights made on different days is too great to be experimental.

Such fluctuations have been reported previously,[4] particularly in connection with balloon flights. They are interpreted as being caused by variations in the primary radiation, and are more pronounced at the higher altitudes.

PART II. WIDE SHOWERS

By the investigation of extensive air showers at B-29 altitudes, it was hoped to gain information which will lead to a better understanding of these complex phenomena. In particular, in this set of experiments an attempt was made to investigate three effects:

A. The shower density as a function of spread of counters at certain fixed altitudes;

B. The development of showers of different size as measured by the altitude effect;

C. The latitude effect for extensive showers.

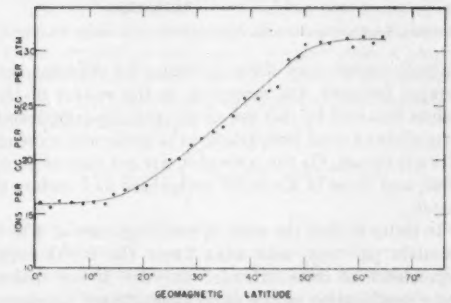

FIG. 2. Latitude effect obtained with an ionization chamber shielded with 11 cm of lead. Points are from both north and south-bound flights averaged over each two degrees of latitude. No comparable data were taken on the June, 1948, series of flights.

A. Shower Density

As pointed out by Cocconi *et al.*,[5] there are two simple methods of measuring shower density by means of coincidence counter arrangements. One (method I) is to compare the coincidence counting rates between various numbers of trays having the same total geometrical spread. In our case, fourfold to sixfold coincidence ratios were used. The other (method II) is to change the sensitive counter area of each tray of counters and compare the counting rates. In using this latter method, the number of counters per tray was reduced from the normal eight to four, by removing counters 2, 4, 5, and 7, as numbered from either side of the tray. To a first approximation this would reduce the sensitive area of each tray by a factor of one-half. However, owing to the zenith-angle dependence of the intensity of air showers,

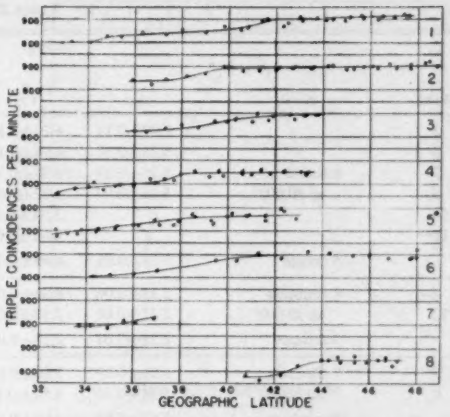

FIG. 3. The counting rates of the average of the two cosmic-ray telescopes are plotted as a function of geographic latitude for ten-minute intervals. All flights were made along the 117° W longitude. Note that flight 5 was made at an altitude of 30,500 ft, and all others at 33,000 ft. Crossed solid circles are going north, solid circles going south. To change from geographic to geomagnetic latitude at this longitude, add approximately seven degrees.

a shading effect takes place so that the effective ratio of areas is closer to 0.6. The methods of approximating this ratio will be treated in more detail later.

Table II gives a tabulation of the counting rates in counts-per-minute taken on each of the flights while the plane was maintained at a constant altitude. The probable errors for each rate and an average of the rates for similar flights are given. Care must be used in comparing counting rates, as in most cases they are not statistically independent. A first inspection shows that as the array is spread further out along the length of the plane, a decrease of about 5 percent per meter occurs in the counting rate. This fact allows an extrapolation to be

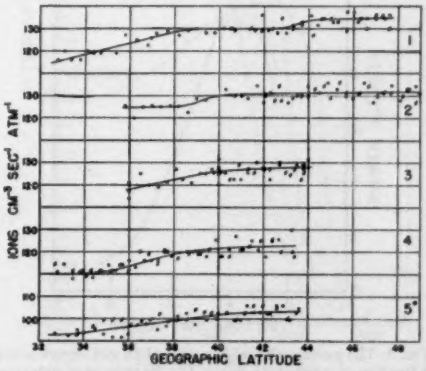

FIG. 4. The ionization as a function of geographic latitude is plotted for five-minute intervals, as obtained by an unshielded ionization chamber. Crossed solid circles are going north, solid circles are going south.

[4] Millikan, Neher, and Pickering, Phys. Rev. **66**, 295 (1944). See also: Biehl, Montgomery, Neher, Pickering, and Roesch, Revs. Modern Phys. **20**, 360 (1948).

[5] Cocconi, Loverdo, and Tongiorgi, Phys. Rev. **70**, 841 (1946).

TABLE II. Shower data.

Flight	Notes	Rates (counts/minute) 4 fold *A* ½ m	*B* 1 m	*C* 1½ m	*D* 3.15 m	6 fold *AB* 1½ m	*BD* 3.15 m
2		5.09±0.11	4.79±0.10	...	...	2.92±0.08	...
3		5.25±0.10	4.94±0.10	...	...	3.02±0.08	...
7	8 counters	5.26±0.11	4.92±0.10	...	...	3.04±0.08	...
8	at 30,000′	5.31±0.09	4.92±0.09	...	...	3.02±0.07	...
10		...	5.04±0.10	4.87±0.10	...	2.92±0.08	...
11		...	4.91±0.08	...	4.64±0.08	...	2.85±0.07
	Average	5.24±0.05	4.89±0.08	4.87±0.10	4.64±0.08	2.986±0.035	2.85±0.07
4	4 counters	2.32±0.06	2.25±0.06	...	...	1.58±0.05	...
12	at 30,000′	2.17±0.05	2.12±0.05	...	...	1.28±0.04	...
	Average	2.23±0.04	2.18±0.04	...	...	1.405±0.03	...
5	8 counters	5.64±0.09	5.20±0.09	...	...	3.10±0.07	...
9	at 22,700′	5.24±0.10	4.84±0.10	...	...	3.01±0.08	...
	Average	5.47±0.07	5.02±0.07	...	...	3.07±0.05	...
5	8 counters at 35,000′	5.47±0.07	5.02±0.07			3.07±0.05	

made so that one may estimate with a fair degree of accuracy the counting rates of those arrays that time or facilities did not permit to be measured directly.

Figure 5 gives the altitude-dependence curve of extended air showers obtained from data taken on flights 2, 3, 5, 6, 7, 8, 9. Those points shown at 22,500 ft; 30,000 ft, and 25,000 ft were computed from the data taken while the plane maintained constant altitude by taking a weighted average of all data obtained for each array on each flight. The intermediate points were obtained by a similar averaging process from data taken while climbing to altitude. It is realized that such an averaging process is not strictly justified in that the altitude curves may differ in shape for different size arrays; however, the reduction in the scatter of the points obtained by this use of all available comparable data allows a good comparison to be made with existing altitude curves. On the same plot, are our data of June, 1948, and those of Kraybill[6] normalized at 6 meters of water.

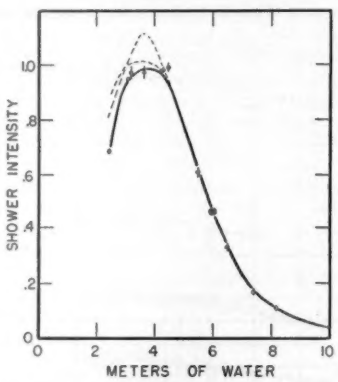

FIG. 5. The average shower intensity of all size arrays is shown as a function of atmospheric depth. For the purpose of comparison, our data of June, 1948 (higher dotted curve), and that of Kraybill (lower dotted curve) are also shown. Normalization has been made at six meters of water. Counting rates are in terms of the rate at the maximum of the curve.

In order to find the ratio of counting rates of 4 to 8 counters per tray, one must know the zenith-angle dependence of these extended showers. If one makes some modification of the usual assumptions[7] necessary to apply the generalized Gross transformation, it is possible to obtain the directional intensity of extended air showers.[8] These assumptions are (1) that the array may be represented by a horizontal flat surface, and (2) that the lateral spread of shower particles at a given depth is inversely proportional to the air density. Both of these assumptions are known to be in error, but it is believed the total error introduced into the final results will be small. Under these assumptions, together with an integral power law spectrum of $k\Delta^{-\delta}$, it can be shown that such a Gross transformation leads to a directional intensity at the vertical given by

$$N_0(h, N)=\tfrac{1}{2}\pi[(3\delta-1)N-h(dN/dh)],$$

where h is the atmospheric depth, and N the counting rate of the shower array. By this means Fig. 6 is obtained from Fig. 5 where we have used a value of $\delta=1.5$. Since the corrections needed to find the ratio of counting rates of 4 to 8 counters per tray are small, the value of δ need not be known accurately for this purpose.

[6] H. L. Kraybill, Phys. Rev. **76**, 1093 (1949).
[7] See L. Janossy, *Cosmic Rays* (Clarendon Press, Oxford, 1948), p. 139.
[8] H. L. Kraybill, Phys. Rev. **77**, 410 (1950).

If we again use the foregoing assumption (2), it is possible to find the zenith-angle dependence for a fixed altitude. We then find that

$$N_0(h, \theta) = N_0(h/\cos\theta, N)[\cos\theta]^{2n-2}.$$

These assumptions yield the zenith-angle curves given in Fig. 7 for 35,000 ft, 30,000 ft, and 22,500 ft. As pointed out previously, it is necessary to know the zenith-angle dependence in order to compute the ratio of the effective area of the 4 and 8 counter trays. This can now be done using numerical integration and the curves of Fig. 7. Actually, it was found to be easier to determine the ratio empirically. This was done by tracing the shadow of the trays cast by a distant light source and finding the mean area over azimuth angles for various zenith angles. Then, by multiplying this mean area by the zenith-angle curves and integrating, the following ratios were found for the effective areas of 4 and 8 counter trays: 22,500 ft, 0.564; 30,000 ft, 0.584; 35,000 ft, 0.641.

Cocconi,[5] as well as Kraybill,[6] has shown that if one assumes that the frequency of occurrence of showers whose density of particles is greater than Δ can be represented by a power law $K\Delta^{-\delta}$, where K is a constant and Δ is the particle density, then the counting rate of an n-fold array is given by

$$C(n, A) = \delta \int_0^\infty (1-e^{-\Delta A})^n K\Delta^{-\delta-1}d\Delta,$$

where A is the effective area of each tray. It may readily be seen that method I is the case where A is held constant and n is varied (in this case the values of n are 4 and 6), and method II is the case where n is held constant and A varied. Table III gives the values of δ computed for these two methods.

The probable errors in the foregoing values of the exponent, δ, are estimated to be of the order of 0.05 by method I, and perhaps slightly higher by method II. Thus, it may be seen that a mean value of 1.50 ± 0.05 may be accepted for δ at 30,000 ft and 22,5000 ft, and 1.65 ± 0.05 for 35,000 ft. It is interesting to note how well methods I and II agree at 30,000 ft.

In attempting to compare this result with that of other experimenters, the difference in geometries must be borne in mind. This dependence on the experimental arrangement was first pointed out by Cocconi *et al.*,[5] and was shown to make comparison difficult. Nevertheless, they find a value of $\delta = 1.46$ near sea level, using counter areas comparable with ours. Kraybill,[6] with his apparatus under somewhat similar circumstances and altitude, finds a value of δ considerably higher (i.e., about 1.73). This difference is believed to be caused by the much larger relative areas used in this experiment, which gave counting rates about ten times as great as Kraybill's. This would make our apparatus more sensitive to the less dense showers.[9] This selectivity of showers with a certain density can perhaps be illustrated in another manner. In an earlier paper Kraybill[10] computes the average density of the showers detected in his apparatus to be $\frac{3}{4}$ particle per counter area (13 sq in.). A similar calculation for our apparatus

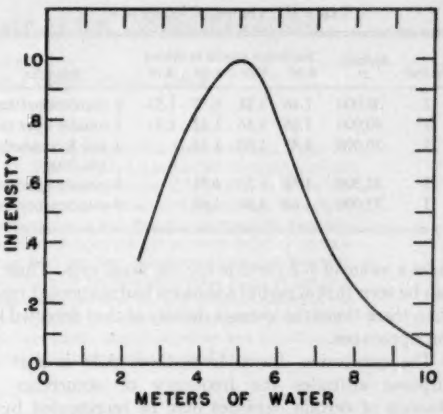

FIG. 6. Directional shower intensity at the vertical as a function of atmospheric depth, as obtained by a generalized Gross transformation of the curve given in Fig. 5.

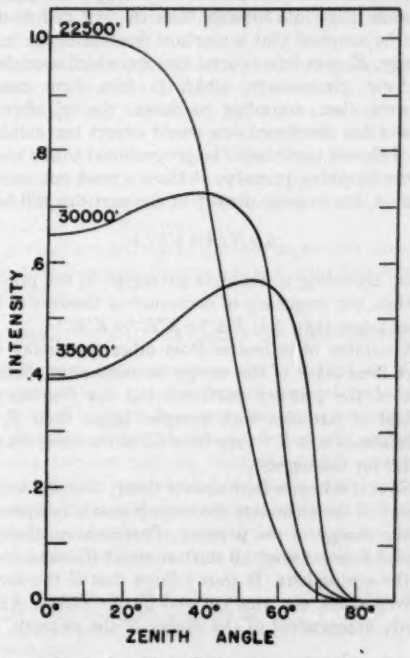

FIG. 7. Derived zenith-angle shower intensity curves for three different altitudes.

[9] See Fig. 6 of reference 5.

[10] H. L. Kraybill, Phys. Rev. 73, 632 (1948).

TABLE III. Computed values of δ.

Method	Altitude ft	Maximum spread in meters 0.50	1.00	1.50	3.16	Remarks
I	30,000	1.46	1.51	1.52	1.55	8 counters per tray
I	30,000	1.46	1.46	1.42	1.41	4 counters per tray
II	30,000	1.55	1.50	1.41		4 and 8 counters per tray
I	22,500	1.55	1.55	1.51		8 counters per tray
I	35,000	1.65	1.66	1.66		8 counters per tray

gives a value of 0.2 particle for the same area. Thus, it can be seen that Kraybill's showers had somewhat more than three times the average density of that detected by our apparatus.

The conclusion drawn from these data is that at airplane altitudes the frequency of occurrence of showers of certain densities may be represented by a power law whose exponent, δ, is close to that found at or near sea level. It is rather remarkable that this is so, since the showers at the higher altitude have not, in general, reached their maximum development, as they have at sea level.

Extensive showers are thought to be caused by primary particles with very high energy, which suffer nuclear collisions near the top of the atmosphere. In these interactions the major part of the energy of the primary appears to go into mesons, both charged and neutral. If it be assumed that a constant fraction of the initial energy, E, goes into neutral mesons, which soon decay to form gamma-rays, which in turn form cascade showers, then, according to shower theory, after the shower has developed one would expect the numbers, N, of shower particles to be proportional to the energy of the incoming primary. If these spread out over an area, A, the average density of the particles will be

$$\Delta = N/A = k'E/A. \tag{2}$$

Now, according to the data presented in the previous section, the frequency of occurence of showers of densities larger than Δ is $K\Delta^{-\delta} = K'E^{-\delta} = K'E^{-1.5}$.

A number of estimates from other cosmic-ray data have been made of the energy or momentum distribution of the primary particles. For the frequency of arrival of particles with energies larger than E, the estimates of n in E^{-n} vary from 1.5 at the lower energies to 1.9 for the highest.

Now, it is known from shower theory that the average energy of the secondary electrons is nearly independent of the energy of the primary. Furthermore, these extended showers must all start at about the same height in the atmosphere. It thus follows that if the shower arrives at all, the area covered by the shower will be nearly independent of the energy of the primary. It is to be expected then that the exponent of the density spectrum would be the same as that for the distribution in energy of the primary particles responsible for the showers. This appears to be approximately the case.

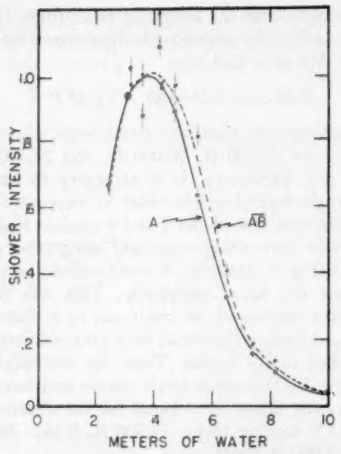

FIG. 8. Shower intensity as a function of atmospheric depth is shown for two different size arrays which have been normalized at 30,000 ft for comparison. Array A is four trays having a spread of one-half meter. Array AB is six trays having a spread of one and one-half meters. Notice the earlier development of the smaller array at high altitudes. The intensity is given in terms of the counting rate at the maximum of the curves.

B. Shower Development

Figure 8 shows a comparison of the altitude effect obtained for a wide and a narrow array. Curve A is that obtained for an array of one-half meter spread. It is interesting to note the manner in which the narrower showers appear to develop nearer the top of the atmosphere than the wider showers. This behavior is to be expected on the basis of current shower theories.

C. Latitude Effect for Extensive Showers

A casual inspection of Table II is sufficient to show that no latitude effect was observed for even the smallest array used. This is in conformity with that found previously,[1] and is what one would expect if the primary particles causing the showers have momenta above 2×10^{10} Bev/c.

In conclusion, the authors wish to thank the Office of Naval Research and the United States Air Forces for making these flights possible. Particularly, we express our appreciation to the officers and men stationed at Inyokern, California. We also wish to thank Dr. R. F. Christy for his many helpful discussions.

Neutrons Produced in the Atmosphere by the Cosmic Radiations*

J. A. SIMPSON
Institute for Nuclear Studies, University of Chicago, Chicago, Illinois
(Received February 19, 1951)

The distribution of disintegration product neutrons in the atmosphere has been measured from the geomagnetic equator to 65°N and up to ~220 g-cm^{-2} air. The measured exponential absorption of the neutron producing radiations in the equilibrium portion of the atmosphere is: $L(0°)=212$, $L(19°)=206$, $L(40°)=181$, $L(53°)=157$, $L(65°)=157$ g-cm^{-2}. It is shown that the neutron component has the largest latitude effect of any known secondary component in the cosmic rays and that the neutrons are part of a low energy nucleonic component in the atmosphere. The yield of neutrons per incident primary particle in an air column one cm^2 area extending through the atmosphere has been calculated at various latitudes. The yield increases by 400 percent between 0° and 55°N. The slow neutron absorption in air at the geomagnetic equator under 312 g-cm^{-2} air was measured. It is concluded that nucleon collision chains in the atmosphere are the principal process by which a low energy nucleonic and neutron component is produced. Measurements at high latitudes over a period of two years have shown that fluctuations and large changes of intensity of the neutron component may occur during solar and terrestrial disturbed days.

I. INTRODUCTION

RECENT measurements[1] indicate that the neutron half-life is approximately 15 minutes so that only a small portion of the primary cosmic radiations is expected to consist of free neutrons. However, neutrons of all energies, up to and including primary particle energies, are produced abundantly in the atmosphere by primary and secondary cosmic-ray particles interacting with oxygen and nitrogen nuclei. The energy ranges of these neutrons may be somewhat arbitrarily defined in this paper according to the kind of nuclear interaction by which they are produced. *High energy neutrons* are defined as being produced by nucleon-nucleon or exchange interactions and may have initial energies extending from primary particle energies down to the order of 40 Mev. Processes in which a portion of the nucleus or the entire nucleus is excited to high temperatures produce evaporation or disintegration products including neutrons, protons, and alpha-particles with initial energies of the order 2–30 Mev; these processes include nucleon-nucleus collisions and photon or π- or μ-meson nuclear capture. These disintegration product neutrons are defined as the *fast neutrons* in this paper. Since these disintegration product neutrons, in general, have insufficient energy to produce further nuclear disintegrations, they are slowed in the atmosphere by elastic and inelastic collisions.[2] Hence, neutrons slowed to less than ~1 ev are defined as *slow neutrons*.

The objectives of this study were (a) to determine the principal nuclear processes which contribute to the production of fast or disintegration product neutrons in the atmosphere, and (b) to determine the relationship of the fast neutron production to primary particle energy and primary particle intensity. Fast and slow neutron intensities in the free atmosphere were obtained as a function of atmospheric depth (Sec. III and Appendix I) and as a function of geomagnetic latitude and longitude (Sec. IV). The measurements were restricted to regions below the air transition maximum for the primary radiations so the fast neutrons would be in equilibrium with their producing radiations. The experiments covered the period of December, 1947 through November, 1949 and were performed in aircraft. Preliminary accounts have been given of some of the measurements.[3]

Prior to these measurements, neutron measurements by several observers had been obtained at high latitudes, indicating satisfactory agreement on the exponential form of the increase of intensity with altitude.[2,4,5] More recently, Yuan[6] has shown the existence of a maximum in the slow neutron intensity curve at high altitudes expected on the basis of the secondary origin of the slow neutrons.

A preliminary account of the time dependent changes of neutron intensity observed at the high latitudes is presented in Sec. VI.

II. APPARATUS AND METHODS OF MEASUREMENT

All neutron measurements were obtained in B-29 type aircraft with boron trifluoride proportional counters enriched in the B-10 isotope. Neutrons are isotropically incident on the detector. Since the most probable processes for fast neutron production emit neutrons isotropically,[7] the orientation of the detectors was not critical. In the equilibrium region of the atmosphere it may be shown[2] that the mean distance from the point of origin of a free fast neutron to the point of detection

* Assisted by the joint program of the ONR and AEC.
[1] A. H. Snell and L. C. Miller, Phys. Rev. 74, 1217 (1948). J. M. Robson, Phys. Rev. 77, 747 (1950).
[2] Bethe, Korff, and Placzek, Phys. Rev. 57, 573 (1940) and references therein.
[3] J. A. Simpson, Jr., Phys. Rev. 73, 1389 (1948); Phys. Rev. 74, 1214 (1948). See also references 8 and 11.
[4] S. A. Korff and E. T. Clarke, Phys. Rev. 61, 422 (1942) and references therein.
[5] Agnew, Bright, and Froman, Phys. Rev. 72, 203 (1947).
[6] L. C. L. Yuan, Phys. Rev. 74, 504 (1948).
[7] G. Cocconi and V. Tongiorgi, Phys. Rev. 76, 318 (1949). J. A. Simpson, Jr. and R. B. Uretz, Phys. Rev. 76, 569 (1949).

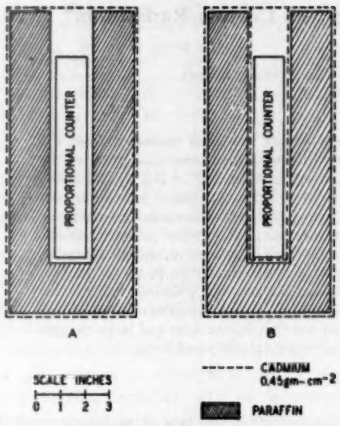

FIG. 1. Cross sections of BF_3 proportional counter geometries used to measure neutron intensity. By inserting the cadmium thimble around the counter as shown in 1(B) the counter background may be measured.

is sufficiently short to assume that the density of neutrons measured at a point in the atmosphere is proportional to the rate of production of neutrons at that point. Thus, a measurement of the rate of production or absorption of neutrons with altitude in the atmosphere is a close approximation of the absorption of the neutron producing radiations by air nuclei. Unless otherwise noted, the Gross transformation has not been used.

The fast neutron measurements are relative, and must be normalized to one absolute measurement in space. Measurements have been reported showing that the energy spectrum of atmospheric neutrons in the range of fast to slow neutrons below the air transition maximum does not appear to change with altitude[5] or latitude.[8] This is in agreement with theory, since this energy distribution arises from the slowing down processes of neutrons in nitrogen and oxygen, and the capture of neutrons by nitrogen and oxygen, and does not depend strongly on the initial kinetic energy of the nuclear disintegration product neutrons. Therefore, in the equilibrium region of the atmosphere at atmospheric depths >200 g-cm^{-2} the relative intensity distribution of fast neutron intensities in the atmosphere is the same as the relative intensity distribution of slow neutron intensities in the atmosphere. Thus, by measuring the absolute intensity of slow neutrons at one point in the atmosphere, the relative fast neutron distribution will give the absolute distribution of slow neutron intensities. It will be shown that there are large changes of neutron intensity with time at high latitudes and altitudes which make it difficult to attempt absolute measurements above approximately 40° geomagnetic latitude. Therefore, slow neutron absorption measurements were obtained at the equator so that all the relative fast neutron data could be normalized at one point, showing negligible time or seasonal dependence.

TABLE I. The exponential absorption L of the neutron producing radiation in the atmosphere at geomagnetic latitude λ.

λ	L (g-cm^{-2})	b (absorption coefficient)
0°	212±4	0.064
19°	206±4	0.067
40°	181±3	0.076
53°	157±2	0.086_5
65°	157±3	0.086

[8] Simpson, Baldwin, and Uretz, Phys. Rev. **76**, 165 (1949).

The slow neutron measurements were made inside a thin aluminum skin in the tail of the aircraft, using pressurized high voltage circuits. The method was similar to that used by Agnew *et al.*[5] in their measurements. One counter was covered with 0.030-in. cadmium; the other counter was covered with brass. These measurements are discussed in Appendix I.

The fast neutron detector was composed of a BF_3 proportional counter surrounded by paraffin inside a cadmium shield as shown in Fig. 1(A). Such a detector is insensitive to neutrons below 0.4 ev and does not depend critically on energy up to the order of 2–5 Mev.[9] Two detectors were operated in parallel to increase the measured counting rate. By locating their cylindrical axes in a vertical plane and approximately 45 cm apart, large and small shower effects were negligible. A second pair of detectors, identical with the exception that they contained non-enriched boron at the same pressure, were used in the early measurements to confirm the negligible contribution of shower effects, star production, and recoils. Cadmium thimbles could be placed around the counters as shown in Fig. 1(B) to measure background from star production in the counter wall and recoil processes. The contribution of these processes is discussed in Sec. III(c).

The vertical meson intensity for mesons of momenta $>4\times10^8$ ev/c and the total vertical charged particle intensity were measured as a function of latitude along with the early neutron measurements in order to confirm the independence of the neutron production processes and the classical charged particle components. Since these latter measurements are incidental to the neutron measurements, they are discussed in Appendix II.

It was important to show that all measurements in aircrafts correspond to free atmosphere measurements. The possibilities of systematic errors and spurious effects are investigated and discussed in Sec. III(b). Local production in materials of high atomic weight and slowing down of neutrons in large amounts of hydrogenous materials were the principal sources of difficulty. Preliminary measurements of the local production of neutrons in materials as a function of atomic

[9] For example, B. Rossi and H. Staub, *Ionization Chambers and Counters* (McGraw-Hill Book Company, Inc., New York, 1949), p. 192.

weight A have been reported at these altitudes.[10] Detectors were located so as to avoid appreciable local production in materials of atomic weight higher than aluminum. No measurements were taken in or near dense cloud formations where the measured intensity is known to be anomalous.[5]

Errors in the determination of the free atmospheric air pressure from a moving aircraft may be appreciable and may lead to serious errors in the determination of the absorption of radiation with atmospheric depth. Some of these errors depend on the location of the measuring system with respect to the slip stream of the aircraft, the gross weight, the speed and yaw of the aircraft, and are independent of the precision of manometers or altimeters. Calibrated and temperature corrected sensitive Kollsman 0–50,000 ft pressure—altitude altimeters were used with provision for eliminating hysteresis caused by friction in the moving parts. All pressure altitudes and pressures are related to the N.A.C.A. "standard" atmosphere and then corrected.

All measurements with BF_3 proportional counters employed negative feedback wide-band amplifiers, pulse size discriminators, and scaling circuits. Both photographic and manual recording of the events, time, and air pressure were provided on most of the flights to assure independent checks on the counting rates. All high potential circuits were regulated, pressurized, and treated for high humidity conditions in the tropics.

It was found that fast neutron measurements at low latitudes could be repeated easily within ± 2 percent, and that all instrument errors were maintained below ± 1 percent.

III. ALTITUDE DEPENDENCE OF DISINTEGRATION PRODUCT NEUTRONS

(a) The Altitude Dependence as a Function of Latitude

The altitude dependence of fast neutrons was measured using detectors of the type shown in Fig. 1(a) at the geomagnetic latitudes λ of 0°, 19°, 40°, 54°, and 65°N and at atmospheric depths 217 g-cm^{-2} to 600 g-cm^{-2}. Series of flights were made in December, 1947–February, 1948, May–June, 1948, April–May, 1949 and August–October, 1949. Since independent sets of detectors were used in the various flight series, their relative efficiencies were measured in the laboratory and at $\lambda=0°$ at an atmospheric depth of 312 g-cm^{-2} (30,000 ft pressure altitude). In this way a normalization factor for each series of flights was determined. The experimental data are given in Fig. 2. The bands of curves at 40° and higher latitudes indicate the changes in intensity observed in these flights except for the data given in Sec. VI. For example, the altitude curves for both 55° and 65° obtained in April, 1949 lie along the upper edge of the 53°–65° band. The lower edge of each band represents the undisturbed day neutron intensity. The longitude and latitude dependence of neutron intensity will be discussed in Sec. IV. It should be noted that the absorption mean-free paths as obtained from the combined data of all the flight series changes slightly the preliminary data of December, 1947–February, 1948.[3] Below approximately one m.f.p. from the top of the atmosphere, these curves are fitted by an expression of the form $D=D_0\varepsilon^{-h/L}=D_0\varepsilon^{-bp}$, where D is the neutron density in events per minute, h is the atmospheric depth in g-cm^{-2}, b is the absorption coefficient in cm^{-1}, and p is in cm Hg air pressure. Although it is not expected that the altitude curves at all latitudes are true exponentials, this exponential function is the simplest expression which provides a good fit with the data below 15 cm Hg atmospheric pressure. It is clear from Fig. 2 that at $\geq 52°$N the neutron altitude curve deviates appreciably from a simple exponential below 55–60 cm Hg.

Table II.

Status of aircraft	Altitude in feet—pressure altitude	Counting rate events per minute
Full tanks on way up	27,050	508± 7
Full tanks on way up	33,150	823±10
Low tanks on way down (later)	33,000	809±10
Low tanks on way down (later)	27,050	499± 7

The values for the exponential absorption length for the neutron producing radiation are obtained from Fig. 2 and are tabulated in Table I. Since there is a large latitude dependence, the aircraft was either flown in a circle over a fixed land mark or along a short segment of a constant geomagnetic line. Experienced navigators were used on all flights where space position was important. It may be shown easily that a 0.5° error in position for any λ between 20° and 45°N would produce a marked error in measuring L. For example, the change in neutron intensity at $\lambda=40°$ at 30,000 ft is $[\delta D/\delta\lambda]_{\lambda=40°}=25$ counts per minute per degree.

Fluctuations in pressure altitudes at 15,000 ft were ± 50 ft; at 30,000 ft were ± 100 ft, and at 36,000 ft or higher were ± 150 ft. Frequent checks on pressure during each measurement reduced the average value of these fluctuations.

(b) Local Neutron Production

The local production and slowing down of neutrons by the aircraft gasoline was checked by measurements at increasing altitudes and then, as the fuel supply became low, at decreasing altitudes so as to repeat the

Table III. Local production of neutrons in paraffin as a function of latitude at 312 g-cm^{-2}.

λ	Local production in paraffin; counts per minute	Fast neutron detector; counts per minute
0°	298	202
55°	975	665
Ratio: λ_{55}/λ_0	3.27±0.03	3.31±0.03

[10] Simpson, Baldwin, and Molner, Phys. Rev. 77, 751 (1950).

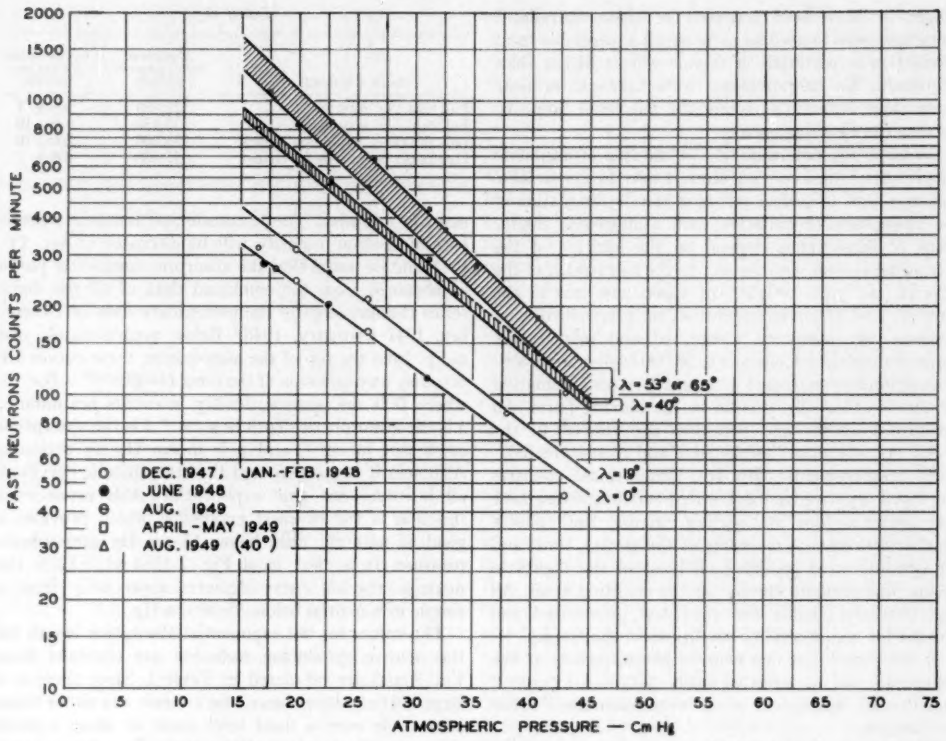

FIG. 2. The measurement of the exponential absorption of the neutron producing radiations or altitude dependence of neutrons. The quiet day curve is shown as the bottom curve of the $\lambda = 53°$ or 65° band, while the top curve corresponds to measurements on a solar disturbed day (see Fig. 5). The data for $\lambda = 40°$ is at 108–112°W longitude.

measurements for comparison. Measurements for $\lambda = 53°$, for example, are shown in Table II. These measurements lie within statistical fluctuations.

Measurements[11] to be reported in a later paper show that the local production in carbon and aluminum is proportional to the production in atmospheric nitrogen and oxygen at all measured altitudes and latitudes. For example, a 9×10^4 g mass of paraffin containing BF_3 proportional counters was arranged so that the detected neutrons came from neutron production in paraffin. Measurements at the equator and above $\lambda = 55°$ showed that the ratio of production rates in carbon and nitrogen-oxygen are the same, as shown in Table III, for an altitude of 30,000 ft. Therefore, the local production in the paraffin cylinders of the fast neutron detectors contributes a background counting rate proportional to the fast neutron production in the atmosphere. Using the absolute measurement of slow neutron absorption, this background was calculated at 30,000 ft and at $\lambda = 55°$. Each cylinder produces approximately 25 counts per minute. Thus, the contribution of local production in the paraffin to the total counting rate is 7–8 percent, which is not important for the relative measurements of the fast neutron intensity. However, the movement of materials of high atomic weight in close proximity to a single detector introduces serious errors. For example, fast neutron measurements made with and without 21 kg of lead or 8.5 kg of aluminum adjoining the paraffin cylinder at 37,000 ft gave the counting rates shown in Table IV.

Thus, the importance of not placing materials of high atomic weight in the vicinity of the detectors or not moving materials during the measurements is evident.

(c) Counter Background

The contribution to the observed neutron counting rates of star production in the walls of the counters, recoils in the BF_3 gas, and electronic showers was investigated. Since these background effects are independent of the boron-10 enrichment factor two pairs of detectors described in Fig. 1 were used, one set being the enriched counters used for the data in Fig. 2, and

[11] J. A. Simpson, Proc. Echo Lake Cosmic-Ray Symposium 252 (1949).

the other set being normal BF_3 counters but otherwise identical.[5] Owing to the large decrease in neutron intensity with decreasing λ, any evidence of showers and recoils should be most pronounced at the geomagnetic equator. The observed data are shown in Table V.

Since the enrichment ratios have been determined only to within ± 3.5 percent it is clear that there are no significant indications of showers or recoils.

By inserting a cadmium thimble around the counter inside the paraffin cylinder as shown in Fig. 1(B), the background caused by star production, recoils, showers, and fast neutron capture may be estimated. These data are summarized for the enriched BF_3 detectors in Table VI.

Thus, the total background from these processes is approximately 2 percent and not greater than 3 percent of the observed detector counting rate. Since this background is approximately proportional to the neutron intensity at all latitudes and altitudes it is assumed that this represents the contribution of stars[7] produced principally in the counter walls.

To show that the contribution of electronic showers was negligible lead (21 kg) was placed beside a single fast neutron detector. The counting rate was determined with and without the inner cadmium shield around the proportional counter. Typical measurements are given in Table VII. It is seen from these measurements that there is a negligible contribution of local showers to the detector counting rate. Also, it is evident that the increase in detector counting rate with the lead present arises from neutron production in the lead and moderator and not additional star production in the counter wall.

IV. THE LATITUDE AND LONGITUDE DEPENDENCE OF NEUTRONS

It is clear from Fig. 2 that a large latitude effect exists for the production of neutrons. This latitude dependence of the neutron intensity demonstrates that the neutrons are produced by primary charged particles. This was observed in detail by flying aircraft at constant air pressures from the geomagnetic equator to 65°N geomagnetic latitude. The time intervals for the individual measurements were approximately 15 to 30 minutes and represented a compromise between statistics and latitude change since the aircraft traversed approximately four degrees per hour. An experienced navigator used two or three independent methods for checking aircraft positions, and positions were established at the beginning and end of each measurement. Some of the flights were along the 80th meridian which closely corresponds to a constant geomagnetic longitude. All flights below 20°N geomagnetic were along 80°±1°W longitude. Flights at the higher latitudes extended as far as 122°W longitude. Thus, between 20° and 48°N geomagnetic latitude the shape of the latitude curve is dependent on the longitude effect. Figures 3, 4, and 5 show the results obtained with the fast neutron detectors. Recently Yuan[12] has confirmed this effect for slow neutrons in flights down to $\lambda = 20°$.

TABLE IV.

	c/min without	c/min with lead	c/min with aluminum
$\lambda = 0°$	157	176	—
$\lambda = 53°$	539	606	545
rate at $\lambda = 53°$ / rate at $\lambda = 0°$	3.4	3.4	—

The selection of the appropriate geomagnetic coordinates for these data is a serious problem. Neither centered dipole nor eccentric dipole[13] field distributions fit all of the data. However, since most cosmic-ray data to date have been fitted to the centered dipole distribution, it is this distribution which was used in Figs. 3, 4, and 5. The coordinates used for the intersection of the dipole axis with the surface of the northern hemisphere are: 78° 32′ N latitude; 69° 8′ W longitude.

Changes in cosmic-ray intensity with longitude are expected to occur[14] since the magnetic center of the earth is approximately 300 km from the center of the earth along a line passing through 10°N geomagnetic latitude and 160°E longitude. The magnetic field distribution of the earth is represented by an equivalent dipole located at this point. Thus, at a given latitude, λ, the distance r from the magnetic center to the given atmospheric depth of the observer will change with longitude. According to the theory of Vallarta and Lemaître[15] the solid angles of the allowed cones for any given primary particle energies will change with this distance. It should be noted that this longitude effect should decrease with increasing magnetic latitude for two reasons. First, owing to the eccentricity, the percentage change in this distance r diminishes with increasing geomagnetic latitude λ. Second, the solid angles of the allowed cones are increasing with λ. However, because of the momentum distribution of the primary particles, the change $\delta I/\delta\lambda$ of neutron intensity I with latitude is greatest in the region of 20°

TABLE V. Neutron measurements using normal and enriched B-10 counters to determine shower backgrounds.

$\lambda = 0°$	15,000 ft	27,000 ft	33,200 ft
Enriched BF_3	45 ±1	154 ±3	243 ±4
Normal BF_3	10.3±0.5	39.9±0.9	57.4±1.4
Enrichment ratio	4.4	4.1	4.3
$\lambda = 53°$	15,000 ft	27,000 ft	33,150 ft
Enriched BF_3	109	507	823
Normal BF_3	26	115	185
Enrichment ratio	4.2	4.4	4.4

[12] L. C. L. Yuan, Phys. Rev. **76**, 1267 (1949).
[13] J. Bartels, Terr. Mag. **41**, 225 (1936).
[14] T. Johnson, Revs. Modern Phys. **10**, 193 (1938).
[15] M. S. Vallarta, Phys. Rev. **47** (1935). G. Lemaître and M. S. Vallarta, Phys. Rev. **50**, 493 (1936).

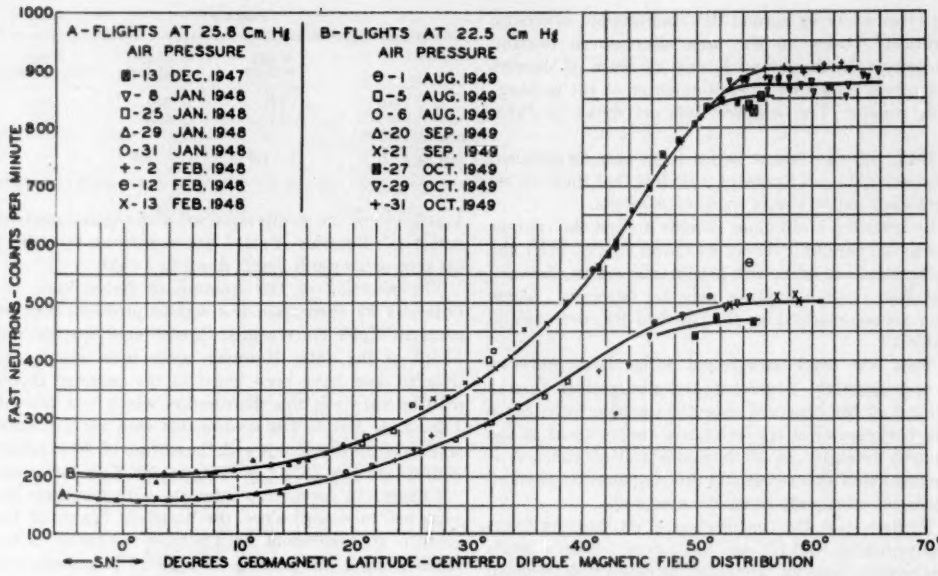

FIG. 3. Latitude dependence of fast neutrons at (A) 27,000 ft and (B) 30,000 ft. Several points lie off the curve between 20° and 40° owing to errors in navigation. The family of curves at high latitude for B show the change of intensity between October 27 and 31, 1949.

to 50°N. Below approximately $\lambda=10°$, $\delta I/\delta\lambda$ is small; above $\lambda=50°$ at atmospheric depths ~ 200 g-cm^{-2} or more, $\delta I/\delta\lambda \to 0$. Since at any λ a change in geomagnetic longitude φ may be represented by a change in latitude, it is seen that the region of 20°–50° latitude is most sensitive to the longitudinal position of measurements. Thus, the shape of the latitude curve in Fig. 3 between 20°–50° is determined by the longitude of the measurements.

Some evidence for the magnitude of the change in neutron intensity with longitude has been obtained in the region of $\lambda=41°$ and $\varphi=95°$–110°W geographic longitude. In Fig. 6 it is seen that $[\delta I/\delta\varphi]_\lambda=-1.5$ percent at 312 g-cm^{-2} and -1 percent at 448 g-cm^{-2}. From Fig. 3 $[\delta I/\delta\lambda]_\varphi=4.6$ percent at 312 g-cm^{-2}; thus, approximately,

$$\left[\frac{\delta I}{\delta\varphi}\Big/\frac{\delta I}{\delta\lambda}\right]_{\lambda=40°}=0.33.$$

TABLE VI.

$\lambda=0°$	37,000′	27,000′	36,200′	30,000′
c/min with Cd thimble	5.5±0.5		9.5±0.4	
c/min without thimble	315±4		300	
$\lambda=55°$				
c/min with Cd thimble	22.5	12±1		19±1.0
c/min without thimble	1072	507		662

These data may be compared with the longitude effect of charged particles as determined by Biehl and Neher[16] using an ionization chamber on the same flight at 312 g-cm^{-2} air. For the ionization chamber at $\lambda=41°$, $\delta I/\delta\varphi=-0.24$ percent and $\delta I/\delta\lambda\approx 0.8$ percent. Thus, for charged particles

$$\left[\frac{\delta I}{\delta\varphi}\Big/\frac{\delta I}{\delta\lambda}\right]_{\lambda=40°}=0.3.$$

It has been shown that these results are in fair agreement with theory.[16]

The sea level latitude dependence was measured for neutron energies above 0.4 ev during the June, 1948 series of flights. Local neutron production in the earth's

TABLE VII. Measurements to estimate the contribution of local showers to the neutron counting rate—see Fig. 1(B).

Time sequence of measurement	$\lambda=54°$N (27,000 ft)	Events per minute
1	detector without lead	252±3
2	detector with 2 kg lead	341±2
3	detector with 2 kg lead plus cadmium thimble surrounding proportional counter	12±1.5
4	detector with cadmium thimble but without lead	12±1.5
5	detector without lead	249±3

[16] A. T. Biehl and H. V. Neher, Phys. Rev. 78, 172 (1950).

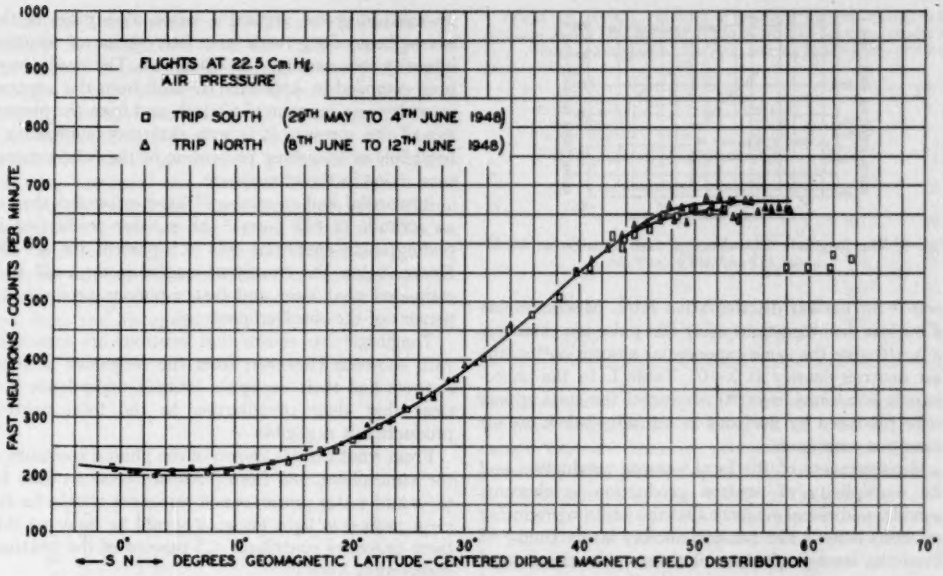

FIG. 4. Latitude dependence of fast neutrons. The time dependent change at high latitudes is shown in Fig. 10.

surface, in addition to the slowing down of neutrons in the earth, increases the neutron intensity at sea level. The results are shown in Table VIII but are difficult to interpret.

V. CONCLUSIONS REGARDING THE PRODUCTION AND DISTRIBUTION OF NEUTRONS IN THE ATMOSPHERE

(a) The Processes for Fast Neutron Production

The measurements described in the foregoing sections represent the neutron production contributions of all the nuclear processes occurring in the atmosphere. Hence, it is essential to estimate, briefly, the individual contributions of neutrons by nuclear disintegrations produced by nucleons, μ- or π-mesons, and photons before attempting to discuss neutron production as a function of primary particle energy. For example, if nonlatitude sensitive radiations contributed 10 percent of the total neutron intensity at the geomagnetic equator at 312 g-cm^{-2} atmospheric depth then the latitude factor between 0° and 55° for neutron production by the remaining kinds of neutron producing processes would be increased from the observed 3.3 to 3.5. Again, on this assumption, if a column atmosphere is defined as a vertical column of one square centimeter area extending through the entire atmosphere, the change of the latitude dependence for neutron production in a column atmosphere would be less than or more than 10 percent, depending on the altitude dependence of the assumed nonlatitude sensitive radiations.

There is evidence from independent kinds of experiments to show that most of the nuclear disintegrations or stars in the atmosphere have low energies and are produced by nucleons. Both photographic emulsion[17,18] and fast electron collection ion chamber[19] measurements at $\lambda > 50°$ show an exponential absorption of 135–150

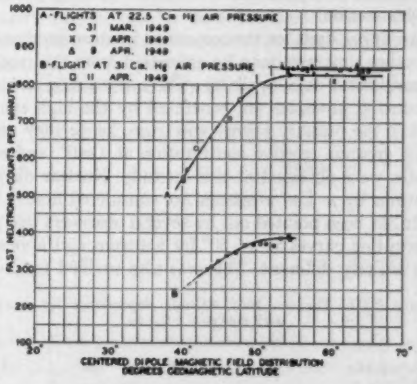

FIG. 5. Latitude dependence of fast neutrons at $\varphi = 116°$W longitude.

[17] For example, Bernardini, Cortini, and Manfredini, Phys. Rev. 76, 1792 (1949); Phys. Rev. 79, 768 (1950) and references therein.

[18] E. P. George and A. C. Jason, Proc. Phys. Soc. (London) 62, 243 (1949); Lord, Schein, and Vidale, Phys. Rev. 76, 171 (1949).

[19] Bridge, Hazen, Rossi, and Williams, Phys. Rev. 74, 1083 (1948).

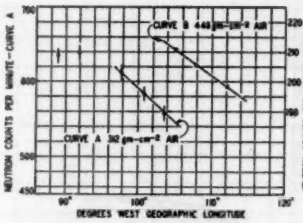
CURVE A 312 g-cm⁻² AIR
NEUTRON COUNTS PER MINUTE—CURVE A
NEUTRON COUNTS PER MINUTE—CURVE B
DEGREES WEST GEOGRAPHIC LONGITUDE

FIG. 6. The longitude dependence of fast neutrons at $\lambda=41°$ under 312 and 448 g-cm^{-2} air.

g-cm^{-2} for nuclear disintegration rates. Measurements of nuclear disintegrations using fast pulse ion chambers at $\lambda=0°$ give the same exponential absorption[20] as the fast neutron density at $\lambda=0°$, Table I. In the photographic emulsions, over 90 percent of the stars appear to be produced by nucleons at altitudes below the air transition maximum.

Measurements of the local neutron production and the multiplicity of neutron production in elements provides additional evidence that the neutron producing processes behave like nucleon-nucleus interactions.[21-22] Even the local production of neutrons in elements of low to intermediate atomic weight has a latitude and altitude dependence which follows closely the corresponding neutron production in the free atmosphere.[22]

Considering the results of all these experiments together, it is to be concluded that >90 percent of the neutrons in the atmosphere are the disintegration product of evaporation type stars produced by high energy nucleons of the order of 300 Mev. Additional arguments to support this conclusion will be given later in this section.

An upper limit for the remaining neutron production by other processes may be estimated from the meager experimental data available. These remaining neutron producing processes are generated by the high energy end of the primary energy spectrum, hence they make their greatest relative contribution at $\lambda=0°$, and estimates were obtained at this latitude. Nuclear disintegrations by μ- and π-mesons are considered first.

It has been pointed out by several observers that the absorption curves at $\lambda\approx 50°$ for neutrons and μ-mesons are entirely different. This was also verified for $\lambda=0°$ by measuring the vertical μ-meson absorption in the atmosphere along with the first series of neutron intensity measurements reported here. The results have been compiled in Appendix II. Both from the μ-meson intensity as a function of altitude and from the properties of the μ-meson it is seen that they contribute a negligible or vanishing proportion of the total neutron production in the atmosphere.

Bernardini and co-workers[17] have estimated that at an altitude of 685 g-cm^{-2} the $\pi\rightarrow$star production in photographic emulsions was <5 percent for $\lambda\sim 50°$. Hence, below the transition maximum at $\lambda=0°$ it is estimated that slow and fast π-mesons produce <3 percent of the observed neutrons.

Tongiorgi[24] has shown that neutrons are associated with showers. However, from the frequency of these showers and their negligible latitude dependence it is clear that their contribution to the total neutron production is negligible.

From what little is known of the photon spectrum in the atmosphere, and from published cross sections for $\gamma-n$ and γ-star processes and resonance widths for the $\gamma-n$ process in light nuclei, it would be expected that these processes contribute <5 percent of the neutrons observed at $\lambda=0°$.

The above comments form the basis for the assumption in Sec. V(b) that the production of neutrons by nucleon-nucleus collisions accounts for >90 percent of the neutron production in a column atmosphere at the geomagnetic equator.

TABLE VIII. The sea level latitude dependence for neutrons with energies >0.4 ev.

Geomagnetic latitude λ	0°	20°	40°	52°
Neutron events per minute	2.5±0.2	2.2±0.3	2.9±0.3	3.4±0.3

(b) The Dependence of the Neutron Component Intensity on Primary Cosmic-Ray Energy

In order to investigate the dependence of neutron production on primary particle energy, the neutron production arising from primary particles arriving vertically in the energy intervals corresponding to the geomagnetic cutoff for $\lambda=0°$, 20°, 40°, 53°, and 65° may be examined. Although primary alpha-particles and heavy nuclei are an important constituent of the primary radiations their role in contributing high energy nucleons in the atmosphere is complex; therefore, for the present it will be assumed that protons are the primary radiation. Geomagnetic cut-off values for *vertical* incidence as calculated from the Stöermer main plus shadow cones have been used. A method of analysis was chosen similar to that used by Bowen, Millikan, and Neher[25] (hereafter referred to as B.M.N.) in their derivation of the primary spectrum from spherical ionization chamber measurements. A comparison of the results will show the relative differences in production of the charged particle and neutron components in the atmosphere at different latitudes or primary proton energies. The B.M.N. measurements neglect a double-neutrino loss. In the B.M.N. analysis

[20] J. Simpson and E. Hungerford, Phys. Rev. **77**, 847 (1950).
[21] V. Cocconi Tongiorgi, Phys. Rev. **76**, 517 (1949).
[22] J. Simpson, Proc. Echo Lake Conf. 252 (1949); Phys. Rev. **77**, 751A (1950).
[23] C. G. Montgomery and A. R. Tobey, Phys. Rev. **76**, 1478 (1949).
[24] V. Tongiorgi, Phys. Rev. **75**, 1532 (1949).
[25] Bowen, Millikan, and Neher, Phys. Rev. **53**, 855 (1938). Millikan, Neher, and Pickering, Phys. Rev. **61**, 397 (1942).

at latitude λ the number of ion pairs measured at each altitude and integrated over the entire depth of the atmosphere is proportional to the amount of energy brought into the atmosphere by all primary protons of energies greater than the cut-off energy defined by λ. The ionization observed at any given altitude is principally caused by particles generated at a higher altitude. Similarly, the fast neutrons detected arise from nearby nuclear disintegrations which are produced by high energy nucleons generated at higher altitudes. The migration length of these disintegration product neutrons has been shown[2] to be short compared with the mean-free path of the neutron producing radiation, and, from the discussion in Sec. II, the energy distribution of disintegration product neutrons is approximately independent of altitude and latitude in the equilibrium region of the atmosphere. Therefore, the difference in areas under two altitude curves at λ_1 and λ_2 is proportional to the neutron production from primary particles which have cut-off energies between E_{λ_1} and E_{λ_2}.

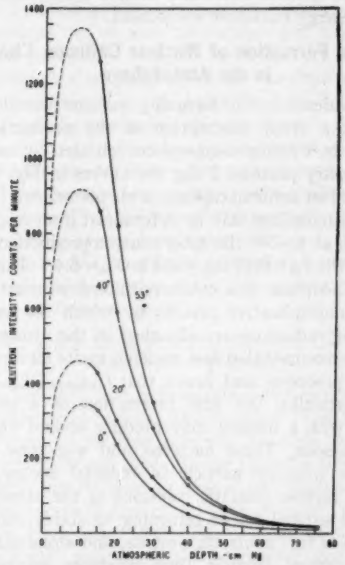

FIG. 7. The points on these curves were derived from the data in Fig. 2. The dashed parts of the curves are extrapolations based on the transition maximum found at $\lambda=54°$ by Yuan (see reference 6).

This method was followed for the interval of atmospheric depths $h=204$ to $h=610$ g-cm^{-2} in the published preliminary account[3] of the dependence of the neutron intensity on primary particle energy. More recently Yuan[6] has reported the shape of the altitude curve at $\lambda=54°$ near the top of the atmosphere. Hence, it will be assumed in the following analysis that the shape of this curve above $\sim$150 g-cm^{-2} is correct and represents the kind of curve to be expected at lower latitudes except that the maxima probably occur at slightly increasing atmospheric depths with decreasing λ owing to the increase in average energy of the primary radiation. With this assumption the experimental curves of Fig. 2 have been extrapolated to the top of the atmosphere. The derived curves are shown in Fig. 7. In arbitrary units the relative areas A of the atmospheric depth *vs.* intensity curves are given in Table IX.

TABLE IX. θ is a function of primary particle energy and intensity and is proportional to the number of neutrons produced in a column atmosphere per Bev energy interval of primary particle energy.

λ	Arbitrary units of areas (proportional to neutron production) A See Fig. 7	Differences in area $=\Delta A$	Vertical proton cut-off energy Bev	Energy differences in Bev $=\Delta E$	$\theta=\frac{\Delta A}{\Delta E}$
		222		21	10
0°	222		14		
		63		3.5	18
20°	285		10.5		
		309		6.2	50
40°	594		4.3		
		252		3.0	84
53°	846		1.3		
		small		0.9	—
65°	846+		0.4		

θ is a function of primary particle energy and intensity and is proportional to the number of neutrons produced in a column atmosphere per Bev energy interval of primary particle energy. The results are plotted as a dashed line histogram in Fig. 8. The results obtained by B.M.N. from their ionization chamber measurements are shown in the solid line histogram without corrections for neutrino loss. The energies given in their paper for electron primaries were changed to energies for proton primaries, and their data were fitted to the neutron data in the range of energies of

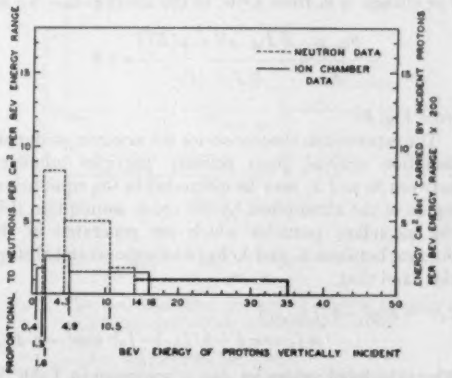
NEUTRON DATA
ION CHAMBER DATA
PROPORTIONAL TO NEUTRONS PER Ce³ PER BEV ENERGY RANGE
ENERGY Ce³ Bev⁻¹ CARRIED BY INCIDENT PROTONS PER BEV ENERGY RANGE × 200
BEV ENERGY OF PROTONS VERTICALLY INCIDENT

FIG. 8. A histogram of the results tabulated in Table IX. The two histograms were normalized at 16–35 Bev. The ion chamber data are the corrected results of Bowen, Millikan, and Neher (see reference 25).

TABLE X. Calculated values for the exponential absorption L of the neutron producing radiation produced by primary particles arriving between λ_2 and λ_1.

λ	$\lambda_2-\lambda_1$	L_λ g-cm^{-2}	Derived values for $L_{\lambda_2-\lambda_1}$ g-cm^{-2}
0°		212	212
	(20°–0°)		187
20°		206	
	(40°–20°)		162
40°		182	
	(50°–40°)		123
55°		157	

vertically incident protons of $E>16$ Bev. The more recent measurements of Biehl, Neher, and Roesch[26] were not used to change the ionization chamber measurements of B.M.N.

Before discussing these graphs, the following terms are defined: J_λ = integrated primary cosmic-ray nucleon intensity over the entire solid angle at the top of the atmosphere at magnetic latitude λ. Q_λ = total neutron capture cm^{-2}-sec^{-1} in a column atmosphere at magnetic latitude λ. $Y_\lambda(\bar{E})$ = yield of disintegration product neutrons in a column atmosphere per incident primary particle of average energy $\bar{E}$.

It is seen that

$$Q_\lambda \sim J_\lambda Y_\lambda(\bar{E}),$$

and that between two latitudes λ_1 and λ_2 with average vertical primary cut-off energies E_{λ_1} and E_{λ_2},

$$Q_{\lambda_2-\lambda_1}K = J_{\lambda_2-\lambda_1}Y_{\lambda_2-\lambda_1},$$

where $Q_{\lambda_2-\lambda_1}$ is proportional to the differences in areas, in Table IX.

Thus:

$$\frac{Q_{\lambda_2-\lambda_1}}{E_{\lambda_1}-E_{\lambda_2}} \rightarrow \frac{\delta Q}{\delta E\lambda} = K_2\theta_{\lambda_2-\lambda_1}.$$

The change in θ_λ from $\lambda=0°$ to the interval $\lambda_{53}-\lambda_{40}$ is,

$$\frac{\theta_{53-40}}{\theta_0} = \frac{\delta[J_{53-40}Y_{53-40}(E)]}{\delta[J_0Y_0(E)]} = 8.4$$

from Fig. 8.

The exponential absorption for the neutron producing radiation derived from primary particles admitted between λ_2 and λ_1 may be estimated in the equilibrium region of the atmosphere by the crude assumption that the secondary particles which are generated in the interval between λ_2 and λ_1 have an exponential absorption, and that,

$$I_0^{\lambda_2-\lambda_1}\exp[-h/L_{\lambda_2-\lambda_1}] = I_0^{\lambda_2}\exp[-h/L_{\lambda_2}] - I_0^{\lambda_1}\exp[-h/L_{\lambda_1}]$$

The calculated values for $L_{\lambda_2-\lambda_1}$ are given in Table X.

Since $L_0>L_{55-40}$ then $Y_{53-40}/Y_0<1$ and $J_{53-40}/J_0>8.4$.

[26] Biehl, Neher, and Roesch, Phys. Rev. **76**, 914 (1949).

The primary energy dependence of Y may be investigated by assuming a knowledge of the integral number spectrum. The best values for J_{55}/J_0 range from 5 to 6 on the basis of recent work by Biehl[26] and Winckler and co-workers.[27] Hence, since $(Q_{55}/Q_0)=(Y_{55}/Y_0)\times(J_{55}/J_0)\approx 4$ then $Y_{55}/Y_0=0.5$ to 0.7. It is seen, therefore, that Y is a slowly varying function of the primary particle energy.

It is evident from Figs. 3 and 8 that with decreasing primary particle energy the ratio of the production of nucleons to the production of high energy charged mesons increases rapidly, especially above $\lambda=40°$. For example, from Fig. 2 at 312 g-cm^{-2} air the fast neutron production increases by $\sim$1.5 between 40° and 50°. This large latitude effect is a unique characteristic of the low energy nucleonic component.[28]

C. The Formation of Nuclear Collision Chains in the Atmosphere

The evidence in the foregoing sections provides the basis for a crude description of the production of neutrons in a column atmosphere initiated by an incident primary particle. Using the curves in Fig. 7, the slow plus fast neutron capture in air per second, Q, in a column atmosphere may be determined from Appendix I. Hence, at $\lambda=55°$ the total neutron production, Q, is $Q=8$. With $J_{55}=0.95$ the yield is $Y_{55}=8.4$. This high yield of neutrons in a column atmosphere must come from a multiplicative process by which the neutron producing radiations are absorbed in the atmosphere. It will be assumed that fast nucleons excite air nuclei by collision processes, and, hence, that $L_{\text{collision}} \lesssim L_{\text{absorption}}$.

In particular, the first interaction of a primary particle with a nucleus may produce several nucleons and π-mesons. These nucleons and π-mesons, along with the primary particle of reduced energy, may produce further inelastic collisions in the atmosphere with the excited nuclei returning to stable states by emission of fast neutrons, protons, and alpha-particles. Each primary particle thus produces several secondary nucleons which, together with the primary, may each produce a few excited nuclei in subsequent collisions at greater atmospheric depths. This crude picture requires the assignment of the following energy dependent multiplicities for measurements at λ: ν_1 = average multiplicity of high energy nucleon production by a primary particle; ν_2 = average multiplicity of nuclear disintegrations per high energy nucleon; and ν_3 = average multiplicity of fast neutrons from a nuclear disintegration.

Values for ν_3 in carbon and aluminum near $\lambda=55°$ and $\lambda=40°$ have been measured[29] with $\nu_3\sim 2$. Also,

[27] Winckler, Stix, Dwight, and Sabin, Phys. Rev. **79**, 656 (1950).

[28] Recently a comparable latitude effect for charged particles, probably protons of momenta >1 Bev, has been found by M. Conversi, Phys. Rev. **76**, 444 (1949).

[29] V. Tongiorgi, Phys. Rev. **76**, 569 (1949). J. Simpson, Proc. Echo Lake Conf. 252 (1949); Phys. Rev. **77**, 751(A) (1950). C. G. Montgomery and A. R. Tobey, Phys. Rev. **76**, 1478 (1949). A. R. Tobey and C. G. Montgomery, Phys. Rev. **81**, 517 (1951).

$\nu_1\nu_2$ may be estimated from the absolute nuclear disintegration rates observed in photographic emulsions.[17,30] One and two prong stars and disintegrations emitting only neutrons are not counted in the emulsions, and they must be estimated. By including these latter events it is estimated that 3–4 events per second which emit neutrons occur in a column atmosphere at $\lambda \approx 50°$; then $\nu_1\nu_2 \approx 4$. Hence, it appears that a low multiplicity ν_1 of secondary high energy nucleons, each making a few inelastic collisions, may account for the entire neutron production in a column atmosphere.

As the average energy of the primary particles is increased, the average energy as well as the multiplicity ν_1 of secondary nucleons increases. In this way collision chain processes extend to greater atmospheric depths with increasing primary particle energy, and the multiplicity ν_2 of star production per high energy nucleon increases. This accounts for the change of exponential absorption L of the neutron producing radiations from $L_{55°}=157$ g-cm^{-2} to $L_0=212$ g-cm^{-2}.

It should be emphasized that this is only a qualitative discussion. J_λ, Q, and the star production in a column atmosphere are not known precisely. In several respects the above remarks are consistent with models proposed by Thomson,[31] Rossi,[32] and Bernardini[17] to describe the behavior of the low energy star producing radiations. Recently Cocconi and co-workers have proposed a model which appears to fit the experimental data at high nucleon energies.[33]

VI. TIME DEPENDENT CHANGES OF THE NEUTRON INTENSITY

On the basis of the measurements described in the preceding sections there do not appear to be significant differences in neutron intensity between winter and summer. Although the optimum times for the measurements would be close to March and September, only measurements in December, 1947–January, 1948 (Fig. 2) and May–June, 1948 (Fig. 4) have been made at both $\lambda=0°$ and $\lambda=54°$. The winter and summer measurements are the same within the experimental error of ± 5 percent. These measurements were made during periods in which no significant geomagnetic or solar disturbances were reported. Also, with a larger experimental error, the slow neutrons measured in January and August, 1949 at $\lambda=0°$ (Table XI) show no significant change between winter and summer (see Appendix I). Neutron intensities on these quiet days have, therefore, been selected as a measure of the quiet day intensity of neutrons from the low energy nucleonic component.

It is evident from a close examination of the statistical fluctuations of the experimental points along a latitude curve that, aside from occasional position errors, the fluctuations of neutron intensity are greater for $\lambda > 50°$ than for $\lambda \to 0°$. In fact, the intensity as a function of time at high latitudes shows periods of relatively large fluctuations. For example, in Fig. 9 two flights are represented which occurred on disturbed days.

In order to investigate time dependent changes, two series of flights were made in 1949 at 30,000 ft pressure altitude. Both series will be described before discussing their interpretation. The first set included March 31, April 7 and 9, 1949, as shown in Fig. 5(A). Considerable solar activity was reported during the period April 5–9. Many stations reported[34] magnetic storms on April 7. The principal increase of neutron intensity above $\lambda=50°$ was ~ 25 percent higher than the quiet day intensity, with this increase apparently occurring before the April 7 flight. Aircraft difficulties prevented flights at 30,000 ft on April 11, but data at 23,000 ft were recorded. Using $L=157$ g-cm^{-2} the extrapolated intensity at 23,000 ft on April 9 would have been 450 events per minute. However, by April 11 the observed intensity was 390 events per minute. This indicates that there was a decrease of neutron intensity toward normal occurring between April 9 and 11.

The second flight series at 30,000 ft was October 27, 29, and 31, 1949, shown in Fig. 3(B). Solar flares were reported of importance 1, 2, and 3 during the period October 25–31.[35] None of the flares occurred with the aircraft in the air. Some of the flares were followed by minor but distinct magnetic storms. The flight positions covered only a small range of longitudes, and corrections were made for this using the measured longitude effect at 41° in Fig. 6. The corrected curves were plotted and shown elsewhere.[36] The quiet day measurements at 40°N are shown in Fig. 2 and were obtained at 110°W longitude. A detailed discussion of these curves and their relation to changes of the primary cosmic-ray intensity has appeared elsewhere,[36] however, it is clear that:

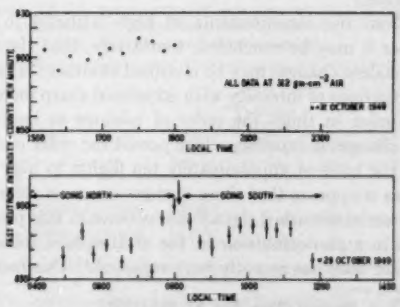

FIG. 9. The time dependent changes of neutron intensity for $\lambda > 55°$ from the latitude measurements of Fig. 3.

[30] S. Lattimore, private communication.
[31] G. P. Thompson, Phil. Mag. **40**, 589 (1949).
[32] B. Rossi, Proc. Echo Lake Conf. (1949).
[33] Cocconi, Tongiorgi, and Widgoff, Phys. Rev. **79**, 768 (1950).
[34] J. Geophys. Research **54**, 301 (1949).
[35] The data covering the solar flare observations in this period were kindly prepared by A. H. Shapley of the Central Radio Propagation Laboratory, National Bureau of Standards. (Private communication.)
[36] J. A. Simpson, Phys. Rev. **81**, 639 (1951).

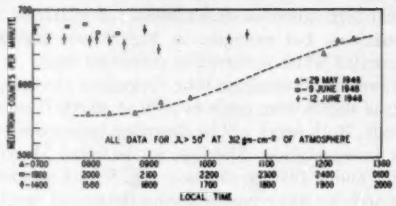

FIG. 10. The time dependence of the neutron intensity for measurements above $\lambda=50°$, as shown in Fig. 4.

1. Above $\lambda=56°$ an increase of $\sim$30 percent over the quiet day neutron intensity has occurred.

2. Beginning before the measurement of October 27, additional primary particles with momenta lower than the limit on quiet days at $\lambda=50°$ arrive at the top of the atmosphere. By October 31, particles arrive with momenta as low as ~ 1 Bev/c, if singly charged, corresponding to a cutoff at $\lambda>56°$.

These neutron measurements have been compared[37] with charged particle measurements obtained in the same aircraft and at the same time; it was concluded that the observations represented a change in primary particle intensity and that the neutron intensity has an order of magnitude greater response to primary intensity change than the charged particle intensity at aircraft altitudes. Because of atmospheric absorption this increase could not have been observed at sea level.[38]

These experimental results are consistent with the conclusions derived from Sec. V B; namely, that the neutron yield as a function of primary energy decreased with increasing latitude, but that the relative cross sections for the production of the low energy nucleonic component to the cross section for the production of high energy charged mesons increased with increasing latitude.

From the measurements at high latitudes in this paper it may be concluded, tentatively, that the time dependent changes may be classified as either: (a) small fluctuations of intensity with occasional sharp increases occurring in times the order of minutes or hours, or (b) changes of intensity which persist the order of days. On the basis of approximately ten flights to high latitudes it appears that these changes occur on solar and terrestrial disturbed days.[39] An increase in star production in a photoemulsion in the stratosphere following a solar flare has recently been reported.[40] This increase may be of the same type as reported here for the neutrons.

In Fig. 4 the intensity decrease observed in the early hours of May 29, 1948 for $\lambda>58°$ is not understood. The neutron intensity as a function of time for $\lambda>50°$ has been plotted in Fig. 10. Although a change of intensity of the kind shown in Fig. 10 is not in disagreement with the phase for a diurnal effect, the observed intensity change is too large.

SUMMARY

The distribution of fast neutrons produced in the atmosphere has been measured from the geomagnetic equator to 65°N over a period of two years. It was shown that these measurements are equivalent to "free atmosphere" measurements. The results may be summarized as follows:

(a) A neutron component exists in the atmosphere which has the largest latitude dependence of any known secondary component in the cosmic radiations. This fact alone shows that the neutrons are secondary particles produced by charged primaries.

(b) The neutrons are produced as part of a low energy nucleonic component which has a latitude effect at least as great as that for the neutrons.

(c) The yield, Y, of fast neutrons in a column atmosphere from a single primary particle is only a slowly varying function of primary energy above approximately 4 Bev. There is still a large latitude effect between $\lambda=40°$ and $\lambda=50°$. These are characteristics of the neutron component.

(d) At high latitudes the ratio at the top of the atmosphere of the cross section for neutron producing radiations to the cross section for high energy meson production increases rapidly for increasing geomagnetic latitude. This is verified from the observed increases of neutron and meson production in the atmosphere at high latitudes and below $\sim$200 g-cm^{-2} air following an increase in primary particle intensity.[37]

(e) Measurements of the exponential absorption of the neutron producing radiations from $\lambda=0°$ to 65°, where $L_0°>L_{20}°>L_{40}°>L_{65}°$, indicate that the neutrons are the disintegration products of stars and that the stars are produced in a series of collisions of a high energy nucleon. Developing at the top of the atmosphere, this process is a nucleon-nucleus collision phenomenon.

(f) From the absolute capture rate of neutrons in the atmosphere and the primary cosmic-ray flux, it has been estimated that the average multiplicities in air for high energy nucleon production, star production per high energy nucleon, and neutrons per star are low.

(g) The slow plus fast neutron capture was measured at the geomagnetic equator at 312 g-cm^{-2}. The average value was $(3.2\pm0.5)\times10^{-3}$ neutron captured in air g^{-1}-sec^{-1}. There may be large errors in this measurement because of the lack of knowledge of the neutron energy spectrum.

(h) At high latitudes and altitudes the neutron component is time dependent, with temporary increases of at least $\sim$30 percent being observed at 30,000 ft and persisting for the order of days.

Although the contribution of primary alpha-particles in the primary cosmic-ray spectrum is important, it was assumed in this paper that all primary particles were protons. The effect of the alpha-particles will be discussed in a later paper.

Rossi has classed both high and low energy nucleon processes as an "N" component. It is seen in the present paper that the definition of a low energy nucleonic component is much more restricted but is

[37] J. A. Simpson, Phys. Rev. **81**, 895 (1951).

[38] A recent report by M. A. Pomerantz [Phys. Rev. **81**, 731 (1951)] indicates that small changes of primary radiation intensity may be detected at balloon altitudes.

[39] Staker, Pavalow, and Korff, Phys. Rev. **81**, 517 (1951) have described balloon flights which show a factor of $\sim$2 increase in intensity between $\sim$54°N and 69°N at all altitudes. It is seen from Figs. 2 and 3 that their anomalous results may be explained by a change of neutron intensity in the time interval between their flights.

[40] Lord, Elston, and Schein, Phys. Rev. **79**, 540 (1950).

clearly a part of the mixed "N" component. The neutrons are predominately produced by low energy processes, and the degradation of energy is completed with the formation of slow neutrons in the atmosphere.

The world-wide distribution of slow neutron intensity shows that the total neutron production in the atmosphere is dominated by the low latitude belt. Hence, large fluctuations of low energy primary particle intensity, such as found in the present investigation, do not change appreciably the total neutron production in the atmosphere of the earth.

On the basis of the neutron measurements and the observed time dependent changes of the nucleonic component, the neutrons appear to be the most responsive component to changes in primary particle intensity observable at low altitudes. Thus, neutron monitoring may become useful for following changes of primary particle intensity.

The author wishes to thank Messrs. H. W. Baldwin (deceased), R. B. Uretz, and E. Hungerford for assistance in collecting the data on several of the flights. The assistance of General Mills Company in launching successful "sky hook" balloon flights with photographic emulsions was greatly appreciated. The officers and men of the U. S. Air Force B-29 group at Inyokern, under the command of Major W. Gustafson, and with navigator Captain George Freyer, were both co-operative and skillful in flying the aircrafts.

APPENDIX I. MEASUREMENT OF THE NEUTRON CAPTURE ABSORPTION IN THE ATMOSPHERE

Since the slow neutrons do not attain thermal equilibrium[2] (most probable energies of ~0.02 ev) but have average energies the order of 0.2 ev, the measurement of the absolute neutron flux becomes difficult. However, as first pointed out by Montgomery and Montgomery,[41] measurement of slow neutron absorption by a detector using boron-10 is not dependent on the form of the slow neutron energy spectrum because both nitrogen and oxygen, as well as boron, have cross sections which follow the $1/v$ law. Measurements of the absolute rate of absorption of slow neutrons by the air nuclei have been described by Bethe, Korff, and Placzek[2] and more recently by Yuan.[6,13,42] (See also Staker[43] and Davis.[44])

An attempt was made to convert the relative distribution of Fig. 2 into the absolute distribution for neutron capture by cadmium difference measurements using BF_3 proportional counters in B-29 aircraft.[45] This has been shown to be equivalent to free-atmosphere measurements.[6,8,46] As indicated in Sec. VI, only measurements below approximately latitude 40° avoid the serious time dependent intensity changes found at high latitudes.

Independent measurements in summer and winter at the geomagnetic equator under 312 g-cm^{-2} of air are given in Table XI. No significance has been attached to the difference in these two measurements.

Since each counter had the same rate of production of nuclear disintegrations and recoils, the "cadmium difference" measurements eliminated these background counting rates. An approximate upper limit for this background effect may be obtained from the data in Sec. III(c). At $\lambda=0°$ and under 312 g-cm^{-2} air the background of a single slow neutron counter is ≈6 counts per minute after correcting for the differences in geometry of the fast neutron detectors used to obtain the data in Sec. III(c) and the slow neutron detectors. This shows that an unshielded BF_3 counter cannot be used to determine the slow neutron density.

The detectors were calibrated at thermal neutron energies using a standardized neutron source and the calibrated counters used by Yuan.[47] The thermal neutron cross section of the unshielded counter was equivalent to 8.8 cm^2. At thermal energies the reported value[48] for the thermal neutron absorption cross section of a nitrogen atom is 1.7×10^{-24} cm^2. Thus, taking into account the ratio of N_2 to O_2 in air, one gram of air has an absorption of 0.055 cm^2. Hence, the unshielded counter has a thermal neutron cross section equivalent to 8.8 cm^2 and a neutron absorption equivalent to 160 g of air.

An energy distribution has been assumed for the slow neutrons, which follows the work of Bethe, Korff, and Placzek[2] but is based on more recent data and includes fast neutrons.[49] The average energy of the slow neutrons is assumed to be near 0.2–0.3 ev. This requires that for cadmium difference measurements the cadmium-covered counter response[50] must be calculated using the energy dependence of the measured cross sections for neutron capture in cadmium.[50] With these assumptions the neutron absorption for cadmium difference measurements is equivalent to the absorption of ~43 g of air.

The average value of the measurements at $\lambda=0°$ and under 312 g-cm^{-2} air using cadmium difference corrections is $(3.2\pm0.5)\times10^{-3}$ slow plus fast neutrons captured g^{-1}-sec^{-1}. Accordingly, the tentative conversion factor for the neutron intensity distributions in Fig. 2 is 1.6×10^{-4}. These measurements are in disagreement with the early measurements of Yuan[6] but are in better agreement with his recent measurements[42] at 52°, provided his data on undisturbed days are used.[51] It should be noted that absolute neutron capture rates, particularly those given in Table XI, are subject to large errors because of uncertainties in the necessary assumptions which are made when using BF_3 detectors. When new measurements of absolute neutron capture become available, the normalizing point for the fast neutron data may be changed.

TABLE XI. The measurement of slow plus fast neutron capture in the atmosphere at the geomagnetic equator and at 30,000 ft pressure altitude using BF_3 proportional counters.

Date	Counter	Events per minute	"Cadmium difference" in neutrons per minute	Cadmium ratio	Neutron capture per g and sec at $\lambda=0°$ under 312 g-cm^{-2} air
1949					
January	Cadmium covered	8.0±0.2			
January	No cadmium	15.6±0.4	7.6±0.6	2.0±0.1	2.9×10^{-3}
August	Cadmium covered	7.6±0.2			
August	No cadmium	16.5±0.5	8.9±0.7	2.2±0.1	3.4×10^{-3}

[41] C. G. Montgomery and D. D. Montgomery, Revs. Modern Phys. **11**, 266 (1939).
[42] L. C. L. Yuan, Phys. Rev. **77**, 728 (1950); Phys. Rev. **81**, 175 (1951).
[43] W. P. Staker, Phys. Rev. **80**, 52 (1950).
[44] W. O. Davis, Phys. Rev. **80**, 151 (1950).
[45] The tail gunner compartment was removed and only a thin aluminum tail piece surrounded the region of the detectors.
[46] L. C. L. Yuan, Phys. Rev. **76**, 1268 (1949).
[47] The author is indebted to Dr. Yuan for loaning his calibrated counter for comparison with the calibrated counters used in the above measurements, and to the Argonne National Laboratory for the use of the neutron source.
[48] Goldsmith, Ibser, and Feld, Revs. Modern Phys. **19**, 259 (1947).
[49] E. Melkonian, Phys. Rev. **76**, 1750 (1949).
[50] Rainwater, Havens, Wu, and Dunning, Phys. Rev. **71**, 65 (1947).
[51] L. C. L. Yuan, J. Geophys. Research **53** (1948); **54**, 661 (1949); **54**, 295 (1949).

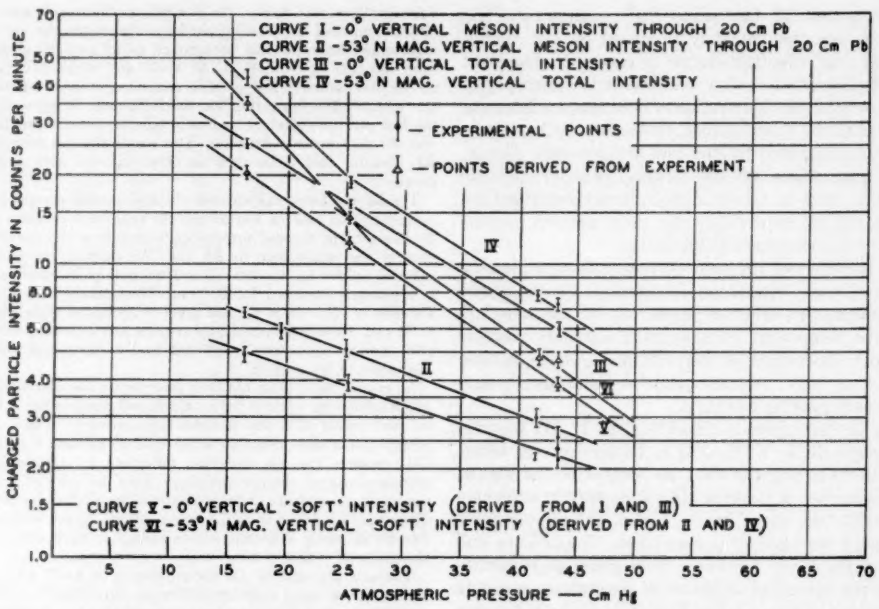
CURVE I - 0° VERTICAL MESON INTENSITY THROUGH 20 Cm Pb
CURVE II - 53° N MAG. VERTICAL MESON INTENSITY THROUGH 20 Cm Pb
CURVE III - 0° VERTICAL TOTAL INTENSITY
CURVE IV - 53° N MAG. VERTICAL TOTAL INTENSITY
— EXPERIMENTAL POINTS
— POINTS DERIVED FROM EXPERIMENT
CURVE V - 0° VERTICAL "SOFT" INTENSITY (DERIVED FROM I AND III)
CURVE VI - 53° N MAG. VERTICAL "SOFT" INTENSITY (DERIVED FROM II AND IV)
CHARGED PARTICLE INTENSITY IN COUNTS PER MINUTE
ATMOSPHERIC PRESSURE — Cm Hg

FIG. 11. The vertical charged particle intensity of the total component and mesons detected under 20 cm lead.

APPENDIX II. THE LATITUDE AND ALTITUDE DEPENDENCE OF THE PENETRATING PARTICLE AND THE TOTAL CHARGED PARTICLE INTENSITY

In order to confirm measurements of the latitude dependence of the charged particle components and to compare the cross sections for production of these components and the low energy nucleonic component, two vertical, three-fold G-M counter telescopes were carried in the aircraft in the January-February, 1948 flights. Penetrating particles, principally μ-mesons of momenta greater than 4×10^8 ev/c, were selected using a 20-cm Pb absorber. The maximum angle from the vertical with which a particle could enter either telescope was $\pm13°$. The counters were 3.8 cm in diameter.

For the total charged particle intensity measurement the absorbing material included a plastic window above the telescope (1.0 g-cm^{-2}) plus the total mean wall mass (3.8 g-cm^{-2} of brass). The diode coincidence circuits had a resolution better than 5×10^{-6} sec. No corrections were made for side showers, since their latitude dependence is small and only relative measurements were required. Knowing the counting rates of the individual counters, corrections for accidental counts in the three-fold telescopes were applied. The data are shown in Fig. 11 with their standard deviations. The classical so-called "soft-component" was determined by subtracting the penetrating particle intensity from the total charged particle intensity. The form of the altitude curves has been represented by exponentials below 15 cm Hg. The altitude dependence of the penetrating particles at $\lambda=0°$ and $\lambda=53°$ is in agreement with the measurements of Gill, Schein, and Yngve[22] and both the penetrating and total vertical intensity altitude dependence are in fair agreement with the recent work of Biehl, Neher, and Roesch.[23]

The latitude dependence of the vertical intensity measurements at $\lambda=0°$ and $\lambda=53°$ are approximately equal below about 22 cm Hg indicating that both the penetrating and nonpenetrating charged particles have nearly the same latitude dependence. This is also the conclusion of Biehl, *et al.* from their more extensive measurements.

[22] Gill, Schein, and Yngve, Phys. Rev. **72**, 733 (1947).

The Fourth-Order Contribution to the Self-Energy of the Electron*

R. M. FRANK†
Department of Physics, Cornell University, Ithaca, New York
(Received February 26, 1951)

The self-energy of a free electron is calculated to order e^4. The modification of quantum electrodynamics suggested by Feynman is used to make the matrix elements finite. After mass renormalization, using the self-energy to order e^2, there remain four Feynman diagrams whose matrix elements must be calculated. Two of these represented the two ways in which two virtual quanta may be emitted and absorbed by the electron, both quanta being present at the same time. The third diagram represents the emission of a virtual quantum which creates a virtual pair, the quantum produced by the pair annihilation being absorbed by the electron. The last diagram corresponds to the emission and absorption of a virtual quantum accompanied by a mass renormalization.

The matrix elements involve an integration over the momenta of all virtual quanta present in each diagram. These integrals are approximated by assuming that the Feynman cutoff, λ, is large compared to the electron mass.

It is found that the result depends upon $(\ln\lambda)^2$, but it is not the square of the second-order self-energy.

I. INTRODUCTION

THE modification in interaction between charges proposed by Feynman[1-4] yields, as he has shown, a convergent result for the self-energy to order e^2. This result used as a mass correction for real processes produces finite matrix elements insensitive to the cut-off width. While it is unlikely that any calculations on real processes will be made to such order that the mass correction to order e^4 will be necessary, still it was thought useful to calculate the self-energy to this order.

One purpose of the calculation was to determine how much more complex and difficult the integrals encountered in higher order processes are likely to be, and what methods of solution will prove advantageous. The self-energy, being the simplest of the processes, is the logical one to attack first.

Furthermore it is interesting to see how this order compares to the e^2 order self-energy and to find the dependence upon the cut-off width λ.

It was found that the integrals are indeed considerably more difficult than those encountered in the lower order terms; and, therefore, the calculation was carried out only to order $\ln\lambda$. An unknown constant is therefore to be added to the results given in this paper.

II. THE MATRIX ELEMENTS

The eight Feynman diagrams representing the process of emission and reabsorption of two virtual quanta and the necessary mass renormalizations reduce to the four shown in Fig. 1 by use of the methods of A, Sec. 6.

The matrix elements representing these four processes are to be computed between states $\bar{u}$ and u for a free electron. This means that $\not{p}u=mu$ and $\bar{u}\not{p}=m\bar{u}$, from the Dirac equation.[5] It follows also that $p^2=m^2$.

Since the matrices will diverge, we introduce the convergence factor $C(k^2)=-\lambda^2/(k^2-\lambda^2)$ for each quantum and imply an integration over λ with weight factor $G(\lambda)$ after Feynman.

The desired matrix element is found by taking the sum of the individual elements for diagrams (a), (b), and (c) and subtracting the element for diagram (d) of Fig. 1.

In evaluating the matrix elements we shall use the methods outlined in A (Appendix) especially Eqs. (1a) through (20a). We shall refer to these as A (1a), etc.

III. MATRIX ELEMENT *A*. DOUBLE SELF-ENERGY

The matrix element corresponding to diagram 1(a) is the element between $\bar{u}$ and u of the matrix:

$$\frac{e^4}{\pi^2}\int d^4k\int d^4J\frac{\gamma_\mu(\not{p}-\not{l}+m)\gamma_\nu(\not{p}-\not{l}-\not{J}+m)\gamma_\nu(\not{p}-\not{l}+m)\gamma_\mu C(k^2)C(J^2)}{[(p-k)^2-m^2][(p-k-J)^2-m^2][(p-k)^2-m^2]k^2J^2}. \tag{1}$$

The numerator after simplification by use of A (4a) becomes $8m^3+8m^2\not{J}-4m\not{J}\not{l}-4ml^2+8ml^2+4\not{l}\not{l}+4\not{J}l\not{J}-4\not{l}l^2$. The integration over J and then k can be performed upon each of the terms by the methods of A (1a) to (20a). Use of $\lambda^2\gg m^2$ simplifies the calculation considerably. The integrals involved after this simplification is made are elementary. There is, however, one point which bears discussion.

From the integration on J there results a term containing $\ln\{[m^2-(p-k)^2]/m^2\}$. In order to make this term of a form suitable for integration over k, we let

* This work was submitted to Cornell University in partial fulfilment of the requirements for a Ph.D. degree.
† Now at Florida State University, Tallahassee, Florida.
[1] R. P. Feynman, Phys. Rev. 74, 939 (1948).
[2] R. P. Feynman, Phys. Rev. 74, 1430 (1948).
[3] R. P. Feynman, Phys. Rev. 76, 749 (1949).
[4] R. P. Feynman, Phys. Rev. 76, 769 (1949), hereafter called A.
[5] We shall use the following notation: Three-vectors are represented in boldface roman; four-vectors are represented in boldface italics; and if a is any four-vector, then lightface German $\mathfrak{a}=a_\mu\gamma_\mu=a_4\gamma_4-a_1\gamma_1-a_2\gamma_2-a_3\gamma_3$. We use natural units throughout (i.e., $\hbar=c=1$).

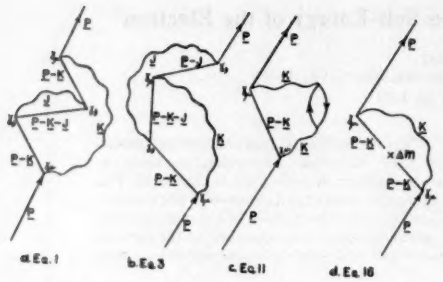

FIG. 1. The fourth-order self-energy, momentum space.

$m^2=x$ and differentiate with respect to x. After integration over k we then integrate the result over x from ∞ to m^2. This latter integration is simplified by splitting the range of integration into $m^2 \leqq x \leqq X$ and $X \leqq x \leqq \infty$, where $m^2 \ll X \ll \lambda^2$ and make the appropriate approximations in each section. In order to avoid the infrared catastrophe we replace k^2 by $k^2-\lambda_{\min}^2$ in the denominator where necessary. The dependence upon $\lambda_{\min}^2$ of the result is not important as this term is canceled by a term from diagram 1(d). We obtain for Eq. (1) the result

$$\frac{e^4}{4\pi^2}\left\{\frac{-m}{8}\ln^2\frac{\lambda^2}{m^2}-\left[\frac{3m}{2}\ln\frac{\lambda^2}{m^2}+\frac{3m}{4}\right]\ln\frac{m^2}{\lambda_{\min}^2}+\frac{9m}{4}\ln\frac{\lambda^2}{m^2}\right\}. \quad (2)$$

IV. MATRIX ELEMENT *B*. CROSSED SELF-ENERGY

The matrix element corresponding to diagram 1(b) is the element between states $\bar{u}$ and u, of the matrix:

$$\frac{e^4}{\pi^2}\int d^4k\int d^4J\frac{\gamma_\mu(\not p-\not l+m)\gamma_\nu(\not p-\not l-\not J+m)\gamma_\mu(\not p-\not J+m)\gamma_\nu C(k^2)C(J^2)}{[(p-k)^2-m^2][(p-k-J)^2-m^2][(p-J)^2-m^2]k^2J^2}. \quad (3)$$

Making use of A (14a) and A (15a), we may write

$$\frac{e^4}{\pi^2}\int\frac{d^4k}{k^2}C(k^2)\int\frac{d^4J}{J^2}C(J^2)\int_0^1 dx\int_0^1 2zdz\frac{\gamma_\mu(\not p-\not l+m)\gamma_\nu(\not p-\not l-\not J+m)\gamma_\mu(\not p-\not J+m)\gamma_\nu}{[(J^2-2p\cdot J)(1-(1-x)z)+(k^2-2p\cdot k)(1-xz)+2J\cdot k(1-z)]^3}. \quad (4)$$

The integration is somewhat simplified by splitting this into two terms, the first containing the $(\not p-\not J+m)$ of the middle factor, the second the $(-\not l)$ thereof. Now the first is integrated over k and then over J, while in the second the order is reversed. Making the change of variable $t=(1-z)y$, $y=(1-xz)^{-1}$, in the first and $t=(1-z)y$, $y=(1-(1-x)z)^{-1}$ in the second allows us to recombine after integration. Use of the relation

$$\gamma_\mu(\not A+a)\gamma_\nu(\not B+b)\gamma_\mu(\not D+d)\gamma_\nu=-8\not A\cdot\not D\not B+4a\not D\not B+4b\not D\not A+4d\not B\not A+4ab\not D+4ad\not B+4bd\not A-8abd$$

then reduces Eq. (4) to

$$\begin{aligned}(e^4/4\pi^2)&\int_1^\infty dy\int_0^1 dt\int_0^1 dz\int_0^1 wdw\\ &\times\left\{[m^3A/4f][(m^2h^2w^2f+\lambda^2(1-w)f+m^2zw)^{-1}-(m^2h^2w^2f+\lambda^2(1-w)f+m^2zw+\lambda^2(1-z)w/z)^{-1}\right.\\ &+(m^2h^2w^2f+\lambda^2[(1-z)/z]w+m^2zw)^{-1}-(m^2h^2w^2f+m^2zw)^{-1}]\\ &\left.+\left[\frac{mB}{8f^2}\right]\left[\ln\frac{m^2h^2w^2f+\lambda^2[(1-z)/z]w+\lambda^2(1-w)f+m^2zw}{m^2h^2w^2f+m^2zw+\lambda^2(1-z)w/z}+\ln\frac{m^2h^2w^2f+m^2zw}{m^2h^2w^2f+m^2zw+\lambda^2(1-w)f}\right]\right\}, \quad (5)\end{aligned}$$

where

$$f=y-1+t-tz,\quad h=1-[tz(1-t)]/[y-1+t(1-tz)],$$
$$A=8-4z+4hwzt-12hw-12hwz-8h^2w^2+12h^2w^2zt+16h^2w^2z-16h^2w^2zt,$$
$$B=-16-16z+96hwzt.$$

Since h, w, z, and t must all lie between zero and one, A and B are both of order one. A detailed examination of the terms in the first bracket shows that they can contribute at most to order constant in λ^2. Similarly, the first logarithm term will contribute, at most, a constant.

The interesting part of this matrix element then comes from

$$(e^4/4\pi^2)\int_1^\infty dy\int_0^1 dt\int_0^1 dz\int_0^1 wdw[m(-16-16z+96hwzt)/8f^2]\ln\frac{h^2w^2f+zw}{h^2w^2f+zw+\lambda^2(1-w)f/m^2}. \quad (6)$$

In order to perform the integrations of Eq. (6), we first neglect k^2w^2f in both numerator and denominator of the logarithm. This will alter the result by at most a constant. After this change the integration over y can be performed. Putting $(m^2/\lambda^2)=a$, we obtain

$$\frac{e^4m}{4\pi^2}\int_0^1 dt\int_0^1 dz\int_0^1 wdw\left\{\frac{2(1+z)-12wzt}{t(1-tz)}\ln\frac{azw+(t-t^2z)(1-w)}{azw}\right.$$
$$\left.+[2(1+z)-12wzt]\frac{1-w}{azw}\ln\frac{azw+(t-t^2z)(1-w)}{(t-t^2z)(1-w)}\right\}$$
$$+\frac{e^4m}{4\pi^2}\int_0^1 dt\int_0^1 dz\int_0^1 wdw\left\{\frac{6wz^2t^2(1-t)}{(t-t^2z)^2}\ln\frac{(t-t^2z)(1-w)+azw}{azw}\right.$$
$$\left.+6wz^2t^2(1-t)\left[\frac{1-w}{azw(t-t^2z)}+\frac{(1-w)^2}{a^2z^2w^2}\ln\frac{(t-t^2z)(1-w)}{azw+(t-t^2z)(1-w)}\right]\right\}. \quad (7)$$

In the first integral replace t by $s=zt$ and then let $r=z/s$; in the second, replace z by $s=tz$ and let $r=1/t$. Next perform the integration over w, then Eq. (7) becomes

$$\frac{e^4m}{4\pi^2}\int_0^1 ds\int_1^{1/s} dr\left\{\frac{1+sr}{1-s}\left[\frac{1-s}{asr^2-(1-s)}-\frac{(1-s)^2}{[asr^2-(1-s)]^2}\ln\frac{asr^2}{1-s}\right]\right.$$
$$+\left[\frac{2s^2(r-1)}{(1-s)^2}-\frac{4s}{1-s}\right]\left[\frac{1-s}{2[asr^2-(1-s)]}-\frac{(1-s)^2}{[asr^2-(1-s)]^2}+\frac{(1-s)^2}{[asr^2-(1-s)]^3}\ln\frac{asr^2}{1-s}\right]$$
$$+\left[\frac{1+sr-6s}{asr^2}\right]\left[-\frac{asr^2}{asr^2-(1-s)}+\frac{a^2s^2r^4}{[asr^2-(1-s)]^2}\ln\frac{asr^2}{1-s}\right]+\left[\frac{4}{ar^2}-\frac{2(r-1)}{a^2r^4}\right]$$
$$\left.\times\left[-\frac{asr^2}{2[asr^2-(1-s)]}-\frac{a^2s^2r^4}{[asr^2-(1-s)]^2}+\frac{a^2s^3r^6}{[asr^2-(1-s)]^3}\ln\frac{asr^2}{(1-s)}\right]+\frac{(r-1)s}{ar^2(1-s)}\right\}. \quad (8)$$

The last term yields $(1/a)(\frac{1}{4}\pi^2-\frac{3}{2})$ when integrated. To integrate the balance of Eq. (8), we replace s by $u=r^2s/(1-s)$, having first changed the order of integration. If we now again change the order of integration, we have to perform integrations over

$$\int_1^\infty dr\int_0^\infty du-\int_4^\infty du\int_{\frac{1}{2}[u+(u^2-4u)^{\frac{1}{2}}]}^{\frac{1}{2}[u+(u^2-4u)^{\frac{1}{2}}]} dr.$$

Performing the integration over r leaves

$$\frac{e^4m}{4\pi^2}\int_0^\infty du\left\{\left[u^{-\frac{1}{2}}\tan^{-1}u^{\frac{1}{2}}+\frac{u}{2(u+1)}\right]\left[\frac{1}{au-1}-\frac{\ln au}{(au-1)^2}\right]\right.$$
$$+\left[u^{-\frac{1}{2}}\tan^{-1}u^{\frac{1}{2}}-\frac{u-1}{u+1}+\ln(u+1)-2\right]\left[\frac{1}{2(au-1)}-\frac{1}{(au-1)^2}+\frac{\ln au}{(au-1)^3}\right]+\left[-2u^{-\frac{1}{2}}\tan^{-1}u^{\frac{1}{2}}+\frac{u+6}{2(u+1)}\right]$$
$$\times\left[-\frac{1}{au-1}+\frac{au}{(au-1)^2}\ln au\right]+\left[2a^{-1}u^{-\frac{1}{2}}\tan^{-1}u^{\frac{1}{2}}-\frac{2}{au(u+1)}+\frac{1}{a^2u(u+1)}-\frac{1}{a^2u^2}\ln(u+1)\right.$$
$$\left.\left.+\frac{2}{a^2u^2}+\frac{1}{a^2u^2(u+1)}-\frac{3}{a^2u^2}u^{-\frac{1}{2}}\tan^{-1}u^{\frac{1}{2}}\right]\left[-\frac{au}{au-1}-\frac{a^2u^2}{(au-1)^2}+\frac{a^3u^3}{(au-1)^3}\ln au\right]\right\}$$
$$-\frac{e^4m}{4\pi^2}\int_4^\infty du\left\{\left[u^{-\frac{1}{2}}\tan^{-1}\frac{(u-4)^{\frac{1}{2}}}{2}+\frac{(u^2-4u)^{\frac{1}{2}}}{2u}\right]\left[\frac{1}{au-1}-\frac{\ln au}{(au-1)^2}\right]\right.$$

Continued on following page.

$$+\left[u^{-\frac{1}{2}}\tan^{-1}\frac{(u-4)^{\frac{1}{2}}}{2}-3(1-4/u)^{\frac{1}{2}}+\ln\frac{1+(1-4/u)^{\frac{1}{2}}}{1-(1-4/u)^{\frac{1}{2}}}\right]\left[\frac{1}{2(au-1)}-\frac{1}{(au-1)^2}+\frac{\ln au}{(au-1)^3}\right]$$

$$+\left[-2u^{-\frac{1}{2}}\tan^{-1}\frac{(u-4)^{\frac{1}{2}}}{2}+\frac{(1-4/u)^{\frac{1}{2}}}{2}\right]\left[-\frac{1}{au-1}+\frac{au}{(au-1)^2}\ln au\right]$$

$$+\left[\frac{2u^{-\frac{1}{2}}}{a}\tan^{-1}\frac{(u-4)^{\frac{1}{2}}}{2}+\frac{3(1-4/u)^{\frac{1}{2}}}{a^2u^2}-\frac{1}{a^2u^2}\ln\frac{1+(1-4/u)^{\frac{1}{2}}}{1-(1-4/u)^{\frac{1}{2}}}\right.$$

$$\left.-\frac{3u^{-\frac{1}{2}}}{a^2}\tan^{-1}\frac{(u-4)^{\frac{1}{2}}}{2}\right]\left[-\frac{au}{2(au-1)}-\frac{a^2u^2}{(au-1)^2}+\frac{a^3u^3}{(au-1)^3}\ln au.\right]\Bigg\}. \quad (9)$$

These integrals may be evaluated by choosing a value $L\gg1$ such that $aL\ll1$. We take the corresponding terms from both integrals together and in the region $L\leqq u\leqq\infty$ expand the first square bracket in each case, while for $0\leqq u\leqq L$ we expand the second square bracket. This procedure yields elementary integrals throughout. The value L disappears after combining results from both regions. The matrix element thus obtained is

$$(e^4/4\pi^2)\{\tfrac{3}{2}m\ln(\lambda^2/m^2)+\tfrac{1}{4}m\ln^2(\lambda^2/m^2)\}. \quad (10)$$

V. MATRIX ELEMENT *C*. VACUUM POLARIZATION

The matrix element corresponding to diagram 1(c) is the element taken between states $\bar{u}$ and u of the matrix

$$\frac{e^2}{\pi i}\int\frac{d^4kC(k^2)k^2\chi(k)C(k^2)\gamma_\mu(\not{p}-\not{k}+m)\gamma_\mu}{[(p-k)^2-m^2]k^4}, \quad (11)$$

where $\chi(k)$ is the vacuum polarization operator

$$\chi(k)=(e^2/2\pi)\int_0^1 dy(1-y^2)\ln[1-(k^2/4m^2)(1-y^2)]$$

$$=\frac{e^2}{\pi}\int_0^1 dy\frac{(y^2-\frac{1}{4}y^4)k^2}{(1-y^2)[k^2-4m^2/(1-y^2)]}. \quad (12)$$

Inserting Eq. (12) into Eq. (11) and using A (4a), (14a), and (20a), we obtain for Eq. (11)

$$-(e^4/4\pi^2)2m\int_0^1[(y^2-\tfrac{1}{4}y^4)/(1-y^2)]dy\int_0^1 dx\int_0^1(z-1)zdz\frac{\lambda^4}{m^4}\frac{1+z-xz}{[z^2(1-x)^2+(4xz/1-y^2)+\lambda^2(1-z)/m^2]^2}. \quad (13)$$

Here again we resort to an approximate solution assuming $\lambda^2\gg m^2$. We write Eq. (13) as

$$-(e^4/4\pi^2)2m(\lambda^2/m^2)\int_0^1(y^2-\tfrac{1}{4}y^4)dy\int_0^1 dx\int_0^1 z(1+z-xz)dz$$

$$\times\left\{-\frac{1}{4xz+\lambda^2(1-z)(1-y^2)/m^2}+\frac{4xz}{[4xz+\lambda^2(1-z)(1-y)/m^2]^2}\right\}. \quad (14)$$

Now it is clear that unless y or z is near unity, neither of these terms will contribute anything of higher order than a constant. Hence, we choose constants β and η such that

$$[\lambda^2/m^2]\eta\beta\gg1 \quad \text{and} \quad \beta\ll1; \quad \eta\ll1.$$

Now we need only perform the integral for values of y in the range $1-\beta$ to 1, z in range 0 to $1-\eta$, or y in the range 0 to $1-\beta$, z in the range $1-\eta$ to 1, or y in the range $1-\beta$ to 1, z in the range $1-\eta$ to 1, since for $y<1-\beta$ and $z<1-\eta$ the integral contributes at most a constant to the result. The integration over the three ranges above mentioned is elementary after the obvious approximations are made. The result is to find for the matrix element here

$$(mc^2/4\pi^2)\{\tfrac{1}{2}\ln^2(\lambda^2/m^2)-(5/3)\ln(\lambda^2/m^2)\}. \quad (15)$$

VI. MATRIX ELEMENT *D*. MASS RENORMALIZATION

The matrix element corresponding to diagram 1(d) is the element between $\bar{u}$ and u of the matrix.

$$\frac{e^2}{\pi i}\int\frac{\gamma_\mu(\not{p}-\not{k}+m)\Delta m(\not{p}-\not{k}+m)\gamma_\mu C(k^2)d^4k}{[(p-k)^2-m^2]^2k^2}, \quad (16)$$

where

$$\Delta m=\frac{e^2}{\pi i}\int\frac{\gamma_\nu(\not{p}-\not{J}+m)\gamma_\nu C(J^2)d^4J}{[(p-J)^2-m^2]J^2}. \quad (17)$$

The integrations here are simply carried out using the results in A (Appendix) yielding for this matrix element

$$(e^4/4\pi^2)[2\ln(\lambda^2/m^2)+\ln(\lambda_{\min}{}^2/m^2)]$$

$$\times[\tfrac{3}{2}m\ln(\lambda^2/m^2)+\tfrac{3}{4}]. \quad (18)$$

Now recalling that this term (18) is to be subtracted from the others including Eq. (2), we note that the term involving $\ln(\lambda_{min}^2/m^2)$ in these elements will cancel. The reason for this is clear: in both elements the infrared terms come from the emission of long wavelength (small k) quanta. For small k the intermediate state $p-k$ is very nearly a free particle state and the self-energy operator

$$\int C(J^2)d^4J\gamma_\nu(\not{p}-\not{l}-\not{J}+m)\gamma_\nu/[(p-k-J)^2-m^2]J^2$$

arising in Eq. (1) is very nearly Δm appearing in (16).

VII. THE FOURTH-ORDER SELF-ENERGY

The fourth-order contribution to the self-energy is found by adding Eqs. (2), (10), and (15) and subtracting (18) from the result. We find for the self-energy

$$m(e^4/4\pi^2)\{-(19/8)\ln^2(\lambda^2/m^2)+(7/12)\ln(\lambda^2/m^2)\}. \quad (19)$$

It is encouraging, from the point of view of the theory, that this result behaves as $\ln^2(\lambda^2/m^2)$ in the leading term, and no stronger dependence upon λ exists. However, there is no cancellation between terms which would make the fourth-order self-energy finite, independently of λ. The contribution from the vacuum polarization term is quite strong; and it must therefore be taken into account here, and presumably therefore in any processes involving virtual quanta.

It has been suggested[6] that the self-energy might be represented as a summable series in Δm [second-order self-energy, Eq. A (21)] which would converge for large λ. Neither the relative signs nor the sizes of the coefficients of our result (19) seem to indicate much hope of this.

The statement made by Feynman just before Appendix A of reference 4 seems fully justified. The extreme complexity of the integrations required in any but the simplest higher order processes is apparent by comparison to those evaluated here.

The author is deeply indebted to Professor H. A. Bethe for his invaluable help during the calculation and his careful reading and criticisms of the manuscript. He is also grateful to Professor R. P. Feynman for suggesting the problem and for many very helpful suggestions.

[6] G. Racah, Phys. Rev. **70**, 406 (1946).

PHYSICAL REVIEW VOLUME 83, NUMBER 6 SEPTEMBER 15, 1951

On the Origin of the Cosmic Radiation

GIUSEPPE COCCONI
Cornell University, Ithaca, New York
(Received June 5, 1951)

Experimental evidence of the isotropy of the cosmic radiation of energy above 10^{13} ev is given. The interpretation of this result leads one to infer that the more energetic particles of the cosmic radiation are not of solar origin, but come from the whole galaxy. On the other hand, a local origin seems necessary for the particles of moderate energy (10^8–10^{10} ev).

DURING the months from August, 1950, to February, 1951, experiments have been performed in a salt mine, at a depth equivalent to 1600 m (geographical latitude 42°N) in order to study various properties of the cosmic radiation underground.[1] The ionizing particles were detected by the fourfold coincidences of a vertical telescope shielded by 14-in. Pb (sensitive surface of the counters 30×30 sq. in., maximum distance between counters 22 in.). The temperature inside the mine is constant throughout the year within a few hundredths of a degree. The operation of the apparatus was excellent; no counters had to be replaced during the experiment.

In 4154 hours of effective running 20,450 coincidences have been recorded (average rate 4.92 per hour) on a running tape, and their time distribution has now been analyzed in correlation with the solar time and the sidereal time. Within the statistical errors (~3 percent), no correlation of the rate of coincidences with either the solar time or the sidereal time has been found.

This result can be of interest in connection with the problem of the origin of the cosmic radiation. In fact, our experiments have indicated that the ionizing particles observed underground are mu-mesons produced in the atmosphere by primaries of energies from 10^{13} to 10^{14} ev; the absence of time correlation for the mu-mesons provides, therefore, experimental evidence of the isotropy of the more energetic particles of the primary cosmic radiation.[2–4] The statement about

[1] A preliminary report of these experiments has been given at the New York meeting of the American Physical Society. See Phys. Rev. **82**, 294 (1951).

[2] Auger, Daudin, Denisse, and Daudin, Compt. rend. **228**, 1116 (1949).

[3] A. Daudin and J. Daudin, J. phys. et radium **10**, 394 (1949).

[4] A variation with sidereal time of the frequency of the extensive showers at mountain altitudes has been reported by

the nature of the particles underground and their correlation with the primary radiation is based on the following facts: (a) the absorption in lead of the particles underground is equal to the absorption deduced from the well-known intensity *versus* depth curves. This shows that the particles observed underground arrive there losing energy all along the way mostly by ionization, and leads one to infer that they were produced with an average energy of about 10^{12} ev; (b) all the ionizing particles underground are accompanied above ground, in the air, by extensive showers containing at sea level on the average 500 to 1000 electrons each. Hence, the production of the particles observed underground must be due to primaries having energies of the order of 10^{13} to 10^{14} ev per nucleon, since otherwise the accompanying shower would not reach the surface of the earth. A primary energy per nucleon of at least the same order of magnitude is obtained, if one accepts the energy-multiplicity relation in the nucleon-nucleon collisions predicted by Fermi.[5]

We can thus make the statement that the particles of the primary radiation with energies from 10^{13} to 10^{14} ev arrive at the earth isotropically, within an accuracy of about 3 percent.

Not considering the possibility of an isotropic source of cosmic radiation spread uniformly over the whole galaxy, the only known mechanism which can give rise to the isotropy of such particles in space is their curling due to the action of irregular magnetic fields, extended over regions larger by some order of magnitude than the radius of curvature, ρ, of the path of the particles,

$$\rho = E/300H \text{ cm (energy } E \text{ in ev, magnetic field } H \text{ in gauss).}$$

An upper limit for the intensity of a magnetic field surrounding the solar system is believed to be $H = 10^{-5}$ gauss. This gives $\rho = 10^{16}$ to 10^{17} cm. The average distance between the stars in the region of the galaxy in the neighborhood of the sun is several light years, 10^{18} to 10^{19} cm, i.e., of the same order of magnitude as the distance which the particles of 10^{13} to 10^{14} ev have to sweep in order to be sufficiently stirred by a field of 10^{-5} gauss. Therefore, it seems likely that at least the more energetic particles of the primary cosmic radiation are not confined to the solar system, but come also from other stars. Possibly the whole galaxy contributes to their production. A galactic origin of the more energetic band of the cosmic radiation, say, above 10^{13} to 10^{14} ev, very likely implies that the length of the path of these particles in the galaxy is at least of the order of 10^{25} to 10^{26} cm. If the density of the interstellar matter is equal to 10^{-24} g cm^{-3}, this length corresponds to a thickness of at least 10 to 100 g cm^{-2}.

Assume that the galaxy is a sphere of radius R and that cosmic rays are produced at its center by a source of strength S.[6] The effect of the curling of the paths of the charged particles by the irregular magnetic fields is equivalent to the effect of an isotropic elastic scattering with mean free path $\lambda \approx \rho$. The diffusion equation in this case is the Laplace equation:

$$\tfrac{1}{3}\lambda v \nabla^2 n + S\delta(r) = 0,$$

where v is the velocity and n the density of the particles at a distance r from the center of the galaxy. With the condition that $n = 0$ when $r = R$, the solution is

$$n = A\left(\frac{1}{r} - \frac{1}{R}\right),$$

where A is a constant. To find the ratio

$$1 + a = \frac{I(0)}{I(\pi)} = \frac{\text{intensity of the radiation coming from the center of the galaxy}}{\text{intensity of the radiation coming from the opposite direction}},$$

assume that the flux per unit surface and unit solid angle of the particles at a point at a distance r from the center is given by the expression,

$$F(\theta) = f + g\cos\theta,$$

where θ is the angle between the tangent to the trajectory of the particle at the point considered and the line connecting that point to the center; g represents the anisotropy of the radiation at the distance r. Thus,

$$1 + a = (f+g)/(f-g) = \sim 1 + 2(g/f)$$

and

$$a = 2g/f.$$

Furthermore,

$$n = 4\pi f/v.$$

The net outward flux, $I(0) - I(\pi)$ can be obtained both from the expression for the flux, $F(\theta)$, and from the diffusion equation. In the first case,

$$I(0) - I(\pi) = 2\pi \int_0^\pi g\cos^2\theta \sin\theta d\theta = \frac{4\pi}{3} g.$$

In the second,

$$I(0) - I(\pi) = -\frac{1}{3}\lambda v \nabla n = -\frac{1}{3}\lambda v \frac{A}{r^2} = \frac{4\pi}{3}\lambda f \frac{R}{r(R-r)}.$$

Equating the two results one obtains

$$g/f = (\lambda/r)R/(R-r)$$

Auger *et al.* (see reference 2). Later (see reference 3), the same group found that the fluctuations observed could be correlated with the fluctuations of the temperature of the atmosphere, hence did not provide evidence for a sidereal effect.

[5] E. Fermi, Prog. Theor. Phys. **5**, 570 (1950).

[6] This is not an oversimplified picture, since most of the galactic matter is concentrated near the center of the galaxy, and the sun is quite far from it. See, for example, A. Unsöld, Z. Astrophys. **26**, 176 (1949).

and finally

$$\lambda/r=(a/r)(1-r/R).$$

The number of "collisions" a particle must suffer before diffusing through a distance r is

$$N=(r/\lambda)^2,$$

hence, the length of the path of the particle in the galaxy before reaching the distance r from the center is

$$s=2\pi\lambda N=2\pi r(r/\lambda)=4\pi r/[a(1-r/R)].$$

From our measurements, $a\leqslant 3\times10^{-2}$, and assuming for r the value of the distance of the sun from the center of the galaxy, $r=3\times10^{22}$ cm, and $r/R=0.5$, one obtains

$$\lambda\leqslant 2\times10^{20}\text{ cm} \quad\text{and}\quad s\geqslant 3\times10^{25}\text{ cm}\equiv 30\text{ g cm}^{-2}.^{7}$$

If, among the primary particles, there are heavy ions, their probability of colliding with the interstellar matter will be quite high, their mean free path for nuclear collision being of about 20 g cm^{-2}. This means, first, that the number of heavy ions which reach the earth is much smaller than the number of ions formed at the center of the galaxy; second, that the charge spectrum of the ions is a continuous one, because in the interactions with interstellar matter all kinds of fission nuclei are formed. The first argument does not apply to the protons, because even if they lose some energy in each collision they will gain energy in the interaction with the irregular magnetic fields, as shown by Fermi.[8]

If this picture is true, we can anticipate that the charge spectrum of the high energy band (above 10^{13} to 10^{14} ev) of the cosmic radiation is very different from that observed for moderate energy particles (10^9 to 10^{10} ev). Namely, it will not show the deficiency of Li, Be, B atoms observed by Bradt and Peters,[9] and the relatively high abundance of heavy ions.

This point needs experimental check. No data are thus far available.

The value found previously for λ determines a lower limit for the intensity of the irregular magnetic fields in the galaxy:

$$H_{\min}=10^{14}eV/300\lambda=\sim10^{-9}\text{ gauss}.$$

The isotropy observed could be considered as a proof of the existence of such fields in the galaxy.

If these fields exist, the particles of the cosmic radiation of moderate energy, e.g., 3×10^9 ev, will move along orbits with a radius of curvature

$$\rho=10^{16}\text{ cm}=\lambda_1,$$

and if they too come from the center of the galaxy, the length of their path before reaching the earth will be at least

$$s_1=2\pi r(r/\lambda_1)=\sim10^{30}\text{ cm}\equiv10^6\text{ g cm}^{-2}.$$

On the other hand, the fact that the cosmic radiation of moderate energy has a charge spectrum quite rich in heavy nuclei and probably very poor in Li, Be, B nuclei strongly suggests, as shown by Bradt and Peters,[9] that these particles have not crossed a thickness of material larger than ~1 g cm^{-2}. The only way out seems to be to assume that the moderate energy particles do not come from very far, but are locally generated by the sun. It may be that they are mostly trapped in the closed orbits of the magnetic field of the sun: in this case their life-time, as shown by Kane, Shanley, and Wheeler,[10] would be of the order of 10^4 years, and the thickness of matter crossed smaller than 1 g cm^{-2}.

In conclusion, the picture we propose is the following. The less energetic particles of the primary cosmic radiation, up to energies of about 10^{10} ev, come from the sun. They are mostly captured by the planets, with a lifetime of 10^4 years. Their charge spectrum reflects the composition of the region of the sun in which they were produced. Their isotropy is insured by their interaction with the magnetic fields of the sun, the earth, and possibly of the planets, as shown by Kane, Shanley, and Wheeler.[10]

The more energetic band of the primary cosmic radiation (energies above 10^{13} to 10^{14} ev) is not produced in the solar system, but comes from the whole galaxy. It consists of the particles which have leaked out from the trapping fields of the producing stars and have possibly undergone further acceleration in the cosmic space. These particles disappear, partly destroyed by collisions with interstellar matter, and partly by diffusing out of the galaxy; anyway their lifetime is at least of the order of 10^8 years and their charge spectrum does not maintain the peculiarities of the composition of the stars from which the particles come.

An intermediate region of energies must be present, whose characteristics are intermediate between those of the two extreme bands.

With a picture of this kind, the density δ of the energy of the cosmic radiation in the galaxy would essentially be the density of the energy of the particles with energy above, say, 10^{13} ev; with the usual 1.8 power spectrum, $\delta=6\times10^{-13}$ erg cm^{-3}; with a lifetime of 10^8 years this corresponds to an output of power 10^8 times smaller than the power going into electromagnetic radiation. The argument of Richtmeyer and Teller[11] against a galactic origin of the cosmic radiation thus loses some of its weight.

The author is grateful to Professor H. A. Bethe and Dr. S. Hayakawa for helpful criticism and suggestions.

[7] Smaller values for λ and larger values for s would be found if, instead of a spherical galaxy, one assumed a disk-like one, as it actually is.

[8] E. Fermi, Phys. Rev. **75**, 1169 (1950).

[9] H. L. Bradt and B. Peters, Phys. Rev. **80**, 943 (1950).

[10] Kane, Shanley, and Wheeler, Revs. Modern Phys. **21**, 51 (1950).

[11] R. D. Richtmeyer and E. Teller, Phys. Rev. **75**, 1729 (1949).

Absorption by Aluminum in the Soft X-Ray Region*

D. H. TOMBOULIAN AND E. M. PELL
Cornell University, Ithaca, New York

(Received June 8, 1951)

Measurements on the absorption by aluminum in the spectral range extending from 80A to 600A have been carried out by the use of a grazing incidence spectrograph. The investigation has revealed that the strong absorption band centered at 129A is a "surface" phenomenon which takes place in the metal-substrate interface of absorbers prepared by evaporation. Thin metallic foils without a substrate do not show this absorption band. The present data have yielded consistent results for the mass-absorption coefficient, whose value ranges from 1.0×10^4 cm²/g to 2.8×10^4 cm²/g in the above spectral region. As observed previously in connection with the K edge, a secondary structure is also present on the short wavelength side of the $L_{2,3}$ edge. The L_1 absorption limit has not been detected.

INTRODUCTION

THE soft x-ray emission spectra of many crystalline metallic and nonmetallic elements of low atomic number have been investigated rather thoroughly.[1,2] The emission spectra referred to are due to electron transitions from the valence band to vacant K or L levels. Since the width of these inner levels is relatively small, the observed intensity distribution in the emission spectrum furnishes information concerning the level density of the populated states of the crystal lattice.

Measurements on the absorption by the light elements are less extensive. Since the absorption process involves the transition of electrons into unoccupied levels such measurements yield additional information concerning the level structure. If the absorber be irradiated by photons of energy greater than $h\nu_q$, where ν_q is the frequency corresponding to the q absorption edge, the incident photon may be absorbed by an electron in the q level. If the photon energy is less than $h\nu_q$ the absorption does not involve the q level. For example, in the case of aluminum, the absorption of photons of energy somewhat greater than $h\nu_L$ involves primarily an L electron; while photons whose energy is less than $h\nu_L$ may only be absorbed by electrons in the conduction band. Thus, the absorption on the short wavelength side of the edge reflects the characteristics of the unoccupied levels, while that on the long wavelength side portrays the combined features of filled as well as unfilled levels.

Measurements on various metallic elements whose absorption edges lie in the soft x-ray region have been reported by several investigators.[3-7] These observations deal with the K-edge of Li; the $L_{2,3}$ edges of Na, Mg, and Al; and the $M_{2,3}$ edges of Ni, Cu, and Zn. A summary of the numerical absorption data for the foregoing elements (except Na) are given in reference 6. Although the K-edge of Be and B; and the L-edges of Si, P, and S also fall in this region, no measurements seem to have been carried out on these elements as yet.†

A survey of the results obtained previously leads to the following summary with regard to the characteristic features of the absorption curve in the neighborhood of the K or L limit.

(1). The metals Li, Na, Mg, and Al show a well-defined K or $L_{2,3}$ absorption edge. A somewhat diffuse L_1 edge should also appear in the spectra of the last three metals. The observations yield no conclusive evidence of the presence of this edge, though it should lie in the wavelength range investigated.

(2). In the M-absorption spectra of Ni, Cu, and Zn, a somewhat diffuse $M_{2,3}$ edge is established, though the M_1 limit is not observed definitely.

(3). The absorption curves in general show secondary structure. On the short wavelength side of the K edge in Li and of the $L_{2,3}$ edge in the case of Mg and Al, there appears a surprisingly intense absorption band. A correspondingly strong absorption is not observed near the K edge of the latter elements.

(4). The reported measurements indicate the presence of large discrepancies in the values of the absorption coefficient as arrived at from absorbers which differ in thickness.

The experimental procedures in the 50 to 500A region, are subject to difficulties. Of prime importance in making reliable absorption measurements is a source of strong more or less continuous radiation. Such a source does not exist. The continuum emitted by x-ray targets is extremely weak in this region. One is therefore limited to the use of line spectra emitted by highly excited atoms in a condensed spark discharge. Aside from the discontinuous nature of such a source, measurements become less reliable due to the variation in the relative intensities of lines and due to the presence and overlapping of higher order spectra.

A second difficulty lies in the preparation of suitable

* Work supported by the ONR.

[1] H. W. B. Skinner and H. M. O'Bryan, Trans. Roy. Soc. (London) **239**, 95 (1940).
[2] W. M. Cady and D. H. Tomboulian, Phys. Rev. **59**, 381 (1941).
[3] V. H. Sanner, Z. Physik. **94**, 523 (1935).
[4] H. M. O'Bryan, Phys. Rev. **49**, 944 (1936).
[5] H. W. B. Skinner and J. E. Johnston, Proc. Roy. Soc. (London) **161**, 420 (1937).
[6] J. E. Johnston, Proc. Cambridge Phil. Soc. **35**, 108 (1939).
[7] H. M. O'Bryan, Phys. Rev. **57**, 995 (1940).

† *Note added in proof:* Preliminary measurements on Be were reported by D. H. Tomboulian and R. W. Johnson at the Washington meetings of the Am. Phys. Soc., Phys. Rev. **83**, 220 (1951).

absorbers. For this purpose one needs uncontaminated metallic films preferably of known thickness not exceeding 5000A. Usually such absorbers are made by evaporating the substance on a transparent supporting film or on a backing layer which can be removed. Samples prepared in this manner may contain traces of impurities or may not be crystalline in character. Furthermore, if absorption coefficients are to be evaluated, one has to contend with the problem of ascertaining the thickness of the absorber with some degree of precision.

Finally, there are the limitations in intensity measurements imposed by the photographic method. This method is at present the one generally used for the comparison of intensities although recent techniques involving photomultipliers show promise.

The foregoing troublesome experimental features are to a large extent responsible for the scarcity and lack of refinement in absorption measurements in the far ultraviolet region.

It was considered worthwhile to select an absorber, such as aluminum, which is convenient to work with and to re-examine the various features of the absorption curve in the neighborhood of the L limit. In particular the investigation was undertaken (1) to institute a search for the L_1 edge, whose location had more recently been predicted[8] on the basis of radiative transitions within the L shell; (2) to investigate the intense selective absorption on the short wavelength side of the edge as indicated by previous measurements; (3) to extend the range of measurements and if possible to arrive at more definitive values for the absorption coefficient.

EXPERIMENTAL

The source of radiation was a condensed spark discharge in a glass capillary. Such a source produces an intense line spectrum superimposed on a relatively weak continuum. The lines emitted by this source are due primarily to ionized atoms of oxygen, nitrogen, silicon, and sodium, and except for the very short wavelengths are sufficiently densely distributed over the range of interest. The intense lines of this spectrum are classified and their wavelengths have been determined accurately by Edlen.[9] A large number of tests have established the fact that if operated under carefully controlled conditions, the relative intensities of the lines from the capillary discharge do not differ by more than a few percent from one exposure to another though the absolute intensities for a dozen or more sparks are subject to somewhat greater variation (about 5 percent).

The dispersing instrument was a grazing incidence spectrograph which in the neighborhood of 200A had a dispersion of 1A per mm. For photometric purposes a slit width of 0.10 mm was used, and for this slit width a practical instrumental resolving power of 400 was readily attainable for the wavelength region specified above.

Several types of absorbers were utilized. The thickest sample consisted of rolled aluminum foil while the thinner ones were prepared by condensing the metal on thin backing films of zapon. Two samples of intermediate thickness were prepared by careful etching of the rolled foil. Foils whose thickness was in excess of 6000A practically absorbed all the wavelengths shorter than that of the edge, while those of only several hundred angstroms in thickness were almost equally transparent on either side of the edge. Calculation[10] indicates that the optimum thickness of the absorber should be about 1500A. The present measurements were conducted with absorbers whose thickness ranged from 200 to 6500A. The backing films used had a transmission of 50 percent in the vicinity of 300A and were considerably more transparent at shorter wavelengths. The absorption by the backing film varied only slowly with wavelength and was free from selective effects.

For the rolled foils, the absorber thickness was arrived at by weighing samples on a microbalance, successive weighings being in agreement within $\frac{1}{2}$ percent. The samples selected were tested for uniformity in thickness by placing a large sample in the path of the incident beam and by comparing the absorption produced by different regions of the foil. The thickness of the etched foils was determined indirectly by a scheme to be mentioned later. In the case of evaporated films the sample thickness was estimated[11] by distilling a known weight of the metal from a battery of tungsten evaporators so arranged as to insure a uniformly deposited layer. The thickness so calculated was checked by weighing a deposit of known area. The two results differed by about 1 percent. It is known[12] that in this procedure the evaporated Al film is not contaminated by tungsten. Extreme precautions were taken to maintain cleanliness of the apparatus and good vacuum conditions within the distilling chamber. The absorbers of different thicknesses were prepared under as reproducible conditions as possible.

Electron diffraction experiments by Stahl[13] seem to indicate that if the evaporation is carried out in an interrupted fashion, the deposits obtained consist of sandwiched layers of the pure metal and its oxide. Such studies indicate further that an amorphous deposit may be present on the outer surface and that on exposure to air the fresh surface layers become oxidized only to a depth of 50A. The present measurements gave no evidence that samples prepared by continuous or by interrupted evaporation were sufficiently different in structure as to affect the character of the observed absorption curves. In all but the thinnest absorbers

[8] D. H. Tomboulian, Phys. Rev. **74**, 1887 (1948).
[9] B. Edlen, Nova Acta Regiae Societatis Scientarium Upsaliensis **9**, No. 6, (1934).
[10] A. Sandstrom, Nova Acta Regiae Societatis Scientiarum Upsaliensis Ser. IV **9**, No. 11 (1935).
[11] R. C. Williams, J. Appl. Phys. **20**, 98 (1949).
[12] J. Strong, *Procedures in Experimental Physics* (Prentice-Hall, Inc., New York, 1946), p. 173.
[13] H. A. Stahl, J. Appl. Phys. **20**, 1 (1949).

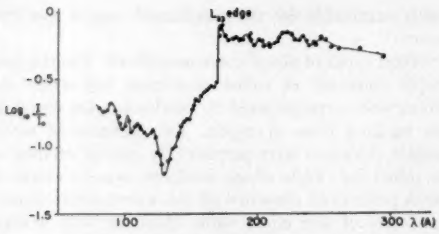

FIG. 1. Absorption curve in the neighborhood of the $L_{2,3}$ edge of aluminum. The absorber was prepared by depositing a 1000A layer of the metal onto a zapon substrate.

used, the influence of the oxide layer was considered to be negligible.

PROCEDURE

For the actual runs, two mountings were prepared from the same zapon film. These two supporting layers received identical treatment with regard to aging and exposure to vacuum conditions except that one of them was coated with the desired thickness of aluminum. The two specimens were then mounted on a rotary shaft behind the spectrograph slit, and as close to the slit as possible. This should minimize fogging and deterioration of the image due to radiation which is scattered by the foil and falls on the grating at angles other than those necessary for focusing. By means of external controls, it was possible to rotate the specimens in the interval between sparks so that either the bare zapon film or the one coated with aluminum was introduced in the path of incident beam. The arrangement of the plate holder was such that it could also be raised or lowered quickly behind an occulator without disturbing the vacuum. Two juxtaposed spectra could thus be obtained on the same plate, one representing the absorption by the bare zapon film and the other that due to the metal and zapon films in combination. In order to smooth out the effect of fluctuations in the intensity of individual sparks, intermingled exposures were made on the same plate by inserting the coated and uncoated films alternately in the path of the beam.

The ratio of the total number of sparks used for the individual exposures was adjusted so as to obtain comparable photographic densities in the adjacent spectra. This ratio was varied from 2 to 20 depending on the thickness of the absorber and no exposures were made in which the total number of sparks was less than 10. The photographic plates (Ilford QI) were calibrated by utilizing the L-emission band of aluminum[2] and also by a procedure described by Skinner and Johnston.[5] Calibration curves were obtained over the required wavelength range by the latter scheme, which assumes the constancy of the intensity ratios of lines in two spectra taken with different number of sparks. Over the region of overlap, the two methods gave results which were in good agreement.

RESULTS

A typical absorption curve obtained by the use of evaporated samples of aluminum is reproduced in Fig. 1. (For the given curve the thickness of the deposit was 1000A.) In the quantity plotted as the ordinate, I_0 represents the intensity of the radiation emergent from the uncoated zapon absorber, while I stands for the intensity of the beam after passage through the absorbing layers of aluminum and zapon. In accordance with the relation $-\mu x=2.30\log_{10}(I/I_0)$ the ordinate corresponding to a given wavelength λ is proportional to the linear absorption coefficient μ since x, the absorber thickness, is fixed. The experimental points represent averages determined from six to ten plates taken with varying exposure ratios. The general features of the absorption curve, such as the $L_{2,3}$ limit at 170A, the intense absorption band centered at 129A, and the secondary structure were also observed on similar curves obtained with five different samples of deposited layers whose thicknesses ranged from 500A to 2500A.

It follows from the aforementioned relation that for a given wavelength, the quantity $\log_{10}(I_0/I)$ should be directly proportional to the absorber thickness x. When the measurements on evaporated samples were tested for this consistency, it was found that, for wavelengths in the neighborhood of the edge, the expected regularity was valid within the limits of experimental uncertainty. It must be mentioned that reproducible values of $\log_{10}(I_0/I)$ were achieved only through the maintenance of scrupulous cleanliness in the evaporation process. However, over the general region of the selective absorption band (110 to 150A) the data failed to follow the expected linear relation. Examples of this behavior are shown in the plot of Fig. 2 for the three wavelengths indicated thereon. The data represented by circles are based on absorbers prepared by distillation. The estimated error in $\log_{10}(I_0/I)$ and that in x is indicated by the sides of the rectangles. The two points designated by triangles (△) were obtained from measurements on rolled metal foil, whose thickness was

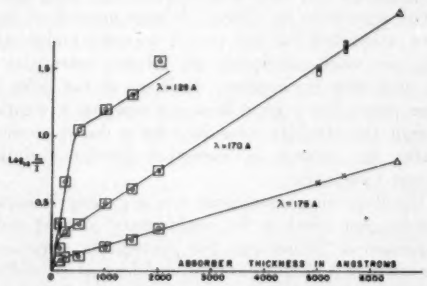

FIG. 2. A plot of $\log_{10}(I_0/I)$ *versus* x, the absorber (Al) thickness. The data for absorbers with zapon substrate are designated by circles. The data for the absorbers thicker than 3000A were obtained by the use of foils without substrate.

determined by weighing. The determinations represented by crosses (×) will be commented upon in the discussion which follows.

The discrepancy observed in connection with the plot of Fig. 2 suggested the desirability of testing absorbers free from zapon backing and led to the use of self-supported metallic foils. When rolled foils were used the intensity transmitted on the high energy side of the edge was too feeble for reliable measurements. It was therefore necessary to reduce the thickness of such absorbers. This was accomplished by etching the foils gradually until samples of sufficient transparency were obtained. The absorption curve of the thinnest sample of this type is reproduced in Fig. 3. Here I_0 represents the intensity of the radiation incident upon the foil and I is the intensity emergent from it. A comparison of the shape of this curve with that of the one shown in Fig. 1 reveals the striking fact that the intense absorption band, which is invariably present in the observations made on evaporated layers, no longer exists when etched foils free from a substrate are used for absorbers. Since the absorption on the long wavelength side of the edge seemed to be linear with x in each case, the thickness of the particular etched sample was determined with the aid of the linear relationship between $\log_{10}(I_0/I)$ and the absorber thickness given in Fig. 2. Thus, from the value of the ordinate of the curve in Fig. 3 at a wavelength (175A) selected previously for one of the linear plots in Fig. 2, the thickness of the etched absorber was found to be 5000A. As a check the value of $\log_{10}(I_0/I)$ at a second wavelength (170A) was plotted in Fig. 2 against the absorber thickness arrived at in the manner just described. Such points, corresponding to the two etched samples, are indicated by crosses in Fig. 2. Unfortunately, due to the extreme fragility of the etched absorbers, it was not practical to prepare thinner specimens.

As a possible cause for the large dip observed in the absorption curves of samples prepared by evaporation one may consider the introduction of impurities, the formation of oxide layers, or the properties of the supporting film. Or, the effect may arise from peculiarities inherent in the crystalline structure of the evaporated film. A similar dip in the absorption is also present in the curve obtained by Johnston[6] who used foils prepared by vaporizing aluminum from a molybdenum crucible under electron bombardment and condensing the metal onto thin backing films of celluloid. Since the absorbers used in the present measurements were prepared by a different procedure, it is unlikely that the effect is due to peculiarities of the distillation process, such as the presence of impurity atoms of tungsten or molybdenum. Absorbers prepared by interrupted evaporation and presumed to contain sandwiched layers of the oxide[13] did not behave differently from other absorbers. The effect cannot arise from the unavoidable surface layer of oxide since the latter must also be present in the case of etched foils which show

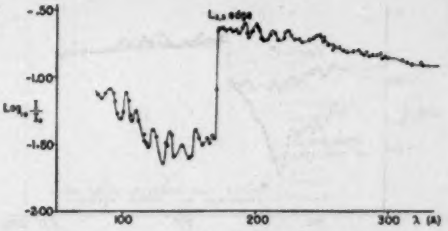

FIG. 3. Absorption curve for aluminum in the region of the $L_{2,3}$ edge. The absorber consisted of a metallic foil (no substrate) 5000A in thickness.

no selective absorption. In addition, the absorption curve of pure Al_2O_3 was determined for comparison purposes. No similarities were found between the absorption curve of the oxide and that of the evaporated metal.

It is possible to determine the thickness of evaporated films very precisely by the methods of multiple-beam interferometry.[14] Such thickness determinations in conjunction with microchemical techniques indicate that thin films (100 to 500A) of Al, Cu, and Ag have densities which are very nearly the same as those of the bulk metal. Furthermore, an electron diffraction pattern of one of our samples has confirmed the crystalline nature of the deposit. Thus, one is led to believe that thin Al films possess the characteristic structure of the metal lattice.

In the present tests both zapon and polystyrene substrates were used and Johnston used a celluloid backing film in his experiments. The absorption by these materials has been studied over the spectral range concerned and is found to be quite free from large fluctuations. When metals are deposited on thin films of these plastics the extra absorption is present in all cases and does not seem to be influenced by the chemical nature of the supporting film.

From the plot shown in Fig. 2, it is seen that, in particular, the 129A radiation is more strongly absorbed in the first 500A of Al than it is in the rest of the sample. By reference to the slope of this curve it is seen that the absorption beyond this thickness is about the same as at 170A, as it should be if the peculiar absorption structure were absent. This suggests that the strong dip in the absorption curve centered at 129A arises from some sort of "surface" effect limited to a depth of about 500A taking place in the region of the aluminum-substrate interface.

Although the unexplained absorption seems to be associated with the metal-backing interface, the mechanism that accounts for it is not known. The absorption may arise from transitions between energy levels in the metal and levels in some element common to the different substrates used. Or it may be due entirely to the

[14] S. Tolanski, *Multiple-Beam Interferometry* (Clarendon Press, Oxford, England, 1948), p. 148.

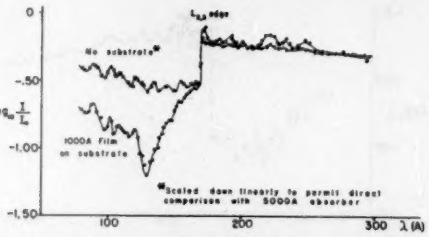

FIG. 4. The effect of substrate on absorption. A comparison of the results shown in Figs. 1 and 3.

metal, the substrate serving only to change the metal lattice near the surface or perhaps serving as a medium into which metallic atoms or ions can diffuse.

That the absorption is characteristic of the metal and not of the substrate appears to be confirmed by the results obtained by Skinner and Johnston[6] who used lithium and magnesium deposits on celluloid. Unexplained dips are present in their results. But in the case of lithium there are two dips instead of one and the distance of either to the absorption edge is appreciably smaller than in the case of Al or Mg. If the absorption is due to an energy level provided by a common element in the substrate, one would not expect an additional absorption band to show up merely through the use of Li instead of the other metals.

It is likely that in the condensation process the metal atoms penetrate the body of the substrate thus forming an interface region several hundred angstroms thick. Only at the pure aluminum boundary is the lattice characteristic of the metal. In the transition region, each metal atom is surrounded by substrate atoms in neighborhood configurations that vary greatly for different metal atoms. Upon the absorption of a photon, the $L_{2,3}$ electron is ejected from the metal atom and goes to an outer level which is essentially atomic in origin and character. Such a selective transition would give rise to a rather sharp absorption line or lines. But because of the difference in the immediate surroundings, the sharp lines may overlap in energy positions and thus give rise to the observed band or dip in absorption.

The wavelengths of the positions of the absorption dips are all within a few electron-volts of the wavelengths corresponding to certain atomic transitions in the metallic ions stripped to their rare gas cores. It may be proposed that the metal might diffuse into the substrate, there forming an ionic structure with the cation stripped of all its valence electrons. This seems possible energetically. Estimates indicate that even if the initial state is strongly localized in the neighborhood of the positive ion, the final state in the absorption process would probably overlap with neighboring negative ions. The energy of the final state would therefore be affected by coulomb and exchange interaction, as well as by the change in the Madelung potential. It is conceivable that these factors might compete with each other, in such a way that the energy would be changed only slightly relative to what it would be in the gaseous ion. No calculations have been made to prove or disprove these hypotheses and such explanations must be regarded as pure speculation.

The lower curve in Fig. 5 is a plot of the present measurements showing the secondary structure on the high energy side of the $L_{2,3}$ edge. The data for this curve were derived from a study of etched-foil absorbers, though many of the characteristic peaks and valleys were also present in the measurements made on absorbers prepared by evaporation (see Fig. 4). It is interesting to note that appreciable structure is observable to within a few electron-volts of the L-edge. The upper curve in Fig. 5 is reproduced from a study[15] of the structure in the neighborhood of the K-limit (7.95A). The vertical scales in Fig. 5 are arbitrary. The curves are drawn so as to match the positions of the K and L limits approximately. The secondary structure observed in these experiments falls within 75 ev of the edge and theerfore cannot be accounted for on the basis of Kronig's theory.[16] The structure in this energy region is usually regarded[17] as atomic in character. The positions of the observed maxima and minima, the shapes of the peaks and valleys should be dependent on the initial state of the photoelectrically ejected electron (s electron from the K shell and p electron from the L shell).

COMMENTS ON THE L_1 EDGE

Studies in the soft x-ray spectra of the light metallic elements have been unsuccessful in detecting the emission band which should be observed when conduction electrons make transition into a vacated L_1 level. The absence of such an emission band is ascribed to the operation of other processes whereby an excited atom may leave the L_1 state by a radiationless transition (Auger effect) or by a radiative transition within the L-shell. Because of such competing transitions the intensity of the L_1 emission band is so weakened and/or broadened as to escape detection. However, in ab-

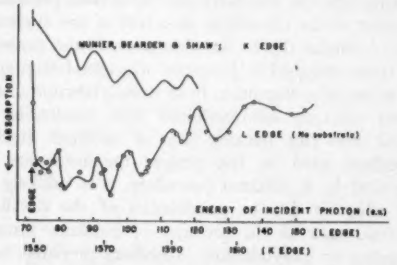
MUNIER, BEARDEN & SHAW: K EDGE
L EDGE (No substrate)
ABSORPTION
EDGE
ENERGY OF INCIDENT PHOTON (e.v.)
70 80 90 100 110 120 130 140 150 (L EDGE)
1550 1570 1590 1610 (K EDGE)

FIG. 5. Secondary structure on the short wavelength side of the $L_{2,3}$ absorption edge of aluminum.

[15] Munier, Bearden, and Shaw, Phys. Rev. 58, 537 (1940).
[16] R. DeL. Kronig, Z. Physik 75, 191 (1932).
[17] D. Coster and S. Kiestra, Phil Mag. 41, 144 (1950).

sorption the L_1 edge should have a better chance of being observed, since it is expected that in the absorption process the transition probability from an L_1 to empty conduction levels ($s \rightarrow p$) should compare favorably (in the ratio 4 to 11 by calculation[18]) with those from $L_{2,3}$ into empty valence levels ($p \rightarrow s$). Previous investigations[5,6] in the absorption spectra of Mg and Al have clearly revealed the position of the $L_{2,3}$ edge. The L_1 edge should be greatly broadened relative to the $L_{2,3}$ edge, because of the above factors reducing its life time. And in fact, the location of the L_1 edge cannot be regarded as experimentally established.

In two previous reports[19,20] experimental evidence has been presented for the existence of radiative transitions within the L-shell of the four light elements Na, Mg, Al, and S. On the basis of such identifications, the L_1 edge in Al should appear at about 105A. Unfortunately, the present measurements do not show evidence of an absorption edge at the predicted position. Presumably, the secondary structure associated with the $L_{2,3}$ edge masks the L_1 absorption edge which is expected to be somewhat weak and very diffuse.

ABSORPTION COEFFICIENT AS A FUNCTION OF WAVELENGTH

The available experimental data on (τ/ρ) the mass absorption coefficient for aluminum over the region 1A to 600A are summarized graphically in Fig. 6. The data in the region of the K limit are taken from the papers by Allen[21] and Hill,[18] while those in the region of the L-edge are based on the present measurements. The experimental determination of the mass absorption coefficient includes the effects of scattering and reflection in addition to the photoelectric absorption which predominates. No direct determination of the scattering is available above 1.6A; and the effect of scattering is assumed to be negligible.

Sabine's[22] measurements on evaporated films of Al indicate that the reflectivity of the metal is less than 3 percent below 600A. Hence the effect of reflection may also be ignored, and the measurements in the region concerned essentially represent the photoelectric absorption only.

A discussion of the photoelectric absorption for x-rays is given by Hall.[23] By the use of the expression for the dependence of (τ/ρ) on frequency, as given by Eq. (6) in Hall's paper, the theoretical values of the mass-absorption coefficient on the short wavelength side of

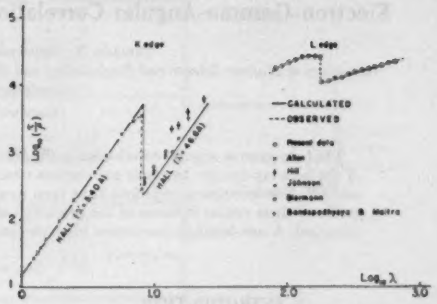

FIG. 6. A plot of the mass absorption coefficient as a function of wavelength. The spectral region extends from 1A to 600A. The present measurements cover the region on either side of the $L_{2,3}$ edge.

the K edge were calculated for the ideal absorption limit $\lambda' = 5.40$A. Similar calculations were carried out for the long wavelength side of the K edge utilizing the general functions listed in Table II of Hall's article. In the latter computation, λ'', the hypothetical wavelength of the L edge was determined using the screening constant for the L-shell as given by Slater.[24] The numerical value of λ'' turns out to be 46.6A.

A more refined value of the wavelength corresponding to the K edge may be predicted on the basis of a formula derived by Kennard and Roess.[25] This relation yields the value of 8.20A for the position of the K edge.

The results of the theoretical calculations mentioned above are indicated on Fig. 6 by the solid limes. The agreement with the experimental measurements is satisfactory as far as the short wavelength side of the K edge is concerned. The departure on the long wavelength side of the K edge is not surprising since the theory ignores the effect of the crystal lattice of the absorber. So far as the authors are aware, the present measurements constitute the only attempt to extend the determination of absorption coefficients into the very soft x-ray region. It is gratifying that the L-region coefficients are not seriously out of line with an extrapolation from the K-region measurements and calculations.

Acknowledgments are due Professor L. G. Parratt and Dr. E. L. Jossem for many helpful discussions throughout the course of this investigation. We also wish to thank Professor J. A. Krumhansl for assistance offered in connection with the problem of the intense absorption band. The research was supported by the Office of Naval Research.

[18] R. D. Hill, Proc. Roy. Soc. (London) **A161**, 284 (1937).
[19] D. H. Tomboulian and W. M. Cady, Phys. Rev. **59**, 422 (1941).
[20] D. H. Tomboulian, Phys. Rev. **74**, 1887 (1948).
[21] S. J. M. Allen, Phys. Rev. **27**, 266 (1926).
[22] G. S. Sabine, Phys. Rev. **55**, 1064 (1939).
[23] H. Hall, Revs. Modern Phys. **8**, 358 (1936).
[24] J. C. Slater, Phys. Rev. **36**, 57 (1930).
[25] E. H. Kennard and L. C. Roess, Phys. Rev. **38**, 1267 (1931).

Electron-Gamma-Angular Correlation Measurements in Radioactive Decay*

DONALD T. STEVENSON AND MARTIN DEUTSCH
Laboratory of Nuclear Science and Engineering, and Department of Physics, Massachusetts Institute of Technology, Cambridge, Massachusetts
(Received June 7, 1951)

The beta-gamma angular correlations in the decay of a number of nuclides have been studied as a function of the beta-ray energy. Isotropic correlations were found in the decay of Co^{55}, Co^{56}, Co^{60}, Na^{22}, Na^{24}, Cs^{134}, and I^{134}. Non-isotropic correlations have been measured in the decay of Rb^{86}, Sb^{124}, and I^{126}. The interpretation of these results in terms of the properties of the emitted radiations and the nuclear energy states is discussed. A non-isotropic conversion electron-gamma-angular correlation was found in the decay of Mo^{99}.

1. INTRODUCTION

IN recent years angular correlation measurements have taken their place with the measurement of internal conversion coefficients, lifetimes, and spectral shapes in the determination of the angular momentum and parity of nuclear levels.[1] In this paper we shall describe measurements of beta-gamma and conversion electron-gamma correlations.

The theory of beta-gamma angular correlation has been dealt with most extensively by Falkoff and Uhlenbeck[2] who have calculated explicit beta-gamma correlation functions for all possible cases involving an angular momentum change of one or two for the beta-ray and the gamma-ray, assuming a zero nuclear charge and assuming a single nuclear matrix element is responsible for the beta-transition. Lennox and co-workers[3] have calculated explicit correlation functions for some special cases assuming a finite nuclear charge and mixtures of matrix elements. The theory of conversion electron-gamma angular correlation has been studied by Ling and Uhlenbeck.[4] They have computed these correlations for K shell conversion using various approximations for the atomic wave functions.

In all of these theoretical studies it is assumed that the lifetime of the intermediate state of the nucleus is so short that no appreciable reorientation takes place before the emission of the second radiation. It is also assumed that the efficiency of the radiation detectors are polarization and spin insensitive. Goertzel[5] has made a theoretical study of the effect of reorientation of the nucleus by the atomic magnetic field and by externally applied magnetic fields.

Some general conclusions of the theoretical studies which apply to all types of angular correlations discussed in this paper are stated here:

1. The correlation function will always be of the form:

$$W(\theta)=1+a_1\cos^2\theta+a_2\cos^4\theta+\cdots.$$

Only even powers of $\cos\theta$ appear.

2. The coefficients a_1, a_2, etc., depend on the angular momenta of the three nuclear states involved and on the nature of the transitions. For a gamma-transition the coefficients depend on the multipole order of the transition but not on parity change. For a beta-transition the coefficients depend on the particular matrix element responsible for the transition. The conversion electron-gamma-correlation coefficients depend on the atomic shell in which the conversion takes place and on the multipole order and parity change of the transition.

3. No higher power of $\cos\theta$ can appear than $2L$, where L is the smaller of the angular momenta carried away by the emitted particles.

4. No higher power of $\cos\theta$ can appear than $2J$, where J is the angular momentum of the intermediate state. For example, if $J=0$ or $J=\frac{1}{2}$ there will be no correlation.

Some further theoretical conclusions applicable only in the beta-gamma case should also be given here:

1. If the beta-transition is allowed there will be no correlation.

2. If the beta-transition is forbidden but the shape of the spectrum is strictly identical with the allowed shape there will be no correlation.

3. For the axial vector and tensor interactions the highest power of $\cos\theta$ that can appear in $2F$ where F is the degree of forbiddenness. For example, for first-forbidden axial vector or tensor interactions $\cos^4\theta$ terms do not appear even though these transitions may involve an angular momentum change of two.

4. The beta-gamma angular correlation depends on the maximum energy of the beta-spectrum involved. If beta-rays of all energies are detected the so-called integral correlation will be observed. If beta-rays of a particular energy only are detected the so-called differential correlation will be observed. The differential correlation depends on the energy of the beta-rays being observed and vanishes as the energy of the beta-rays being observed tends to zero.

5. The correlation computed assuming the actual value of Z for cases where matrix elements like $\int \sigma \times \mathbf{r}$ are involved is substantially lower in absolute value

* This work has been supported in part by the joint program of the ONR and AEC.
[1] E. L. Brady and M. Deutsch, Phys. Rev. **78**, 558 (1950).
[2] D. L. Falkoff and G. E. Uhlenbeck, Phys. Rev. **79**, 334 (1950).
[3] M. Fuchs and E. S. Lennox, Phys. Rev. **79**, 221 (1950); E. S. Lennox, private communication.
[4] D. S. Ling, thesis, University of Michigan (1948), unpublished.
[5] G. Goertzel, Phys. Rev. **70**, 897 (1946).

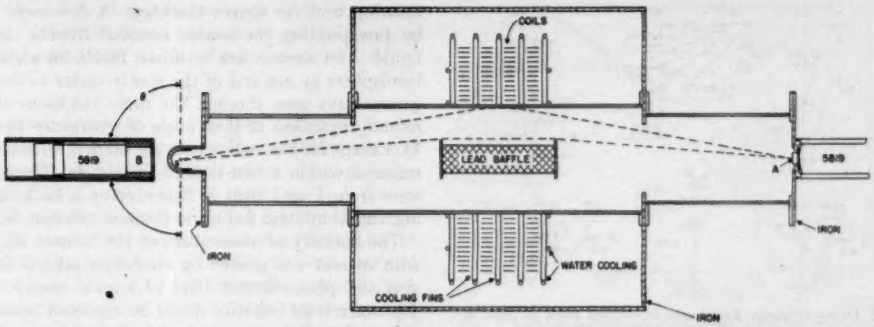

FIG. 1. Apparatus for observing beta-gamma angular correlations. S is the source, A is the thin anthracene crystal of the beta-counter, and B is the NaI crystal of the gamma-counter.

than that computed from the $Z=0$ approximation. When matrix elements like B_{ij} are involved the correlation is nearly independent of Z.

2. EXPERIMENTAL PROCEDURE

The simplest experimental arrangement would consist of a source set up between a beta-counter and a gamma-counter, one of which could be rotated around the source. Appropriate electronic equipment to operate the counters and record the coincidences would also be needed. Several such experimental arrangements have been described recently.[6] In these arrangements the energy of the beta-particles being observed is fixed by the amount of absorber in front of the counter and if a scintillation counter is used by the height of pulse accepted by the counting equipment. For this research this simple arrangement was modified by inserting a thin-lens beta-ray spectrometer between the source and the beta-counter to select the energy of the beta-rays being observed. By selecting beta-particles in a narrow range of energy we are able to measure the differential correlation. A sketch showing the position of the source, counters, and the spectrometer is given in Fig. 1.

At energies near the maximum beta-energy the differential correlation is expected to be larger than the integral correlation and might be easier to find. Furthermore, if a correlation is found we are able to measure the differential correlation as a function of energy. This provides additional information when comparing the experiments with the theory.

The use of a lens spectrometer has certain advantages from an experimental point of view. Its use allows the beta-counter to be placed at some distance from the gamma-counter. Since the electrons follow curved paths in the spectrometer, the direct line of travel from the source to the beta-counter can be filled with sufficient lead-absorber to prevent any gamma-rays from being counted in the beta-counter. In the decay of a nucleus such as Co^{60} where a gamma-gamma correlation exists, a spurious beta-gamma correlation might be observed if the gamma-ray efficiency of the beta-counter were not very small. If the nucleus being studied is a positron emitter the possibility of observing a spurious beta-gamma correlation is much increased since the two gamma-rays emitted when the positron is annihilated always come off with an angle of 180 degrees between them. In any case eliminating gamma-counts in the beta-counter reduces the chance coincidence rate. Locating the beta-counter some distance away from the gamma-counter also eliminates the possibility of registering a coincidence when a gamma-ray is Compton scattered from one counter to the other.

The spectrometer used in this experiment was of the conventional thin lens type.[7] This type of spectrometer was chosen because of its simplicity and because it can be adjusted so that the angular spread of electrons transmitted and the momentum resolution are satisfactory for angular correlation experiments. Furthermore, its use allows both the source and the detectors to be placed outside the magnetic field. The coil, wound around the center of the spectrometer chamber, is surrounded by $\frac{3}{16}$-inch steel plate and the spectrometer endplates are made of steel so as to reduce the magnetic field at the positions of the counters. This is necessary since the amplification of the photomultipliers used in the scintillation counters is very sensitive to changes in the magnetic field. The spectrometer baffles were set so that the momentum resolution $\Delta p/p$ was about 0.15. With this baffle setting the transmission of the spectrometer for electrons of a given energy was about $\frac{3}{4}$ percent.

The beta-counter consists of a small crystal of anthracene about $\frac{3}{4}$-inch square and $\frac{1}{4}$-inch thick and an RCA 5819 photomultiplier. The crystal is mounted on the vacuum side of a glass plate which seals a hole in

[6] R. L. Garwin, Phys. Rev. **76**, 1876 (1949); Grace, Allen, and Halban, Nature **164**, 538 (1949); T. B. Novey, Phys. Rev. **78**, 66 (1950); R. Stump and S. Frankel, Phys. Rev. **79**, 243 (1950); S. L. Ridgeway, Phys. Rev. **79**, 243 (1950); **78**, 821 (1950); J. R. Beyster and M. L. Wiedenbeck, Phys. Rev. **79**, 728 (1950); **79**, 169 (1950); I. Shaknov, Phys. Rev. **82**, 333 (1951).

[7] Deutsch, Elliott, and Evans, Rev. Sci. Instr. **15**, 178 (1944).

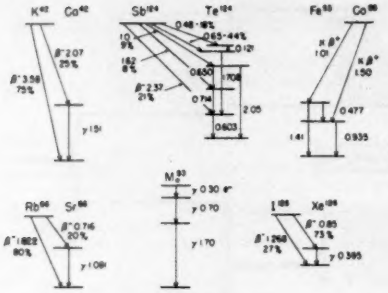

FIG. 2. Decay schemes. References to original work on these may may be found in reference 12.

the end plate. The photomultiplier is mounted outside the vacuum (see Fig. 1). The gamma-counter in some of the earlier experiments consisted of a cylinder of anthracene 1.8 inches in diameter and 1.7 inches high and a 5819. Later the efficiency of the counter was increased by replacing the anthracene by a cylinder of thallium activated sodium iodide. The sides of the crystal are protected from stray and scattered radiation by $\frac{1}{4}$-inch of lead. Sufficient lead is placed between the source and the gamma-counter to prevent the detection of gamma-rays scattered through large angles near the source. Both photomultipliers are surrounded by Permalloy cylinders to reduce the effect of magnetic fields. The tubes with their Permalloy shields are placed in grounded brass cylinders which serve to eliminate electrical pick-up and stray light.

Pulses from the multipliers are amplified by a pair of Model 501 amplifiers.[8] The coincidence circuit consists of a pair of blocking oscillators giving pulses about 0.1 μsec long. The blocking oscillator pulses are fed to separate grids of 6AS6 coincidence tube. Coincidences and the single counts in each channel are recorded simultaneously.

It is evident that to observe an angular correlation we must observe the direction of the particles just as they come from the nucleus. Any scattering between source and detector will reduce the observed correlation. In any angular correlation experiment where gamma-rays are involved care must be taken to avoid counting Compton scattered radiation since the energy and intensity of the scattered radiation is strongly dependent on angle. As noted previously we have placed sufficient lead in front of the gamma-counter to keep Compton scattered quanta out of it.

The scattering of the beta-particles in the source and the source backing is an even more serious problem. We have used the thinnest possible sources consistent with a reasonable counting rate. Most of the sources were vacuum evaporated onto a very thin backing, assuring uniform source thickness. A few were made by precipitating the source material from a drop of liquid. The sources are mounted inside an aluminum hemisphere at one end of the spectrometer so that the gamma-rays pass through the same thickness of aluminum regardless of their angle of emergence (see Fig. 1). Except for the source backing there is no scattering material within a half-inch of the source. The sources were from $\frac{1}{8}$ to $\frac{3}{8}$ inch in diameter on a backing of $\frac{1}{4}$ mg/cm^2 aluminum foil or on thinner collodion films.

The linearity of momentum of the focused electrons with current was proved by measuring several conversion and photoelectron lines of known energy. Some departure from linearity might be expected because of the steel used for magnetic shielding. Apparently the steel is far enough away from the coil to have little effect on the field inside the spectrometer tank.

With an external source of gamma-radiation the counting rates in both counters were substantially independent of a spectrometer current showing that sufficient magnetic shielding was present. Variations of about 2 percent in the gamma-counting rate as a function of angle were noted. This is attributed to a slight misalignment of the source and the axis of rotation of the counter and also to scattering by the spectrometer end plates. The effect of this variation on the measured correlation was corrected for in first order by dividing all coincidence rates by the single counting rate in the gamma-counter. The angle of the gamma-counter was changed frequently during a run to minimize errors arising from changing efficiencies, spectrometer current, resolving time, etc. The principal proof of the symmetry of the apparatus was provided by the numerous symmetrical (or zero) angular correlations observed in the decay of various nuclides.

The angular correlation was corrected for finite angular resolution assuming a theoretical correlation of the form $1+a\cos^2\theta$. For our arrangement all measured values of the angular correlation must be raised by 11 percent in absolute value. The energy dependence of the correlation was corrected for the finite momentum resolution of the spectrometer by using the observed dependence as a first approximation.

3. BETA-GAMMA ANGULAR CORRELATION RESULTS

We subtract the chance rate from the gross coincidence rate at a given angle and divide the result by the gamma single rate at that angle to obtain a number $N(\theta)$. We define $\epsilon_\theta=[N(\theta)-N(90°)]/N(90°)$. Then $E(\theta)=A\epsilon_\theta+R$, where A is the angular resolution correction factor which for our arrangement was 1.11, and R is a small correction for the momentum resolution of the spectrometer. $E(\theta)$ is to be compared with $[W(\theta)-1]$ as computed theoretically. Most of our data was taken at 180° and 90° and hence we obtain $E(180°)$ which is to be compared with the theoretical value, $(a_1+a_2+\cdots)$. In most cases enough data was

[8] W. C. Elmore and M. Sands, *Electronics; Experimental Techniques*, National Nuclear Energy Series, V-1 (McGraw-Hill Book Company, Inc., New York, 1949).

taken at 135° to show that no large $\cos^4\theta$ terms were present. The errors given in this paper are the standard deviation based only on the number of counts.

A. Rb^{86}

The decay scheme is shown in Fig. 2. Our results for E_β plotted *vs* the energy of the focused electrons are given in Fig. 3. The solid points were obtained using sources of RbCl 0.5 mg/cm² thick and 1.1 cm in diameter vacuum evaporated onto ¼ mg/cm² aluminum foil. The source material was made available to us through the kindness of Dr. C. S. Wu, who had obtained it from Chalk River. Our earlier results obtained from sources about 6 mg/cm² thick made from lower specific activity RbCl from Oak Ridge are plotted in Fig. 3 as open circles. The standard deviations of these points are approximately the same as for the solid circles at corresponding energies. It can be seen that at 525 kev both sources give the same result while at lower energies the correlation measured with the thicker source is smaller than that with the thinner sources. We take this to mean that at 525 kev and probably also at 330 kev our thin sources were thin enough to allow us to measure the true correlation. Below 300 kev our values are probably lower than the true value.

In all cases the large amount of Cs^{134} present in the source material was removed by repeated cesium silicotungstate precipitation. The absence of Cs^{134} in the purified Rb^{86} was proved by noting the absence of gamma-gamma-coincidences.

The integral correlation in Rb^{86} of +0.13 was calculated assuming an allowed spectrum shape[9] and a differential correlation passing through our observed points with the thinner sources.

The high energy beta-spectrum has a shape corresponding to the B_{ij} matrix element.[9,10] Since Sr^{86} is an even-even nucleus its ground state is expected to have spin zero and hence the ground state of Rb^{86} probably has spin two. The low energy spectrum has a shape

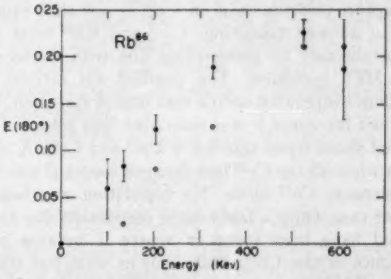

FIG. 3. Beta-gamma angular correlation of Rb^{86}. Solid circles are data obtained with the thin sources. Open circles are data obtained with thick sources. Standard deviations in the thick source data are approximately the same as for the solid circles at corresponding energies.

[9] H. R. Muether and S. L. Ridgeway, Phys. Rev. **80**, 750 (1950).
[10] Zaffarano, Kern, and Mitchell, Phys. Rev. **74**, 682 (1948).

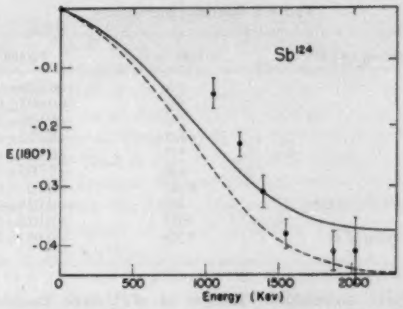

FIG. 4. Beta-gamma angular correlation of Sb^{124}. The solid line is the theoretical correlation for spins 3–2–0 and the dotted line the theoretical correlation for spins 1–1–0 with the B_{ij} matrix element responsible for the beta-transition in both cases.

consistent with an allowed transition or with some types of first-forbidden transitions.[9] An allowed transition is ruled out by the existence of a beta-gamma angular correlation. The excited level in Sr^{86} is probably one or two.

The experimental correlation is not consistent with any theoretical correlation from reference 2. Lennox and co-workers[11] have been unable to fit the data with any correlation calculated assuming a single matrix element operative but taking the nuclear charge into account. They are currently trying to fit the data with mixtures of matrix elements.†

B. Sb^{124}

Ridgeway,[6] and Beyster and Wiedenbeck[6] have reported an integral beta-gamma correlation in the decay of Sb^{124}. Our results for Sb^{124} as a function of energy are given in Fig. 4. The source material was obtained from Oak Ridge. Three different sources were used. Each consisted of metallic antimony about 1.5 mg/cm² vacuum evaporated onto a 3 mg/cm² mica backing. Although no thick sources were made for comparison it is felt that the values given in Fig. 4 are nearly the true correlation since the high electron energy reduces the scattering. Assuming the scheme given by Kern *et al.*,[12] shown in Fig. 2, the correlation above 1620-kev beta-energy involves only the 2.29-Mev negatron spectrum and the 602-kev gamma-ray. Below 1620 kev a second spectrum begins to contribute beta-gamma-coincidences to the measured rate. At about this energy the correlation is seen to drop rapidly in absolute value presumably because these additional coincidences are isotropic or perhaps even have a

[11] E. S. Lennox (private communication).
† *Note added in proof:* M. Fuchs [thesis, University of Michigan (1951), unpublished] has fitted our experimental value of the correlation in Rb^{86} by assigning an angular momentum of 2 to the excited state in Sr^{86} and using a mixture of the B_{ij}^{β} and $\int\beta\alpha$ matrix elements.
[12] K. Way *et al.*, *Nuclear Data*, National Bureau of Standards Circular 499 (1950).

TABLE I. Isotropic correlations.

Decaying nuclide	Energy (kev)	$E_\phi(180°)$
Co^{60}	111	-0.028 ± 0.02
	252	$+0.005\pm0.017$
	277	-0.023 ± 0.025
Cs^{134}	467	$+0.017\pm0.03$
Na^{22}	277	-0.021 ± 0.027
	436	-0.005 ± 0.041
Na^{24}	1045	$+0.02\ \pm0.019$
$Co^{55}-Co^{56}$ (source A)	609	$+0.026\pm0.024$
	1074	$+0.028\pm0.024$
Co^{56} (source B)	1074	$+0.013\pm0.02$

positive correlation. Langer *et al.*[13] were unable to determine whether or not the 1.69-Mev spectrum has a forbidden shape. They found the shape of the 2.29-Mev negatron spectrum to correspond to the first-forbidden matrix element B_{ij} ($\Delta J=0, \pm1, \pm2$ and parity change). Assuming all beta-transitions eventually lead to the 602-kev level they find the 602-kev gamma-ray to be electric dipole. In Fig. 4 the solid line is the theoretical correlation for angular momenta 3–2–0 and the dotted line that for 1–1–0 with the beta-transition due entirely to the B_{ij} matrix element and zero nuclear charge in both cases. As we have said the correlations involving only B_{ij} type transitions are nearly insensitive to Z. The scheme 3–1–0 with B_{ij} matrix element proposed by Langer *et al.*[13] leads to a theoretical value of $E(180°) = -0.14$ at maximum beta-energy and seems definitely ruled out by our results. The 1–1–0 scheme would seem to fit our data best since we might expect that any scattering effects would reduce the observed correlation. However, in this case the transition direct to the ground state of Te^{124} would be allowed or first forbidden only. The scarcity of these direct transitions could be accounted for by assuming that the gamma-transition is magnetic dipole and that the $L=1$ first-forbidden matrix elements $\int \beta\sigma\times\mathbf{r}$ and $\int \boldsymbol{\alpha}$ are small compared with the B_{ij} matrix element. The correlation resulting from the 3–2–0 scheme nearly fits the observed points and this scheme would explain satisfactorily the absence of direct transitions to the ground state. Perhaps a mixture of matrix elements with only a small amount of an $L=1$ matrix element with the B_{ij} matrix element would raise the correlation slightly without changing the characteristic B_{ij} shape noticeably. The 3–2–0 scheme would obviously require the gamma-ray to be quadrupole. No other plausible spin assignments with unmixed matrix elements and $L=1$ or 2 yield acceptable correlation functions for Sb^{124}. No gamma-gamma angular correlation has been found in the decay of Sb^{124} by Beyster and Wiedenbeck[14] or by the present authors. A further study is necessary before anything definite can be said about the spins and parities of the levels involved in the decay of Sb^{124}.

[13] Langer, Moffat, and Price, Phys. Rev. **79**, 808 (1950).
[14] J. R. Beyster and M. L. Wiedenbeck, Phys. Rev. **79**, 169 (1950).

C. I^{126}

The decay scheme given in Fig. 2 is due to Mitchell *et al.*[15] We have found a beta-gamma angular correlation of about 0.13 for 460-kev beta-rays in the decay of I^{126}. The source was made by evaporating a drop of water solution of NaI to dryness on a very thin collodion film. The average thickness of the source was about 2 mg/cm². The source material was obtained by an (α,n) reaction on antimony in the MIT cyclotron. The decay scheme is similar to that of Rb^{86} and from our preliminary data the correlations of the two nuclides appear to be similar. Additional measurements of the I^{126} correlations are being made in this laboratory.

D. Co^{55}, Co^{56}, Co^{60}, Na^{22}, Na^{24}, Cs^{134}, I^{124}

No beta-gamma angular correlation was found in the decay of any of the above nuclides. The results are given in Table I.

The Co^{60} source was vacuum evaporated onto a collodion backing 30 μg/cm² thick. The source material was $CoCl_2$ of specific activity 0.77 mc/mg obtained from Oak Ridge. The source strength was about 15 μc and the area $\frac{1}{3}$ cm² making the thickness about 60 μg/cm². The beta-spectrum has an allowed shape.[16]

The Cs^{134} source was vacuum evaporated onto a backing of $\frac{1}{4}$ mg/cm² aluminum foil and was about 2 mg/cm² thick. Waggoner *et al.*[16] have found some evidence that the spectrum deviates slightly from the allowed shape.

The Na^{22} source was vacuum evaporated onto a thin collodion film and was less than 100 μg/cm² thick. The spectrum has an allowed shape.[12]

The Na^{24} source was vacuum evaporated onto $\frac{1}{4}$ mg/cm² aluminum foil and was about 20 mg/cm² thick. The spectrum has an allowed shape.[17]

Approximate decay schemes of Co^{55} and Co^{56} are shown in Fig. 2. As far as is known the shape of the spectrum of Co^{56} is allowed.[18] However, Deutsch and Hedgran[19] have obtained data which indicates that the K-capture-positron ratio in Co^{55} is not that expected for an allowed transition. Co^{55} and Co^{56} were made simultaneously by bombarding iron with deuterons in the MIT cyclotron. The purified Co activity was vacuum evaporated onto a thin film of collodion. From the half-life curve it was estimated that source A contained about equal activity of Co^{55} and Co^{56}. A month later when all the Co^{55} had decayed source B was made to measure Co^{56} alone. No correlation was found in either case. Only a fairly large correlation due to Co^{55} would have been found in source A because of the presence of the Co^{56}. Both sources were less than 10 mg/cm².

[15] Mitchell, Mei, Maienschen, and Peacock, Phys. Rev. **76**, 1450 (1950).
[16] Waggoner, Moon, and Roberts, Phys. Rev. **80**, 420 (1950).
[17] K. Siegbahn, Phys. Rev. **70**, 127 (1946).
[18] L. G. Elliott and M. Deutsch, Phys. Rev. **64**, 321 (1943).
[19] M. Deutsch and A. Hedgran, Phys. Rev. **75**, 1443 (1949).

The source of I^{126} (see C) when first prepared contained a large amount of I^{124}. We found no gamma-rays in coincidence with the 2.20-Mev positron spectrum of I^{124} in contradiction with the decay scheme of Mitchell *et al.*[12] Preliminary results indicate that coincidences involving the 1.50-Mev positrons are isotropic.

4. CONVERSION ELECTRON-GAMMA ANGULAR CORRELATION

A conversion electron-gamma angular correlation was looked for in the decay of Hf^{181} and Mo^{93}. With L and M conversion electrons from the 130- and 134-kev gamma-transitions of Hf^{181} focused in the spectrometer we found the electron-gamma coincidence rate to be isotropic. The source used was very thick and it is probable that any correlation present was obscured by the scattering.

The decay scheme of Mo^{93} given by Kundu *et al.*[20] is shown in Fig. 2. With a strong electron line at 240 kev focused in the spectrometer we found a correlation of $E(180°)=+0.33$. Data at angles between 180° and 90° indicate that terms higher than $\cos^2\theta$ may be present. Interpretation of these results is not possible at this time because both K and L conversion electrons were counted and because two gamma-rays follow the conversion electron. We have measured a gamma-gamma angular correlation of about $E(180°)=+0.20$ in the decay of this nuclide.

It is a pleasure to acknowledge the advice of Professor J. W. Irvine on the chemical separations and the collaboration of Dr. J. W. Shearer in the design of the spectrometer.

[20] Kundu, Hult, and Pool, Phys. Rev. **77**, 71 (1950).

PHYSICAL REVIEW VOLUME 83, NUMBER 6 SEPTEMBER 15, 1951

The Schrödinger Equation in Quantum Electrodynamics

F. J. DYSON
Department of Mathematical Physics, University of Birmingham, Birmingham, England
(Received April 27, 1951)

Concluding a program begun in earlier papers, this paper is occupied with the analysis of the hamiltonian occurring in the Schrödinger equation of quantum electrodynamics in a new representation called the intermediate representation. It is proved that the hamiltonian is free of divergences, either explicit or implicit. The intermediate representation therefore provides a complete divergence-free formulation of quantum electrodynamics, applicable to all physical situations. The divergences which are eliminated are the well-known ultraviolet divergences. The hamiltonian is still expressed as a power series in the fine-structure constant; the convergence of the series is not proved.

I. INTRODUCTION

THIS paper is one of a series[1] dealing with the applications of the idea of renormalization in quantum electrodynamics. It is a direct continuation of (D), and the notations of (D) will generally be used without explanation. The purpose of the paper is to prove that, after the state-vector is transformed by the unitary operator $S(t)$ defined by Eq. (D35), the Schrödinger equation of quantum electrodynamics is free of divergences.

The Schrödinger equation after transforming with $S(t)$ is

$$i\hbar(\partial\Phi/\partial t)=H'(t)\Phi, \tag{1}$$

$$H'(t)=S^{-1}(t)[H_1(t)-i\hbar(d/dt)]S(t). \tag{2}$$

Here $H_1(t)$ is given by Eqs. (D10)–(D14). The physical meaning of $H'(t)$ is discussed in (E). In this paper Secs. II–VI will be occupied with the proof that $H'(t)$ is divergence-free. In Sec. VIII the form of $H'(t)$ will be described, and the problems connected with the practical use of the Schrödinger equation (1) will be briefly considered.

[1] F. J. Dyson, Phys. Rev. **75**, 486 and 1736 (1949); Phys. Rev. **82**, 428 (1951); Phys. Rev. **83**, 608 (1951); Proc. Roy. Soc. **A207**, 395 (1951). These five papers will be referred to hereafter as (A), (B), (C), (D), (E), respectively. References to equations and sections in them will be made as follows: Eq. (D35) means Eq. (35) in (D); Sec. CII means Section II in (C).

II. THE STRUCTURE OF THE TRANSFORMED HAMILTONIAN

The series expansion of $S(t)$ given by Eq. (D35) depends on t in two ways. First, t appears as the upper limit of the multiple integrals; second, t appears in the functions $g(t-t_j)$, contained in $H_e(x, x_j)$ according to Eqs. (D21)–(D30). The total differentiation with respect to t in Eq. (2) can thus be separated into two partial differentiations,

$$(d/dt)=(\partial/\partial t)+(\Delta/\Delta t), \tag{3}$$

where $(\Delta/\Delta t)$ operates only on the g-functions. The operation of $(\partial/\partial t)$ on $S(t)$ gives

$$i\hbar(\partial S/\partial t)=\left[\int H_e(x, x')d_4x'\right]S, \tag{4}$$

where the integration with respect to x' extends over

3-dimensional space at the time t. By Eqs. (D17) and (D21), when x and x' are points with the same time-coordinate, one obtains

$$H_\sigma{}^0(x, x') = H^I(x'). \tag{5}$$

Therefore, Eqs. (2) and (4) give

$$H'(t) = S^{-1}\left[-(1/c)\left(\int H_{\sigma d}(x, x')d_4x'\right) - i\hbar(\Delta/\Delta t)\right]S, \tag{6}$$

$$H_{\sigma d}(x, x') = \delta(t-t')[H_{\sigma a}(x, x') + H_{\sigma b}(x, x')]. \tag{7}$$

Note that in consequence of Eq. (D18), the term $H_{\sigma b}$ in Eq. (7) vanishes. The term $H_{\sigma a}$ involves the second derivative $[g''(0)]$ and does not vanish. It is convenient not to use Eq. (D18) at this point, and to leave Eq. (7) as it stands.

Substituting into Eq. (6) the series expansion for S, the transformed hamiltonian H' takes the form,

$$H'(t) = -\sum_{n=0}^{\infty}\left(\frac{i}{\hbar c}\right)^n \int_{-\infty}^{t} dx_1 \int_{-\infty}^{t_1} dx_2 \cdots \int_{-\infty}^{t_{n-1}} dx_n \times\Big[H_\sigma(x, x_n), \Big[\cdots\Big[H_\sigma(x, x_1), \times\Big\{(1/c)\left(\int H_{\sigma d}(x, x')d_4x'\right) + i\hbar(\Delta/\Delta t)\Big\}\Big]\cdots\Big]\Big]. \tag{8}$$

Here the commutator $[H_\sigma(x, x_1), (\Delta/\Delta t)]$ is to be interpreted as $[(-d/dt)H_\sigma(x, x_1)]$. With a change in the labeling of the variables of integration, Eq. (8) may be rewritten

$$H'(t) = -(1/c)\int_{-\infty}^{t} d_4x' K_\sigma(x, x'), \tag{9}$$

$$K_\sigma(x, x') = \sum_{n=0}^{\infty}\left(\frac{i}{\hbar c}\right)^n \int_{-\infty}^{t'} dx_1 \int_{-\infty}^{t_1} dx_2 \cdots \int_{-\infty}^{t_{n-1}} dx_n \times[H_\sigma(x, x_n), [\cdots[H_\sigma(x, x_1), \times H_{\sigma t}(x, x')]\cdots]], \tag{10}$$

$$H_{\sigma t}(x, x') = H_{\sigma d}(x, x') + (d/dt)H_\sigma(x, x'). \tag{11}$$

In Eq. (10), t' is the time at the point x'.

Let $H'(t)$ be expanded into its normal constituents according to the rules given in Sec. C-II. Let M be the coefficient multiplying any particular normal product given by Eq. (D41). As in Sec. D-IV, M is a sum of contributions $M(G)$ from various Feynman graphs G. Each G has $(n+1)$ vertices x', x_1, $\cdots$, x_n, corresponding to the operator factors in a particular term of the expansion in Eq. (10). The vertex x' now takes the place which x occupied in (D); but whereas only a single photon line was incident at x in (D), the vertex x' may have two electron lines and a photon line, or two electron lines only, or two photon lines only. The operator operating at x' may be any one of the six given by Eq. (D58), all of which occur as terms in $H_{\sigma t}(x, x')$. So far as the structure of G is concerned, there is nothing to distinguish the special vertex x' from the others. All the graphs obtained from G by permuting the labels x', x_1, $\cdots$, x_n of the vertices will give contributions to M together with G.

The analysis of Secs. D-IV and D-V can be followed through for the operator $H'(t)$, with only minor changes arising from the substitution of $H_{\sigma t}(x, x')$ for $A_\mu(x)$. Just as the $H_\sigma(x, x_i)$ were divided into terms $Z_i(x, x_i)$, given by Eqs. (D46)–(D48), so $H_{\sigma t}(x, x')$ is now divided into terms $Z'(x, x')$. If Z' is taken from Eq. (D22), (D23), or (D24), then by Eq. (11),

$$Z' = Q'e_1{}^{m'}[(d/dt)(g(t-t'))^{m'}]Y'(x'). \tag{12}$$

If Z' is taken from Eq. (D30), then by Eqs. (7) and (11)

$$Z' = Q'e_1{}^{m'}[(\delta(t-t') + (d/dt)) \times\{g'(t-t')(g(t-t'))^{m'-1}\}]Y'(x'), \tag{13}$$

and if from Eq. (D29)

$$Z' = Q'e_1{}^{m'}[(\delta(t-t') + (d/dt))\{(g''(t-t')g(t-t') + (m'-2)(g'(t-t'))^2)(g(t-t'))^{m'-2}\}]Y'(x'). \tag{14}$$

Here Y' is one of the operators listed in Eq. (D58).

Given a particular graph G, only one term Z' is supposed to operate at x'. Let

$$\Lambda' = \Gamma_1 + \cdots + \Gamma_{m'} \tag{15}$$

be the sum of the m' vectors, Γ appearing when the functions g, g', g'' in Eqs. (12)–(14) are expanded by Eq. (D16). Let

$$\Delta' = \Lambda' + \Lambda_1 + \cdots + \Lambda_n \tag{16}$$

be the sum of the vectors Γ arising from all the terms Z', Z_1, Z_2, $\cdots$, Z_n. The number of these vectors is

$$N' = N + m'.$$

Since Γ_1, $\cdots$, $\Gamma_{m'}$ already appear in Eq. (15), it is convenient to relabel the variables of integration in Eq. (D52) so that

$$\Lambda_1 + \cdots + \Lambda_n = \Gamma_{m'+1} + \cdots + \Gamma_{N'}. \tag{17}$$

It is now possible to write down the formula for $H'(t)$ corresponding to Eq. (D55). Instead of being given by Eq. (D51), S_T is defined by

$$S_T = \sum \theta(x'-x_1)\cdots\theta(x_{n-1}-x_n) \times[Y_n(x_n), [\cdots[Y_1(x_1), Y'(x')]\cdots]]. \tag{18}$$

Let J_s and $I_n(\Lambda, p)$ be defined by Eqs. (D56) and (D57),

with S_Y given by Eq. (18), and with the labeling of variables in Eq. (D56) altered to correspond with Eq. (17). Using Eqs. (9), (10), (12), (13), (14), $H'(t)$ becomes

$$H'(t)=\left(\frac{1}{2\pi}\right)^4\sum_{n=0}^{\infty}\left(\frac{i}{\hbar c}\right)^n\Sigma_s Q'Q_s e_1^{N'}$$

$$\times\int_0^\infty G(\Gamma_{10})d\Gamma_{10}\cdots\int_0^\infty G(\Gamma_{n'0})d\Gamma_{n'0}J_s', \quad (19)$$

$$J_s'=\int_{-\infty}^{t}dx'\int_{-\infty}^{\infty}dp\exp[\Delta'\cdot(x-x')+ip\cdot x']E''J_s. \quad (20)$$

Here E'' derives from the factor in square brackets in Eqs. (12), (13), (14), and is given by

$$E''=\Lambda_0', \quad (21)$$

$$E''=-c\Gamma_{i0}\{\Lambda_0'-(1/c)\delta(t-t')\}, \quad (22)$$

$$E''=c^2\{\Gamma_{i0}^2+(m'-2)\Gamma_{i0}\Gamma_{j0}\}\{\Lambda_0'-(1/c)\delta(t-t')\}, \quad (23)$$

these three equations corresponding respectively to Z' given by Eqs. (12), (13), (14). The vectors Γ_i and Γ_j are any two terms taken from the sum (15); the value of $H'(t)$ is independent of the choice of i and j.

Since J_s is independent of x', the integration over x' can be immediately performed in Eq. (20). This gives

$$J_s'=(2\pi)^3\int_{-\infty}^{\infty}dp\delta_3(p)\exp(ip\cdot x)[\Delta_0'-ip_0]^{-1}E'J_s, \quad (24)$$

where

$$E'=\Lambda_0', \quad (25)$$

$$E'=-c\Gamma_{i0}[\Lambda_0'-\Delta_0'+ip_0], \quad (26)$$

$$E'=c^2[\Gamma_{i0}^2+(m'-2)\Gamma_{i0}\Gamma_{j0}][\Lambda_0'-\Delta_0'+ip_0], \quad (27)$$

in the three cases corresponding to Eqs. (12), (13), (14). In Eq. (24) the δ_3 denotes an ordinary 3-dimensional δ-function operating on the first three components of p.

Consider now the coefficient $M(G)$ in the expansion of $H'(t)$ into normal constituents. The formula which now replaces Eq. (D59) is

$$M(G)=\int_0^\infty G(\Gamma_{10})d\Gamma_{10}\cdots\int_0^\infty G(\Gamma_{N'0})d\Gamma_{N'0}N(G,\Lambda). \quad (28)$$

The definition of $N(G,\Lambda)$ is as follows. Let $M(G,\Lambda)$ be the momentum-space integral discussed in Sec. D-V, only constructed with $Y'(x)$ replacing $A_s(x)$ in Eq. (D60). According to Eq. (C52), $M(G,\Lambda)$ contains as a factor the 4-dimensional δ-function

$$\delta(p+\Sigma l_i). \quad (29)$$

Here (Σl_i) is the 4-vector expressing the difference between the total momenta and energies of the particles in the final and initial states, in the transition effected by the operator Eq. (D41). Let $M'(G,\Lambda)$ be $M(G,\Lambda)$ with the factor (29) omitted. When the integration over p in Eq. (24) is carried out,

$$N(G,\Lambda)=[\delta_3(\Sigma l_i)]\exp(-ip_0ct)$$
$$\times[\Delta_0'-ip_0]^{-1}E_\Gamma E'M'(G,\Lambda). \quad (30)$$

In Eq. (30), p_0 is no longer a variable of integration, but a constant equal to minus the fourth component of (Σl_i). Thus $H'(t)$ has nonzero matrix elements only for transitions in which the total momentum of the system is conserved. The total energy, on the other hand, is not conserved in transitions effected by $H'(t)$, and the quantity $(\hbar cp_0)$ is equal to the energy difference between initial and final states.

Summarizing the results of the analysis so far, the general coefficient $M(G)$ in the expansion of $H'(t)$ is given by Eqs. (28) and (30), with $M'(G,\Lambda)$ defined by Eq. (D72).

The discussion of derivative interactions in Sec. D-VI applies without change to $H'(t)$. Only one new point arises. It may happen that the operator H_{ps}, given by Eq. (D81), operates at the special vertex x'. Then either x_1 or x_2 in Eqs. (D83)–(D87) will be replaced by x'. Suppose that the two ends of the line λ_j are x' and x_1. The contribution $M(G_T,\Lambda)$, in which Eq. (D84) occurs as a factor, appears in $M(G)$ according to Eq. (30) with the additional multiplying factor,

$$E'=\Lambda_0', \quad (31)$$

given by Eq. (25). This factor (31) was not present in the analysis of $A_{ps}(p)$ in (D). When the line λ_j is removed from G_T and the vertices x' and x_1 replaced by a single vertex x', the resulting doubled graph is G_T'. In $M(G_T',\Lambda)$ there appears instead of Eq. (31) the factor,

$$E'=\Lambda_0'+\Lambda_{10}, \quad (32)$$

which is the sum of all the Γ_{j0} corresponding to both the vertices x' and x_1 in G_T. Therefore, the singular contribution to $M(G_T,\Lambda)$ derived from Eq. (D87) is no longer equal to a multiple of $M(G_T',\Lambda)$. However, there is another doubled graph G_T^* which gives a contribution $M(G_T^*,\Lambda)$ to $M(G)$; G_T^* is the graph obtained by exchanging the labels of the vertices x' and x_1 in G_T. In $M(G_T^*,\Lambda)$, there appears the factor,

$$E'=\Lambda_{10}, \quad (33)$$

instead of E' given by Eq. (31). Apart from the factors (31) and (33), the singular contributions to $M(G_T,\Lambda)$ and $M(G_T^*,\Lambda)$ are identical. According to Eq. (32), when the singular contributions from $M(G_T,\Lambda)$ and $M(G_T^*,\Lambda)$ are added together, the result is a multiple of $M(G_T',\Lambda)$.

In this way the conclusions of Sec. D-VI remain valid for operators involving time-derivatives operating at the special vertex x'. It is correct to calculate $H'(t)$, ignoring completely the terms $F_{s4}F_{s4}$ in Eqs. (D24) and (D58), if at the same time the singular contributions are dropped from the momentum integrals $M'(G,\Lambda)$.

III. THE MOMENTUM-SPACE INTEGRALS

The general structure of $M(G)$ is given by Eqs. (28) and (30) of Sec. II. It is necessary now to analyze in greater detail the effect of the special vertex x' upon the momentum-space integral $M'(G, \Lambda)$ appearing in Eq. (30). According to Eq. (D72) the integrand of $M'(G, \Lambda)$ is a product of factors, one corresponding to each internal line λ_s of G. When λ_j is a doubled line, the corresponding factor in $M'(G, \Lambda)$ involves the vector,

$$R_j = l_j + i\eta_j\Delta_j, \tag{34}$$

according to Eq. (D69). Suppose that the shape of the graph G is kept fixed, while the label x' is moved from one vertex to another within G; then $M'(G, \Lambda)$ will depend on the position of x' only in so far as the vectors R_j in Eq. (34) depend on the position of x'.

The definitions of l_j, η_j, and Δ_j have been given in Secs. D-IV and D-V. First, the "tree" formed by the doubled lines of G is supposed to have its "root" at x'. Each doubled line λ_j cuts the tree into two parts, a part "below" λ_j containing x', and a part "above" λ_j not containing x'. According as the "down" direction in λ_j runs with or against the direction of the arrow, the value of η_j is defined to be ± 1. Δ_j is defined as the sum of the Λ_i corresponding to vertices x_i on the part of the tree above λ_j. And $(-\eta_j l_j)$ is defined as the algebraic sum of the vectors l_i and k_a corresponding to external lines and undoubled internal lines incident at vertices x_i on the part of the tree above λ_j. These definitions depend on the position of x' in G.

The sum of the Λ_i corresponding to vertices x_i on the part of the tree below λ_j is, according to Eq. (16),

$$(\Delta' - \Lambda' - \Delta_j). \tag{35}$$

The algebraic sum of the l_i and k_a corresponding to lines incident at vertices x' and x_i on the part of the tree below λ_j is

$$(-p + \eta_j l_j), \tag{36}$$

where $p = -\sum l_i$ is the 4-vector with components

$$(0, 0, 0, p_0). \tag{37}$$

Using Eqs. (35) and (36), it is possible to make a new definition of R_j which no longer refers explicitly to the position of x' in G. Let the vertex x' be given the alternative name x_{n+1}, meaning that it is to be treated on the same footing as the other vertices x_j. Let Λ_{n+1} be defined by

$$\Lambda_{n+1} = \Lambda' - \Delta' + ip. \tag{38}$$

Then the sum of the Λ_j corresponding to vertices x_i, including x_{n+1}, on the part of the tree below λ_j is

$$(ip - \Delta_j), \tag{39}$$

instead of being given by Eq. (35).

Irrespective of the position of x', λ_j cuts the tree of doubled lined into two parts. The arrow in λ_j points away from one of the two parts and toward the other. The part toward which the arrow leads, will be said to lie "after" λ_j; the other part will be said to lie "before" λ_j. If $\eta_j = +1$, then the part after λ_j is below λ_j, and the part before λ_j is above λ_j; if $\eta_j = -1$ the reverse relations hold. Let D_j be defined as the sum of the Λ_i corresponding to all vertices x_i lying on the part of the tree before λ_j, including the vertex x_{n+1} if $\eta_j = -1$. Let $(-w_j)$ be defined as the algebraic sum of the l_i and k_a corresponding to lines incident at all vertices x_i lying on the part of the tree before λ_j. Then, by Eqs. (36) and (39), one obtains

$$D_j = \eta_j\Delta_j + \tfrac{1}{2}ip(1 - \eta_j), \tag{40}$$

$$w_j = l_j + \tfrac{1}{2}p(1 - \eta_j). \tag{41}$$

Hence, using Eq. (34), one obtains

$$R_j = w_j + iD_j. \tag{42}$$

Equation (42) gives a definition of the R_j which is independent of any special property of the vertex x', provided that the vector Λ' associated with x' is replaced by Λ_{n+1} given by Eq. (38). The integral $M'(G, \Lambda)$ may be calculated, using Eq. (42), as a function of $\Lambda_1, \Lambda_2, \cdots, \Lambda_{n+1}$, in which Λ_{n+1} occurs in exactly the same manner as the other Λ_i. If the shape of G is held fixed and the position of the label x' is changed from one vertex to another, the only effect on $M'(G, \Lambda)$ is a permutation of the vectors $\Lambda_1, \cdots, \Lambda_{n+1}$.

This new definition of the R_j will simplify to some extent the analysis of the divergences in $M(G, \Lambda)$ in Secs. VIII–X of (D). The explicit appearance of η_j in the formulas will be avoided. A more important advantage of the new definition is that it enables the analysis of divergences in (D) to be extended immediately to the integrals $M'(G, \Lambda)$ appearing in $H'(t)$.

IV. DISCUSSION OF DIVERGENCES

The divergences in $H'(t)$ are of exactly the same types[2] as those which appeared in $A_{\mu\nu}(p)$ and were discussed in Sec. D-VII. Moreover, the methods of Secs. D-VIII–D-X apply unchanged to the analysis of divergences in $H'(t)$, and the divergences cancel out exactly as before, except when x' lies inside that part of the graph G which is giving rise to the divergence. Henceforth, it will be necessary to consider only the divergences in $H'(t)$ associated with vertex and self-energy parts containing x'.

First consider an ordinary proper vertex part V, with $(d+1)$ vertices x', x_2, $\cdots$, x_{d+1}. This gives rise to a logarithmically divergent integral I^V defined by Eq. (D123). The divergent part of I^V is

$$I_D{}^V = L\gamma_\mu, \tag{43}$$

[2] This statement is strictly true of all normal constituents of $H'(t)$, except the normal constituent H_0' which is a multiple of the identity operator. H_0' is the expectation value of $H'(t)$ in the vacuum state of the non-interacting fields, and is not an observable quantity. The results of Secs. IV–VI apply to the operator $H'(t)$ with the term H_0' dropped. The meaning of H_0', and the justification for dropping it from $H'(t)$, will be discussed in Sec. VII.

according to Eq. (D129), and is unaffected by the presence of x' in V. In $M'(G,\Lambda)$ the term (43) is multiplied by an expression which does not involve any of the vectors $\Gamma_1, \cdots, \Gamma_{d+1}$ associated with the vertices of V. According to Eqs. (28) and (30), in $M(G)$ the divergence (43) is multiplied by

$$[\Delta_0'-ip_0]^{-1}, \tag{44}$$

which is a symmetric function of $\Gamma_1, \cdots, \Gamma_{d+1}$, and by the factor E'. By Eqs. (15) and (25), in this case, one obtains

$$E'=\Lambda_0'=\Gamma_{10}. \tag{45}$$

If G is any graph containing V, contributions $M(G')$ will be obtained from all the graphs G' obtained from G by moving the label x' in turn to each of the $(d+1)$ vertices of V. Each of these $M(G')$ will contain the same divergent part, given by $I_D{}^V$ multiplied by Eqs. (44) and (45). Because the integration in Eq. (28) is symmetrical in the variables $\Gamma_{10}, \cdots, \Gamma_{d+1,0}$, the sum $\sum M(G)$ of the $(d+1)$ contributions $M(G')$ has a divergent part which may be written in a symmetric form as follows. $\sum M(G)$ contains the factor (34), multiplied by Eq. (44) and by the factor

$$E'=\Gamma_{10}+\cdots+\Gamma_{d+1,0}. \tag{46}$$

The total effect of the presence of x' in V is thus to insert the two factors (44) and (46) into the divergent term arising from V in $H'(t)$.

Next consider an ordinary proper electron self-energy part W with d vertices $x_2, \cdots, x_d, x'$. This gives rise to a linearly divergent integral I^W defined by Eq. (D123). As in Sec. D-IX, let λ_1 and λ_2 be the lines adjoining W in G, with the arrow in λ_2 pointing towards W. Because x' lies inside W, Eqs. (D134) and (D135) are no longer valid. On the contrary, if λ_1 is a doubled line, then it follows that $\eta_1=-1$; and if λ_2 is doubled, it follows that $\eta_2=+1$. Using the notations of Sec. III and Eqs. (40)–(42), the vectors R_1 and R_2 associated with λ_1 and λ_2 are given by

$$R_1=l+iD_1, \quad R_2=l+iD_2, \tag{47}$$

where

$$l=w_2=l_2=w_1=l_1+p, \tag{48}$$

$$D_2=\Delta_2, \tag{49}$$

$$D_1=-\Delta_1+ip. \tag{50}$$

By Eqs. (49), (50), and (38), the relation,

$$D_1-D_2=\Gamma_2+\cdots+\Gamma_d+\Lambda_{n+1}, \tag{51}$$

holds, replacing Eq. (D135).

The analysis of Sec. D-IX can now be applied in order to separate the divergent part $I_D{}^W$ from I^W. The same process of symmetrization which led to Eq. (D148) now leads to

$$I_D{}^W=X+E^0[(l_\mu+i\bar{\Delta}_\mu)\gamma_\mu-im], \tag{52}$$

with the same coefficients X and E^0 as before, and

$$\bar{\Delta}=\tfrac{1}{2}(D_1+D_2). \tag{53}$$

By Eqs. (49) and (50), $\bar{\Delta}$ and $I_D{}^W$ are independent of $\Gamma_1, \cdots, \Gamma_d$. Therefore, the graphs G', obtained from G by moving the position of x' in W, give contributions $M(G')$ to M which can be added together to form the sum $\sum M(G)$ exactly as in the discussion of vertex parts. In $\sum M(G)$, the divergent term $I_D{}^W$ appears multiplied by Eq. (44) and by the factor,

$$E'=\Gamma_{10}+\cdots+\Gamma_{d0}. \tag{54}$$

Lastly, consider an ordinary proper photon self-energy part W with d vertices $x_2, \cdots, x_d, x'$. Equations (47)–(51) are again valid in this case. The quadratically divergent integrals I^W are to be grouped together into the sums I^c, exactly as in Sec. D-VIII. The divergent part of I^c is given by

$$I_D{}^c=B(q\cdot q'\delta_{\alpha\beta}-q_\alpha q_\beta'), \tag{55}$$

with the same coefficient B as in Eq. (D113). The vectors q, q' are given by

$$q=l+iD_2+i\Gamma_i, \quad q'=l+iD_1-i\Gamma_j, \tag{56}$$

provided that the two end-vertices x_i and x_j of W, adjoining λ_2 and λ_1, respectively, are different from x'. If, however, x' is the vertex adjoining λ_2, then it follows that

$$q=l+iD_2+i\Lambda_{n+1}; \tag{57}$$

and if x' is the vertex adjoining λ_1, then it follows that

$$q'=l+iD_1-i\Lambda_{n+1}. \tag{58}$$

Thus, Eq. (55) is not, like Eq. (52), independent of the position of x' in W.

In Sec. D-VIII, $M(G_c)$ was defined as the sum of $M(G')$ over the graphs G' obtained by substituting for W in G every self-energy part W' belonging to the class C. Let now $\sum M(G')$ denote the sum of the $M(G'')$, the summation running over the d graphs G'' which can be obtained from a given G' by changing the position of the label x' to any of the d vertices of W'. Let $\sum M(G_c)$ denote the double sum obtained by summing $\sum M(G')$ over the graphs G' which give contributions to $M(G_c)$. In $H'(t)$ the $M(G)$ will always occur grouped together into sums of the form $\sum M(G_c)$; thus, it is sufficient to prove that the divergences cancel out in the sums $\sum M(G_c)$, without considering each $M(G_c)$ separately.

According to Eqs. (55)–(58), the divergent part of $\sum M(G_c)$ contains as a factor,

$$\begin{aligned}\sum I_D{}^c=B[&(d-2)(q\cdot q'\delta_{\alpha\beta}-q_\alpha q_\beta')\\&+q\cdot(l+iD_1-i\Lambda_{n+1})\delta_{\alpha\beta}-q_\alpha(l+iD_1-i\Lambda_{n+1})_\beta\\&+(l+iD_2+i\Lambda_{n+1})\cdot q'\delta_{\alpha\beta}\\&-(l+iD_2+i\Lambda_{n+1})_\alpha q_\beta'],\end{aligned} \tag{59}$$

with q and q' given by Eq. (56). In $\sum M(G_c)$ there also

appear factors (44) and (45). Apart from the three factors given by Eqs. (44), (45), and (59), the divergent part of $\sum M(G_e)$ does not involve the parameters $\Gamma_1, \cdots, \Gamma_d$ at all.

The results of this section will now be summarized. Let G be any graph containing the vertex part V. As in Sec. D-IX, let M_d denote the sum of the $M(G')$ obtained from graphs G' derived from G by replacing V by any ordinary proper vertex part with $(d+1)$ vertices. M_d is obtained from $\sum M(G)$ when I^V is replaced by a sum I^d. The divergent part of I^d is

$$I_D{}^d = L_d \gamma_\mu, \tag{60}$$

with L_d given by Eq. (D133). Besides Eq. (60), M_d contains the factors (44) and (46).

Again, let G be any graph containing the electron self-energy part W. Let M_d be the sum of the $M(G')$ obtained from graphs G' derived from G by replacing W by any ordinary proper electron self-energy part with d vertices. M_d is obtained from $\sum M(G)$ when I^W is replaced by $J^{d'}$. The divergent part of $J^{d'}$ is

$$J_D{}^{d'} = iK_d m + E_d[(l_\mu + i\tilde{\Delta}_\mu)\gamma_\mu - im], \tag{61}$$

with K_d and E_d given by Eqs. (D152) and (D153). Besides Eq. (61), M_d contains the factors (44) and (54).

Finally, let G be any graph containing the photon self-energy part W. Let M_d' be the sum of the $M(G')$ obtained from graphs G' derived from G by replacing W by an ordinary proper photon self-energy part with d vertices. M_d' is obtained from $M(G_e)$ when I^e is replaced by a sum I^d. The divergent part of I^d is by Eq. (59)

$$\begin{aligned} I_D{}^d = -B_d[&d(q\cdot q'\delta_{\alpha\beta} - q_\alpha q_\beta') + iq\cdot(\Gamma_j - \Lambda_{n+1})\delta_{\alpha\beta} \\ &- iq_\alpha(\Gamma_j - \Lambda_{n+1})_\beta - i(\Gamma_i - \Lambda_{n+1})\cdot q'\delta_{\alpha\beta} \\ &+ i(\Gamma_i - \Lambda_{n+1})_\alpha q_\beta'], \end{aligned} \tag{62}$$

with B_d given by Eq. (D115). Besides Eq. (62), M_d' contains the factors (44) and (45).

V. REMOVAL OF DIVERGENCES ARISING FROM PHOTON SELF-ENERGY PARTS

Consider the cancellation of divergences arising from photon self-energy parts, which was described in Sec. D-VIII. The cancellation was brought about by the terms of degree $\epsilon_1{}^d$ in H_{gp}, H_{ga}, and H_{gb}. These terms, operating at a single-vertex photon self-energy part W_0, exactly compensated the divergent part of I^d given by Eq. (D114). In $H'(t)$ the compensation occurs in essentially the same way, but with a few additional complications.

If G is any graph containing the ordinary photon self-energy part W, with x' included in W, then G_0 will denote the graph obtained by replacing W by W_0, with the label x' at the vertex W_0. Let M_{dp}, M_{da}, M_{db} be the contributions $M(G_0)$, arising from G_0 with the term of degree $\epsilon_1{}^d$ in H_{gp}, H_{ga}, H_{gb}, respectively, operating at x'. In $H'(t)$, these contributions M_{dp}, M_{da}, M_{db} will always occur together with the M_d' defined in the last paragraph of Sec. IV. Thus, only the sum,

$$M_d = M_d' + M_{dp} + M_{da} + M_{db}, \tag{63}$$

appears in $H'(t)$.

The variables of integration in M_d' according to Eq. (28) are

$$\Gamma_{10}, \cdots, \Gamma_{N+1,0}, \tag{64}$$

where Γ_1 corresponds to x' and $\Gamma_2, \cdots, \Gamma_d$ correspond to the remaining vertices of W. In M_{dp}, M_{da}, M_{db}, the variables of integration are the same, all the vectors $\Gamma_1, \cdots, \Gamma_d$ corresponding to the single vertex x'. Let $\int G d\Gamma$ denote the $(N+1)$-fold integration appearing in Eq. (28), including the $(N+1)$ functions G. By Eqs. (44), (45), and (62), the divergent part of M_d' is

$$\begin{aligned} M_{dD}' = B_d \int G d\Gamma [\Delta_0' - ip_0]^{-1} C \Gamma_{10} \\ \times [-d(q\cdot q'\delta_{\alpha\beta} - q_\alpha q_\beta') - i(q\cdot(\Gamma_j - \Lambda_{n+1}) \\ - (\Gamma_i - \Lambda_{n+1})\cdot q')\delta_{\alpha\beta} + i(q_\alpha(\Gamma_j - \Lambda_{n+1})_\beta \\ - (\Gamma_i - \Lambda_{n+1})_\alpha q_\beta')]. \end{aligned} \tag{65}$$

Here C is a product of factors arising from the part of G outside W, and is independent of $\Gamma_1, \cdots, \Gamma_d$. The integration $\int G d\Gamma$ and the factors C are identical in M_d', M_{dp}, M_{da}, M_{db}.

According to Eqs. (D116), (25), and (15), M_{dp} is given by

$$\begin{aligned} M_{dp} = B_d \int G d\Gamma [\Delta_0' - ip_0]^{-1} C[\Gamma_{10} + \cdots + \Gamma_{d0}] \\ \times [(l+iD_2)\cdot(l+iD_1)\delta_{\alpha\beta} - (l+iD_2)_\alpha (l+iD_1)_\beta]. \end{aligned} \tag{66}$$

By Eqs. (D117), (27), and (15), M_{da} is given by

$$\begin{aligned} M_{da} = B_d \int G d\Gamma [\Delta_0' - ip_0]^{-1} C[\Gamma_{i0}{}^2 + (d-2)\Gamma_{i0}\Gamma_{j0}] \\ \times [\Gamma_{10} + \cdots + \Gamma_{d0} - \Delta_0' + ip_0][\delta_{\alpha\beta} - \delta_{\alpha 4}\delta_{\beta 4}]. \end{aligned} \tag{67}$$

By Eqs. (D118), (26), and (15), M_{db} is given by

$$\begin{aligned} M_{db} = B_d \int G d\Gamma [\Delta_0' - ip_0]^{-1} C \Gamma_{i0} [\Gamma_{10} + \cdots + \Gamma_{d0} \\ - \Delta_0' + ip_0][\delta_{\alpha 4} l_\beta - \delta_{\beta 4} l_\alpha]. \end{aligned} \tag{68}$$

In Eq. (66), the factor $[\Gamma_{10} + \cdots + \Gamma_{d0}]$ can by symmetry be replaced by $[d\Gamma_{10}]$. In Eqs. (67) and (68), Γ_{i0} can be replaced by Γ_{10}.

When Eqs. (65), (66), (67), (68) are added together, many terms disappear as a result of the cancellations in Sec. D-VIII. There remains an expression M_{dD}, which is the divergent part of M_d defined by Eq. (63). After some rather lengthy reductions, M_{dD} becomes

$$M_{dD} = B_d \int G d\Gamma [D_{10} - D_{20} - \Gamma_{j0}] C \Gamma_{10} (\delta_{\alpha\beta} - \delta_{\alpha 4}\delta_{\beta 4}). \tag{69}$$

The important feature of Eq. (69) is that the factor $[\Delta_0'-i\not{p}_0]^{-1}$ which appeared in Eqs. (65)–(68) has now canceled against a factor $(\Delta_0'-i\not{p}_0)$ in the numerator. Moreover, the factors C and $[D_{10}-D_{20}-\Gamma_{j0}]$ in Eq. (69) are independent of Γ_{10}. Therefore, the integration over Γ_{10} can be carried out at once, and this gives

$$M_{dD}=0 \tag{70}$$

in virtue of Eq. (D18). That is to say, M_d given by Eq. (63) is free from divergences.

This completes the proof that $H'(t)$ is free from divergences associated with photon self-energy parts. In the proof, the condition (D18) plays a decisive role. It is noteworthy that Eq. (D18) is used nowhere else, in (D) or in the present paper up to the end of Sec. VI, except at this one point in order to prove that M_{dD} given by Eq. (69) is zero. If Eq. (D18) is dropped, the operator $A_{\mu 0}(\not{p})$ is still divergence-free but $H'(t)$ is not. The meaning of Eq. (D18) will be further elucidated in Sec. VIII.

VI. REMOVAL OF REMAINING DIVERGENCES

There remain to be canceled the divergences arising from vertex and electron self-energy parts. These are given by Eqs. (60) and (61). They will be canceled by following the method of Sec. D-X. The addition of $(H_{gq}-H_{0q})$ to H_0 produces effects in $H'(t)$ precisely analogous to those produced in $A_{\mu 0}(\not{p})$. The graphs G giving contributions $M(G)$ to $H'(t)$ are made more numerous by inserting into all electron lines any number of P-vertices and N-vertices, as described in Sec. D-X. There are only two new points to be considered. First, in any graph G the label x' may be attached to a P-vertex or to an N-vertex. Second, it is necessary now to consider graphs G which consist entirely of P- and N-vertices, joined by a single open polygon of electron lines with one external electron line at each end; such graphs did not occur in the previous analysis.

Consider the effect of a P- or an N-vertex x', at which the term of degree e_1^d in the expansions of H_{0q} or of $(-H_{0q})$ is operating. If G is a graph in which this vertex occurs, then the factor contributed by the vertex to $M(G)$ is given by Eq. (D162) or (D163) as before; but $\bar{\Delta}$ is now given by Eq. (53), where λ_1 and λ_2 are the two lines adjacent to x'. There also appears in $M(G)$ a factor E' given by Eq. (54).

The analysis in Sec. D-X of the effects of inserting P-vertices, in all possible ways, into the electron lines of a graph G_0 originally without P-vertices, extends immediately to $H'(t)$. As before, the effect of the insertions is precisely to multiply the interaction operating at every E-vertex of G_0 by the factor (D191). To see that this is so, only two observations are necessary. First, the identities (D172) and (D181) remain valid when one of the vectors $\Lambda_1, \cdots, \Lambda_r$, is replaced by Λ_{n+1}, according to the remarks at the end of Sec. III. Second, let G be any graph formed by inserting P-vertices in the electron lines of G_0; the factor E' given by Eq. (54), which occurs in $M(G)$ when x' is a P-vertex, adds together with the factor E' which occurs in $M(G)$ when x' is a vertex of G_0, to give precisely the correct factor E' which occurs in $M(G_0)$ associated with the vertex x' of G_0 when the interaction operating at that vertex is multiplied by Eq. (D191).

Consider the effect of the multiplying factor (D191) at the vertex x' of G_0, when x' is an ordinary vertex. The term of order e_1^d in Eq. (D191), by Eqs. (D157) and (D160), will give rise to a term,

$$-L_d\gamma_\mu, \tag{71}$$

in $M(G_0)$, which is multiplied by a factor,

$$E'=\Gamma_{10}+\cdots+\Gamma_{d+1,0}, \tag{72}$$

according to Eq. (25). In Eq. (72) one of the Γ_{j0} is derived from the interaction H_{0i} originally operating at x', and the remainder come from the multiplying factor Eq. (D191). The term (71) multiplied by Eq. (72) exactly cancels Eq. (60) multiplied by Eq. (46). Therefore, the effect of Eq. (D191), multiplying the interaction operating at an ordinary vertex x', is to cancel all the divergences produced by vertex parts inserted at x'. That is to say, the cancellation of vertex part divergences in Sec. D-X is valid for $H'(t)$. Next consider the effect of the multiplying factor Eq. (D191) at an N-vertex or an S-vertex, when this vertex happens to be x'. The term of degree e_1^d in the interaction at x', as modified by the multiplication by Eq. (D191), produces in $M(G_0)$ a term given by Eq. (D193) or Eq. (D195), exactly as before. This term in $M(G_0)$ is multiplied by a factor E' given by Eq. (54). Therefore, the sum of Eqs. (D193) and (D195) cancels the divergence Eq. (61). The effect of Eq. (D191), multiplying the interactions operating at x' when x' is an N-vertex or an S-vertex, is to cancel all the divergences produced by ordinary electron self-energy parts which contain x'. That is to say, the cancellation of electron self-energy part divergences in Sec. D-X is valid for $H'(t)$.

The cancellation of divergences in $H'(t)$ is now complete, except for the contributions $M(G_P)$ arising from graphs which consist entirely of P-vertices. Graphs which are composed of both P- and N-vertices give contributions which are included in the previous analysis; these contributions were used to cancel the divergences arising from graphs consisting entirely of electron self-energy parts. Only the contributions $M(G_P)$ remain uncanceled, and must now be considered separately.

Let G_P be an open polygon with the vertices $y_1, \cdots, y_{r+1}$, in order reading in the direction following the arrows in the lines of G_P. At each y_i the term of order $e_1^{d_i}$ in H_{0q} is operating. One of the y_i, say, y_k, is x'. For $i\neq k$, let Λ_i be the sum of the d_i vectors Γ_j associated with y_i. Let Λ_k be written for the vector Λ_{n+1} defined by

Eq. (38), in this case

$$\Lambda_k = i\not{p} - \Lambda_1 - \cdots - \Lambda_{k-1} - \Lambda_{k+1} - \cdots - \Lambda_{r+1}. \quad (73)$$

Then in analogy with Eq. (D165), one obtains

$$D_i = \Lambda_1 + \cdots + \Lambda_i, \quad D_0 = 0. \quad (74)$$

Let l be the momentum vector in the external line at y_1, and l' the vector in the external line at y_{r+1}. The definition of p in this case is

$$p = l - l'. \quad (75)$$

The factors arising in $M(G_P)$ from the lines and vertices of G_P are

$$K = C d_{r+1}[(l_\mu + \tfrac{1}{2}i(D_{r+1,\mu} + D_{r\mu}))\gamma_\mu - im]F, \quad (76)$$

where F is given by Eq. (D166) with each $(\eta\Delta_i)$ replaced by D_i. Let K'' denote the product $Cd_1Cd_2\cdots Cd_{r+1}$, and K' the product of the remaining factors in Eq. (76).

According to Eq. (D173), summing K' over the permutations of $\Lambda_1, \cdots, \Lambda_r$ gives

$$\sum_r K' = r! f_r[(l_\mu + \tfrac{1}{2}i(D_{r+1,\mu} + D_{r\mu}))\gamma_\mu - im], \quad (77)$$

making use of the Dirac equation satisfied by the incoming particle of momentum l. By Eq. (77), if K' is summed over all permutations of $\Lambda_1, \cdots, \Lambda_{r+1}$, the result is

$$\sum_{r+1} K' = r! f_r[((r+1)l_\mu + (r+\tfrac{1}{2})iD_{r+1,\mu})\gamma_\mu - (r+1)im]. \quad (78)$$

Now by Eqs. (73), (74), and (75), one obtains

$$l + iD_{r+1} = l - p = l'. \quad (79)$$

Therefore, it follows that

$$\sum_{r+1} K' = \tfrac{1}{2}r! f_r[(l_\mu\gamma_\mu - im) + (2r+1)(l_\mu'\gamma_\mu - im)]. \quad (80)$$

When the Dirac equations satisfied by both the incoming and the outgoing particles are used, Eq. (80) vanishes identically.

When the contributions $M(G_P)$ to $H'(t)$ are added together, the factors M' will always be grouped together in symmetrical sums $\sum_{r+1} K'$. Therefore, the sum of the $M(G_P)$ is identically zero. This completes the proof that $H'(t)$ is divergence-free.

VII. NOTE ON THE VACUUM SELF-ENERGY

As previously stated in a footnote,[2] the analysis of Secs. IV–VI applies to $H'(t)$ after dropping the constant numerical term H_0'. The term H_0' is a sum of contributions $M(G)$ from the graphs G which have no external lines whatever. It is independent of t, because the vector p in Eq. (30) is zero for graphs without external lines. When the wave function $\Phi(t)$ is multiplied by the numerical phase-factor $\exp[iH_0't/\hbar]$, the hamiltonian $H'(t)$ in the Schrödinger equation (1) is replaced by $[H'(t) - H_0']$. This transformation corresponds to a redefinition of the zero-level of energy, eliminating the unobservable constant energy H_0'. Therefore, it is allowable to take as the hamiltonian in Eq. (1) the operator $H'(t)$ with the term H_0' dropped. This procedure leads to a divergence-free Schrödinger equation, and is certainly the correct procedure to use in practical applications of the theory. Nevertheless, it is of some interest in principle to formulate the theory in such a way that a divergent vacuum self-energy does not arise, so that the theory is free even from this very harmless kind of divergence. In the following paragraphs an alternative treatment of the vacuum self-energy will be described, which leads to a divergence-free Schrödinger equation and avoids any arbitrary discarding of constant terms.

The physically correct zero-level of energy is the energy of the vacuum-state of the fully interacting fields. The energy of the vacuum-state of the non-interacting fields lies above this zero-level by an amount H_{00}. Therefore, referred to the correct zero-level, the Schrödinger equation of quantum electrodynamics in the interaction representation is

$$i\hbar[\partial\Psi/\partial t] = \left[\int H'(x)d_3x + H_{00}\right]\Psi. \quad (81)$$

This leads to a Schrödinger equation in the intermediate representation,

$$i\hbar[\partial\Phi/\partial t] = [H'(t) + H_{00}]\Phi. \quad (82)$$

The hamiltonian in Eq. (82) is equal to the hamiltonian previously considered, plus the constant term,

$$E_0 = H_0' + H_{00}. \quad (83)$$

The true vacuum self-energy in the intermediate representation is $(-E_0)$.

Consider the form of the contribution $M(G)$ to H_0' from a graph G without external lines. The vector $(\sum l_i)$ in Eq. (30) being zero, the three-dimensional δ-function gives a factor,

$$(2\pi)^{-3}\Omega, \quad (84)$$

where Ω is the volume of the 3-dimensional space over which the vacuum self-energy is to be calculated; it is obviously correct that H_0' and H_{00} should be proportional to Ω. Thus, by Eqs. (28) and (30), one obtains

$$M(G) = (2\pi)^{-3}\Omega\int Gd\Gamma E_\Gamma E'(\Delta_0')^{-1}M'(G, \Lambda), \quad (85)$$

where $\int Gd\Gamma$ denotes the multiple integration in Eq. (28). The divergences in $M'(G, \Lambda)$ arising from parts interior to G are supposed all to have been removed by the methods of Secs. IV–VI. There remains a divergence produced by the integration over the momenta in $M'(G, \Lambda)$ considered as a whole. This divergence is different from any which have been previously analyzed; according to the criterion formulated in Sec. B-V, the divergence at large momenta may increase with the fourth power of the momentum variables.

Following the method of Sec. D-VIII, $M'(G,\Lambda)$ may be separated into a finite part $M_F(G,\Lambda)$ and a divergent part which is a polynomial P_4 of degree at most 4 in the parameters Λ_{j0}. Since all internal divergences are supposed already canceled in $M'(G,\Lambda)$, the vertices of G are all ordinary and the parameters Λ_{j0} are given by

$$\Lambda_{j0}=\Gamma_{j0},\quad j=2,\cdots,n,$$
$$\Lambda_{n+1,0}=-\Gamma_{20}-\cdots-\Gamma_{n0}, \tag{86}$$

according to Eq. (38). Also, in Eq. (85), one has

$$E_\Gamma=1,\quad E'=\Gamma_{10},\quad \Delta_0'=\Gamma_{10}+\cdots+\Gamma_{n0}. \tag{87}$$

Therefore, it follows that

$$M(G)=M_F(G)+\int GdI\Gamma[\Gamma_{10}/(\Gamma_{10}+\cdots+\Gamma_{n0})]P_4(\Lambda_{j0}), \tag{88}$$

where $M_F(G)$ is finite. Now let $M(G)$ be summed over the graphs G' derived from G by moving the label x' in turn to the n vertices of G. The result is

$$\sum M(G)=\sum M_F(G)+\int GdI\Gamma[\Gamma_{10}/(\Gamma_{10}+\cdots+\Gamma_{n0})]P_4'(\Lambda_{j0}), \tag{89}$$

where $P_4'(\Lambda_{j0})$ is a symmetrical polynomial in $\Lambda_{20},\cdots,\Lambda_{n+1,0}$. Now let the integrand in Eq. (89) be symmetrized with respect to the variables $\Gamma_{10},\cdots,\Gamma_{n0}$; this does not affect the value of $\sum M(G)$. The symmetrical sum,

$$\sum \Gamma_{10}P_4'(\Lambda_{j0}),$$

is a polynomial of the fifth degree in the Γ_{j0}, which is exactly divisible by $[\Gamma_{10}+\cdots+\Gamma_{n0}]$ and which involves no pure power $(\Gamma_{j0})^a$ with $a>1$. Therefore, it follows that

$$\sum \Gamma_{10}P_4'(\Lambda_{j0})=[\Gamma_{10}+\cdots+\Gamma_{n0}]Q_4(\Gamma_{j0}), \tag{90}$$

where Q_4 is a polynomial of the fourth degree, symmetric in the Γ_{j0} and not involving any pure power $(\Gamma_{j0})^a$ with $a>0$. Substituting Eq. (90) into Eq. (89), the integrations over the Γ_{j0} can be carried out at once, using Eqs. (D17) and (D18). The result is

$$\sum M(G)=\sum M_F(G)+A_G+B_G[g''(0)]^2, \tag{91}$$

where A_G and B_G are divergent constants independent of the function g. Summing Eq. (91) over all graphs G without external lines,

$$H_0'=H_{Fg}+A+B[g''(0)]^2, \tag{92}$$

where A and B are divergent absolute constants, and H_{Fg} is finite and depends on g.

Now consider the limit in which g tends to 1 and the intermediate representation tends to the Heisenberg representation. In this limit, all the parameters Λ_i tend to zero, and $M'(G,\Lambda)$ becomes $M'(G,0)$. Then $M_F(G)$ in Eq. (88) is zero, and Eq. (92) becomes $H_0'=A$. But the vacuum self-energy in the Heisenberg representation, which is the limit of H_0' as $g\to 1$, is by definition $(-H_{00})$. Therefore, it follows that

$$A=-H_{00}, \tag{93}$$

and so Eq. (92) gives

$$E_g=H_{Fg}+B[g''(0)]^2. \tag{94}$$

According to Eq. (82), the hamiltonian in the Schrödinger equation, without discarding any vacuum self-energy term, is

$$[H'(t)-H_0']+E_g. \tag{95}$$

By Eq. (94) this hamiltonian will be divergence-free, if in addition to Eqs. (D17) and (D18) the function g satisfies the condition,

$$g''(0)=0. \tag{96}$$

To impose the condition (96), in order to make the vacuum self-energy E_g finite, is for practical purposes an unnecessary luxury. This whole discussion of the vacuum self-energy in Sec. VII is intended to be of academic interest only, and should be ignored by anybody concerned with the practical use of the theory.

VIII. THE USE OF THE SCHRÖDINGER EQUATION

It was proved in Sec. D-III that the operator $S(t)$ is of the form,

$$S(t)=\exp(iH_0t/\hbar)S\exp(-iH_0t/\hbar), \tag{97}$$

where S is time-independent. This has the consequence that $H'(t)$ is of the form,

$$H'(t)=\exp(iH_0t/\hbar)H'\exp(-iH_0t/\hbar), \tag{98}$$

where H' is the time-independent operator defined by Eq. (E12). As explained in (E), the equation,

$$i\hbar(\partial\Phi_0/\partial t)=(H_0+H')\Phi_0, \tag{99}$$

with H' given by Eq. (98), is a divergence-free Schrödinger equation, giving an exact description of the behavior of all systems of quantum electrodynamics in the Schrödinger representation. To obtain the operator H' from $H'(t)$, it is only necessary to drop the phase-factor $[\exp(-ip_0ct)]$ in Eq. (30). For solving problems of quantum electrodynamics involving bound states, Eq. (99) will be a possible starting-point. The statement that Eq. (99) is divergence-free means that H' is defined by a power-series in e_1, each term of which is individually finite. Equation (99) will be of practical use, only if the power-series itself converges. The discussion in Sec. D-XII is intended to make it plausible that the series is convergent; to prove the convergence is the outstanding unsolved problem in quantum electrodynamics. In the remaining paragraphs of this paper, the convergence of the series will be taken for granted.

Let H' be written in the form,

$$H' = H_1' + H_e', \tag{100}$$

where H_1' is a first-order term proportional to e_1, and H_e' is of order e_1^2 and higher. Let M_i be any matrix element of the original interaction,

$$H_i = -ie_1 \int \bar{\psi}(x)\gamma_\mu \psi(x) A_\mu(x) d_3x, \tag{101}$$

regarded now as a time-independent operator. M_i will refer to some process in which a photon is emitted or absorbed, with conservation of momentum but with an energy difference $(\hbar c p_0)$ between the initial and final states. By Eqs. (28) and (30), H_1' will have a matrix element for the same process, given by

$$M_i' = M_i \int_0^\infty G(\Gamma_0)\Gamma_0[\Gamma_0 - ip_0]^{-1} d\Gamma_0$$

$$= M_i\left[-\int_0^\infty g'(a)\exp(ip_0 ca)da\right]. \tag{102}$$

For low frequency processes, when p_0 is small, Eq. (102) shows that M_1' is approximately equal to M_i. Thus, H_1' is approximately equivalent to H_i so far as low frequency processes are concerned. On the other hand, at high frequencies when p_0 is large, $[M_i'/M_i]$ becomes small, and so H_1' differs from H_i by a cut-off factor which effectively cuts out the high frequency processes.

To see how strong the cut-off factor is, one may use instead of Eq. (102) the asymptotic expansion valid for large p_0,

$$\left[\frac{M_i'}{M_i}\right] = -\sum_{n=1}^{\infty}\left(\frac{i}{p_0 c}\right)^n g^{(n)}(0). \tag{103}$$

Thus Eq. (D18) is sufficient to make $[M_i'/M_i]$ tend to zero at least as fast as p_0^{-2}. If, in addition, Eq. (96) should hold, $[M_i'/M_i]$ would tend to zero at least as fast as p_0^{-3}. The strength of the cutoff depends directly on the degree of smoothness with which $g(a)\to 1$ as $a\to 0$.

The term H_e' represents the effects of the high frequency processes, which were not included in H_1', in the form of a higher order radiative correction. H_e' contains a great variety of matrix elements, similar in their general properties to the radiative corrections which are encountered in the Schwinger theory. In particular H_e' will include the part of the Lamb shift which arises from high frequency virtual transitions, the remainder of the Lamb shift being due to the second-order effects of H_1'.

Every matrix element of H_e' will contain, according to Eqs. (28) and (30), a factor giving a cutoff at high frequencies like the cut-off factor in Eq. (102). In particular, when Eq. (D18) is satisfied, every matrix element in H', referring to a process in which energy is not conserved by an amount $(\hbar c p_0)$, tends to zero at least as fast as p_0^{-2} as p_0 tends to infinity. This has an important consequence. Suppose that the Schrödinger equation (99) is to be solved by some kind of a perturbation expansion in powers of H'. The sums over intermediate states in such a perturbation treatment can never introduce any new divergences into the theory to replace those which have been eliminated. The sums over intermediate states will always be convergent by virtue of the cut-off factors in the high frequency matrix elements of H'. This is true whether or not the perturbation expansion in powers of H' is either convergent or physically reasonable.

There is just one exception to the statement made in the preceding paragraph. If the self-energy of the vacuum state is calculated from Eq. (99), using a perturbation expansion in powers of H', the result will still diverge if the cut-off factors in H' are proportional to p_0^{-2} for large p_0. To obtain a finite vacuum self-energy, the cut-off factors must tend to zero at least as fast as p_0^{-3}, which requires that Eq. (96) be satisfied.

These results make it clear why the conditions (D18) and (96) are important in the present theory. They also make it clear that the theory is totally divergence-free; not only is the hamiltonian in Eq. (99) free from explicit divergences, but also it is impossible to obtain high frequency divergences in the theory by any subsequent perturbation expansions.

If the methods of this paper have a useful application in practice, it will be to bound-state problems in which the Schrödinger equation (99) must be solved without treating H' as a perturbation. The method to be used in solving the equation must then be adapted to the particular problem. Since the equation is divergence-free, all the well-known approximate methods, trial wave functions, variation methods, iteration methods, and if necessary numerical integration, may be applied to it freely. The techniques developed in this series of papers may thus be instrumental in restoring to the theoretical physicist working in quantum field theory the freedom of action which he enjoys when solving partial differential equations in other branches of physics.

Electron-Capture Cross Sections for Protons Passing through Hydrogen Gas

F. L. RIBE
Department of Physics and Institute for Nuclear Studies, University of Chicago, Chicago, Illinois
(Received June 4, 1951)

Measurements have been made of the electron-capture cross sections σ_c in hydrogen gas for protons moving with kinetic energies between 34 and 149 kev. At these energy limits, σ_c has the values 1.52×10^{-16} and 2.29×10^{-18} cm^2, respectively. Using the values of the electron-loss cross sections σ_l for hydrogen atoms in hydrogen gas recently measured in this laboratory, the ratio σ_l/σ_c was derived from the results of the present measurements. Direct measurements of this ratio agreed with the values derived from the separate measurements of σ_l and σ_c to within 10 percent.

In the present case σ_l/σ_c is unity at an ion velocity of 1.44 Bohr units ($e^2/\hbar$). This may be compared with the traversal of metals by protons, for which $\sigma_l/\sigma_c=1$ is attained at 0.95 Bohr unit.

I. INTRODUCTION

THE processes by which ions capture and lose electrons in passing through matter were the subject of many early investigations using low energy canal rays and the high energy alpha-particles from radioactive sources.[1] Recent measurements by Hall,[2] on the ratio of loss and capture cross sections for protons in various metals, and by Montague,[3] on the loss cross sections for hydrogen atoms in hydrogen gas have extended these studies to intermediate energies (35 to 400 kev).

Rudnick[4] and Bartels,[5] in their low energy work on ions in gases, made use of the fact that an initially charged beam acquires a neutral component as the gas is introduced into its path, until at sufficiently high densities there occurs an equilibrium distribution of neutral and charged particles which is unchanged by further increases in gas pressure. The ratio of the charged to the neutral component of the beam, after it had passed through a gas chamber, gave a measure of the ratio of loss and capture cross sections. From this measurement and a measurement of the variation of the charged-to-neutral ratio with gas pressure, before equilibrium, the capture and loss cross sections could be obtained. Meyer[6] has also used this method at higher energies, obtaining, among his results, three measurements of the capture cross sections for protons in hydrogen gas at energies between 35 and 145 kev.

In the work of Montague[3] a direct measurement was made of the loss cross section without using the equilibrium ratios as an intermediate step. By causing the moving neutral atoms to be deflected out of the beam immediately upon becoming charged, an exponential decay of the neutral-beam intensity with gas pressure was obtained, from which the cross sections were determined.

Goldmann,[7] Rostagni,[8] Wolf,[9] and, more recently, Keene,[10] using low energy ions, have determined capture cross sections by using a known current of ions and measuring the positive-ion current arising in a known path length from the stripped gas atoms as a function of pressure. Smith[11] measured capture cross sections in the same energy range by observing the exponential decrease in ion-beam current at three positions along the path of the ions in the gas, assuming that only capture events occurred at the pressures used. Bartels[5] also applied this principle, obtaining values of the capture cross sections for protons in hydrogen in good agreement with those measured by the equilibrium method.

In the present experiment the capture cross sections for protons in hydrogen gas in the intermediate range of energies were obtained by a method similar to that used by Montague for the loss cross sections. A beam of protons entered an evacuated chamber, sealed from the beam-defining tube by a thin window. Traversing the chamber was a magnetic field which bent the proton orbits along a circular path which ended in a faraday cage. As hydrogen gas at low pressure was introduced into the chamber, some of the protons captured orbital electrons from the gas molecules, thus becoming neutral; they then moved off tangentially to the circular path, missing the faraday cage. Using Montague's notation, the ratio of the number $N(p)$ of protons in the attenuated beam corresponding to gas pressure p, to the number $N(0)$ of protons entering the faraday cage when the chamber was evacuated, is

$$\rho(p)\equiv N(p)/N(0)=\exp[-n(p)\sigma_c d], \qquad (1)$$

where $n(p)$ is the number of atoms per cubic centimeter of the gas, d is the length of the circular path from entrance window to detector, and σ_c is the electron-capture cross section per atom of hydrogen for protons

[1] E. Rüchardt, Hand. Physik XXII/2, 103 (1933). This article contains a review of the subject and a summary of the older results. Further references are contained in the papers of Hall and Montague (references 2 and 3, below).
[2] T. Hall, Phys. Rev. 79, 504 (1950).
[3] J. H. Montague, Phys. Rev. 81, 1026 (1951).
[4] P. Rudnick, Phys. Rev. 38, 1342 (1931).
[5] H. Bartels, Ann. Physik 6, 957 (1930); 13, 373 (1932). The latter reference contains the results for protons in hydrogen gas.
[6] H. Meyer, Ann. Physik 30, 635 (1937).
[7] F. Goldmann, Ann. Physik 10, 460 (1931).
[8] A. Rostagni, Nuovo cimento 15, 117 (1939).
[9] F. Wolf, Z. Physik 74, 575 (1932).
[10] J. P. Keene, Phil. Mag. 40, 369 (1949).
[11] R. A. Smith, Proc. Cambridge Phil. Soc. 30, 514 (1934).

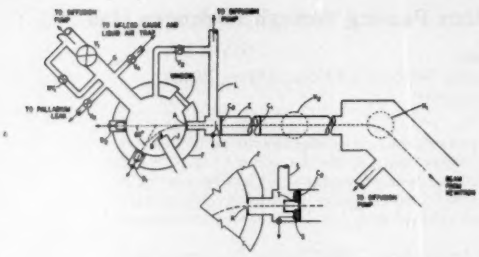

FIG. 1. Apparatus, schematic.

of the energy under consideration. In the following $\rho(p)$ will be called the "attenuation ratio."

In applying capture and loss information to the calculation of the energy loss by moving ions at intermediate energies, the ratio of loss and capture cross sections is of primary interest. This ratio, as a function of energy, can now be obtained by dividing the loss cross sections measured by Montague by the capture cross sections of this experiment.

The consistency of the separate measurements of loss and of capture cross sections was checked at a few energies by means of an equilibrium method similar to that employed by Bartels and others. Using no magnetic field, a well-defined beam of protons was directed from the entrance aperture straight across the chamber to a faraday cage (which would not register neutral particles). As gas was admitted, some of the original protons became neutralized, and the proton current to the cage decreased to an equilibrium value. If σ_l/σ_c is the ratio of loss and capture cross sections, and the incident beam is composed entirely of protons, equilibrium value of $\rho(p)$ is given by

$$\rho_e=(\sigma_l/\sigma_c)/(1+\sigma_l/\sigma_c). \quad (2)$$

Thus the measured values of ρ_e could be compared with those calculated from the values of σ_c and σ_e at corresponding energies.

II. APPARATUS

Figure 1 is a schematic diagram of the apparatus, the main components of which were the beam-defining tube E, the electron-exchange chamber F, and the vacuum manifold G. This diagram will be referred to throughout this section.

A. Experimental Arrangement for Measuring the Capture Cross Sections

1. The Beam-Defining Apparatus

The beam of protons was provided by the University of Chicago 400-kev Cockcroft-Walton accelerator, or kevatron. After either the atomic or the molecular component was selected by the analyzing magnetic field H_1, the beam entered the beam-defining tube E with diaphragms C_1 and C_2 (hole diameter=0.158 cm, spacing=86 cm). The beam then passed through a monitoring screen H and entered the electron-exchange chamber F through a thin aluminized zapon window A which provided a vacuum seal between the exchange chamber and the beam-defining tube. For the range of energies used in this experiment the windows had an average thickness of 6.2 kev. A weak magnetic field H_2 provided fine adjustment of the beam position in the horizontal plane.

It was necessary to shield the beam from the stray magnetic field during its passage through tube E; hence, the tube itself was made of steel and was surrounded by an outer steel tube to a distance of 71 cm from the exchange chamber. Additional magnetic shielding was placed around the beam-defining tube to a distance of 22 cm from the exchange chamber.

2. The Electron-Exchange Chamber

This chamber, as well as the monitoring screen H and the current-measuring amplifiers, has been described in some detail in Montague's paper.[12] It had an inside diameter of 12.70 cm and an over-all (outer) height of 3.17 cm. An axial magnetic field was provided by an electromagnet between whose pole faces the chamber fitted snugly. The inside diameter of the chamber and that of the poles was the same, so that the slits of detectors D_1 and D_2, as well as window A, lay directly between the circular edges of the pole faces.

The bent beam, indicated by the dashed circular line, entered detector D_1, after being deflected by 60 degrees, through a 1.06-mm slit defined by a pair of knife edges and was collected by a faraday cage. After amplification, the current to the detector (and similarly, the monitor current) was read on a galvanometer. The length of the circular arc from entrance window A to the opening of the faraday cage was 12.02 cm. The amount by which the actual path length of the protons differed from this, owing to edge effects of the magnetic field, will be discussed later. Can J, projecting into the chamber, allowed a synchronous-motor-driven fluxmeter to be introduced between the pole faces.

The foregoing arrangement provided a magnetic analyzer for measuring beam energies after the entrance window, and it was so used in the experiment. The magnetic field was exactly zeroed, as indicated by the fluxmeter, and the electromagnet current then gave a measure of the momentum of the protons. A calibration was carried out by removing window A and tabulating magnet currents and corresponding beam energies, the latter being measured by means of a cylindrical electrostatic analyzer.[13]

In addition to the charged beam a neutral component, indicated by the straight dotted line, emerged from window A because capture processes take place in the

[12] See reference 3, p. 1028.
[13] S. K. Allison *et al.*, Rev. Sci. Instr. **20**, 735 (1949).

window material. Another effect arising from the window was elastic scattering of the proton beam. Although the faraday cage in detector D_1 could be expected to be insensitive to neutral atoms, those formed by capture processes in the scattered beam were prevented from entering the detector by means of baffle B. This baffle intercepted most of the scattered particles which could give rise to neutral atoms entering the 60-degree detector D_1.

Detector D_2 was used in measuring the equilibrium attenuation ratios ρ_ϵ, as will be described later. Figure 2 shows the cross section of a detector.

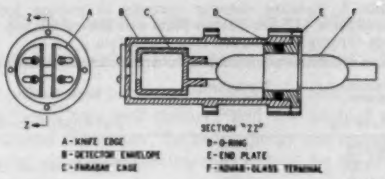

FIG. 2. Cross section of faraday-cage detector.

3. *The Vacuum System*

The electron exchange chamber could be evacuated or filled with hydrogen at the low operating pressures used in the experiment (of the order of 10^{-2} mm Hg) through manifold G. In the following discussion needle valve NV_1 may be assumed to be closed. With valve V_1 open the high vacuum obtained was about 4×10^{-6} mm Hg. Upon closing this valve, the rate of rise of pressure, in the absence of hydrogen, never exceeded 2×10^{-3} mm Hg per hour, corresponding to a leak rate of about 4×10^{-3} cc per hour. Since the time lapses between successively pumping out the system did not exceed ten minutes, this leak rate was negligible.

With valve V_1 closed, hydrogen from a palladium leak could be admitted to the system through valve V_3. Pressures were measured by means of a McLeod gauge, connecting through valve V_4.

An additional diffusion pump was attached through line L to the collimating tube. Valve V_2 was provided in order to equalize the pressures on both sides of window A while the system was pumped down and was closed when a high vacuum was obtained.

B. Experimental Arrangement for Measuring the Equilibrium Attenuation Ratios

In making these measurements it was desirable to have as nearly pure a proton beam as practicable and hence to eliminate the excessive neutral component arising from capture processes in window A. Therefore, the window was replaced by a small brass diaphragm K with a 0.51-mm diameter hole (No. 76 drill), having a sharply beveled edge, as shown in the detail drawing at the bottom of Fig. 1. Since the individual wires of the monitoring screen H could cover an appreciable fraction of the area of such a hole, the screen was replaced by a thimble T, separated by a Lucite spacer S from diaphragm C_2. The hole in the end of T had a diameter of 1.19 mm and, therefore, intercepted a portion of the collimated beam, passing the rest to diaphragm K.

The diffusion pump on line L evacuated the space behind diaphragm K and thus provided differential pumping to isolate the exchange chamber from the high vacuum of the beam-defining tube. The pressure in the exchange chamber was maintained at the desired magnitudes by matching the rate of flow of hydrogen into the exchange chamber with the effusion rate through the hole in diaphragm K. Needle valve NV_1, leading back to the diffusion pump, provided a fine adjustment on the rate of flow of hydrogen into the chamber.

The proton beam in this part of the experiment was collected by the faraday cage of detector D_2 whose slits were opened to 3.5 mm.

III. EXPERIMENTAL PROCEDURE

A. The Electron Capture Cross Sections

1. *Procedure Used in Obtaining the Data*

The energy of the ion beam was set; and with the exchange chamber evacuated, a "profile" of the current to the 60-degree detector *versus* magnet current was obtained. As always, the magnetic field was carefully adjusted to zero by means of the fluxmeter before beginning, and the magnet current was increased throughout the desired range, with no decreases to give hysteresis errors. The profiles had widths at half-maximum of from 8 to 14 percent, a large fraction of which could be attributed to elastic scattering in the entrance window rather than to inhomogeneity of the beam energy. For convenience in obtaining protons at the lower energies, the molecular beam from the kevatron was often used; the molecules were dissociated in the window, giving protons of half the molecular beam's energy.

Having determined the beam energy from the peak of the profile, the magnet current was set at peak value and maintained at this value during the course of the run. The magnet coils and their series rheostats were water-cooled, so that there was very little drift of the magnet current, and only slight adjustments were required during a run to compensate small fluctuations in the voltage of the motor-generator set supplying the coils. Both magnet current and accelerator voltage were held constant to within less than one percent during the runs.

With the beam thus held in position on the 60-degree detector the ratio $r(0)$ of the detector-galvanometer deflection to the monitor-galvanometer deflection was measured with the electron-exchange chamber evacuated to less than 10^{-4} mm Hg. Hydrogen was admitted to the chamber, during which process the detector

TABLE I. Relative detector currents at various hydrogen pressures for a 44.5-kev proton beam and the calculation of the electron-capture cross section from these data.

Hydrogen pressure p 10^{-2} mm Hg	Normalized detector current r	Attenuation ratio $\rho(p)=r(p)/\text{mean } r(0)$
<0.01	0.636	
0.97	0.322	0.322/0.630=0.511
<0.01	0.624	
1.61	0.199	0.199/0.167=0.322
<0.01	0.611	
0.75	0.339	0.339/0.595=0.570
<0.01	0.580	

Calculation of the capture cross section:

s = slope of straight line in Fig. 3 = 30.9 ± 0.9 (mm Hg)$^{-1}$

T = room temperature = 294.7°K.

σ_e' = uncorrected capture cross section = $2.959\times10^{-18}s(T/298)$ = $(9.04\pm0.27)\times10^{-17}$ cm^2,

σ_e = corrected cross section = $\sigma_e'+\sigma_g=\sigma_e'+0.108\times10^{-17}$ = $(9.15\pm0.27)\times10^{-17}$ cm^2.

current decreased; and when a suitable pressure had been reached, the flow was stopped. The ratio $r(p)$, at hydrogen pressure p, was then determined, and the hydrogen pressure was measured with the McLeod gauge. Finally, the chamber was evacuated and the ratio $r(0)$ measured again. The cycle was then repeated for a different pressure.

It should be emphasized that since only ratios of the currents were required, the absolute values were not important in the cross-section measurements. These values were, however, a few thousandths of a microampere. The linearity of the amplifier-galvanometer

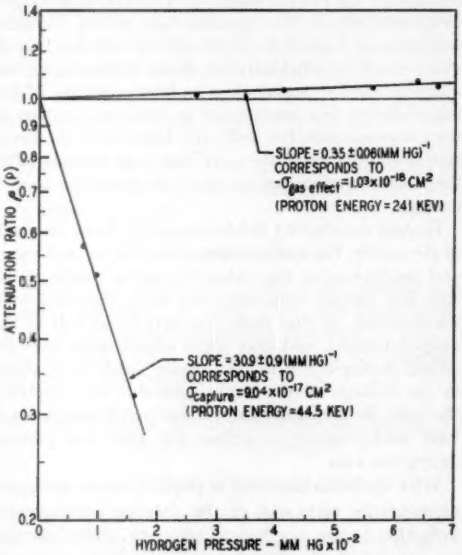
ATTENUATION RATIO ρ(p)
HYDROGEN PRESSURE - MM HG x 10⁻²
SLOPE = 0.35 ± 0.06 (MM HG)⁻¹
CORRESPONDS TO
-σ gas effect = 1.03 x 10⁻¹⁸ CM²
(PROTON ENERGY = 241 KEV)
SLOPE = 30.9 ± 0.9 (MM HG)⁻¹
CORRESPONDS TO
σ capture = 9.04 x 10⁻¹⁷ CM²
(PROTON ENERGY = 44.5 KEV)

FIG. 3. Lower curve: Attenuation curve for a 44.5-kev proton beam at the 60-degree detector. Upper curve: Variation of detector response with hydrogen pressure.

arrangements (exclusive of input resistors) was checked over the operating range and found to be good to better than one percent.

In measuring the ratios $r(0)$ and $r(p)$, three or more readings were taken and averaged; and in each run a minimum of two, and usually three or four, pressures were used. In terms of these ratios the attenuation ratio $\rho(p)$ of Eq. (1) is given by

$$\rho(p)=r(p)/r(0). \tag{3}$$

The data for a typical run at a beam energy of 44.5 kev are given in Table I and plotted in Fig. 3 (lower curve). Using $d=12.02$ cm, Eq. (1) gives for the electron-capture cross section per atom,

$$\sigma_e=2.959\times10^{-18}s(T/298), \tag{4}$$

where s is the slope of the line ("attenuation curve") in Fig. 3, expressed in (mm Hg)$^{-1}$, and T is the absolute temperature. In the sample calculation of Table I the value of σ_e derived from the slope of the attenuation curve is called σ_e'. It is necessary to correct this value by adding a small quantity $-\sigma_g$ due to the effect of gas on the detector, as will presently be explained, to obtain the value σ_e of the electron capture cross section.

2. *Tests for Experimental Errors*

When the faraday cage was used in measuring proton current in this part of the experiment, it was always situated in a strong magnetic field, which varied from about 1900 to 5500 gauss for the energy range of protons used. Therefore, it was not necessary to bias the cage in order to trap completely all secondary electrons produced by the proton beam in the cage. In order to check this point, the voltage from a well-insulated battery was applied between the grid of the beam-current amplifier and the faraday cage of the 60-degree detector (faraday cage positive). With proton beams of 61 and 258 kev and the exchange chamber evacuated, no difference was observed in the detector-galvanometer deflections for the conditions of zero and 100 volts on the faraday cage. Thus, it can safely be assumed that the cage did not respond to neutral atoms whose effect would be to produce secondary electrons from the surfaces which they struck. Therefore, no correction of the path length, owing to the entry of neutral-hydrogen beam atoms from positions at small distances in front of the detector, was applied. Neither were neutral atoms arising from capture processes in the proton beam scattered by the entrance window registered. A large fraction of these were excluded by means of baffle B of Fig. 1 whose knife edge was separated from the center of the bent beam by about 2 mm.

However, with a beam entering the faraday cage, the response of the detector itself was found to be somewhat affected by the presence of hydrogen gas. In order to measure this effect the beam energy was set at a value sufficiently high (295 kev) that the effect of

electron capture (as given by σ_e') was certainly negligible. With the proton beam bent into the faraday cage at the 60-degree position, the normalized detector current rose by a few percent as the pressure of hydrogen was increased up to the maximum value (about 7×10^{-3} mm) used in the experiment. The percent rise was also found to be independent of beam current. At slightly lower energies where there was some residual capture cross section, this rise decreased. However, by using the values of σ_e' extrapolated from the working energy region (32 to 150 kev), it was possible to correct for this. When this was done, the rise was found to be independent of beam energy within experimental error. The data for a typical rise corresponding to a beam energy of 241 kev are plotted in Fig. 3 (upper curve). Such a rise can be represented by an equivalent negative cross section.

In order to estimate the effect at lower energies where capture processes caused a large attenuation of the bent beam, the 60-degree detector was inserted at the zero-degree position, and a 0.025-mg/cm² aluminized zapon foil was placed about 3 mm in front of the detector. Capture and loss processes occurring in the gas of the chamber did not affect the faraday cage current, since the beam emerging from the foil covering the cage had an equilibrium distribution of protons and atoms, regardless of the composition of the beam impinging on the foil. With a magnetic field of about 100 gauss it was possible to prevent secondary electrons ejected from the foil from entering the cage and still to work on the portion of the beam scattered slightly by the entrance window. Measurements at 109 and 137 kev gave gas effects which were of the same size as those obtained before, indicating that the effect was independent of energy and magnetic field.

Table II gives the data for the gas effect. In the second column are the equivalent negative cross sections corresponding to the slopes of the gas-effect rises. Column 3 gives the extrapolated values of σ_e' added to their magnitudes to correct them, and the last column gives the gas effect $-\sigma_g$ itself. It can be represented as a constant correction to be added to the cross sections σ_e', giving for the corrected capture cross section:

$$\sigma_e=\sigma_e'+\sigma_g. \tag{5}$$

Such an effect was also observed by Montague,[14] who used a different type of detector in his measurements of loss cross sections and attributed the effect to ionization produced by the beam in the detector. In the present case the correction is somewhat smaller, but it is difficult to see how it is produced by ionization in view of the geometry of the detector. It should perhaps be mentioned that the voltage developed by the beam current across the input resistor to the beam-current amplifier (100 megohms) never exceeded 0.11 volt.

[14] See reference 3, p. 1031.

B. The Equilibrium Attenuation Ratios

1. Procedure Used in Obtaining the Equilibrium Data

Since there was no entrance window in this case, the proton beam was well defined, and the profiles were quite narrow. Therefore, the beam energy was measured simply by visually observing the peak of the 60-degree detector currents.

With the beam energy held constant, the field was carefully zeroed and then increased to a value of about 60 gauss in order to trap secondary electrons in the faraday cage. The slits of the zero-degree detector were set sufficiently wide that the beam still entered the faraday cage at this weak field. Hydrogen pressure was then allowed to build up in the exchange chamber, and needle valve NV_1 of Fig. 1 was adjusted so that the pressure remained approximately constant at the desired value. The ratio $r(p)$ of detector- and monitor-galvanometer deflections was then read, the flow of hydrogen was stopped, and the system was pumped to high vacuum. Finally, the ratio $r(0)$ was determined.

TABLE II. Effect of hydrogen gas on detector response, expressed as an equivalent negative cross section.

Proton energy kev	Negative cross section corresponding to gas effect cm² × 10⁻¹⁸	Extrapolated capture cross section σ_e' cm² × 10⁻¹⁸	Corrected gas effect $-\sigma_g$ cm² × 10⁻¹⁸
295	1.07±0.06	0	1.07±0.06
241	1.03±0.18	0.033	1.06±0.18
208	0.94±0.42	0.10	1.04±0.42
190	0.86±0.17	0.25	1.11±0.17
137	1.10±0.28	···	1.10±0.28
109	0.84±0.16	···	0.84±0.16

Equivalent gas-effect cross section used in correcting the data: $-\sigma_g=(1.08\pm0.10)\times10^{-18}$ cm².

The process was repeated for a number of hydrogen pressures. As pressure increased, the attenuation ratio $\rho(p)$ at first decreased and then reached an approximately constant value. A slight rise at saturation occurred because of the gas effect discussed in the last section, and the data were corrected for this effect. In taking each point, the ratio $r(p)$ was read quickly in order to minimize fluctuations in pressure, and gas was trapped in the McLeod-gauge bulb at the time of reading the galvanometer deflections.

Three such runs were made at energies of 59.0, 66.7, and 73.0 kev. In order to obtain decreases in attenuation ratio which were sufficiently large for its accurate determination, it was necessary to run at low energies where σ_1/σ_c is close to unity. However, since there was no entrance window, dissociated molecules could not be used to furnish low energy protons, and the lowest proton energy used was, therefore, that for which the beam from the kevatron focused sufficiently well to give a workable beam.

The data are plotted in Fig. 4 with the equilibrium value, ρ_∞, of $\rho(p)$ indicated for each curve. It can be

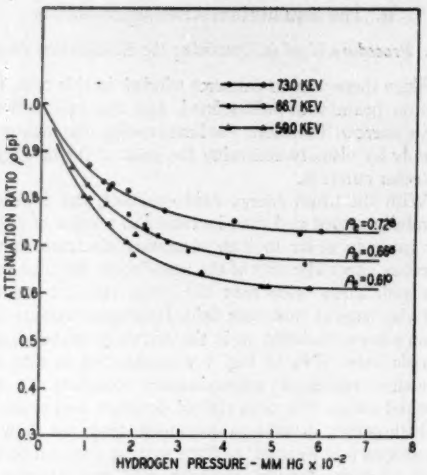

FIG. 4. Attenuation curve, showing the attainment of charge equilibrium, for mixed neutral-atom and protom beams at the zero-degree detector.

shown[15] that these curves should be of the form

$$\rho(p)=\rho_e+(1-\rho_e)\exp[-(\sigma_l+\sigma_e)n(p)d'], \qquad (6)$$

where d' is the distance between the entrance to the exchange chamber and the zero-degree detector. The curves shown in Fig. 4 were obtained by using this form to fit the data. It may be noted that this equation allows a determination of $(\sigma_l+\sigma_e)$; however, no attempt was made to determine this quantity accurately from these data, since instabilities in pressure did not allow an accuracy comparable to that obtained for the cross sections themselves. Such small variations in pressure did not affect the accuracy of the determination of ρ_e, however.

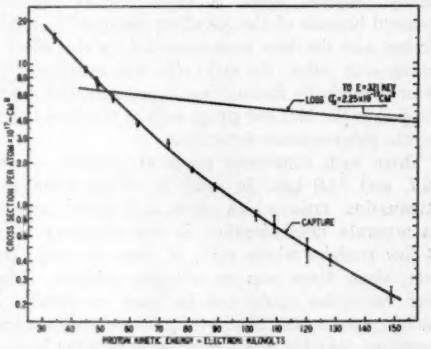

FIG. 5. Electron capture and loss cross sections as functions of ion energy for hydrogen beams in hydrogen gas.

[15] See reference 2, p. 507.

2. Tests for Experimental Errors

It was further verified that the faraday cage at the zero-degree position in these runs did not respond to a neutral beam. With chamber evacuated and sufficient magnetic field to deflect away the protons, no detector-galvanometer deflection was observed when the entrance hole was replaced by an aluminized zapon window which gave a neutral component of beam entering the cage.

An attempt was made to see if the presence of hydrogen gas caused a broadening of the beam as measured at the 60-degree detector. With the 0.5-mm entrance hole and the detector slit set at 1.06 mm, profiles were taken with and without gas in the chamber. No increase due to the presence of hydrogen was observed in the half-width for a pressure of about 3×10^{-2} mm Hg pressure, at a beam energy of 60 kev. This indicated that scattering by the gas in the chamber was negligible.

IV. RESULTS

A. The Electron Capture Cross Sections and the Ratio σ_l/σ_c

The results of the measurements of electron-capture cross sections are summarized in Fig. 5 in which σ_c is plotted as a function of energy. For comparison, the results obtained by Montague[3] in this energy range for the electron-loss section σ_e are also plotted in this graph.

The values of σ_c are tabulated in the second column of Table III; in the third column are the values of σ_l/σ_c obtained by dividing the magnitudes of the loss cross sections measured by Montague by those of the capture cross sections obtained here. This ratio is plotted as a function of energy in Fig. 6 (the curve marked M & R).

B. Consistency of the Measurements of σ_l and σ_c

The consistency of the measurements of the two cross sections, at least in the range of energies in which the equilibrium ratio ρ_e was measured, is indicated by the graph in Fig. 7. In the upper curve the values of ρ_e given in Fig. 4 are plotted as a function of energy. The lower curve is a plot of ρ_e derived from Eq. (2), using the values σ_l/σ_c obtained from Fig. 6. The discrepancy between the two results can be attributed to a small component of neutral atoms in the incident beam of the equilibrium-ratio experiment which arose from capture and loss processes taking place on the periphery of the entrance hole to the exchange chamber and in the residual gas in the beam-defining tube. If one assumes a fraction ν of neutral atoms in the incident beam, Eq. (2) should be modified to read

$$\rho_e=(\sigma_l/\sigma_c)/[(1-\nu)(1+\sigma_l/\sigma_c)]. \qquad (2')$$

Solving this equation for ν, using the values of ρ_e and σ_l/σ_c corresponding to 59.0, 66.7, and 73.0 kev, gives, respectively, 4.5, 2.4, and 4.2 percent. These values are about what might be expected from edge effects.

An attempt was made to estimate the neutral component using a secondary-emission detector described by Montague.[18] Measurements made by comparing the responses of this detector (at the zero-degree position) to the total beam and to the neutral beam, when the protons were deflected away by the magnetic field, indicated a small neutral component. However, the relative responses of the detector to neutral and charged particles, as well as the dependence of its multiplication on magnetic field, were not known and could not be determined without further, rather extensive, experiments.

The measurements of ρ_e provide estimates of σ_l/σ_e. From the foregoing it is concluded that the values derived from the separate measurements of σ_l and σ_e are consistent with the direct estimates of their ratio to within 10 percent.

TABLE III. The electron-capture cross sections σ_e and the ratio, σ_l/σ_e, of loss and capture cross sections for hydrogen beams passing through hydrogen gas.

Hydrogen-beam energy E kev	Electron-capture cross section per atom σ_e 10^{-17} cm²	Ratio of loss and capture cross section σ_l/σ_e
34.0	15.2 ±0.85	...
44.5	9.15 ±0.27	0.728
48.3	7.65 ±0.21	0.851
48.7	7.05 ±0.16	0.922
53.9	5.73 ±0.51	1.10
62.5	3.76 ±0.11	1.61
72.9	2.75 ±0.29	2.07
81.1	1.77 ±0.02	3.09
88.8	1.36 ±0.17	3.86
103	0.842±0.069	5.79
109	0.733±0.017	6.41
120	0.485±0.098	9.20
128	0.410±0.033	10.5
149	0.229±0.028	17.1

C. Accuracy of the Measurements

The limits of random error in the measurements of σ_e are given in Table III and indicated on the experimental points of Fig. 5. They were estimated from the spread of points about the attenuation curves and thus take into account instrument-reading errors and fluctuations in the experimental conditions. In addition, there were systematic errors which are enumerated below.

1. The Effect of Gas on the Detector Response

Values of σ_e are given for energies up to the maximum at which measurements were made of 149 kev. At this end of the energy range, however, the capture cross sections have small magnitudes, comparable with the correction $-\sigma_g$ due to the detector gas effect. This correction rapidly becomes less important at lower energies and represents only 0.71 percent at the lowest energy (34 kev) used. The systematic error in capture cross section due to this correction is estimated to be 0.07 and 5 percent at the lower and upper energy extremes of the measurements, respectively.

[18] See reference 3, p. 1029.

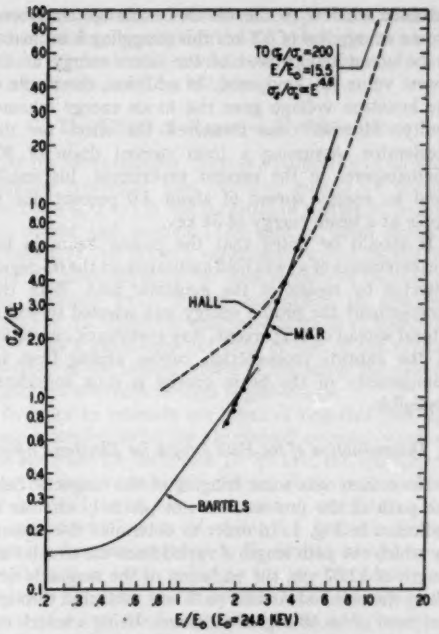

FIG. 6. Ratio of loss to capture cross section σ_l/σ_e as a function of ion energy E. Curve M & R and that of Bartels: Hydrogen beams in hydrogen gas. Curve of Hall: Hydrogen beams in the metals Be, Al, and Ag.

2. Inhomogeneity of the Beam Energy

Some inhomogeneity was introduced into the beam energy by straggling arising from energy loss in the

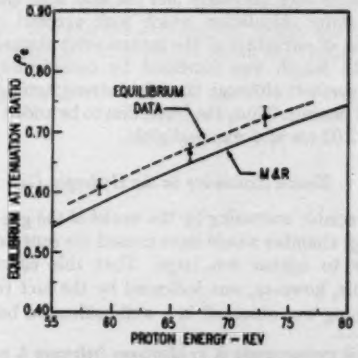

FIG. 7. Comparison of the equilibrium attenuation ratios ρ_e derived from the separate measurements of σ_l and σ_e (the curve marked M & R) with those measured directly.

entrance window to the electron-exchange chamber.[17] For an energy loss of 6.5 kev this straggling is estimated to be about 0.9 percent of the beam energy at the lowest value (34 kev) used. In addition, the ripple of the kevatron voltage gave rise to an energy inhomogenity. Morrish[18] has measured the effect for this accelerator. Assuming a total current drain of 400 microamperes in the present experiment, his results yield an energy spread of about 3.0 percent due to ripple at a beam energy of 34 kev.

It should be noted that the proton beam in the measurements of σ_e was held accurately on the 60-degree detector by means of the magnetic field. With this arrangement the proton energy was selected to within a total spread of 1.8 percent. Any systematic correction of the capture cross-section curves arising from inhomogeneity of the beam energy is thus considered negligible.

3. *Determination of the Path Length for Electron Capture*

Since there was some fringing of the magnetic field, the path of the protons was not precisely circular as indicated in Fig. 1. In order to determine the amount by which the path length d varied from the circular-arc length of 12.02 cm, the variation of the magnetic field along the nominal circular path was measured throughout most of its 60-degree extension. Using a search coil of 1-cm diameter on the generating fluxmeter, the field was found to be weakened by respectively 9 and 26 percent at the entrance and detector ends of this circular arc and to be homogeneous to within 1 percent over 60 percent of this arc. The difference in fringing at the ends of the arc was due to the magnetic shielding about the entrance window.

Since the ends of the protons' path were fixed at the positions of the entrance window and of the detector, the main effect of this field inhomogeneity was merely to require a larger field at the center of the exchange chamber for bending protons of a given energy than would have been necessary had the field been uniform. A first-order calculation which took account of the variation of curvature of the proton orbit showed that the path length was increased by considerably less than 1 percent; although the "field strengthening" was about 2 percent. Thus, the correction to be added to the value 12.02 cm of d was negligible.

4. *Elastic Scattering in the Hydrogen Gas*

Appreciable scattering by the nuclei of the gas in the exchange chamber would have caused the capture cross sections to appear too large. That this effect was negligible, however, was indicated by the fact that no broadening was observed in a well-collimated beam at the 60-degree detector. In addition, since the beam in the measurements of σ_e was spread by elastic scattering in the entrance window to a width considerably greater than that of the detector slit, the "geometry" was poor for observing such scattering in the gas. Bartels,[5] using good collimation and thicknesses of hydrogen gas comparable to those used here, observed no elastic scattering of protons at 30 kev. If there were such an effect in the present experiment, it would be included in the measured detector gas-effect correction $-\sigma_g$.

5. *McLeod-Gauge Calibration*

The McLeod guage was calibrated by measuring the volume of its bulb and the diameter of its capillary. The consistency of several measurements indicated a calibration error of less than 1 percent.

V. DISCUSSION

A. The Capture Cross Section

From Fig. 5 it is seen that the capture cross section varies much more rapidly with energy than does the loss section. A log-log plot of the data shows that σ_e varies approximately as $E^{-3.5}$ at the upper end of the energy range (100 to 150 kev), while the value of the exponent reported by Montague for σ_l in the region 120 to 329 kev is -0.70. This difference is qualitatively in accord with previous observations and theory. Rutherford[19] obtained the value -2.8 for this exponent for the capture by doubly-charged alpha-particles in air and the value -0.5 for the corresponding loss cross section. Brinkmann and Kramers,[20] using the first Born approximation, calculated the cross sections for capture into the Bohr orbits of a moving ion from hydrogen. Their result gives a variation of σ_e as E^{-6}, asymptotically for $E \gg E_0$, where E_0 is the kinetic energy at which the ion velocity is equal to that of an electron in the first hydrogen Bohr orbit ($v_0 = e^2/\hbar$). In the present experiment, however, E/E_0 varies between 1.37 and 6.01, so that this condition is not met. A decrease in the numerical value of the exponent at lower energies is predicted, however; and it might be worth noting that the value of the exponent obtained from their equation in the energy range 100 to 150 kev is about -3.8.

The difference between the exponent -3.5 observed in this experiment ($1.17 \leq v/v_0 \leq 2.46$) and Rutherford's value of $-2.8 (4.1 \leq v/v_0 \leq 8.3)$ indicates a more rapid decrease of σ_e with increasing ion velocity for hydrogen than for heavier stopping atoms. On classical grounds, Bohr[21] estimates the value -3 for this exponent for heavy stopping atoms. This difference in exponents for light and heavy stopping materials is in qualitative accord with the Brinkmann-Kramers result, which indi-

[17] In his measurements of σ_l Montague (reference 3, p. 1033) overestimated this straggling in setting 45 kev as the lowest beam energy at which his results could be considered reliable.

[18] A. H. Morrish, Phys. Rev. **76**, 1651 (1949).

[19] E. Rutherford, Phil. Mag. **47**, 277 (1924).

[20] H. C. Brinkmann and H. A. Kramers, Proc. Akad. Amsterdam **33**, 973 (1930).

[21] N. Bohr, Kgl. Danske Videnskab. Selskab, Mat.-fys Medd. **18**, 115 (1948).

cates a decrease in the numerical value of the negative exponent, at a given velocity, with increasing atomic number of the stopping material.

Keene[22] has published a summary of the previous measurements of σ_c for protons in hydrogen gas. Of these measurements those of that author, of Bartels, and of Meyer extend to sufficiently high energies for comparison with the present data. At low energies both Keene and Bartels observe a maximum of the curve $\sigma_c(E)$ at about 7 kev, but they disagree appreciably on the magnitude of σ_c. The present data appear to agree quite well with those of Bartels, forming a reasonable extension of his curve, which is given for proton energies up to about 32 kev. The data of Meyer and the present data differ appreciably in the region about 32 kev, with the former showing a smaller exponent in the dependence of σ_c on E.

B. The Ratio σ_l/σ_c

In Fig. 6 are plotted curves of the ratio σ_l/σ_c obtained from the present experiment and that of Montague and also from the data of Bartels.[5] The curve given by Hall[23] for protons in the metals Be, Al, and Ag is also plotted for comparison.

A striking fact that appears from the data for protons in metals is that σ_l/σ_c for a given energy is approximately independent of the atomic number of the stopping material. The ratio σ_l/σ_c has the value unity for a proton velocity v of about one Bohr unit ($v/v_0=1$). Hall gives for this critical ratio the value 0.95. The present data, however, indicate a value 1.44 for this critical ratio; and this difference between the values obtained for metals and for hydrogen is confirmed by Bartels's data for protons in hydrogen gas given in Fig. 6.

In calculating the effective charge of moving ions it is assumed that roughly all electrons of velocities less than the speed of the ion are stripped off, since σ_l/σ_c increases rapidly from unity for $v/v_0>1$. In some of the calculations on the stopping of heavy ions in heavy gases the value $v/v_0\approx 1$ obtained from previous measurements has been a rough guide. On this basis the higher value 1.44 obtained here would result in a lower effective charge for ions moving in hydrogen.

C. The Effect of Negative Hydrogen Ions

At the lower energies, there is a possibility of forming negative hydrogen ions (binding energy of second electron=0.71 ev) in the traversal of matter by hydrogen atoms and protons. The capture cross sections obtained in the present experiment would hardly be affected, however, since the cross section for capture of two electrons by a proton can safely be assumed negligible. In Montague's measurements of σ_l, however, there was a possibility not only of loss of the orbital electrons of the neutral atoms of the beam but also of capture of electrons to form negative ions.

In order to estimate the effect of negative ions the beam emerging from the aluminized entrance window was analyzed for such ions. At 35 kev, the fraction of negative ions was about 3 percent of the proton component, while at 90 kev none were observed to within an experimental error of about 0.1 percent. Fewer negative ions are expected to be formed in hydrogen gas than in a metal owing to the smaller density of electrons per atom in the former. Since the measurements of σ_l extended only down to 45 kev, it seems safe to neglect the effect of negative hydrogen ions in these measurements. At lower energies, such as those used by Bartels in his measurements of σ_l/σ_c, there may, however, be such an effect, so that his results would represent $(\sigma_l/\sigma_c)+\sigma_c^*/\sigma_l^*$ instead of σ_l/σ_c, where the starred quantities refer to transitions involving negative hydrogen ions and neutral atoms.

The author wishes to express his thanks to Professor S. K. Allison for suggesting this problem and for extending the facilities of his laboratory for its execution and for his helpful advice. Thanks also are due Mr. H. Kanner and Mr. D. S. Bushnell for their aid in taking the data, and to Dr. J. H. Montague for helpful discussions. Grateful acknowledgment is also made of an AEC Predoctoral Fellowship granted the author.

[22] See reference 9, p. 385, Fig. 18.
[23] See reference 2, Fig. 3. The curve plotted in Fig. 6 is the solid curve given by Hall.

Magnetic Neutron Diffraction from Exchange-Coupled Lattices at High Temperatures

M. SLOTNICK
Randall Physics Laboratories, University of Michigan, Ann Arbor, Michigan
(Received April 9, 1951)

The magnetic scattering of slow neutrons from a crystal lattice with exchange coupling at temperatures much higher than the (ferromagnetic or antiferromagnetic) Curie point is investigated. The residual short-range order is shown to manifest itself in coherent and inelastic effects, which are calculated by means of an expansion in $1/T$. These effects can yield information on the strength of the exchange interactions, the ratio of nearest neighbor to next nearest neighbor interactions, etc. Conditions for the observability of these effects are more favorable in the antiferromagnetic case.

I. INTRODUCTION

COHERENT effects in the magnetic scattering of neutrons from the antiferromagnetic substance MnO at room temperature were first observed by Shull and Smart.[1] Recently, more detailed experiments have been performed on MnO by Bendt and Rainwater.[2] Since MnO has a Curie temperature of 122°K, the scattering effects constitute one of the very few detectable effects of exchange coupling at temperatures far above the Curie point. It was therefore thought of interest to make a detailed theoretical calculation of the magnetic neutron diffraction pattern in this temperature region, particularly since here the rigorous high temperature expansion methods are available and make possible relatively unequivocal statements. These enable one, at least in principle, to obtain from the experimentally observed pattern a considerable amount of information on the exchange interaction strengths, etc.

In Sec. II, the specifically coherent scattering effects are investigated for a lattice with nearest neighbor and next nearest neighbor exchange coupling, for both the ferromagnetic and antiferromagnetic cases. In Sec. III, several inelastic effects neglected in Sec. III are taken into account.

II. THE COHERENT MAGNETIC SCATTERING

The magnetic scattering of slow neutrons (i.e., that part of the scattering due to the interaction of the neutron magnetic moment with the electronic magnetic moments) has been studied by Halpern and Johnson[3] and many others. They found that for neutrons of momentum $\mathbf{k}$ and spin s incident on a lattice in a state L, the ratio of measured intensity of neutrons of momentum $\mathbf{k}'$ and spin s' in a solid angle range $d\Omega$ to incident neutron intensity is

$$di=(2e^2\mu_N/m)^2|(s'L'|\textstyle\sum_n(\mathbf{s}\cdot\mathbf{S}_n-\mathbf{q}^*\cdot\mathbf{s}\mathbf{q}^*\cdot\mathbf{S}_n)\times\exp(-\mathbf{q}\cdot\mathbf{R}_n)|sL)|^2F(q)d\Omega. \quad (1)$$

Here L' is the final lattice state, m is the electronic mass, μ_n is the magnetic moment of the neutron, $\mathbf{s}$ is the neutron spin operator, $\mathbf{S}_n$ and $\mathbf{R}_n$ are the spin operator and position respectively of the nth ion, and the sum is over all N ions in the lattice. Further, $\hbar$ and c have been taken as unity and

$$\mathbf{q}=\mathbf{k}'-\mathbf{k};\quad \mathbf{q}^*=\mathbf{q}/|\mathbf{q}|, \quad (2)$$

and

$$F^1(q)=\mathcal{S}^{-1}(B|\exp(-\mathbf{q}\cdot\mathbf{r}_l)\mathbf{s}_l\cdot\mathbf{S}|B)\quad(\mathcal{S}\equiv S(S+1)) \quad (3)$$

is the magnetic form factor of the individual ion, B being the state of the individual ion, $\mathbf{s}_l$ and $\mathbf{r}_l$ the spin and location of its lth electron, and $\mathbf{S}$ its total spin.

It has been assumed that the orbital magnetic interactions are absent or quenched, and that the neutrons are being detected with an efficiency inversely proportional to the velocity, so that a $|\mathbf{k}'|/|\mathbf{k}|$ term is absent in (1). We assume also that the region of observation is far from a nuclear Bragg peak, so that there is no interference with nuclear scattering. The nuclear scattering may then simply be subtracted from the total measured scattering to give the magnetic scattering.

Of experimental interest is the total intensity of scattered neutrons in a given direction $\mathbf{k}^{*\prime}=\mathbf{k}'/|\mathbf{k}'|$. If we therefore sum (1) over all possible final states for which $\mathbf{k}'$ lies in the specified direction, and average over the initial neutron spin states (assuming an unpolarized beam) we obtain for the ratio of intensity in the direction $\mathbf{k}^{*\prime}$ (per unit solid angle) to incident neutron intensity:

$$I(\mathbf{k},\mathbf{k}^{*\prime})=\sum_L Z^{-1}\exp(-E_L/T)\sum_{\text{ad }L'}(e^2\mu_N/m)^2F(q)\cdot|(L'|\sum_n(\mathbf{S}_n-\mathbf{q}^*\mathbf{q}^*\cdot\mathbf{S}_n)\exp(-i\mathbf{q}\cdot\mathbf{R}_n)|L)|^2. \quad (4)$$

Here $Z^{-1}\exp(-E_L/T)$ is the probability of occupation of the lattice state L, where

$$Z(T)=\textstyle\sum_L\exp(-E_L/T). \quad (5)$$

(T measured in energy units) and E_L is the exchange energy of the state L, which we take to be the eigenfunction of a hamiltonian

$$H=J\sum_{\text{nbr }l,l'}\mathbf{S}_l\cdot\mathbf{S}_{l'}+K\sum_{n\text{ nbr }l,l'}\mathbf{S}_l\cdot\mathbf{S}_{l'}. \quad (6)$$

The specifications "nbr l, l'" and "n nbr l, l'" refer to

[1] C. J. Shull and J. S. Smart, Phys. Rev. **76**, 1256 (1949).
[2] P. J. Bendt and L. J. Rainwater, Phys. Rev. **83**, 235 (1951).
[3] O. Halpern and M. H. Johnson, Phys. Rev. **55**, 898 (1939).

the fact that the first sum is taken over all ions l and l' that are nearest neighbors, the second over all l and l' that are next nearest neighbors. J and K are proportional to certain exchange integrals and are positive in the antiferromagnetic, negative in the ferromagnetic case. The instruction "ad L'" in the sum over final states in (4) means that only those final lattice states with admissible energies are to be included. That is, the kinetic energy of the scattered neutron

$$k'^2/(2M)=k^2/(2M)+E_L-E_{L'} \tag{7}$$

must be $\geqslant 0$, or $E_{L'}\leqslant E_L+k^2/(2M)$. ($M$ is the neutron mass.)

To proceed with the evaluation of (4), two approximations are made, which will be examined more closely in Sec. III. First, we assume that in the admissible transitions, $\mathbf{q}$ is seldom very far from its value $\mathbf{q}_0$ for a purely elastic transition:

$$q_0=2k\sin\tfrac{1}{2}\vartheta;\quad |\mathbf{k}'|=|\mathbf{k}|, \tag{8}$$

where ϑ is the angle between $\mathbf{k}$ and $\mathbf{k}'$. We thus substitute $\mathbf{q}_0$ for $\mathbf{q}$ in the matrix element of (4) and in the argument of the form factor. Second, we assume that the final lattice states L' to which a nonzero matrix element exists in (4) are almost all energetically accessible, so that in the summation over final states, we may sum over all states to which a nonzero matrix element exists. The first approximation depends on q being fairly large compared to the rms energy change, the second on k being fairly large.

$I(\mathbf{k},\mathbf{k}^{*\prime})$ then becomes (with $\mathbf{R}_{nn'}$ written for $\mathbf{R}_n-\mathbf{R}_{n'}$)

$$\begin{aligned}I(\mathbf{k},\mathbf{k}^{*\prime})&=(e^2\mu_N/m)^2F(q_0)Z^{-1}\textstyle\sum_L\exp(-E_L/T)\\&\quad\cdot(L|\textstyle\sum_{nn'}(\mathbf{S}_n-\mathbf{q}^*_0\mathbf{q}^*_0\cdot\mathbf{S}_n)\cdot(\mathbf{S}_{n'}-\mathbf{q}^*_0\mathbf{q}^*_0\cdot\mathbf{S}_{n'})\\&\quad\times\exp(i\mathbf{q}_0\cdot\mathbf{R}_{nn'})|L)\\&=(e^2\mu_N/m)^2F(q_0)Z^{-1}\\&\quad\times\mathrm{Sp}\{\textstyle\sum_{nn'}(\mathbf{S}_n\cdot\mathbf{S}_{n'}-\mathbf{q}_0{}^*\cdot\mathbf{S}_n\mathbf{q}_0{}^*\cdot\mathbf{S}_{n'})\\&\qquad\times\exp(i\mathbf{q}_0\cdot\mathbf{R}_{nn'})\exp(-H/T)\}.\end{aligned} \tag{9}$$

Next, the $\exp(-H/T)$ is expanded:

$$\exp(-H/T)=\sum_{m=0}^{\infty}(-1)^m/m!(H/T)^m$$

in both the argument of the spur in (9) and in

$$Z(T)=\textstyle\sum_L(L|\exp(-H/T)|L)=\mathrm{Sp}\exp(-H/T), \tag{10}$$

and a series is obtained for $I(\mathbf{k},\mathbf{k}^{*\prime})$:

$$I(\mathbf{k},\mathbf{k}^{*\prime})=I_0+T^{-1}I_1+T^{-2}I_2+\cdots. \tag{11}$$

To terms in $1/T^2$,

$$Z(T)=(2S+1)^N\{1+T^{-2}(N\mathcal{S}^2/3)(J^2z_n+K^2z_{nn})\} \tag{12}$$

where z_n and z_{nn} are the numbers of nearest and next nearest neighbors respectively of a given lattice point. It is characteristic that because of the factor N, the number of ions in (12)—the expansion for Z, an extensive property of the lattice, is in powers of $(N^{\frac{1}{3}}/T)$, and is thus extraordinarily poor at laboratory temperatures. The series for $I(\mathbf{k},\mathbf{k}^{*\prime})$, however, is in powers of $1/T$, and is usable at ordinary temperatures. (In all of these calculations, frequent use is made of the following formulas for taking spurs:

$$\begin{aligned}&\mathrm{Sp}'S_\mu=0\\&\mathrm{Sp}'S_\mu S_\nu=\mathcal{S}/3\delta_{\mu\nu}\\&\mathrm{Sp}'S_\mu S_\nu S_\kappa=i/6\mathcal{S}e_{\mu\nu\kappa}\\&\mathrm{Sp}'S_\kappa S_\lambda S_\mu S_\nu=\mathcal{S}/30[(2\mathcal{S}+1)(\delta_{\kappa\lambda}\delta_{\mu\nu}+\delta_{\kappa\nu}\delta_{\mu\lambda})\\&\qquad\qquad+(2\mathcal{S}-4)\delta_{\kappa\mu}\delta_{\lambda\nu}],\end{aligned}$$

where $e_{\mu\nu\kappa}$ is the permutation symbol, S_μ is the μ-component of a spin vector whose square is $S(S+1)\equiv\mathcal{S}$, and Sp' indicates the spur divided by the number of states.) Further, it is found that

$$I_0(q_0)=(e^2\mu_N/m)^2F(q_0)\cdot\tfrac{2}{3}N\mathcal{S}, \tag{13}$$

which is the ordinary incoherent paramagnetic scattering (see reference 3) and

$$\begin{aligned}I_1(\mathbf{k},\mathbf{k}^{*\prime})&=(e^2\mu_N/m)^2F(q_0)\cdot\tfrac{2}{3}N\mathcal{S}\cdot(-\tfrac{2}{3}\mathcal{S})\\&\quad\times\{J\textstyle\sum_1\cos(\mathbf{q}_0\cdot\mathbf{R}_{ll'})+K\sum_2\cos(\mathbf{q}_0\cdot\mathbf{R}_{ll'})\},\end{aligned} \tag{14}$$

where $\sum_1$ is taken over all nearest neighbors l' of a single given lattice point l, and $\sum_2$ is over next nearest neighbors l' of l.

Actually, most experiments are performed with a microcrystalline powder, so that a typical lattice vector $\mathbf{R}_{ll'}$ will on the average be randomly located with respect to $\mathbf{q}_0$. We must, therefore, replace $\cos(\mathbf{q}_0\cdot\mathbf{R}_{ll'})$ by its average over-all directions of $\mathbf{R}_{ll'}$, which is

$$(q_0R_{ll'})^{-1}\sin(q_0R_{ll'}).$$

(14) then becomes (I_1 depends now only on k and the angle ϑ)

$$\begin{aligned}I_1(k,\vartheta)&=I_0(q_0)\cdot(-\tfrac{2}{3}\mathcal{S})\\&\quad\times\left\{Jz_n\frac{\sin q_0\Delta_n}{q_0\Delta_n}+Kz_{nn}\frac{\sin q_0\Delta_{nn}}{q_0\Delta_{nn}}\right\}\end{aligned} \tag{15}$$

where Δ_n and Δ_{nn} are the spacings between nearest and next nearest neighbors on the lattice respectively.

Note that to this approximation, the effects of nearest and next nearest neighbor interactions are completely additive—as are indeed the effects of any other interactions that may be present. This contrasts strongly with the situation below the Curie point, where the ordered lattice state may be determined by just one of the interactions.[4] In fact, it is possible by comparing the experimental location of the maxima or minima of the magnetic scattering pattern with those of (15) to infer the ratio of J to K, which can be used to check the theory of Anderson.[4]

[4] P. Anderson, Phys. Rev. 79, 705 (1950).

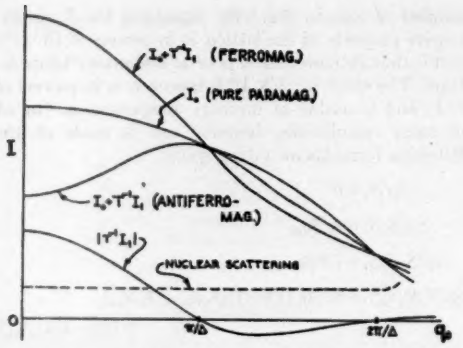

FIG. 1. Magnetic neutron scattering intensity per unit solid angle per unit incident beam (I) as function of $q_0=2k\sin\frac{1}{2}\vartheta$.

The relation between the ferro- and antiferromagnetic pattern is shown schematically in Fig. 1, where for simplicity we have assumed only one interaction, and plotted the intensity as functions of q_0. $I_0(q_0)$ [Eq. (13)], is just the form-factor pattern for an uncoupled paramagnetic lattice. The next term in the intensity, I_1 [Eq. (15)] is seen to be negative for the antiferromagnetic, positive for the ferromagnetic pattern, and is a coherent effect of the exchange coupling. In the ferromagnetic case, its principal effect is to increase the scattering for small q_0. This is difficult to observe first because of experimental difficulties at small q_0 (i.e., small angle or small neutron momentum k), and second because the inelastic effects to be discussed in Sec. III are very large in this region. The antiferromagnetic pattern, however, shows a coherent peak in the neighborhood of $q_0=\pi/\Delta$, and is readily observed. The inelastic effects, in fact, decrease the cross section at small q_0 and make the peak even more pronounced. The antiferromagnetic case is, therefore, much more accessible to experimental observation.

The antiferromagnetic coherent peak is the high temperature residue of the large coherent peak visible below the Curie temperature.[1] By examining the calculation of I_1, it is seen that the coherent effect arises from the correlation of ions directly coupled by an interaction [see Eq. (14)], and is thus an effect of the residual short-range order at high temperatures. It is in fact easy to compute the lowest order term in the temperature expansion for the average correlation of two ions at positions a and b in the lattice. The result is:

$$\langle(L|S_\alpha^{(a)}S_\beta^{(b)}|L)\rangle_{Av}=\tfrac{1}{3}\mathcal{S}\delta_{\alpha\beta}(-2J\mathcal{S}/3T)^{n_{ab}}s_{ab}, \quad (16)$$

where α and β refer to components of the spins of ions a and b, K has been assumed zero, n_{ab} is the minimum number of steps between a and b, counting distance between two neighbors as one step, and s_{ab} is the number of "shortest paths" between a and b, i.e., the number of ways of reaching b from a going from lattice point to lattice point, in precisely n_{ab} steps.

From (16), it is seen that the high temperature expansion is certainly poor at $T\lesssim 2|J|\mathcal{S}/3$, where the lowest order terms (16) indicate long-range order. The parameter $2J\mathcal{S}/(3T)$ is thus at high temperatures an indication of the degree of order, and is probably of the order of magnitude of unity at the Curie point.

The result for I_2 is, after some computation,

$$I_2=I_0\{J^2[-\tfrac{1}{3}\mathcal{S}\textstyle\sum_1\cos\mathbf{q}_0\cdot\mathbf{R}_{ll'}+(4/9)\mathcal{S}^2\sum_{1'}\cos\mathbf{q}_0\cdot\mathbf{R}_{ll'}]$$
$$+K^2[-\tfrac{1}{3}\mathcal{S}\textstyle\sum_2\cos\mathbf{q}_0\cdot\mathbf{R}_{ll'}+(4/9)\mathcal{S}^2\sum_{2'}\cos\mathbf{q}_0\cdot\mathbf{R}_{ll'}]$$
$$+JK\cdot(8/9)\mathcal{S}^2\textstyle\sum_3\cos\mathbf{q}_0\cdot\mathbf{R}_{ll'}\}, \quad (17)$$

where $\sum_1$ and $\sum_2$ have been defined above [Eq. (14)]. $\sum_{1'}$ is taken over all l' defined as follows: Pick any nearest neighbor of a given lattice site l. Then every nearest neighbor of this nearest neighbor, except l itself is taken as an l' in the sum. $\sum_{2'}$ is defined similarly—for "nearest neighbor" merely read "next nearest neighbor." In $\sum_3$, l' can be either a next nearest neighbor of a nearest neighbor of l, or the nearest neighbor of a next nearest neighbor.

After averaging over orientations of the microcrystals, (17) becomes

$$I_2=I_0\Big\{J^2\Big[-\frac{1}{3}\mathcal{S}z_n\frac{\sin q_0\Delta_n}{q_0\Delta_n}+\frac{4}{9}\mathcal{S}^2z_n\sum_\alpha\omega_\alpha^{(1)}\frac{\sin q_0D_\alpha^{(1)}}{q_0D_\alpha^{(1)}}\Big]$$
$$+K^2\Big[-\frac{1}{3}\mathcal{S}z_{nn}\frac{\sin q_0\Delta_{nn}}{q_0\Delta_{nn}}+\frac{4}{9}\mathcal{S}^2z_{nn}\sum_\alpha\omega_\alpha^{(2)}\frac{\sin q_0D_\alpha^{(2)}}{q_0D_\alpha^{(2)}}\Big]$$
$$+JK\cdot\frac{8}{9}\mathcal{S}^2z_nz_{nn}\sum_\alpha\omega_\alpha^{(3)}\frac{\sin q_0D_\alpha^{(3)}}{q_0D_\alpha^{(3)}}\Big\}. \quad (18)$$

Table I gives the $\omega_\alpha^{(i)}$, $D_\alpha^{(i)}$, etc., for several lattice types. It is not difficult to extend the results to other lattice types and to include other interactions. For each interaction, a term of the structure of the J^2 term in (17) must be included, and a cross-term like the JK term in (17) for every pair of interactions. To this order, there are no cross-terms involving more than two interactions.

III. INELASTIC EFFECTS

The approximations made in going from Eq. (4) for $I(\mathbf{k},\mathbf{k}^{*\prime})$ to Eq. (9) have led us to the expressions (11), (13), (15), and (18). These expressions are functions only of $q_0=2k\sin\frac{1}{2}\vartheta$, instead of both k and ϑ, so that if (as in the experiments of reference 2) $I(k,\vartheta)$ is measured as a function of k for several fixed angles $\vartheta_1,\vartheta_2,\cdots$ and the curves are plotted with q_0 as abscissa (as in Fig. 1), the curves taken at angles ϑ_1, ϑ_2, etc., should all coincide. We shall show now that if we take into account the neglected effects, the intensities are reduced somewhat (particularly for small q_0). Moreover, the curves for large ϑ are further depressed than those

TABLE I. Coefficients for Eq. (18).

Lattice type	$\frac{\Delta_{nn}}{\Delta_n}$	z_n	z_{nn}	i	$\omega_1^{(i)}$	$D_1^{(i)}$	$\omega_2^{(i)}$	$D_2^{(i)}$	$\omega_3^{(i)}$	$D_3^{(i)}$	$\omega_4^{(i)}$	$D_4^{(i)}$
Simple cubic	$\sqrt{2}$	6	12	1	4	$\sqrt{2}\Delta_n$	1	$2\Delta_n$				
				2	4	$\sqrt{2}\Delta_n$	2	$2\Delta_n$	4	$\sqrt{6}\Delta_n$	1	$\sqrt{8}\Delta_n$
				3	3	Δ_n	3	$\sqrt{3}\Delta_n$	3	$\sqrt{5}\Delta_n$		
Body-centered cubic	$\sqrt{2}$	8	6	1	3	Δ_{nn}	3	$\sqrt{2}\Delta_{nn}$	1	$\sqrt{3}\Delta_{nn}$		
				2	4	$\sqrt{2}\Delta_{nn}$	1	$2\Delta_{nn}$				
				3	1	$\frac{\sqrt{3}}{2}\Delta_{nn}$	1	$\frac{\sqrt{11}}{2}\Delta_{nn}$				
Face-centered cubic	$\sqrt{2}$	12	6	1	4	$\frac{\sqrt{2}}{2}\Delta_{nn}$	2	Δ_{nn}	4	$\frac{\sqrt{6}}{2}\Delta_{nn}$	1	$\sqrt{2}\Delta_{nn}$
				2	4	$\sqrt{2}\Delta_{nn}$	1	$2\Delta_{nn}$				
				3	3	$\frac{\sqrt{2}}{2}\Delta_{nn}$	3	$\frac{\sqrt{6}}{2}\Delta_{nn}$	3	$\frac{\sqrt{10}}{2}\Delta_{nn}$		

for smaller ϑ, so that the curves for ϑ_1, $\vartheta_2\cdots$ are actually separated. Otherwise, the results of Sec. II are not seriously modified.

We examine first the effect of having included in Eq. (9) transitions to a few states that would require the neutron to transfer more than its total kinetic energy to the lattice. To this end, we must compute the distribution of energy losses in the transitions admitted in Eq. (9), and decrease our computed intensity by the fraction of energetically inaccessible transitions. It will prove practicable to calculate only the lowest few moments of the energy loss distribution, and the shape of the entire curve will be inferred from these. In fact, since the entire effect is generally not very large, it will be sufficient to assume that the distribution is gaussian, with suitably fitted mean energy loss and rms energy loss.

The mean energy loss of the neutron, $\bar{\epsilon}(\mathbf{k}, \mathbf{k}^{*\prime})$ is obtained by inserting a factor $(E_{L'}-E_L)$ into the summand of Eq. (4), and dividing by the total intensity $I(\mathbf{k}, \mathbf{k}^{*\prime})$. (Note that for this purpose it is essential to sum over all states L', including the inaccessible, in both numerator and denominator.) We assume then that in the matrix element and the form factor, $\mathbf{q}$ may still be replaced with sufficient accuracy by $\mathbf{q}_0$. This yields:

$$\bar{\epsilon}(\mathbf{k}, \mathbf{k}^{*\prime})=\frac{\mathrm{Sp}\{\sum_{nn'} \exp(-i\mathbf{q}_0\cdot\mathbf{R}_{nn'})(\mathbf{S}_{n'}-\mathbf{q}^*_0\mathbf{q}^*_0\cdot\mathbf{S}_{n'})\cdot[H, (\mathbf{S}_n-\mathbf{q}^*_0\mathbf{q}^*_0\cdot\mathbf{S}_n)]\exp(-H/T)\}}{\mathrm{Sp}\{\sum_{nn'} \exp(-i\mathbf{q}_0\cdot\mathbf{R}_{nn'})(\mathbf{S}_{n'}-\mathbf{q}^*_0\mathbf{q}^*_0\cdot\mathbf{S}_{n'})\cdot(\mathbf{S}_n-\mathbf{q}^*_0\mathbf{q}^*_0\cdot\mathbf{S}_n)\exp(-H/T)\}} \tag{19}$$

where $[A, B]=AB-BA$. Expanding the $\exp(-H/T)$ and using the result

$$[H, \mathbf{S}_n]=-2Ji\sum_{\substack{\text{nbrs}\\ n' \text{ of } n}}\mathbf{S}_{n'}\times\mathbf{S}_n-2Ki\sum_{\substack{n \text{ nbrs}\\ n' \text{ of } n}}\mathbf{S}_{n'}\times\mathbf{S}_n \tag{20}$$

we find that $\bar{\epsilon}$ approaches zero at high temperatures. The lowest nonvanishing term in the high temperature expansion is (after performing the microcrystalline averaging)

$$\bar{\epsilon}(k, \vartheta)=+4S/(3T)\left\{J^2z_n\left(1-\frac{\sin q_0\Delta_n}{q_0\Delta_n}\right)+K^2z_{nn}\left(1-\frac{\sin q_0\Delta_{nn}}{q_0\Delta_{nn}}\right)\right\} \tag{21}$$

indicating that the neutron tends to lose rather than gain energy at the lower temperatures. To this order, the interactions contribute additively to (21).*

To obtain the mean square neutron energy loss $\langle\epsilon^2(\mathbf{k}, \mathbf{k}^{*\prime})\rangle_{Av}$, one proceeds identically, inserting, however, a factor $(E_{L'}-E_L)^2$ rather than $(E_{L'}-E_L)$ in Eq. (4). One finds for $\langle\epsilon^2\rangle_{Av}$ an equation identical to (19), except that $[H, (\mathbf{S}_n-\mathbf{q}^*_0\mathbf{q}^*_0\cdot\mathbf{S}_n)]$ is replaced by

$$[H, [H, (\mathbf{S}_n-\mathbf{q}^*_0\mathbf{q}^*_0\cdot\mathbf{S}_n)]].$$

The lowest term in the high temperature expansion is then found to be

$$\langle\epsilon^2(k, \vartheta)\rangle_{Av}=\frac{8\bar{S}}{3}\left\{J^2z_n\left(1-\frac{\sin q_0\Delta_n}{q_0\Delta_n}\right)+K^2z_{nn}\left(1-\frac{\sin q_0\Delta_{nn}}{q_0\Delta_{nn}}\right)\right\}. \tag{22}$$

This is temperature-independent, the interactions again contributing additively, and reduces for large $q_0\Delta_n$ and $K=0$ to an analogous result obtained by Van Vleck.[5]

* Including inaccessible states in the sum limits the use of (21) to neutrons of kinetic energy large compared to T. In general, (21) gives an upper limit to the magnitude of the neutron mean energy loss.

[5] J. H. Van Vleck, Phys. Rev. 55, 924 (1939), Eq. (7). Note in this connection that if it is desired to express the results in terms of magnetic susceptibility data [as in Eqs. (9) (10) of the reference], the expression $\Theta=\frac{2}{3}S(Jz_n+Kz_{nn})$ should be used for the constant Θ in the susceptibility law $\chi=C(T+\Theta)^{-1}$. Comparing (18) and (15) shows that rapid convergence of (11) depends on the smallness of Θ/T. This must be remembered in applications to substances such as MnO for which Θ is much larger than the Curie temperature.

The probability that a neutron loses energy between ϵ and $\epsilon+d\epsilon$ in the scattering process is then taken to be

$$P(\epsilon)d\epsilon=(2\pi\langle\epsilon^2\rangle_{Av})^{-\frac{1}{2}}\exp\{-(\epsilon-\bar{\epsilon})^2/2\langle\epsilon^2\rangle_{Av}\} \quad (23)$$

so that since transitions for which $\epsilon>k^2/2M$ are prohibited, the previously determined intensity must be multiplied by the factor

$$\gamma(k,\vartheta)=1-\int_{k^2/2M}^{\infty}P(\epsilon)d\epsilon$$
$$=\tfrac{1}{2}[1+\Phi((k^2-2M\bar{\epsilon})/(8M^2\langle\epsilon^2\rangle_{Av})^{\frac{1}{2}})] \quad (24)$$

where Φ is the error function.[6] Note that $\gamma(k,\vartheta)$ depends on k and ϑ, not merely on q_0, so that the intensity curves for 2 different values of ϑ and varying k, will be separated. Since $k^2/2M=(8M\sin^2\frac{1}{2}\vartheta)^{-1}q_0^2$, it is seen from (24) that γ is larger for larger ϑ ($\bar{\epsilon}$ and $\langle\epsilon^2\rangle_{Av}$ depend only on q_0). $\gamma(k,\vartheta)$ is slightly greater than $\frac{1}{2}$ at $q_0=0$, rises fairly rapidly, and is rather close to unity in the region of antiferromagnetic coherent peak.

The second effect we consider is that of having replaced $\mathbf{q}$ by $\mathbf{q}_0$ in the form-factor in Eq. (4). Since the values of ϑ of interest are not too large (below the angle of the first Debye-Scherrer ring), q will be larger than q_0 for most transitions, whether the neutron gains or loses energy. Since the form-factor decreases monotonically with q, we exaggerate the intensity by replacing q by q_0, the exaggeration being worse, for given q_0, for larger ϑ.

To correct for this effect, we note that in the region of interest the form factor can be expressed sufficiently accurately as

$$F(q)\approx 1-\alpha q^2. \quad (25)$$

Furthermore, if the energy change is not too large compared to the initial neutron energy, we have using Eq. (7)

$$q^2=k^2+k'^2-2kk'\cos\vartheta\approx q_0^2+4M(E_L-E_{L'})\sin^2\tfrac{1}{2}\vartheta$$
$$+(1/k^2)M^2(E_L-E_{L'})^2\cos\vartheta. \quad (26)$$

Inserting (26) and (25) into (4), replacing $\mathbf{q}$ by $\mathbf{q}_0$ elsewhere in (4), and neglecting the effect of the energetically inaccessible states, $I(k,\vartheta)$ takes the form

$$I(k,\vartheta)=I_0(q_0)+T^{-1}I_1(q_0)+T^{-2}I_2(q_0)+\cdots$$
$$+\delta I_{FF}(k,\vartheta) \quad (27)$$

where I_0, I_1, and I_2 are given in (13), (15), and (18).

[6] Notation of Magnus and Oberhettinger, *Special Functions* (Chelsea Publishing Company, New York, 1949), p. 96.

For δI_{FF} we obtain, because of the factors $(E_L-E_{L'})$ and $(E_L-E_{L'})^2$ in (26), expressions much like the numerator of (19), etc. These may be evaluated by expansion of $\exp(-H/T)$ and give to lowest order the temperature-independent term

$$\delta I_{FF}(k,\vartheta)=-(e^2\mu_N/m)^2(\tfrac{3}{4}NS)((32/3)\alpha S M^2\sin^2\tfrac{1}{2}\vartheta\cos\vartheta)$$
$$\cdot(J^2z_n\Delta_n^2R(q_0\Delta_n)+K^2z_{nn}\Delta_{nn}^2R(q_0\Delta_{nn})) \quad (28)$$

where $R(x)=x^{-2}(1-x^{-1}\sin x)$ is a monotonically decreasing function of x, which is $\frac{1}{6}$ at $x=0$ and is again not very large in the region of interest.

Lastly we examine the effect of having replaced $\mathbf{q}$ by $\mathbf{q}_0$ in $\exp(-i\mathbf{q}\cdot\mathbf{R}_n)$ in Eq. (4). To this end we put

$$\exp(-i\mathbf{q}\cdot\mathbf{R}_n)\approx\exp(-i\mathbf{q}_0\cdot\mathbf{R}_n)(1-i\delta\mathbf{q}\cdot\mathbf{R}_n-\tfrac{1}{2}(\delta\mathbf{q}\cdot\mathbf{R}_n)^2)$$

where using (7)

$$\delta\mathbf{q}\equiv\mathbf{q}-\mathbf{q}_0=(k'-k)\mathbf{k}^{*\prime}\approx(Mk^{-1}(E_L-E_{L'})$$
$$-M^2k^{-3}(E_L-E_{L'})^2). \quad (29)$$

This results, after a somewhat tedious microcrystalline averaging, using methods similar to these used in the previous two calculations, in the addition to Eq. (27) of a term

$$\delta I_{exp}(k,\vartheta)=-(e^2\mu_N/m)^2\cdot 8F(q_0)\cdot(1/9)S^2N\cdot k^{-2}M^2$$
$$\cdot\{J^2z_n\Delta_n^2G(q_0\Delta_n)+K^2z_{nn}\Delta_{nn}^2G(q_0\Delta_{nn})\}, \quad (30)$$

where $G(x)=x^{-1}d/dx\,(x^{-1}\sin x)$.

Equation (3) is the first term in a high temperature expansion, and in its evaluation, $\mathbf{q}$ was replaced by $\mathbf{q}_0$ except in the exponential, and again the loss of energetically inaccessible transitions was neglected. Equation (30) is not reliable for very small q_0, since (29) is inaccurate there, but the effect is quite negligible in this region, and is in fact nowhere very large.

To recapitulate, the intensity pattern computed in Sec. II must be corrected by the term δI_{FF} [Eq. (28)] as in Eq. (27), and to this must be added the term δI_{exp} [Eq. (30)]. Finally, the resulting expression must be multiplied by the factor γ [Eq. (24)] to correct for the inclusion of energetically inaccessible transitions. These corrections may be observed directly experimentally as a separation in the $I(k,\vartheta)$ *vs* q_0 curves for 2 different ϑ and varying k, and may be employed as a further check on the values of J and K deduced from the strength and location of the antiferromagnetic coherent peak.

The author would like to thank Professor L. J. Rainwater and Dr. P. Bendt for stimulating this research, and for many useful discussions.

On the Formalism of Thermodynamic Fluctuation Theory*

RICHARD F. GREENE† AND HERBERT B. CALLEN
Department of Physics, University of Pennsylvania, Philadelphia, Pennsylvania
(Received March 16, 1951)

From the statistical mechanical occupation probability of microstates Einstein has inferred a distribution function for the macroscopic states of a canonical ensemble. The conventional theory of thermodynamic fluctuations proceeds by making certain series expansions in the Einstein function and by dropping all cubic and higher order terms. In this paper we establish that: (*a*) The correlation moments for the extensive thermodynamic parameter fluctuations may be computed directly from the distribution function for the microstates, without introducing an intermediate macroscopic distribution function. (*b*) These same moments can be evaluated from the Einstein function without making series expansions or invoking approximations. (*c*) All moments computed by methods (*a*) or (*b*) agree exactly. (This may be taken as an alternative derivation of the Einstein function.) (*d*) The second moments computed by the conventional method are correct, but all higher moments are incorrect.

I. INTRODUCTION

STATISTICAL mechanics predicts both the average values of the thermodynamic variables of a system in equilibrium and the characteristics of the fluctuations of these variables about their average values.[1] In this paper we discuss and, to some degree, extend the theory of the fluctuations of the extensive thermodynamic parameters.[2] In particular we investigate the Einstein method[3] which, by introducing macroscopic concepts at the fundamental level of the distribution function, affords great insight into macroscopic fluctuation phenomena.

The general subject of fluctuations is of interest for a number of reasons. Recent developments in cryogenics have led to the increasing application of thermodynamics at low temperatures. Problems of thermodynamic stability, of critical points,[4] and of phase transitions[5] have also received extensive recent attention. In each of these cases the fluctuations play a fundamental role, as they do in all "marginal" applications of thermodynamics. Finally, in a recent paper[6] by Welton and one of us, it has been conjectured that a logical approach to a theory of linear irreversible processes lies through the analysis of equilibrium fluctuations, and it is in connection with this program that the present investigation of fluctuation theory is undertaken.

II. THE DISTRIBUTION FUNCTION FOR MICROSTATES

In order to introduce a convenient notation we briefly restate the results of statistical mechanics in giving the occupation probabilities of the microstates in a canonical ensemble.

For the set of extensive parameters $x_0, x_1, x_2, \cdots$ which determines the macroscopic state of a thermodynamic system, we adopt the convention that x_0 shall represent the internal energy, whereas $x_1, x_2, x_3, \cdots$ are parameters such as the volume, mole numbers, etc. The expectation values of these parameters in an equilibrium state will be denoted by $X_0, X_1, X_2, \cdots$.

The entropy may be considered as a single-valued first-order homogeneous function of the extensive parameters, $S(X_0, X_1, X_2, \cdots)$; the inverse function, $X_0(S, X_1, X_2, \cdots)$, being similarly single-valued, first-ordered, and homogeneous. Whereas the latter functional form is the more convenient for the conventional development of thermodynamics, we shall find the former form to be considerably more convenient in the analysis of fluctuations. Indeed much of the awkwardness of fluctuation formalisms has arisen from the habitual maintenance of the second form as fundamental.

The intensive parameters are conventionally defined by the equations,

$$T\equiv\partial X_0/\partial S, \quad P_k\equiv\partial X_0/\partial X_k; \quad k=1,2,3,\cdots. \tag{1}$$

Alternatively, we shall find it convenient to define a set of intensive parameters by the equations,

$$F_k\equiv\partial S/\partial X_k; \quad k=0,1,2,\cdots, \tag{2}$$

whence

$$F_0=1/T, \quad F_k=-P_k/T; \quad k=1,2,3,\cdots. \tag{3}$$

By Euler's theorem on homogeneous functions we have

$$X_0=TS+\textstyle\sum_1 P_kX_k \tag{4}$$

and

$$S=\textstyle\sum_0 F_kX_k. \tag{5}$$

A set of partial Legendre transforms of the energy (the so-called generalized Gibbs' functions) may be defined by the equations,

$$X_0[T, P_1, P_2, \cdots, P_r]\equiv X_0-TS-\sum_1^r P_kX_k. \tag{6}$$

* This work was supported in part by the ONR. It is taken from a Ph.D. thesis submitted to the University of Pennsylvania by one of the authors (RFG).
† John F. Frazer Fellow.
[1] R. C. Tolman, *The Principles of Statistical Mechanics* (Oxford University Press, England, 1938).
[2] A theory of fluctuations of intensive thermodynamic parameters will be given in a subsequent paper.
[3] A. Einstein, Ann. phys. **33**, 1275 (1910).
[4] M. J. Klein and L. Tisza, Phys. Rev. **76**, 1861 (1949).
[5] L. Tisza, Technical Report No. 127, Research Lab. of Electronics, M.I.T. (1949) (unpublished).
[6] H. B. Callen and T. A. Welton, Phys. Rev. **83**, 34 (1951).

The possibility of considering these transforms as functions of the parameters $T, P_1, P_2, \cdots, P_r, X_{r+1}, X_{r+2}, \cdots$, instead of parameters $S, X_1, \cdots, X_r, X_{r+1}, X_{r+2}, \cdots$, is determined by the nonvanishing of the jacobian of this transformation. This jacobian is identical with the discriminant of the quadratic forms determining the stability of the system,[5] and thus vanishes only at critical points. One thus obtains the relations,

$$\left.\begin{aligned}(\partial/\partial T)X_0[T, P_1, \cdots, P_r]&=-S,\\ (\partial/\partial P_k)X_0[T, P_1, \cdots, P_r]&=-X_k;\\ k&=1, 2, \cdots, r.\end{aligned}\right\} \quad (7)$$

A set of analogous Legendre transforms of the entropy (which we shall call the generalized Massieu[7] functions) may be defined by the equations,

$$S[F_0, F_1, \cdots, F_r]\equiv S-\sum_0^r F_kX_k. \quad (8)$$

Except at critical points the generalized Massieu functions may be considered as functions of the parameters, $F_0, F_1, \cdots, F_r, X_{r+1}, X_{r+2}, \cdots$, and satisfy the equations,

$$(\partial/\partial F_k)S[F_0, \cdots, F_r]=-X_k; \quad k=0, 1, 2, \cdots, r. \quad (9)$$

We now consider a macroscopic system and its environment in equilibrium. The system parameters $x_{r+1}, x_{r+2}, \cdots$ are assumed to be fixed:

$$x_{r+k}=X_{r+k}; \quad k=1, 2, 3, \cdots, \quad (10)$$

but we assume the interaction with the environment to be such that the parameters, $x_0, x_1, x_2, \cdots, x_r$, are able to fluctuate about their equilibrium values; i.e., we consider a system "canonical with respect to $x_0, x_1, \cdots, x_r$ and microcanonical with respect to $x_{r+1}, x_{r+2}, \cdots$."[8]

The distribution function for the occupation probability of the microstates is then

$$f_n=\exp[(X_0[T, P_1, \cdots, P_r]-x_0^n+\sum_1^r P_kx_k^n)/kT] \quad (11)$$

or

$$f_n=\exp[-(S[F_0, \cdots, F_r]+\sum_0^r F_kx_k^n)/k], \quad (12)$$

where f_n is the occupation probability for the n^{th} microstate and x_k^n is the expectation value of x_k in the n^{th} microstate.

[7] E. A. Guggenheim, *Thermodynamics* (North Holland Publishing Company, Amsterdam, 1949).

[8] Implicit in the canonical formalism is the assumption that the environment is so large that its "capacity" places no bounds upon the variation of $x_0, x_1, \cdots, x_r$. Except in the region of critical points, the fluctuations are generally sufficiently small so that the effect of finite environmental "capacity" is negligible.

III. CORRELATION MOMENTS FROM THE MICRODISTRIBUTION FUNCTION

We now show that the correlation moments of the fluctuating extensive parameters can be computed directly from the distribution function for the microstates [Eq. (12)]; i.e., if δx_k denotes the deviation of x_k from its equilibrium value: $\delta x_k\equiv(x_k-X_k)$, and if $\langle b\rangle$ denotes the expectation value, or ensemble average, of any quantity b, then a typical moment which we may wish to calculate is (taking $i, j, k\leqq r$) the third moment

$$\langle(x_i^n-X_i)(x_j^n-X_j)(x_k^n-X_k)\rangle\equiv\langle\delta x_i\delta x_j\delta x_k\rangle.$$

If ω_n is the degeneracy of the n^{th} microstate, the ensemble average can be written more explicitly as

$$\langle\delta x_i\delta x_j\delta x_K\rangle=\textstyle\sum_n \omega_nf_n(x_i^n-X_i)(x_j^n-X_j)(x_k^n-X_k). \quad (13)$$

However it follows from the form of f_n that

$$\begin{aligned}\partial f_n/\partial F_k&=-((\partial/\partial F_k)S[F_0, \cdots, F_r]+x_k^n)f_n/k\\ &=-(x_k^n-X_k)f_n/k, \quad (14)\end{aligned}$$

whence

$$\begin{aligned}&\langle\delta x_i\delta x_j\delta x_k\rangle\\ &\quad=-k\textstyle\sum_n \omega_n(\partial f_n/\partial F_i)(x_j^n-X_j)(x_k^n-X_k)\\ &\quad=-k(\partial/\partial F_i)[\textstyle\sum_n \omega_nf_n(x_j^n-X_j)(x_k^n-X_k)]\\ &\qquad+k\textstyle\sum_n \omega_nf_n[(x_j^n-X_j)(\partial/\partial F_i)(x_k^n-X_k)\\ &\qquad\qquad+(x_k^n-X_k)(\partial/\partial F_i)(x_j^n-X_j)],\end{aligned}$$

$$\begin{aligned}\langle\delta x_i\delta x_j\delta x_k\rangle&=-k(\partial/\partial F_i)\langle\delta x_j\delta x_k\rangle\\ &\quad-k\langle\delta x_k\rangle\partial X_j/\partial F_i-k\langle\delta x_k\rangle\partial X_j/\partial F_i.\end{aligned}$$

However,

$$\langle\delta x_j\rangle=0=\langle\delta x_k\rangle$$

and we obtain

$$\langle\delta x_i\delta x_j\delta x_k\rangle=-k(\partial/\partial F_i)\langle\partial x_i\delta x_j\delta_k\rangle. \quad (15)$$

The form of this equation is clearly maintained for moments of any order higher than the third, so that we have, for instance;

$$\begin{aligned}&\langle\delta x_i\delta x_j\delta x_k\delta x_l\rangle\\ &\quad=-k(\partial/\partial F_l)\langle\delta x_i\delta x_j\delta x_k\rangle-k(\partial X_i/\partial F_l)\langle\delta x_j\delta x_k\rangle\\ &\quad-k(\partial X_j/\partial F_l)\langle\delta x_i\delta x_k\rangle-k(\partial X_k/\partial F_l)\langle\delta x_i\delta x_j\rangle. \quad (16)\end{aligned}$$

The second moments must be considered separately. We have

$$\begin{aligned}\langle\delta x_i\delta x_j\rangle&=\textstyle\sum_n \omega_nf_n(x_i^n-X_i)(x_j^n-X_j)\\ &=-k\textstyle\sum_n \omega_n(x_j^n-X_j)\partial f_n/\partial F_i\\ &=-k(\partial/\partial F_i)[\textstyle\sum_n \omega_nf_n(x_j^n-X_j)]\\ &\qquad+k\textstyle\sum_n \omega_nf_n(\partial/\partial F_i)(x_j^n-X_j)\\ &=-k\partial\langle\delta x_j\rangle/\partial F_i-k(\partial X_j/\partial F_i)\textstyle\sum_n \omega_nf_n\\ &=-k\partial X_j/\partial F_i. \quad (17)\end{aligned}$$

Equations (15), (16), and (17) form a set of iteration

equations from which we immediately obtain

$$\langle \delta x_i \delta x_j \delta x_k \rangle = k^2 \partial^2 X_k / \partial F_i \partial F_j \tag{18}$$

and

$$\langle \delta x_i \delta x_j \delta x_k \delta x_l \rangle = -k^3 \partial^3 X_i / \partial F_j \partial F_k \partial F_l + k^2 (\partial X_i / \partial F_l)(\partial X_j / \partial F_k) + k^2 (\partial X_j / \partial F_l)(\partial X_i / \partial F_k) + k^2 (\partial X_k / \partial F_l)(\partial X_i / \partial F_j). \tag{19}$$

Equations (17), (18), and (19) are then the fundamental equations for the correlation moments of the thermodynamic extensive parameters. It is, of course, clear that the indices appearing on the right sides of these equations may be freely permuted. It should also be noted that in performing the differentiations indicated, the fundamental set of independent parameters is to be considered to be $F_0, \cdots, F_r, X_{r+1}, X_{r+2}, \cdots$.

IV. THE MACROSCOPIC DISTRIBUTION FUNCTION

We shall now briefly review the logic whereby the distribution for the microstates may be transformed into a distribution function for macroscopic states.[8] It follows immediately from Eq. (12) that the probability $W dx_0 \cdots dx_r$ of finding a system, canonical with respect to $x_0, x_1, \cdots, x_r$ with parameters instantaneously in the ranges $dx_0, dx_1, \cdots, dx_r$ is

$$W dx_0 \cdots dx_r = \Omega dx_0 \cdots dx_r \times \exp(-(S[F_0, \cdots, F_r] + \sum_0^r F_k x_k)/k) \tag{20}$$

where $\Omega dx_0 \cdots dx_r$ is the total number of microstates, each state being weighted with its degeneracy, in the range $dx_0, dx_1, \cdots, dx_r$.

We now let Ω_0 denote the value of Ω corresponding to unit density of states in the space of $x_0, x_1, \cdots, x_r$ and recall that the entropy in a *microcanonical* ensemble having parameters in the range $dx_0, dx_1, \cdots, dx_r$ is defined[9] as

$$s \equiv k \ln(\Omega/\Omega_0) \tag{21}$$

whence

$$W = \Omega_0 \exp[-(S[F_0, \cdots, F_r] - s + \sum_0^r F_k x_k)/k] \tag{22}$$

or

$$W = \Omega_0 \exp[-\{S - s + \sum_0^r F_k (x_k - X_k)\}/k]. \tag{23}$$

The essential point of the argument is to now note that although S is the entropy of a *canonical* ensemble with parameters $X_0, X_1, \cdots, X_r$ and s is the entropy of a *microcanonical* ensemble with parameters $x_0, x_1, \cdots, x_r$, nevertheless s is the same function of its parameters as S is of its parameters. This fact is a fundamental theorem of statistical mechanics, rooted in the enormously high dimensionality of the phase spaces (speaking classically) of thermodynamic systems, and responsible for the fact that there is a single general thermodynamics, rather than a "microcanonical thermodynamics" and a separate "canonical thermodynamics." Thus we may now simply say that s is the entropy of a system in equilibrium, with parameters $x_0, x_1, \cdots, x_r$.

To recapitulate, the probability of finding a system with deviations from equilibrium between $\delta x_0 = (x_0 - X_0)$ and $\delta x_0 + d\delta x_0 = [(x_0 + dx_0) - X_0]$, and between $\delta x_1 = (x_1 - X_1)$ and $\delta x_1 + d\delta x_1 = [(x_1 + dx_1) - X_1]$, and

. . . . . ,

between $\delta x_r = (x_r - X_r)$ and $\delta x_r + d\delta x_r = [(x_r + dx_r) - X_r]$ is

$$W dx_0 \cdots dx_r = \Omega_0 dx_0 \cdots dx_r \times \exp[-(S - s + \sum_0^r F_k \delta x_k)/k], \tag{24}$$

where S and s are the entropies of systems in equilibrium with parameters $X_0, X_1, \cdots, X_r$ and $x_0, x_1, \cdots, x_r$, respectively.

Although we shall adopt Eq. (24) as the fundamental macroscopic distribution function and shall show that all quantities of interest can be computed directly from it, the conventional procedure at this point has been to expand either $(s - S)$ or $(x_0 - X_0)$ in a Taylor series and to drop the cubic and higher order terms in the expansion. Of these two procedures, the expansion of $(x_0 - X_0)$ is the more awkward, but has nevertheless been the more common. We shall illustrate the more reasonable, but still unnecessary procedure of expanding $(s - S)$. We obtain

$$s - S = \sum_0^r F_k \delta x_k + \tfrac{1}{2} \sum_{j,k=0}^r S_{jk} \delta x_j \delta x_k + (1/3!) \sum_{i,j,k=0}^r S_{ijk} \delta x_i \delta x_j \delta x_k + \cdots, \tag{25}$$

where

$$S_{jK} = S_{kj} = \partial^2 S / \partial X_j \partial X_k = \partial^2 s / \partial x_j \partial x_k \tag{26}$$

(the latter evaluated at $X_0, X_1, \cdots, X_r$), and similarly for $S_{ijk}, S_{ijkl}, \cdots$. Dropping the cubic the cubic and higher order terms, we obtain

$$W \simeq A \exp(\sum_{j,k=0}^r S_{jk} \delta x_j \delta x_k / 2k), \tag{27}$$

where A is a renormalization constant. We shall refer to Eq. (25) as the "approximate macroscopic distribution function," as distinguished from the true macroscopic distribution function of Eq. (24).

V. CORRELATION MOMENTS FROM THE MACROSCOPIC DISTRIBUTION FUNCTION

We shall now show that the correlation moments of the fluctuating extensive parameters can be computed directly from the true macroscopic distribution function, (23), without invoking approximations, such as cutting off a series expansion. We shall also find that all the correlation moments so computed are identical

[8] A. I. Khinchin, *Mathematical Foundations of Statistical Mechanics* (Dover Publications, New York, 1949).

with those obtained from the microdistribution function, so that the two distribution functions are completely equivalent. The calculation of this section may therefore be considered as constituting an alternate derivation of the macroscopic distribution function.

Consider a typical third moment,

$$\langle \delta x_i \delta x_j \delta x_k \rangle = \Omega_0 \int \cdots \int dx_0 \cdots dx_i \delta x_i \delta x_j \delta x_k \times \exp[-(S - s + \sum^r F_t \delta x_t)/k]. \quad (28)$$

As in Eq. (14) we now have

$$\partial W/\partial F_k = -W(x_k - X_k)/k. \quad (29)$$

The procedure following Eq. (14) may now be repeated, with sums replaced by integrations, and one easily obtains the iteration Eqs. (15) and (16). Again the second moments must be considered separately, and we easily obtain Eqs. (17), (18), and (19). We thus see that the macroscopic distribution function may be directly used as the basis of calculation and yields the correct results in all cases.

VI. AN ALTERNATE FORM FOR THE SECOND MOMENTS

We have seen that the correct second correlation moments are given by

$$\langle \delta x_j \delta x_k \rangle = -k \partial X_j / \partial F_k$$

where, in the partial differentiation, the independent variables are to be taken as $F_0, \cdots, F_r, X_{r+1}, X_{r+2}, \cdots$. We now develop an alternative, and more familiar, form for these second moments, which is of interest in the theory of critical fluctuations,[10] and which bears on the calculation which proceeds from the approximate macroscopic distribution function. Let the inverse matrix to the $(r+1)$ by $(r+1)$ matrix S_{jk} have the elements,

$$\mathcal{S}_{jk} \equiv (\text{cofactor } S_{jk})/\|S_{jk}\| \equiv \mathcal{S}_{kj}. \quad (30)$$

Then we shall show that

$$\langle \delta x_j \delta x_k \rangle = -k \mathcal{S}_{jk}. \quad (31)$$

Consider the quantity $\partial X_j/\partial F_k$. Recalling the independent variables implied therein, and employing jacobian notation, we have

$$\frac{\partial X_j}{\partial F_k} = \frac{\partial(X_j, F_0, \cdots, F_{k-1}, F_{k+1}, \cdots, F_r)}{\partial(F_k, F_0, \cdots, F_{k-1}, F_{k+1}, \cdots, F_r)} = \frac{\partial(F_0, \cdots, F_{k-1}, X_j, F_{k+1}, \cdots, F_r)}{\partial(F_0, \cdots, F_{k-1}, F_k, F_{k+1}, \cdots, F_r)} = \frac{\partial(X_0, \cdots, X_r)}{\partial(F_0, \cdots, F_r)} \cdot \frac{\partial(F_0, \cdots, F_{k-1}, X_j, F_{k+1}, \cdots, F_r)}{\partial(X_0, \cdots, X_r)}. \quad (32)$$

[10] M. J. Klein and L. Tisza, Phys. Rev. 76, 1861 (1949).

Consider the first of the two jacobians in this equation:

$$\frac{\partial(X_0, \cdots, X_r)}{\partial(F_0, \cdots, F_r)} = \left(\frac{\partial(F_0, \cdots, F_r)}{\partial(X_0, \cdots, X_r)} \right)^{-1} = \left(\frac{\partial[(\partial S/\partial X_0), \cdots, (\partial S/\partial X_r)]}{\partial(X_0, \cdots, X_r)} \right)^{-1} = \|S_{jk}\|^{-1}. \quad (33)$$

The second jacobian in Eq. (32) is identical with the determinant of the matrix, except that the elements of column k are $\partial X_j/\partial X_0$, $\partial X_j/\partial X_1$, $\cdots$, $\partial X_j/\partial X_r$. Thus column k has a unity in position j and zeros elsewhere. Making a laplace expansion of the determinant according to the elements of column k we thus obtain

$$\frac{\partial(F_0, \cdots, F_{k-1}, X_j, F_{k+1}, \cdots, F_r)}{\partial(X_0, \cdots, X_r)} = (\text{cofactor } S_{jk}) \quad (34)$$

which, together with Eqs. (32) and (33) establishes our result, Eq. (31).

VII. APPROXIMATE CORRELATION MOMENTS

Having now obtained the correct correlation moment by direct calculation based on the true distribution functions, without recourse to approximations, we shall examine the validity of the results obtained by the conventional methods, based on the approximate macroscopic distribution function of Eq. (25).

We shall find it convenient to define

$$(\delta f_k) = k(\partial/\partial \delta x_k) \cdot \log_e W \quad (35)$$

and we shall see in a subsequent paper that this function plays a fundamental role in the theory of fluctuations of *intensive* parameters. With

$$W = A \exp\Big(\sum_{j,k=0}^{r} S_{jk} \delta x_j \delta x_k / 2k \Big)$$

we find that

$$(\delta f_k) = \sum_{j=0}^{r} S_{jk} \delta x_j \quad (36)$$

which, except at critical points, may be inverted:

$$\delta x_j = \sum_{k=0}^{r} \mathcal{S}_{kj} (\delta f_k). \quad (37)$$

Now let ϕ be a function of the form,

$$\phi \equiv (\delta x_0)^{n_0} (\delta x_1)^{n_1} \cdots (\delta x_r)^{n_r}, \quad (38)$$

where the n_j are non-negative integers, and consider the

quantity

$$\langle\phi(\delta f_m)\rangle=\int\cdots\int d(\delta x_0)\cdots d(\delta x_r)W\phi(\delta f_m)$$

$$=k\int\cdots\int d(\delta x_0)\cdots d(\delta x_r)\phi\partial W/\partial\delta x_m$$

$$=k\int\cdots\int d(\delta x_0)\cdots d(\delta x_r)$$

$$\times[\partial(\phi W)/\partial\delta x_m-W\partial\phi/\partial\delta x_m]. \quad (39)$$

Integrating the first term with respect to δx_m we see that this term vanishes because of the vanishing of ϕW at the limits of integration. Thus

$$\langle\phi(\delta f_m)\rangle=-k\langle\partial\phi/\partial\delta x_m\rangle=-kn_m\langle\phi/\delta x_m\rangle. \quad (40)$$

Using Eq. (37) we can now put

$$\langle\phi\delta x_k\rangle=\sum_{m=0}^{r}s_{mk}\langle\phi(\delta f_m)\rangle=-k\sum_{m=0}^{r}s_{mk}n_m\langle\phi/\delta x_m\rangle. \quad (41)$$

This equation furnishes us with an iteration equation for the approximate correlation moments, the moments on the right being two orders lower than the moment on the left. If we take $\phi=1$ so that $n_m=0$ for all m we obtain $\langle\delta x_k\rangle=0$ as is to be expected. If we put $\phi=\delta x_j$ we have $n_m=\delta_{mj}$ (where δ_{mj} is the Kronecker delta) and

$$\langle\delta x_j\delta x_k\rangle=-ks_{jk} \quad (42)$$

which is identical with (32). This result shows that all the second moments computed with approximate macroscopic distribution function are exact. It has heretofore been considered, on the contrary, that the dropping of the higher terms in the exponent of W must cause small but nonzero errors in the results (42) for the second moments, and that these errors might conceivably become significant near critical points.

It is also easy to see that all the third, fifth, seventh, . . . moments are given as zero in the aforementioned approximate scheme, since our iteration procedure reduces them all to a linear combination of first moments, which latter must vanish. Furthermore all the fourth, sixth, eighth, . . . moments are also incorrectly given by the approximate macroscopic distribution function: For consider a fourth moment

$$\langle\delta x_i\delta x_j\delta x_k\delta x_l\rangle=-k(s_{il}\langle\delta x_j\delta x_k\rangle+s_{jl}\langle\delta x_i\delta x_k\rangle+s_{kl}\langle\delta x_i\delta x_j\rangle)$$

$$=k^2(s_{il}s_{jk}+s_{jl}s_{ik}+s_{kl}s_{ij}). \quad (43)$$

If we compare the right-hand members of Eqs. (43) and (19) we note that each contains certain purely thermodynamic quantities and different powers of Boltzmann's constant; but transformations among purely thermodynamic quantities cannot involve Boltzmann's constant, so that Eqs. (43) and (19) cannot be identical. Therefore we see that the approximate macroscopic distribution function yields all the second moments of the thermodynamic extensive parameter fluctuations exactly, but that all the higher moments are incorrectly given.

VIII. CONCLUSION

In considering the various fluctuation moments of thermodynamic extensive parameters, we may either take a microscopic point of view and proceed directly from the distribution function for the microstates in the canonical ensemble, or we may take a completely macroscopic viewpoint and proceed from the Einstein function which gives the probability of each instantaneous macroscopic fluctuation. In both cases we may proceed entirely without approximation, and the results of both methods agree completely. The macroscopic point of view provides insight into various phenomena, such as irreversibility and the fluctuations in the intensive parameters, which is not so directly afforded by the microscopic point of view.

The Magnetostriction of Single Crystals of Iron-Silicon Alloys*

W. J. Carr, Jr.,† and R. Smoluchowski
Carnegie Institute of Technology, Pittsburgh, Pennsylvania

(Received May 9, 1951)

The spontaneous magnetostriction of iron-silicon alloys can be adequately described by two constants h_1 and h_2. For ordered alloys h_1 goes through zero at about 11 atomic percent silicon, h_2 at about 9 atomic percent silicon. In disordered alloys, in the composition range around 10 percent silicon, h_1 is somewhat larger than for the ordered alloys.

A method is given for calculating accurately the constants from the experimental data. The form effect is calculated and a semi-empirical theory is given of the influence of silicon on magnetostriction.

1. INTRODUCTION

THE magnetostriction of a ferromagnetic can be described[1] as consisting of three parts: (a) the strain produced in the crystal lattice by the spontaneous magnetization, which we shall take as that observed in a specimen having no "demagnetizing" field; (b) a part called the "form effect" which depends upon the shape of the specimen and may be calculated classically from the interaction of the demagnetizing field with the spontaneous magnetization; and (c) the "forced" or volume magnetostriction which does not interest us here since it is observed principally as a small volume strain in large applied fields.

In the following, the results of measurements of the single crystal magnetostriction constants of a series of Fe–Si alloys are presented. Since the specimens used had a small, but not entirely negligible demagnetizing factor, calculations are given for the form effect (b) so that the part (a) can be obtained. Most previous measurements have been made on similar samples having small demagnetizing factors. The alloys here studied have a cubic symmetry and so only a small number of measurements is necessary in order to specify the magnetostriction in any direction $(\beta_1, \beta_2, \beta_3)$ for a crystal magnetized to saturation in any direction $(\alpha_1, \alpha_2, \alpha_3)$ with respect to the crystal axes.

The strain in any direction in terms of the strain tensor A_{ij} is given by

$$\epsilon=\beta_i\beta_j A_{ij} \tag{1}$$

(we use the convention of summation over the repeated subscripts). With the axes selected to coincide with the unstrained cubic axes of the crystal, the components of the strain tensor, from lattice symmetry are of the form,[2]

$$\begin{aligned} A_{11}&=a_0+a_1\alpha_1^2+a_2 s+\cdots, \\ A_{12}&=\alpha_1\alpha_2[b_0+b_1\alpha_3^2+b_2 s+\cdots], \end{aligned} \tag{2}$$

where $s=\alpha_1^2\alpha_2^2+\alpha_1^2\alpha_3^2+\alpha_2^2\alpha_3^2$ and the same a's and b's are used for the other components.[3] The series (2) can be expanded to as many terms as desired, but since the higher order terms tend to make the function, plotted against angle, oscillate rapidly, which is contrary to experiment, one would expect their coefficients to be small. The a's and b's are constants to be determined by measurements which in our case consist of obtaining the strain (1) in a fixed direction while varying the α's in (2).

With precise measurements, all of the constants in (2) can be determined from observations in a single crystallographic plane, providing none of the α's vanishes for all directions in the plane [which is not true of a (100)]. A thin oblate spheroid with major axes in the (110) plane is a convenient specimen to use since the ellipsoidal shape insures uniform magnetization and if the magnetization is confined to the plane of the major axes the demagnetizing effect is small. In our study only two constants are required to describe the results: $a_1=h_1=3\lambda_{100}/2$ and $b_0=h_2=3\lambda_{111}/2$.

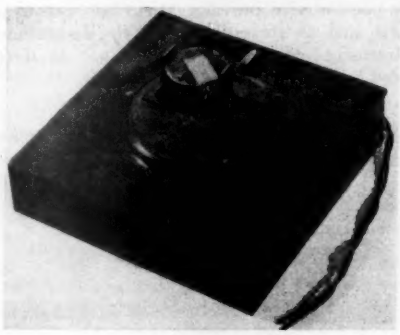

FIG. 1. Spheroid mounted on turntable.

2. PREPARATION OF SPHEROIDS AND METHODS OF MEASUREMENT

From single crystals[4] of silicon content varying from 4.9 to 14.8 at. percent (2.5 to 8 percent by weight) disks

* Taken largely from a dissertation submitted by the former author in partial fulfillment of the requirements for the degree of Doctor of Science at Carnegie Institute of Technology.

† Now at the Westinghouse Research Laboratories, East Pittsburgh, Pennsylvania.

[1] R. Becker and W. Döring, *Ferromagnetismus* (Julius Springer, Berlin, 1939).

[2] See reference 1, p. 274.

[3] Since the a_0 term does not depend upon the direction of the spontaneous magnetization, it is of no interest here.

[4] Grown by Mr. R. K. McGeary at the Westinghouse Research Laboratories, East Pittsburgh, Pennsylvania.

were cut 1 in. in diameter and 0.1-in. thick with the desired crystallographic orientation. Both (110) and (100) planes were obtained, the latter being used as a check on measurements on the former. The low percentage silicon disks were machined on a lathe into oblate ellipsoids of major and minor axes given above. Because of the brittleness of the higher silicon alloys, they had to be ground into shape. In order to prevent the growth of new crystallites during annealing, approximately 0.001 in. was etched off the surface of the specimens. They were then annealed in hydrogen five hours at 850°C and furnace cooled (50–100°C/hr) as first heat treatment. The measurements were made by means of resistance strain gauges:[5,6] One-eighth-inch gauges were cemented on both sides of the specimens and the output of the resistance bridge connected directly to a galvanometer with a five meter long light beam. With a battery voltage of 10 volts a strain sensitivity of 5×10^{-8} per mm deflection was obtained.

The specimens were mounted on a small turntable (Fig. 1),[7] which was covered with a brass cup to keep the temperature constant and the assembly was placed

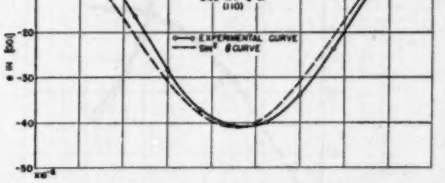

FIG. 2. Strain in the [001] direction in a (110) sample.

between the poles of an electromagnet. A field of 3300 gauss[8] was used for all the measurements. Starting with the field in the [001] direction, the crystal was rotated through various angles in the field and the change of strain thus produced in the particular direction in which the strain gauges were fastened was measured. By so doing we avoided the ambiguities of the demagnetized state which has been used as a reference in previous magnetostriction measurements. If $\gamma_1, \gamma_2, \gamma_3$ are the direction cosines of the magnetization in the reference state, the strain which we measure is, from (1)

$$e'=\beta_i\beta_j A_{ij}(\alpha_1,\alpha_2,\alpha_3)-\beta_i\beta_j A_{ij}(\gamma_1,\gamma_2,\gamma_3). \quad (3)$$

3. EVALUATION OF THE CONSTANTS

Although in principle the evaluation of the constants in (2) is quite straightforward, one must not allow small

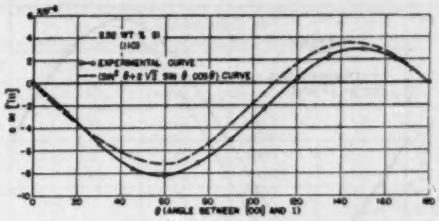

FIG. 3. Strain in the $[\bar{1}11]$ direction in a (110) sample.

errors in the measurements to produce large errors in the values for the constants. For reasons which will become apparent, measurements of the strain have been made for the (110) plane in the directions [001] and $[\bar{1}11]$. From (1) the strain for the first of these is A_{33} and for the second $\frac{1}{3}(A_{11}+A_{22}+A_{33})+\frac{2}{3}(A_{23}-A_{12}-A_{13})$. (The strain tensor is symmetric, $A_{ij}=A_{ji}$.) Substituting from (2) and subtracting the strain of the reference state as in (3) ($\gamma_1=\gamma_2=0$, $\gamma_3=1$) one obtains

$$e_{[001]}'=-a_1\sin^2\theta+\tfrac{1}{4}a_2(\sin^2 2\theta+\sin^4\theta+)\cdots, \quad (4)$$

$$e_{[\bar{1}11]}'=\tfrac{1}{3}a_2(\sin^2 2\theta+\sin^4\theta)+\cdots+\tfrac{1}{3}b_0(\sin^2\theta+\sqrt{2}\sin 2\theta)+\frac{b_1}{3}\left(\frac{\sin^2 2\theta}{4}+\frac{\sin^2\theta\sin 2\theta}{\sqrt{2}}\right)+\frac{b_2}{12}(\sin^2\theta+\sqrt{2}\sin 2\theta)(\sin^2 2\theta+\sin^4\theta)+\cdots, \quad (5)$$

where θ is the angle the magnetization makes with the [001] direction ($\alpha_2=-\alpha_1=\sin\theta/\sqrt{2}$, $\alpha_3=\cos\theta$). The a's can be obtained from (4) and the b's from (5). In deciding how many terms are necessary to describe the measurements, one must examine the symmetry of the measured curves. It is also helpful to note that the slope of (5) at $\theta=0$ is given by the b_0 term.

Typical examples of curves obtained are shown in Figs. 2 and 3 (also Figs. 4 and 5 for the (100) plane). From symmetry considerations it was concluded that in none of the measurements terms other than a_1 and b_0 in (4) and (5) were important.[9] Although deviations

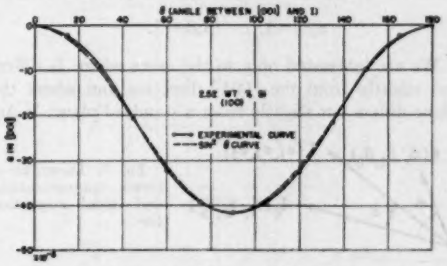

FIG. 4. Strain in the [001] direction in a (100) sample.

[5] J. E. Goldman, Phys. Rev. **72**, 529 (1947).
[6] J. E. Goldman and R. Smoluchowski, Phys. Rev. **75**, 140 (1949).
[7] The strain produced by the clamps holding the specimen in place was kept in the order of 10^{-6}.
[8] High enough to keep the direction of magnetization within one or two degrees of the field direction.
[9] Of all the curves there were two cases for which the measurements were accurate enough to indicate an additional $\sin^2 2\theta$ term,

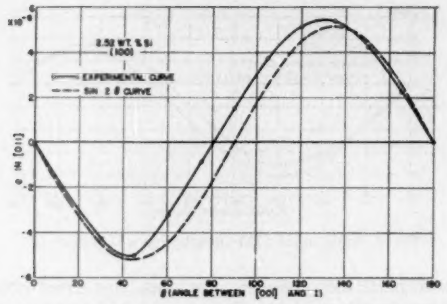

FIG. 5. Strain in the [011] direction in a (100) sample.

from these terms appear in the curves, the discrepancies do not have the symmetry of additional terms in (4) and (5). We attribute these to slight uncertainties in the crystal orientation and discuss below a method of avoiding them in evaluating the constants.

4. CORRECTIONS FOR NONIDEAL ORIENTATION

Using the established notation of Becker and Döring, we replace a_1 with h_1 and b_0 with h_2, where $\lambda_{100}=2h_1/3$ and $\lambda_{111}=2h_2/3$. Thus for these alloys (2) becomes

$$A_{ii}=a_0+h_1\alpha_i^2, \quad A_{ik}=h_2\alpha_i\alpha_k$$

and (3) can be written

$$e'=(h_1-h_2)(\beta_i^2\alpha_i^2-\beta_i^2\gamma_i^2) + h_2(\alpha_i\alpha_j\beta_i\beta_j-\gamma_i\gamma_j\beta_i\beta_j). \quad (6)$$

We wish to know the magnetostriction in a plane, Fig. 6, in which the magnetization I, and the direction of strain measurement make angles θ and φ with the initial direction of magnetization. The last term in (6) becomes $h_2[\cos^2(\varphi-\theta)-\cos^2\varphi]$ and if δ_1, δ_2, δ_3 are the direction cosines of a normal to the plane, the α's and β's in the first term can be expressed in terms of the δ's, γ's, θ and φ by the equations,

$$\begin{aligned} &\alpha_i\delta_i=0, && \beta_i\delta_i=0, \\ &\alpha_i\gamma_i=\cos\theta, && \beta_i\gamma_i=\cos\varphi, \\ &\alpha_i\alpha_i=1, && \beta_i\beta_i=1. \end{aligned} \quad (7)$$

We are interested only in the cases where I_0 differs but slightly from the [001] direction and where the plane differs but slightly from a standard plane. If $\Delta\eta_1$ and $\Delta\eta_2$ are small angles we can write

$$\gamma_1=\cos(\tfrac{1}{2}\pi-\Delta\eta_1)\simeq\Delta\eta_1, \quad \gamma_2=\cos(\tfrac{1}{2}\pi-\Delta\eta_2)\simeq\Delta\eta_2, \quad \gamma_3\simeq 1$$

and similarly the δ's for a given plane can be expressed in terms of small angles of deviation. Using these to solve for the α's and β's in (7) and substituting in (6) one obtains to *a* first approximation for a plane near the (100)

$$e'=-h_1\sin^2\theta\cos2\varphi+\tfrac{1}{2}h_2\sin2\theta\sin2\varphi + \Delta\eta_2(h_1-h_2)(2\sin^2\theta\sin2\varphi-\sin2\theta\cos2\varphi). \quad (8)$$

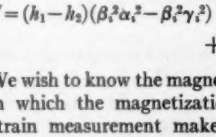

FIG. 6. Directions of strain, magnetization, and initial magnetization.

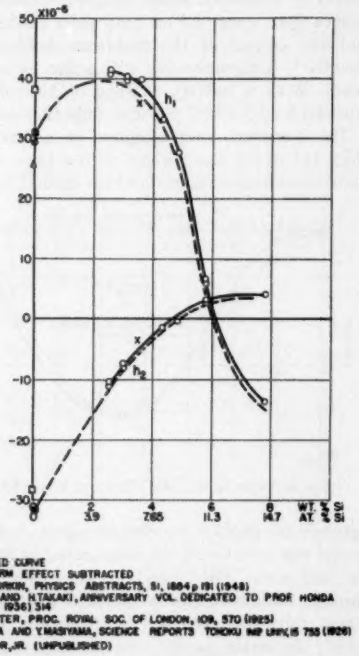
X10⁻⁶
h1
h2
WT. % Si
AT. % Si
O—O MEASURED CURVE
– – – WITH FORM EFFECT SUBTRACTED
X — D.A. SHTURKIN, PHYSICS ABSTRACTS, 51, (864 p 191 (1948)
□ — S.KAYA AND N.TAKAKI, ANNIVERSARY VOL. DEDICATED TO PROF. HONDA (SENDAI 1936) 314
● — W.WEBSTER, PROC. ROYAL SOC. OF LONDON, 109, 570 (1925)
Δ — K. HONDA AND Y.MASIYAMA, SCIENCE REPORTS TOHOKU IMP. UNIV. (1) 755 (1926)
■ — W.J. CARR, JR. (UNPUBLISHED)

FIG. 7. Magnetrostriction of annealed iron-silicon alloys.

All the angles except $\Delta\eta_2$ appear in the second order and have been dropped. Even though $\Delta\eta_2$ is only of the order of 1 or 2 degrees, this term will tend to obscure one of the first two in (8) if one of the constants is large compared with the other.

In addition, because of our method of strain measurement, there is a small uncertainty $\Delta\varphi$ in the angle in which the strain gauges lie. Substituting $\varphi=\varphi_0+\Delta\varphi$ in (8) one obtains

$$e'=-h_1\sin^2\theta\cos2\varphi_0+\tfrac{1}{2}h_2\sin2\theta\sin2\varphi_0 + \Delta\eta_2(h_1-h_2)(2\sin^2\theta\sin2\varphi_0-\sin2\theta\cos2\varphi_0) + \Delta\varphi(2h_1\sin^2\theta\sin2\varphi_0+h_2\sin2\theta\cos2\varphi_0). \quad (9)$$

which could not arise from any known error in the measurement. The magnitude of this term in the curves was 5×10^{-7} and we are justified in neglecting it here. It would be important, however, in a determination of the volume change.

The terms in $\Delta\eta_2$ and $\Delta\varphi$ have a symmetry which can account for most of the discrepancy in Fig. 5. To obtain the necessary constants we made measurements for $\varphi_0=0$ and $\varphi_0=45°$. In the first case (Fig. 4) the value of ϵ' at $\theta=90°$ is $-h_1$; in the second case (Fig. 5) $\epsilon'_{\theta=45°}-\epsilon'_{\theta=135°}=h_2$.

In the (110) plane a similar analysis shows that for $\varphi_0=0$ (Fig. 2)

$$\epsilon'=-h_1\sin^2\theta+(1/\sqrt{2})(\Delta\eta_1-\Delta\eta_2)(h_1-h_2)\sin 2\theta + \Delta\varphi h_2\sin 2\theta. \quad (10)$$

Whence, at $\theta=90°$ we have $\epsilon'=-h_1$. In order to obtain h_2 in this plane, it is best to let φ_0 be the angle between the $[\bar{1}11]$ and $[001]$ directions, whereupon (Fig. 3)

$$\epsilon'_{\theta=45°}-\epsilon'_{\theta=135°}=\tfrac{3}{2}h_2(\sqrt{2}-\Delta\varphi)\simeq\tfrac{3}{2}\sqrt{2}h_2.$$

Thus one can evaluate the constants to the same accuracy as that in the measurement of strain, which for most of our measurements was ±3 percent. The results are given in Table I and plotted in Fig. 7.

TABLE I. Magnetostriction constants in iron-silicon alloys (annealed condition).

At. percent Si	Wt. percent Si	I	Plane	Measured $h_1\times10^6$	Measured $h_2\times10^6$	With form effect subtracted $h_{1_0}\times10^6$	With form effect subtracted $h_{2_0}\times10^6$
4.92	2.52	1640	(100)	41.5	−10.4	39.7	−11.2
4.92	2.52		(110)	40.7	−10.7	35.9	−11.5
5.88	3.03	1620	(100)	39.9	−8.0	38.1	−8.7
5.88	3.03		(110)	40.2	−7.28	38.4	−8.0
6.93	3.59	1590	(100)	40.0		38.3	
8.28	4.32	1560	(100)	33.2	−1.4	31.5	−2.1
9.22	4.83	1535	(110)	27.7	−0.43	26.1	−1.1
10.95	5.80	1490	(100)	6.45	3.03	4.9	2.4
10.95	5.80		(110)	6.7	2.93	5.2	2.3
14.82	7.79	1370	(110)	−13.6	4.28	−14.9	3.7

5. EFFECT OF ORDER AND DISORDER

It has been shown by Goldman and Smoluchowski[10] that ordering in an alloy can appreciably change the magnetostriction. Since, over a certain range of composition, the Fe–Si system is known to order one would expect to measure different constants for annealed and quenched crystals. The values given in Table I and plotted in Fig. 7 were obtained on annealed material, furnace cooled (50–100°C/hr) and presumably ordered for those compositions for which ordering can take place.

Above 12.5 atomic percent silicon ordering definitely has been observed by a number of investigators and the superstructure is of the Fe_3Si type.[11–13] Below 12.5 percent no superlattice lines have been detected in the x-ray photographs, but there are reasons to believe that ordering, at least of short-range character, commences at about 9 or 10 atomic percent since there is a discontinuity in the curve of lattice constant *versus* percent silicon near this composition.[12,13] Also a discontinuity appears at 9.86 atomic percent silicon in a plot of the magnetic anisotropy constant against percent silicon.[14]

TABLE II. Magnetrostriction constants in iron-silicon alloys (quenched in oil).

At. percent Si	Wt. percent Si	Plane	Quenching temperature	$h_1\times10^6$	$h_2\times10^6$
4.92	2.52	(110)	900°C	39.4	−10.7
8.28	4.32	(100)	900°C	34.0	−1.0
10.95	5.80	(110)	900°C	12.0	3.3
10.95	5.80	(100)	700°C	13.0	4.9
14.44	7.79	(110)	900°C	No significant change from annealed material.	

Measurements of the magnetostriction for specimens quenched in oil, shown in Table II and plotted in Fig. 8, add credence to the belief that ordering begins to take place in the region of 9 to 10 atomic percent. Due to the brittleness of the specimens it was not possible to subject these crystals to a severe quench. The indicated heat treatment often produced small cracks in the specimens and made magnetostriction measurements difficult. For this reason the foregoing measurements are not so accurate as values for the annealed specimens. Comparing the values with those of Table I, one sees that the only significant change that has occurred is the value of h_1 for the 10.95 at. percent (5.8 wt. percent) alloy. The constant h_1 for the quenched alloy is nearly double that for the annealed; h_2 has changed but little and within the accuracy of the measurements no change

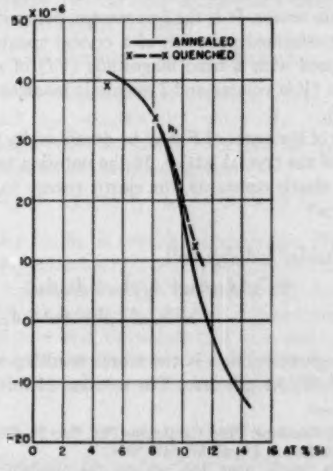

FIG. 8. Influence of heat treatment on magnetostriction.

[10] J. E. Goldman and R. Smoluchowski, Phys. Rev. **75**, 140 (1949).
[11] G. Phragmen, J. Iron Steel Inst. **114**, 397 (1926).
[12] E. R. Jette and E. S. Greiner, Trans. Am. Inst. Mining Met. Engrs. **105**, 259 (1933).
[13] Farquhar, Lipson, and Weill, J. Iron Steel Inst. **152**, 457 (1945).
[14] L. P. Tarasov, Phys. Rev. **56**, 1231 (1939).

has occurred in the constants for specimens with smaller amounts of silicon. Also no change appears in the values for the 14.44 at. percent (7.79 wt. percent) alloy. The latter in the annealed condition should possess some order. Since no difference large enough to measure was detected in its magnetostriction after an oil quench from 900°C, one may suppose either that the magnetostriction of this alloy is insensitive to order or that the disordered condition, if any, cannot be undercooled by the employed rate of quench. The critical temperature, from magnetostriction measurements, for the 10.95 at. percent (5.8 wt. percent) alloy was found to be somewhere in the neighborhood at 450°C. Near the composition where ordering first appears, however, the critical temperature theoretically should rise rapidly as the alloying element is increased.[15]

6. CALCULATION OF THE FORM EFFECT

The effect of the shape of the specimen on its magnetostriction has been calculated by Becker[16] for the case of a prolate spheroid of isotropic material. We must calculate this for a single crystal oblate spheroid and will use a somewhat different method.

It is desired first to write the magnetostriction strains in terms of an energy function (the magnetostriction part of the free energy) and the Hooke constants of the material. A way of doing this is given by Becker and Döring, where the free energy is expressed as $F=F_0+F_1+F_2$, with the subscripts denoting that the three terms on the right are respectively independent of strain, linear in strain, and quadratic. The expression F is to be regarded, at constant temperature, as a function of the direction of magnetization and the components of the strain tensor. It is the free energy, per unit volume of the unstrained material, of a crystal spontaneously magnetized with a fixed magnitude (VI) of magnetic moment (V is volume and I magnetic moment per unit volume).

Each of the parts of F may be described by the symmetry of the crystal lattice. In the notation to be used for the elastic constants, the elastic energy for a cubic crystal is[17]

$$F_2=\tfrac{1}{2}C_{11}(A_{11}^2+A_{22}^2+A_{33}^2)+C_{12}(A_{11}A_{22}+A_{11}A_{33}+A_{22}A_{33})+2C_{44}(A_{12}^2+A_{13}^2+A_{23}^2). \quad (11)$$

The magnetostriction is the strain resulting when the stress,[18] $\partial F/\partial A_{ij}$, is zero. The solution of this yields

$$A_{11}=\frac{C_{12}}{(C_{11}+2C_{12})(C_{11}-C_{12})}\left(\frac{\partial F_1}{\partial A_{22}}+\frac{\partial F_1}{\partial A_{33}}\right)-\frac{(C_{11}+C_{12})}{(C_{11}+2C_{12})(C_{11}-C_{12})}\frac{\partial F_1}{\partial A_{11}}, \quad (12)$$

$$A_{12}=-\frac{1}{4C_{44}}\frac{\partial F_1}{\partial A_{12}}, \quad \text{etc.}$$

To obtain the form effect, the part of F_1 which depends upon the dimensions of the ellipsoid is substituted into (12). The ratios of the axes of the ellipsoid enter into the energy expression through the interaction of the demagnetizing field with the spontaneous magnetization. Most of the calculation required for this has been performed by Powell.[19] In the Appendix we show that for an oblate spheroid which is magnetized in the equatorial plane ($\alpha_1'=0$),

$$\Delta F_{1f.e.}=\tfrac{1}{2}\mu I^2[A_{22}'\alpha_2'^2-A_{33}'(\alpha_3'^2-1)]+\tfrac{2}{3}\mu I^2 A_{23}'\alpha_2'\alpha_3' \quad (13)$$

where $\Delta F_{1f.e.}$ is the change in F_1, contributed by the demagnetizing field, when the magnetization is rotated out of the z (subscript 3) axis and the primes indicate that the quantities are referred to the principal axes of the spheroid. The value of μ depends upon the dimensional ratio of the spheroid and is given in the Appendix.

A general expression for F_1 for crystals of cubic symmetry is given by Becker and Döring. For ΔF_1, defined by $F_1(\alpha_1, \alpha_2, \alpha_3)-F_1(0, 0, 1)$, only the following terms are important in the Fe–Si alloys:

$$\Delta F_1=k[A_{11}\alpha_1^2+A_{22}\alpha_2^2+A_{33}(\alpha_3^2-1)]+m(A_{12}\alpha_1\alpha_2+A_{13}\alpha_1\alpha_3+A_{23}\alpha_2\alpha_3) \quad (14)$$

which substituted in (12) give

$$A_{ii}=-k\alpha_i^2/(C_{11}-C_{12}),\ A_{ik}=-m\alpha_i\alpha_k/4C_{44},\ k\neq i \quad (15)$$

where k and m are constants of the material. From (6) one identifies the constant h_1 with $-k/(C_{11}-C_{12})$ and h_2 with $-m/4C_{44}$.

We must now examine more closely the derivation of (14). In the expression of Becker and Döring the only consideration was the cubic symmetry of the crystal lattice; but as we know, the shape of the boundary of the crystal must also play a role. The crystal cannot be cubic in shape since an ellipsoidal boundary is required for uniform field (which is tacitly assumed by taking all the variables of state to be uniform throughout the volume). For the boundaries of interest, only the sphere has all the symmetry elements of a cube and so we conclude that Becker and Döring's expression and (14) actually apply only to a spherical crystal with a cubic lattice. The difference between the magnetostriction of a sphere and that of an arbitrary

[15] C. E. Easthope, Proc. Cambridge Phil. Soc. 33, 502 (1937).
[16] R. Becker, Z. Physik 87, 547 (1934).
[17] As is usually done, this neglects the possibility that the Hooke coefficients (measured with VI fixed) depend upon the direction of magnetization.
[18] Appendix, Eq. (2).
[19] F. C. Powell, Proc. Cambridge Phil. Soc. 27, 561 (1931).

ellipsoid is determined by the difference between the contribution to F_1 of the "demagnetizing" energy for the two cases (Appendix).

We shall discuss only the special case where the magnetization is confined to a single plane, the equatorial plane of an oblate spheroid, and shall add the further restriction that it contain the [001] crystallographic direction, which shall be the z axis of the spheroid. For such a plane, which makes an angle ψ with the (100) plane, $\alpha_1=-\alpha_2'\sin\psi$, $\alpha_2=\alpha_2'\cos\psi$, and $\alpha_3=\alpha_3'$ where the primed and unprimed quantities refer, respectively, to the direction cosines of magnetization referred to the principal axes of the spheroid and the cubic axes of the crystal. The transformation for the strain components can be obtained easily from the requirement that the strain $\epsilon=A_{ij}\beta_i\beta_j=A_{ij}'\beta_i'\beta_j'$ for any direction given by the β's and β''s. In this manner, (13) becomes

$$\Delta F_{1f.e.}=\tfrac{1}{3}\mu I^2[A_{11}\alpha_1^2+A_{22}\alpha_2^2+A_{33}(\alpha_3^2-1)]$$
$$+\tfrac{2}{3}\mu I^2(A_{12}\alpha_1\alpha_2+A_{13}\alpha_1\alpha_3+A_{23}\alpha_2\alpha_3), \quad (16)$$

which for this case has the same form as (14) and justifies the use of expressions for strain such as (2) in Part. I. We can now write

$$h_{1f.e.}=-\tfrac{1}{3}\mu I^2/(C_{11}-C_{12}), \quad h_{2f.e.}=-\tfrac{1}{6}\mu I^2/C_{44} \quad (17)$$

and for a given spheroid

$$h_1=-k/(C_{11}-C_{12})-h_{1f.e.\text{ sphere}}+h_{1f.e.\text{ spheroid}},$$
$$h_2=-m/4C_{44}-h_{2f.e.\text{ sphere}}+h_{2f.e.\text{ spheroid}}. \quad (18)$$

The first two terms on the right in each equation shall be designated h_{1_0} and h_{2_0}, respectively. They are the values of the constants for an infinite sheet and are given in Table I by subtracting the calculated form effect of the spheroid from the measured constants.

7. MAGNETIC DIPOLE INTERACTION

The task of a magnetostriction theory is to calculate the constants k and m (and additional ones for higher order terms in materials such as nickel) in the energy expression for a spherical crystal. As of the present no such satisfactory theory is known. The first attempts at a magnetostriction theory made by Akulov[20] and Becker[21] were based upon magnetic interactions between the atomic dipoles. The dipoles were assumed to be situated at lattice points and the energy, obtained as a function of strain, is then of the form (14). The constant calculated on that basis are too small but in some cases not negligible. The two authors obtained different results and the discrepancy as shown by Powell[19] is due to the fact that Akulov's calculations would apply for an infinite sheet while Becker's were for a sphere. The theory thus, indeed, leads to what we have described in terms of "form effect." Since the effect of shape is well established without resort to atomic interactions, we shall discuss the simpler type of calculation of Becker.

If the part of the free energy F_1, can be obtained by a summation over all pairs of atoms of an expression E_{MN} for the interaction of the M^{th} and N^{th} atoms in their respective lattice positions then

$$F_1=\frac{1}{2V_0}\sum_{M,N}\frac{\partial E_{MN}}{\partial X_k}\Delta X_k=\frac{1}{2V_0}\sum_{M,N}\frac{\partial E_{MN}}{\partial X_k}A_{kl}X_l. \quad (19)$$

where V_0 is the volume of the crystal and X_1, X_2, X_3 (instead of X, Y, Z) are used for the coordinates of the N^{th} lattice point with the M^{th} at the origin. As usual, the repeated subscripts are to be summed over 1, 2, 3 and the summation sign indicates a sum over all atoms in the crystal.

For the present problem, E_{MN} is the magnetic energy of a pair of parallel dipoles. In the case of the Fe–Si alloys, we assume the silicon atoms have no magnetic moment while the dipole moment of the iron atoms is unaffected by the presence of the silicon. By this assumption, if f is the atomic fraction of silicon atoms, the ratio of the intensity of magnetization, I, of the alloy, to that for pure iron, I_0, is $I/I_0=1-f$, an expression which is approximately correct for alloys of low silicon. Thus for the alloy we use the expression E_{MN} for two iron atoms and multiply it by the probability of iron atoms being at both the M^{th} and N^{th} positions. For a random alloy this is simply $(I/I_0)^2$ so F_1 and the constants h_1 and h_2 for the alloy are the same as those for pure iron multiplied by $(I/I_0)^2$.

A comparison of (14) with Eq. (4) of Becker's paper shows that this theory gives for iron $k=-6SI^2$ and $m=8SI^2$ where $S=0.36$ from McKeehan's work.[22] For a spherical iron crystal we have

$$h_1=6.65\times10^{-6}, \quad h_2=-1.9\times10^{-6}. \quad (20)$$

From (17) the form effect of a sphere in $h_{1f.e.}=7.75\times10^{-6}$ and $h_{2f.e.}=3.34\times10^{-6}$ when the value of $-12\pi/5$ appropriate for a sphere is used for μ. Thus for an infinite sheet the theory gives

$$h_{1_0}=-1.1\times10^{-6}, \quad h_{2_0}=-5.2\times10^{-6}. \quad (21)$$

The value for h_{1_0} is considered negligible. We multiply the h_{2_0} value by $(I/I_0)^2$ and subtract it from the measured constants in Fig. 9, leaving the resultant curve which remains to be explained. Considering only the case of pure iron, the values (20) of h_1 and h_2 for a spherical crystal would have to be respectively 6 and 13 times larger to give correctly the observed magnetostriction.[23]

The question arises as to whether a quantum-

[20] N. Akulov, Z. Physik **52**, 389 (1928).
[21] R. Becker, Z. Physik **62**, 253 (1930).
[22] L. W. McKeehan, Phys. Rev. **43**, 1022 (1933).
[23] Previously published results for this have a tendency to be misleading. Akulov's and Becker's figures are not correct for reasons which Powell points out. Secondly, the quantity Powell compares with experiment is essentially $h_{1_0}-h_{2_0}$.

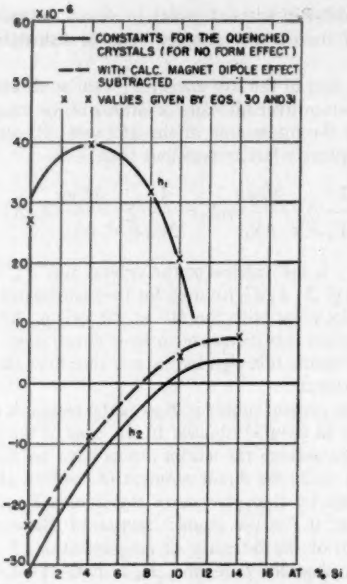
X10⁻⁶
CONSTANTS FOR THE QUENCHED CRYSTALS (FOR NO FORM EFFECT)
WITH CALC. MAGNET DIPOLE EFFECT SUBTRACTED
X X VALUES GIVEN BY EQS. 30 AND 31
h1
h2
AT % Si

FIG. 9. Comparison of experiment with semi-empirical theory.

mechanical calculation of this interaction would appreciably change the results. The assumption of point dipoles situated at the lattice points is equivalent to assuming non-overlapping spherically symmetric wave functions for the electrons responsible for the magnetism. The use of the actual wave functions would probably change the interaction between nearest neighbors and possibly next nearest neighbors, but we would not expect the result to be appreciably different. The reason for this is the following: the energy of (14) is of the form which would arise from dipole-dipole interaction, whereas the effect of a nonspherical charge distribution is to introduce quadrupole and higher order terms in the direction cosines. If the dipole terms were greatly altered by the nonspherical wave function then probably quadrupole terms also would be appreciable. Experimentally, however, none is observed in these alloys.

8. A SEMI-EMPIRICAL THEORY

If the magnetostriction energy can be expressed as resulting from an interaction between pairs of atoms, one can construct a semi-empirical description of the curves in Fig. 9 in the following manner:

Let the free energy of an iron atom with the rest of the lattice be given by

$$F_I=p_{II}'F_{II}'+p_{II}''F_{II}''+\cdots +(1-p_{II}')F_{IS}'+(1-p_{II}'')F_{IS}''+\cdots, \quad (22)$$

where $\frac{1}{2}F_{II}'$ is the energy between a pair of iron nearest neighbors, p_{II}', the probability the iron atom under consideration has a nearest neighbor which is iron, and $\frac{1}{2}F_{IS}'$ is the energy of an iron-silicon pair of nearest neighbors. The double primes are the appropriate quantities for the next nearest neighbors, etc. All of the F's are to be regarded as expressions having the form of (14).

We now write the magnetostriction energy of a silicon atom with the rest of the lattice as

$$F_S=p_{SI}'F_{IS}'+p_{SI}''F_{IS}''+\cdots, \quad (23)$$

with p_{SI}' the probability that a silicon atom has an iron nearest neighbor, etc. We have assumed that Si–Si interactions contribute nothing to this energy. The magnetostriction energy per unit volume is thus

$$F_1=\tfrac{1}{2}N_IF_I+\tfrac{1}{2}N_SF_S, \quad (24)$$

where N_I and N_S are respectively the number of iron and silicon atoms per unit volume.

We shall concern ourselves only with the case of a random alloy for which all the probabilities in (22) and (23) may be replaced by $1-f$, if f is the atomic fraction of silicon. Also $N_I=N(1-f)$ and $N_S=Nf$ where N is the total number of atoms per unit volume. Let $F_{II}=F_{II}'+F_{II}''+\cdots$ and similarly for F_{IS}. Thus (24) becomes

$$F_1=\tfrac{1}{2}N(1-f)[(1-f)F_{II}+2fF_{IS}] \quad (25)$$

and since the F's have the form of (14), m and k are expressions like (25). From (15)

$$h_1=\frac{-N(1-f)}{2(C_{11}-C_{12})}[(1-f)k_{II}+2fk_{IS}],$$
$$h_2=\frac{-N(1-f)}{8C_{44}}[(1-f)m_{II}+2fm_{IS}] \quad (26)$$

with the notation obvious.

We do not suppose the k's and m's in (26) to be independent of composition. This is for two reasons: (a) the lattice constant of these alloys changes appreciably with composition,[24,25] a condition which obviously might change the interaction, and (b) the interaction to be assigned to a pair might depend upon the environment of the pair and thus upon composition. Also the elastic constants may depend upon composition.

We assume that for small amounts of silicon the dependence on composition may be expressed by

$$\frac{k_{II}}{C_{11}-C_{12}}=\frac{k_{II_0}}{(C_{11}-C_{12})_0}(1+K_{II}f),$$
$$\frac{m_{II}}{C_{44}}=\frac{m_{II_0}}{C_{44_0}}(1+M_{II}f) \quad (27)$$

[24] E. R. Jette and E. S. Greiner, Trans. Am. Inst. Mining Met. Engrs. 105, 259 (1933).
[25] Farquhar, Lipson, and Weill, J. Iron Steel Inst. 152, 457 (1945).

with similar expressions for k_{IS} and m_{IS}. The subscript zero refers to values for nearly pure iron, while the K's and M's are new constants.

Equations (26) now become

$$h_1=\frac{-N(1-f)}{2(C_{11}-C_{12})_o}[k_{II_o}+(k_{II_o}K_{II}+2k_{IS_o}-k_{II_o})f+(2k_{IS_o}K_{IS}-k_{II_o}K_{II})f^2],$$
$$h_2=\frac{-N(1-f)}{8C_{44_o}}[m_{II_o}+(m_{II_o}M_{II}+2m_{IS_o}-m_{II})f+(2m_{IS_o}M_{IS}-m_{II_o}M_{II})f^2]. \quad (28)$$

These are suitable to describe the curves of Fig. 9 if one sets the constants equal to the following values

$$\begin{aligned} k_{II_o}&=-6\times10^{-16},\\ k_{II_o}K_{II}+2k_{IS_o}-k_{II_o}&=-138\times10^{-16},\\ 2k_{IS_o}K_{IS}-k_{II_o}K_{II}&=1450\times10^{-16},\\ m_{II_o}&=23.8\times10^{-16},\\ m_{II_o}M_{II}+2m_{IS_o}-m_{II_o}&=-423\times10^{-16},\\ 2m_{IS_o}M_{IS}-m_{II_o}M_{II}&=1340\times10^{-16} \end{aligned} \quad (29)$$

giving the equations,

$$h_1=(1-f)(27+620f-6550f^2)\times10^{-6}, \quad (30)$$
$$h_2=(1-f)(-23+410f-1300f^2)\times10^{-6}. \quad (31)$$

One cannot solve for all the constants in (29); however, the expressions,

$$m_{IS_o}(1+M_{IS})=470\times10^{-16}$$

and

$$k_{IS_o}(1+K_{IS})=653\times10^{-16}$$

can be obtained and they show that, unless M_{IS} and K_{IS} are very large compared with unity, the energy ascribed to the Fe−Si interaction is larger than that for the Fe−Fe. This all presupposes, of course, that our original assumptions were correct.

A possible explanation of this might be found in Van Vleck's[28] suggestion that the magnetostriction energy arises as a result of interactions between orbital momenta. In our case both the iron and silicon atoms would participate in this and the interaction would become a function of the direction of magnetization through the spin-orbit coupling in the iron atom.

[28] J. H. Van Vleck, Phys. Rev. 52, 1178 (1937).

APPENDIX

Let the free energy of a system consisting of a single crystal ellipsoid of magnetization I in the field H of a permanent magnet be given by f. If one does work, at constant temperature, by applying stresses τ_{ij} to the ellipsoid and also by applying a translational force which moves it into the field of the permanent magnet, the change in free energy is

$$df=-VI_i dH_i+V_0\tau_{ij}dA_{ij}, \quad (A\text{-}1)$$

where V is the volume and V_0 the unstrained volume of the ellipsoid.[27] Letting $V_0F=f+VI_iH_i$, one has

$$dF=(H_i/V_0)d(VI_i)+\tau_{ij}dA_{ij}, \quad (A\text{-}2)$$

where V_0F is equal to the free energy of a strained ellipsoid possessing magnetization I in zero applied field, since VI_iH_i is the work required to remove such an ellipsoid from the field H if I and A are held constant. If $F(VI_i, A_{ij})$ is imagined as the free energy of a crystal spontaneously magnetized at a given strain, to a fixed VI, it becomes a function of the strain and direction cosines of I.

We shall integrate (A-2) along a path P which starts with the crystal magnetized in the Z direction (subscript 3), with no stresses applied. The strain is defined as initially zero. If the crystal is now strained, holding VI constant a term F_{el} quadratic in A_{ij} is obtained since it is assumed that for constant VI the material obeys a Hooke law. Next, keeping the strain constant, the magnetization is rotated into an arbitrary direction. Thus the change in free energy is

$$\Delta F=F_{el}+(V/V_0)\int_P H_i dI_i. \quad (A\text{-}3)$$

Substituting $H_i=H_i^{(i)}+N_{ij}I_j$ where H^i is the internal field and N_{ij} the demagnetizing coefficients (the off-diagonal components of which are zero) one gets

$$\Delta F=F_{el}+\frac{V}{V_0}\int_P H_i^{(i)}dI_i+\frac{V}{V_0}\frac{N_{ij}I_iI_j}{2}-\frac{V}{V_0}\frac{N_{33}I_3^2}{2}. \quad (A\text{-}4)$$

The last two terms give the form effect part of the energy due to changing the direction of magnetization. The part $\Delta F_{ll.e.}$ which depends linearly on the strain is given by

$$(\partial\Delta F_{ll.e.}/\partial A_{1m})_{A=0}A_{1m}.$$

Therefore

$$\Delta F_{ll.e.}=\frac{V_0}{2}\left[I_iI_j\frac{d(N_{ij}/V)}{dA_{1m}}-I_3^2\frac{d(N_{33}/V)}{dA_{1m}}\right]. \quad (A\text{-}5)$$

Making use of Powell's[29] calculations for an oblate spheroid magnetized in the equatorial plane

$$\Delta F_{ll.e.}=\tfrac{1}{2}\mu I^2[A_{22}'\alpha_2'^2-A_{33}'(\alpha_3'^2-1)]+\tfrac{1}{2}\mu I^2A_{23}'\alpha_2'\alpha_3' \quad (A\text{-}6)$$

where the primes indicate the quantities are referred to the principal axes of the spheroid and

$$\mu=(3\pi/2\epsilon^3)[(1-\epsilon^2)(3+2\epsilon^2)(3/\epsilon)(1-\epsilon^2)^{\frac{1}{2}}\sin^{-1}\epsilon]. \quad (A\text{-}7)$$

In terms of the principal axes a, b, and c, the eccentricity ϵ is given by

$$a=b=C/(1-\epsilon^2)^{\frac{1}{2}}.$$

For a sphere

$$\mu=-12\pi/5.$$

[27] We always assume the strain to be uniform throughout the volume.
[29] F. C. Powell, Proc. Cambridge Phil. Soc. 27, 564 (1931).

Letters to the Editor

PUBLICATION of brief reports of important discoveries in physics may be secured by addressing them to this department. The closing date for this department is five weeks prior to the date of issue. No proof will be sent to the authors. The Board of Editors does not hold itself responsible for the opinions expressed by the correspondents. Communications should not exceed 600 words in length.

Half-Life of Li^8

WALDO RALL AND KENNETH G. MCNEILL*
Yale University, New Haven, Connecticut†
(Received August 3, 1951)

MANY determinations have been made of the half-life of Li^8. Those using the Li(d, p) reaction as a source of Li^8 have so far not been so accurate as the more recent experiments using Li(n, γ) or Be(γ, p) reactions, the most recent published figures for the half-lives being, respectively,[1,2,3] 0.88 ± 0.1 sec, $0.89+0.02$, and 0.88 ± 0.03 sec for the three methods of formation. Preparatory to a search for a β-ray from H^4 described below[4] the half-life of Li^8 produced by the (d, p) reaction on Li was measured.

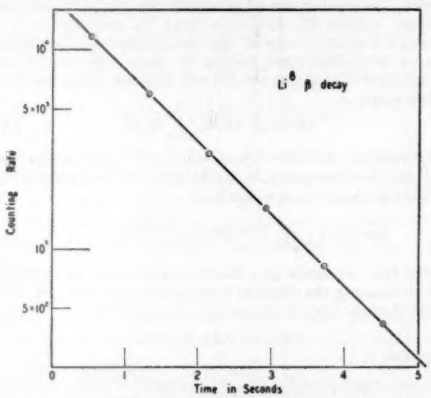

FIG. 1. Decay curve of $Li^8 \rightarrow Be^8$ β-decay; the observed half-life is 0.825 ± 0.02 sec.

A 0.5-μa beam of 4-Mev cyclotron deuterons was used. This was first focused on a gold leaf covered shutter which could be swung away out of the beam by a remotely controlled solenoid arrangement, allowing the beam to fall on the Li. After three seconds irradiation of the Li, the beam was instantaneously cut off by breaking the rf power supplies to the cyclotron. A NaI(Tl) crystal and photomultiplier were used to detect the beta-rays, which passed through 2.5 g/cm^2 of brass before entering the crystal. The pulses from the photomultiplier were fed through conventional circuits to two scalers. The circuit constants were so adjusted that there was no detectable background before the beam was switched on. The pulses from the scalers could be fed to the Y plates of a self-triggered CRO adjusted to have a sweep speed of 100 μsec. The data displayed on the CRO were recorded by means of a shutterless movie camera, the film in which was driven at a speed of 40 cm/sec by a motor switched on simultaneously with the cutting of the beam. One scaler, which ran continuously, was set to record every 128th count, while the output of the other, which recorded every 32nd count, was switched in 2 sec after the beam interruption. This avoided saturating the CRO at the beginning of the run, while extending the number of half-lives measured. Timing pips were displayed every 8/60 sec from a scaler actuated by the 60-cps line voltage. Runs usually lasted 5 sec. In all, 17 acceptable runs were taken and analyzed.

After development of the film, it was possible to obtain from the data the counting rate over a period of six half-lives. Figure 1 is a plot of the experimental data. The value of the half-life obtained is 0.825 ± 0.02 sec. This is somewhat lower and outside the error of the most closely specified result of 0.89 sec reported by Hughes *et al.*[3] Hughes[5] points out that their analysis may contain overcorrections for the dead time of the G-M counter used, since the He^6 half-life of 0.89 sec[6] obtained using the same corrections has been remeasured to be 0.82 sec.[7,8]

To check that it was in fact the high energy Li^8 beta-rays that were being counted, the crystal and photomultiplier were roughly calibrated using the 1.28-Mev gamma-rays from Na^{22}. Since the maximum pulses from the Li were approximately a factor of 10 larger than the photoelectron pulses from the 1.28-Mev gamma-rays, it was estimated that 12-Mev betas were being detected in the main experiment, in agreement with the known maximum energy of the betas.

It is considered that this method of measuring half-lives is useful in the range 0.01 to 1.0 sec, usually regarded as being somewhat difficult.

* Dill-Overlander-Loomis Post Doctorate Fellow. Now at Glasgow University, Glasgow, Scotland.
† Assisted by the joint program of the ONR and AEC.
[1] Lever, Burcham, and Chang, Nature **139**, 24 (1937).
[2] Hughes, Hall, Eggler, and Goldfarb, Phys. Rev. **72**, 646 (1947).
[3] G. C. Baldwin, Phys. Rev. **76**, 182A (1949).
[4] K. G. McNeill and W. Rall, Phys. Rev. **83**, 1244 (1951).
[5] Private communication.
[6] D. J. Hughes and W. D. B. Spatz, private communication listed in G. T. Seaborg and I. Perlman, Revs. Modern Phys. **20**, 585 (1948).
[7] W. J. Knox, Phys. Rev. **74**, 1192 (1948).
[8] J. E. R. Holmes, Proc. Phys. Soc. (London) **A62**, 293 (1949).

The Possibility of the Reaction $H^3(d, p)H^4$

KENNETH G. MCNEILL* AND WALDO RALL
Yale University, New Haven, Connecticut†
(Received August 3, 1951)

EXPERIMENTS have been conducted to investigate the possibility of the reaction $H^3(d, p)H^4$. The stability of H^4 is doubtful, and it was considered that an investigation into its possible formation was desirable.

The research falls into two parts. In the first, an air-cooled target of H^3 on zirconium, supplied by the Oak Ridge National Laboratory was bombarded by cyclotron deuterons of energies between 0.5 and 3.8 Mev. A search was made for the protons which would arise from the (d, p) reaction if it existed. A "peaked" proportional counter was used to detect protons at the end of their range. Difficulty was experienced due to the presence of oxygen, nitrogen, and carbon impurities on the target, all of which yielded (d, p) protons. These could be distinguished from $H^3(d, p)H^4$ protons by their shift in range with altered deuteron energy. The impurities, however, gave a background which prevented a search for low yield $H^3(d, p)H^4$ protons of small range. The following limits can be put on the reaction: either the reaction's Q value is less than 4.4 Mev, which implies that the mass value of H^4 is greater than 4.019 mass units, or the probability of the reaction is at least 1500 times as small as that of the $H^3(d, n)He^4$ reaction. This latter conclusion was reached after measurement of the neutron flux from the target using the $Ag^{107}(n, 2n)$ and $C^{12}(n, 2n)$ reactions and measuring the activity of the Ag^{106} and Cu^{62}.

The experiments do not exclude the possibility of Q being less than 4.4 Mev, since protons would not have been detected for such Q. Part of the corresponding mass range of H^4 could correspond perhaps to sufficient stability against mechanical disintegra-

tion to make β-emission possible. The β-emission $H^4 \rightarrow He^4 + \beta^-$ would give rise to high energy ($\sim$15 Mev) β-rays with a likelihood of short half-life. A search for these was made using a NaI (Tl) scintillation detector.

To study the region of half-lives of about 1 second, the same technique was used in the Li^8 half-life determination described in the previous letter.[1] The discriminator in the circuit was set so that only high energy electrons would be counted. The observation of Li^8 produced by the $Li^7(d, p)Li^8$ reaction was used as an indicator of the sensitivity of the apparatus and made it possible to relate the expected ratio of β-intensities from H^4 and Li^8 to the ratio of cross sections of the reactions $H^3(d, p)H^4$ and $Li^7(d, p)Li^8$. For a bombarding energy of 3.82 Mev there were 2000 counts observed from Li^8 after bombardment for 3 seconds. There were no counts attributable to H^4 after bombardment of the H^3 target with the same current and energy in the interval extending from 0.006 to 3 seconds after shutting off the cyclotron beam. This experiment was repeated 8 times, and not a single H^4 β-ray was observed.

For half-life investigations in the region of 100 seconds, H^3 was irradiated for 3 minutes and counts were simply looked for on the scaler after cutting the beam. Again, no counts were recorded, though as before, while the beam was on, neutrons from the $H^3(d, n)He^4$ reaction gave many counts.

The β-ray experiments were repeated with 4.1-Mev deuterons and 1/20 of the current of the first set of runs, and again no β-rays were detected. The combined evidence of absence of protons for Q values which would make their detection feasible, together with the absence of β-rays, decreases the probability of the existence of a stable H^4, as is more fully discussed in the following note.[2]

We wish to thank Professor Breit for many helpful discussions and Professor Pollard for his continued interest in the problem.

* Dill-Overlander-Loomis Post Doctorate Fellow. Now at Glasgow University, Glasgow, Scotland.
† Assisted by the joint program of the ONR and AEC.
[1] Waldo Rall and Kenneth G. McNeill, Phys. Rev. **83**, 1244 (1951).
[2] G. Breit and J. S. McIntosh, Phys. Rev. **83**, 1245 (1951).

Evidence Regarding Instability of H^4

G. Breit and J. S. McIntosh
*Yale University, New Haven, Connecticut**
(Received August 3, 1951)

McNeill and Rall's attempts[1] to find protons or β-rays from $H^3(d, p)H^4$ failed to detect these particles, decreasing the probability of there being a stable H^4. The mass of a mechanically stable H^4 must be greater than 4.0211, for otherwise $Li^8 \rightarrow He^4 + H^4$ would compete with β-decay of Li^8. It must be less than 4.0259, for otherwise $H^4 \rightarrow H^3 + n$ could take place. The lower limit agrees with the value 4.019 obtained experimentally;[1] E_β for $H^4 \rightarrow He^4 + \beta^-$ is accordingly between 22.0 and 17.3 mMU, and the corresponding values of Q for $H^3(d, p)He^4$ are -2.23 and $+2.23$ Mev. The first of these is directly $H^3 - H^3 - n$[1]. Calculations give half-lives as in Table I.

Under "Notes," *N.C.* is a normalization correction for a p neutron taking account of overlap probability with a He^4 proton. The notation is as in the paper by Konopinski.[5] The "forbid." factors give lengthening of the half-life. Uncertainties in Table I are: (a) the *N.C.* may be different for ^1D; (b) just below dissociation into $H^3 + n$ the *N.C.* (^1S) is large and $t_{\frac{1}{2}}$ unobservably long; (c) an uncertainty of a factor of 2 is possible on account of variability of ft values, (d) vector coupling effects in the ^3P states are neglected. A trace of Fermi interaction would seriously shorten $t_{\frac{1}{2}}$ for $^1S_0$.

From data on β-counts, estimates have been made regarding the lower limit of Y_H/Y_L, where Y_H and Y_L are yields of $(\ , p)H^4$ and of $(\ , p)Li^8$. Factors considered are: (1) ratios of barrier penetrations for first stage as in OBJ,[6] (2) ratio of velocities for second stage, (3) ratio of geometric cross sections. Effects of Zr in target and of stopping powers are as in the following note.[7] Curve *A* in Fig. 1 is derived from data.[1] Absence of counts forbids the region below *A*. Probable regions of t are marked for states of H^4; w, Q are shown at end points of regions. Curves marked $a, \cdots, d'$ show yield ratios *versus* Q. Primed letters refer to lower E_d. Unprimed letters deal with $E_d = 4.1$ Mev. The graphs for these have been displaced up by $\log_{10}20$ to allow for the smaller current. The 4.1-Mev experiment gives less information but provides more certainty regarding errors in energy scales, because for $Q = -2.23$ Mev the 3.82-Mev experiment would barely make the reaction possible. The $^1D_2$, $^1S_0$ states are probably[8] unstable to n emission. The $^3P_2$ state appears likely to have lowest energy from shell structure spin-orbit coupling theory.[9] The more likely possibility is made improbable by the experiments[1] within the reservations mentioned together with uncertainties in yields of reactions. The writers are grateful to Drs. McNeill and Rall for a helpful discussion of data.

TABLE I. Expected half-lives of H^4.

State of H^4	Type of transition	Limits on $t_{\frac{1}{2}}$ (sec)	Notes
$^3P_2$ odd	$\Delta I = 2$ (yes)	$4.5 < t < 16$ $w = 41.2$ to 32.5	($w = 41.2$, *N.C.* = 3) ($w = 32.5$, *N.C.* = 2) Theory as in references 2, 3, and 4.
$^3P_{1,0}$ odd	$\Delta I = 0, \pm 1$ (yes)	$0.03 < t < 0.12$ $w = 41.2$ to 32.5	
$^1P_1$ odd (pure)	$\Delta I = 0, \pm 1$ (yes)		
$^1P_1$ $+0.001$ $^3P_1$	$\Delta I = 0, \pm 1$ (yes)	$30 < t < 120$	
$^1D_2$, $^1S_0$ even		$0.4 < t < 3$ $w = 41.2$ to 32.5	15, 25 = forbid. factor for $w = 41.2$, 32.5

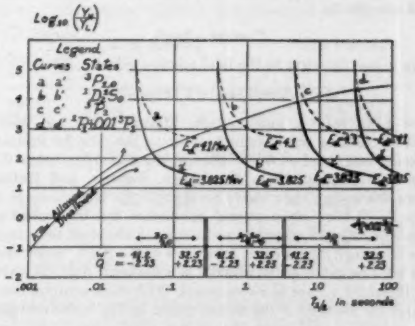

FIG. 1. Allowed and excluded regions. For each state of H^4, parts of curves $a, \cdots d'$ below curve *A* are excluded.

* Assisted by the joint program of the ONR and AEC.
[1] K. G. McNeill and W. Rall, Phys. Rev. **83**, 1244 (1951).
[2] E. J. Konopinski and G. E. Uhlenbeck, Phys. Rev. **60**, 308 (1941).
[3] C. S. Wu, Revs. Modern Phys. **22**, 386 (1950).
[4] F. B. Shull and E. Feenberg, Phys. Rev. **75**, 1768 (1949).
[5] E. J. Konopinski, Revs. Modern Phys. **15**, 209 (1943).
[6] Ostrofsky, Breit, and Johnson, Phys. Rev. **49**, 22 (1936).
[7] J. S. McIntosh, Phys. Rev. **83**, 1246 (1951).
[8] S. S. Share, Phys. Rev. **53**, 875 (1938).
[9] M. G. Mayer, Phys. Rev. **78**, 16 (1950).

Effect of Target Thickness in the Search for H^4

J. S. McIntosh
*Yale University, New Haven, Connecticut**
(Received August 3, 1951)

IN connection with the search for H^4 by McNeill and Rall,[1] it was found necessary[2] to estimate the ratio

$$R=[Y/\sigma(E_{\max})]_H/[Y/\sigma(E_{\max})]_{Li}, \quad (1)$$

where Y is the total reaction yield, $\sigma(E_{\max})$ is the collision cross section for the maximum energy of the bombarding deuterons (i.e., before they have been slowed down), and subscripts H and Li refer to the reactions $H^3(d,p)H^4$ and $Li^7(d,p)Li^8$, respectively. The yield is given by[3]

$$Y=(N_\sigma/N)\int_{E(\min)}^{E(\max)}[\sigma/(\epsilon\sigma)]dE, \quad (2)$$

where N_σ/N is the ratio of the number of nuclei taking part in the reaction to the total number in the target, σ the collision cross section, $\epsilon\sigma$ the stopping cross section, and E the energy of the bombarding deuterons. For the targets used $E_{\min}\cong 0$.

For tritium occluded on zirconium,[1] $N_\sigma/N\cong\frac{1}{2}$ and $\epsilon\sigma\cong\frac{1}{2}[\epsilon\sigma(H^3)+\epsilon\sigma(Zr)]$. The values of $\epsilon\sigma$(air) (adapted to deuterons) are obtained from Livingston and Bethe,[4] and the ratios of $\epsilon\sigma$ for H^3 and Zr to that for air are estimated to be 0.3 and 3.0, respectively.[4] For the energy dependence of σ, reference is made to Ostrofsky, Breit, and Johnson,[5] Eqs. (7), (12), and abstract.

$$\sigma\cong\text{const.}\ (P/v_i^2)/[\exp(2\pi\eta_i)-1], \quad (3)$$

where v_i is the initial relative velocity, P the probability that once the deuteron is in the bombarded nucleus a reaction will occur, and

$$\eta_i=\alpha Z_d Z_p c/v_i, \quad \alpha\cong 1/137. \quad (4)$$

As suggested by Professor Breit, P may be estimated by the principle of detailed balance from the reverse reaction. This leads for small energies to

$$P\propto\exp(-2\pi\eta_f), \quad (5)$$

where $\eta_f=\alpha c/v_f$ refers to the final relative velocity. Thus

$$\sigma\propto[\eta_i^2/\exp(2\pi\eta_i)-1]\exp(-2\pi\eta_f). \quad (6)$$

For $Li^7(d,p)Li^8$ a pure metallic lithium target was used so $N_\sigma/N=1$, and $\epsilon\sigma$ was obtained as above, the ratio for lithium to air being estimated at 0.5. Values of σ for energies below 0.770 Mev were obtained from Rumbaugh, Roberts, and Hafstad.[6] Above this energy the σ curve breaks sharply. Experimental data above 0.770 Mev[7] show several resonances, but for present purposes these may be smoothed and the σ calculated on two assumptions of energy dependence: (case a) $\sigma\propto(E-E_{th})^{\frac{1}{2}}$, which would have been expected in the absence of a coulomb field (E_{th} = reaction threshold); (case b) σ = constant. With these assumptions one obtains for the ratio R the curves drawn in Fig. 1, for energies of the bombarding deuterons $E=3.825$ Mev and $E=4.1$ Mev, respectively, and for assumed Q values from -2.226 to $+2.227$ Mev.

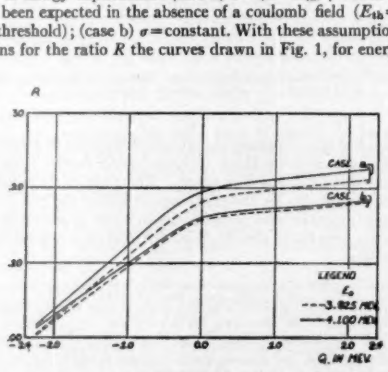

FIG. 1. Double ratio R of yield to cross section at maximum energy, plotted against assumed Q.

The writer wishes to thank Professor Breit for a helpful discussion.

* Assisted by the joint program of the ONR and AEC.
[1] K. G. McNeill and W. Rall, Phys. Rev. **83**, 1244 (1951).
[2] G. Breit and J. S. McIntosh, Phys. Rev. **83**, 1245 (1951).
[3] Yale Nuclear Physics Lectures, by G. Breit.
[4] M. S. Livingston and H. A. Bethe, Revs. Modern Phys. **9**, 270 (1937).
[5] Ostrofsky, Breit, and Johnson, Phys. Rev. **49**, 22 (1936).
[6] Rumbaugh, Roberts, and Hafstad, Phys. Rev. **54**, 666 (1938).
[7] Hornyak, Lauritsen, Morrison, and Fowler, Revs. Modern Phys. **22**, 309 (1950).

Scattering of Pi-Mesons by the Deuteron

JOHN S. BLAIR
*Department of Physics, University of Illinois, Urbana, Illinois**
(Received July 30, 1951)

THE scattering of charged spin zero mesons by the deuteron has been examined in the weak-coupling approximation[1] and compared with the familiar weak-coupling results for single-nucleon scattering. Ferretti and Gallone[2] have already pointed out that the scattering of mesons by the deuteron would differ from the single-nucleon case because of certain interference effects unique to the deuteron. It is believed, however, that Ferretti and Gallone have not explored all likely modes of scattering.

The chief interference effect occurs because the calculated scattering amplitudes from single neutrons and protons have nearly the same magnitude but may be of differing sign. Thus, large destructive or constructive interference may arise in the scattering amplitude of the deuteron, which for low energy mesons is a sum of single-nucleon amplitudes. An additional interference effect arises from the fact that the Pauli exclusion principle must operate in intermediate states; this, together with conservation of angular momentum, leads to restrictions on the parity of meson waves. It is found, however, that this latter effect decreases the ratio of deuteron to single-nucleon cross sections only in those cases where the ratio is already small because of the first interference effect.

The results of the calculations can be summarized as follows: For scalar coupling, the ratio of elastic to the single-nucleon cross section, $d\sigma_1$, is quite small and approximately (2 kinetic energy of mesons/rest-mass energy of nucleon)$^2\cos^2\theta$, where

$$d_1=\sigma(g^2/4\pi)^2(1/\hbar\omega)^2d\Omega;$$

θ is the angle between the incident and final mesons; g, the meson-nucleon coupling parameter; and $\hbar\omega$, the total energy of the meson. The inelastic scattering cross section into final nucleon states of odd parity is larger. The cross section is small and has a backward angular distribution $(1-\cos\theta)$ for low energy mesons (kinetic energy <20 Mev). But, as the energy is increased, the cross section slowly approaches the magnitude $2d\sigma_1$, and rapidly approaches the isotropic angular distribution predicted for scalar scattering from two free nucleons.

In discussing pseudovector coupling, it suffices to give only the cross sections arising from the spin coupling term in the interaction; cross sections due to the γ^5-term are masked either by coulomb or spin coupling cross sections. Elastic scattering with spin flip gives the largest contribution to the cross section. The ratio of the elastic to single-nucleon cross section, $d\sigma_2$, is for low energy mesons about $(8/3)\sin^2\theta$, where $d\sigma_2=d\sigma_1(p/mc)^4$, p is the momentum, and m is the rest mass of the meson. Elastic scattering without spin flip is negligible. The ratio of inelastic to single-nucleon cross section is negligible compared with the elastic to single-nucleon ratio for low energy mesons, and for high energy mesons is qualitatively the same as that found with scalar coupling. For an incident meson of energy 88 Mev, the ratio of deuteron to single nucleon cross sections is approximately $1.2\sin^2\theta+0.5$, where the first term results from elastic and the second term inelastic deuteron scattering. The inelastic term above is an

overestimate at small scattering angles; more accurately, the inelastic scattering, instead of remaining nearly isotropic, approaches 0 at small angles. To obtain the above numbers, the zero range deuteron wave function was employed; when the more refined Hulthén wave function is used, the elastic scattering is reduced and the inelastic scattering is increased.

Details will be given in a future paper with B. Segall.

The author wishes to thank Professor S. M. Dancoff for his guidance and Professor G. F. Chew, Professor J. M. Blatt, and Mr. B. Segall for much helpful comment.

* Supported in part by the joint program of the ONR and AEC.

[1] Ph.D. thesis of author, University of Illinois, 1951.

[2] B. Ferretti and S. Gallone, Phys. Rev. 77, 153 (1950). Also see the recent work of Fernbach, Green, and Watson, Phys. Rev. 82, 980 (1951).

Charge Exchange Scattering of π-Mesons in Deuterium

BENJAMIN SEGALL

Department of Physics, University of Illinois, Urbana, Illinois

(Received July 30, 1951)

SINCE ordinary scattering[1] and absorption[2] of fast π-mesons of spin zero in deuterium have already been studied in the weak-coupling approximation, the calculation of the exchange scattering cross section in deuterium,

$$\pi^+ + d \rightarrow p + p,$$

completes the list of important meson reactions in the two-body system. After carrying out this calculation, we find the deuteron cross section to be directly expressible in terms of the corresponding single-nucleon cross section. An outline of the argument follows.

It was first found that the result obtained from a second-order perturbation calculation, with the most general type of coupling, is consistent with the result obtained by the impulse approximation method,[2] in which one assumes that the scattering amplitude of the deuteron as a whole can be taken to be a linear superposition of the single-nucleon amplitudes. The essential point here is simply that the lifetime of the intermediate state is very short compared with the period of the deuteron. Thus, it is plausible to assume the validity of the impulse approximation even if the meson-nucleon coupling is not weak.

The results of applying the impulse approximation are particularly simple if the deuteron crosss section is expressed as a function of the nuclear recoil, $\mathbf{K}_f = \mathbf{q}_0 - \mathbf{q}_f$, where $\mathbf{q}_0$ and $\mathbf{q}_f$ are initial and final meson momenta. The probability for scattering per unit interval of K_f^2 is given by

$$d\sigma/d\mathbf{K}_f^2 = \{\tfrac{1}{4}\int d\mathbf{k}_f |I_S|^2 + \tfrac{3}{4}\int d\mathbf{k}_f |I_T|^2\} d\sigma_A/d\mathbf{K}_f^2 + \{\int d\mathbf{k}_f |I_T|^2\} d\sigma_B/d\mathbf{K}_f^2, \quad (1)$$

where the integration variable $\mathbf{k}_f$ is the final relative momentum of the nucleon system and the integration is to be carried out only over those values of $\mathbf{k}_f$ compatible with the conservation of energy. In Eq. (1), I_S and I_T are the singlet and triplet overlap integrals defined by

$$I_S = \int \psi_f^{e*} \exp(\tfrac{1}{2} i \mathbf{K}_f \cdot \mathbf{r}) \psi_i d\mathbf{r}, \qquad I_T = \int \psi_f^{o*} \exp(\tfrac{1}{2} i \mathbf{K}_f \cdot \mathbf{r}) \psi_i d\mathbf{r},$$

where ψ_i, ψ_f^e, and ψ_f^o are the nuclear wave functions for the initial state (deuteron), final state (di-proton) with even parity, and final state with odd parity, respectively. The quantities $d\sigma_A/d\mathbf{K}_f^2$ and $d\sigma_B/d\mathbf{K}_f^2$ are the single-nucleon exchange cross sections corresponding to spin flip and no spin flip, respectively.

From the above expression, one can easily deduce the important result that the deuteron cross section cannot be larger than the neutron cross section. Evaluation of the integrals in Eq. (1) has been performed in both the plane wave and closure approximations;[4] however, for the sake of brevity, only the closure result, which is found to be a reasonable approximation, will be presented here. The formula for the cross section is

$$d\sigma/d\mathbf{K}_f^2 = [1 - \tfrac{1}{4}F(\mathbf{K}_f)](d\sigma_A/d\mathbf{K}_f^2) + [1 - F(\mathbf{K}_f)]\, d\sigma_B/d\mathbf{K}_f^2. \quad (2)$$

The function $F(K_f)$, which is defined by

$$F(\mathbf{K}_f) = \int \exp(i\mathbf{K}_f \cdot \mathbf{r}) \psi_i^2(\mathbf{r}) d\mathbf{r},$$

is plotted against K_f in Fig. 1. Since $F(\mathbf{K}_f)$ is very nearly equal to unity for values of K_f in the neighborhood of zero, only the spin flip terms will contribute appreciably for small nuclear recoils.

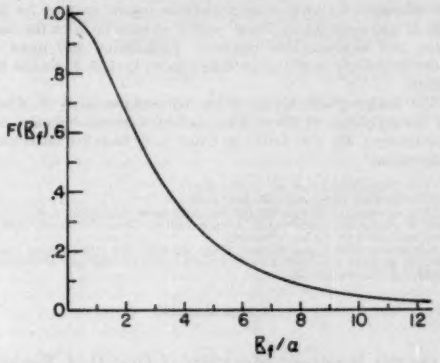

FIG. 1. $F(\mathbf{K}_f)$ versus K_f.

TABLE I. Weak-coupling single-nucleon cross sections. In this table g is the charged meson coupling parameter; g_N and g_P are coupling parameters of the neutral meson to the neutron and proton, respectively; and $(\mu)^{-1}$ is the meson Compton wavelength.

Charged π ↓ \ Neutral π →	Scalar coupling	Spin coupling
Scalar coupling	$d\sigma_A = 0$	$d\sigma_A = \frac{g^2}{16\pi}\frac{g_P^2}{\mu^2}\frac{(\mathbf{\varepsilon}_P - \mathbf{\varepsilon}_N)^2}{q_0^2\hbar^2\omega_0^2} d\mathbf{K}_f^2$
	$d\sigma_B = \frac{g^2}{16\pi}\frac{(\mathbf{\varepsilon}_P - \mathbf{\varepsilon}_N)^2}{q_0^2\hbar^2\omega_0^2} d\mathbf{K}_f^2$	$d\sigma_B = 0$
Spin coupling	$d\sigma_A = \frac{g^2}{16\pi}\frac{(\mathbf{\varepsilon}_P - \mathbf{\varepsilon}_N)^2}{\mu^2\hbar^2\omega_0^2} d\mathbf{K}_f^2$	$d\sigma_A = \frac{g^2}{16\pi}\frac{(\mathbf{\varepsilon}_P + \mathbf{\varepsilon}_N)^2}{\mu^4 q_0^2 \hbar^2 \omega_0^2}(\mathbf{q}_0 \times \mathbf{q}_f)^2 d\mathbf{K}_f^2$
	$d\sigma_B = 0$	$d\sigma_B = \frac{g^2}{16\pi}\frac{(\mathbf{\varepsilon}_P - \mathbf{\varepsilon}_N)^2}{\mu^4 q_0^2}\frac{(\mathbf{q}_0 \cdot \mathbf{q}_f)^2}{\hbar^2\omega_0^2} d\mathbf{K}_f^2$

This can easily be understood in terms of the Pauli principle. For, in the case of no change in spin, the final state consists of two identical nucleons with their spins aligned. This is forbidden unless the nuclear system is kicked into a state of odd orbital angular momentum.

As an example, the relevant weak-coupling single-nucleon cross sections for the various possible combinations of parities of spin zero neutral and charged mesons are listed in Table I. In Table II

TABLE II. Total cross sections.

Meson energy (Mev)	Deuteron $\sigma_A \times 10^{27}$ cm^{-2} $\left[\frac{g^2(\mathbf{\varepsilon}_P + \mathbf{\varepsilon}_N)^2}{(4\pi\hbar c)^2}\right]$	Deuteron $\sigma_B \times 10^{27}$ cm^{-2} $\left[\frac{g^2(\mathbf{\varepsilon}_P - \mathbf{\varepsilon}_N)^2}{(4\pi\hbar c)^2}\right]$	Single nucleon $\sigma_A \times 10^{27}$ cm^{-2} $\left[\frac{g^2(\mathbf{\varepsilon}_P + \mathbf{\varepsilon}_N)^2}{(4\pi\hbar c)^2}\right]$	Single nucleon $\sigma_B \times 10^{27}$ cm^{-2} $\left[\frac{g^2(\mathbf{\varepsilon}_P - \mathbf{\varepsilon}_N)^2}{(4\pi\hbar c)^2}\right]$
28	19.6	4.06	24.5	14.6
56	59.4	16.0	70.1	34.7
90	120	34.0	133	68.2

are tabulated the total cross sections at several energies for the case of spin coupling for the π^+ and π^0 mesons for both the deuteron and single-nucleon reactions. Elaboration and proof of these results will be given in a future paper by J. S. Blair and the author.

The author gladly expresses his indebtedness to G. F. Chew for his suggestion of the problem and his constant help and encouragement. He also wishes to thank J. S. Blair for his helpful suggestions.

[1] J. S. Blair, Phys. Rev. **83**, 1246 (1951).
[2] W. Cheston, Phys. Rev. **82**, 335 (1951).
[3] The application of the impulse approximation is similar to the treatment of photomeson production in deuterium by Chew and Lewis, and by Feshbach and Lax (to be published).
[4] Fernbach, Green, and Watson, Phys. Rev. **82**, 980 (1951), have evaluated the impulse approximation in a similar way for the case of ordinary scattering with no spin flip.

On the Magnetic Moments of Odd-Odd Nuclei

IGAL TALMI*
Physikalisches Institut der Eidgenössischen Technischen Hochschule, Zürich, Switzerland
(Received July 24, 1951)

It was pointed out by Feenberg[1] and others that the magnetic moments of odd-odd nuclei are very close to the values calculated with the assumption that the two odd nucleons move in a central field and their angular momenta combine in the j-j coupling scheme. This excellent agreement is rather astonishing in view of the large deviations of the magnetic moments of odd-even nuclei from the Schmidt values (also in the case of light nuclei).

The aim of this note is to point out that the apparent contradiction between these two facts disappears upon consideration of the mutual compensation of the changes in the magnetic moment due to the odd proton and odd neutron. This compensation can occur in many reasonable theories which explain the deviations from the Schmidt values. It represents itself in a simple way if that deviation can be expressed as a change of the g factor which belongs to the j of the odd nucleon. This is the case with the theory which assumes that the anomalous magnetic moment of the proton and neutron is quenched when they are bound in the nucleus.[2,3]

If the two odd nucleons have the same l and j (according to the shell model), their angular momenta will have equal projections on their resultant. We may assume that the changes in the individual g factors are then roughly equal in magnitude (they have opposite signs) if there are as many protons as neutrons. As a result, the changes would cancel and the magnetic moment would have the calculated value. In case the odd proton and odd neutron do not have the same l and j, the situation will not be the same; but it is still possible to estimate the sign and order of magnitude of the deviation from the calculated value.

Turning to the experimental material (Table I), we find that in all the cases where the proton and neutron configurations are the same, the calculated and experimental values agree within a few percent. The only case where the proton and neutron are in different orbits is K^{40}, and only in this case is the deviation not small. Elementary calculation shows that the deviation in this case should be

$$\Delta\mu=(8/5)[(4/7)\Delta\mu_N+(1/3)\Delta\mu_P].$$

The deviation found could have well been caused by changes in the individual magnetic moments $\Delta\mu_N$ and $\Delta\mu_P$ of the sign and order of magnitude found for odd $f_{7/2}$ neutron and $d_{3/2}$ proton-nuclei. The magnetic moment of Lu^{176} can also be explained on these lines, but the lack of exact knowledge of the spin and the ambiguity of the orbit assignment in this region do not allow a clear discussion. The magnetic moment of Li^6 agrees better with the value calculated in LS-coupling; this result is not unexpected for this light nucleus. (If LS-coupling is assumed, the simple cancellation described above would take place if the deviations from the Schmidt values can be expressed as a change in the g_s or g_l of the odd nucleon.) It may be noted that the assignment $d_{3/2}$ in the case of Na^{22} will not give a good agreement.

TABLE I. Calculated and observed magnetic moments.

Nucleus	I obs	Neutron state	Proton state	Coupling scheme	Ground state	Magnetic moment Calculated	Observed[a]
Li^6	1	$p_{3/2}$ $\bar{p}$	$p_{3/2}$ $\bar{p}$	jj LS	$J=1$ $^3S_1$	0.63 0.88	0.8221
B^{10}	3	$p_{3/2}$ $\bar{p}$	$p_{3/2}$ $\bar{p}$	jj LS	$J=3$ $^3D_3$	1.88 1.88	1.801
N^{14}	1	$p_{1/2}$	$p_{1/2}$	jj	$J=1$	0.37	0.403
Na^{22}	3	$d_{5/2}$ $(d_{5/2})^3$, $J_N=\frac{3}{2}$	$d_{5/2}$ $(d_{5/2})^3$, $J_P=\frac{3}{2}$	jj jj	$J=3$ $J=3$	1.73 1.73	1.7454
K^{40}	4	$f_{7/2}$	$d_{3/2}$	jj	$J=4$	−1.68	−1.29

[a] *Nuclear data*, Natl. Bur. Standards (U. S.) Circ. 499 (1950).

[*] Hebrew University, Jerusalem, Israel.
[1] E. Feenberg, Phys. Rev. **76**, 1275 (1949).
[2] A. de Shalit, Helv. Phys. Acta, to be published.
[3] F. Bloch, Phys. Rev. **83**, 839 (1951).

The Systematics of Nuclear Energies

ALEX E. S. GREEN
University of Cincinnati, Cincinnati, Ohio
(Received July 12, 1951)

THE Weizsäcker semi-empirical formula for nuclear energies may, by straightforward analysis, be placed in the form,

$$E(A,D)=A\epsilon_v(A)+J(A)[D-D_v(A)]^2+H(A)\delta, \quad (1)$$

where $D=N-Z$ and δ is ±1 or 0 according to the nuclear type. On the basis of this expression the Q value of a nuclear reaction,

$$Q=E(A,D)+e(a,d)-E(A',D')-e(a',d'), \quad (2)$$

may be written in the convenient form,

$$Q=Q_1+Q_2+Q_3, \quad (3)$$

where

$$Q_1\approx e-e'-(a-a')\bar{S}_v, \quad (4)$$
$$Q_2=\delta H-\delta' H'\approx(\delta-\delta')\bar{H}, \quad (5)$$
$$Q_3=\theta^2 J-\theta'^2 J'\approx(\theta^2-\theta'^2)\bar{J}, \quad (6)$$
$$S_v=d(A\epsilon_v)/dA, \quad (7)$$

and

$$\theta=D-D_v(A). \quad (8)$$

The bar signifies that the functions are to be evaluated at

$$\bar{A}=\tfrac{1}{2}(A+A')=A+\tfrac{1}{2}(a-a'), \quad (9)$$

and $\approx$ signifies "very nearly equal to."

The key functions ϵ_v, D_v, J, H, and S_v, although quite complicated from the computational standpoint, have relatively small variations. Thus graphical representations of these functions, once prepared, are adequate for most purposes.

Alternatively, one may replace the complicated key functions derived from the Weizsäcker surface by the simple analytical functions:

$$E_v(A)=A\epsilon_v(A)=c_1-c_2A+c_3A^{\frac{2}{3}}, \quad (10)$$
$$J(A)=c_4/A, \quad (11)$$
$$H(A)=c_5/A^{\frac{1}{3}}, \quad (12)$$
$$D_v(A)=\gamma A^{\frac{2}{3}}/(A+B), \quad (13)$$

and

$$S_v(A)=-c_2+2c_3A. \quad (14)$$

A graphical analysis of Rosenfeld's[1] table of nuclear energies, the known pairing correction function, and other empirical con-

siderations have led to the constants (the c's are in Mev)

$$c_1=26.00,\quad c_2=9.560,\quad c_3=0.00780,\quad c_4=22.5,$$
$$c_5=33.5,\quad \gamma=0.400 \text{ and } B=200.$$

Together with Eq. (1) these simple key functions characterize an empirical energy surface which does not deviate significantly from the Weizsäcker surface for the great range of mass numbers and which lies significantly closer to the true nuclear surface for very heavy nuclei. Furthermore, Eq. (4) is now exact.

Apart from systematizing nuclear data, it is thought that this empirical surface will be very useful as a base surface for investigating the irregularities of the actual surface. Thus if $E_{es}(A, D)$ is the deviation of the true surface from the empirical surface at the A, D point then any discrepancy between an experimental Q value and the calculated Q value is given by

$$Q_{exp}-Q_{calc}=E_{es}(A, D)-E_{es}(A', D'). \quad (15)$$

I would like to thank the many students who have assisted in this study, in particular Mr. Robert Minogue who determined the values of c_1, c_2, and c_3 quoted above. Mr. Minogue has also carried out a survey of experimental and calculated neutron binding energies and alpha-decay energies as well as a study of the shell correction in the neighborhood of mass number 208. These results will be reported in a detailed communication.

[1] L. Rosenfeld, *Nuclear Forces* (Interscience Publishing Company, Inc., New York, 1949).

On the Spin and Quadrupole Moment of Cl^{36}

C. M. Johnson and Walter Gordy
*Department of Physics, Duke University, Durham, North Carolina**
and
Ralph Livingston,
Oak Ridge National Laboratory, Oak Ridge, Tennessee†
(Received July 23, 1951)

FROM observation of the hyperfine structure of the $J=0\rightarrow1$ transition of CH_3Cl^{36} we have confirmed the assignment of 2 for the nuclear spin of Cl^{36} by Townes and Aamodt.[1] This is the only known nuclear spin value of 2.

The hyperfine structure of a $0\rightarrow1$ transition is particularly simple, consisting of only three lines for any spin value. The ratios of the frequency intervals differ widely for different spin value, so that an unquestionable assignment of a spin can be made by a precise measurement of these ratios. Table I lists the

Table I. Frequency ratios of hyperfine components for different spin values.

Spin	Theoretical ratio	Observed ratio
1	1.500	
2	0.556	0.547 ± 0.017
3	0.350	
4	0.257	

frequency ratios for spin values 1 to 4, together with the measured value for CH_3Cl^{36}. It is seen that all theoretical values except those for $I=2$ are considerably outside the range of limits of error.

Tables II and III list the various constants which were evaluated. The quadrupole moment is determined from the coupling ratio, using the Cl^{35} moment -0.07894×10^{-24} cm^2, as revised by Jaccarino and King.[2] The value agrees with that of Townes and Aamodt,[1] $-0.0172\pm0.0004\times10^{-24}$ cm^2,[3] within the limits of error of the two observations.

Table II. Measured frequencies of CH_3Cl^{36}.

Transition	Observed frequency Mc/sec	B_0 Mc/sec
$J=0\rightarrow1$, $F=2\rightarrow2$	26,372.42 ± 0.05	
$2\rightarrow3$	26,376.01	13,187.66[a]
$2\rightarrow1$	26,377.97	

[a] D_J is assumed to be 26.5 kc/sec.

Table III. Cl^{36} constants.

Spin	Coupling Mc/sec	Quadrupole moment cm^2
2	−15.87 ± 0.09[a]	$-0.0168\pm0.0001\times10^{-24}$

[a] The accuracy of relative frequency measurements is ±0.03 Mc/sec.

Figure 1 shows a cathode-ray presentation of the spectrum, with bars to indicate the theoretical spectrum for $I=2$. One of the lines of CH_3Cl^{35} in an excited vibrational state falls among the Cl^{36} group. Although this could not be completely "frozen out," it was easily identified and resolved from the Cl^{36} lines. The observations were made at dry ice temperature with a 20-foot Stark cell. A 100-kc square wave Stark modulating voltage was employed, with the field adjusted so as to remove the Stark

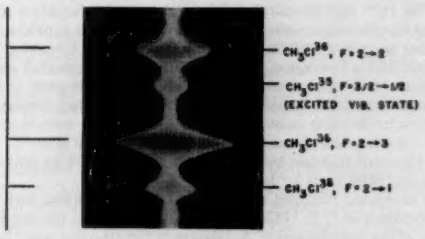

Fig. 1. Oscilloscope picture of $J=0\rightarrow1$ hyperfine pattern for CH_3Cl^{36}, with the calculated pattern below.

components completely from the undisplaced group (zero field components). The methyl chloride was synthesized by reacting NaCl with H_2SO_4 and CH_3OH. The Cl^{36} was made by neutron capture in Cl^{35} in a reactor. Its concentration was less than 1 percent.

Since the hyperfine structure lines of an excited vibrational state of CH_3Cl^{35} occur so near the Cl^{36} group, the frequencies of these lines were also measured during this experiment in order to determine whether or not the quadrupole coupling remained the same as in the ground state. The coupling was found to be −74.70 Mc/sec, which is not significantly different from the latest value,[4] −74.77 Mc/sec, given for the ground state.

We wish to thank Ralph Trambarulo, J. Q. Williams and C. F. Luck for assisting with the measurements.

* The research at this institution was sponsored by the Geophysical Research Directorate of Air Force Cambridge Research Laboratories.
† The research at this institution was performed for the AEC.
[1] C. H. Townes and L. C. Aamodt, Phys. Rev. **76**, 691 (1949).
[2] V. Jaccarino and J. G. King, private communication.
[3] This value has not been corrected for the revised moment of Cl^{35}.
[4] Geschwind, Gunther-Mohr and Townes, Phys. Rev. **81**, 288 (1951).

The Specific Alpha-Radioactivity of Pu^{240}

Edgar F. Westrum, Jr.*
Argonne National Laboratory, Chicago, Illinois†
(Received July 26, 1951)‡

THE small concentrations of Pu^{240} produced by the reaction $Pu^{239}(n, \gamma)Pu^{240}$ during irradiation of uranium or plutonium samples in thermal neutron reactors make possible the calculation of the half-life of Pu^{240} from a determination of the relative specific

alpha-activities and the isotopic compositions of the plutonium fractions of such samples.

The plutonium fractions of several samples subjected to different neutron fluxes were separated and carefully purified to spectrochemical freedom from foreign cations, to the absence of uranium (detected by a sensitive fluorescence test), and to radioactive purity. Duplicate portions of each plutonium fraction were converted to PuF_3 and reduced to high purity metal by microscale methods.[1]

Milligram globules of plutonium metal were massed against calibrated weights and dissolved in weighed quantities of solution. Aliquots were plated on platinum by a very precise gravimetric technique,[2] and counted on a parallel plate nitrogen counter (N-4) by methods previously described.[3] The isotopic compositions of the samples were available from the mass spectrometric examinations of Bartlett and Swinehart.[4] A minor change in the isotopic composition of sample C indicated by a recent determination has been incorporated into the present calculation after correcting for the accumulated radioactive disintegration.[5]

Appropriate corrections for Pu^{239} and the small amounts of Pu^{238} and Pu^{241} present were made in calculating the half-life of Pu^{240} from the observed[3] specific activity of the samples relative to that of Pu^{239}.

The Pu^{240} half-life calculated from three such plutonium fractions in order of increasing Pu^{240} content were sample A, 6180±360 years; sample B, 6100±200 years; and sample C, 6310±130 years; with a best value of 6240±120 years. The indicated probable errors in these measurments includes consideration of the uncertainties in the mass spectrometry and weighing, limitation of spectrochemical sensitivity, observed standard deviations in the counting, and the probable error in the half-life of Pu^{239}.

It is noted that this half-life value is in accord with an estimate of about 6000 years by James *et al.*[6]

The general direction of Professor Glenn T. Seaborg and the cooperation of P. R. O'Conner and D. C. Stewart in the preparation of the samples and of A. Ghiorso in the counting procedures is gratefully acknowledged.

* Present address: Department of Chemistry, University of Michigan, Ann Arbor, Michigan.
† Formerly the Metallurgical Laboratory.
‡ Based on Manhattan Project Document CC-3894 (1946).
[1] E. F. Westrum, Jr., Manhattan Project Reports CK-1586 (1944), CN-2495 (1945). Reported in J. Am. Chem. Soc. 70, 3543 (1948).
[2] E. F. Westrum, Jr., *The Transuranium Elements: Research Papers* (McGraw-Hill Book Company, Inc., New York, 1949), National Nuclear Energy Series, Vol. II, p. 1185.
[3] Westrum, Hindman, and Greenlee, *The Transuranium Elements: Research Papers* (McGraw-Hill Book Company, Inc., New York, 1949), National Nuclear Energy Series, Vol. II, p. 1717.
[4] A. A. Bartlett and O. F. Swinehart, Manhattan Project Document LA-561 (1946).
[5] M. G. Ingham and D. C. Hess (private communications).
[6] James, Florin, Hopkins, and Ghiorso, *The Transuranium Elements: Research Papers* (McGraw-Hill Book Company, Inc., New York, 1949), National Nuclear Energy Series, Vol. II, p. 1604.

Half-Life of Plutonium-240 by Determination of Its Uranium-236 Daughter

M. G. Ingham, D. C. Hess, P. R. Fields, and G. L. Pyle
Argonne National Laboratory, Chicago, Illinois
(Received July 27, 1951)

A NEW measurement of the Pu^{240} half-life has been made using a technique which depends on the growth of the uranium daughters from a plutonium sample of known isotopic composition. The decays involved in this experiment are

$$Pu^{239} \xrightarrow[\alpha]{24{,}410\ \text{yr}^{\dagger}} U^{235} \xrightarrow[\alpha]{7\times10^{8}\ \text{yr}}, \qquad (1)$$

$$Pu^{240} \xrightarrow[\alpha]{\sim 6000\ \text{yr}^{\S}} U^{236} \xrightarrow[\alpha]{\sim 2\times10^{7}\ \text{yr}^{\S}}. \qquad (2)$$

Since the time necessary to complete the experiment was short in comparison to the half-lives involved, the following simplified analytical expression can be obtained for the Pu^{240} half-life:

$$T_{\frac{1}{2}}(Pu^{240}) = \frac{\text{moles of } U^{235}}{\text{moles of } U^{236}} \times \frac{\text{moles of } Pu^{240}}{\text{moles of } Pu^{239}} \times T_{\frac{1}{2}}(Pu^{239}).$$

The half-life thus obtained depends on the isotopic ratios of the uranium daughters and of the plutonium parents as determined by the mass spectrometer, and on the known half-life of Pu^{239}. Previous measurements of the Pu^{240} half-life have been dependent on the Pu^{239} half-life and on the ratio of the plutonium isotopes, but have also been subject to the errors inherent in specific activity measurements.

The plutonium used for this experiment was chosen because it contained a relatively large amount of Pu^{240} and because it had been purified several years earlier with respect to the other heavy elements. After a chemical separation of the uranium daughters and subsequent purifications, an analysis on the alpha-differential pulse analyzer indicated that the final uranium fraction was sufficiently free of plutonium for mass spectrometric determinations.

The calculation of the half-life of Pu^{240} involved two experimental errors: (1) The error in the half-life of Pu^{239}, which is given by Westrum as ±0.3 percent;[1] (2) the error in the mass spectrometric measurements of the isotopic ratios, which is about ±0.3 percent. It should be noted that the usual mass discriminations inherent in a mass spectrometer cancel in the present case. Substituting in the analytical expression, the values obtained on the mass spectrometer for the isotopic ratios of Pu^{240}/Pu^{239} and U^{235}/U^{236} and the value $T_{\frac{1}{2}}^{239}=24{,}410$ years,[1] gives the half-life of Pu^{240} as 6580±40 years. This value and its limits of error is to be compared with those of 6240±120 yr,[4] 6850±150 yr,[5] and 6650±150 yr,[5] as determined by specific activity measurements.

The authors wish to express their appreciation to Dr. W. M. Manning for his helpful discussions of this problem.

[1] E. F. Westrum, Jr., *The Transuranium Elements: Research Papers*, (McGraw-Hill Book Company, Inc., New York, 1949), National Nuclear Energy Series, Division IV, 14B, Paper No. 22.80.
[2] James, Florin, Hopkins, Ghiorso, *The Transuranium Elements: Research Papers*, (McGraw-Hill Book Company, Inc., New York, 1949), National Nuclear Energy Series, Division IV, 14B, Paper No. 22.8.
[3] Ghiorso, Brittain, Manning, and Seaborg, Phys. Rev. 82, 558 (1951).
[4] E. F. Westrum, Jr., Phys. Rev. 83, 1249 (1951).
[5] Thompson, Street, Ghiorso, and Reynolds, to be published.

Low Excited States of Nuclei and the Quasi-Atomic Model*

L. J. Koester,† H. L. Jackson,‡ and R. K. Adair
University of Wisconsin, Madison, Wisconsin
(Received July 23, 1951)

THE independent particle, or quasi-atomic model of the nucleus, has been used to discuss the ground states of nuclei[1,2] and the doublet splitting in light nuclei.[3] Recent experiments[4] on the elastic scattering of protons by He^4, C^{12}, O^{16}, and of neutrons by He^4 have been analyzed,[4,5] and assignments of angular momentum and parity have been made to the excited states observed. These quantum numbers have also been determined for some of the low states of Al^{25} by an analysis of the scattering[6] of protons by Mg^{24}. Although these assignments are not all quite conclusive, we shall assume them to be correct for the purpose of discussion. The resulting series of energy levels, which are about 4 Mev in extent and lie near the ground states, show an interesting correlation with the predictions of an independent particle model with strong spin-orbit coupling.

One assumes that the nucleons of the target nucleus form a core of zero resultant angular momentum and that the influence of this core on the extra nucleon can be represented by an average potential. As a first approximation, this potential might be considered similar to that of a three-dimensional harmonic oscillator.

Since the coulomb repulsion is small in light nuclei, the density of nucleons is greatest near the origin. This[5] suggests a potential more singular at the origin than that of the harmonic oscillator. The result is a splitting of degenerate states with the same oscillator number, such that the energy of the state of lower orbital angular momentum is decreased. Finally, if we assume (LS) spin-orbit coupling, a state for which $J=L+\frac{1}{2}$ is depressed by an amount proportional to L, and one for which $J=L-\frac{1}{2}$ is raised by an amount proportional to $L+1$.

In Figs. 1c and 2c, we have plotted the levels of He^5, Li^5, and F^{17} relative to their ground states. The rest of Figs. 1 and 2 show how these levels can be fitted qualitatively into the above scheme. In Fig. 3 we have worked the levels of N^{15} and Al^{25} into the same type of scheme, but it is noticeable that the "closed shell plus one" nuclei, He^5, Li^5, and F^{17}, show the better correlation.

The degree of validity of the single particle approximation for a state is given roughly by the ratio of its reduced width[7] to the single particle limit $\hbar^2/\mu a$, where a is the interaction radius and μ the reduced mass of the system. On this basis, the dotted $S_{1/2}$ and the $F_{7/2}$ resonances in F^{17} can be excluded from the discussion because their reduced widths are very small. The other levels in F^{17} all have reduced widths comparable with the limit, and the reduced widths of the He^5, Li^5 levels are about equal to the limit. The large spin-orbit splitting is obvious in these three nuclei.

In N^{15} the $P_{3/2}$ resonance is the only one whose reduced width is small enough to indicate considerable multiple particle excitation. The mixing of a large number of wave functions to form this state may account for its abnormally large depression below the corresponding oscillator level.

Since the lowest excited states of He^4, C^{12}, and O^{16} lie well above the highest energy considered here, we expect a relatively small amount of core excitation in these low states of Li^5, He^5, N^{15}, and F^{17}. In Mg^{24}, however, there is a well known excited state at 1.38 Mev, which enhances the probability of core excitation. The Al^{25} excited states shown are the lowest three observed in the elastic scattering of protons by Mg^{24}, and their reduced widths are of the order of 15–20 percent of the single particle limit. Higher levels in this nucleus are narrower and of less definite assignment.

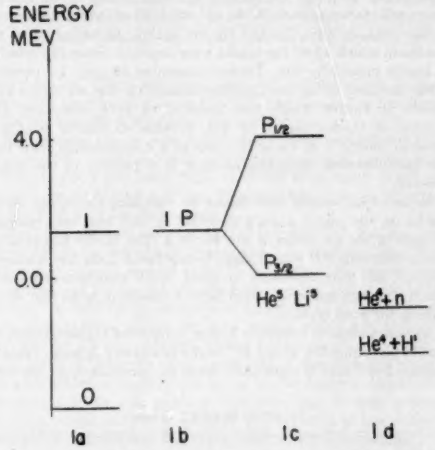

FIG. 1. Energy levels of the Li^5 and He^5 nuclei. (a) The ground state and first excited level of a simple harmonic oscillator. The ground state of Li^5 or He^5 is taken as the energy zero. (b) The corresponding level of the nuclear potential. (c) The observed levels of Li^5 and He^5, showing the large splitting and inversion of the $P_{3/2}$ and $P_{1/2}$ doublet. (d) Dissociation energies of He^4+n and He^4+H^1.

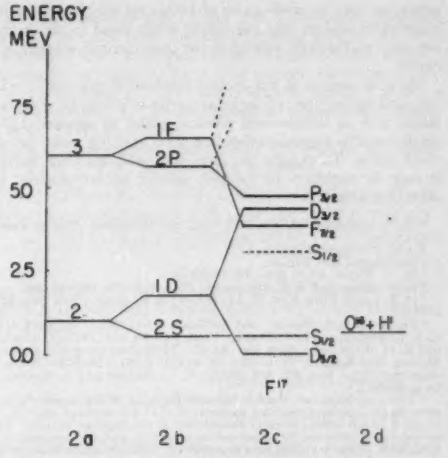

FIG. 2. Energy levels of the F^{17} nucleus. (a) The second and third excited levels of a harmonic potential. (b) The corresponding levels of the nuclear potential showing removal of degeneracy in L. (c) The ground state and known excited levels in F^{17}. The second $S_{1/2}$ level is probably not a single particle level. The splitting and inversion of the $D_{5/2}D_{3/2}$ doublet is clearly shown and that of the $P_{3/2}P_{1/2}$ and $F_{7/2}F_{5/2}$ doublets is suggested. (d) The dissociation energy of $O^{16}+H^1$. The ground state of F^{17} is taken as the energy zero.

Resonance energies are determined by the behavior of the wave function at infinity. In order to relate the resonance energies to the specifically nuclear characteristic energies, one must make a correction for the effect of the part of the wave function which lies outside of the range of nuclear forces. These corrections are calculable[8] and are proportional to the reduced widths, but since we do not know the reduced widths of the ground states, we have presented the observed energy in every case. The magnitude of the

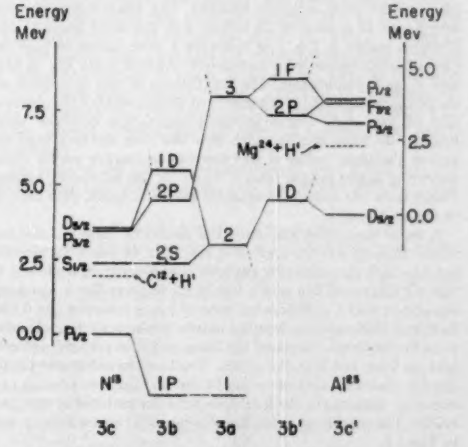

FIG. 3. Energy levels of the N^{15} and Al^{25} nuclei. (a) The first three excited levels of a harmonic potential. (b) and (b') Splitting of oscillator levels in N^{15} and Al^{25}, respectively, as a result of the departure of the nuclear potential from that of the harmonic oscillator. (c) Ground state and observed levels in N^{15}. (c') Ground state and observed excited levels of Al^{25}. The left ordinate measures energy from the ground state of N^{15} and the right ordinate measures energy from the ground state of Al^{25}.

correction may be of the order of 1 Mev for very broad levels. It is therefore evident that the energy levels listed in the diagrams are only qualitatively related to the characteristic energies of the nuclei.

These sequences of low excited states of simple nuclei exhibit two striking features: (1) large spin-orbit splitting; (2) good correlation with an independent particle model. It appears that the single particle approximation is a good starting point for more exact study. To explain the large spin-orbit splitting, however, it may be necessary to consider specific nucleon-nucleon spin-orbit interactions.[9]

* Work supported by the AEC and the Wisconsin Alumni Research Foundation.
† AEC Predoctoral Fellow.
‡ Kimberly-Clark Fellow.
[1] M. G. Mayer, Phys. Rev. **78**, 16 (1950).
[2] E. Feenberg and K. C. Hammack, Phys. Rev. **75**, 1877 (1949).
[3] D. R. Inglis, Phys. Rev. **82**, 181 (1951); R. K. Adair, Phys. Rev. **82**, 750 (1951).
[4] Freier, Lampi, Sleator, and Williams, Phys. Rev. **75**, 1345 (1949); C. L. Critchfield and D. C. Dodder, Phys. Rev. **76**, 602 (1949); G. Goldhaber and R. M. Williamson, Phys. Rev. **82**, 495 (1951); Laubenstein, Laubenstein, Mobley, and Koester, Phys. Rev. **81**, 654(A) (1951); Bashkin, Petree, and Mooring, Phys. Rev. **82**, 378 (1951); H. L. Jackson and A. Galonsky, to be published.
[5] These analyses are feasible because the spin of the target nucleus is zero; hence, the total angular momentum J of a compound state is $L \pm \frac{1}{2}$, where L is the orbital angular momentum of the incident particle. The $\pm$ ambiguity is removed by conservation of parity, and the designation of a level by S, P, D, $\cdots$ is merely a statement of this fact, which does not imply that orbital angular momentum is conserved.
[6] Mooring, Goldberg, Kaufmann, Koester, and Saxon (to be published).
[7] E. P. Wigner and L. Eisenbud, Phys. Rev. **72**, 29 (1947); T. Teichmann, Ph.D. Dissertation, Princeton (1949).
[8] J. B. Ehrmann, Phys. Rev. **81**, 412 (1951).
[9] C. H. Blanchard and R. Avery, Phys. Rev. **81**, 35 (1951).

Proton-Proton Scattering Near 30 Mev*

FRANKLIN L. FILLMORE†
Radiation Laboratory, Department of Physics, University of California, Berkeley, California
(Received July 9, 1951)

THE work reported in an earlier paper[1] has been continued with a few improvements in technique. The entire apparatus was completely overhauled, and mechanical tolerances in the plate holder were carefully checked. The beam collimator was lengthened to a total of 21 inches, and the three graphite diaphragms shown in Fig. 7 of reference 1 were spaced so that the photographic plates were completely shielded from the $\frac{1}{16}$-inch and $\frac{1}{32}$-inch diaphragms. The lengthening of the collimator reduced the background of slit scattered tracks, making the observation of low angle tracks in the photographic emulsion more reliable. By using swaths which were less than one inch from the axis of the plate holder it was possible to observe tracks whose scattering angles ranged from 5° to 82° in the laboratory system. Plates from the same photographic emulsion batch were used as in the earlier work.

A set of three runs was made and results of these are reported below. Run 46 was the scattering run. Run 44 was a background run in which the scattering chamber was evacuated, while run 47 was a background run which was in all respects like a scattering run except that a molybdenum tube of $\frac{3}{4}$ inch diameter and 0.030-inch wall thickness was inserted axially in the scattering chamber so as to completely surround the beam and thus prevent scattered protons from reaching the plates. Tracks observed in the photographic plates for this run must be due to knock-on protons produced by neutrons in the hydrogen or in the material of the plate holder. The conditions prevailing during each run are summarized in Table I.

The criteria for reading tracks were the same as described in Sec. III-B of reference 1. Each swath was 2.300 inches long and 127±0.5 microns wide. The tracks were counted by Mr. R. C. Terzian, to whom the author is greatly indebted, and over half of the counts were checked by the author to determine the reliability of the counting. In order to speed the gathering of data in the region of small scattering angles, it was decided to try counting only tracks whose scattering angles were in the intervals 5° to 26° and 64° to 82° in the laboratory system. However, after twelve swaths had been counted in this manner, it was decided that the increase in speed was too small to justify the decrease in the reliability of counting tracks, so the method was abandoned. This accounts for the low number of tracks shown in Table I for the angular interval from 26° to 64°. All 1129 of the tracks counted in this manner were checked by the author, as were half of the swaths in which all of the tracks were counted. Since the number of tracks missed by Mr. Terzian amounted to only 1.5 percent, it was assumed in the cross section calculation that no tracks were missed on swaths which were counted by both observers. The number of tracks missed by Mr. Terzian on twelve swaths is given in column 3 of Table II. Column 4 is included to show that the two observers disagreed on only 0.56 percent of the tracks checked.

TABLE I. Summary of runs.

Run No.	Type of run	Time for pressure to reach 10^{-4} mm (sec)	Temp. (°C)	Pressure (mm of Hg)	Charge collected (coulombs X10⁹)	Number of swaths scanned
44	background	0.6	···	10^{-4}	1.095	8
46	scattering	0.5	19.1	764.1	1.083	36
47	background	0.4	19.1	764.1	1.065	8

In order to enable the reader to visualize the types of all tracks on the plates a random swath $\frac{1}{4}$ inch long was scanned on each of the six plates of run 46. Of a total of 689 tracks of all kinds observed, 360 were judged to represent bona fide scattered protons, 320 were obviously no good, and 9 were spurious tracks which although appearing good failed to conform to all four of the criteria for good tracks.

As was shown in reference 1, the number of scattered protons should be symmetric about 45° in the laboratory system. Data in column 2 of Table II show that this is so, particularly at low scat-

TABLE II. Summary of data.

Angular interval (θ_{lab})	Total number of tracks counted	Number of tracks missed in 12 swaths by R.C.T.	Number of tracks on 12 swaths on which F.L.F. and R.C.T. disagreed	Number of tracks in both background runs
5° to 6°	60	2	0	2
6° to 10°	204	7	0	0
10° to 14°	246	4	2	0
14° to 18°	343	5	0	0
18° to 22°	463	5	0	0
22° to 26°	576	2	2	0
26° to 30°	436	2	1	1
30° to 34°	455	0	0	0
34° to 38°	527	2	0	0
38° to 42°	523	1	0	0
42° to 48°	761	0	0	0
48° to 52°	506	2	1	0
52° to 56°	483	1	1	0
56° to 60°	430	0	1	0
60° to 64°	398	0	1	0
64° to 68°	525	1	2	0
68° to 72°	464	0	4	0
72° to 76°	338	1	3	1
76° to 80°	267	2	0	3
80° to 82°	82	14	1	0
Total	8087	51	19	7

Of the 8087 tracks counted, 1129 were on swaths where tracks with scattering angles from 26° to 64° were omitted, 3432 of the remaining were checked by F.L.F., and 3526 were unchecked.

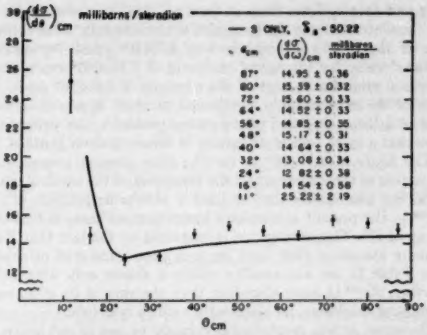

FIG. 1. Data based on 8087 tracks tabulated from run 46. The probable errors indicated on the graph are just those due to statistics. The s-wave curve shown was taken from Fig. 17 of reference 1 and is included here in order to facilitate the comparison of the present data with the earlier results.

tering angles. While the data near 45° do not show as good symmetry as one might hope, it is felt that the lack of symmetry is not serious and is accounted for statistically.

The primary energy was determined by the method described in reference 1. The range and scattering angle was measured for 202 tracks and a plot made from which the mean range at 45° was found to be 1120±4.3 microns. This corresponds to an energy of 30.14±0.08 Mev before scattering.

The cross sections were calculated by reflecting the raw data about 45° in the laboratory system and then applying Eq. (20) of reference 1 to each angular interval. This was done for each pair of swaths and the results averaged to give the uncorrected cross section. Corrections for background and number of tracks missed were then applied, giving the final results which are plotted in Fig. 1. The relative probable errors which are shown in Fig. 1 were obtained from the counting statistics. The probable error of the absolute cross section was found in the manner described in reference 1 to be 2.68 percent. The error due to lack of beam centering in the scattering chamber was found to be less than 0.2 percent. This correction was not applied to the cross section.

As can be seen from Fig. 1, these results do not conflict with the results reported earlier.[1,2] The high cross section at low angles which was not investigated in the earlier work is in qualitative agreement with expectations.

* This work was performed under the auspices of the AEC.
† Now with North American Aviation, Inc.
[1] Franklin L. Fillmore, Phys. Rev. 79, 57 (1950).
[2] Franklin L. Fillmore, Phys. Rev. 79, 71 (1950).

j-j Coupling Shell Model and Beta-Decay

H. HORIE AND M. UMEZAWA
Physics Department, University of Tokyo, Tokyo, Japan
(Received June 12, 1951)

BECAUSE of the success of the nuclear shell structure,[1] it seems probable that the individual particle model for nuclear structure has been given a rather strong foundation. However, Wigner's concept of supermultiplets[2] does not hold, since there is a strong spin-orbit interaction according to Mayer's shell model. On the other hand, we may assume charge independence of nuclear forces so far as the nuclear structure is concerned. Therefore, the charge multiplicity of nuclear states is still a good quantum number, especially for light nuclei.

We calculate the nuclear matrix elements for allowed β-transitions based on the above-mentioned assumptions. According to Fermi's β-decay theory,[3] the nuclear matrix elements related to the allowed transitions are $\int 1$ and $\int \sigma$. These matrix elements, except for the radial parts (for the time being we shall not write them explicitly), are evaluated in the TJT_fM_J-scheme, where T is the charge multiplicity, J the total angular momentum, T_f is the third component of T (i.e., half of neutron excess), and M_J is the z component of J. The calculations are similar to the atomic case in the SLM_SM_L-scheme.

In the j^n configurations, these matrix elements for the transitions $j^nTJT_f \to j^nT'J'T_f \pm 1$ are given as follows:

$$|\int 1|^2 = |(TJT_f \pm 1 M_J | \Sigma_i \tau_i^{\pm} | TJT_f M_J)|^2 = (T \mp T_f)(T \pm T_f + 1),$$

$$|\int \sigma|^2 = [3/(2J+1)] \Sigma_{M_J} |(T'J'T_f \pm 1 M_J | \Sigma_i \tau_i^{\pm} \sigma_{iz} | TJT_f M_J)|^2$$
$$= [2/(2J+1)] (j \| \sigma \| j)^2 (j^n T'J' \| V^{(\sigma\tau)} \| j^n TJ)^2 V(T'T1; -T_f \pm 1 T_f \pm 1)^2,$$

where the notation of Racah[4] is used and the values of $(j\|\sigma\|j')$ are given in the following formulas. When $n=1$ (one particle case), they become

$$|\int 1|^2 = 1,$$

$$|\int \sigma|^2 = (1/2j+1)(j\|\sigma\|j)^2 = \begin{cases} (2l+3)/(2l+1) & (j = l+\frac{1}{2}) \\ (2l-1)/(2l+1) & (j = l-\frac{1}{2}) \end{cases}.$$

For, other configurations, we may evaluate the matrix elements by a trivial generalization. For example (for the one-particle case), we have

$$|\int \sigma|^2 = (1/2j+1)(j'\|\sigma\|j)^2 = \begin{cases} 4l/(2l+1) & (j = l+\frac{1}{2} \to j' = l-\frac{1}{2}) \\ 4(l+1)/(2l+1) & (j = l-\frac{1}{2} \to j' = l+\frac{1}{2}) \end{cases}.$$

Of course, these results agree with those of Konopinski. We have calculated the matrix elements for more complicated configurations when they were necessary, but do not show them all here for the sake of simplicity.

The squares of total matrix elements $|M|^2$ for allowed β-transitions should be linear combinations of $|\int 1|^2$ and $|\int \sigma|^2$ which are evaluated above. By the relation

$$ft|M|^2 = 2\pi^3 \log(2/G^2),$$

the experimental ft values multiplied by $|M|^2$ should be constant for all allowed β-transitions, though there are still ambiguities of $|M|^2$ caused by radial overlapping. For β-transitions of mirror nuclei, we examined this situation, taking $|M|^2$ as $|\int 1|^2$ and $|\int \sigma|^2$ separately. The results are shown in Table I. We see at once the values of $ft/|\int \sigma|^2$ vary too violently even if the variation of radial overlapping is taken into account. On the contrary, $ft/|\int 1|^2$ show fairly constant values. Therefore, it seems reasonable to consider that the Fermi-type interaction is the main part of the allowed β-transitions and that the Gamow-Teller one is subsidiary.

For most of the allowed β-transitions of even nuclei and odd nuclei other than mirror nuclei, only the matrix element $\int \sigma$ is

TABLE I. β-decay of mirror nuclei.[a]

	Configuration	$ft/\lvert\int 1\rvert^2/10^3 = ft/10^3$	$\lvert\int\sigma\rvert^2$	$ft/\lvert\int\sigma\rvert^2/10^3$
$n \to H^1$	$(s_{1/2})^1$	1–3	3	3–9
$H^3 \to He^3$	$(s_{1/2})^{-1}$	1.1	3	3.3
$C^{11} \to B^{11}$	$(p_{1/2})^{-1}$	3.9	5/3	6.5
$N^{13} \to C^{13}$	$(p_{1/2})^1$	4.8	1/3	1.6
$O^{15} \to N^{15}$	$(p_{1/2})^{-1}$	3.7	1/3	1.2
$F^{17} \to O^{17}$	$(d_{5/2})^1$	2.2[b]	7/5	3.1
$Ne^{19} \to F^{19}$	$(s_{1/2})^{-1}$	2.0	3	6.1
$Si^{27} \to Al^{27}$	$(d_{5/2})^{-1}$	3.6	7/5	5.0
$P^{29} \to Si^{29}$	$(s_{1/2})^1$	3.8	3	11.4
$S^{31} \to P^{31}$	$(s_{1/2})^{-1}$	3.4	3	10.2
$Cl^{35} \to S^{35}$	$(d_{3/2})^1$	4.0	3/5	2.4
$A^{35} \to Cl^{35}$	$(d_{3/2})^0$	3.4	121/375	1.1
$Sc^{41} \to Ca^{41}$	$(f_{7/2})^1$	2.6	9/7	3.3

[a] The ft-values used are calculated by making use of G. L. Trigg and E. Feenberg's curves (see reference 5).
[b] The maximum energy of F^{17} decay is taken from Natl. Bur. Standards (U. S.) Circ. 499 (1950).

TABLE II. β-decay of even-mass nuclei.

	Configuration	ft	$\lvert\int\sigma\rvert^2$	$ft\lvert\int\sigma\rvert^2$
$He^6 \rightarrow Li^6$	$(p_{3/2})^2$	590	10/3	2.0×10^3
$B^{12} \rightarrow C^{12}$	$(p_{3/2})^{-1}(p_{1/2})^1 \rightarrow (p_{3/2})^2$	1.4×10^4	16/9	2.5×10^4
$N^{12} \rightarrow C^{12}$	$(p_{3/2})^{-1}(p_{1/2})^1 \rightarrow (p_{3/2})^2$	1.5×10^4	16/9	2.6×10^4
$F^{18} \rightarrow O^{18}$	$(s_{1/2})^2$	3.7×10^3	2	7.4×10^3
$Al^{28} \rightarrow Mg^{28}$	$(d_{5/2})^{-2}$	2.3×10^3	14/15	2.2×10^3
$P^{34} \rightarrow Si^{34}$	$(s_{1/2})^2$	5.1×10^3	2	1.0×10^4
$Cl^{34} \rightarrow S^{34}$	$(d_{3/2})^2$	9.9×10^3	2/5	4.0×10^3

nonvanishing. Since assignment of the configurations are rather difficult for these nuclei and most of the spins of odd-odd nuclei have not yet been determined experimentally, we could not obtain as definite a conclusion as was obtained from mirror nuclei. Some of the $ft|\int\sigma|^2$ are shown in Table II. In Table II the $(p_{3/2})^2$ configuration assigned to He^6 and Li^6 yields extremely poor results for the magnetic moment and quadrupole moment of Li^6. However, we adopt it for these nuclei for the sake of simplicity. Detailed investigations of the magnetic moment, quadrupole moment of Li^6, and the transition $He^6 \rightarrow Li^6$ will be published soon by one of the authors (H) and S. Yoshida.

As seen in Table II, three elements, that is to say, He^6, F^{18}, and Al^{28} have ft values of the order 10^3. But, as was pointed out by Feenberg,[5] among all direct transitions of even nuclei there are only three which have ft value of the order 10^3, so it may be justifiable to treat the three elements mentioned above as exceptional cases. If so, $ft|\int\sigma|^2$ becomes one order greater than $ft|\int 1|^2$, and the result concerning even nuclei may be said to be compatible with the one concerning mirror nuclei. However, if it is not permitted to treat them as exceptions, our results contradict that of Moszkowski.[6] But, it should be noted that his analysis is limited only to the comparison of $ft|M|^2$ for $H^2 \rightarrow He^3$, $He^6 \rightarrow Li^6$ and for the branching K-capture of $Be^7 \rightarrow Li^7$ and disregards other allowed transitions.

Thus, in order to explain the shape of β-ray spectra and the ft values (or $ft|M|^2$), the following type of matrix elements are necessary: 1 (mirror nuclei), $\int\sigma$ (even mass nuclei), B_{ij} (a-shape spectra of Y^{90}, Sr^{90}, etc.), S_{ijk} (c-type spectrum of B^{10}), S_{ijkl} (K^{40}), and probably A_{ij}, T_{ij} (Cl^{38}, RaE^{210}, Tc^{99}). In order to include all these matrix elements, more than two interactions are necessary; that is, (I) T and one of S or V interactions, or (II) V and A V interactions are necessary.

It is interesting to note the following. In the meson theory of β-decay, a vector τ-meson with V and T coupling is permitted in the analysis of various decay processes.[7] Recently, it has been shown by Nakamura that such a meson theory of β-decay includes all the matrix elements mentioned above.[8] Thus, the vector τ-meson with V and especially T coupling is consistent with the facts discussed above.

Our thanks are due to Professors S. Nakamura and T. Yamanouchi for their helpful discussions.

[1] E. Feenberg and K. C. Hammack, Phys. Rev. 75, 1877 (1949); L. W. Nordheim, Phys. Rev. 75, 1894 (1949); M. G. Mayer, Phys. Rev. 78, 16 (1950); Umezawa, Nakamura, Ono, Yamaguchi, and Taketani, Prog. Theor. Phys., to be published.
[2] E. Wigner, Phys. Rev. 51, 106 (1937).
[3] E. J. Konopinski, Revs. Modern Phys. 15, 209 (1943).
[4] G. Racah, Phys. Rev. 62, 438 (1943).
[5] E. Feenberg and G. Trigg, Revs. Modern Phys. 22, 399 (1950).
[6] S. A. Moszkowski, Phys. Rev. 82, 118 (1951).
[7] Private communication from S. Nakamura and Y. Tanikawa; R. Caianiello, Phys. Rev. 81, 625 (1951).
[8] S. Nakamura, to be published.

I^{129} and the Age of the Elements

H. E. SUESS AND HARRISON BROWN
Institute for Nuclear Studies, University of Chicago, Chicago, Illinois
(Received July 30, 1951)

IN a recent paper of considerable importance, Katcoff, Schaeffer, and Hastings[1] reported the half-life of I^{129} to be $(1.72\pm0.09)\times10^7$ years. Combining this result with relevant geochemical data and assumptions, these authors conclude that the length of the time interval from the formation of the elements to the formation of the earth's atmosphere was 2.7×10^8 years. By adding Holmes' value for the age of the earth of 3.35×10^9 years, they obtain a value for the age of the elements of 3.6×10^9 years. In view of the extraordinary significance of these figures in a wide field of astronomical and cosmogonical problems, the writers believe that a more critical discussion of these values is justified.

The figure of 2.7×10^8 yr for the time interval between the formation of the elements and the formation of the earth is based upon the assumption that at least a noticeable fraction of the Xe^{129} in the present atmosphere has originated from radioactive decay of I^{129}. This assumption is suggested by the fact that Xe^{129} is more abundant than both its even mass numbered neighbors (see Table I), an abnormality which it shares only with Pt^{195}. Further, Xe^{129} is more abundant than the sum of its even mass numbered neighbors, an abnormality which is unique.

However, as was mentioned previously by one of us,[2] it can be shown by a careful study of the systematics of nuclear abundances that this abnormality can be explained in a way other than by assuming a radiogenic origin of atmospheric Xe^{129}. It can then be seen that in the case of xenon the even isotopes 128 and 130 have an abnormally low abundance, whereas the abundance curve for the odd nuclei shows only a flat maximum in this region and no marked irregularity. The reason for the exceptionally low abundance of Xe^{128} and Xe^{130} might then be interpreted in the following way: both isotopes are "shielded" by stable tellurium isotopes. It is a general rule that in this mass region "shielded" isotopes always have a lower cosmic abundance than their unshielded isotopes. This rule is one of the indications which justify the assumption that the nuclei in this mass region have, in substantial fraction, originally been formed from their neutron-rich β^- unstable isobars.[3]

In the tellurium-xenon region this "shielding" apparently was more effective than elsewhere. The ratios of the abundances of unshielded to shielded isobars are exceptionally large if one determines the elementary abundances by interpolation. Possibly this effect is connected with the filling of the $g_{9/2}$ proton shell, the $h_{11/2}$ neutron shell and the resulting large spin values of the unstable odd-odd nuclei in this region. It is to be expected from Mayer's theory[4] that the "pairing energies" and therefore the "even-odd" effect in this region will be correspondingly large.

The possibility that the abundance of Xe^{129} is not abnormally high, but that instead the abundances of Xe^{128} and Xe^{130} are abnormally low, can most easily be seen from the fact that Xe^{131} possesses about the same abundance as does Xe^{129}.

The possibility that a fraction of the atmospheric Xe^{129} was produced by decay of I^{129} cannot, of course, be excluded. We wish to stress, however, that in view of the present state of our knowledge of abundance regularities, radiogenic origin of atmospheric Xe^{129} can by no means be proved. As a result, the value of 2.7×10^8 years given by Katcoff, Schaeffer, and Hastings should be interpreted only as an approximate lower limit for the time interval between the formation of the elements and the formation of the earth's atmosphere.

We would like to point out in addition that the actual lower limit might be somewhat higher than that given by Katcoff, Schaeffer, and Hastings. They have assumed that the fraction of

TABLE I. Relative abundances of tellurium and xenon isotopes in percent (in mass number region 124 to 132).

Te^{124}	Te^{125}	Te^{126}		Te^{128}		Te^{130}		
4.6	7.0	18.7		31.8		34.3		
			I^{127} 100					
Xe^{124} 0.094		Xe^{126} 0.088		Xe^{128} 1.91	Xe^{129} 26.2	Xe^{130} 4.06	Xe^{131} 21.2	Xe^{132} 26.9

Xe^{129} liberated is about the same as the fraction of A^{40} liberated. Actually, in view of the probability that the earth was in considerable upheaval during its early history, one might expect nearly all of the Xe^{129} formed from iodine since the origin of the earth to have found its way into the atmosphere. As the total iodine content of the earth is probably of the order of 1000 g/cm² of earth surface, the lower limit for the interval would be raised by about 50 percent to 4×10^8 years.

[1] Katcoff, Schaeffer, and Hastings, Phys. Rev. 82, 688 (1951).
[2] H. E. Suess, Z. Physik 125, 386 (1948); Experientia 5, 376 (1949).
[3] For references, see R. A. Alpher and R. C. Herman, Revs. Modern Phys. 22, 153 (1950).
[4] M. G. Mayer, Phys. Rev. 78, 22 (1950).

Magneto-Optics of an Electron Gas for Guided Microwaves: Propagation in Rectangular Wave Guide*

L. Goldstein, M. Lampert, and J. Heney
Federal Telecommunication Laboratories, Inc., Nutley, New Jersey
(Received July 6, 1951)

WE have previously described[1] magneto-optical effects in microwave propagation experiments in circular wave guide. The magneto-electronic medium in the guide was an electron gas immersed in a uniform dc magnetic field parallel to the axis of the guide. The main experimental results consisted of polarization transformations of a TE_{11} wave initially launched in the guide with linear polarization. The results were interpreted satisfactorily in terms of the different propagation characteristics in the anisotropic medium of the two oppositely-rotating, circularly-polarized TE_{11} modes which the empty circular guide supports.

The purpose of this note is to describe the results of propagation experiments with the same magneto-electronic medium in rectangular wave guide. Both the results and their interpretation are quite different from those briefly mentioned above. In this case, the empty guide, at the frequency employed, supports only one propagating mode, namely the TE_{10} mode, so that no polarization transformations can take place. The relevant propagation measurements in the empty guide outside of the medium are those of the amplitudes and phases of the transmitted and reflected waves. The main results of these measurements are—(1) very large attenuations of the signal in the region of magnetic field intensities where the gyrofrequency of the electrons approximates the signal frequency; (2) large reflections at magnetic field intensities immediately on either side of gyroresonance; and (3) small or negligible reflection at gyroresonance. Thus, the very large attenuation at gyroresonance appears to be the result of absorption in the medium, in accordance with theoretical prediction. In the accompanying figure these results are illustrated for a particular experiment under conditions there indicated.

Further results are—(1) increasing the gas pressure tends to widen the resonance and decrease its magnitude; (2) at sufficiently low pressure (below about 0.1 mm Hg in our experiments) the width of resonance appears to be determined by other factors than pressure, such as non-uniformity of magnetic field in the medium; and (3) the phase of the reflected wave varies very sharply in the gyroresonance region. That these results are essentially independent of the gas is evidenced by the fact that similar phenomena were observed also in Kr, Xe, H_2, and Hg vapor.

The resonance curves have precisely the shape to be expected from the typical anomalous dispersion of the dielectric constant in the region of a proper frequency of the medium, here the electron gyrofrequency. The anomalous dispersion of the magneto-electronic medium has been previously established[2] at lower frequencies. However, in our experiments the length of the anisotropic medium exceeded two free-space wavelengths; so that true propagation phenomena have been observed.

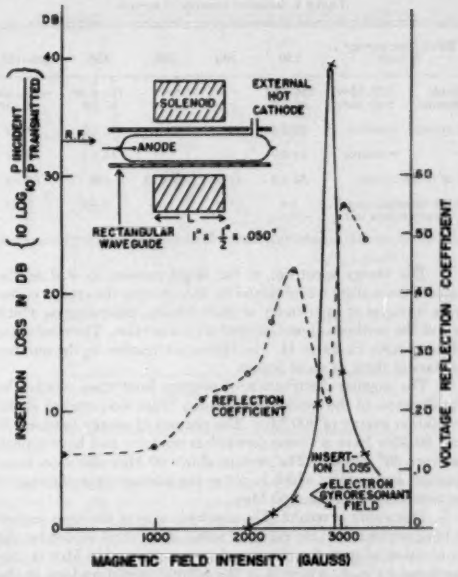

FIG. 1. Transmission and reflection characteristics vs magnetic field intensity. Signal frequency: 8200 Mcps. Gas: Ne+1 percent A at 0.1 mm Hg pressure. Discharge conditions: steady dc plasma at 465 v and 30 ma (current limiting resistor of 10,000 ohms included). Length L of solenoid = 5 inches (approximately 2 guide wavelengths).

We believe that the observed phenomena are general, to the extent that they are characteristic of electromagnetic wave propagation in the magneto-electronic medium (with longitudinal magnetic field) in any guiding system that supports only a single mode of propagation at the frequency employed.

* This work was sponsored by the Signal Corps.
[1] Goldstein, Lampert, and Heney, Phys. Rev. 82, 956 (1951).
[2] S. Benner, Naturwiss. 17, 120 (1929); H. Gutton, Ann. phys. 13, 62 (1930); L. Tonks, Phys. Rev. 37, 1458 (1931); E. Appleton and F. Chapman, Proc. Phys. Soc. (London) 44, 246 (1932).

On the Photonuclear Dissociation of Nuclei by High Energy Gamma-Rays*

Seishi Kikuchi
Laboratory of Nuclear Studies, Cornell University, Ithaca, New York
(Received July 25, 1951)

THE stars produced in photographic emulsions exposed directly to a beam of synchrotron gamma-rays were analyzed further by using 600-micron G5 emulsions.[1] The results are summarized as follows.

1. Table I shows the relative frequency of appearance of different sorts of events. The values corresponding to the different energy of excitation are normalized to the same number of equivalent quanta using the previous data.[1] The meson coming out of a star was identified chiefly by multiple scattering measurements.

2. The absolute cross section averaged over light and heavy atoms, except hydrogen, was redetermined carefully at the excitation energy of 300 Mev. It came out to be $6.1\pm0.3\times10^{-27}$ cm² per equivalent quantum for stars of three or more prongs.

TABLE I. Relative number of events.

Excitation energy in Mev		150	200	250	300	300–150
Single protons	<20 Mev	256±64	···	···	170±20	−86±67
	>20 Mev	45±6	···	···	47±8	2±10
2 prongs	positive	20±3	···	···	47±6	27±7
	probable	11±2	···	···	46±7	35±7
3 or more prongs		32±4	42±4	93±13	100	68±4
Stars from which a meson comes out		~0	···	···	5±2	5±2

3. The energy spectrum of the single protons as well as the protons from stars was obtained by determining the energy either from its range or gap density or grain density, depending on which one of the methods gives the most accurate value. The results are given roughly in Table II. The figures are relative to the number of stars of three or more prongs.

4. The angular distribution of protons from stars relative to the direction of the incident gamma-ray beam were studied at the excitation energy of 300 Mev. The protons of energy between 20 and 60 Mev have a strong forward asymmetry and have a peak between 30° and 60°. The protons above 60 Mev also show some forward asymmetry, which is not so conspicuous as in the case of protons between 20 and 60 Mev.

5. Discussion of results. The absolute value of the cross section is in agreement with the expected value, if the cross section for the production of stars for photons of energy above 150 Mev is proportional to $\sigma_m A$, where A is the atomic weight and σ_m is the cross section for the photomeson production by a nucleon including both the charged and neutral mesons. The percentage of the stars from which a meson is coming out is about twice as small as the value expected from the known data. This might be due to the fact that the mesons starting in the emulsion without being associated with a star were not taken into account in the figures given in Table I.

The forward asymmetry of the angular distribution of the protons of energy between 20 and 60 Mev in the case of 300-Mev excitation can be explained by assuming that they are mostly those protons which are knocked out by the primary process, in which a meson is produced by the interaction of a photon with a nucleon. If the high energy protons above 60 Mev are due to the absorption of a meson, their angular distribution should be more or less isotropic, contrary to the result. But the interpretation of the angular distribution of the protons of this group is expected to be fairly complicated. For the protons of this group might consist partly of protons knocked out by the meson producing process, partly of protons produced by the absorption of a meson, partly of the prongs confused with mesons, and finally of protons produced by electromagnetic photodissociation, if any.

These results, together with the excitation curve for star production obtained previously, indicate that most of the stars produced by the photons of energy between 150 and 300 Mev are due to the production and absorption of a meson inside the nucleus. The fact that the number of single protons is rather small compared with the number of protons from stars indicates that the high energy photoprotons excited by the high energy gamma-rays observed by other people[2] by counter methods are likely to have come from stars.

Thanks are due to Professor R. R. Wilson, Professor H. A. Bethe, and Mr. S. Hayakawa and other members of the Laboratory for valuable discussions. Thanks are also due to the crews of the microscope laboratory for the scanning of plates.

TABLE II. Energy distribution of protons.

Excitation energy in Mev	Single protons		Protons from stars	
	Between 20 and 60 Mev	Above 60 Mev	Between 20 and 60 Mev	Above 60 Mev
300	0.38±0.07	0.05±0.03	0.56±0.05	0.18±0.04
150	1.5±0.2 (>20 Mev)		0.45±0.08 (>20 Mev)	

* This work was done under ONR contract.

[1] S. Kikuchi, Phys. Rev. **80**, 492 (1950); **81**, 1060 (1951).

[2] C. Levinthal and A. Silverman, Phys. Rev. **82**, 822 (1951); D. Walker, Phys. Rev. **81**, 634 (1951); J. Keck (to be published).

On the Angular Distribution and the Polarization of the Deuteron in the Reaction $p+p\rightarrow d+\pi^+$

K. M. WATSON AND C. RICHMAN
*Radiation Laboratory, University of California, Berkeley, California**

(Received July 27, 1951)

CROSS sections at several angles for the reaction $p+p\rightarrow\pi^++d$ have been measured.[1-3] For energies not too far above threshold (i.e., for those at which the cross sections have been measured) and in the center-of-mass frame of reference, there is reason to believe[4,5] that only orbital S- and P-states of the meson with respect to the deuteron contribute appreciably to the cross section.

There will be no S- and P-wave interference in the differential cross section, so for the moment we can restrict our considerations to just the contribution from meson P-waves. Combining the intrinsic angular momentum of the deuteron with the P-wave orbital motion, we obtain a total angular momentum $j=0, 2$ ($j=1$ is forbidden by parity considerations[5] if the meson is assumed to be pseudoscalar, in accord with present evidence). These values of j arise from the $^1S_0$ and $^1D_2$ states, respectively, of the initial $p-p$ system.

The wave functions for the orbital motion of the meson will then be described by the spherical harmonics $Y_1^\mu(\theta,\phi)$ (with the polar axis defined by the proton beam direction), and those of the internal coordinates of the deuteron by Σ_1^μ ($\mu=1, 0, -1$). Then the linear combinations of these, Q_0 and Q_2^0, which transform as a scalar and as the spherical harmonic Y_2^0, will arise from the $^1S_0$ and $^1D_2$ states, respectively, of the initial $p-p$ system.

The asymptotic form of the outgoing wave will be proportional to

$$(e^{iqr}/r)[Q_0+\eta Q_2^0], \tag{1}$$

where q is the meson momentum and η is a parameter. If one writes $\eta=\epsilon e^{i\sigma}$, the resulting angular distribution of the mesons will be

$$F(\theta)=1+\tfrac{1}{2}\epsilon^2+\sqrt{2}\epsilon\cos\sigma+3\cos^2\theta(\tfrac{1}{2}\epsilon^2-\sqrt{2}\epsilon\cos\sigma). \tag{2}$$

Including an arbitrary amount of contribution to the cross section from mesons in S-states, we arrive at the following generalization of the cross section given previously:[4]

$$d\sigma=\sigma_0(d\Omega/4\pi)[1+a(q^2/\mu^2c^2)F(\theta)], \tag{3}$$

where $F(\theta)$ is given by Eq. (2) and μ is the mass of the meson. Near threshold it is assumed that a is a constant and that σ_0 is just q (from the phase space factor) times a constant. Integrating, we obtain the total cross section

$$\sigma=\sigma_0[1+a(1+\epsilon^2)(q^2/\mu^2c^2)], \tag{4}$$

which is of the specific form given previously,[4] with $a(1+\epsilon^2)=b$. We see that ϵ^2 represents the relative amounts of $^1S_0$ and $^1D_2$ contribution of the initial $p-p$ system to the P-wave partial cross section.

The approximate value, $b=8$, was deduced earlier.[4] This value is consistent with the observed angular distribution,[3] which however implies that b cannot be much less than 8. From the experimental cross sections,[3] it would then follow that at 340 Mev, $\sigma_0\simeq 5(10)^{-30}$ cm^2. The observed angular distributions are consistent with a pure $\cos^2\theta$ dependence from the meson P-states, which would imply $\cos\sigma=-1$, $\epsilon^2=2$ (the quoted experimental errors

imply that these relations are also quite approximate). Of more positive significance is the conclusion from the observed angular asymmetry that the large contribution from the $^1D_2$ state of the initial protons implies, independently of a specific model, that noncentral interactions are involved[8] (since the deuteron is mostly in an S-state).

Equation (1) suggests that the deuterons observed at an angle (Θ, Φ) may be polarized.[7] Indeed, the direction of the polarization is given by the average values of the components of intrinsic angular momentum of the deuteron, which are $J_x = -R\sin\Phi$, $J_y = R\cos\Phi$, $J_z = 0$ (i.e., at right angles to the plane defined by the direction of the protons and the deuterons).

The degree of polarization (considering just the P-wave component of the cross section), $R'(0<R'<1)$, is given by the numerical magnitude of

$$R = 3\sqrt{2}\,\epsilon \sin\sigma \cos\Theta \sin\Theta[F(\Theta)]^{-1}, \qquad (5)$$

where F is given by Eq. (2). R vanishes for a pure $\cos^2\theta$ angular distribution.

The detection of this polarization, if nonvanishing, would appear feasible. The beam of deuterons produced is more intense than the accompanying meson beam,[8] which has been used to study meson scattering.[9] A possible means of detection would be by means of (d, p) scattering, the polarization effects of which have been used by Wouters[10] to measure polarization in (n, p) scattering.

* This work was performed under the auspices of the AEC.
[1] Cartwright, Richman, Whitehead, and Wilcox, Phys. Rev. **78**, 823 (1950).
[2] Peterson, Iloff, and Sherman, Phys. Rev. **81**, 647(A) (1951).
[3] C. Richman and M. H. Whitehead, Phys. Rev. **83**, 855 (1951).
[4] Brueckner, Serber, and Watson, Phys. Rev. **81**, 575 (1951).
[5] K. Watson and K. Brueckner, Phys. Rev. **83**, 1 (1951).
[6] It has been noted previously by K. Brueckner, Phys. Rev. **82**, 598 (1951), that on the basis of meson theory one must assume that tensor forces are involved to give an angular asymmetry to the mesons produced.
[7] The authors are indebted to Professor R. Serber for the suggestion that the deuterons should be polarized.
[8] Richman, Skinner, Merritt, and Youtz, Phys. Rev. **80**, 900 (1950).
[9] M. Skinner and C. Richman, Phys. Rev. **83**, 217(A) (1951).
[10] L. Wouters (private communication).

Some Excitation Functions for Protons on Magnesium*

J. W. Meadows and R. B. Holt
Nuclear Laboratory, Harvard University, Cambridge, Massachusetts
(Received July 24, 1951)

In continuation of our study of proton-induced reactions on light and intermediate nuclei[1] we have determined the yield of Na^{22} as a function of energy for protons on Mg^{24}, Mg^{25}, and Mg^{26}. The experimental method has been previously described.[1,2]

Bombardments were made on natural MgO and on MgO enriched[3] in Mg^{25} and Mg^{26}, at initial energies of 100 and 70 Mev. Al metal foils were placed in the target stack with the MgO, and the Mg reactions were monitored by comparing them with the known excitation curve for $Al(p, 3pn)Na^{24}$ as measured by Hintz.[3] Bombardment times of approximately 12 hours were required to obtain sufficient activity for accurate counting. Since the half-life of Na^{24} is only 15 hours, some error may have been introduced by variations in the beam intensity during the bombardment.

The monitor foils were counted 24 hours after the end of the bombardment, when all activities with half-lives shorter than the 15-hour Na^{24} had disappeared. The MgO targets were counted after three weeks, when only the 2.6-year Na^{22} remained. The Al foils were also counted at this time, and the previous Na^{24} count was corrected for Na^{22} activity. All samples were counted, as nearly as possible, under the same geometry and mounting arrangements. Corrections were made for self-absorption and scattering and for absorption due to the air and counter window. The yield of Na^{22} from Mg^{24} was determined by subtracting the contributions of Mg^{25} and Mg^{26} from the yield obtained with the natural isotopic mixture. The results are shown in Fig. 1.

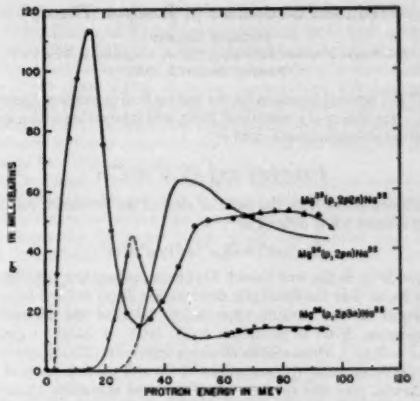

FIG. 1. Excitation function for protons on magnesium.

The thresholds to be expected, including the coulomb barrier heights, for the lowest energetically possible reaction and for single particle emission are shown in Table I. These lowest thresholds compare fairly well with the Mg^{25} and Mg^{26} excitation curves. However, accurate threshold energies cannot be determined by this method due to the thickness of the targets (20–30 mg/cm^2) and the finite energy spread of the beam (0.5 Mev) on the target face.

It is evident that the emission of alpha-particles is a major mode of decay of these compound nuclei at low energies. It might be expected that the emission of other heavy fragments such as H^3 or He^3 would also be an important mode of decay. This does not seem to be the case. The observed threshold for $Mg(p, 2pn)Na^{22}$ at 20–25 Mev indicates a $(p, 2pn)$ or (p, dn) reaction rather than (p, He^3). Also if the emission of H^3 or He^3 were very probable, the minimum found in $Mg^{25}(p, 2p2n)Na^{22}$ at 30 Mev should not be so pronounced.

TABLE I. Thresholds in the laboratory system.

Reaction	$-Q$	$-Q$+barrier
$Mg^{24}(p, He^3)Na^{22}$	16.6 Mev	22.5 Mev
$(p, 2pn)$	24.4	32.2
$Mg^{25}(p, \alpha)Na^{22}$	2.3	8.2
$(p, 2p2n)$	31.6	39.2
$Mg^{26}(p, \alpha n)Na^{22}$	14.1	20.0
$(p, 2p3n)$	43.3	50.9

* Assisted by the joint program of the ONR and AEC.
[1] J. W. Meadows and R. B. Holt, Phys. Rev. **83**, 47 (1951).
[2] N. M. Hintz, Phys. Rev. **83**, 185 (1951).
[3] Obtained from Oak Ridge National Laboratory, Oak Ridge, Tennessee.

Erratum: Non-Equilibrium Thermodynamics of Two-Fluid Models

[Phys. Rev. **81**, 1070 (1951)]

S. R. De Groot, L. Jansen, and P. Mazur
Institute for Theoretical Physics, The University, Utrecht, The Netherlands

The line following Eq. (1) should read: "between the two effects (v is the specific volume). We can derive. . . ."

Fredholm Structures in Positron Theory*

MAURICE NEUMAN
Brookhaven National Laboratory, Upton, Long Island, New York
(Received August 2, 1951)

THE integral equation for the matter field in positron theory—the theory of a quantized Dirac field interacting with a given external electromagnetic field—

$$\psi(x)=\psi_0(x)+e\int K^F(xx')\psi(x')dx' \tag{1}$$

was investigated from the point of view of the Fredholm method.[1] The symbol K^F is defined as

$$K_{\alpha\beta}{}^F(xx')\equiv iS_{\alpha\sigma}{}^F(xx')\gamma_{\sigma\beta}{}^\mu A^\mu(x'), \tag{2}$$

where $S^F(x)$ is the well-known Feynman propagation function. It was found that the Fredholm determinant $D_0(e)$ derived from (2) is equal to the vacuum expectation value of the Heisenberg S-operator. A set of operators $\Delta_0(e)$, $\Delta_1(e)$, $\cdots\Delta_n(e)\cdots$ [where $\Delta_0(e)=D_0(e)$], whose matrix elements $\langle x_1x_2\cdots x_n|\Delta_n(e)|y_1y_2\cdots y_n\rangle$ are determinantal representations of the nth particle parts of the S matrix, was also constructed. The set of operators $\{\Delta_n(e)\}$ is isomorphic to a set of operators $\{D_n(e)\}$ whose matrix elements $\langle x_1x_2\cdots x_n|D_n(e)|y_1y_2\cdots y_n\rangle$ are the nth Fredholm minors constructed on K^F. The set $\{\Delta_n(e)\}$ has many but not all of the functional properties of $\{D_n(e)\}$. The situation is somewhat similar to that obtaining between an ordinary exponential function and the chronologically ordered exponential of Dyson.

The properties of $\{D_n(e)\}$ have been extensively investigated in classical analysis. One can therefore utilize the isomorphism between $\{\Delta_n(e)\}$ and $\{D_n(e)\}$ to construct various representations of $\langle S\rangle_n$. The determinantal representation of $\{\Delta_n(e)\}$ are interesting in so far as they clearly exhibit the operation of the exclusion principle for real and virtual particles.

We shall illustrate the method by considering the somewhat trivial case of $\Delta_0(e)$ where the isomorphism degenerates into an equality $\Delta_0(e)=D_0(e)$.

We write

$$H=ieT(\psi_\alpha(x)\phi_\alpha(x)). \tag{3}$$

Here T is the ordering operator of Wick[2]

$$T(\psi_\alpha(x)\phi_\alpha(x'))=\theta(x^0-x'^0)\psi_\alpha(x)\phi_\alpha(x')-\theta(x'^0-x^0)\phi_\alpha(x')\psi_\alpha(x); \tag{4}$$

$\theta(x)$ is the usual step function: $\theta(|x|)=1$, $\theta(-|x|)=0$ for $x\neq0$; $\theta(0)=\frac{1}{2}$. The letter $\phi_\alpha(x)$ stands for $\bar\psi_\beta(x)\gamma_{\beta\alpha}{}^\mu A^\mu(x)$. We also have

$$\langle T(\psi_\alpha(x)\phi_\beta(x'))\rangle_0=-iK_{\alpha\beta}{}^F(xx'). \tag{5}$$

$\langle S\rangle_0$ may then be written as

$$\langle S\rangle_0=\sum_{n=0}^{\infty}[n!]^{-1}(-ie)^n\langle T[\psi(X_1)\phi(X_1)\cdots\psi(X_n)\phi(X_n)]\rangle_0, \tag{6}$$

where $\psi(X_1)=\psi_{\alpha(1)}(x_1)$, $\phi(X_1)=\phi_{\alpha(1)}(x_1)$ and all the repeated variables and indices are integrated and summed over, respectively. The convention $\theta(0)=\frac{1}{2}$ in the definition (4) guarantees the charge symmetry of Eq. (6). Wick's theorem[2] and Eq. (5) yield

$$\langle T[\psi(X_1)\phi(X_1)\cdots\psi(X_n)\phi(X_n)]\rangle_0 =(-i)^n\epsilon^{\alpha(1)\cdots\alpha(n)}K^F(X_1X_{\alpha(1)})\cdots K^F(X_nX_{\alpha(n)}), \tag{7}$$

and, consequently,

$$\langle S\rangle_0=D_0(e). \tag{8}$$

Having established contact with the Fredholm theory, we may now exploit the known properties of $D_0(e)$ to find another representation for $\langle S\rangle_0$. The integral equation for $f(x)$,

$$f=f_0+\lambda Kf, \tag{9}$$

is solved in the Fredholm theory by

$$f_0=f-\lambda[D_0(\lambda)]^{-1}D_1(\lambda)f_0. \tag{10}$$

Moreover,[3] we have

$$\mathrm{Tr}\,D_1(\lambda)=-D_0'(\lambda), \tag{11}$$

where the prime denotes differentiation with respect to the argument. Comparing (10) with the Liouville-Neumann solution,

$$f_0=f-\lambda[1-\lambda K]^{-1}Kf_0, \tag{12}$$

and making use of Eq. (11) and of $D_0(0)=1$, we immediately deduce the expressions

$$D_0(\lambda)=\exp[\mathrm{Tr}\log(1-\lambda K)], \tag{13}$$

$$D_1(\lambda)=K[1-\lambda K]^{-1}\exp[\mathrm{Tr}\log(1-\lambda K)]$$
$$=K\exp[\sum_{n=1}^{\infty}n^{-1}\lambda^n(K^n-\mathrm{Tr}\,K^n)]$$
$$=K\prod_{n=1}^{\infty}\exp[n^{-1}\lambda^n(K^n-\mathrm{Tr}\,K^n)]. \tag{14}$$

For $\langle S\rangle_0$ we get

$$\langle S\rangle_0=\exp[\mathrm{Tr}\log(1-eK^F)]. \tag{15}$$

Expression (15) could be derived more simply by an elegant method due to Glauber,[4] but the connection with the Fredholm theory is then somewhat obscured.

The author is grateful to Dr. E. J. Kelly and Dr. H. S. Snyder for many discussions and criticisms.

* Research carried out at Brookhaven National Laboratory, under the auspices of the AEC.

[1] R. Courant and D. Hilbert, *Methoden der Mathematischen Physik*, second edition, Vol. I, Chapter III.
[2] G. C. Wick, Phys. Rev. **80**, 268 (1950).
[3] See reference 1, Eq. (77).
[4] R. J. Glauber, Harvard University thesis, June, 1949. Also "Some notes on multiple boson processes," to be published.

Isotope Shift in the Spectrum of Os I and the Magnetic Moment of Os^{189}

S. SUWA
Institute of Science and Technology, Komaba, Meguro-ku, Tokyo, Japan
(Received July 23, 1951)

IN order to determine the ratio of the distances between the components due to even isotopes in the spectrum of osmium and the magnetic moment of Os^{189}, the hyperfine structure (hfs) of Os I[1] was studied, using a water-cooled hollow cathode discharge tube and a Fabry-Perot etalon.

The hfs of any clearly resolved line was found to consist of six components. Four of them, which are spaced equidistantly to a rough approximation, are due to the even isotopes (186, 188, 190, 192), and the remaining two are due to the odd isotope 189. The number of components due to Os^{189} in each line and their intensity ratio were found to be in harmony with the assumption of the nuclear spin $\frac{3}{2}$. Kawada[2] had previously shown that Os^{189} might have probably a spin of $\frac{3}{2}$.

The result of the measurements is given in Table I. In each line listed the heavier isotopes have greater wavelength, as expected from the indicated electron configuration of the terms. The

TABLE I. Displacement effect of the even osmium isotopes and the splitting of Os^{189} in the spectrum of Os I (in unit of 10^{-3} cm^{-1}).

		Even isotopes			Os^{189}
		$\Delta\nu$	$\Delta\nu$	$\Delta\nu$	Doublet
λ(A)	Combination[a]	(186–188)	(188–190)	(190–192)	distance
4794	$d^6s^2\,{}^5D_3-d^6sp\,{}^7D_3$		51.4	48.7	236
4447	$(14)_3-(53)_3$		100.3	95.2	···
4420	$d^6s^2\,{}^5D_4-d^6sp\,{}^7D_4$	67	57.5	55.4	350
4261	$d^6s^2\,{}^5D_4-d^6sp\,{}^7D_5$	67	64.5	58.8	538
4135	$d^6s^2\,{}^5D_3-d^6sp\,{}^7P_4$	58	54.4	47.9	333
4112	$d^6s^2\,{}^5D_1-(36)_2$		58.4	55.6	···
3876	$(9)_4-(53)_3$	~100	87.0	84.4	···
3752	$d^6s^2\,{}^5D_3-(35)_3$?		51	49	371
	Mean ratio	1.1	: 1.05	: 1	

[a] See reference 1.

ratio $\Delta\nu(186\text{–}188):\Delta\nu(188\text{–}190):\Delta\nu(190\text{–}192)$ can be regarded as constant within experimental error for all lines except λ4135, whose structure was possibly disturbed by the overlapping of another line of the combination $(13)_3$–$(60)_2$, though this was not well confirmed. The mean value of the ratio, excluding λ4135, is given in the last row of Table I. This ratio is not in agreement with the measurements of Kawada;[2] but the present investigation might be considered the more accurate, owing to the improved resolving power of the spectroscopic apparatus.

The ratios of the isotopic displacements of even isotopes in the heavy elements with even atomic number $Z(Z=74-82)$, are summarized in Table II. The magnitude of the shift decreases as

TABLE II. Ratio of spacings between consecutive even isotopes in heavy elements.

	Z \ N	126	124	122	120	118	116
Pb[a,b]	82		1 : 0.90				
Hg[a]	80			1 : 0.99 : 0.88			
Pt[c]	78					1 : 0.97	

	Z \ N	116	114	112	110	108	106
Os	76		1 : 1.05 : 1.15				
W[d]	74				1 : 1.13 : 1.02		

[a] K. Murakawa and S. Suwa, J. Phys. Soc. Japan **5**, 429 (1950); **5**, 382 (1950).
[b] F. E. Geiger, doctoral thesis, university of Wisconsin (1950).
[c] S. Tolansky and E. Lee, Proc. Roy. Soc. (London) **A158**, 110 (1937).
[d] J. A. Vreeland and K. Murakawa, Phys. Rev. **83**, 229 (1951).

the neutron number N decreases from $N=126$ to 116, increases from $N=116$ to 108, and again begins to decrease from $N=108$. This indicates a variation in the effect caused by adding two neutrons to a nucleus.

The magnetic moment of Os^{189} can be calculated from the hfs of λ4420 and λ4261 (see Table I). Neglecting any splitting of the final term $d^5s^2\ {}^5D_4$ of Os^{189}, the coupling constant of the $6s$ electron, $a(6s)$, was found to be 0.79 cm^{-1}. Putting this value and $I=\frac{1}{2}$ into the well-known Goudsmit-Fermi-Segrè formula,

$$\mu(Os^{189}) = +0.6\pm0.1 \text{ nm}$$

was obtained.

The writer wishes to express his sincere thanks to Professor K. Murakawa for his kind guidance in this work.

[1] W. Albertson, Phys. Rev. **45**, 304 (1934).
[2] T. Kawada, Proc. Phys. Math. Soc. Japan **20**, 653 (1938).

Quantum Corrections to Transport Properties at High Temperatures

J. DE BOER AND R. BYRON BIRD
Institute for Theoretical Physics, University of Amsterdam, Amsterdam, Netherlands
(Received August 3, 1951)

IN the quantum theory of transport phenomena[1] the following formulas are given in Boltzmann statistics for the "cross sections," $\phi^{(1)}$ for diffusion, thermal diffusion, and viscosity of mixtures, and $\phi^{(2)}$ for viscosity and thermal conductivity:

$$\phi^{(1)}(g) = \frac{2g}{k^2}\sum_{l=0}^{\infty}(l+1)\sin^2(\eta_{l+1}-\eta_l), \tag{1a}$$

$$\phi^{(2)}(g) = \frac{2g}{k^2}\sum_{l=0}^{\infty}\frac{(l+1)(l+2)}{(2l+3)}\sin^2(\eta_{l+2}-\eta_l), \tag{1b}$$

in which $k=\mu g/\hbar$, μ and g are the reduced mass and the initial relative velocity of a pair of colliding molecules, and $\eta_l(k)$ is the phase-shift corresponding to the orbital quantum number, l.

At very low temperatures formulas analogous to Eq. (1b), written for Fermi-Dirac and Bose-Einstein statistics, have been used for the calculation of the viscosity of the light and heavy isotopes of helium[2,3] and for light and heavy hydrogen,[4] by numerical evaluation of the phase shifts. At higher temperatures this method is not feasible because of the large number of phase-shifts required. Consequently, it is important that another method of attack be developed for those temperatures for which the deviations from classical behavior are small.

In this temperature region we have succeeded in expressing the cross sections (and hence all of the transport coefficients) as power series in Planck's constant; this was accomplished by using Kahn's[5] expressions for the phase shifts, which are derived from the W.K.B. method:

$$\eta_l(k) = \eta_l^{I}(k) + \eta_l^{II}(k) + \cdots, \tag{2}$$

$$\eta_l^{I}(k) = (\pi/2)bk - kr_m + k\int_{r_m}^{\infty}[(1-F)^{-\frac{1}{2}}-1]dr, \tag{2a}$$

$$\eta_l^{II}(k) = (\pi/16bk) - (1/24k)\int_{r_m}^{\infty}[(F'''/F') - (F''/F')^2][1-F]^{-\frac{1}{2}}dr, \tag{2b}$$

in which the variable, b, defined by $\hbar^2l(l+1)=\mu^2g^2b^2$, has been introduced; r_m is the distance of closest approach in a collision; $F(r)=[\varphi(r)/(\frac{1}{2}\mu g^2)]+[b^2/r^2]$, $F'=dF/dr$, etc., and $\varphi(r)$ is the intermolecular potential function.

The differences in the phase-shifts which occur in Eqs. (1a) and (1b) can be expressed in terms of the various derivatives of η_l with respect to b, with the result that

$$[\eta_{l+1}-\eta_l] = \tfrac{1}{2}\chi + \tfrac{1}{48}b\chi'(\hbar/\mu gb) + \tfrac{1}{384}[\chi - \psi + b\psi' + (4/3)b^2\chi''](\hbar/\mu gb)^2 + O(\hbar^3), \tag{3a}$$

$$[\eta_{l+2}-\eta_l] = \chi + b\chi'(\hbar/\mu gb) + \tfrac{1}{8}[\chi - \psi + b\psi' + (16/3)b^2\chi''](\hbar/\mu gb)^2 + O(\hbar^3), \tag{3b}$$

in which the primes on χ and ψ indicate differentiation with respect to b; χ, defined as $(2/k)(\partial\eta^I/\partial b)$, or

$$\chi(b,g) = \pi - 2b\int_{r_m}^{\infty}[1-F]^{-\frac{1}{2}}r^{-2}dr, \tag{4a}$$

is the classical angle of deflection, and $\psi=16bk\eta^{II}$ or

$$\psi(b,g) = \pi - \tfrac{1}{2}b\int_{r_m}^{\infty}[(F'''/F') - (F''/F')^2][1-F]^{-\frac{1}{2}}dr. \tag{4b}$$

The final expressions for the cross sections may be obtained by substituting Eqs. (3a, b) into Eqs. (1a, b), developing $\sin(\eta_{l+n}-\eta_l)$ in a power series in $(\hbar/\mu gb)$, and transforming the summation over into an integration over b [using $dl=db(\mu g/\hbar)\{1-\frac{1}{2}(\hbar/\mu gb)^2+\cdots\}$]. The first term, proportional to $\hbar^0$, is the classical expression for $\phi^{(n)}$. The terms proportional to odd powers of $\hbar$ may be seen to vanish by partial integrations; we may finally write

$$\phi^{(n)} = \phi_{cl}^{(n)} + \phi_{qu}^{(n)}, \tag{5}$$

where

$$\phi_{cl}^{(n)} = g\int_0^{\infty}[1-\cos^n\chi]bdb, \tag{5a}$$

$$\phi_{qu}^{(1)} = (\hbar^2/8\mu^2g)\int_0^{\infty}[\chi - \psi + b\psi' + \tfrac{1}{3}b^2\chi'']\sin\chi(db/b) + O(\hbar^4), \tag{5b}$$

$$\phi_{qu}^{(2)} = (\hbar^2/8\mu^2g)\int_0^{\infty}\{[\chi - \psi + b\psi' + (4/3)b^2\chi'']\sin 2\chi - \sin^2\chi\}(db/b) + O(\hbar^4). \tag{5c}$$

Chapman and Cowling[1] have shown that the transport properties may be expressed directly in terms of a set of quantities, $\Omega^{(n)}(s)$, which are functions of the temperature and are defined in terms of the quantities $\phi^{(n)}$ calculated above:

$$\Omega^{(n)}(s) = \pi^{\frac{1}{2}}\int_0^{\infty}\exp(-\gamma^2)\gamma^{2s+3}\phi^{(n)}d\gamma, \tag{6}$$

where $\gamma^2=\mu g^2/2\kappa T$, κ being Boltzmann's constant. Consequently, substitution of the expression (5) into Eq. (6) leads to a series development of each of the transport coefficients in a series of powers of $\hbar^2/\mu\kappa T$, the coefficients of which are functions of T and

depend parametrically on the intermolecular potential. The first term, not containing $\hbar$, is the well-known classical expression for each of the transport properties. Obviously, this series converges only in the temperature region where the deviations from classical theory are relatively small.

If the intermolecular potential function may be written as $\varphi(r)=\epsilon f(\sigma/r)$, in which ϵ and σ are units of energy and length, respectively, then the quantities σ and ϵ characterizing the potential field can be used to define "molecular units" for each of the transport quantities. In classical theory[6] the thus "reduced" transport coefficients are universal functions of the reduced temperature, $T^*=\kappa T/\epsilon$. When quantum corrections must be taken into account, one may, in general, expect deviations from the classical result depending on the quantum mechanical parameter, $\Lambda^*=[\hbar/\sigma(m\epsilon)^{\frac{1}{2}}]$, characteristic for each substance. The results of this paper are in agreement with this "quantum mechanical principle of corresponding states":[7] the series development for each of the transport properties is a power series in Λ^{*2}/T^*, the coefficients being functions of T^* only.

A detailed account of this work, accompanied by numerical results, will be published elsewhere. One of the authors (R.B.B.) wishes to acknowledge the financial assistance provided him by the Fulbright exchange program.

[1] S. Chapman and T. G. Cowling, *The Mathematical Theory of Non-Uniform Gases* (Cambridge University Press, London, 1939).
[2] J. de Boer, Physica **10**, 348 (1943).
[3] J. de Boer and E. G. D. Cohen, Physica (to be published).
[4] R. Miyako, Proc. Phys. Math. Soc. Japan **24**, 852 (1942).
[5] B. Kahn, dissertation, Utrecht (1938).
[6] J. de Boer and J. van Kranendonk, Physica **14**, 442 (1948); Hirschfelder, Bird, and Spotz, J. Chem. Phys. **16**, 968 (1948).
[7] J. de Boer, Physica **14**, 139 (1948).

Limits on the Energy of the Antiferromagnetic Ground State

P. W. Anderson
Bell Telephone Laboratories, Murray Hill, New Jersey
(Received July 16, 1951)

THE energy of the ground state of a simple antiferromagnetic lattice remains one of the unsolved problems of quantum mechanics, except in the simplest case of atoms of angular momentum quantum number $S=\frac{1}{2}$ on a linear chain.[1] For such a lattice, the hamiltonian is effectively

$$H=J\Sigma_i\Sigma_j\mathbf{S}_i\cdot\mathbf{S}_j. \tag{1}$$

The double sum runs over all pairs of neighbors i and j. Hereafter, it will be understood that atoms labeled i are on sublattice (1), while those labeled j are on sublattice (2). We shall assume the lattice is sufficiently simple, as, for example, is the simple or body-centered cubic, that it can be divided into two sublattices, the nearest neighbors of atoms on one sublattice laying all on the other and *vice versa*. The naive expectation is then that the spins on sublattice (1) lie all in one direction, while the spins on (2) all lie antiparallel to those on (1). The average energy for such a situation, represented by the wave function

$$\Psi=\Pi_i\psi_i(+S)\Pi_j\psi_j(-S) \tag{2}$$

(where here again i and j are atoms on sublattices (1) and (2), respectively), is easily obtained, and is

$$(\Psi, H\Psi)=-\tfrac{1}{2}NZJS^2, \tag{3}$$

where N is the number of atoms and Z the nearest neighbor number. Unfortunately, the state (2) is not an eigenstate, and so all that can be said is that, by the variational principle, the energy E_g of the ground state lies lower than Eq. (3):

$$E_g<-\tfrac{1}{2}NZJS^2. \tag{4}$$

A second, lower bound may be placed on the ground state energy in the following way: For the two-sublattice situation, it is clear that the hamiltonian (1) may be decomposed into a sum of terms:

$$H=\Sigma_i H_i, \tag{5}$$

$$H_i=J\Sigma_j\mathbf{S}_i\cdot\mathbf{S}_j. \tag{6}$$

The sum in Eq. (6) runs over all atoms j of sublattice (2) which are neighbors to the atom i of sublattice (1). Now the diagonal energies of the H_i are well known.[2] The lowest energy is

$$E_i=-JS(ZS+1), \tag{7}$$

which is obtained when the cluster of neighbor spins S_j is given its maximum angular momentum $\Sigma_j S_j=ZS$, and S_i is then set as nearly antiparallel to the surrounding cluster as possible. Unfortunately, there is no way to make up a full eigenfunction for the lattice out of such least-energy wave functions—for instance, we find that $(S_{ix})_{kl}\neq-(S_{ix})_{kl}$, which shows that such a wave function would not be self-consistent. On the other hand, one can easily see that the least eigenvalue of the total hamiltonian must be greater than the sum of the least eigenvalues of its parts:

$$\begin{aligned} E_g&>\Sigma_i\{-JS(ZS+1)\},\\ E_g&>-\tfrac{1}{2}NZJS^2(1+1/ZS). \end{aligned} \tag{8}$$

This statement follows from the fact that the ground-state energy, or least eigenvalue E_g, must be the sum of diagonal elements of H_i by Eq. (5), but the variational theorem says that all possible diagonal elements of any matrix are greater than or equal to the least element. Physically, this means that the interaction with the rest of the lattice necessarily "spoils" the wave functions for the clusters which lead to the energy (7), and increases the energies of the clusters.

Thus, the bounds on the energy of the lowest state are

$$-\tfrac{1}{2}NJZS^2>E_g>-\tfrac{1}{2}NJZS^2(1+1/ZS). \tag{9}$$

In most practical cases of interest, these are very strong bounds: MnF_2, for instance, has $Z=8$, $S=5/2$, so that the possible fractional variation for E_g is 1/20. This in turn is a good indication that the wave function of the ground state is usually not greatly different from the "naive" expectation (2).

In Hulthén's case,[1] $1+1/ZS$ is 2. He found the corresponding factor for his rigorous ground state to be 1.773:

$$E_g(S=\tfrac{1}{2}, Z=2)=-1.773(\tfrac{1}{4}NZ)JS^2, \tag{10}$$

while a somewhat better upper bound than Eq. (4), 1.5, may be obtained with a simple "bond eigenfunction." We see that the limits are correct, if somewhat wide, in this, the worst possible case.

[1] L. Hulthén, Arkiv. Mat. Astron. Fysik **26A**, No. 11 (1938).
[2] See, for instance, P. R. Weiss, Phys. Rev. **74**, 1493 (1948).

The New State in Li^7 at Low Bombarding Energy*

R. W. Gelinas, C. M. Class, and S. S. Hanna
Department of Physics, Johns Hopkins University, Baltimore, Maryland
(Received July 20, 1951)

GOVE and Harvey[1] have revealed the existence of a state in Li^7 at 4.77 ± 0.10 Mev from observations on the $Be^9(d,\alpha')Li^{7*}$ reaction and on the inelastic scattering of protons, deuterons, and alphas by Li^7, at bombarding energies of 7.9, 14, and 31 Mev. In a survey of the $Be^9(d,\alpha)Li^7$ reaction,[2] at bombarding energies of 0.68 and 1.03 Mev, we examined the alpha-spectrum at 90° using magnetic analysis.[3] Above $E_{ex}=2.5$ Mev in Li^7 a continuum of alpha-particles is encountered, and in the neighborhood of $E_{ex}=4.7$ Mev Li^{+++} recoils from the doublet ground-state transition interfered with our observations. With photographic detection, discrimination between the lithium particles and alphas is difficult because they have practically the same range in emulsion. The two lithium groups are separated by only 135

kev on the alpha-energy scale. We have now reexamined the region around $E_{ex}=4.7$ Mev, using thinner targets and more favorable bombarding energies and target orientations than in the survey work.

With magnetic analysis, alpha-particles corresponding to a 4.77-Mev state will coincide with the ground state. Li^{+++} recoils at a bombarding energy of 1.64 Mev and with the first excited state recoils at 1.20 Mev. Interference from deuterons scattered elastically from Be, C, and O will be experienced at bombarding energies of 1.84, 1.55, and 1.37 Mev, respectively. We have selected a bombarding energy near 0.5 Mev, which produces a separation of about 200 kev between the predicted alpha-position and the closest lithium recoils, making possible a search on either side of the expected location.

The beryllium target (on solid backing) was set at an angle of 22° to the deuteron beam. This orientation produces a relatively large spread in energy in the impinging deuterons; but the lithium recoils receive only 2/11 of the bombarding energy, and for them the effective thickness is only 8 percent above that for normal emergence. The oblique setting also has the advantage of increasing the yield from a given thin target. In the first run, the results of which are shown in the lower part of Fig. 1, a fairly thick target of approximately 3000A was used. The spectrum was calibrated with the proton peak from $Be^9(d, p')Be^{10*}$. The breadth of this peak is due in large measure to the target orientation which is not favorable for the proton reaction. Despite the poor resolution a group of particles can be seen partially resolved on the low energy side of the lithium recoils.

The second run, shown in the upper part of Fig. 1, was made with a considerably thinner target (conveniently prepared from the stock of evaporated targets on hand by dissolving away a portion of the beryllium in very dilute sulfuric acid). With the increased sharpness of the lithium peaks it was possible to use them to calibrate the plate. The energy scale obtained agreed satisfactorily with that from the first run when compared on the basis of the magnetic field settings. The group of particles on the low energy side of the recoils is well resolved and falls in the right region to be identified with the alpha-group observed by Gove and Harvey[1] at a bombarding energy of 14 Mev. Using the Q values of $Be^9(d, p')Be^{10*}$ and $Be^9(d; Li, Li^*)He^4$ given in the literature,[4] we obtain a Q of 2.53 ± 0.02 Mev and an excitation energy in Li^7 of 4.62 ± 0.02 Mev. The intensity of the transition is estimated to be about 25 percent that of the ground state alpha-transition at this bombarding energy. In comparing the two spectra in Fig. 1, one observes the shift in peak maxima arising from target thickness. The rising edge on the high energy side of the ground state lithium group, however, agrees satisfactorily between the two runs. In computing energy values we have attempted to utilize the high energy edge of the peaks in a consistent fashion.

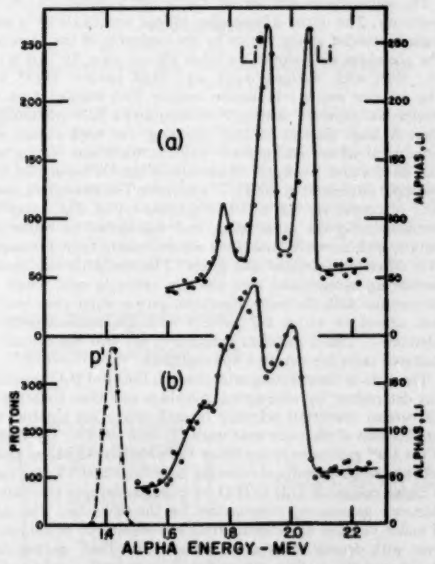

FIG. 1. Magnetic spectra of Be^9+d, in the neighborhood of $E_{ex}=4.7$ Mev in Li^7. The background arises from $Be^9(d, \alpha)He^4+H^3$, the proton peak from $Be^9(d, p')Be^{10*}$, and the lithium peaks from $Be^9(d; Li, Li^*)He^4$. The lithium particle energy is 9/7 the alpha-energy. (a) $E_d=0.47$ Mev. The target, approximately 1000A, is set at 22° to the deuteron beam. Magnetic field $=12.3$ kilogauss. (b) $E_d=0.48$ Mev. The target, approximately 3000A, is set at 25° to the deuteron beam. Magnetic field $=11.6$ kilogauss.

* Assisted by a contract with the AEC.

[1] H. E. Gove and J. A. Harvey, Phys. Rev. **82**, 299, 658 (1951).

[2] R. W. Gelinas and S. S. Hanna, Phys. Rev. **82**, 298 (1951).

[3] For a description of the instrument see D. R. Inglis, Phys. Rev. **78**, 104 (1950).

[4] W. W. Buechner and E. N. Strait, Phys. Rev. **76**, 1547 (1949); W. Whaling and C. W. Li, Phys. Rev. **81**, 150 (1951); Strait, Van Patter, Buechner, and Sperduto, Phys. Rev. **81**, 747 (1951).

Stars Produced in Nuclear Emulsions by Carbon Ions from the Cyclotron

JAMES F. MILLER
Crocker Laboratory, University of California, Berkeley, California
(Received July 20, 1951)

NUCLEAR emulsions have been exposed to carbon ions accelerated in the 60-inch cyclotron at Crocker Laboratory,[1-5] and a study of salient features is being made. This note reports early results on the observation of inelastic nuclear events with the atoms of the emulsion. Ilford E-1 and D-1 nuclear emulsions were used. In the E-1 emulsion, the track of a carbon ion has a solid core, covered with electron spurs less than 2 microns long in the early part of the track and none in the later part. The track tapers appreciably and may have gaps near the end. In the D-1 emulsion the track is less dense and the tapering less noticeable.

The plates are exposed in the cyclotron vacuum to the external beam, with nothing interposed between them and the beam. A set of three slits over a length of 26 inches serves to exclude all but a few extraneous charged particles. The plates are inclined so that the tracks dig into the emulsion at an angle of five degrees. Both C^{12} and C^{13} ions, completely stripped, have been used. C^{12} ions of 120-Mev energy have a range in the emulsion of 175 microns; C^{13} ions of 130-Mev energy have a range of 190 microns. Carbon ions ionized twice, rather than six times, can be accelerated in the cyclotron, using the cyclotron frequency as the third harmonic of their orbital frequency. These C^{3+} appear in great quantity in the internal cyclotron beam, and of these a small fraction is often found in the external beam. Their energy is one-ninth that of the C^{4+}, and their range in the emulsion is about 2.5 microns.

Inelastic events in which charged particles are emitted are the only kind that can be definitely identified, and only these are included here. From these events can be calculated a composite cross section for all the elements of the emulsion. In Ilford emulsions, the stated composition gives, out of 100 atoms, approximately 13 atoms each of silver, bromine, and oxygen, 17 of carbon, 41 of hydrogen, and 3 of minor constituents.

In calculating a cross section, the hydrogen atoms have been included here as capable of producing a star in contrast to the usual procedure when bombardment is with protons or neutrons. The full length of the carbon ion track has been used in the calculation. With C^{12} ions, 102 events have been found out of 181,000 tracks; with C^{13}, 108 events out of 188,000. These correspond to

cross sections of 0.40 ± 0.03 barn for C^{12}, 0.37 ± 0.03 barn for C^{13}. Table I shows the number of emergent prongs from the stars.

TABLE I. Number of emergent prongs from the stars.

Prongs	2	3	4	5	6	7	Total
C^{12}	23	49	24	3	2	1	102
C^{13}	32	44	30	2	0	0	108

Two-prong stars are included only when they could not have been elastic.

A feature of the stars is the high percentage of alphas emerging. Of protons emerging from carbon stars, the longest track lying wholly in the emulsion was 1046 microns, corresponding to an energy of 14.2 Mev. No "hammer tracks" from Li^8 have as yet been observed.

The mosaic of Fig. 1 shows a C^{12} ion stopped in Ilford 100μ E−1 emulsion without a nuclear reaction and one which entered another nucleus, with seven emergent prongs. The C^{12} ion had traveled 63 microns when it entered the target nucleus and accordingly had about 90-Mev kinetic energy remaining. The seventh prong is hidden in the main mosaic, since it is short and goes downward. Its presence is shown by the three pictures at the upper right, taken at increasing depths.

The interest and encouragement of Professors Ernest O. Lawrence, J. G. Hamilton, and E. M. McMillan are acknowledged with gratitude. The writer is particularly indebted to the operations staff of the 60-inch cyclotron under Mr. T. M. Putnam, Jr., and Mr. G. B. Rossi. Much painstaking work has been done by Mr. A. Oliver of the nuclear emulsion group of the Radiation Laboratory in preparing mosaics of nuclear events from carbon ions, of which those reproduced here are part.

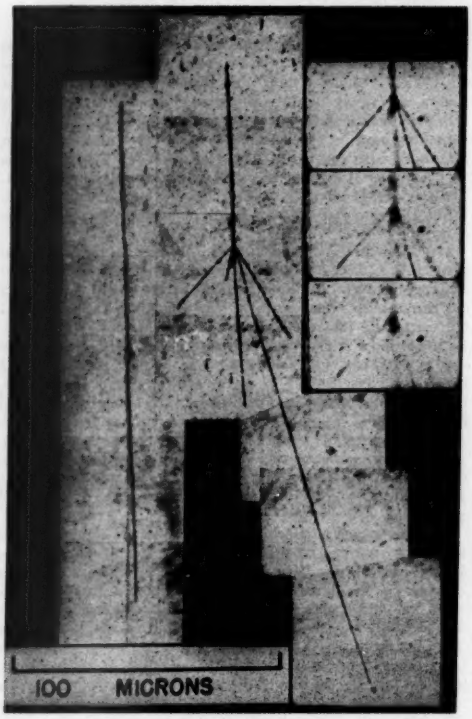

FIG. 1. C^{12} ion tracks in Ilford E-1 emulsion. One stopped without nuclear event; the other produced a seven-pronged star.

[1] L. W. Alvarez, Phys. Rev. **58**, 192 (1940).
[2] C. A. Tobias, Ph.D. thesis, University of California, Berkeley (1941).
[3] R. I. Condit, Ph.D. thesis, University of California, Berkeley (1942), and Phys. Rev. **62**, 301 (1942).
[4] York, Hildebrand, Putnam, and Hamilton, Phys. Rev. **70**, 446 (1946).
[5] Miller, Hamilton, Putnam, Haymond, and Rossi, Phys. Rev. **80**, 486 (1950).

The Photodisintegration Cross Section of the Deuteron

STIRLING A. COLGATE
Laboratory of Nuclear Studies, Cornell University, Ithaca, New York*
(Received July 30, 1951)

THE photodisintegration cross section of deuterium by gamma-rays of ThC″ has been observed by measuring the difference between the total gamma-ray absorption cross sections in D_2O and H_2O. Although the difference is very small (approximately 0.3 percent), the effect can be magnified in a balance-type experiment by observing the difference in counting rates through many mean free paths of absorber. The ratio of the counting rates through two-dimensionally identical absorbers of D_2O and H_2O was observed for the sources Co^{60} and ThC″. The photodisintegration cross section obtained for 2.62-Mev gamma-rays of the ThC″ was (1.47 ± 0.22) millibarns, which agrees within the statistical accuracy with the excellent measurements by Bishop *et al.*[1]

The sources were 300 mC of ThC″ and 3 curies of Co^{60}, respectively. The initial columnation in lead was (6.1×10^{-5}) solid angle subtended at the source by the beginning of the absorber. The absorbers were aluminum tubes 187 cm long, $1\frac{1}{2}$″ o.d.$\times1\frac{1}{8}$″ i.d., filled with distilled water and 99.88 percent D_2O.[2] The The detector was a scintillation counter with stacked 4-cm diameter NaI crystals totaling 9 cm long and a 5819 photomultiplier. A large amount of lead shielding was used around the detector to reduce background. The electronic bias setting was such as to count the upper 50 percent of the Co^{60} spectrum and the upper 30 percent of the ThC″ spectrum. The absorption coefficient of copper for the 2.62-Mev gamma-ray of ThC″ was determined using the same setup, and this agreed to within 0.2 percent with accurate absorption measurements made previously with different apparatus and setup.[3] This could be used to determine an extrapolated zero absorber counting rate, which, in conjunction with the water absorbers, gave a water cross section that agreed to within 0.2 percent with the measurements in reference 3. This is sufficient evidence to say that the amount of scattered radiation detected was negligible.

The ratio of the counting rates through D_2O and H_2O absorbers was determined by alternating absorbers and then counting to 1.5 percent statistical accuracy in each trial. One hundred determinations of the ratio were made for both sources. The energy of the Co^{60} gamma-rays are below the photodisintegration threshold and so give a ratio of counting rates determined by the ratio of molar volume of D_2O to H_2O, or in particular give the ratio of electronic gamma-ray cross section for the two tubes. The ratio of molar volumes so determined agreed within the experimental error with density determined values.[4] The ThC″ gamma-rays should give rise to the same electronic cross-section ratio and in addition include the photodisintegration cross section. The ratio of counting rates of D_2O/H_2O for the Co^{60} source was (1.0361 ± 0.0020) in 11.85 mean free paths. The ratio for ThC″ was (1.0060 ± 0.0023) in 7.96 mean free paths. This results in a differ-

ence of (0.0183±0.0027) in the counting rate due to D_2 in 187.1 cm of D_2O at 22°C. This gives a photodisintegration cross section of (1.47±0.22) millibarns per deuterium nucleus.

I am grateful for the encouragement of Dr. R. R. Wilson throughout the course of this experiment.

* This work was supported by the ONR.
[1] Bishop, Collie, Halban, Hedgran, Siegbahn, Du Toit, and Wilson, Phys. Rev. 80, 211 (1950).
[2] The D_2O was furnished by The Stuart Oxygen Company, San Francisco, California.
[3] Thesis, S. A. Colgate.
[4] E. Swift, Jr., J. Am. Chem. Soc. 61, 198 (1939).

Erratum: Quantum Statistics of Fields

[Phys. Rev. 83, 125 (1951)]
A. E. Scheidegger and C. D. McKay
Department of Physics, Queen's University, Kingston, Ontario, Canada

THE following changes should be made in the article with the above title:

Equations (2.5) and (2.11): The factor T should be omitted.

Equation (3.13) should read:

$$S/V=-(2\pi)^{-3}k\int_0^\infty \log\{1-\exp(-h^2K^2/2mkT)\}4\pi K^2dK$$
$$+\frac{1}{(2\pi)^3}\frac{1}{T}\int_0^\infty \frac{h^2K^2}{2m\{\exp(h^2K^2/2mkT)-1\}}4\pi K^2dK.$$

Equation (4.14): add the factor mc^2.

Cosmic-Ray Star Production in Argon at Sea Level*†

W. W. Brown and E. W. Hones
Department of Physics, Duke University, Durham, North Carolina
(Received August 1, 1951)

THE sea level rate of cosmic-ray star production in argon has been measured by direct observation of the N-ray nuclear interactions in the gas of an ionization chamber contained in a cloud chamber. The ionization chamber, a 3¼ in. diameter and ⅛-in. walled brass cylinder 8 in. in length, open at both ends, and having a ⅛-in. steel central wire, is mounted coaxially with the cloud chamber which has a useful rectangular volume 10 in.×10 in. ×8 in. depth[1] (Fig. 1). The gas, argon at 75 lb-in.$^{-2}$ absolute pressure saturated with iso-amyl alcohol, is common to both the cloud chamber and ionization chamber. A burst occurring in the ionization chamber generates a pulse which is used to trigger the expansion mechanism. Rapid reduction of the cylinder voltage from minus 1400 volts to ground, after electron collection is over, prohibits any appreciable motion of the positive ions and thus permits observation of the tracks of the burst producing particles. The regions exterior and interior to the ionization chamber are illuminated with Amglo flashlamps and photographed stereoscopically. A photographed array of neon bulbs indicates which of the counters (each 1 in.×16 in. effective area) above the chamber are discharged in coincidence with a burst. The chamber was operated under a light roof in an insulated box and maintained within a few degrees of 37°C. Only those bursts releasing more than 7 Mev (1.3 Po-alpha) were permitted to trigger the chamber. Oscillograph traces of the ionization chamber pulses were photographed.

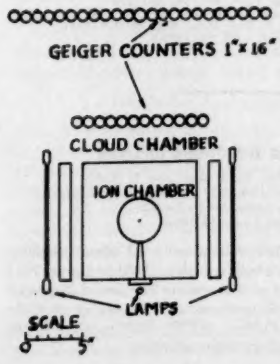

FIG. 1. Arrangement of ionization chamber, cloud chamber, and counters.

FIG. 2. A neutral particle interacts with an argon nucleus to produce a star in which 11 emitted ionizing particles are visible in the original negative. Protruding through the wall at the lower right is a wire carrying a Po-alpha calibrating source.

Bursts were produced by stars occurring in the wall and gas (see Fig. 2) of the ionization chamber and by electronic showers. In Table I the numbers of the above ionizing phenomena causing bursts in 365 hours of sensitive operating time are given. A plot of the spacial distribution of the origins of the stars occurring in the gas indicated that those occurring near the wall and the ends of the ionization chamber had less chance of being detected than those occurring nearer the axis and center of the chamber. In a centrally located cylindrical volume 7.16 cm in diameter and 12.2 cm long, where the wall and end effects are negligible, 37 stars of 1 or more prongs occurred in the gas in the sensitive time interval. Of these 27 were of three or more prongs. Since the photographs of the oscillograph traces of the bursts indicated the ionization chamber was working properly during this interval, the few instances in which blank pictures of the cloud chamber were obtained were attributed to inefficiency in the cloud chamber operation. The rate of star production in argon, after correcting

TABLE I. Number of ionizing phenomena causing bursts.

Sensitive time, hr	Stars in brass wall of 1 or more prongs	Stars in argon 1 or more prongs	Stars in argon 3 or more prongs	Bursts due to electronic showers
365	135	46	33	14

for this inefficiency (7 percent) and for the expansion of the gas (15 percent) is 0.78 ± 0.13 g^{-1} day^{-1} and 0.57 ± 0.13 g^{-1} day^{-1} for one or more and three or more prongs, respectively. The ratio of the latter rate to the rate measured in photographic plates[3] is 1.42 ± 0.34, while the ratio of the nuclear area per gram of argon to that of the photographic emulsion, not counting the hydrogen present, is 1.17. Our results are thus not in disagreement with the emulsion work if N-rays have geometric cross section for nuclear interaction.

In a total operating period of 1009 hours, during which the chamber was not always operating at high enough efficiency for absolute rate measurements, the total number of gas stars observed was 95. In 5 cases the initiator was identified as a charged particle by its low ionization, its location in the upper hemisphere with reference to the star origin as center, and by the requirement that the backward extension of its path pass through counters above the cloud chamber which were discharged in coincidence with the ionization chamber. If charged and neutral N-rays have the same mean free path for nuclear interaction, this indicates that about 5 percent of the sea level N-rays are charged.

The authors are grateful to Professor W. M. Nielsen for his interest in the project and for his efforts which made the work possible.

* This work was supported by the joint program of the ONR and AEC.
† Based in part on a thesis to be submitted by E. W. Hones to the Graduate School of Duke University in partial fulfillment of the requirements for the Ph.D. Degree.
[1] Lewis, Brown, Seevers, and Hones, Rev. Sci. Instr. **22**, 259 (1951).
[2] E. P. George and A. C. Jason, *Cosmic Radiation*, Colston Papers, (Butterworth Scientific Publications, London, 1949), p. 31.

Induced Infrared Absorptions of H_2, N_2, and O_2 in the First Overtone Regions

H. L. Welsh, M. F. Crawford, J. C. F. MacDonald, and D. A. Chisholm*
McLennan Laboratory, University of Toronto, Toronto, Canada
(Received July 23, 1951)

INFRARED absorptions at the fundamental frequencies have been observed in the compressed gases H_2, N_2, and O_2 and in mixtures of these with foreign gases.[1-3] The experimental evidence is consistent with the hypothesis that the absorption is caused by the distortion of the charge distribution of the absorbing molecule during a close two-body collision. The theoretical calculations of Van Kranendonk and Bird[4] support this hypothesis. In recent experiments on H_2, N_2, and O_2 at high densities, absorptions in the regions of twice the fundamental frequencies have been observed.

These absorptions were obtained using two transmission cells: a medium pressure (150 atmos) cell of 85-cm path length, and a high pressure (1500 atmos) cell of 30-cm path length. The medium pressure cell could be cooled to liquid air temperatures, and was used to investigate the temperature dependence of the H_2 absorption.

The integrated absorption coefficient of the overtone absorption in H_2 at both 80°K and 300°K varies as the square of the density up to 426 and 676 Amagat, respectively. The specific integrated absorption coefficient for the overtone is 3.5×10^{-6} cm^{-1} per cm path per Amagat[2] at 80°K and 6.2×10^{-6} at 300°K; for the fundamental it is 1.1×10^{-2} cm^{-1} per cm path per Amagat[2] at 80°K and 2.5×10^{-2} at 300°K. The specific absorption coefficient for the overtone plotted against wave number is shown in Fig. 1 for both temperatures. The low temperature contour shows five distinct components. The frequencies 8080, 8415, and 8645 cm^{-1} are in good agreement with those calculated for the Q, $S(0)$, and $S(1)$ lines of the $v=0$ to $v=2$ transition using the constants of the free molecule.[5] The frequencies 8320, 8645, and 8865 cm^{-1}, marked Q', $S'(0)$, and $S'(1)$ in Fig. 1, agree with those calculated using the expression $2\omega_e-4x_e\omega_e$ for the frequency of the Q-branch. The variation in the intensities of the lines as the temperature, and hence the ortho-para ratio, was changed confirms the above assignments. Thus we conclude that the observed absorption is a superposition of two bands. The frequency analysis suggests that the lower frequency band is the first overtone and that the higher frequency band corresponds to a double transition in which both H_2 molecules in the collision undergo the fundamental transition simultaneously. This interpretation is as yet speculative, and is being tested by experiments on the enhancement of the absorption by foreign gases.

An absorption at the overtone frequency of N_2, 4632 cm^{-1}, was observed in a 22.6-cm path of liquid N_2, and in the 30-cm path of the high pressure cell at room temperature with a gas density 81 percent that of the liquid. On the assumption of a density-squared dependence, the specific integrated absorption coefficient in both the liquid and the gas is 1.4×10^{-6} cm^{-1} per cm path per Amagat.[3] The ratio of the specific integrated absorption coefficient of the overtone to that of the fundamental absorption is 1:66. An absorption was also observed in the region of twice the fundamental frequency of the O_2 molecule, 2900–3300 cm^{-1}, using the 85-cm cell at room temperature and O_2 densities up to 134 Amagat. The ratio of overtone to fundamental intensity is 1:30 in this case.

The authors are indebted to the National Research Council of Canada for financial assistance in the construction of high pressure apparatus.

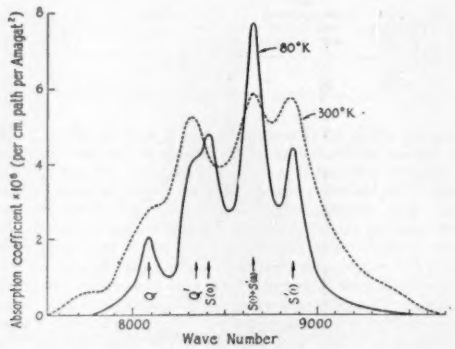

FIG. 1. Contours of the induced infrared absorption of hydrogen in the overtone region.

* Holder of the E. F. Burton Fellowship in Physics, School of Graduate Studies, University of Toronto, 1950–1951.
[1] Crawford, Welsh, and Locke, Phys. Rev. **75**, 1607 (1949).
[2] Welsh, Crawford, and Locke, Phys. Rev. **76**, 580 (1949).
[3] Crawford, Welsh, MacDonald, and Locke, Phys. Rev. **80**, 469 (1950).
[4] J. Van Kranendonk and R. B. Bird, Phys. Rev. **82**, 962 (1951).
[5] G. Herzberg, Can. J. Research A **28**, 144 (1950).

Photoproton Reactions in Lead

A. G. W. Cameron, W. Harms, and L. Katz
Betatron Group, Department of Physics, University of Saskatchewan, Saskatoon, Saskatchewan, Canada
(Received July 30, 1951)

IN 1946 Baldwin and Klaiber[1] obtained a 4.5-minute thallium activity when lead was irradiated with 100-Mev x-rays. They attributed this to a mixture of 4.76-minute Tl^{207} and 4.23-minute Tl^{206} (at that time incorrectly assigned to Tl^{204}). Any or all of the reactions $Pb^{208}(\gamma, p)Tl^{207}$, $Pb^{207}(\gamma, p)Tl^{206}$, $Pb^{208}(\gamma, d)Tl^{206}$, and $Pb^{208}(\gamma, pn)Tl^{206}$ would produce these activities.

We have measured the activation curve for the combined reactions up to 27 Mev, making no attempt to separate the two half-lives. Thin lead and copper disks of identical shape were irradiated together in the betatron beam and counted alternately with an end-window counter. The known $Cu^{63}(\gamma, n)Cu^{62}$ activation curve[2] thus served as a monitor for the lead reactions. The energy thresholds for the (γ, p) reactions in Pb^{208} and Pb^{207} are 7.7 and 7.8 Mev, respectively,[3] but due to the high potential barrier for protons the yields below 15 Mev were too small to be counted.

Although the counting geometries were the same for both types of sample, the corrections for self-absorption in lead and copper were quite different. Because of the changing angular distribution of beta-particles from circular disks as a function of sample thickness, it is necessary to measure specific activities in extremely thin samples in order to make this correction. This was not possible in the case of the lead samples, so a curve of specific activity *versus* sample thickness was measured using saturation backscattering, and a correction given by Yaffe and Justus[4] was applied.

The resulting activation curve was analyzed by the photon difference method[5] to determine the sum of the contributing photonuclear cross sections. This is plotted as the solid curve (a) in Fig. 1. A cross section maximum of 5.3 millibarns occurs at 26 Mev.

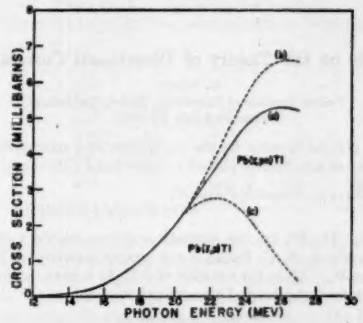

FIG. 1. Cross-section curves for (γ, p) and (γ, pn) reactions in lead. (a) Observed cross-section curve assuming that only the reactions $Pb^{207}(\gamma, p)Tl^{206}$ and $Pb^{208}(\gamma, p)Tl^{207}$ produced the measured activities. (b) Sum of (γ, p) and (γ, pn) cross sections computed from (a) and statistical theory. (c) The (γ, p) cross section computed from (a) and statistical theory. The difference in ordinates between curves (b) and (c) represents the (γ, pn) cross section.

It is possible to draw some theoretical conclusions regarding the contribution of the various possible reactions to this cross-section curve. In the following considerations we assume the (γ, d) reaction cross section to be small compared to those for the (γ, p) and (γ, pn) reactions.

If the absorption of high energy photons results in the formation of a compound nucleus, then, according to the statistical theory of Weisskopf,[6] protons will be emitted with an energy distribution.

$$I(E_p) \propto E_p \sigma(E_p) \exp 2[a(h-Q-E_p)]^{\frac{1}{2}}, \qquad (1)$$

where E_p is the proton energy, $\sigma(E_p)$ is the capture cross section for protons of energy E_p by the residual nucleus, and the exponential factor represents the level density of the residual nucleus at the excitation in which it is left after the proton emission. This residual nucleus will decay by γ-ray emission, or, if the energy is sufficient, by neutron emission (thus resulting in a (γ, pn) reaction). Since proton emission becomes easier as the nuclear excitation is raised, it is probable that the majority of the (γ, pn) events observed here involved the prior emission of a proton in the above manner.

With the value $a = 10$ (Mev)$^{-1}$ for $A = 207$, proton energy distributions corresponding to photon energies between 15 and 27 Mev were computed. It was then assumed that the fractional part of the distribution, which would leave the residual nucleus sufficiently excited to emit a neutron, would result in a (γ, pn) reaction (this fraction was negligible below 20 Mev). The observed cross-section curve (a) of Fig. 1 is the sum of (γ, p) cross sections in two lead isotopes and a (γ, pn) cross section in Pb^{208}. Thus, assuming equal cross sections in the different lead isotopes at a given photon energy, it was possible to find what fraction of curve (a) represented the $Pb^{208}(\gamma, pn)Tl^{206}$ reaction at any photon energy. Curve (b) is the computed sum of (γ, p) and (γ, pn) cross sections in lead, and curve (c) is the (γ, p) cross section alone. These two curves are insensitive to the nuclear radius assumed in the computations.

The above value of a from Eq. (1) for the description of Tl level densities is a smooth extrapolation of Weisskopf and Blatt's values.[6] From the work of Stelson and Goodman[7] and of Whitmore[8] on the inelastic scattering of 14-Mev neutrons from lead, a value $a = 22$ (Mev)$^{-1}$ may be obtained for the "magic number" lead nuclei. This larger value would decrease the peak position of curve (c) by less than one Mev. On the other hand, if many of these photoprotons are directly excited in the nucleus and escape before a compound nucleus can be formed,[9,10] the (γ, p) cross sections will comprise a much larger fraction of curve (a). To settle such questions it is necessary to determine the energy distribution of the photoprotons from lead.

[1] G. C. Baldwin and G. S. Klaiber, Phys. Rev. **70**, 259 (1946).
[2] Johns, Katz, Douglas, and Haslam, Phys. Rev. **80**, 1062 (1950).
[3] K. Way, Phys. Rev. **75**, 1448 (1949).
[4] L. Yaffe and K. M. Justus, "Conference on absolute beta counting," National Research Council Preliminary Report No. 8 (1950); J. Chem. Soc. Supplementary Issue No. 2, 5, S 341 (1949).
[5] A. G. W. Cameron and L. Katz, Phys. Rev. **83**, 892 (1951).
[6] J. M. Blatt and V. F. Weisskopf, "The theory of nuclear reactions," Technical Report No. 42, Laboratory for Nuclear Science and Engineering, Massachusetts Institute of Technology (unpublished).
[7] P. H. Stelson and C. Goodman, Phys. Rev. **82**, 69 (1951).
[8] B. G. Whitmore (private communication).
[9] E. D. Courant, Phys. Rev. **82**, 703 (1951).
[10] L. Katz and A. G. W. Cameron, Phys. Rev. **83**, 892 (1951).

Yields of α-, n-, and γ-Radiation from Chlorine Bombarded with Protons

K. J. BROSTRØM AND B. S. MADSEN,
Institute for Theoretical Physics, University of Copenhagen, Denmark,
AND
C. B. MADSEN,
Physical Institute, University of Aarhus, Denmark
(Received July 30, 1951)

THE $Cl(p, \gamma)A$ reaction was first studied by Curran and Strothers[1] who found indications of three broad resonances at 650, 800, and 1000 kev. Tangen *et al.*[2,3] found four sharp resonances at 427, 447, 500, and 532 kev.

Weimer, Kurbatow, and Pool[4,5] found that bombardment of chlorine with fast protons resulted in a radioactive gas with a half-life of 34 days. They ascribed the activity to A^{37} formed in the process $Cl^{37}(p, n)A^{37}$. Richards *et al.*[6,7] detected the neutrons from this process and studied the excitation function. They found the threshold energy of the protons to be 1639 kev.

Using targets of unseparated chlorine ($PbCl_2$) and with the technique of proton bombardment and γ-detection previously described,[8] we have found 86 γ-resonances in the voltage region from 500 to 2150 kev. (See Fig. 1.) A few of the strongest of these peaks have also been detected with targets of separated chlorine prepared by Dr. J. Koch and Mr. K. O. Nielsen by the methods previously used for neon and argon.[9,10] These peaks are: Cl^{35}: 858, 888, 1102, 1258, 1484, and 1510 kev; Cl^{37}: 1090 kev.

Neutrons have been searched for with boron-filled proportional counters surrounded by paraffin wax. In the voltage region from 1600 to 2300 kev, 47 neutron-emitting levels have been found,

the lowest situated at 1637 kev in fair agreement with the threshold found by Richards *et al.*

Six of these resonances, i.e., 1928, 1974, 2014, 2028, 2079, and 2108 kev, have been detected in Cl^{37} targets, whereas none was found in Cl^{35}. This is in accordance with the highly negative Q-value calculated from accepted mass values for the $Cl^{35}(p, n)A^{35}$ process.

α-particles have been looked for (at a right angle to the proton beam) with a proportional counter, magnetic deflection being used to separate α-particles from scattered protons. In the interval from 1450 to 2040 kev, 10 resonances giving rise to α-emission have been found. The energy of the α-particles has been estimated from pulse size and gives a Q-value of 3.2 Mev. As the Q-value for the process $S^{32}(\alpha, p)Cl^{35}$ is known to be -2.1 Mev,[11,12] the α-particles are ascribed to the process $Cl^{37}(p, \alpha)S^{34}$.

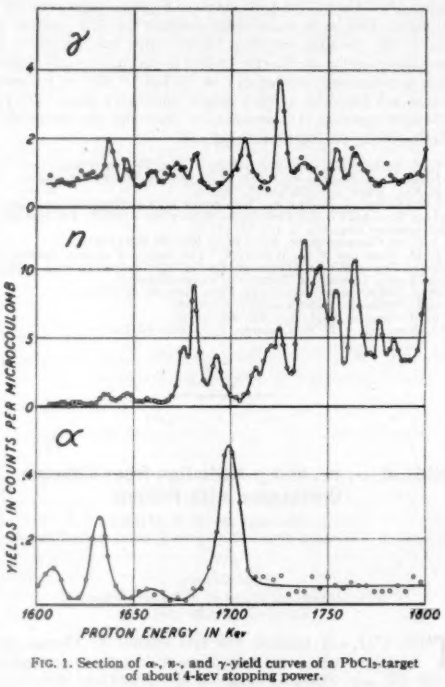

FIG. 1. Section of α-, n-, and γ-yield curves of a $PbCl_2$-target of about 4-kev stopping power.

At most resonance voltages more than one sort of radiation has been observed, e.g., at 1838 kev, 1928 kev, and at 1974 kev we have found conspicuous peaks in both the α-, γ- and n-curves, but a few strong peaks (e.g., the n-peak at 1693, the γ-peak at 1707, and the α-peak at 1699 kev) show up only in one of the yield curves.

In order to decrease the effect of voltage uncertainties, measurements were always made either of the n- and γ-yields simultaneously or of the n- and α-yields simultaneously.

In the whole voltage region the resonance widths are smaller than the experimental widths, which are for γ- and neutron peak 6–8 kev and for α-peaks 15 kev.

The average distance between the observed neutron peaks is about 14 kev. For the γ-peaks the distance is the same in the interval from 800 to 1500 kev whereas it is 25 kev from 1500 to 2150 kev. From this, however, it cannot be inferred that the density of γ-levels decreases with increasing energy, as the number of small peaks which are concealed by the background rises markedly with voltage. This is not the case with the neutron curve, where the background is much smaller. A more detailed account of the experiments and a closer discussion of the results will shortly appear in the Communications of the Copenhagen Academy (Kgl. Danske Videnskab. Selskab. Mat.-fys. Medd.).

The investigation has been carried out in the Institute for Theoretical Physics, University of Copenhagen, Copenhagen, Denmark. The authors wish to express their thanks to Professor Niels Bohr for his continued interest in the work and to Dr. J. Koch and Mr. K. O. Nielsen for their kind help in preparing the targets with separated isotopes.

[1] Curran and Strothers, Proc. Roy. Soc. (London) **A172**, 72 (1939).
[2] Hole, Holtsmark, and Tangen, Z. Physik **118**, 48 (1941).
[3] Tangen, Kgl. Norske Videnskab. Selskab. Skrifter 1946, No. 1 (1948).
[4] Weimer, Kurbatov, and Pool, Phys. Rev. **60**, 469 (1941).
[5] Weimer, Kurbatov, and Pool, Phys. Rev. **66**, 209 (1944).
[6] H. T. Richards and R. V. Smith, Phys. Rev. **74**, 1257(A) (1948).
[7] Richards, Smith, and Browne, Phys. Rev. **80**, 524 (1950).
[8] Brostrøm, Huus, and Tangen, Phys. Rev. **71**, 661 (1947).
[9] Brostrøm, Huus, and Koch, Nature **160**, 498 (1947).
[10] Brostrøm, Huus, and Koch, Nature **162**, 695 (1948).
[11] W. Low and C. H. Townes, Phys. Rev. **80**, 609 (1950).
[12] Wentink, Walter, Koski, and Cohen, Phys. Rev. **81**, 948 (1951).

A Note on the Theory of Directional Correlation

K. ALDER
Federal Institute of Technology, Zürich, Switzerland
(Received July 30, 1951)

As a general formula for the correlation of 2 successive emissions of any nuclear particles, Falkoff and Uhlenbeck[1] found

$$W(\vartheta)=\Sigma_{M_aM_bM_c}P_{M_aM_b}(0)P_{M_bM_c}(\vartheta)$$
$$=Q+R\cos^2\vartheta+S\cos^4\vartheta+\cdots, \quad (1)$$

where M_a, M_b, M_c are the magnetic quantum numbers of the 3 energy levels A, B, C. $P_{M_aM_b}$ is the relative probability for the transition $M_a\rightarrow M_b$ in the notation of F.U. In a more natural way $W(\vartheta)$ can be expanded in Legendre polynomials:

$$W(\vartheta)=\Sigma a_k P_k(\cos\vartheta). \quad (2)$$

Here a_k is a product of 2 factors I_k and II_k, which are dependent only upon the first and upon the second of the two transitions, respectively,

$$a_k=\mathrm{I}_k\mathrm{II}_k. \quad (3)$$

For pure transitions

$$\mathrm{I}_k=\{\Sigma_m C_{LmL-m}{}^{k0}(-1)^m F_L{}^M(0)\}W(I_BI_AkL|LI_C), \quad (4)$$

and the same formula holds for II_k with I_C replacing I_A. $W(I_BI_AkL|LI_B)$ is the Racah coefficient,[2] $C_{LmL-m}{}^{k0}$ the Clebsch-Gordon coefficient as used, for example, in the paper of Gardner.[3] If the influence of the magnetic field of the electronic shells on the angular correlation has to be taken into account, the general formula is

$$a_k=\mathrm{I}_k\mathrm{II}_kG_k, \quad (5)$$

where G_k is an attenuation factor, given by

$$G_k=\sum_{FF'}\frac{(2F+1)(2F'+1)|W(I_BJkF|F'I_B)|^2}{1+(\nu_{FF'}|2\gamma)^2}. \quad (6)$$

Following Goertzel,[4] J denotes the electronic angular momentum, F the total angular momentum, $\nu_{FF'}$ the hyperfine splitting, and $4\pi\gamma$ the total transition probability of the intermediate nuclear state B. G_k is completely independent of multipole order and of the spins of initial and final state. G_k can be split up into a part $F=F'$ and into interference terms $F\neq F'$. The latter are negligible when the interaction is strong $\nu_{FF'}\gg 2\gamma$. We are left then with a minimum correlation.

$$(G_k)_{\min}=\Sigma_F(2F+1)^2|W(I_BJkF|FI_B)|^2.$$

The case $J=\frac{1}{2}$ can be easily discussed. The sum of the Racah

coefficients gives

$$G_k = 1 - \frac{k(k+1)}{(2I_B+1)^2}T, \quad T = \frac{(\Delta\nu/2\gamma)^2}{1+(\Delta\nu/2\gamma)^2}$$

with the minimum value

$$(G_k)_{\min} = 1 - k(k+1)/(2I_B+1)^2.$$

For $\Delta\nu/2\gamma = 2\pi\Delta\nu c\tau_B = 1$ (τ_B mean life of the level B) the attenuation is exactly half of its maximal value; $(2\pi\Delta\nu c)^{-1} = \tau_0$ is a characteristic time for this attenuation. The values of τ_0 for different values of $\Delta\nu$ is shown in Table I. The variation of $G_{k,\min}$ as a function of k and I_B may be seen in Table II. An application of

TABLE I. τ_0 as a function of $\Delta\nu$.

$\Delta\nu$	0.001 cm^{-1}	0.01 cm^{-1}	0.1 cm^{-1}	1 cm^{-1}	10 cm^{-1}
τ_0	$5.3\cdot10^{-9}$ sec	$5.3\cdot10^{-10}$ sec	$5.3\cdot10^{-11}$ sec	$5.3\cdot10^{-12}$ sec	$5.3\cdot10^{-13}$ sec

formula (4) which permits the determination of the multipole order and the character of an electromagnetic transition is the following.

TABLE II. $G_{k,\min}$ as a function of k and I_B.

I_B \ k	2	4	6	8	10
1	0.33				
3/2	0.52				
2	0.76	0.20			
5/2	0.83	0.44			
3	0.88	0.59	0.15		
7/2	0.91	0.68	0.34		
4	0.93	0.75	0.48	0.11	
9/2	0.94	0.80	0.58	0.28	
5	0.95	0.84	0.65	0.40	0.09

If in addition to the correlation of the $\gamma-X$ transition (where X stands for any particle) it is possible to measure the $\varepsilon^- - X$ correlation of the respective $\varepsilon^- - X$ transition (ε^- conversion electrons), then the ratio A_k/B_k is dependent only upon k and the multipole order. A_k and B_k are the coefficients of the Legendre polynomials for the $\gamma-X$ and $\varepsilon^- - X$ transition, respectively.

For an electric 2^l transition we get, with $A_0 = B_0 = 1$,

$$A_k/B_k = 1 - [k(k+1)/2l(l+1)].$$

For a magnetic 2^l transition we get

$$\frac{A_k}{B_k} = \frac{l+1}{2l+1}\,\frac{k(k+1)-2l(2l+1)}{k(k+1)-2l(l+1)}.$$

Both formulas are valid for low Z and nonrelativistic energies.

I would like to express my thanks to Professor Pauli, Professor Weisskopf, Dr. Frauenfelder, and Dr. Schafroth for their interest and many discussions.

[1] D. L. Falkoff and G. E. Uhlenbeck, Phys. Rev. 79, 323 (1950).
[2] G. Racah, Phys. Rev. 62, 438 (1942).
[3] J. W. Gardner, Proc. Phys. Soc. (London) 62, 763 (1949).
[4] G. Goertzel, Phys. Rev. 70, 897 (1946).

Properties of Plutonium-243

J. C. SULLIVAN, G. L. PYLE, M. H. STUDIER, P. R. FIELDS, AND W. M. MANNING
Argonne National Laboratory, Chicago, Illinois
(Received July 23, 1951)

TO build up an appreciable concentration of higher plutonium isotopes by successive neutron capture, a sample of Pu^{239} was subjected to a prolonged neutron irradiation. After irradiation the plutonium was isolated from fission products and other impurities by extraction with di-ethyl ether. The isotopic composition of this plutonium was determined mass-spectrometrically by Inghram and Hess.[1] In addition to Pu^{239} they found measurable amounts of Pu^{240}, Pu^{241}, and Pu^{242}.

Samples of a nitrate solution of this plutonium were evaporated to dryness in a quartz tube and irradiated in the thimble of the Argonne heavy water reactor for periods of time varying from two to twenty-four hours. At the end of each irradiation the plutonium was rapidly purified from all extraneous activity by a series of precipitations and solvent extractions. The purifications were continued until the ratio of beta-activity (corrected for decay) to alpha-activity became constant. A five-hour beta-activity remained with the plutonium despite many attempted separations, and was formed with the same cross section in each of the irradiations.

Samples of Pu^{239} containing negligible quantities of higher plutonium isotopes, when subjected to irradiation and subsequent chemical purification under conditions identical to the test samples, showed no traces of the induced five-hour activity.

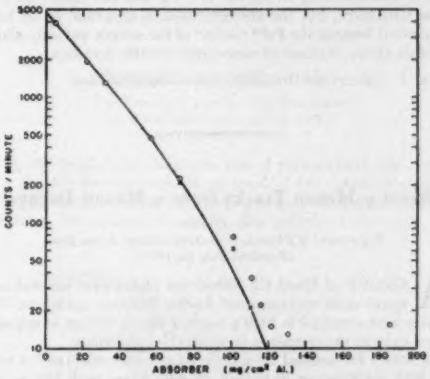

FIG. 1. Aluminum absorption curve with a helium filled, mica end-window tube. The circles represent values corrected for decay, and the crosses represent values corrected for both decay and the constant Geiger background of the plutonium.

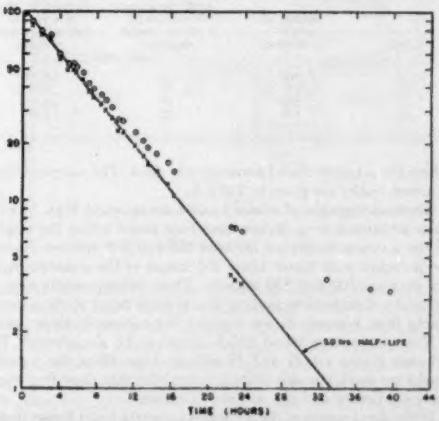

FIG. 2. Decay of Pu^{242}. The circles represent the actual values obtained, while the crosses are these values corrected for the constant Geiger background of the plutonium.

Absorption measurements indicated that the maximum beta-energy for the five-hour plutonium activity is approximately 0.5 Mev. Absorption and decay data are shown in Figs. 1 and 2.

From these results, we conclude that the five-hour activity is due to a plutonium isotope, most probably Pu^{242}. The mass 243 is favored by the following considerations: 1. The difference in yield of five-hour activity from this plutonium sample and from another sample of plutonium containing smaller amounts of Pu^{242}, Pu^{241}, and Pu^{240} fits best with the assumption that the activity was produced by neutron excitation of Pu^{242}. Moreover, except for the unlikely possibility of a short-lived isomer of the observed long-lived Pu^{242}, all plutonium isotopes of lower mass which could conceivably have been formed are long-lived. 2. Odd mass plutonium isotopes 243 or greater are certainly beta-unstable since Pu^{241} is beta-unstable. 3. Plutonium isotopes of mass higher than 243 can almost certainly be ruled out from considerations of yield and the maximum energy of the new beta-ray activity.

The capture cross section of Pu^{242} for pile neutrons, based on the yield of the five-hour activity from five separate irradiations, was estimated to be of the order of one hundred barns. The individual yields, corresponding to 90, 97, 112, 94, and 113 barns, were in close agreement, but the absolute value is uncertain by at least 50 percent because the Pu^{242} content of the sample was only about twofold above the limit of mass-spectrometric detection.

[1] M. C. Inghram and D. C. Hess (private communication).

Short μ-Meson Tracks from π-Meson Decays*

W. F. Fry
Department of Physics, Iowa State College, Ames, Iowa
(Received July 24, 1951)

A GROUP of Ilford C2 200-micron plates were exposed in a spiral orbit spectrometer[1] to the Berkeley cyclotron. The plates were arranged in such a manner that π-mesons of opposite signs entered the emulsions from opposite directions.

A search for unusual $\pi-\mu$-decays has been continued.[2] A total of 3018 $\pi-\mu$-decays have been studied where both the π- and μ-meson tracks stopped in the emulsion. Four cases were found where the μ-meson tracks are unusually short. The ranges of these μ-meson tracks are given in Table I.

TABLE I. Data for four π-meson decays with short μ-meson tracks.

Event	Range of μ-track, in microns	Angle between directions of π- and μ-tracks, degrees	Energy in Mev of π-meson, assuming decay in flight
1	260	113	0.73
2	258	93	1.7
3	185	20	16.6
4	120	73	5.0

Photomicrographs of events 1 and 3 are shown in Figs. 1 and 2. Four additional $\pi-\mu$-decays have been found where the lengths of the μ-meson tracks are between 485 and 500 microns. Sixteen $\pi-\mu$-decays were found where the ranges of the μ-meson tracks are between 500 and 520 microns. These twenty events may be examples of extreme straggling. The average range of the μ meson tracks from π-meson decays is about 594 microns in these plates.

Two events were found which appear to be $\pi-\mu$-decays. The μ-meson tracks are 57 and 25 microns long. Since the μ-meson tracks are short, it seems difficult to establish that these two events are $\pi-\mu$-decays and not scattered μ-mesons.

If the short ranges of the μ-mesons in events 3 and 4 were due to the decay in flight of the π-mesons, the energy of the π-mesons at the time of decay would be 16.6 and 5 Mev, respectively. The grain density near the end of the π-meson tracks is much greater than along a 5-Mev meson track; hence it is concluded that the short ranges of the μ-mesons in events 3 and 4 are not due to the decay in flight of the π-mesons.

In all of the 26 cases where the μ-meson tracks are shorter than 520 microns, the π-mesons entered the emulsions from such a direction as to indicate that the π-mesons were positively charged. Approximately 3300 π-meson events have been studied in these plates. Only 5 π-meson events have been observed where the sign of the charge, as determined from the direction of the π-meson, is inconsistant with the phenomena associated with the meson. Since no conclusive evidence has been found for the decay of negative π-mesons in photographic emulsions, and since the scattering in the spectrometer is small, it is concluded that the π-mesons which give rise to the short μ-meson tracks are positively charged. It is believed that events 1 through 4 are examples of an alternative mode of π-meson decay.

FIG. 1. Photomicrograph of an usual $\pi-\mu$-decay. The π-meson enters the emulsion at point *A* and decays at point *B*. The μ-meson stops at point *C*. The μ-meson track is only 260 microns long. The grain density near the end of the π-track is much greater than along the beginning of the μ-track.

An unusual $\pi-\mu$-decay was found by Smith,[3] where the μ-track is 275 microns long. Another $\pi-\mu$-decay was found by Powell.[4]

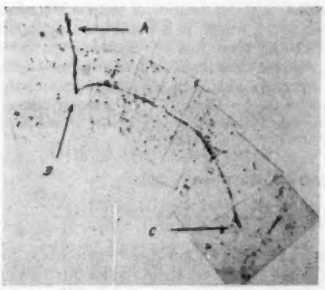

FIG. 2. Photomicrograph of a $\pi-\mu$-decay where the μ-meson track is only 185 microns long. The track of the π-meson is indicated by arrow *A*. The π-meson decay is indicated by arrow *B*. The μ-meson track ends at point *C*. The track of the μ-meson is more nearly perpendicular to the plane of the emulsion than the π-meson track; nevertheless, the grain density is greater near the end of the π-meson track than along the beginning of the μ-meson track.

The μ-track did not end in the emulsion, but by grain counting and scattering it was estimated that the μ-track would have been less than 350 microns long.

The author is indebted to Dr. R. Sagane for the exposed plates and to Dr. J. K. Knipp and Dr. M. Schein for many interesting and helpful discussions.

* Supported in part by a grant from the Research Corporation.
[1] R. Sagane and P. C. Giles, Phys. Rev. 81, 653 (1951).
[2] W. F. Fry, Nuovo cimento, to be published.
[3] F. M. Smith, Reported at the Washington Meeting, American Physical Society (1951).
[4] C. F. Powell, *Cosmic Radiation*, Colston Papers (Butterworth Scientific Publications, London, 1949).

Band Spectra of the Selenium Isotopes

SUMNER P. DAVIS AND F. A. JENKINS
Department of Physics, University of California, Berkeley, California
(Received July 30, 1951)

AN investigation of the rotation structure of the $^1\Sigma_u^+ \rightarrow {}^1\Sigma_g^+$ band system of Se_2 in the region 3700–3815A has been undertaken in an attempt to resolve the discrepancy[1] that exists between the value of the nuclear spin of $_{34}Se^{77}$ indicated by optical hyperfine structure[2] and by microwave spectra.[3] The former method indicates $I=7/2\pm1$ and the latter $I=\frac{1}{2}$, although with certain reinterpretations[2,4] either value may be reconciled with the other. Under these circumstances it seemed logical to apply the method originally used[5] to establish the value $I=0$ for Se^{80}, namely observation of the alternating intensities in the rotational lines of the electronic band spectrum. For this purpose spectrograms have been obtained of the separated isotopes[6] in which the major components were Se^{77}, Se^{78}, and Se^{80}, respectively. They were taken in the second order of the 21-foot grating, which gives a dispersion of 0.67 A/mm. The source was a small quartz tube containing about 10 mg of selenium and 1–5 mm of argon excited by a 60-Mc oscillator. This source may be scaled down in size to yield band spectra of the nonmetallic elements with much smaller samples. Preliminary studies of the possibility of measuring the spin of P^{32} in this way show that the P_2^{32} spectrum may be obtained with as little as 2 μg of phosphorus.

FIG. 1. Tracing of last five lines of 10,5 band of Se_2^{77}, enlarged 40 times from the original plate. The abrupt ending of the P branch due to predissociation is apparent.

$P(45)(44)(43)(42)(41)$

Even though the bands of Se_2 become much simpler when produced by the separated isotopes, only a few at the ultraviolet end are sufficiently free from overlapping to permit an analysis of the rotational structure. Measurements of the 10,4 and 10,5 bands confirm the analysis given by Olsson,[5] who reported on bands due to Se_2^{80} and Se^{78} Se^{80}. The state $v'=10$ shows strong perturbations, while the predissociation occurring in this state at $K'=49$ in Se_2^{80} comes at $K'=44$ in Se_2^{77}. The 9,4 and 9,5 bands appear to be free from such irregularities, and are most suitable for observing the intensity alternation. Our plates of Se_2^{78}, from a sample containing 82.6 percent of Se^{78}, show a very simple structure consisting of singlet P and R branches with alternate lines missing. Hence, as expected, the spin of this isotope is zero.

The first plates with enriched Se^{77} gave evidence of a pronounced alternation,[7] with the lines of odd K stronger since the nucleus obeys Fermi statistics. This sample had a concentration of 58.4 percent Se^{77}, but overlapping by lines due to the next most abundant molecule, Se^{77} Se^{80}, prevented an accurate measurement of the alternation ratio. Hence a special separation was made by the Stable Isotopes Division[6] yielding 50 mg of 91.7 percent Se^{77}. Using 9.5 mg of this material, successful spectrograms were obtained on which the alternation of intensities was essentially free from disturbances. Photographic photometry on the last five lines of the P branch in the 10,5 band, a microphotometer trace of which is shown in Fig. 1, was done by the method previously used by one of the authors[8] in determining the spin of P^{31}. The average ratio obtained was 3.0:1, showing definitely that the nuclear spin of Se^{77} is $\frac{1}{2}$. The band spectrum method, it should be emphasized, is the only way of determining nuclear spins which gives a positive result in cases where $I=0$ or $\frac{1}{2}$. Our value agrees with the conclusion of Canada and Mitchell,[9] based on measurements of the beta-ray spectrum of As^{77}. It also confirms the presumption of Mayer[10] that the odd neutron in Se^{77} is in the $p_{1/2}$ state, rather than in $g_{9/2}$.

In the course of this work, an accidental contamination of air in one tube yielded a well-resolved band system which is evidently that now attributed[11] to SeO, but not as yet studied in detail. By using the separated isotopes, a complete analysis of the rotational structure of these bands will be possible.

[1] J. E. Mack, Revs. Modern Phys. **22**, 64 (1950).
[2] J. E. Mack and O. H. Arroe, Phys. Rev. **76**, 173 (1949).
[3] Strandberg, Wentink, and Hill, Phys. Rev. **75**, 827 (1949); Geschwind, Minden, and Townes, Phys. Rev. **78**, 174 (1950).
[4] Townes, Foley, and Low, Phys. Rev. **76**, 1415 (1949).
[5] E. Olsson, Z. Physik **90**, 138 (1934). A more complete account is given in E. Olsson, Dissertation, Stockholm (1938).
[6] All enriched isotopes were supplied by the Stable Isotopes Research and Production Division, Y-12 Area, Oak Ridge National Laboratory.
[7] S. P. Davis and F. A. Jenkins, Phys. Rev. **83**, 891 (1951). The final result, as reported in the present letter, was given in this paper at the Vancouver meeting.
[8] F. A. Jenkins, Phys. Rev. **47**, 783 (1935).
[9] R. Canada and A. C. G. Mitchell, Phys. Rev. **81**, 485 (1951).
[10] M. G. Mayer, Phys. Rev. **78**, 16 (1950).
[11] Asundi, Jan-Khan, and Samuel, Proc. Roy. Soc. (London) **157**, 28 (1936).

Photodisintegration of He^4

T. S. BENEDICT AND W. M. WOODWARD
Cornell University, Ithaca, New York[*]
(Received July 27, 1951)

CROSS sections for the production of protons from He^4 using the 300-Mev bremsstrahlung beam of the Cornell synchrotron have been measured for proton energies ranging from 45 to 120 Mev. The apparatus consists of a pressure vessel (Fig. 1)

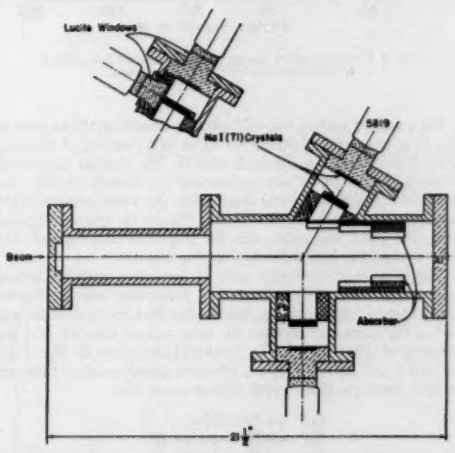

FIG. 1. Schematic diagram of the apparatus.

capable of withstanding pressures up to 2000 lb/in.^{2}, with counting arms mounted at 60° and 90° with respect to the γ-ray beam. Two NaI(Tl) crystals are mounted inside each arm in such a way as to form a proton counter telescope. The light from the crystals is piped out of the vessel through Lucite windows which are about 4 cm thick. The scintillations are detected by RCA 5819 photomultiplier tubes. The front counter, in conjunction with a multi-channel pulse-height discriminator, was used to measure the ionization of those particles which pass through the front crystal and subsequently lose >15 Mev in the back crystal.

With this arrangement one observes a pulse-height distribution with a width at half-maximum of 3 Mev corresponding to an energy spread for protons incident on the first crystal of about 20 Mev. This method distinguishes protons from mesons and electrons because, although it is possible for the latter to produce 15-Mev pulses in the back crystal (i.e., stars), they will produce considerably smaller pulses in the front crystal. The energy of those protons counted could be varied by sliding lead absorbers in front of the counting arms as shown in Fig. 1.

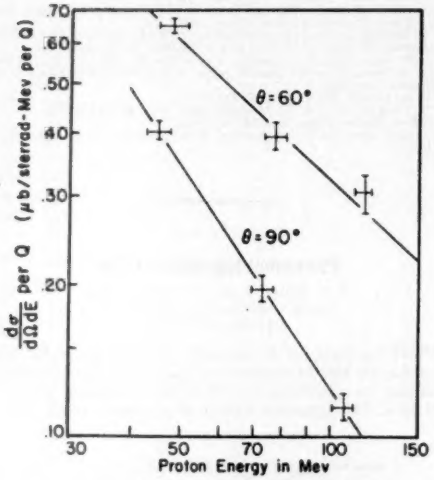

FIG. 2. Cross section vs energy for photoprotons from He^4 at 60° and 90° relative to the γ-ray beam.

The counting system was calibrated by observing the number of counts in the proton distribution curve as a function of discriminator bias setting for the back crystal. The number of protons counted should go to zero approximately linearly as the bias setting for the back crystal approaches the value corresponding to the energy thickness of the crystal. This energy was also checked using the ThC″ end point, and the two calibrations agreed. The front crystal was calibrated in a similar manner.

The beam was monitored with an ionization chamber behind one-quarter inch of lead which had previously been calibrated against the pair spectrometer. Measurements were made at 60° and 90° in the laboratory system for three proton energies at a gas pressure of 1800 lb/in.[2] The cross sections given in Fig. 1 are plotted in μb/sterrad-Mev per effective quantum, since there are at least three reactions which yield protons, viz:

(a) $\gamma+He^4\rightarrow H^3+p$,
(b) $\gamma+He^4\rightarrow p+n+H^2$,
(c) $\gamma+He^4\rightarrow p+p+n+n$.

If we assume that the predominant reaction is (a), the cross sections at 101° in the c.m. system per photon are $d\sigma/d\Omega=25$, 17, and 14μb at γ-ray energies of 78, 112, and 153 Mev, respectively.

It should be noted that the resolution of the arrangement was not sufficient to distinguish between protons, deuterons, and tritons; however, energetic considerations show that the heavier particles should contribute only a small fraction of the observed coincidences.

The errors given in Fig. 2 are relative errors. The error to be assigned to the absolute cross sections is 30 percent.

† Supported by the joint program of the ONR and AEC.

The Nature of the Second-Order Transition in ND_4Br

HENRI A. LEVY AND S. W. PETERSON
*Oak Ridge National Laboratory, Oak Ridge, Tennessee**
(Received July 25, 1951)

SECOND-ORDER phase transitions in the ammonium halides have been interpreted as the onset of free rotation[1] or of orientational disorder[2] of ammonium ions. Recent spectroscopic evidence[3] supports the latter hypothesis. We have obtained direct evidence also favoring the disorder hypothesis from complete crystal structure determinations of two phases of ND_4Br by means of neutron diffraction. A contrary result in ND_4Cl was recently reported by Goldschmidt and Hurst[4] from a neutron diffraction study of that material.

ND_4Br undergoes the following changes[5] as the temperature is lowered:

$$\text{f.c. cubic} \xrightarrow{\sim 125^\circ} \text{simple cubic (CsCl type)} \xrightarrow[\text{second order}]{-58.4^\circ}$$
$$\text{tetragonal} \xrightarrow{-105^\circ} \text{simple cubic (CsCl type).}$$

Neutron diffraction data from all four phases have been collected, and those of the two CsCl-type structures have been analyzed in detail. Scattering cross sections used were those reported by Shull and Wollan.[6] Observed data and comparison with calculation are presented in Table I.

TABLE I. Neutron diffraction data[a] from ammonium bromide.

Indices	Low temperature phase Calc.	Obs.	Uncertainty	Room temperature phase Calc.	Obs.	Uncertainty
100	17.9	17.9	±0.4	17.8	17.7	±0.35
110	72.0	72.3	1.4	67.5	67.3	1.3
111	15.4	16.1	0.8	3.9	3.6	0.4
200	5.4	5.0	0.6	6.2	6.8	0.7
210	0.6	1.7	1.0	0.2	0	1.0
211	84.5	87.1	2.4	32.0	32.1	1.6
220	31.1	30.8	2.0	18.9	19.5	1.4
221–300	79.1	76.0	3.5	8.7	7.8	0.8
310	2.4	4.1	2.1	3.9	3.7	1.8
311	13.1	13.3	3.5	3.0	3.0	1.5
222	43.3	41.5	8	11.3	11.3	1.7
320	8.4	5.8	4	2.0	3.7	1.8
321	159.5	163.2	8	72.8	77.8	5.8
400	0.2	0	1	0.1	0	1.0
410–322	27.2	27.4	3	4.8	6.1	3.0
411–330	124.1	117.5	15	45.9	48.0	4.8
331	27.5	33.4	15	6.8	9.6	4.8
420	77.7	93.2	15	31.3	36.9	5.5
421	23.4	40.9	15	2.5	5.2	2.6
332	32.0	25.0	10	18.8	18.1	2.7

[a] The quantities listed are the square of the structure factor multiplied by the multiplicity of the reflection, jF^2. The calculated values are for the final models and include the effects of temperature motion. Intensities were measured on an absolute scale, so that absolute as well as relative agreement is significant.

The phase at −195°C was found to give a simple cubic pattern with $a_0=3.96$A. Peak intensities were satisfactorily matched by calculation from a model conforming to symmetry T_d^1 with deuterium atoms placed in fourfold positions (*e*),[7] along the body diagonals of the cube. The required temperature factor for deuterium corresponded to a mean amplitude of vibration of about 0.14A. Thus, the lowest temperature phase consists of an ordered structure closely similar to that found for low temperature ND_4Cl.

The room temperature pattern corresponds to a simple cubic unit with $a_0=4.05$A. The model which gave satisfactory agreement placed the four deuterium atoms at random in the eightfold positions (*g*) of space group O_h^1, corresponding to twofold randomness in the orientation of the tetrahedral ammonium ions. The model required anisotropic temperature motion of the deuterium atoms, the distribution being greatly extended in directions near the plane normal to the N—D link. This anisotropy could result from torsional oscillation of the ammonium ion about the two

equilibrium orientations in its cubic cage of bromide ions. In the simplified model used for calculation, each deuterium was treated as a spherical cloud whose center was distributed with uniform probability around a circle centered on the cube body diagonal, the root-mean-square radius of the cloud and the half-angle subtended by the circle at the nitrogen atom being treated as parameters whose final values were 0.21A and 10°, respectively. Models involving ordered structures of symmetry T_d^1 with or without anisotropic temperature motion and models with freely rotating ammonium ions failed to give agreement with the data. Also eliminated were models in which the ammonium ions rotate about their twofold axes, space group O_h^1, and about their threefold axes with and without randomness of orientation, space group T_d^1 and O_h^1 (simulated), respectively.

Thus, in room-temperature ND_4Br there exists orientational disorder of the ammonium ions, and the crystal belongs to symmetry class O_h, simulating the space-group symmetry O_h^1. The reported chloride structure, in contrast, is ordered, with symmetry T_d^1, although involving temperature motion similar to that found in ND_4Br. This difference between the room temperature phases of ND_4Br and ND_4Cl is surprising and calls for further study to confirm its reality. A disagreement exists on the value of the coherent scattering cross section of deuterium (5.2 barns[8] in this work *versus* 5.8 used in reference 4). We find that use of the latter value does not change our conclusions with regard to the nature of the structure; however definitely better agreement is achieved with the value 5.2.

Our study yields the values 0.99 ± 0.02A for the length of the N−D link, equal within experimental uncertainty in both phases. Further work on the atomic arrangements in the two remaining phases is planned. A complete description will be published elsewhere.

* This work was performed for the Atomic Energy Commission.
[1] L. Pauling, Phys. Rev. 36, 430 (1930).
[2] J. Frenkel, Acta Physicochim. U.R.S.S. 3, 23 (1935).
[3] E. L. Wagner and D. F. Hornig, J. Chem. Phys. 18, 296, 305 (1950).
[4] G. H. Goldschmidt and D. G. Hurst, Phys. Rev. 83, 88 (1951).
[5] A. Smits and D. Tollenaer, Z. physik. Chem. B52, 222 (1942).
[6] C. G. Shull and E. O. Wollan, Phys. Rev. 81, 527 (1951).
[7] *International Tables for the Determination of Crystal Structures* (Edwards Brothers, Inc., Ann Arbor, Michigan, 1944), revised edition.

The Spins and Parities of the 3.7–3.9-Mev Doublet in C^{13}

J. ROTBLAT
The Physics Department,
Medical College of St. Bartholomew's Hospital, London, England
(Received August 1, 1951)

THE energy of the nuclear level of C^{13}, following after the 3.11-Mev state, has been variously given in the literature as 3.7 and 3.9 Mev. Thus Heydenburg *et al.*[1] in a study of the protons from $C^{12}(d, p)C^{13}$ give the energy value of the state as 3.91 Mev, while recently Malm and Buechner,[2] in a careful measurement of the alpha-particles from $N^{15}(d, \alpha)C^{13}$, found a value of 3.68 Mev. Actually both of these values are nearly correct. In a detailed study of the protons from the $C^{12}(d, p)C^{13}$ reaction, using an 8-Mev deuteron beam and employing the photographic emulsion technique for recording the protons (the experimental arrangement is described by Rotblat *et al.*)[3] two groups of protons, of slightly different ranges, were found to be present in this energy region, indicating the existence of two closely lying levels in C^{13}. The protons of longer range have a much lower intensity than those of the shorter range; at some angles the intensity of the former is only 2 percent of that of the latter. For this reason the longer range group tends to be lost in the "tail" of the more intense group. Nevertheless, after measuring a large number of tracks at 20 angles of emission and analyzing the histograms of the proton groups, the existence of both levels has been established beyond doubt. The Q-values for the two states were found to be -0.967 and -1.168 Mev; assuming a Q-value for the ground state of 2.716 Mev[4] we obtain for the energy values of the two states 3.683 and 3.884 Mev. It is possible that these correspond to the states which were observed by Creagan[5] from the $B^{10}(\alpha, p)C^{13}$ reaction and for which he gave values 3.76 and 4.00 Mev. It is also interesting to note that, unlike the $C^{12}(d, p)$ process in which the 3.7-Mev level is formed relatively rarely, in the $N^{15}(d, \alpha)$ reaction this level appears to be formed predominantly.

Apart from establishing the existence of the doublet, the angular distributions of the two groups of protons have also been investigated. According to Butler's[6] stripping process the spins and parities of the corresponding nuclear states can be determined

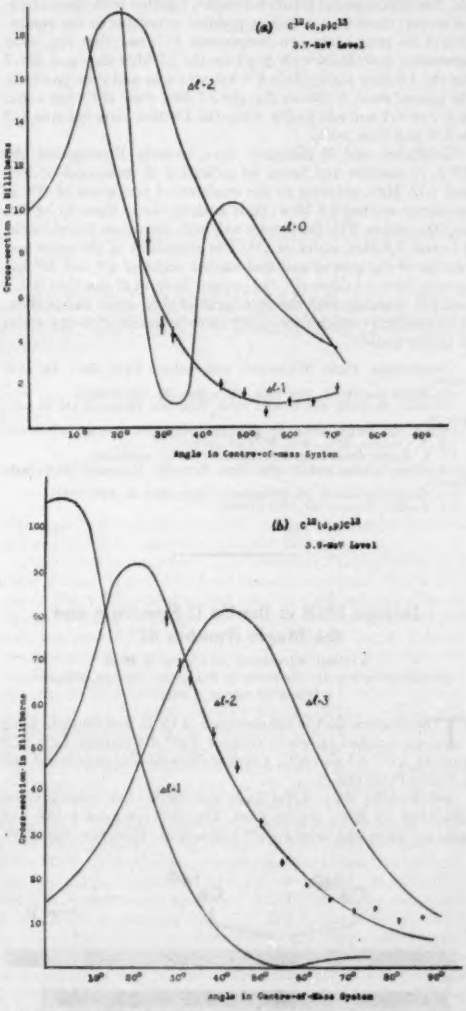

FIG. 1. Angular distributions of protons from $C^{12}(d, p)C^{13}$ in the center-of-mass system. The full curves give the theoretical distributions for various values of the angular momentum transfer. The experimental points are given with their probable errors. Figure 1(a) is for the formation of C^{13} in the 3.7-Mev state and Fig. 1(b) for the 3.9-Mev state.

from the angular distributions. The analysis of the histograms into the two components gives the number of protons in each group, and from this the differential cross sections can be calculated.[7] Unfortunately the distribution could not be studied in the most interesting region, at small angles, owing to the overlap of a group of protons from the elastic scattering of deuterons on hydrogen (the target gas was acetylene), but the accuracy with which the cross sections were determined at the larger angles was sufficient to establish the spins and parities of the two states. The observed angular distributions up to angles of about 90° are indicated in Figs. 1(a) and (b) for the 3.7- and 3.9-Mev levels, respectively. The full curves are the distributions calculated on the basis of Butler's theory for various values of the angular momentum transfer. The experimental points are shown together with the statistical errors; these do not include possible errors due to the separation of the groups into two components. It is seen that very good agreement is obtained with $\Delta l=1$ for the 3.7-Mev state and $\Delta l=2$ for the 3.9-Mev state. Since C^{12} has zero spin and even parity in the ground state, it follows that the 3.7-Mev state of C^{13} has a spin of 1/2 or 3/2 and odd parity, while the 3.9-Mev state has spin 3/2 or 5/2 and even parity.

Goldhaber and Williamson[8] have recently investigated the $C^{12}(\phi, \phi)$ reaction and found an indication of resonances at 1.68 and 1.73 Mev, pointing to the existence of two levels of N^{13} at an energy around 3.5 Mev; their analysis shows these to be $P_{3/2}$ and $D_{3/2}$ states. This fits in very well with our values found for the 3.7- and 3.9-Mev states of C^{13}. The agreement of the spins and parities of the ground and first excited states of C^{13} and N^{13} has already been established.[9] The present findings of doublets in C^{13} and N^{13}, together with the agreement of their spins and parities, is an excellent confirmation of the correspondence of energy states in mirror nuclei.

[1] Heydenburg, Inglis, Whitehead, and Hafner, Phys. Rev. **75**, 1147 (1949).
[2] R. Malm and W. W. Buechner, Phys. Rev. **81**, 519 (1951).
[3] Rotblat, Burrows, and Powell, Proc. Roy. Soc. (London) (to be published).
[4] Strait, von Patter, Buechner, and Sperduto, Phys. Rev. **81**, 747 (1951).
[5] R. J. Creagan, Phys. Rev. **76**, 1769 (1949).
[6] S. T. Butler, Proc. Roy. Soc. (London) (to be published).
[7] Burrows, Gibson, and Rotblat, Proc. Roy. Soc. (London) (to be published).
[8] G. Goldhaber and R. M. Williamson, Phys. Rev. **82**, 495 (1951).
[9] J. Rotblat, Nature **167**, 1027 (1951).

Isotope Shift in the Ce II Spectrum and the Magic Number 82*

KIYOSHI MURAKAWA AND JOHN S. ROSS
Department of Physics, University of Wisconsin, Madison, Wisconsin
(Received August 1, 1951)

THE isotope shift in the spectrum of Ce II was studied,[1] using an enriched sample of cerium[2] (Ce^{138} 4.4 percent, Ce^{140} 92.0 percent, Ce^{142} 3.5 percent), a hollow-cathode discharge tube,[3] and a Fabry-Perot etalon.

λ4628 ($4f^26s\ ^4H_{9/2}-4f^26p\ ^4I_{9/2}{}^o$) was studied first, since it is not disturbed by other cerium lines. The Ce^{142}-component was well resolved from the strong Ce^{140}-component. However, the Ce^{138}-component was not resolved, although Ce^{138} is somewhat more abundant than Ce^{142}. The distance 140–142 was found to be 0.055 cm^{-1}, which agrees with the measurement of Brix and Frank[4] within experimental error. The upper limit of the distance 138–140 was found to be about 0.029 cm^{-1}. Figure 1 illustrates some of the spectrograms of λ4628. Here λ4528 ($4f^26s\ ^4H_{13/2}-4f^26p\ ^4I_{13/2}{}^o$) was also found to have the same structure as λ4628.

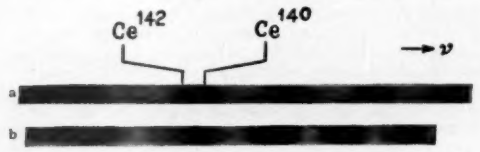

FIG. 1. Fabry-Perot patterns of Ce II λ4628. (a) Natural cerium (Ce^{140} 88.5 percent, Ce^{142} 11.1 percent); 20-mm etalon. (b) Enriched sample (Ce^{138} 4.4 percent, Ce^{140} 92.0 percent, Ce^{142} 3.5 percent); 30-mm etalon.

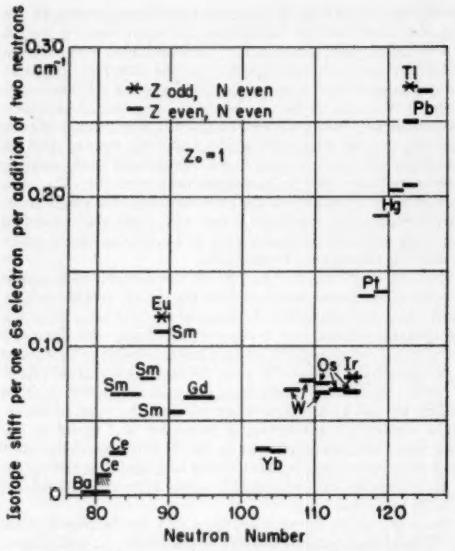

FIG. 2. Plot of the isotope shift per one 6s electron in the neutral atom per addition of two neutrons as a function of the neutron number.

This result shows that the upper limit of the distance 138–140 is about half of the distance 140–142. Since the neutron number (N) of the isotope 140 is 82, the above-mentioned anomaly can be very probably ascribed to the stable nuclear structure connected with the magic number 82.[5]

The isotope shift in the spectra of heavy elements was treated theoretically by Rosenthal and Breit[6] and by Crawford and Shawflow.[7] It is characteristic of similar theories that the isotope shift is proportional to $\psi^2(0)$, the square of the nonrelativistic wave function at the position of the nucleus. It is expressed by

$$\psi^2(0)=Z_iZ_e^3(dn^*/dn)/[\pi a_H^3 n^{*3}],$$

where the symbols have their usual meaning.

Using the same considerations as those of Crawford and Shawlow[7] and the above-mentioned formula, we can calculate from experimental data, for most heavy elements, the isotope shift per one 6s electron in the neutral atom ($Z_0=1$), per addition of two neutrons, the accuracy being 10–15 percent. Figure 2 represents the above-mentioned quantity[8] as a function of the neutron number. The isotope Sm^{148} does not exist, so the value for the isotope $Sm^{144}-Sm^{148}$ is divided by 2 and plotted. Since no gross multiplet analysis of Nd I is available, no value for the Nd isotopes is plotted. However, a rough estimate, obtained by using the data of Klinkenberg,[9] shows that the plots for Nd fall fairly close to those of Sm, and the irregularity for the pair N88–90 is especially conspicuous for Nd also.

Figure 2 shows that there is a distinct rise in the diagram when we pass from $N=80$ to $N=82$, and the above-mentioned anomaly in the isotope shift for $N=88$–90 is especially large, an idea which was expressed by Klinkenberg. Investigation of the physical meaning of the neutron number 88 or 90 will be important.

The idea that the neutron number is more important than the proton number in considering the isotope shift in the spectra of heavy elements is not altogether new, but we believe that the diagram given in Fig. 2 will be useful in arranging isotope shift data.

We are looking forward to the availability of the enriched cerium isotope 136.

* Supported by the ONR.
[1] Harrison, Albertson, and Hosford, J. Opt. Soc. Am. **31**, 439 (1941).
[2] Loaned by Union Carbon and Carbide Corporation, Oak Ridge, Tennessee.
[3] O. H. Arroe and J. E. Mack, J. Opt. Soc. Am. **40**, 386 (1950).
[4] Z. Physik **127**, 289 (1950).
[5] M. G. Mayer, Phys. Rev. **78**, 16 (1950).
[6] J. Rosenthal and G. Breit, Phys. Rev. **41**, 459 (1932).
[7] M. F. Crawford and A. L. Shawflow, Phys. Rev. **76**, 1310 (1949).
[8] In the calculation, besides the articles quoted by J. E. Mack, Revs. Modern Phys. **22**, 64 (1950), the following data were utilized: Ba: O. H. Arroe, Phys. Rev. **79**, 836 (1950); Gd: P. F. A. Klinkenberg, Physica **12**, 33 (1946); W: J. A. Vreeland and K. Murakawa (to be published); Os: S. Suwa (to be published); Ir: K. Murakawa and S. Suwa (to be published); Pb: K. Murakawa and S. Suwa, J. Phys. Soc. Japan **5**, 429 (1950); F. E. Geiger, doctoral thesis, University of Wisconsin (1950).
[9] P. F. A. Klinkenberg, Physica **11**, 327 (1945).

β-Ray Spectrum and the *ft* Value in the Second Forbidden Transition

SEITARO NAKAMURA, MINORU UMEZAWA, AND HISAO TAKEBE
Department of Physics, University of Tokyo, Tokyo, Japan
(Received June 25, 1951)

RECENTLY, a new type of forbidden β-ray spectrum of Cl^{36} was explained by Wu and Feldman[1] by means of a linear combination of A_{ij} and T_{ij} terms in the second forbidden tensor interaction C_{2T}. This provides a valuable basis for further interpretation and also for the eventual discovery of forbidden spectra. We have tried to reinterpret the forbidden spectra of Tc^{99} and Sb^{124} following this principle, i.e., using a correction factor

$$C_{2T}\sim k^2(3a)+(1/12)(3D_+-c)-kE,$$

where a, $3D_+-c$, and E are as defined in Konopinski's[2] paper, and

$$k^2=\Sigma|A_{ij}|^2/\Sigma|T_{ij}|^2. \quad (1)$$

The quantity k will be determined so that a straight-line Fermi plot may result by using the correction factor C_{2T}.

$_{43}Tc_{56}^{99}$:—If we take $k=7.7$, the forbidden Fermi plot becomes a straight line up to $W=1.35\ mc^2$ from the maximum energy, as is seen in Fig. 1. The experimental material used here was given in Taimuty's[3] paper. The spin of the ground state of $_{43}Tc_{56}^{99}$ has been determined[4] to be 9/2. On the basis of the nuclear shell model, we can expect the ground state of $_{43}Tc_{56}^{99}$ to arise from the combination of a $g_{9/2}$ proton with an even state neutron; the resultant state should then have even parity. The ground state of $_{44}Ru_{55}^{99}$ presumably may be constructed by the $d_{5/2}$ (or $g_{7/2}$) neutron with an even state proton. If the ground state of Ru^{99} is $d_{5/2}$, the required selection rule, $\Delta J=\pm 2$, no parity change, will be satisfied.

Sb^{124}:—We found that $k=13$ results in a straight line forbidden Curie plot down to $W=4\ mc^2$ for the highest energy β-ray of Sb^{124} (see Fig. 2). The data were presented by Langer, Moffat, and Price,[5] who showed that the "a"-type interaction C_{1T} provides a good explanation for it. In the light of their analysis concerning $Sb^{124}\rightarrow Te^{124}$ decay schemes, we can take the alternative explanation: i.e., if a C_{2T} transition ($\Delta J=\pm 2$, no) is valid, the odd parity and spin 3 ground state ($g_{7/2}$, $h_{11/2}$) of Sb^{124} goes to the odd parity excited state (presumably spin 1) of Te^{124}, which is accompanied by the electric dipole ratiation, 0.607-Mev γ-ray, reaching the even parity and spin 0 ground state of Te^{124}. On Mayer's nuclear shell model, however, it seems more reasonable to assume a ($g_{7/2}$ proton, $s_{1/2}$ neutron)-state, thus even parity for the ground state of Sb^{124}, and also to assign even parity for the excited state of Te^{124}.

Once the ratio k is determined, one can evaluate the *ft* values of β-decay in these cases. By using the forbidden *f*-functions,[6]

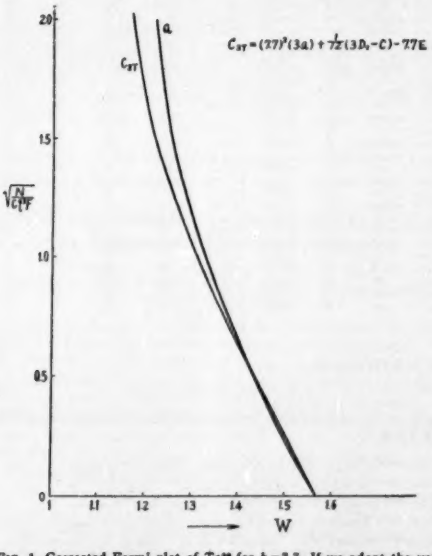

FIG. 1. Corrected Fermi plot of Tc^{99} for $k=7.7$. If we adopt the value $k\geq 7.8$ instead of $k=7.7$, the curve will deviate downward from the straight line about the point $W=1.32$. And for $k\leq 7.6$, the curve tends to bend upward for W less than 1.37. The curve might be a straight line up to $W<1.35$, if we take for k a value a little smaller than 7.7.

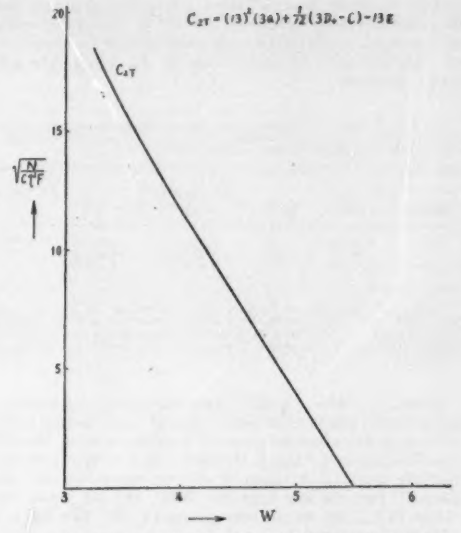

FIG. 2. Corrected Fermi plot of Sb^{124} for $k=13$. If we adopt the value $k<13$, the curve is nearly straight up to $W\sim 3.5$, but the curve deviates slightly from a straight line about $W=4.5$. This deviation, however, can be removed by a small modification of the lines joining the empirical data in Langer's graph.

we have the results shown in Table I. It is interesting to note that they fall into a distinct group, i.e., $ft \sim 10^{13}$. In view of this result, one can expect to find some reasons which indicate the interpretation that Sb^{124} is to be classified into the C_{2T} group ($\Delta J = \pm 2$, parity change no).

TABLE I. ft values of β-decay in the second forbidden transition.* f_{1T}, f_{2T} are the first and second forbidden f-functions, respectively (see reference 6); the coulomb corrections are also made.

Element	t(sec)	$W_0(mc^2)$	$\Delta J = \pm 2$, yes ft_{1T}	$\Delta J = \pm 2$, no ft_{2T}	k
Cl^{36}	1×10^{13}	2.4	6.1×10^{13}	9.8×10^{13}	$\sqrt{18}$
Tc^{99}	7×10^{12}	1.57	1.1×10^{11}	8.4×10^{13}	7.7
Sb^{124}	5×10^{6}	5.5	1.0×10^{10}	2.4×10^{12}	13

* If we take into account the fact that all β-emitters of the "a" type group ($\Delta J = \pm 2$, yes) have $ft = 10^8$ (see references 7, 9, and 8), it seems more natural to classify Cl^{36}, Tc^{99}, and Sb^{124} into C_{2T} groups ($\Delta J = \pm 2$, no), rather than into "a"-type groups. Theoretically, ft_{2T} should be proportional to $\Sigma |T_{ij}|^2$.

In fact, C_{1T} ($\Delta J = \pm 2$, parity change yes) gives an ft value for $_{51}Sb_{73}^{124}$ (see Table I) which seems too great to be classified in the "a" type group, where the corrected ft values are about $10^7 \sim 10^8$ (see Taketani, *et al.*,[7] also J. Davidson).[8] It is interesting to note that the empirical ft values of different transitions, i.e., the allowed ($\int \sigma$), the first forbidden (ΣB_{ij}), and the second forbidden (ΣT_{ij}), fall into distinct groups, i.e., 10^4, $10^6 \sim 10^9$, and $10^{13} \sim 10^{12}$, respectively.[9]

In conclusion it is suggested that, when carrying out an analysis of β-decay, one can get useful and effective information from the evaluation of corrected ft values in addition to the usual analysis of the spectrum shape and the analysis of the selection rule on the basis of the shell model.

[1] C. S. Wu and L. Feldman, Phys. Rev. **82**, 457 (1951). The authors are greatly indebted to Professor Wu for sending the manuscript before publication.
[2] E. J. Konopinski, Revs. Modern Phys. **15**, 209 (1943).
[3] S. I. Taimuty, Phys. Rev. **81**, 461 (1951).
[4] K. G. Kessler and W. F. Meggers, Phys. Rev. **80**, 901 (1950).
[5] Langer, Moffat, and Price, Phys. Rev. **79**, 808 (1950).
[6] Nakamura, Shima, and Kobayashi, J. Phys. Soc. Japan **4**, 166 (1949).
[7] Taketani, Nakamura, Umezawa, Ono, and Yamaguchi, Phys. Rev. **82**, 441 (1951).
[8] J. Davidson, Phys. Rev. **82**, 48 (1951).
[9] Taketani, Nakamura, Ono, and Umezawa, Prog. Theor. Phys. **6**, 266 (1951).

Third-Order Elastic Coefficients of Crystals

FAUSTO G. FUMI
Institute of Theoretical Physics, University of Milan, Milan, Italy

(Received May 21, 1951)

THE independent nonzero third-order elastic coefficients of crystals $C_{pqr} = C_{prq} = C_{qpr}$ ($p, q, r = 1, 2, 3, 4, 5, 6$) (sixth-order polar tensor) have hitherto been known only for cubic groups and for C_3.[1,2] Here they are derived for all the crystal classes S_2; C_{1h}, C_2, C_{2h}; C_{2v}, D_2, D_{2h}; C_4, S_4, C_{4h}, C_{4v}, D_{2d}, D_4, D_{4h}; C_3, S_6, C_{3v}; T, T_h, T_d, O, O_h in which one can find orthogonal cartesian coordinates that do not transform into linear combinations of themselves under the symmetry operations of the crystal,[3] and for D_{3d}($C_{3v} \times i = D_3 \times i$) and D_3, which are equivalent to C_{3v} for polar properties of even order. The numbers of coefficients agree in all cases with those found group-theoretically by Bhagavantam and Suryanarayana[3] and by Jahn.[3] The coefficients for symmetry C_3, T, O, T_h, O_h agree with those given by Birch.[1]

For symmetry C_1 the number of independent third-order elastic coefficients equals the numbers of combinations with repetition of class 3 of 8 objects: $8!/5!3! = 56$. They are listed in Table I. Symmetry $S_2 = C_1 \times i$ is equivalent to C_1.

For symmetry C_{1h}

$$\sigma_h: x \to x, \quad y \to -y, \quad z \to z, \tag{1}$$

the 24 coefficients with indices odd in y must vanish, since they change sign under σ_h (Table I). Symmetries C_{2h}($C_{1h} \times i = C_2 \times i$) and C_2($C_3 = C_2(y)$) are equivalent to C_{1h}.

For symmetry C_{2v}

$$\sigma_v: x \to -x, \quad y \to y, \quad z \to z; \quad \sigma_v': x \to x, \quad y \to -y, \quad z \to z, \tag{2}$$

σ_v requires that the 12 independent nonzero coefficients for C_{1h} with indices odd in x vanish (Table I). Symmetries D_{2h}($C_{2v} \times i = D_2 \times i$) and D_2 are equivalent to C_{2v}.

TABLE I. Third-order elastic coefficients of crystals.

C_1, S_2	C_{1h}, C_s C_{2h}	C_{2v}, D_2 D_{2h}	C_3, S_6	C_{3v}, D_{3d} D_{3d}	C_4, S_4 C_{4h}	C_{4v}, D_{2d} D_4, D_{4h}	T, T_h	T_d, O O_h
xxxxxx	xxxxxx	xxxxxx	xxxxxx	xxxxxx	xxxxxx	xxxxxx	xxxxxx	xxxxxx
xxxxyy	xxxxyy	xxxxyy	xxxxyy	xxxxyy	xxxxyy	xxxxyy	xxxxyy	xxxxyy
xxxxzz	xxxxzz	xxxxzz	xxxxzz	xxxxyy	xxxxzz	xxxxzz	xxxxzz	xxxxyy
xxxxyz	0	0	xxxxyz	xxxxyz	0	0	0	0
xxxxzx	xxxxzx	0	xxxxzx	xxxxzx	0	0	0	0
xxxxxy	0	0	xxxxxy	xxxxzx	xxxxxy	0	0	0
xxyyyy	xxyyyy	xxyyyy	xxyyzz	xxxxyy	xxxxyy	xxxxyy	xxxxzz	xxxxyy
xxyyzz	xxyyzz	xxyyzz	xxyyzz	xxyyzz	xxyyzz	xxyyzz	xxyyzz	xxyyzz
xxyyyz	0	0	xxyyyz	xxyyyz	0	0	0	0
xxyyzx	xxyyzx	0	xxyyzx	xxyyzx	0	0	0	0
xxyyxy	0	0	xxyyxy	xxyyzx	0	0	0	0
xxzzzz	xxzzzz	xxzzzz	xxxxyy	xxxxyy	xxzzzz	xxzzzz	xxxxyy	xxxxyy
xxzzyz	0	0	xxyyzx	xxyyyz	0	0	0	0
xxzzzx	xxzzzx	0	xxyyxy	xxyyxy	0	0	0	0
xxzzxy	0	0	xxyyyz	xxyyyz	xxzzxy	0	0	0
xxyzyz	xxyzyz	xxyzyz	xxyzyz	xxyzyz	xxyzyz	xxyzyz	xxyzyz	xxyzyz
xxyzzx	0	0	xxyzzx	xxyzzx	xxyzzx	0	0	0
xxyzxy	xxyzxy	0	xxyzxy	xxyzzx	0	0	0	0
xxzxzx	xxzxzx	xxzxzx	xxzxzx	xxzxzx	xxzxzx	xxzxzx	xxzxzx	xxzxzx
xxzxxy	0	0	xxzxxy	xxzxxy	0	0	0	0
xxzxyy	xxzxyy	xxzxyy	xxzxyy	xxzxzx	xxzxyy	xxzxyy	xxzxyy	xxzxzx
yyyyyy	yyyyyy	yyyyyy	xxxxxx	xxxxxx	xxxxxx	xxxxxx	xxxxxx	xxxxxx
yyyyzz	yyyyzz	yyyyzz	xxxxyy	xxxxyy	xxxxzz	xxxxzz	xxxxyy	xxxxyy
yyyyyz	yyyyzx	0	xxxxyz	xxxxyz	0	0	0	0
yyyyzx	yyyyzx	0	xxxxzx	xxxxyz	0	0	0	0
yyyyxy	0	0	xxxxzx	xxxxzx	−xxxxxy	0	0	0
yyzzzz	yyzzzz	yyzzzz	xxxxzz	xxxxyy	xxzzzz	xxzzzz	xxxxzz	xxxxyy
yyzzyz	0	0	xxyyxy	xxyyxy	0	0	0	0
yyzzzx	yyzzzx	0	xxyyyz	xxyyyz	0	0	0	0
yyzzxy	0	0	xxyyzx	xxyyyz	−xxzzxy	0	0	0
yyyzyz	yyyzyz	yyyzyz	xxxyxy	xxzxzx	xxzxzx	xxzxzx	xxxyxy	xxzxzx
yyyzzx	0	0	xxyzxy	xxyzzx	−xxyzzx	0	0	0
yyyzxy	yyyzxy	yyyzxy	xxzxzx	xxzxzx	0	0	0	0
yyzxzx	yyzxzx	yyzxzx	xxyzyz	xxyzyz	xxyzyz	xxyzyz	xxyzyz	xxyzyz
yyzxxy	yyzxxy	yyzxxy	xxyzzx	xxyzyz	xxyzzx	xxyzyz	xxyzyz	xxyzyz
zzzzzz	zzzzzz	zzzzzz	xxxxxx	xxxxxx	zzzzzz	zzzzzz	xxxxxx	xxxxxx
zzzzyz	0	0	xxxxzx	xxxxzx	0	0	0	0
zzzzzx	zzzzzx	0	xxxxyz	xxxxyz	0	0	0	0
zzzzxy	0	0	xxxxzx	xxxxzx	0	0	0	0
zzyzyz	zzyzyz	zzyzyz	xxzxzx	xxzxzx	zzyzyz	zzyzyz	xxzxzx	xxzxzx
zzyzzx	0	0	xxyzyz	xxyzyz	0	0	0	0
zzyzxy	zzyzxy	0	xxyzzx	xxyzyz	0	0	0	0
zzzxzx	zzzxzx	zzzxzx	xxyzyz	xxyzzx	0	0	0	0
zzzxxy	0	0	xxyzxy	xxyzzx	zzyzxy	0	0	0
zzzxyy	zzzxyy	zzzxyy	xxyzzx	xxyzyz	zzyzxy	0	0	0
yzyzyz	0	0	yzyzyz	yzyzyz	0	0	0	0
yzyzzx	yzyzzx	0	yzyzzx	yzyzzx	0	0	0	0
yzyzxy	0	0	yzyzxy	yzyzzx	yzyzxy	0	0	0
yzzxzx	0	0	yzyzxy	yzyzzx	0	0	0	0
yzzxxy	yzzxxy	yzzxxy	yzzxxy	yzzxxy	yzzxxy	yzzxxy	yzzxxy	yzzxxy
yzzxyy	0	0	yzyzzx	yzyzzx	0	0	0	0
zzzxzx	zzzxzx	0	yzyzzx	yzyzzx	0	0	0	0
zzzxyy	zzzxyy	0	yzyzzx	yzyzzx	−yzyzxy	0	0	0
zzzxyy	zzzxyy	0	yzyzxy	yzyzzx	0	0	0	0
xyxyxy	0	0	yzyzyz	yzyzyz	0	0	0	0

For symmetry C_4

$$C_4: x \to y, \quad y \to -x, \quad z \to z, \tag{3}$$

there are 16 independent nonzero coefficients (listed in column 6 of Table I):

$$C_{xxxxxx} = C_{yyyyyy}, \quad C_{xxxxyy} = C_{xxyyyy}, \quad C_{xxxxzz} = C_{yyyyzz},$$
$$C_{xxxxzx} = -C_{yyyyyz}, \quad C_{xxyyzz} = C_{xxzzyy} = -C_{xxyyyz} = 0,$$
$$C_{xxzzzz} = C_{yyzzzz}, \quad C_{xxzzzx} = -C_{yyzzyz}, \quad C_{xxyyzx} = C_{yyzzyz},$$
$$C_{xxyyzz} = -C_{yyyyzz}, \quad C_{xxzzxz} = C_{yyyyzz}, \quad C_{xxzzyy} = C_{yyyyyz}, \quad C_{xxzzzx},$$
$$C_{xxzzzx} = -C_{xxzzzy} = 0, \quad C_{xxyyzx} = C_{xxzzxz}, \quad C_{xxyyxz} = -C_{xxyyzz} = 0,$$
$$C_{xxyyxy}, \quad C_{yyyyzy} = -C_{xxzzxy}, \quad C_{yyzzxy}, \quad C_{xyzxyz} = -C_{xyzyzx} = 0. \tag{4}$$

The 24 components odd in x or in y vanish. Symmetries C_{4h}($C_4 \times i = S_4 \times i$) and S_4 are equivalent to C_4.

For symmetry C_{4v},

$$C_4: x\to y,\quad y\to -x,\quad z\to z;\quad \sigma_v: x\to y,\quad y\to x,\quad z\to z, \tag{5}$$

σ_v imposes four additional relations among the 16 coefficients (4):

$$C_{xxxxzz}=C_{yyyyzz},\quad C_{zzxxxy}=C_{zzyyxy},\quad C_{zxyxzx}=C_{yyyzyz},\quad C_{yzyzxy}=C_{xxxzzy}. \tag{6}$$

Thus, these 4 coefficients vanish (Table I). Symmetries $D_{4h}(C_{4v}\times i = D_4\times i = D_{2d}\times i)$, D_4 and D_{2d} are equivalent to C_{4v}.

For symmetry C_3,

$$C_3: x\to y,\quad y\to z,\quad z\to x, \tag{7}$$

there are 20 independent coefficients (Table I),[1] while for symmetry C_{3v},

$$C_3: x\to y,\quad y\to z,\quad z\to x;\quad \sigma_v: x\to x,\quad y\to z,\quad z\to y, \tag{8}$$

there are 14, since σ_v imposes six additional relations among the coefficients for C_3 (Table I). Symmetries $D_{3d}(C_{3v}\times i = D_3\times i)$ and D_3 are equivalent to C_{3v}.

For symmetry T,

$$C_3': x\to y,\quad y\to z,\quad z\to x;\quad C_3'': -x\to y,\quad y\to z,\quad z\to -x, \tag{9}$$

12 of the coefficients for C_3 vanish (Table I) owing to the additional relations imposed by C_3''. Symmetry $T_h = T\times i$ is equivalent to T.

For symmetry T_d,

$$C_3': x\to y,\quad y\to z,\quad z\to x;\quad C_3'': -x\to y,\quad y\to z,\quad z\to -x;\quad \sigma_d: x\to x,\quad y\to z,\quad z\to y, \tag{10}$$

only 8 of the relations imposed by C_3'' are distinct, owing to the relations imposed by σ_d: 8 of the 14 independent coefficients for C_{3v} vanish (Table I). Symmetries $O_h(T_d\times i = O\times i)$ and O are equivalent to T_d.

The writer wishes to thank Professor Bhagavantam and Mr. Hearmon for correspondence.

[1] F. Birch, Phys. Rev. **71**, 809 (1947).
[2] S. Bhagavantam and D. Suryanarayana, Nature **160**, 750 (1947), have shown group-theoretically that Birch's number of coefficients for symmetry T_d(=8) is in error; the correct number is 6, as was also confirmed by H. A. Jahn, Acta Cryst. **2**(1), 30 (1949). This result is actually obvious, even in more complete form, since symmetries T_d, O, and O_h ($T_d\times i = O\times i$) are equivalent for polar properties of even order.
[3] F. G. Fumi, Acta Cryst. (1951), to be published.
[4] After the writer had undertaken this work, he was informed by private communication that Mr. R. F. S. Hearmon, Physics Section, Forest Products Research Laboratory, England, had been applying to the third-order elastic tensor the direct method described in C. E. Love, *The Mathematical Theory of Elasticity* (Cambridge University Press, London 1927), Chapter VI.

Experimental Evidence for the Vacancy Mechanism in Diffusion in Metals and Alloys*

FOSTER C. NIX AND FRANK E. JAUMOT, JR.†
Randal Morgan Laboratory of Physics, University of Pennsylvania, Philadelphia, Pennsylvania
(Received July 25, 1951)

THERE has been much discussion among the workers in the field of metallic diffusion as to the possibility of using an alloy system such as iron-aluminum, nickel-aluminum or cobalt-aluminum, near the fifty-fifty atomic percent composition, to test the vacancy theory of diffusion, but to our knowledge only one previous report[1] on experimental work has been given. FeAl,[2] NiAl,[3] and CoAl[4] are body-centered cubic with ordered structures at room temperature, aluminum atoms going to cube corners and the ferrous atoms to cube centers. The lattice spacings at the ideal composition (50–50 atomic percent) rise to a maximum. On the cobalt-rich side of the ideal composition (to take a specific example), the cobalt replaces aluminum, atom for atom, and a fall in the lattice spacing results from the replacement of large aluminum atoms by the smaller cobalt atoms. On the aluminum-rich side the number of atoms per unit cell is less than two.[4] For the ordered structure the cube corners are filled by aluminum atoms, but there are insufficient cobalt atoms to fill up the cube centers and the vacancies are not made up by the larger aluminum atoms to that there is a contraction in the cell dimensions. These vacancies have then been considered as a possible source of information on the vacancy mechanism of diffusion. Smoluchowski and Burgess[1] have raised doubt as to the ability of these vacancies to play a role in diffusion, due to their relatively small size compared to the size of an aluminum atom, in connection with an experiment on nickel-aluminum alloys. Their experiments seemed to uphold the arguments presented there, in that no increase in the diffusion coefficient was found for compositions on the aluminum-rich side in NiAl.

The arguments raised by Smoluchowski and Burgess are only applicable to a highly ordered structure and rapidly lose validity under the experimental conditions at elevated temperatures where the actual diffusion takes place. At these temperatures there must exist a considerable degree of disorder permitting vacancy diffusion to take place, where vacancies are distributed in a random fashion over lattice sites.

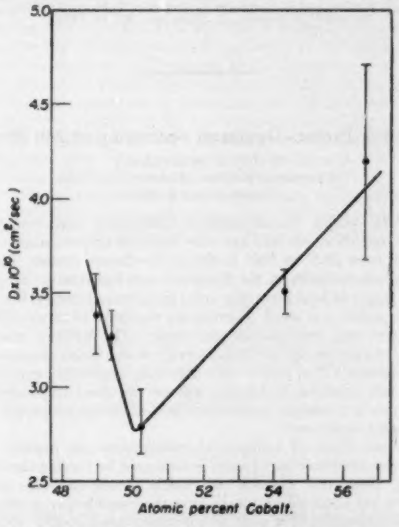

FIG. 1. Values of the diffusion coefficient of cobalt in cobalt-aluminum alloys as a function of cobalt concentration, at 1250°C.

Even though the ordered structure persists at elevated temperatures where the diffusion experiments were carried out, it seems highly unlikely, with such a large number of excess vacancies present, that they would not be of consequence in any process which took place as a result of vacancies. Even admitting that a cobalt or aluminum atom could not move into the cobalt vacancy created, as suggested by Smoluchowski and Burgess,[1] the sheer number of these vacancies would greatly increase the probability of a vacancy being adjacent to a normal lattice defect (e.g. a cobalt atom on a cube corner) or to a vacancy due to thermal excitation, and thus increase the mobility of the vacancies and consequently increase the diffusion coefficient.

We have investigated the diffusion of cobalt into five compositions of cobalt-aluminum alloys near the ideal composition, using radioactive Co^{60} as the diffusing atom. The experimental technique used was similar to that employed in our work on self-diffusion in cobalt.[5] The diffusion was carried out at three temperatures, 1050°C, 1150°C, and 1250°C. The preliminary results

at all temperatures show a minimum in the diffusion coefficient at the ideal composition and a definite increase on the aluminum-rich side. Figure 1 shows this for diffusion at 1250°C, with the data spread indicated. The diffusion of cobalt in samples of the same composition at different temperatures follow the usual law

$$D = Ae^{-Q/RT},$$

thus allowing us to calculate the activation energies for the process at the various compositions of the alloy. The activation energy, as expected, drops off sharply on the vacancy-rich side of CoAl.

These preliminary results have large possible errors and do not determine the exact form of the curve of D as a function of composition. Consequently, the experiment is being continued using a greater number of compositions of the alloy and with emphasis on reducing the many possible errors involved.

* This work was supported by the ONR.
† This discussion is part of a dissertation by Frank E. Jaumot, Jr. presented to the Faculty of the Graduate School of the University of Pennsylvania in partial fulfillment of the requirements for the Ph.D. degree.
[1] R. Smoluchowski and H. Burgess, Phys. Rev. **76**, 309 (1949).
[2] A. J. Bradley and A. H. Jay, Proc. Roy. Soc. (London) **136**, 210 (1932).
[3] A. J. Bradley and A. Taylor, Proc. Roy. Soc. (London) **159**, 56 (1937).
[4] A. J. Bradley and G. C. Seager, J. Inst. Metals **64**, 81 (1939).
[5] F. C. Nix and F. E. Jaumot, Jr., Phys. Rev. **82**, 72 (1951).

Elastic Proton-Deuteron Scattering at 240 Mev*

ROBERT D. SCHAMBERGER
University of Rochester, Rochester, New York
(Received July 9, 1951)

THE elastic proton-deuteron differential scattering cross section at 240 Mev has been measured for proton-scattering angles from 20.5° to 100° in the center-of-mass system. The internal proton beam of the Rochester synchrocyclotron strikes a thin target of heavy paraffin and coincidences between the scattered proton and recoil deuteron are observed using scintillation counters and conventional electronics. The incident beam is determined from the C^{11} beta-activity of the target produced by the reaction $C^{12}(p, pn)C^{11}$. The scattering apparatus, electronics, and beta-counting techniques will be described in detail in a paper to be published on proton-proton scattering performed with the same equipment.[1]

Several types of background coincidences are present. The chance coincidence background is measured by moving the target away from the position at which proton-deuteron coincidences are observed and measuring the coincidences at different beam intensities. The part which varies quadratically with the beam intensity, as monitored by the singles counts in either counter, is ascribed to chance. The linear term is due to events in the carbon in which two charged particles are emitted and reach the counters. For all of the measurements except that at 100° there was a background from inelastic proton-deuteron scattering. Only that portion of the inelastic process which results in a low energy neutron and two protons with approximately the same energy and angular relationship as in proton-proton scattering is observed. For small scattering angles proton-proton scattering from the hydrogen impurity in the target was an additional background. Scattering at 75° and 79° was observed at the same target position. It was not possible to completely separate the two effects. The cross sections at these two angles were obtained by splitting the total number of coincidences in such a way that the center-of-mass cross sections do not differ greatly.

The experimental values of the cross section are given in Fig. 1. The errors indicated at 20.5°, 31°, 42°, 54°, and 100° are the standard deviation in the coincidences. The error on the other points has been increased because of uncertainties in the background. The error in the calibration of the beta-counter is 5 percent. A value of 49 millibarns has been used for the $C^{12}(p, pn)C^{11}$ cross section.[2] The proton-proton scattering cross section at 90° in the center-of-mass system measured with the same apparatus is 4.9 millibarns.

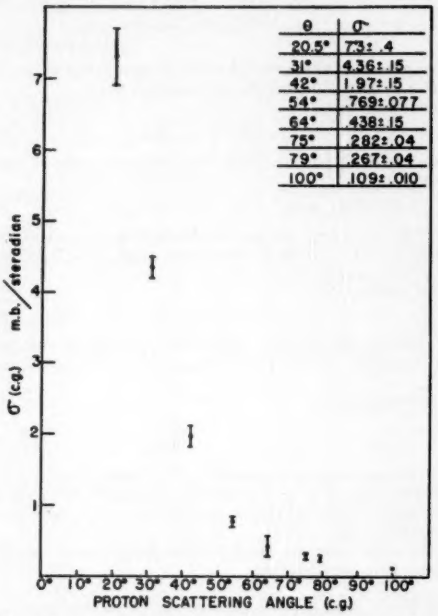

FIG. 1. Elastic proton-deuteron scattering cross section at 240 Mev.

Mr. T. Auerbach, of this laboratory, has calculated the cross section in the Born approximation[3] with the Serber mixture for the neutron-proton interaction and the three proton-proton interactions used by Gluckstern and Bethe.[4] The results of Auerbach's calculation and the experimentally determined cross sections are summarized in Table I. The experimental cross sections do not agree with any of these calculations, which is not surprising since the assumed forces do not explain the observed proton-proton scattering. Further theoretical calculations are clearly necessary.

TABLE I. Theoretical and experimental differential scattering cross sections.

Proton scatt. angle in c.m. system	Theoretical cross section, cm²/sterad			Experimental cross section cm²/sterad
	Direct	Pure exchange	Serber	
20.5°	21×10^{-27}	6.0×10^{-27}	13×10^{-27}	$7.3\pm0.4\times10^{-27}$
31°	6.8	1.82	3.9	4.36±0.15
42°	1.95	0.55	1.06	1.97±0.15
54°	0.55	0.145	0.30	0.769±0.77
64°	0.24	0.052	0.112	0.44±0.15
75°	0.104	0.016	0.026	0.28±0.04
79°	0.083	0.010	0.017	0.27±0.04
100°	0.040	0.001	0.014	0.109±0.010

Some data have been obtained on the inelastic scattering mentioned above. These data will be published later with a more detailed discussion of the elastic scattering.

The author is indebted to Professor C. L. Oxley for his generous assistance on many phases of this investigation.

* Assisted by the joint program of the ONR and the AEC.
[1] C. L. Oxley and R. D. Schamberger (to be published).
[2] Aamodt, Peterson, and Phillips, UCRL-526 (1949) (unpublished).
[3] G. F. Chew, Phys. Rev. **74**, 809 (1948).
[4] R. L. Gluckstern and H. A. Bethe, Phys. Rev. **81**, 761 (1951).

Small-Angle Scattering of 3.27-Mev Neutrons by Deuterons

I. Hamouda and G. de Montmollin
Physikalisches Institut der Eidgenössischen Technischen Hochschule, Zürich, Switzerland
(Received July 24, 1951)

THEORETICALLY calculated angular distributions of neutrons elastically scattered by deuterons show a marked dependence on the assumed type of forces between two nucleons.[1-4] In view of the experimental difficulties in determining the angular distribution, there are discrepancies among the various data obtained by different experimenters.[5-7] However, for neutrons of a few Mev, the data show, in common, a strong maximum of the distribution at $\theta=180°$, a minimum around 90°, and a tendency to form another maximum at 0°, where $\theta=$ the neutron-scattering angle in the c.m. system. Although the shape of the distribution at small scattering angles seems very important for the comparison with the theory, the experimental data were, to our knowledge, not extended far enough into this region to allow for reliable extrapolation of the value of the differential cross section at 0°, nor to show whether the pronounced maximum of the distribution lies at 0° or at 180°.

In an earlier published experiment[7] we measured the angular distribution of 3.27-Mev $(d, \bar{d})$-neutrons scattered by deuterons in a cloud chamber. The investigation covered the range of $\theta=50°$–180°, and the distribution was then extrapolated for smaller scattering angles. However, it seemed desirable to extend the measurements as low as possible beyond 50° in order to obtain the shape of the distribution in this region.

With the same experimental procedure used in the former experiment, we studied the angular distributions of the neutron-proton as well as the neutron-deuteron scattering. In this case, the incident neutron beam was made to penetrate perpendicularly into the cloud chamber through its upper glass cover. This arrangement was chosen to facilitate the photographing and measuring of recoil tracks projected at large angles from the neutron beam. Four thousand proton recoils and four thousand deuteron recoils lying in the angular range between 18° and 70° have been photographed and measured. The angular distribution of the neutron-proton scattering was found to be isotropic throughout the investigated angular range, which suggested the reliability of the measurements in the case of the neutron-deuteron scattering. In Fig. 1, we have plotted the intensity of scattered neutrons *versus* angle of scattering in the c.m. system. The curves represent the data of the two experiments which were made to join at about 60° and so represent the angular distributions throughout the range from 18° to 180°.

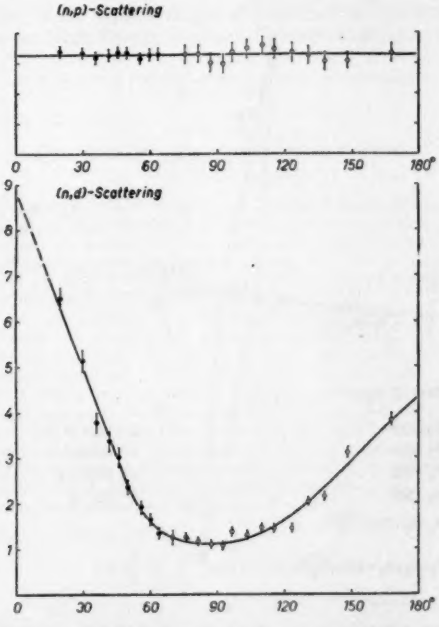

FIG. 1. Intensity of scattered neutrons *versus* angle of scattering in c.m. system. The open circles represent the data of the former experiment; the closed circles represent the data of the present experiment.

Our data were extended far enough into the region of small scattering angles, and they show clearly that more neutrons are scattered forward than backward. This distribution with its pronounced maximum at 0° does not agree qualitatively with either of the two theoretical distributions at 2.5 Mev calculated by Massey and Buckingham.[2] The disagreement is more marked in the case of the exchange force distribution, especially as Buckingham[8] points out that a refinement of the exchange force theory (by taking into account the contribution of d-angular momentum state) tends to enhance backward scattering at the expense of forward scattering of the neutrons. Verde[3] has given numerical calculations of the angular distributions at 20 Mev, and he states generally that a pronounced maximum at 0° disagrees with the "characteristic feature" of the symmetrical theories. We believe that it is rather early to draw theoretical conclusions from the experimental data because the spin-orbit coupling is not taken into consideration in any theory of this process.

We wish to express our sincerest gratitude to Professor P. Scherrer for his continuous encouragement and valuable advise.

The detailed experiment will be published in *Helvetica Physica Acta*.

[1] R. A. Buckingham and H. S. Massey, Proc. Roy. Soc. (London) **A179**, 123 (1941).
[2] H. S. Massey and R. A. Buckingham, Phys. Rev. **71**, 558 (1947).
[3] M. Verde, Helv. Phys. Acta **22**, 339 (1949).
[4] A. Troesch and M. Verde, Helv. Phys. Acta **24**, 39 (1951).
[5] J. H. Coon and H. H. Barschall, Phys. Rev. **70**, 592 (1946).
[6] J. F. Darby and J. B. Swan, Australian J. Sci. Research **A1**, 18 (1948).
[7] Hamouda, Halter, and Scherrer, Phys. Rev. **79**, 539 (1950); Helv. Phys. Acta **24**, 217 (1951).
[8] Martin, Burhop, Alcock, and Boyd, Proc. Phys. Soc. (London) **63A**, 884 (1950). (See note added by Buckingham.)

On the Nuclear Scattering of Negative Pi-Mesons*

G. Bernardini, E. T. Booth, and L. Lederman
Columbia University, New York, New York
(Received July 20, 1951)

THE analysis of the interactions of artificially produced pi-mesons of well-known energy has yielded direct evidence of the anticipated nuclear scattering. Although the number of scatterings detected and studied in detail is not very large, evidence collected to date eliminates any doubt as to the real existence of some rather peculiar features of these meson-nuclear phenomena.[1] These features are (1) the relatively high probability for very large angle scatterings, (2) the existence of inelastic scatterings with exceedingly large energy losses, (3) the dependence of these peculiar scatterings on the incident meson's energy.[2]

These conclusions are based on the results of combined plural scattering and grain density measurements made upon tracks of incident and scattered particles in Ilford G5 plates. Figure 1 illustrates a typical plot of these measurements. This figure represents the inelastic scatterings ($\Delta E/E>0.15$) suffered by mesons of 70–110 Mev. The energy values were deduced from the Snyder and Scott formula,[3] recently checked very satisfactorily by Bramson and Havens.[4] The precision of the measurements depends on

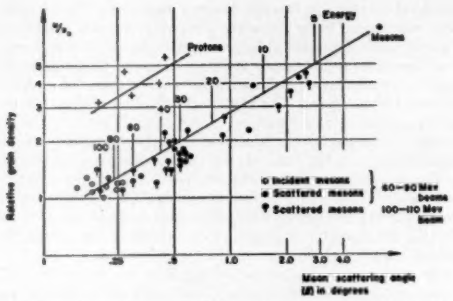

FIG. 1. Grain density vs multiple scattering angle of π^--mesons incident and scatttered in Ilford G5 emulsion. The noise level is included. Angles are measured by successive chords.

E_2 and the lengths of the tracks. All cases in which the measure of $\langle q \rangle$ would have a statistical error greater than 20 percent were considered as doubtful and not plotted.

The frequency and angular distribution of all measured scatterings at various incident energies are given in Fig. 2. To render the contribution of coulomb and shadow scatterings negligible, the elastic scatterings are plotted only for angles $>30°$. Shrinkage effects limit the precision of space angles in the emulsion to $\pm 5°$. As a check on the scanning efficiency, all the elastic scatterings $>10°$ for mesons of 30–50 Mev, and scatterings $>5°$ for mesons of 70–110 Mev were also considered. The results were very consistent with the numbers expected from the Rutherford law and the composition of the emulsion supplied by the manufacturer.

Figures 1 and 2 form the basis of the conclusions stated above. Some remarks remain to be added. The large angle events are rather frequent both in the inelastic and in the elastic scatterings, and we believe that they are correlated with some unknown process occurring in the interaction of pi-mesons with nuclear matter. Cloud-chamber experiments[5] now in progress indicate that a similar effect takes place in carbon; and, thus, the backscattering appears to be independent of nuclear size.

The frequency of strongly inelastic scatterings, $\Delta E = E_2 - E_1 > E_1/2$ Mev, has already been shown[6] to cast doubt upon a model based on single elastic pi-nucleon collisions in nuclear matter. The possibility of multiple elastic collisions inside the nucleus can probably also be ruled out by the results of Chedester *et al.*,[7] which give a very small cross section for pi-proton scattering. An alternative model is suggested to us by the grouping of the E_2's (Fig. 1) independently of incident energy and by the strong energy dependence of these scatterings. The mesons apparently are capable of raising nuclear matter to some excited state in a sort of mesic Raman effect. This means that in complex nuclei, the

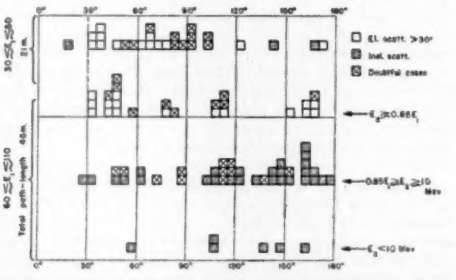

FIG. 2. Angular distribution of elastic and inelastic scatterings of π^- at various incident energies.

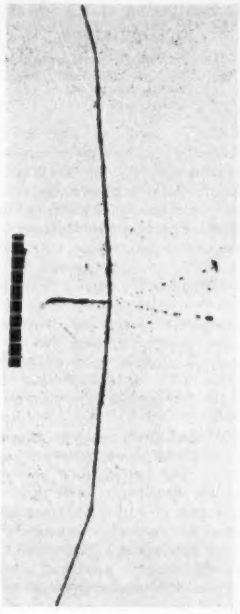

(a)

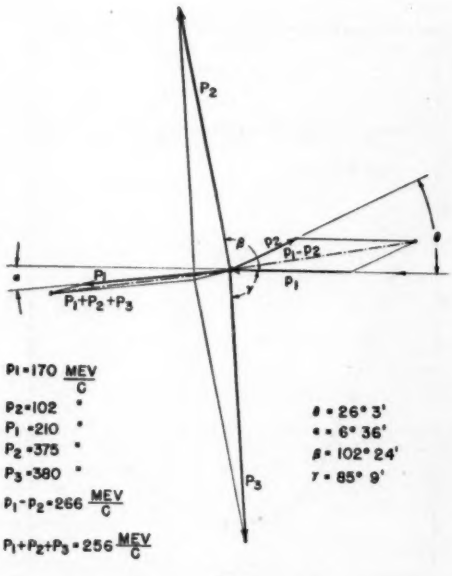

(b)

FIG. 3. Inelastic scattering of an 82-Mev π^- on a C^{12} nucleus (observed by Mrs. E. Wimmer). Each division of the scale in Fig. 3(a) is equivalent to 5 microns. Figure 3(a) is a photomicrograph of the event. Figure 3(b) is the corresponding momentum diagram.

scattering as well as the absorption is a many-body process. This probably naive picture of the nuclear scatterings is, to some extent, supported by some particular cases which are especially difficult to reconcile with a single pi-nucleon encounter. One of these cases is shown in Fig. 3(a). A meson of $E_1=82\pm5$ Mev (track length 2400μ) is scattered through 157°. The scattered meson (track length 8400μ) energy $E_2=33\pm3$ Mev. At the vertex, the three heavy prongs all end in the emulsion and have ranges, $R_1=21\mu$, $R_2=138\mu$, $R_3=145\mu$. If these are assumed to be 3 α-particles, the reaction would be $\pi_1^-+{}_6C^{12}\rightarrow3\alpha+\pi_2^-$. The α's are practically coplanar. The energy balance is

$$Q=(82-33)-(6+18.5+19)=5.5\pm6 \text{ Mev},$$

and the Q of the process ${}_6C^{12}\rightarrow3\alpha$ is 7.2 Mev. Figure 3(b) illustrates the consistency of the momentum balance. In another case, the meson has $E_1=73\pm10$ Mev, and the scattered meson, $E_2=2.2\pm0.2$ Mev. At the vertex, a proton track is found to have an energy $E_p=80\pm10$ Mev. No correlation of momenta is observed. These and other similar cases give us the impression that it will be difficult to explain the scattering of mesons and its energy dependence with any simple model based on the known properties of nuclei and conventional meson-nucleon interactions.

* This research was jointly supported by the ONR and AEC.

[1] G. Bernardini, Phys. Rev. **82**, 313 (1951).
[2] Bernardini, Booth, and Lederman, Phys. Rev. **83**, 1075 (1951).
[3] Snyder and Scott, Phys. Rev. **76**, 220 (1949); Corson, Phys. Rev. **80**, 303 (1950); Voyvodic and Pickup, Phys. Rev. **81**, 471 (1951).
[4] H. Bramson and W. W. Havens, Jr., Phys. Rev. **83**, 361 (1951).
[5] Byfield, Kessler, and Lederman, private communication.
[6] Bernardini, Booth, Lederman, and Tinlot, International Conference on Elementary Particles, Bombay, December, 1950; M. H. Johnson, Phys. Rev. **83**, 510 (1951).
[7] Chedester, Isaacs, Sacks, and Steinberger, Phys. Rev. **82**, 959 (1951).

The Mean Square Angle of Emission of Nucleons in High Energy Nucleon-Nucleus Collisions

H. MESSEL,
School of Theoretical Physics, Dublin Institute for Advanced Studies, Dublin, Ireland
AND
H. S. GREEN,
Department of Mathematical Physics, University of Adelaide, Adelaide, Australia
(Received July 30, 1951)

IN previous work[1,2] we consider the problem of finding the mean square angle of emission of nucleons in high energy nucleon-nucleon collisions. In the present case we are concerned with obtaining the mean square angle of emission of nucleons resulting from a collision of a high energy nucleon with a nucleus using the results obtained in references 1 and 2.

Let $n(U, C, z)dUdC$ be the probability of finding a nucleon at a depth z in homogeneous nuclear matter with energy in the interval U, $U+dU$ and making an angle with the downward vertical whose cosine lies in the interval C, $C+dC$. Further, let $W(U, c)dUdc$ be the probability of finding a nucleon with energy in the interval U, $U+dU$ and scattered at an angle whose cosine lies in the interval c, $c+dc$. Denote by ω the angle between the plane containing the vertical and the direction of motion of a scattered nucleon and the plane passing through the directions of motion of both the incident and scattered nucleons.

The fundamental equation for $n(U, C, z)$ is

$$C[\partial n(U, C, z)/\partial z]+n(U, C, z)$$
$$=2\int_U^\infty\int_{c_0}^1\int_0^{2\pi} n(U', Cc+Ss\cos\omega, z) \times W(U, U', c)dU'dcd\omega/2\pi, \quad (1)$$

where

$$S=(1-C^2)^{\frac{1}{2}} \text{ and } s=(1-c^2)^{\frac{1}{2}}.$$

The mean square angle of scatter of nucleons at a depth z in homogeneous nuclear matter is given by

$$\langle\theta^2(U_0, U, z)\rangle=\left\{\int_{-1}^1 n(U, \cos\theta, z)\sin^2\theta d(\cos\theta)\right\} \times\left\{\int_{-1}^1 n(U, \cos\theta, z)d(\cos\theta)\right\}^{-1}. \quad (2)$$

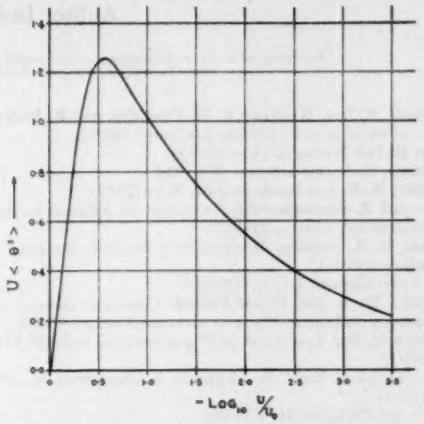

FIG. 1. A plot of $U\langle\theta^2(U_0, U)\rangle$ against the logarithm of the ratio of the energy U above which particles are emitted from a nucleus, to the primary energy U_0. The energies are measured in proton mass units. $\langle\theta^2(U_0, U)\rangle$ gives the mean square angle of emission in radians squared of nucleons resulting from a nucleon-nucleus collision. The curve is valid for nitrogen and oxygen nuclei.

Using the solution we have found for Eq. (1) and assuming that the nuclei are spherical in shape, we can show that the mean square angle of emission of nucleons with energies greater than U, resulting from a nucleon-nucleus collision is equal to

$$\langle\theta^2(U_0, U)\rangle=I_1/I_2, \quad (3)$$

where

$$I_1=\frac{1}{2\pi i}\frac{1}{2U}\int_{s_0-i\infty}^{s_0+i\infty}\left(\frac{U}{U_0}\right)^{-s}\left\{\frac{2-\alpha(s)-\alpha(s+1)}{\alpha(s)}\right\}f[D_A\alpha(s)]\frac{ds}{s+1} \quad (4)$$

and

$$I_2=\frac{1}{2\pi i}\int_{s_0-i\infty}^{s_0+i\infty}\left(\frac{U}{U_0}\right)^{-s}\frac{1-f[D_A\alpha(s)]}{s}ds. \quad (5)$$

Both the primary energy U_0 and the secondary energy U are measured in proton mass units. In the above expressions

$$f(x)=1-2[1-(1+x)e^{-x}]/x^2, \quad (6)$$
$$\alpha(s)=1-240[(s+2)(s+3)(s+4)(s+5)]^{-1}, \quad (7)$$

and D_A is the average number of collisions suffered by a primary nucleon in making a diametrical passage through a nucleus whose atomic weight is A.

The result of a calculation for light nuclei using Eq. (3) (D_A was taken equal to 3·7 and hence should be valid for nitrogen and oxygen nuclei) is given in Fig. 1. The apparent approach to zero in the limit $U\rightarrow U_0$ may be fallacious, since the method for evaluating the integrals becomes precarious for $U/U_0>\frac{1}{2}$, i.e., to the left of the maximum. However, this region has little physical significance.

These results ought to enable us to estimate the energy of the primary nucleon from a statistic of the angles of secondary nucleons in high energy photographic plate stars.

We shall present the details of the above work and a comparison with experiments in a subsequent publication. Results will also be presented for the heavy nuclei, silver and bromine.

We are indebted to Professor E. Schrödinger for many stimulating discussions throughout the course of the above work.

[1] H. S. Green and H. Messel, Phys. Rev. **83**, 842 (1951).
[2] H. S. Green and H. Messel, Proc. Phys. Soc. (London), to be published.

Author Index to Volume 83

References with (A) are to abstracts of papers presented at meetings of the American Physical Society, and those with (T) designate title only. References with (L) are to Letters to the Editor.

Aamodt, R. Lee, Wolfgang K. H. Panofsky, and R. Phillips. π^- absorption in D_2 and the *n-n* force—1057(L)
Abe, H. (see Kumagai, H.)—1077(L)
Accardo, C. A. (see Lehovec, K.)—603
Achter, M. R. (see Smoluchowski, R.)—219(A)
—— **and R. Smoluchowski.** Anisotropy of diffusion in grain boundaries—163(L), 219(A)
Adair, R. K. Angular distribution of neutrons scattered by helium—873(A)
—— (see Koester, L. J.)—1250(L)
Adams, W. R. and Ernest Pollard. Combined thermal and primary ionization effects on a bacterial virus—230(A)
Ajzenberg, Fay. Low states of F^{17} and neutrons from $O^{16}+D$—693(L)
—— Neutrons from the deuteron bombardment of O^{16}—875(A)
—— (see Richards, H. T.)—994
Alburger, David E. Gamma-ray transitions in B^{10}—184(L)
Alcock, N. Z. and D. G. Hurst. Neutron diffraction by the gases N_2, CF_4, and CH_4—1100
Alden, E. D. (see Koller, L. R.)—684(L)
Alder, K. Note on the theory of directional correlation—1266(L)
Alexander, James D. and Griffin Carmichael. Calculations on distributions of lattice vibration frequencies—488(A)
Alford, William L. (see Leighton, R. B.)—843(L)
Alford, W. P. (see Hamilton, Donald R.)—215(A)
Allen, A. J. (see Neiler, John H.)—242(A)
Allen, Clayton H. Upper limit for sound pressure in a spherically diverging field—193(A)
Allen, J. S. (see Rodeback, G. W.)—215(A)
Allen, K. W. (see Almqvist, E.)—202(A)
Allen, William A., John S. Rinehart, and W. C. White. Phenomena associated with the flight of ultra-speed pellets. Part I: Ballistics—889(A)
—— (see Rinehart, John S.)—890(A)
—— (see White, W. C.)—889(A)
Allred, J. C., D. D. Phillips, and Louis Rosen. Erratum: Angular distribution of protons from the $D(d,p)T$ reaction at 10.3-Mev bombarding energy—1077(L)
—— (see Armstrong, A. H.)—218(A)
Almqvist, E., K. W. Allen, J. T. Dewan, and T. P. Pepper. He^4+T reactions—202(A)
Alpher, R. A. and R. C. Herman. Formation of the elements in the expanding universe—236(T)
Althaus, Edward J. Two unstable *V* mesons observed in a cloud chamber at sea level—896(A)
Amble, E. Structure and dipolmoment of trioxane—210(A)
Ampariotis, P. A. (see Petropoulos, G. M.)—658(L)
Anderson, A. B. C. and H. W. Wedaa. Sources of energy degradation and side thrust in Laval rocket nozzles—890(A)
Anderson, C. D. (see Leighton, R. B.)—896(A)
Anderson, H. L. and John Marshall. 170-inch synchrocyclotron at the University of Chicago—232(A)
Anderson, James L. and Peter G. Bergmann. Constraints in covariant field theories—1018
Anderson, P. W. Limits on the energy of the antiferromagnetic ground state—1260(L)
Anderson, Roy S., Charles M. Johnson, and Walter Gordy. Resonant absorption of oxygen at 2.5 millimeter wavelength—1061(L)
Anslow, Gladys A. and Helen H. Fife. Effects of aging and cooling on the ultraviolet spectra of alcohols—192(A)
Anthony, R. L. (see Forster, M. J.)—204(A)
Anthony, Romuald. Atmospheric absorption of solar infrared radiation—888(A)
Apker, L. (see Taft, E.)—479(L)
Appleyard, R. K. Behavior of hemoglobin under irradiation—231(A)
Arfken, G. B. (see Biedenharn, L. C.)—586, 683(L)
—— **and L. C. Biedenharn.** Note on angular distribution of gamma-radiation from 16-Mev C^{12*}—238(A)
Armstrong, A. H., J. C. Allred, R. O. Bondelid, and L. Rosen. Scattering of 9.7-Mev protons by deuterons—218(A)
Arnold, J. T. (see Packard, M. E.)—210(A)
Ashburn, Edward V. and Dorothy Davis Locanthi. On the (O I) airglow in the night sky—888(A)
Ashkin, A. (see DeWire, J. W.)—505
Astin, A. V. Current research programme of the National Bureau of Standards—221(T)
Austern, Norman. Mechanism of nD capture—672(L)
Averbach, B. L. (see Flinn, P. A.)—1070(L)
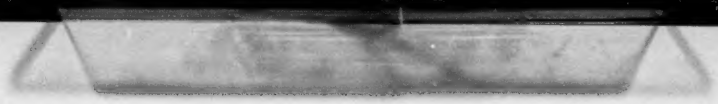
Bailey, V. A. Relativistic theory of electro-magneto-ionic waves—439
Bair, Joe Keagy (see Maienschein, Fred C.)—477(L)
Baker, William B. (see Maienschein, Fred C.)—477(L)
Balasubrahmanyam, V. K. (see Rao, A. S.)—173(L)
Baldock, Russell and John R. Sites. Mass spectrometer studies of the dissociation of some metal carbonyls—488(A)
—— (see Sites, John R.)—488(A)
Baldwin, Ewart M. Neutron-proton scattering in the energy range of 18 to 21 Mev—495
Baldwin, George. Nuclear research with x-rays up to 100 Mev—870(T)
Ball, W. P. (see Richardson, R. E.)—859(L)
Ballario, C., B. Brunnelli, A. De Marco, and G. Martelli. On the diurnal variation of extensive air shows of high density at 3500 m above sea level—666(L)
Baltensperger, Walter. Contribution to the theory of impurity centers in silicon—1055(L)
Band, William. Exclusion principle and the theory of superconductivity—885(A)
Bardeen, J. (see Hall, Harry H.)—879(A)
Barile, Sam. Study of x-ray induced optical absorption bands in CaF_2—227(A)
—— (see Groetzinger, Gerhart)—227(A)
Barkas, Walter H. Meson masses and the energetics of meson decay—236(T)
—— (see Birnbaum, Wallace)—895(A)
Baroody, E. M. Application of Wooldridge's theory of secondary emission—857(L)
Barr, E. Scott and Lugene G. Hungerford. Infrared absorption spectra of some citrus oils—486(A)
Barredo, J. G. Concept of active surface—243(A)
Barrett, Paul H. Absorption of extensive showers by water—896(A)
Barschall, H. H. (see Bockelman, C. K.)—873(A)
Bartholomew, G. A. (see Kinsey, B. B.)—234(A), 519
Beach, L. A. (see DeWire, J. W.)—233(A), 476(L), 505
Basri, S. (see Messiah, A. M. L.)—652(L)
Bay, Z. Differential coincidence counting method—242(A)
Beams, J. W. (see Ross, J. D.)—242(A)
Beard, D. B. and H. A. Bethe. Field corrections to neutron-proton scattering in the new mixed meson theory—1106
Bearden, J. A. and H. M. Watts. Erratum: A re-evaluation of the fundamental atomic constants—457(L)
Beattie, J. W. (see Laughlin, J. S.)—231(A), 692(L)